

Alma Mater Studiorum - Università di Bologna

DOTTORATO DI RICERCA IN
CHIMICA

Ciclo 34

Settore Concorsuale: 03/A1 - CHIMICA ANALITICA

Settore Scientifico Disciplinare: CHIM/12 - CHIMICA DELL'AMBIENTE E DEI BENI CULTURALI

INNOVATIVE METHODS FOR PHYSICOCHEMICAL AND DYNAMIC
CHARACTERIZATION OF AMBIENT AEROSOLS AND OTHER
ENVIRONMENTAL SYSTEMS

Presentata da: Pietro Morozzi

Coordinatore Dottorato

Domenica Tonelli

Supervisore

Laura Tositti

Esame finale anno 2022

Index

Abstract.....	1
Riassunto.....	3
CHAPTER 1 - General Introduction	5
1.1 – Foreword	5
1.2 – Atmospheric Aerosols	7
1.2.1 – Morphology and dimension.....	8
1.2.2 – Origin and formation	12
1.2.3 – Aerosol environmental fate	14
1.2.4 – Emission sources	16
1.2.5 – Chemistry	20
1.2.6 – Effects on the earth system, climate, and human health.....	25
1.3 – Published scientific articles and work in progress	30
References	36
CHAPTER 2 - Particulate matter emission sources and meteorological parameters combine to shape the airborne bacteria communities in the Ligurian coast, Italy	41
Abstract	41
1 – Introduction	42
2 – Results	43
2.1 – Particulate matter emission sources and atmospheric parameters.....	43
2.2 – AM overall composition.....	45
2.3 - Variation of the AM topological structure and association with PM emission sources and meteorological parameters	46
2.4 - Compositional specificity and prevalent microbiological source of the four AM clusters.....	48
3 – Discussion	49
4 – Materials and methods	51
4.1 – Site description	51
4.2 – Sample collection and atmospheric parameters	52
4.3 – Chemical characterisation of the samples	53
4.4 – Positive Matrix Factorization analysis	53
4.5 – Microbial DNA extraction, 16S rRNA gene amplification and sequencing.....	53
4.6 – Bioinformatics and statistics.....	54
5 – Data availability	55
Supplementary Information (only available online)	55
Acknowledgements	55
Author contributions	55
Competing Interests	55
References	55

CHAPTER 3 - Ultraviolet–Visible Diffuse Reflectance Spectroscopy (UV–Vis DRS), a rapid and non-destructive analytical tool for the identification of Saharan dust events in particulate matter filters	61
Highlights	61
Abstract	61
1 – Introduction	62
2 – Materials and methods	64
2.1 - Particulate matter samples.....	65
2.2 - The UV–Vis DRS methodology	65
2.3 - Validation of the methodology.....	68
3 – Results and Discussion.....	70
3.1 - Colorimetric data and results	70
3.2 - Iron oxide minerals	72
3.3 - Validation of UV–Vis DRS results	75
3.4 - Diagnosis and validation of Saharan mineral dust.....	77
Conclusions	81
CRediT authorship contribution statement	82
Acknowledgements	82
References	82
CHAPTER 4 - Chemiluminescent fingerprints from airborne particulate matter: A luminol-based assay for the characterization of oxidative potential with kinetical implications	89
Highlights	89
Abstract	90
1 – Introduction	90
2 – Materials and Methods	92
2.1 –Particulate matter and certified PM reference materials samples	92
2.2 – Chemical speciation and source apportionment of PM ₁₀	94
2.3 – Chemiluminescent assay	94
2.4 –Chemometrics.....	95
3 – Results and discussion.....	95
3.1 – The chemiluminescent assay: Analysis of the chemiluminescence profile	95
3.2 – Chemometric analyses.....	97
3.3 – Source apportionment of the PM samples.....	99
3.4 – Spearman correlation analysis	101
4 – Conclusions	102
Funding	103
CRediT authorship contribution statement	103
Acknowledgements	104
References	104
CHAPTER 5 - How to Get the Best from Low-Cost Particulate Matter Sensors: Guidelines and Practical Recommendations	109
Abstract	109
1 – Introduction	109

2 – Materials and Methods	112
2.1 Instrumentation	112
2.2 Number Concentration to Mass Conversion	114
2.3 Sensor Performance Metrics	115
3 – Results and Discussion	115
3.1 Particle Mass Concentrations	116
3.2 Particle Number Densities and Particle Size Distributions	129
4 – Conclusions	133
Funding	134
Acknowledgements	134
Conflicts of Interest	134
Appendices	135
References	135

CHAPTER 6 - Development and evolution of an anomalous Asian dust event across Europe in March 2020

Abstract	140
1 – Introduction	141
2 – Materials and methods	143
2.1 – Sampling sites	143
2.2 - Synoptic-scale conditions	143
2.3 - Optical Aerosol Counters (OPCs)	144
2.4 - Particulate matter concentrations and chemical speciation data	146
2.5 - AERONET (AErosol RObotic NETwork)	146
2.6 - LIDAR Ceilometer	147
3 – Results and discussions	147
3.1 – Synoptic analysis	147
3.2 – Optical Aerosol Counters (OPCs)	151
3.3 – Ancillary analyses	155
4 – Conclusions	158
Data availability	159
Author contributions	159
Competing interests	160
Acknowledgments	160
Financial support	160
Appendix	160
References	160

CHAPTER 7 - ATR-FTIR Spectroscopy, a New Non-Destructive Approach for the Quantitative Determination of Biogenic Silica in Marine Sediments

Abstract	167
1 – Introduction	168
2 – Results and Discussion	170
2.1 ATR Spectra	170
2.2 Results: Procedure 1	172

2.3 Results: Procedure 2	173
3 – Materials and Methods	174
3.1 Study Area	174
3.2 Samples.....	175
3.3 ATR-FTIR Analysis	176
3.4 Chemometrics.....	177
4 – Conclusions	178
Author Contributions	179
Funding	179
Acknowledgements	179
Conflicts of Interest.....	180
References	180
CHAPTER 8 - Deposition processes over complex topographies: Experimental data meets atmospheric modeling.....	183
Highlights.....	183
Abstract	184
1 – Introduction	184
2 –Materials and methods	187
2.1 Site description and sample collection	187
2.2 Analytical methods.....	189
2.3 Statistical methods and elaboration tools	190
3 –Results and discussion.....	192
3.1 Atmospheric radionuclides and depositional patterns.....	192
3.2 Sampling stations and their association with atmospheric radiotracers ...	195
3.3 Organic compounds.....	198
3.4 Pollutant dispersion in the Terni basin valley: CALPUFF modeling.....	199
4 –Conclusions	202
CRedit authorship contribution statement	203
Declaration of competing interest	203
Acknowledgements	203
Appendix A. Supplementary data	203
References	204
CHAPTER 9 - Chemical characterization of drip and river waters in the Pertosa Auletta cave (SA, Italy).....	209
1 – Introduction	209
2 – Materials and methods	212
2.1 – Pertosa-Auletta cave.....	212
2.2 – Sampling and chemical characterization	214
2.3 – Classification and factor analysis	216
3 – Results and discussions	217
3.1 – Non-Negative Matrix Factorization (NMF)	217
3.2 – Boxplots and Analysis of variance (ANOVA).....	219
4 – Conclusions	222

References	222
CHAPTER 10 - Radioactivity measurements of innovative and sustainable building materials: Geopolymers	224
1 – Introduction	224
2 – Materials and methods	224
2.1 – Geopolymers and their precursors	224
2.2 – High-Resolution Gamma-Ray Spectroscopy	226
2.3 – Data processing	227
3 – Results and discussions	228
3.1 – Principal Component Analysis (PCA).....	228
3.2 – Radionuclide Boxplots	229
3.3 – Dosimetric indices	232
4 – Conclusions	233
References	233
CHAPTER 11 - Applications of non-destructive spectroscopic techniques and multivariate statistics for the analysis of Spanish atmospheric aerosol collected on membranes	235
1 – Introduction	235
2 – Materials and methods	236
2.1 – Sampling sites.....	236
2.2 – Traditional chemical speciation and source apportionment of PM ₁₀	237
2.3 – Fourier transform InfraRed (FT-IR) analysis	237
2.4 - Ultraviolet–Visible Diffuse Reflectance Spectroscopy (UV–Vis DRS) analysis	240
3 – Results and discussions	241
3.1 – PMF on traditional chemical data.....	241
3.2 – IR results.....	243
3.3 – UV-Vis DRS results	245
3.4 – Validation of non-destructive spectroscopic techniques results.....	248
4 – Conclusions	251
References	251
General Conclusions	254

Abstract

The present Thesis reports the main scientific achievements in my PhD research activity based on the application of multivariate statistical methods for Environmental Chemistry (academic discipline: CHIM/12) and, in particular, in the treatment of atmospheric aerosols data. During the three-year PhD period, I have faced several topics which have led to the publication of eight scientific articles including three as the first author. My publications can be conceptually grouped into three distinct parts:

- 1) Design and optimization of innovative experimental methodologies for the analysis of Airborne Particulate Matter (PM) and data interpretation, as related to human health, air quality, and climate change.
- 2) Definition of practical guidelines and optimal use of PM low-cost sensors based on the Optical Particle Counting (OPC) developed on laser scattering devices.
- 3) Analysis of other environmental matrices (different from airborne particulate matter) and data interpretation.

Furthermore, this Thesis describes the preliminary results of other research work presently in progress including:

- 1) Physico-chemical and meteorological characterization of atmospheric aerosols in southern Spain as part of the FRESA¹ project.
- 2) Study and characterization of the processes and dynamics of atmospheric aerosol in the touristic Pertosa-Auletta cave (Italy, SA).
- 3) Characterization and quantification of radionuclides in innovative building materials defined as “Geopolymers”.

My contribution to these scientific works (both published and unpublished) encompasses several activities including:

- 1) chemical analysis with both spectral and chromatographic techniques of particulate matter samples (especially anion and cation chromatography, their optimization, and quality control, as dictated by the lowest aerosol concentration levels often encountered in this PhD research activity);
- 2) development and design of experimental and/or statistical methodologies;
- 3) formulation and/or evolution of overarching research goals and aims;
- 4) R Programming;
- 5) Application of statistical, mathematical, computational techniques to analyze or synthesize study data;
- 6) paper writing.

In spite of the heterogeneity, which is only ostensible, more than 90% of this thesis work concerns various aspects of ambient aerosol properties and multivariate analysis. The common thread of the overall work is substantially the expert use of multivariate statistics (particularly chemometric tool) enhancing the interpretative and diagnostic capabilities of

¹ Impact of dust-laden African air masses and of stratospheric air masses in the Iberian Peninsula. Role of the Atlas mountains. Ref: CGL2015-70741-R

experimental research work and complex chemical matrices, basically focusing on ambient aerosols. The publications reported in this Thesis are highly transdisciplinary and arise from the collaborations with several national and international research groups, including:

- Unit of Microbiome Science and Biotechnology, FaBiT (UNIBO, Italy), coordinated by Prof. Marco Candela;
- SCOLAb, Department of Applied Physics, University Miguel Hernandez de Elche, Spain (Prof. J.A.G. Orza);
- LABRADIQ, Faculty of Sciences, University of Granada, Spain (Prof. Ferro-Garcia, M.A.);
- Lab for Chemistry and Technologies of the Environment and Materials – Faenza (UNIBO, Italy) coordinated by Dr. Sara Arcozzi;
- Analytical Chemistry Lab, FaBiT (UNIBO, Italy), coordinated by Prof. Stefano Girotti.
- Department of Physics and Astronomy (UNIBO, Italy), Dr. Erika Brattich;
- Department of Chemistry, Biology and Biotechnologies, University of Perugia (Italy)
- Department of Biological, Geological, and Environmental Sciences (BiGeA), UNIBO, Italy;
- MIIdA Foundation and the University of Salerno (UNISA), PhD student Rosangela Addesso;
- Department of Civil, Chemical, Environmental, and Materials Engineerin (DICAM), UNIBO (Italy), Prof. Maria Bignozzi.

RIASSUNTO

La presente Tesi riporta i principali risultati scientifici ottenuti nell'ambito della mia attività di ricerca basata specialmente sull'applicazione di metodi statistici multivariati al servizio della Chimica Ambientale (disciplina accademica: CHIM/12) e, in particolare, l'aerosol atmosferico. Durante il dottorato di ricerca ho affrontato diversi temi che hanno portato alla pubblicazione di otto articoli scientifici, di cui tre come primo autore. Le pubblicazioni possono essere raggruppate in tre blocchi concettuali:

- 1) Progettazione e ottimizzazione di metodologie innovative per l'analisi del particolato atmosferico (PM) e l'interpretazione dei dati così ottenuti, in relazione alla salute umana, alla qualità dell'aria ed ai cambiamenti climatici.
- 2) Definizione di linee guida per l'utilizzo ottimale di sensori ottici *low-cost* di PM denominati OPC (dall'inglese Optical Particle Counter).
- 3) Analisi di altre matrici ambientali (diverse dall'aerosol atmosferico) e interpretazione dei dati.

Inoltre questa tesi descrive i risultati preliminari di altri progetti di ricerca attualmente in corso di attuazione tra cui:

- 1) La caratterizzazione chimico-fisica e meteorologica degli aerosol atmosferici nel sud della Spagna nell'ambito del progetto FRESA².
- 2) Studio e caratterizzazione dei processi e le dinamiche degli aerosol nella grotta turistica di Pertosa-Auletta (Italia, SA).
- 3) Caratterizzazione e quantificazione di radionuclidi in materiali da costruzione innovativi chiamati Geopolimeri.

Il mio contributo a questi lavori scientifici (sia pubblicati che inediti) comprende diverse attività tra cui:

- 1) Lo svoglimento di analisi chimiche su campioni di PM con tecniche spettroscopiche e cromatografiche (in particolare la cromatografia anionica e cationica, l'ottimizzazione del metodo analitico ed il controllo qualità dei dati, come dettato dai bassi livelli di concentrazione di aerosol spesso riscontrati nella mia attività di ricerca);
- 2) Sviluppo e progettazione di metodologie sperimentali e/o statistiche;
- 3) Formulazione degli obiettivi e delle finalità generali della ricerca;
- 4) Programmazione R;
- 5) Applicazione di tecniche statistiche, matematiche e computazionali per analizzare dati ed ottenere risultati significativi;
- 6) scrittura di articoli scientifici.

Nonostante l'eterogeneità dei temi di ricerca affrontati, che è solo apparente, più del 90% di questo lavoro di Tesi riguarda vari aspetti delle proprietà dell'aerosol atmosferico e l'analisi statistica multivariata. Il filo conduttore complessivo del lavoro è essenzialmente l'uso

² Impact of dust-laden African air masses and of stratospheric air masses in the Iberian Peninsula. Role of the Atlas mountains. Riferimento: CGL2015-70741-R

pratico della statistica multivariata (in particolare della chemiometria) che può incrementare le capacità interpretative e diagnostiche del lavoro di ricerca sperimentale, in particolar modo su matrici chimiche complesse quali il particolato atmosferico. Le pubblicazioni riportate in questa Tesi sono altamente interdisciplinari e nascono dalle collaborazioni con diversi gruppi di ricerca nazionali e internazionali, tra cui:

- Unità di Scienze e Biotecnologie dei Microbioti, FaBiT (UNIBO, Italia), coordinata dal Prof. Marco Candela;
- SCOLAb, Dipartimento di Fisica Applicata, Università Miguel Hernandez di Elche, Spagna (Prof. J.A.G. Orza);
- LABRADIQ, Facoltà di Scienze, Università di Granada, Spagna (Prof. Ferro-Garcia, M.A.);
- Laboratorio di Chimica e Tecnologie per l'Ambiente e per i Materiali – Faenza (UNIBO, Italia) coordinato dalla Dott.ssa Sara Arcozzi;
- Laboratorio di Chimica Analitica, FaBiT (UNIBO, Italia), coordinato dal Prof. Stefano Girotti.
- Dipartimento di Fisica e Astronomia (UNIBO, Italia), Dott.ssa Erika Brattich;
- Dipartimento di Chimica, Biologia e Biotecnologie, Università di Perugia (Italia);
- Dipartimento di Scienze Biologiche, Geologiche ed Ambientali (BiGeA), UNIBO, Italia;
- Fondazione MIIdA e Università degli Studi di Salerno (UNISA), dottoranda Rosangela Adesso;
- Dipartimento di Ingegneria civile, chimica, ambientale e dei Materiali (DICAM), UNIBO (Italia), Prof.ssa Maria Bignozzi.

CHAPTER 1 - General Introduction

1.1 – Foreword

Human population is certainly facing one of the most relevant ages as far as environmental "imbalances" are concerned.

Undoubtedly, the Severe Acute Respiratory Syndrome Coronavirus 2 (SARS-CoV-2) pandemic is currently representing the more intense impacting problem in our lives, from a health, social, and economic perspective (Harapan et al., 2020). Most of the scientific community agrees that this latest global epidemic, formally declared on 11 March 2020 by the World Health Organization (WHO), was favored by the impact of humans on the environment and ecosystems. Indeed, the most accredited cause of this virus in humans is related to the transmission of a pathogen from an animal to a human (i.e, a zoonotic spillover), occurrences that unfortunately are and could be more and more frequent in this epoch of intense anthropogenic climate changes (Marani et al., 2021). Therefore, the current pandemic may turn out to be just only the “tip of the iceberg” of a larger problem.

The most relevant challenge that the human kind has to face is global warming, i.e. the current rapid increase in Earth's average surface temperature whose start dates back to the mid-18th century. The latest ONU Intergovernmental Panel on Climate Change (IPCC) Report (IPCC, 2021) clearly shows how human influence has unequivocally warmed the atmosphere, the ocean, and the land, with severe meteorological outcomes that are increasingly impacting and damaging to our society.

This influence consists basically in a remarkable and still ongoing perturbation of the Earth's energy balance, described by the amount of energy that the Earth receives from the Sun and the amount of energy that is lost to space in the form of reflected sunlight and thermal radiation basically induced by a significant alteration in the tropospheric (and in part stratospheric) composition. The progressive increase in concentration and number of greenhouse gases and modification of atmospheric aerosol chemical-physical properties has altered the energy budget of the Earth, causing globally the increase in temperature showing a departure from thermal equilibrium conditions for our planet. Currently, greenhouse gas emissions from human activities are responsible for about 1.1 °C of warming compared to the period 1850-1900. Unfortunately, according to the same IPCC report, global temperatures are expected to reach or exceed 1.5 °C of warming over the next 20 years.

The ongoing global warming is impacting every region of the planet with multiple and progressively worse consequences as the temperature rises: decreases in permafrost, snow, glaciers, ice sheets, lake, and arctic sea ice; increases in extreme heat events that can impact everything from agriculture to human health, intensification of tropical cyclones and extra tropical storms, river floods, fire weather, increased overall rainfall, and increased dryness. Tendentially, these extreme events are going to increase in severity and frequency, as reported in the same IPCC report:

“If global warming increases, some compound extreme events with low likelihood in past and current climate will become more frequent, and there will be a higher likelihood that events with increased intensities, durations and/or spatial extents unprecedented in the observational record will occur”

In addition to global warming, global pollution must be considered a not negligible issue tightly associated with global change issues (von Schneidemesser et al., 2015). This link can be found in the co-emission of multiple chemical species from each emission source,

encompassing primary and secondary pollutants and greenhouse gases. The increase in atmospheric pollution originated by anthropogenic activities has significantly changed the natural characteristics of the atmosphere with a progressive deterioration in the quality of the air that people breathe every day. This has severe implications on human health such as birth defects, kidney and liver damage, skin rash and cancer. Air pollutants can also trigger heart attacks, stroke and cardiac arrhythmia especially in people who are already at risk for these conditions. Air pollution is estimated to cause seven million premature deaths every year (WHO, 2021).

The global environmental problems we are currently experiencing, are undoubtedly unprecedented, consequence of an indiscriminate overexploitation of natural resources and inadequate expertise and adaptability to fragile environmental balances.

Firstly, it is mandatory to deepen our knowledge on the various environmental compartments (air, water, soil, biosphere), and their interactions with the “anthroposphere”, i.e. the part of the environment that is managed and/or modified by humans, in order to propose effective solutions to the ongoing global challenge. Environmental problems are intricate and highly interconnected. Therefore, it is necessary to investigate these issues with a non-circumscribed and holistic approach. The proposed solutions have to be the result of collective and multidisciplinary scientific efforts, aware that extraordinary problems require equal endeavors to resolve them.

Thereafter, scientific evidence needs to be integrated and implemented globally. Nations and Institutions should cooperate to address, together, environmental problems. However, the responsibility cannot be delegated solely to the political and business sector but requires a change of mindset of human society. Long-term sustainability of the Earth must become the ethical responsibility of every single person. Scientific research must continue to study and analyze the climate changes underway and provide more and more varied and innovative tools.

In this scenario, this Thesis shows the main scientific achievements in my PhD research activity mostly related to Environmental Chemistry and Atmospheric Aerosols (one of the most important category of air pollutant detailed later in this Chapter). The common thread of all my scientific investigation is multivariate statistics for environmental assessment purposes. Multivariate Statistics includes all the mathematical-statistical methods to study complex sets of data, a typical situation in environmental chemistry, in order to extract tangible and exhaustive quali-quantitative information. The term Chemometrics is going to often be used in this Thesis to indicate mathematical-statistical methods applied to Chemistry.

The present Thesis consists of 12 chapters and is organized as follows:

Chapter 1 describes and poses the scientific basis for environmental chemistry and, specifically, atmospheric aerosol science (paragraph 1.2). Additionally, the same Chapter highlights the connection between atmospheric chemistry and the scientific works detailed in this Thesis (paragraph 1.3). From **Chapter 2** to **Chapter 8** are stated the ultimate published versions of the articles I worked on during my PhD time. **Chapter 9, 10, and 11** briefly describe the preliminary and unpublished results of the ongoing scientific activities. Eventually, a general conclusion completes this Thesis.

1.2 – Atmospheric Aerosols

The Earth's atmosphere is commonly considered as formed by nitrogen (78%), oxygen (21%), and other trace gases (1%). However, this definition is somewhat simplistic as it represents only the gaseous part of the air. Actually air is a multiphase and heterogeneous system consisting of two parts:

- a dispersed phase comprising solid, semi-solid, and liquid components of microscopic dimensions (from a few nm to hundreds of μm);
- a continuous dispersing phase, which is represented by the gaseous mixture defined above.

Although non-entirely accurate, the term “atmospheric aerosol” is often used to refer only to the particulate component of this suspension, used interchangeably with particulate matter (PM), which refers only to the particle phase.

An in-depth study of this system is essential for its role in air quality and climate change. Unfortunately, in recent decades it has been widely demonstrated how the composition and concentration of PM has changed significantly over the past 150 years due to a substantial increase in human activities (Pöschl, 2020). Several epidemiological studies demonstrate the harmful effects of anthropic particulate material on omnifarious biological apparatus, resulting in an increased risk of death: The European Environment Agency (EEA) estimates that, in 2018, approximately 379000 premature deaths were attributable to fine particles ($\text{PM}_{2.5}$) in the 27 EU Member States and the United Kingdom (EEA Report No 9/2020).

As further evidence of the hazard presented by PM, very recently the World Health Organization has further lowered the recommended limits of atmospheric aerosols (PM_{10} & $\text{PM}_{2.5}$) compared to the previous guidelines of 2005 (WHO, 2021).

Other studies show how PM, depending on its composition, can increase the planet's temperature (global warming) (IPCC, 2021) whose consequences range from a reduced availability of food and freshwater, an impoverishment of biodiversity, sea-level rise, and desertification, which inevitably leads to an increase of poverty, wars, and migratory flows (unfortunately, an absolutely crucial issue).

PM is an extremely complex entity under all points of view: sources, origin, chemical composition, size distribution, and morphology. Furthermore, it is an extremely dynamic system, whose characteristics change incessantly over time and space depending on the meteorology, activities of the emission sources, chemical reactivity, and deposition (Figure 1). All these aspects have to be considered concurrently and holistically for a comprehensive understanding of atmospheric PM.

The following paragraphs are going to describe the fundamentals of PM and its role on climate, environment, and human health. For more details see: Capello & Gaddi, 2018; Fuzzi et al., 2015; Kim et al., 2015; Seinfeld & Pandis, 2016; and references therein included.

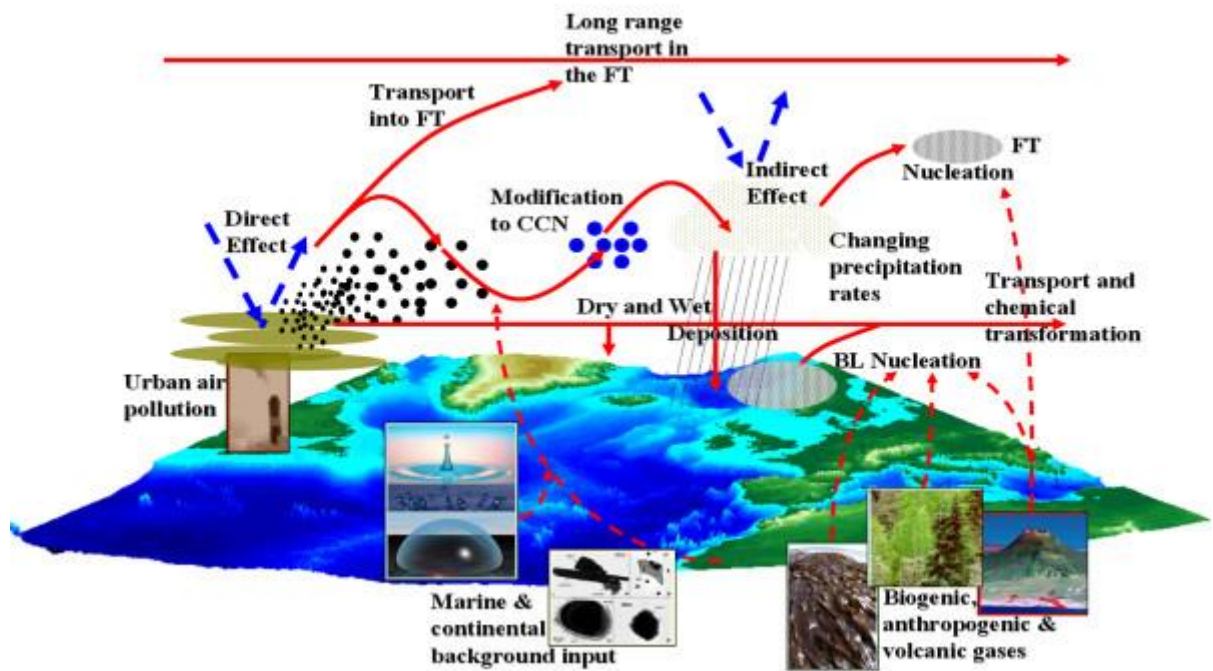


Figure 1. Bio-geo-chemical cycle of atmospheric aerosols (Image downloaded from the Centre for Atmospheric Science, <http://www.cas.manchester.ac.uk/resactivities/aerosol/>)

1.2.1 – Morphology and dimension

The first fundamental characteristics of PM is its wide particle size range, from few nanometers ($1 \text{ nm} = 10^{-9} \text{ m}$) to about 100 microns ($1 \text{ }\mu\text{m} = 10^{-6} \text{ m}$).

In most cases, airborne particles do not have a regular and well-defined geometry but rather irregular and shapeless (China & Mazzoleni, 2018). SEM (scanning electron microscopy) and TEM (transmission electron microscopy) images provides the most disparate particle shapes: from the rough edge-shape of dust particles, to the long-branched chains of soot particles, to the cubic shape of a sodium chloride crystal, etc... (Figure 2):

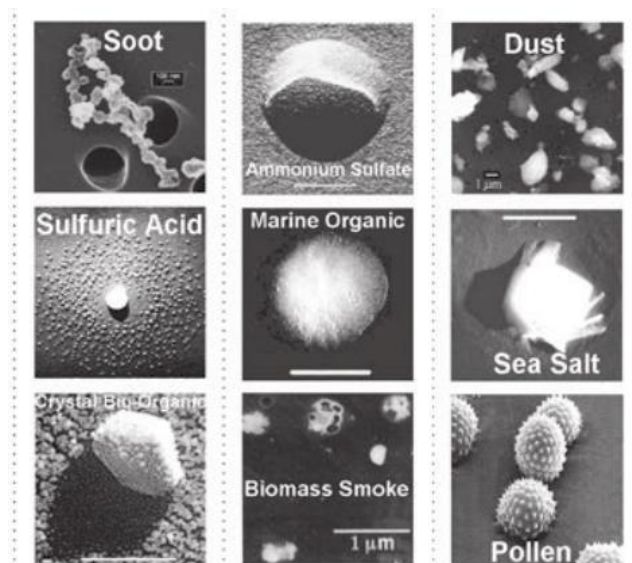


Figure 2. Variegated and complex morphologies of atmospheric particles (adapted from Capello & Gaddi, 2018)

For this reason, particle size can only be conventionally defined by the equivalent spherical diameter, comparing the irregular particle with a spherical one on the basis of a specific physical property of the examined particle. This implies that the dimension thus defined is operational, i.e. it depends both on the instrument used for the measurement and on the physical property used for this comparison.

There are several types of diameters but the most relevant is the aerodynamic diameter (D_a), that is the diameter of a reference sphere of unit density (1 g cm^{-3}) which has the same terminal velocity of an environmental, real-world particle (Heyder & Porstendörfer, 1974). The mathematical law that describes D_a is:

$$D_a = D_g \cdot k \cdot \sqrt{\rho_p / \rho_0}$$

where D_g is the geometrical diameter, k a spatial factor (equal to 1.0 in the case of a spherical particle), ρ_p the particle density, and ρ_0 the density of the reference spherical particle.

Based on this definition, the aerodynamic diameter depends on the real shape, the real size, and the real density of the examined particle. It can be measured by inertial aerosol particle collection devices, such as cascade impactors, or filtration-based systems allowing to select aerosol particle size according to PM_x metrics, defined as airborne particulate matter with a mean aerodynamic diameter equal to or lower than $X \mu\text{m}$ (typical values of the upper aerosol size threshold are 10, 2.5 or 1 μm).

According to the last definition, these classes of atmospheric aerosols resemble a matryoshka as the PM_{10} contains within it all the other metrics with an aerodynamic diameter smaller than 10 microns, $\text{PM}_{2.5}$ contains all the other metrics with an aerodynamic diameter smaller than 2.5 microns, etc. An overview of PM_x metrics is illustrated in Figure 3.

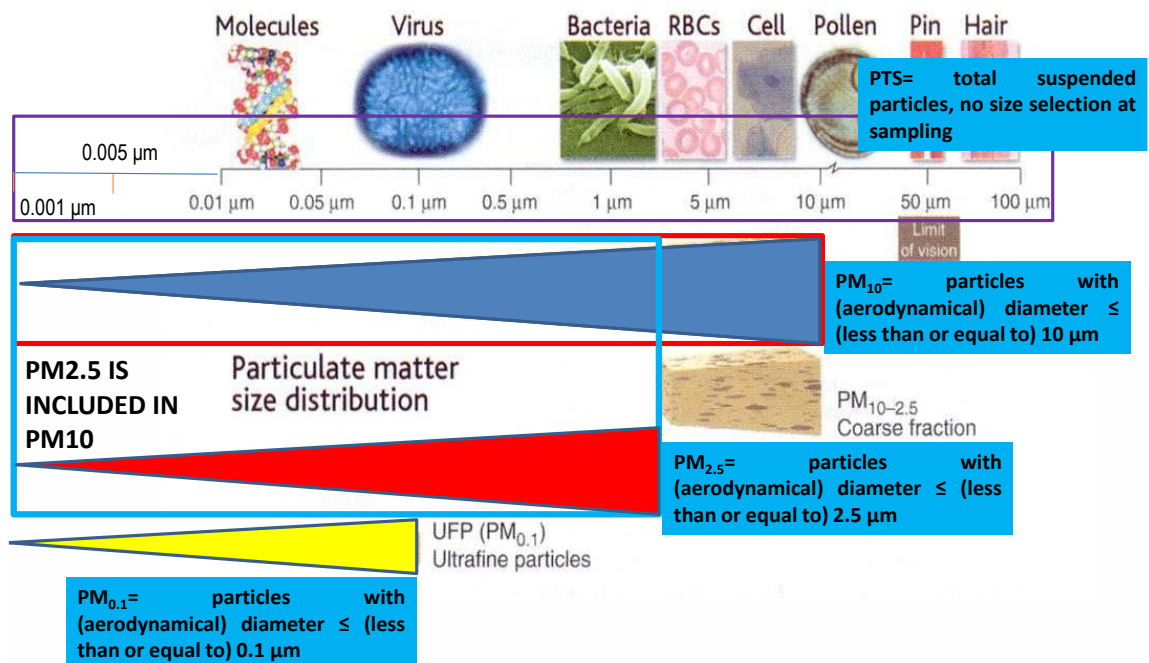


Figure 3. Size-based PM metrics: PTS, PM_{10} , $\text{PM}_{2.5}$ and PM_1 (lesson slide by Prof. Laura Tositti)

Another kind of instrumentation based on aerosol particle size include the so-called Optical Particle Counters (OPCs) based on the particle optical diameter, that is the diameter of the

sphere which has the same refractive index (RI) of the studied particle. It can be determined by means of the light scattering particles induce when hit by a suitable laser beam (Welker, 2012). These instruments can be used as a complement of filtering-based devices and provide another fundamental information such as particle size distribution in the range above 150 nm, therefore excluding ultrafine particles owing to the physical constraint posed by light wavelength as compared to particle size.

The wide range of possible sizes allows the categorization of the airborne particulates into three macro-classes:

- Coarse particles, which have a diameter greater than 2.5 μm ;
- Fine particles, which have a diameter between 100 nm and 2.5 μm ;
- Ultrafine particles, which are less than 0.1 micron in size.

These classes greatly differentiate the aerosol sources, physico-chemical characteristics, formation and removal mechanisms, and effects on climate and human health. These aspects are going to be extensively discussed in this Chapter.

PM is characterized by a multimodal behavior with frequency distribution peaks around well-define particle sizes (John, 2011). PM distribution modes are as follows:

- Condensation nuclei peaking at 10-12 nm;
- Aitken nuclei with a maximum at 70-80 nm;
- Accumulation mode covering the range 200-800 nm;
- Coarse particles > 2.5 μm .

Figure 4 shows formation, growth, and deposition processes for the four particle size modes.

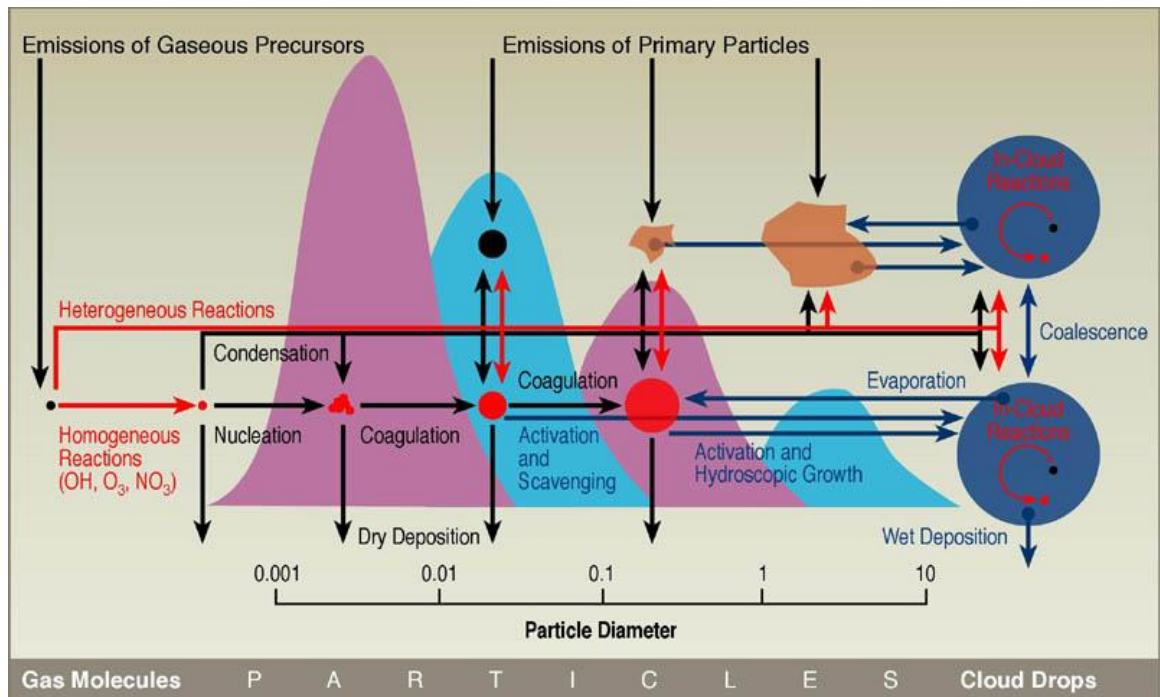


Figure 4. Ideal size distribution of atmospheric aerosol (adapted from Raes et al., 2000)

The smallest ones are the nucleation and Aitken modes, which therefore include ultrafine particles ($< 0.1 \mu\text{m}$). These particles have been freshly formed after the emission of primary gaseous precursors followed by gas-to-particle oxidation reactions; condensation of primary species is also a possible particle source (Kulmala et al., 2013). This process is called homogeneous nucleation and takes place in supersaturation conditions, i.e. when the partial pressure in the gaseous phase of a substance is greater than its vapor pressure. The oxidative chemical reactions typical of ambient atmosphere favors the change of phase within a heterogeneous process owing to the influence of electrostatic interactions induced by the larger polarity of the reaction products usually containing more oxygen than the precursor (see further in this chapter). The particles deriving from homogeneous nucleation are therefore very small and numerous, due to the proximity to the gas phase from which they derive and, also, due to a very fast formation that can only occur under certain thermodynamically favorable conditions. The particles are therefore subject to collisions and phenomena such as coagulation (a phenomenon that involves both solid and liquid particles, which interact with those produced by homogeneous nucleation, colliding and aggregating forming a smaller number of larger particles, i.e. clusters) and condensation (heterogeneous nucleation phenomenon which begins when the equilibrium shifts towards the aerosol phase, i.e. when gas molecules give particle nuclei) (Kulmala et al., 2013). Due to these rapid reactions, the life span of these particles ranges from the order of seconds up to a few minutes, the shorter atmospheric residence time of the four distribution modes. Most of the ultrafine particles are subjected to high-frequency collisions to rapid coagulation or condensation, thus shifting towards the accumulation mode, due to their small size and high number concentration.

Accumulation mode particles includes all the particles with a diameter ranging from 0.1 to $1 \mu\text{m}$, i.e. fine particles. These airborne particles are prone to condensation and coagulation processes and have a fairly long-life span, which can reach up to two weeks. Therefore, they can be transported up to long distances before being removed, mainly, by rainout or evaporation;

The coarse mode relates to particles $> 1\mu\text{m}$, which are mainly formed by mechanical processes such as solid abrasion, wind erosion of rocks and soils, organic debris, volcanic emission, and sea-salt aerosol. Pollen, a part of bacteria, spores and various plant and animal fragments largely contributes to this fraction of atmospheric aerosol. Coarse particles remain in the atmosphere from a few hours to a few days, having a residence time that is halfway between the nucleation and accumulation fractions. They are in fact subject to the influence of their high weight, which results in their removal by gravitational settling. The distance achievable by coarse particles during atmospheric transport is a function of particle mass, gravitational constraint and kinetic energy of air masses in which they are entrained; their resuspension and subsequent transport is usually promoted by dry conditions and thermal convection leading to enhanced uplift in the warm season and subsequent advection (Coude-Gaussen et al., 1987). Wind speed in fact is enhanced with increasing height in the troposphere promoting the long range transport of coarse particles.

Airborne particles volume and mass are largest in the coarse mode and decrease with decreasing size, while surface area and number density (number of particles per unit air volume) increase more than proportionally as size decreases (Figure 5).

The population of particles $< 300\text{nm}$ (therefore including nucleation, Aitken, and the lowest fraction of accumulation modes) represent in number around 84% of all particulate matter (Kumar et al., 2014), while in mass is only 1-2%.

Therefore, the total mass of ultra-fine particles can even be considered negligible, even if is remarkably crucial for health issues (see paragraph 1.2.6).

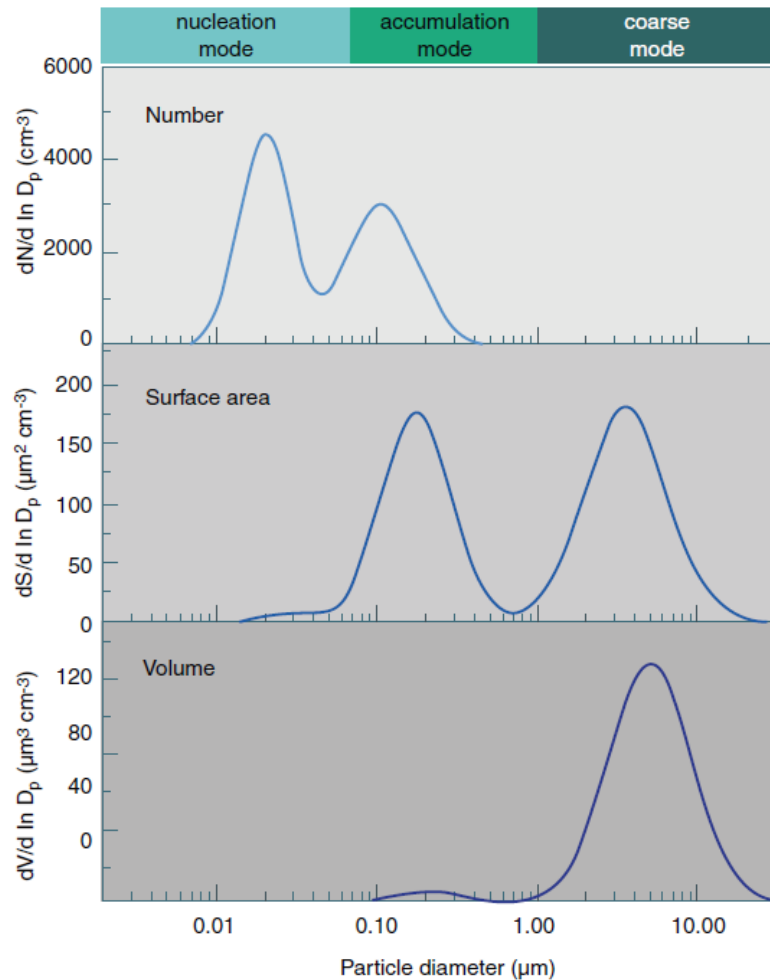


Figure 5. PM number, surface and volume as a function of particle size (Tositti, 2018).

1.2.2 – Origin and formation

The second fundamental concept for PM classification and characterization is the difference between primary and secondary aerosol.

Primary aerosol is constituted by particles which are formed and are directly emitted into the atmosphere as soon as they formed within the corresponding emissions sources. It includes airborne particles from both natural (plant debris, dust, volcanos, sea, and bioaerosol) and anthropogenic (soil dust, mechanical abrasion, etc...) sources, and involve both coarse particles and part of the condensation nuclei, the former being more relevant.

Instead, secondary aerosol derives from gaseous precursors in the atmosphere that condense and chemically react to form condensed aggregates suspended in the air, i.e. some gases undergo heterogeneous chemical reactions. The formation of this kind of aerosol, differently from primary aerosol, has already been explained in the previous paragraph (see paragraph 1.2.1). Figure 6 depicts the main secondary aerosol formation process, that is the transition from free gaseous molecules to nano-dimensional clusters which, in turn, collide and coalesce to give gradually larger particles. This process leads to a change of physical state

from the gas phase to the condensed phase and, therefore, the latter is a condensation process (i.e., “gas-to-particle conversion”).

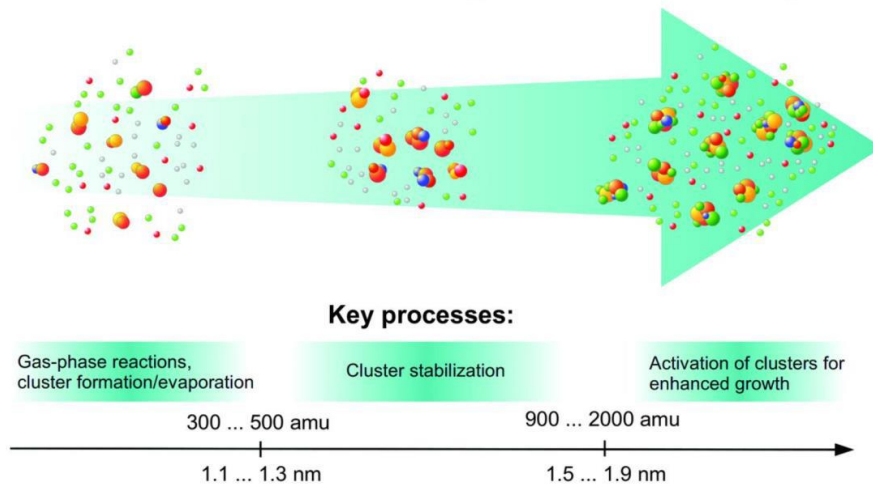


Figure 6. Schematic description of secondary atmospheric aerosol formation (Kulmala et al., 2013).

Therefore, the size of airborne particles is closely linked to its origin and formation, as shown in Figure 7 (John, 2001).

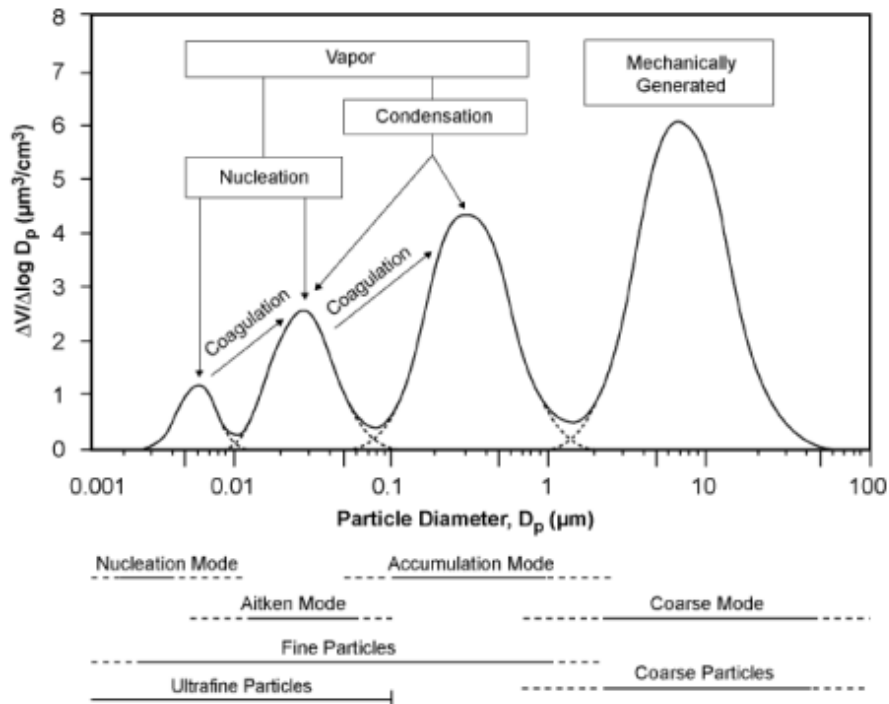


Figure 7. An idealized dimensional distribution of PM volume and respective origin and generation processes (EPA, 2004).

As it will be shown further on, this process concerns gaseous species such as SO₂, NO_x, and a number of VOCs whose environmental fate is being transformed in some of the major chemical components, i.e. ammonium sulfate and nitrate and Organic Carbon (OC).

1.2.3 – Aerosol environmental fate

Once released into the atmosphere, any atmospheric component, aerosol included, is transported over distances that can be long or short, depending on its atmospheric residence time. The atmospheric residence time of an aerosol is defined as the average time it spends in the atmosphere as a mutual result of the process of formation/production against those of removal (Molinarioli & Masiol, 2006). It depends not only on the size, as described in the previous paragraphs, but also on the chemical composition and atmospheric conditions. There are two possible pathways of removal, i.e. wet and dry deposition.

Wet deposition includes rain, snow, hail, and fog (known as occult precipitation owing to the reduced water volume associated as compared to the other hydrometeors). It is largely dominant over dry deposition relying on very efficient mechanisms largely mediated by particle composition, hygroscopicity, and the local climatology. The residence time is then substantially associated with atmospheric water cycle and may reach up to 8-9 days on average. This deposition method accounts for roughly 80% of the total aerosol removal (Zhang et al., 2004). In turn, this removal pathways can be divided into two types of consecutive process:

- in-cloud processes (in-cloud scavenging): the hygroscopic particles (usually saline and/or polar aerosol components) act as Condensation Nuclei of the Clouds, the so-called CCN, which grow in size by condensing the water vapor to give rise to the formation of clouds. When the hygroscopic growth process causes the drops to reach a sufficient size, precipitation is formed which thus falls and reaches the surface of the planet. Otherwise, the particulates can be removed by evaporation/sublimation according to the thermodynamic conditions of the surrounding air mass;
- below-cloud processes (below-cloud scavenging): the removal of particles also occurs during the fall of rain or snow with interception of water drops, or snowflakes, of suspended particles which, in this way, are transported to the ground.

Of these two processes, the first type is the most efficient, because the removal by interception of aerosols is based on the probability that rain or snow will collide with the particles during their path. Snow, however, is more efficient than rain, due to the greater surface area and slower speed that characterize the falling flakes capable to entrap even less polar substances by adsorption such as some organic pollutants. Figure 8 shows a graphical representation of these two deposition processes.

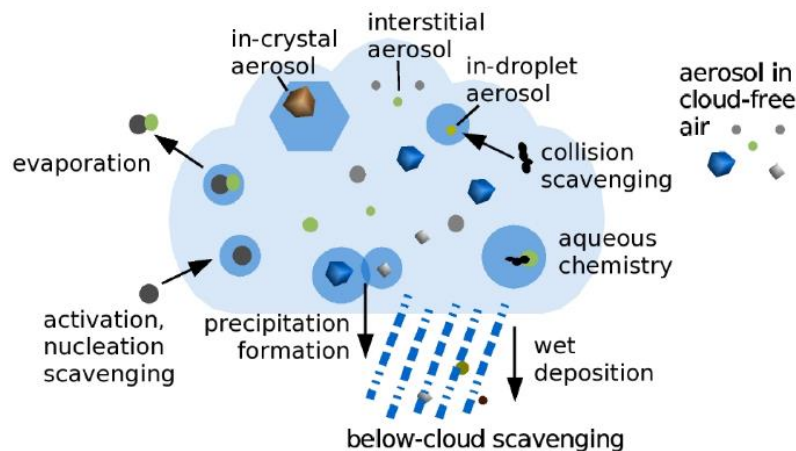


Figure 8. Wet deposition of airborne particles (Hoose et al., 2008).

Dry deposition (Figure 9) instead occurs by gravitational settling and/or impaction. The former mechanism occurs mainly for coarse particles whereas impaction typically favors intermediate size particles, and coagulation is one-way smaller particles can aggregate with larger ones, leading to their eventual deposition by wet or dry processes. Particle injection height, subsequent air mass advection, size, and other factors affect the rate at which dry deposition operates, with a velocity regulated by the Stokes law.

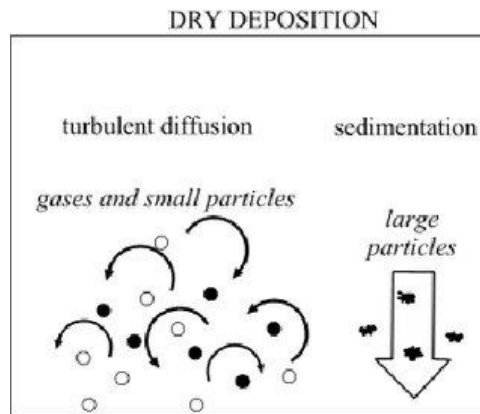


Figure 9. Dry deposition of airborne particles. Adapted from Leelőssy et al., 2014.

The shortest-lived particles are both the coarse and the ultrafine ones. The accumulation mode particles are small enough to remain in suspension in the atmosphere until atmospheric motion will end up in impacts on any surface encountered during transport or until they will be affected by wet deposition. Moreover, aerosol lifetime is also dependent on location, climatology and height in the atmosphere as shown in Figure 10.

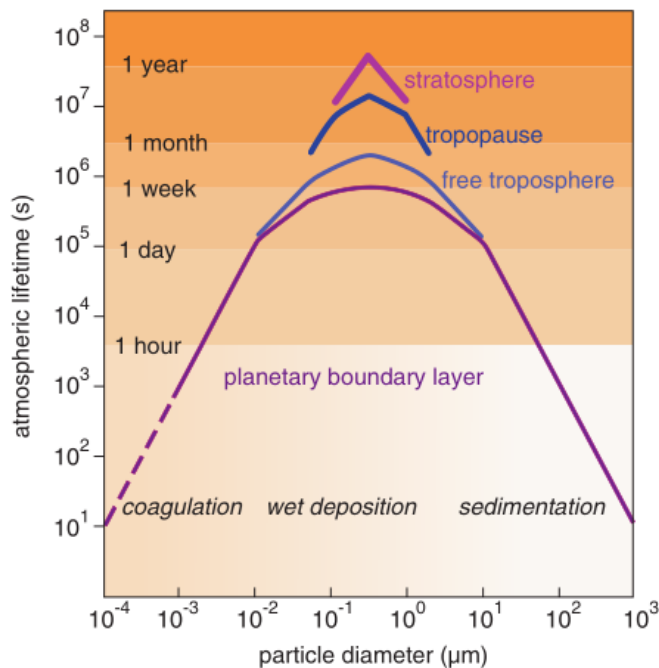


Figure 10. Atmospheric lifetime of aerosol as a function of size and of atmospheric height (Tositti, 2018).

1.2.4 – Emission sources

PM has multiple both natural and anthropogenic sources, which are mixed in variable ratios with the relative distance and intensity of each active source. The pervasiveness of human activities on the planet makes a clear distinction between natural and anthropogenic sources problematic. In fact, even sources that are unequivocally attributable to natural phenomena are now influenced by human's activity and, consequently, are not entirely background conditions but actually represent a natural-anthropogenic fusion.

Major natural aerosol sources include volcanic emissions, sea spray, mineral dust, forest fires, spores and pollen, etc. (Figure 11).

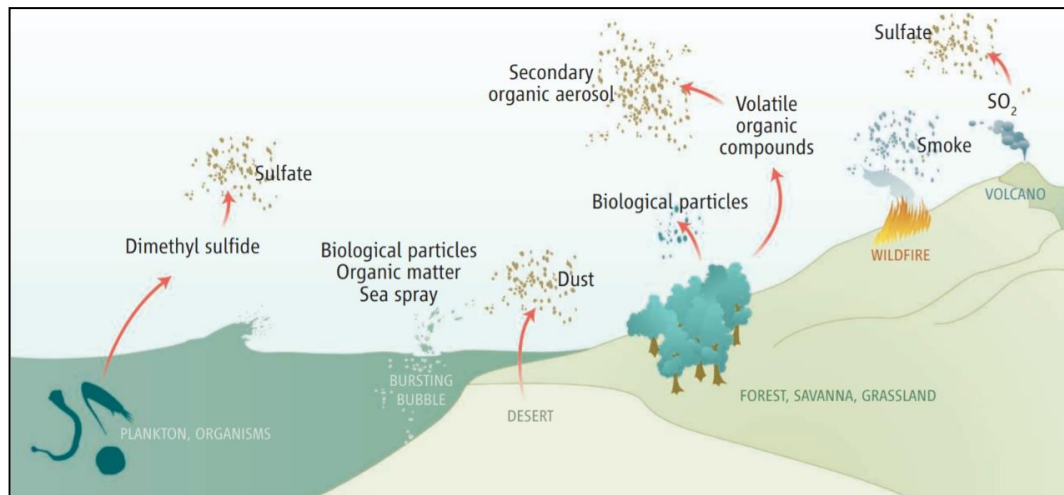


Figure 11. Natural sources of atmospheric aerosols (Andreae, 2007).

Instead, anthropogenic sources include all the airborne particles by human's activity, both intentional and unintentional emissions. PM from anthropogenic sources derives mainly from combustion and high temperature processes, such as the combustion of biomass, fossil fuels, wood, or mineral and material transformation; in this class we also find particulate matter emitted by fires, traffic emissions, wear of brakes and tires, transport, industrial activities, energy production, waste incineration etc. (Figure 12).

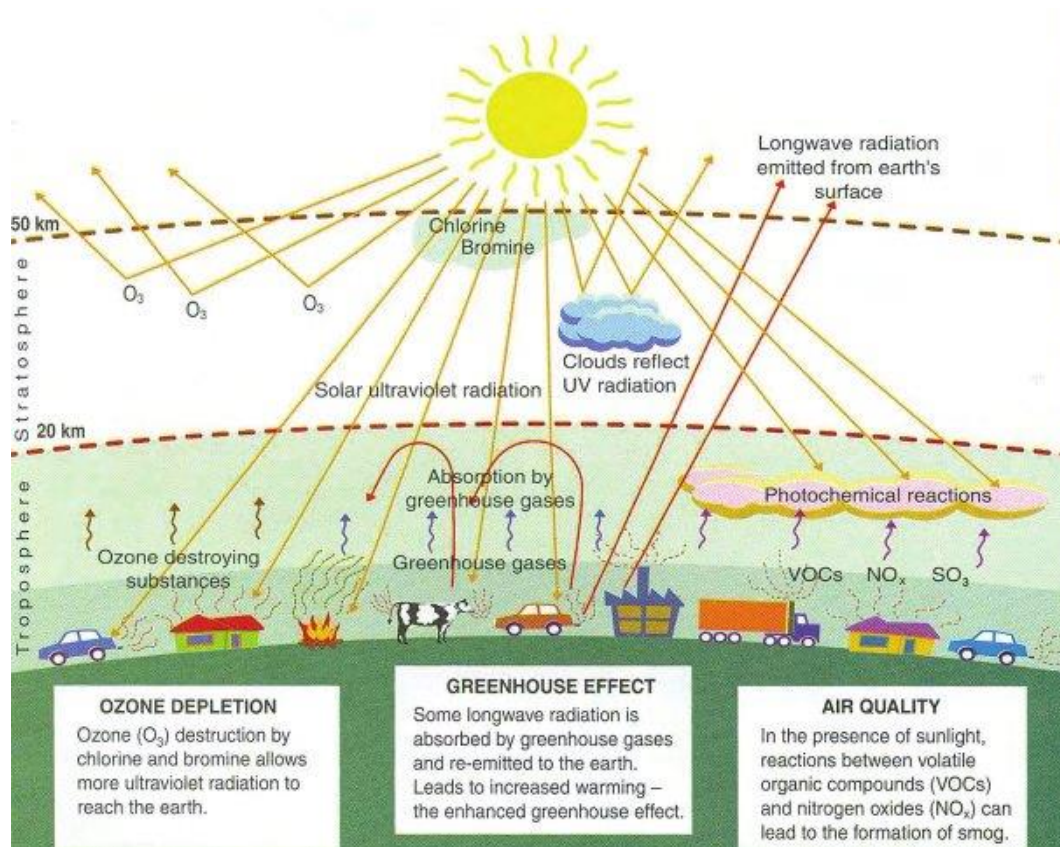


Figure 12. Anthropogenic sources of atmospheric aerosols (Gheorghe et al., 2011).

Worldwide, the estimated annual flow of both natural and anthropogenic contributions reaches 2500 - 24000 Tg y^{-1} . On a global scale, natural contributions prevail on anthropogenic ones. Indeed, about 94% of the total atmospheric particulate matter is natural (2200-23500 Tg y^{-1}) while the rest derives from humans (300-450 Tg y^{-1}) (Karagulian et al., 2015). However, the proportion natural/anthropogenic can be inverted locally, e.g. in urban areas, significantly influenced by traffic, industrial activities, domestic fuel burning, and unspecified sources of human origin highly concentrated in these type of environments (Karagulian et al., 2015). The main sources of atmospheric aerosols with their relative average annual fluxes, are shown in Table 1.

Table 1. Aerosol contributions from natural and anthropogenic sources on the global scale expressed as average annual fluxes (Tositti, 2018).

Source	Present flux		
	Low	High	Best
Natural			
<i>Primary</i>			
Soil dust (mineral aerosol)	1000	3000	1500
Sea-salt	1	10000	1.3
Volcanic dust	4	10000	33
Biological debris	26	80	50
<i>Secondary</i>			
Sulphates from biogenic sources	60	110	90
Sulphates from volcanic SO ₂	4	45	12
Organics from biogenic NMCH ^a	40	200	55
Anthropogenic			
<i>Primary</i>			
Industrial dust etc.	40	130	100
Black carbon (soot and charcoal)	10	30	20
<i>Secondary</i>			
Sulphates from SO ₂	120	180	140
Biomass burning (w/o blackcarbon)	50	140	80
Nitrates from Nox	20	50	36
Organics from anthropogenic NMCH ^a	5	25	10
Total	2390	24000	3450

^aNMHC = non-methan hydrocarbons

The main natural emission sources are described below.

- Sea Spray refers to aerosol particles that are formed directly from the seas and oceans. It is formed when the wind, whitecaps and breaking waves mix air into the sea surface, regrouping it into bubbles, which are released aloft and finally burst and de-hydrate, releasing the so-called sea spray (Lewis et al., 2004). In windy conditions, sea spray can also be obtained through the mechanical removal of water droplets from crests of breaking waves. The major non-water chemical components of sea spray aerosol include organic carbon (OC) and sea salt (mainly NaCl, but with other ions such as K⁺, Mg²⁺, Ca²⁺, SO₄²⁻). These ions are in known composition ratio, see for example the composition of Standard Seawater as from Haynes, 2014. Organic matter, complexed with the metallic ions, is in high concentrations due to the drying of air bubbles at the organic-rich sea surface.
- Volcanic emissions include all emissions caused by the leakage to the surface of magmatic and gaseous materials from within the Earth. Volcanic ash is composed of glass, sulfates, minerals, and magmatic fragments (Sierra-Vargas et al., 2018). Trace elements covering all the periodic table are also present in the volcanic plumes. This source is mainly centered around active zones of tectonic plates margins, except for massive eruptions (for example the eruption of Eyjafjallajökull, in Iceland, in 2010,

which caused the interruption of flights for several weeks due to the imposing resulting ash cloud);

- Mineral dust originates from the resuspension in the air of soil dust and minerals uplifted and transported from arid regions through the atmosphere by strong winds over long distances and also by local surfaces, such as soil, pavement, mines, construction, and agricultural activities. It is mainly composed of the oxides and carbonates that make up the Earth's crust, in particular silicates, silico-aluminates and alkali metal carbonates (CaCO_3 , MgCO_3) (Linke et al., 2006; Rodríguez et al. 2020). Mineral dust emissions are estimated to reach about 1000-5000 million tons per year (Huneeus et al., 2011), mostly released from deserts. However, 25-30% of these spreads are attributed to human activities, through the processes of desertification and land use change (Ginoux et al., 2012). The Sahara Desert is the largest source of mineral dust on the planet. North African dust is uplifted at high altitudes by the convective motions over the hot desert areas, and then transported for thousands of kilometers. These powders are characterized by a peculiar reddish color due to the presence of iron oxides (in particular hematite and goethite) (Formenti et al., 2014; Morozzi et al., 2021);
- Biological aerosol consists of various types of microorganisms, such as bacteria, algae, fungi, and their producing and dispersing units, such as fungal spores, pollen, viruses and biological fragments and detritus directly emitted into the atmosphere from their sources (Fröhlich-Nowoisky et al., 2016).

As previously reported, about 10% of global atmospheric aerosol mass is generated by human activity but it is focused in metropolitan/urban areas and downwind (Chin & Kahn, 2009). Although it has steadily decreased over the years (EEA IND-366-en, 2019), it continues to be an issue for human health. According to World Health Organization (WHO, anno), there is no actual safe threshold in PM ambient concentration below which health effects risk is negligible. The main anthropogenic emission sources are described below:

- Agricultural sources are the major biogenic sources of atmospheric PM. The main emissions from this kind of source are ammonia, mainly from livestock farms and natural fertilizers; NO_x , from soil cultivation and heating; and Volatile Organic Compounds (VOCs), from plant metabolism and combustion of agricultural residues. Most of the airborne particulate produced by this source are fine and secondary, but the coarse fraction is not missing (Amann et al., 2017);
- High temperature sources include the combustion of fossil fuels for vehicles, the production of energy, the industrial production of materials and artifacts, the combustion of biomass and waste, transport (by land, by water, and by air), traffic, domestic heating, food cooking processes, etc. These sources are both mobile, such as traffic and transport, and stationary, such as for example, fireplaces/stoves and industrial plants. These combustion reactions release into the atmosphere a number of chemical species, such as the already known precursors of secondary aerosol, i.e. SO_2 (deriving from combustion with sulfur impurities, especially coal and fuel oils), NO_x (produced by the combination of nitrogen and gaseous oxygen at high temperatures developed by combustion reactions, highly exothermic), VOCs (including polycyclic aromatic hydrocarbons, PAHs) and elemental carbon, whose structure, similar to graphite, is emitted directly into the atmosphere due to the incomplete combustion of fuels and biomass or in the exhausts of vehicles engine (Wang et al., 2019). The size of the particulate matter deriving from combustion processes is generally submicronic, in relation to chemical species originally emitted

in the gaseous phase (free molecules) which, subsequently, are condensed following gas-to-particle conversion reactions (see paragraph 1.2.2);

Physical sources of aerosol formation include the resuspension of volatile and soil dust, both inorganic and organic particles (VOCs), wear of tires, brakes and road surface (from vehicular traffic), building/demolition activities and the spreading of salt to thaw the streets. The PM produced by physical causes is usually coarse.

1.2.5 – Chemistry

Atmospheric aerosol composition is extremely intricate and strongly depends on the size class (paragraph 1.2.1), the formation processes (paragraph 1.2.2), emission sources (paragraph 1.2.4), and meteorology. The average composition of aerosols includes major and minor components, virtually covering substantially the whole periodic table of elements beside the complex chemodiversity of the carbonaceous derivatives making up included in OC (see further on in this chapter) (Figure 13).

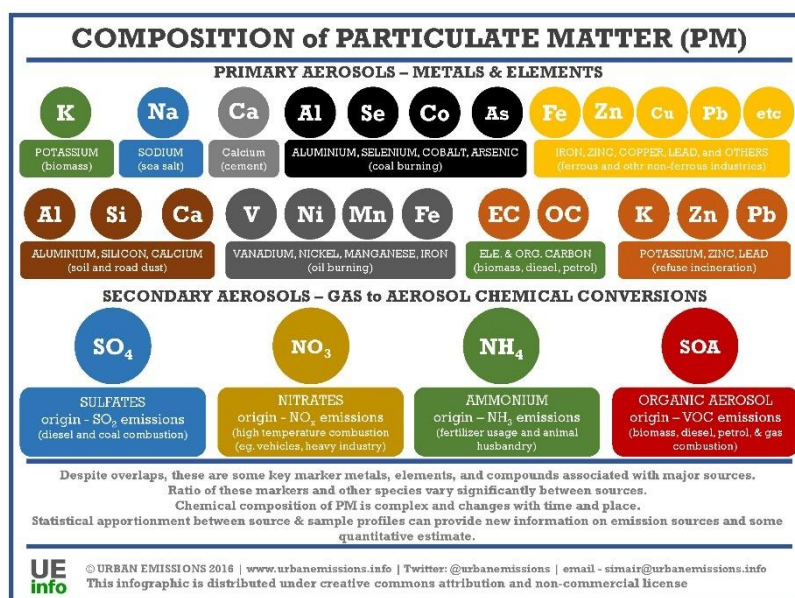


Figure 13. Chemical composition of the atmospheric aerosols (Image downloaded from UrbanEmissions.Info, available at <https://urbanemissions.info/blog-pieces/whats-polluting-delhis-air/>)

Figure 14 shows a schematic representation of the main mechanisms of formation of atmospheric aerosols with their corresponding chemical components.

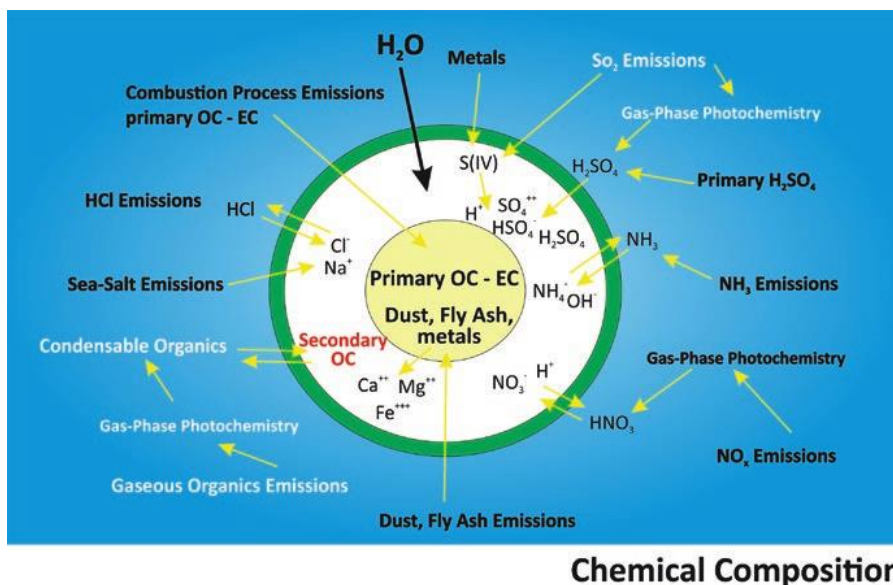
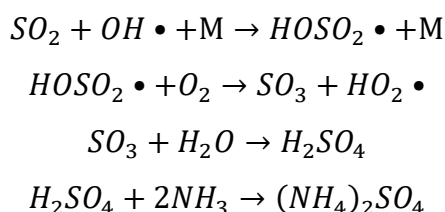
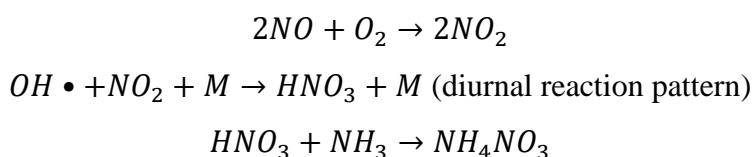


Figure 14. Chemical composition, physico-chemical behaviour, reactivity, and origin of the atmospheric aerosols (Tositti, 2018).

The **inorganic part** of PM includes both primary and secondary particles. The primary aerosol involves metals and nonmetals (cumulatively about 3% by weight of the particulate) and insoluble minerals. Examples are metals associated with the mineral dust (i.e., Si, Al, Fe, Ca) and sea spray (i.e., Na^+). The secondary inorganic aerosol (SIA) includes ionic species such as ammonium sulfates and nitrates, deriving respectively from the oxidation of SO_2 and NO_x respectively to H_2SO_4 and HNO_3 neutralized by atmospheric NH_3 or CaCO_3 . SO_2 is a primary gaseous precursor deriving from the combustion of fossil fuels or, possibly, from natural sources such as volcanic emissions or the oxidation of dimethyl sulfide (DMS) produced by marine phytoplankton. Sulfur dioxide is further oxidized by the OH radical, the most important atmospheric oxidant (Prinn, 2003). If not quantitatively neutralized (actually “titrated”) by the gaseous ammonia, they can generate acid rain (Harrison & Kitto, 1992). The reaction scheme is shown below:



NO_x , on the other hand, are formed at high temperatures; they can react with VOCs to product ozone, but can also be reacted by the OH radical and other oxidizing species to form very rapidly NO_2 and, finally, nitric acid. At this point, HNO_3 can be neutralized by NH_3 to form ammonium nitrate NH_4NO_3 . The reaction scheme is shown below:



Other important components of the inorganic fraction are seasalt in coastal areas and silico-aluminates and carbonates, which constitute the inorganic carbonaceous portion of the atmospheric aerosol. They can derive either from natural sources, such as crustal materials from rocks and soils abrasion, eroded and/or leached by atmospheric agents, or from anthropogenic sources, quarries, mines, and construction sites;

The most abundant carbonaceous fractions are elemental carbon (EC) and organic carbon (OC). They are commonly determined as single macro-components of PM using thermo-optical techniques allowing to fulfil the budget requisite in PM mass balance problems aside other major components, but preventing from the due characterization, since both these components are fairly complex owing to the multiplicity of sources converging in each PM sample.

EC comprises particles of primary origin with a graphitic structure and smaller quantities of heteroatoms, mainly nitrogen and oxygen (Seinfeld & Pandis, 2016). It is formed during high-temperature combustion of both natural (for example spontaneous forest fires) and anthropogenic (such as heating with wood and pellets) material. The mass contribution to submicron particulate matter reaches up to 10-15% and remains practically unaffected during its lifetime in the atmosphere. However, this value can increase in highly polluted areas, such as urban and industrial centers (Tositti, 2018).

Elemental Carbon is also referred to as soot or Black Carbon (BC). These terms are often incorrectly used as synonyms and an internationally unique notation has not yet been defined. However, these terms are used in the scientific literature on an operational basis, i.e. according to the experimental method used for the characterization of this aerosol component. EC is commonly determined using thermo-optical methods based on the evolution of gases (CO_2 or CH_4) at high temperature in controlled conditions, while BC is related to its high peculiar optical properties. In fact, its black color is responsible for a significant absorbance of visible light and, therefore, capable of altering the planet's radiative energy exchanges and influencing the climate (see paragraph 1.2.6). EC has a peculiar structure and morphology that can promote adhesion of organic molecules to its surface, such as VOC and semi-volatile substances. This process continues with their desorption as it is, or chemical reactions can occur that modify the substances initially adsorbed.

BC (soot) can be observed on surfaces exposed to combustion fumes (soiling), such as for example the walls of urban buildings exposed to traffic exhaust, though each combustion source emits it; its formation process is shown in Figure 15.

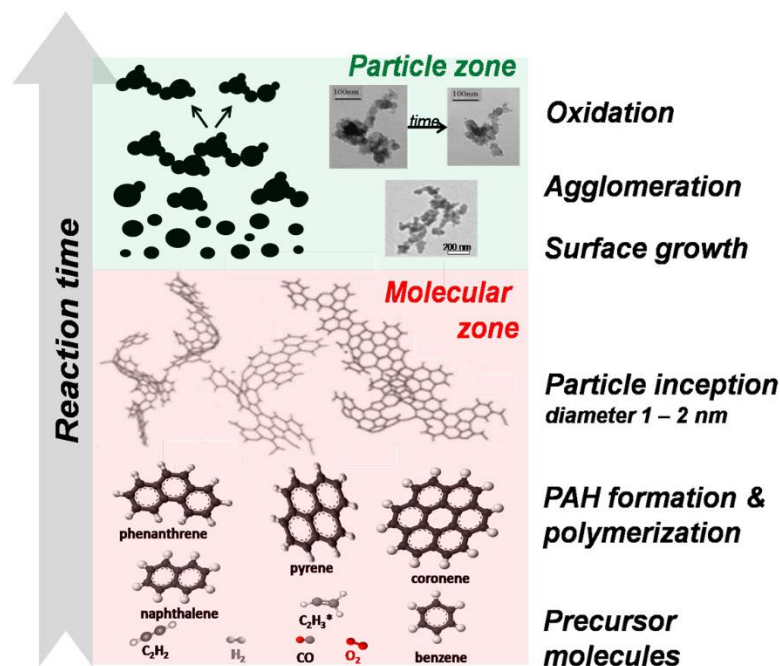


Figure 15. Soot formation mechanism (Image downloaded from the Department of Chemical Engineering – University of Melbourne, <https://chemical.eng.unimelb.edu.au/aerosols/research>)

Both EC and BC are insoluble in water and organic solvents, absorb light, and cause damage to human health, as they are recognized as strong pollutants as well as collectors of various carcinogenic compounds (Briggs & Long, 2016). EC and BC are usually strongly correlated when measuring emissions from the same emission source, even if the total quantified mass is different. Instead, they are not significantly correlated when comparing different sources, when there is variation in meteorological conditions, and/or in the absorption of radiation by carbonaceous material (Briggs & Long, 2016; Salako et al., 2012; WHO, 2012). Another carbonaceous fraction named Brown Carbon has recently been introduced, which is a colored organic fraction that mainly derives from the combustion of biomass and coexists with black carbon when released into the atmosphere. As BC, it tends to absorb solar radiation even if with a lesser extent due to its lighter color (Andreae & Gelencsér, 2006).

The **organic fraction** is a mixture of hundreds up to thousands different organic compounds of which only a tenth has been instrumentally characterized (Lazaridis, 2008). It can be divided into primary (POA) and secondary (SOA) compounds. POAs are polar species such as carboxylic and dicarboxylic acids, hydrocarbons of variable molecular weight, including highly toxic substances such as PAHs, beside nitrogen and sulfur derivatives. SOAs include oxidation products from gaseous precursors with low vapor pressure mostly classified as Volatile Organic Compounds (VOCs) (Lazaridis, 2008). Other important constituents of the organic fraction are the biological component, coming from both natural sources (pollen, spores, vegetation, microorganisms, etc.) known as Primary Biological Aerosol Particles (PBAP) and anthropogenic (agriculture, combustion, traffic and transport, petrochemical industry, etc.). Organic carbon (OC) consists of a wide range of different substances and derives from both primary and secondary sources. OC is still poorly characterized. In fact, only around 10% of the molecular components has been identified so far basically by means of chromatographic hyphenated techniques in agreement with the range of different molecular mass, volatility and detection limits, a relevant problem due to the small amounts

of sample usually available. It was found that OC includes multiple and different classes of organic molecules, such as alkanes, monocarboxylic and dicarboxylic acids, PAHs, aldehydes, ketones, organic nitrates, organic sulfur compounds, amino derivatives etc. Anyhow, chemical speciation analysis is still very difficult and sometimes inconclusive (Choi et al., 2015; Lazaridis, 2008).

Organic carbon is one of the macro-components of PM and its quantification is usually carried out measuring the amount of carbon dioxide and methane released during a controlled combustion of the particulate material. The OC thus determined does not include the presence of heteroatoms, and this lack of information is troublesome for a correct reconstruction of the aerosol mass balance. Therefore, it is necessary to introduce an additional parameter defined as organic matter (OM) (Turpin et al., 2000). OM corrects OC for heteroatoms such as O and N, by means of a multiplicative empirical coefficient. OM compounds originate both from primary sources, such as PBAP, industrial and vehicle exhaust, and from secondary sources, such as the oxidation of volatile organic compounds in the atmosphere. The photo-oxidative processes of VOCs, precursors of numerous chemical species in atmospheric aerosols, are briefly illustrated in Figure 16:

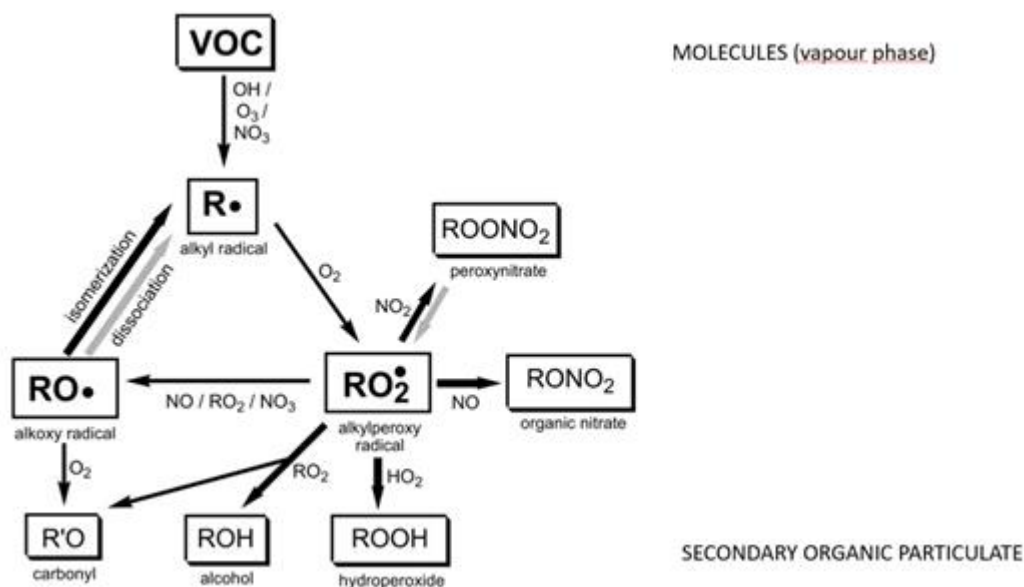


Figure 16. SOA production mechanism from VOCs (Kroll & Seinfeld, 2008)

Eventually, the **aqueous fraction** depends on the hygroscopicity of some of the major water-soluble components of PM (such as SIA), as well as on the atmospheric properties such as relative humidity.

The average composition of PM varies according to the size fraction and the formation processes. The variation of the composition of the particulate material as a function of the aerodynamic diameter is shown in Figure 17.

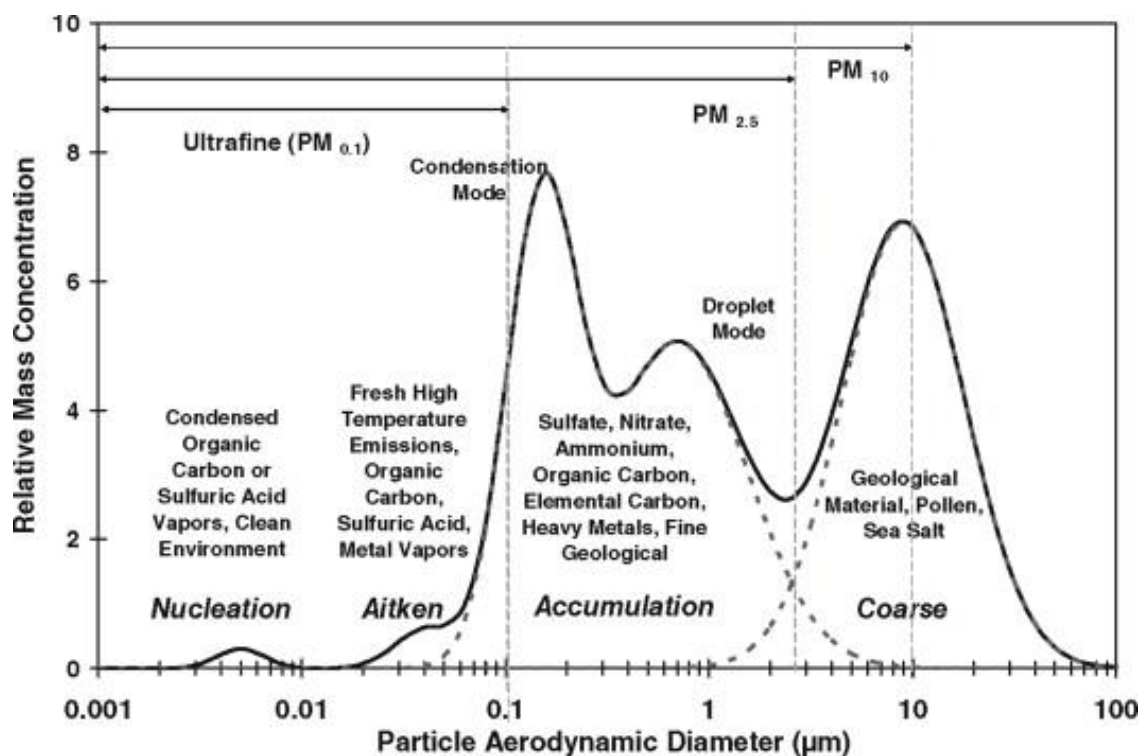


Figure 17. Generic compositional scheme of PM as a function of airborne particle size (Watson & Chow, 2007).

1.2.6 – Effects on the earth system, climate, and human health

It is widely recognized that atmospheric PM influences the global climate system and air quality (Fuzzi et al., 2015; Kim et al., 2015). Figure 18 presents a general scheme of the large-scale effects of atmospheric aerosols.

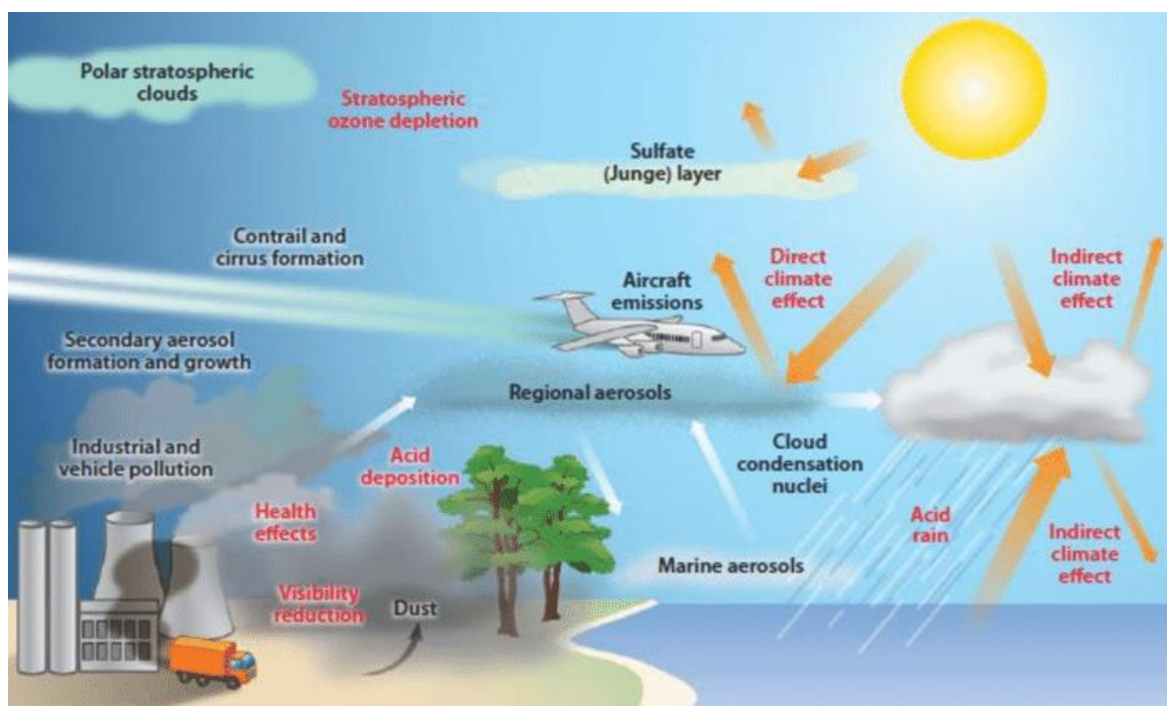


Figure 18. Graphical representation of the aerosol effects (Bimenyimana, 2018).

Atmospheric aerosol affects both directly and indirectly the Earth's climate by optically interacting with the incoming and outgoing electromagnetic radiation field (Bellouin et al., 2020). Indeed, airborne particles can absorb and/or scatter the solar radiation as a function of their chemical properties. Moreover, they may act as condensation nuclei for the formation of clouds (cloud condensation nuclei, CCN) that, in turn, reflect or absorb the solar radiation in the troposphere. Recently a further aerosol influence on climate has been enlightened and has to do with cloudwater precipitability, i.e. a situation in which cloud droplet cannot reach the critical size for precipitating owing to chemical components capable to decrease the surface tension of the droplets themselves, causing indirectly aridity at ground level (Bauer et al., 2010). Atmospheric aerosol contributes both positively (warming) and negatively (cooling) to the effective radiative forcing (ERF), an Earth's energy imbalance index defined as the energy flux (W m^{-2}) in the atmosphere caused by natural and/or anthropogenic factors of climate change (Shindell et al., 2013). Changes in atmospheric aerosol composition reflect a change in the Earth's energy balance (presently >0) and, therefore, justifying the measured increase in its surface temperature (IPCC, 2021).

Aerosol containing Black Carbon (BC) plays a dominant role because it has a remarkable ability to absorb solar radiation and contributes significantly to the warming of the lower atmosphere at the global and regional levels. Conversely, aerosols containing compounds with sulfates or mineral components scatter solar photons promoting the cooling of the atmosphere.

The indirect effect of the aerosol on climate takes place when the increase of numerical concentration of particles, produced from anthropogenic sources, contributes to an increase of the concentration of CCN. These are particles involved in the formation of clouds in the atmosphere. A part of solar radiation is reflected by the top of the clouds towards the outer space resulting in an overall cooling effect by reducing the incoming energy flux; however, if the aerosol particles entrained in clouds contains soot particles, the cloud assumes a greyish tone turning its behavior from reflecting into absorbing and, therefore, causing a warming effect. An increase in the number of "droplets" brings to an intensification of the cloud ability to reflect light, and to an increase of the cloud lifetime.

The Figure 19 shows the contributions of atmospheric aerosol to climate radiative forcing.

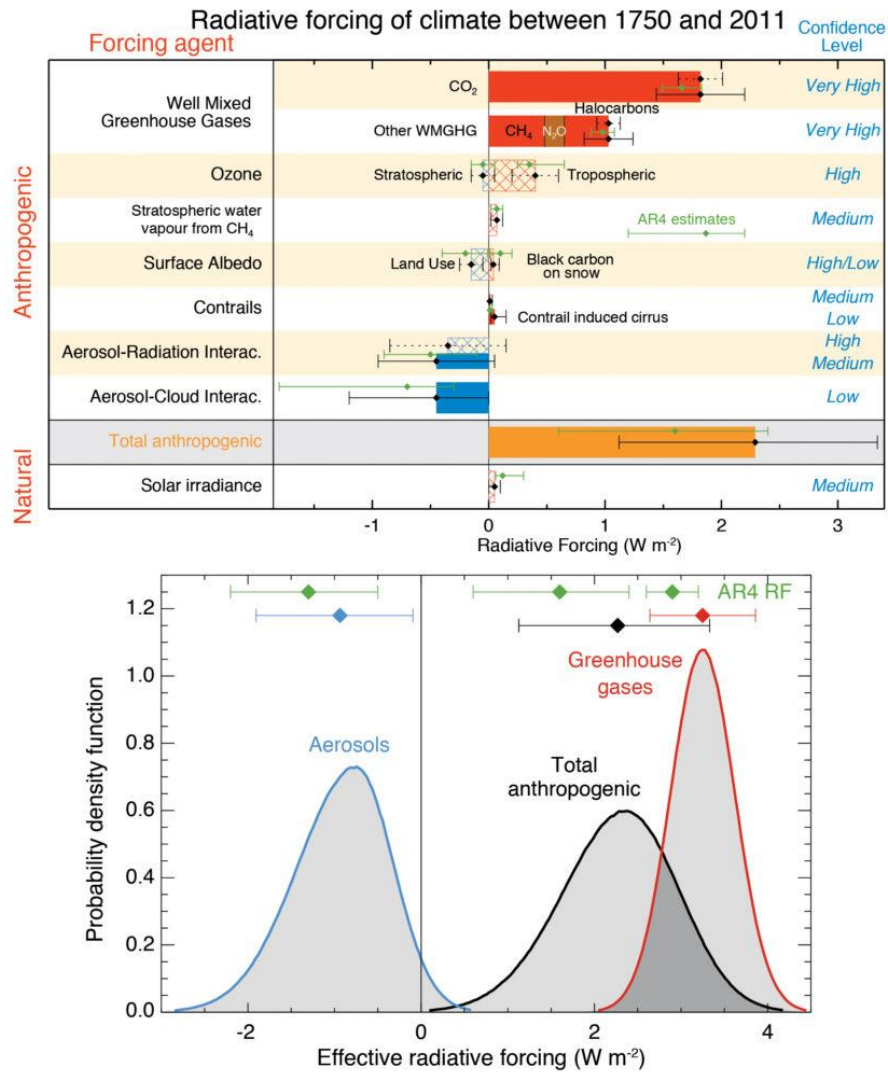


Figure 19. Contribution to ERF from component emissions from 1750 to 2011 (Cubasch, 2013).

Drawing the attention only on the aerosol contribution, a net cooling effect is observed. In fact, atmospheric aerosols contributed an ERF of -0.82 [-2.1 to $+0.17$] W m^{-2} over the period 1750 to 2011. This cooling effect is due to both aerosol–cloud interactions (ERF ≈ -0.55 W m^{-2}) and aerosol–radiation interactions (ERF ≈ -0.27 W m^{-2}). SO_2 emission changes contribute to a negative (cooling) ERF from aerosol–cloud interactions, as precursor of hygroscopic aerosols that act as CCN. Black carbon has a prevailing positive (warming) ERF as light-absorber, while Organic Carbon has a negative ERF as light-reflector.

Another effect connected directly with cloud composition concerns precipitation. The precipitation formation within the cloud depends on the size distribution and on the droplets that constitute the cloud: for a given water content, the occurrence of a low number of large drops produces precipitation. A characteristic growth of the droplets in clouds occurring within convective clouds at temperature above 0°C is the coalescence, in which large drops are pushed aloft while smaller droplets increase in size by collision. In the presence of drops of about $200\ \mu\text{m}$ size, these currents become insensitive to uplifting, thus large drops begin to fall furling the hydrological cycle. The decrease of rainfall, due to the reduction of the

size of cloud droplets, causes not only an increase of the cloud lifetime, but also the in reduction of the hydrological cycle and, ultimately, draught.

PM has been long associated with severe health hazard (WHO, 2021). Particle size and composition are the main drivers since size is connected with the penetration depth by inhalation into the breathing system, while particle toxicity depends on the chemical properties of specific PM components (Kim et al., 2015; Schraufnagel, 2020). Following inhalation, the particles are subjected to a sorting effect at various levels according to size; in brief, supermicron particle are lost progressively from the nasal cavity down to the bronchios, while the numerous fine and ultrafine particles may reach the alveoli and access the blood and lymphatic system (Figure 20).

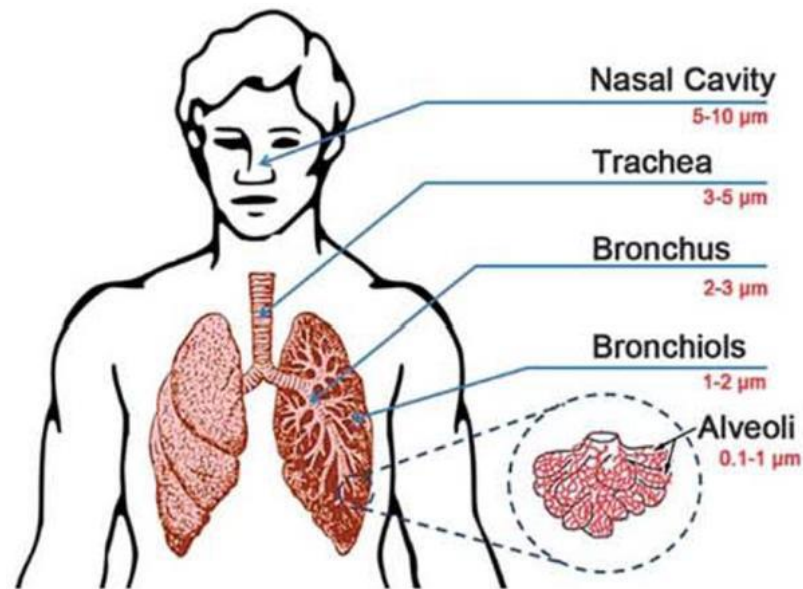


Figure 20. Deposition of airborne particles in respiratory tract, depending on the particle size (Kumar et al., 2013).

Coarse particles (from 10 to 1 μm) penetrate to a lesser extent into the respiratory system, limiting itself to the upper tract, thus affecting nose, mouth, throat, and trachea. Instead fine particles (from 2.5 to 0.1 microns) are able to penetrate to the innermost respiratory tract, down to the bronchus, bronchioles, alveoli and lung tissue, potentially causing serious damage to health such as the formation of tumors (Raaschou-Nielsen et al., 2016). $PM_{0.1}$, the most dangerous, can even cross the blood barrier and enter the bloodstream directly through the alveoli, for example by altering the coagulating capacity of the blood with consequent serious, sometimes fatal, cardio-vascular damage (Schraufnagel, 2020).

The toxicity of atmospheric particulate matter depends not only on its size, but also on its chemical composition, reactivity morphology, dose (concentration) and exposure (contact time of the individual with PM), and can generate various pathologies from allergies as well as the development of serious chronic diseases and premature deaths.

The aerosol components mainly responsible for health hazard, with the exception of soot (high surface area, capable to exchange substances and catalyze chemical reaction beside being conductive) at concentration levels comparable to the major PM components, are typically at trace level and include trace elements and a series of organic compounds.

Altogether, the main toxicity mechanism involved concerns the capacity of trace elements of triggering Reactive Oxygen Species (ROS, e.g. H_2O_2 , OH , O_3 , O_2^-) formation by Fenton-like reactions, a condition promoting oxidative stress from which many types of diseases originate. Oxidative stress consists of the breakdown of the physiological balance between the generation of free-radicals and their scavenging by antioxidants of human tissues.

To the scope, the concept of oxidative potential (OP, i.e the ability to create oxidative stress) of PM has been introduced, in order to provide a metric of aerosol toxicity. Figure 21 depicts the basic scheme of oxidative stress and ROS formation triggered by particulate matter.

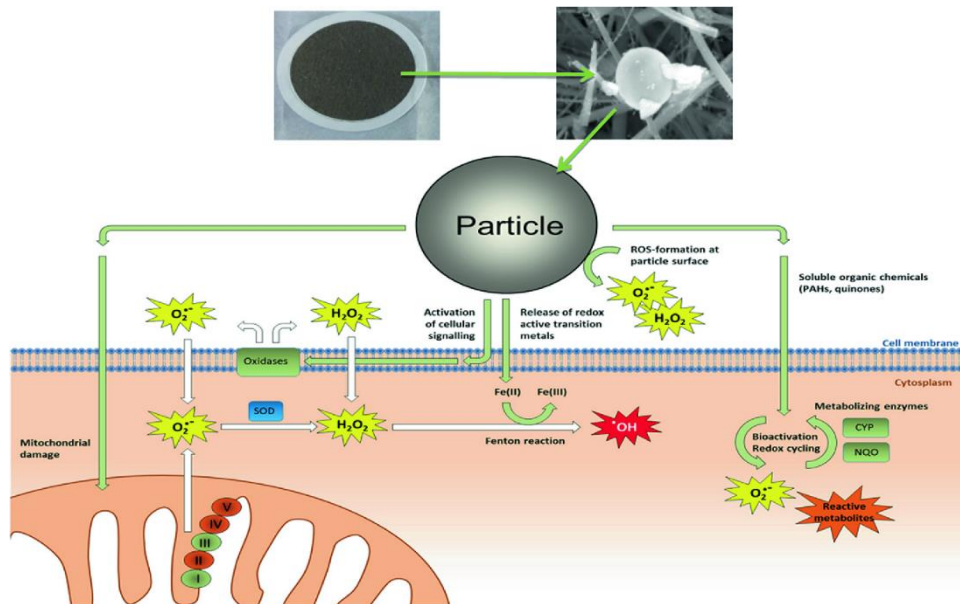


Figure 21. Oxidative stress promotion in cells exposed to atmospheric aerosol (Yadav, 2020)

Non-neutralized radicals are generated by chain reactions and may generate several metabolic disorders and a wide range of cardiovascular and autoimmune diseases (Rajagopalan et al., 2018; Zhao et al., 2019). Many studies have shown a significant correlation between the increase in air pollution and the upsurge of many other less apparently connected pathologies such as, for example, an increase in the risk of dementia. For example, the increase of airborne particles with a $\text{Da} < 2.5$ is associated with delayed psychomotor development in children (Schraufnagel et al., 2019). Other studies also link air pollution to a weakening of the immune system, an increase in allergies, osteoporosis, inflammatory bowel diseases and an increase in intravascular coagulation (Schraufnagel et al., 2019).

1.3 – Published scientific articles and work in progress

Following the premise of the Thesis and the fundamentals of atmospheric aerosols, below are stated the main topics of the following Chapters and how the latter are related to environmental chemistry and, specifically, to atmospheric aerosols.

Chapter 2 refers to atmospheric particles released from the biosphere to the atmosphere (Primary Biological Aerosol, in short bioaerosol), that represent one of the most innovative and challenging research areas in Aerosol Science. Bioaerosol includes living and dead microorganisms (such as bacteria, fungi, and viruses), their dispersal units (e.g., pollen and spores), as well as tissue fragments from decay processes. In this perspective, a scientific article was published on Scientific Reports (Nature) relating to Bacterial DNA sequencing from collected particulate matter in Savona (Italy) over a six months campaign in 2012. This work was carried out with the collaboration of the Laboratory of Microbiology, FaBiT (UNIBO), coordinated by Prof. Marco Candela. Bacterial DNA advanced sequencing techniques represents a frontier approach in aerosol science, allowing to obtain information on the relative abundance of the bacterial families that inhabit PM samples, wherein the biological component is always a matter of fact, but which so far has been scarcely characterized. This analytical approach required a significant interface of chemists and biologists so far unprecedented in this field. My specific role in this research was to optimize chemometric techniques capable to intercept the association between the bacterial and the chemical information obtained on PM samples investigated for environmental diagnosis, meteorological conditions, and data interpretation. The importance of this kind of studies is very important, especially considering the recent global SARS-CoV-2 pandemic. Indeed, the potential role of PM in the spreading of COVID-19 and consequent increase of morbidity and mortality is still obscure and a comprehensive discussion within the scientific community is required.

Chapter 3 describes another relevant research theme in Aerosol Science that involves "Saharan dust", i.e. mineral dust uplifted into the troposphere by atmospheric turbulence and wind in the North African desert. It is well-known how this aerosol component of PM can move across thousands of kilometers, including the Mediterranean basin, altering climate by modifying PM radiative forcing as well as triggering and/or amplifying adverse effects on human health. In this framework, a scientific article was published on Atmospheric Environment (Elsevier) where the feasibility of UV-visible diffuse reflectance spectroscopy (UV-VIS DRS) was described as a rapid, inexpensive, and non-destructive method for the rapid identification of Saharan dust events in PM filters. This non-destructive analytical method allows to parameterize the color of the analyzed filter and obtain semi-quantitative information on the iron oxide minerals present. While the color component is important in the field of climate change as it interferes with the radiative transfer in the visible range of incoming solar radiation and in the IR for the outgoing terrestrial radiation, Iron is a bioactive element capable to interfere negatively with living systems through Fenton-like mechanisms which depend on its chemical speciation/redox state. The analyses were performed at the Lab for Chemistry and Technologies of the Environment and Materials– Faenza (UNIBO). I have been responsible of the experimental setup, and designed and 3D-printed a dedicated sample holder for PM analysis. This technique was initially tested with a preliminary number of PM samples mainly containing "mineral dust", collected at Sierra Nevada (Southern Spain) and provided by the Radiochemistry and Environmental Radiology Laboratory of the Inorganic Chemistry Department of Granada (LABRADIQ). It has been mathematically demonstrated how, as the concentration of hematite increases, the samples have a more reddish-brown color, with an increase in PM₁₀ above the EU Air quality standards. Therefore, this technique can be extremely useful in identifying unambiguously and in a fast

and cheap way an incursion of desert dust in the atmosphere. These episodes are not due to pollution but to “natural” processes and therefore need to be eliminated from the samples above the law threshold. However, it is important to underline that these events, although considered natural according to current legislation, their frequency and intensity have significantly increased due to desertification, a consequence of global warming caused by humans.

Chapter 4 faces the airborne particulate toxicity mainly attributed to oxidative stress, i.e. a pathological condition originated from the breakdown of the physiological balance between the generation of Reactive Oxygen Species (ROS, including H_2O_2 , $\text{O}_2^{\cdot-}$, $^1\text{O}_2$, $^{\cdot}\text{OH}$, O_3 , hypohalous acids, organic peroxides, ...) and the antioxidant capacity of human tissues. Non-neutralized free radicals lead to the damage of cells, tissues, and organs. Therefore, ROS concentration is considered as an efficient predictor of PM hazard and the term oxidative potential (OP), the ability to produce oxidative stress, has been consequently introduced as a suitable metric. In this framework, a scientific article was published on Science of the Total Environment (Elsevier) concerning a new and original chemiluminescent method based on the dependence of luminol (5-Amino-2,3-dihydrophthalazine-1,4-dione) light emission induced by free radicals in airborne PM. This analytical technique allows to obtain semi-quantitative information on the ROS and therefore, information regarding PM OP. This work was carried out with the collaboration of the Analytical Chemistry Lab, FaBiT (UNIBO), coordinated by Prof. Stefano Girotti. I have been responsible of the experimental methodology for PM analysis and statistical data analysis. This technique was tested with certified reference materials and applied to two series of PM samples previously subjected to thorough chemical speciation and subsequent source apportionment. The results show the effectiveness of the luminescent method, allowing the quick assessment of particulate matter oxidative potential, but providing further evidence on the complexity of the oxidative potential determination, characterized by multiple and differentiated mechanisms/kinetics observed in this kind of environmental samples.

Chapter 5 includes miniaturized, low-cost sensors based on laser scattering devices for aerosol characterization. These kinds of devices are increasingly used for air quality monitoring, as they allow to collect PM data at high space and time resolution on account of the remarkable inhomogeneity of PM sources and resulting concentration levels. However, while the easy availability of OPCs, management standardization protocols accounting for PM physico-chemical properties are often neglected, leading to loss of reliability of the potentially precious PM data collected. In this context, a scientific article was published on Sensors (MDPI) based on the results of an intensive field campaign performed on the roof of the Department of Physics and Astronomy DIFA (UNIBO) under different weather conditions. Briefly, the performances of a series of sensors were evaluated against a calibrated mainstream OPC with a heated inlet, using a robust approach based on a suite of statistical indexes capable of evaluating both correlations and biases in respect to the reference sensor. The results of this study indicate that low-cost OPC sensors may be affected by relevant biases depending on the explored temporal resolution, PM chemical composition, and prevailing weather conditions.

Chapter 6 presents the analysis of an exceptional event of mineral dust transport that impacted northern Italy at the end of March 2020. The event originated over the Aralkum region, a desert area formed in recent times owing to the almost complete drying of the Aral Lake, that is recently drawing ever-increasing attention by researchers owing to a multitude of climatic and environmental implications. The event was observed through aerosol number concentrations retrieved by OPCs located at three different sites in north-eastern Italy,

namely Bologna, Trieste, and the high altitude WMO-GAW observatory of Mt. Cimone (<https://cimone.isac.cnr.it/>). Data analysis includes an accurate meteorological assessment in order to identify the peculiar synoptic conditions leading to the event. Back-trajectories analysis was used to identify the source region. Aerosol behavior during transport over Italy was analyzed by optical particle spectrometry, while multiple data based on remote sensing (satellites, LIDAR, and AERONET sun photometers) were employed to gain a dynamical 3D characterization of the mineral dust transport. My specific role in this research was mainly linked to back-trajectories analysis, which allows to simulate the transport of air masses at the three locations of the OPCs over the whole period of the event. This analysis allowed to confirm and support the origin of the studied mineral dust event from Central Asia. This work was recently submitted to Atmospheric Chemistry and Physics (ACP) and the preprint version is currently under review.

Chapter 7 consist of a scientific article published on *Molecules* (MDPI) concerning an innovative and non-destructive method for the quantification of biogenic silica (biosilica) in marine sediments by total reflection Fourier transform infrared (ATR-FTIR) spectroscopy combined with chemometrics. Biosilica represents the major component of the external skeleton of marine micro-organisms, such as diatoms, which, after the organisms death, settle down onto the seabed. These micro-organisms are involved in the CO₂ cycle because they remove it from the atmosphere through photosynthesis. Therefore, the quantification of biosilica in marine sediments may represents an interesting indicator of primary productivity related to CO₂ trends, both in the present and past epochs. My specific role in this research has mainly been to support the optimization of sample preparation and analysis by ATR-FTIR. Indeed, these experimental steps are fundamental in order to provide a reliable background useful to solve reproducibility problems, which may constitute a drawback of such a simple instrumental approach.

Chapter 8 illustrates a scientific article published on *Science of the Total Environment* (Elsevier) that depicts the assessment of the atmospheric deposition processes over an area of complex topography capable to affect the dispersal of atmospheric pollution. The study required a multidisciplinary approach based on the data collected within an extensive physico-chemical characterization of the soils, combined with the local meteorology and complemented by suitable multivariate analysis and atmospheric modelling. Specifically, this paper is based on a transect of surface soil cores collected at ten stations along a mountainous transect across the Terni Basin, an area heavily impacted by human activities in Umbria, Central Italy. At each station, radionuclides, inorganic, and organic pollutants were determined as a function of station height and soil depth. Finally, their connections with atmospheric deposition were analyzed. My specific role in this research was mainly related to multivariate statistical analysis to intercept similarity between soil sampling stations, their association with atmospheric radionuclides, and the occurrence of the atmospheric components into the soils.

Chapter 9 reports the preliminary study and characterization of the processes and dynamics of atmospheric aerosol in the touristic Pertosa-Auletta cave (Italy, SA), in collaboration with MIIdA Foundation and the University of Salerno (UNISA). This activity is based on the sampling of cave aerosol and drip water samples, assisted by meteorological analysis tools typical of both outdoor and indoor atmospheric environments, to understand the complex phenomenologies and outline the best strategies for the correct maintenance of the cave, vulnerable from both the chemical and biological point of view. My role in this work has been the analysis of drip waters by Ion Chromatography (IC) and data processing and interpretation. So far this study has covered the analysis (anions and cations) of almost 90 samples and multivariate analysis of this data together with parallel extensive analysis data

(elements, total organic carbon, total nitrogen, pH, ORP, conductivity) carried out at UNISA. More samples for a complete seasonal coverage are expected in the next months.

Chapter 10 presents the preliminary results of another research in progress that concerns the characterization and quantification of radionuclides in innovative building materials defined as “Geopolymers”, i.e. inorganic polymers obtained by the Alkali activation of an aluminosilicate precursor. The main sources of aluminosilicates can be natural minerals such as clays, kaolinite, etc. but also industrial waste materials, for example: red mud (waste from industrial production of aluminum), fly ash (by-product of coal combustion), slag produced by the separation of a metal from its ore, etc. The most used alkaline activator is sodium hydroxide (NaOH). The possibility of reusing waste materials for geopolymer synthesis, in addition to the economic advantage, lead them to be considered as eco-sustainable materials. However, despite the environmental and economic benefits (reduction of CO₂ emission typical of cement as well as waste reduction), it is mandatory to estimate the health risk associated with the radioactivity of building materials as required by the recent Euratom Directive on Radiation Protection. This work is in progress with the collaboration of the Laboratory of Prof. Maria Bignozzi in the Department of Civil, Chemical, Environmental and Materials Engineering (DECAM - UNIBO). My role in this work consists on the analysis of geopolymers and their precursors by High-Resolution Gamma-Ray Spectroscopy, data interpretation, and calculation of dosimetric indices for health risk assessment as required by the DL 101/2020 (Italian Decree Law N.101 31st July 2020).

Chapter 11 reports the preliminary results of an extensive work in progress within the FRESA³ project, in collaboration with the research group of Professor J.A.G. Orza from the Department of Applied Physics of the University Miguel Hernandez of Elche, in Spain. This project is certainly my main research project in terms of time spent and scientific skills. This challenging project involves the study of Mineral dust uplifted into the atmosphere by the wind in arid and semi-arid regions of North Africa reaching the Mediterranean basin and, in this specific case, southern Spain. The issue is pressing because the ongoing global warming has led to an increase in the frequency and intensity of Saharan Dust outbreaks, with direct effect on climate by modifying PM radiative forcing as well as their adverse effects on human health. As part of this project, PM samples with PTFE support were collected simultaneously at the two Spanish stations of Sierra Nevada and Granada. The sampling site of Granada is located at the faculty of Sciences of the University of Granada, represents an urban environment. Instead, the Sierra Nevada sampling site (2550 m asl) is located near Pico Veleta, just 25 Km away from Granada, but in an high altitude environment slightly affected by anthropogenic activities. Over the past 3 years, around 800 filters have been sampled and analyzed by an integrated methodology based on the synergistic use of different analytical techniques: Ion Chromatography (IC) for the quantification of the main water-soluble cations and anions, which represent a large mass fraction of ambient PM; Particle Induced X-ray Emission (PIXE), an IBA (Ion Beam Analysis) technique that allows to identify and quantify simultaneously and in a non-destructive way, a significant number of chemical elements present in the analyzed sample; UV-VIS DRS, that is a non-destructive analytical method that allows to parameterize the color of the analyzed filter, by mathematical model known as colorimetric space, and obtain semi-quantitative information on the iron oxide minerals present; InfraRed (IR) analysis in transmission mode, that is an unusual analytical technique for PM membranes allowing to obtain, in a non-destructive way, fingerprints of the IR-active functional groups. The innovation in the approach proposed mainly concerns the choice of a series of analytical techniques most of which are

³ Impact of dust-laden African air masses and of stratospheric air masses in the Iberian Peninsula. Role of the Atlas mountains. Ref: CGL2015-70741-R

uncommon in aerosol analysis, like IR spectroscopy and UV-VIS DRS, beside PIXE, while obtaining extensive compositional information on a relevant number PM samples. While chemical speciation is only a preliminary step, this project also aims at source apportionment and at the synergistic integration of physical and meteorological characterization and, in particular, "backtrajectories" modeling (an issue that I studied in depth during my research period abroad as part of the Marco Polo grant). My role in this work concerns the chemical characterization of the hundreds PM filters by IC, UV-VIS DRS, and IR, data processing through multivariate statistics and interpretation of the results. At present, all the chemical analyses have been almost completed (the PIXE analysis lacks about 100 samples, owing to the need of applying for beam time at AN2000 accelerator at scheduled times in the year). Advanced multivariate techniques have been applied to IC, FT-IR and UV-Vis Reflectance data.

Table 2 summarizes the published scientific works and work in progress reported in this Thesis.

Table 2. Lists of the scientific publications and work in progress

<i>Chapter</i>	<i>Title</i>	<i>Journal</i>
2	Particulate matter emission sources and meteorological parameters combine to shape the airborne bacteria communities in the Ligurian coast, Italy	Scientific Reports (Nature) ^a
3	Ultraviolet–Visible Diffuse Reflectance Spectroscopy (UV–Vis DRS), a rapid and non-destructive analytical tool for the identification of Saharan dust events in particulate matter filters	Atmospheric Environment (Elsevier) ^b
4	Chemiluminescent fingerprints from airborne particulate matter: A luminol-based assay for the characterization of oxidative potential with kinetical implications	Atmospheric Environment (Elsevier) ^b
5	How to Get the Best from Low-Cost Particulate Matter Sensors: Guidelines and Practical Recommendations	Sensors (MDPI) ^c
6	Development and evolution of an anomalous Asian dust event across Europe in March 2020 (preprint)	Atmospheric Chemistry and Physics (EGU) ^d
7	ATR-FTIR Spectroscopy, a New Non-Destructive Approach for the Quantitative Determination of Biogenic Silica in Marine Sediments	Molecules (MDPI) ^e
8	Deposition processes over complex topographies: Experimental data meets atmospheric modeling	Science of The Total Environment (Elsevier) ^f
9	Chemical characterization of drip and river waters in the Pertosa Auletta cave (SA, Italy)	<i>Not yet published article</i>
10	Radioactivity measurements of innovative and sustainable building materials: Geopolymers	<i>Not yet published article</i>
11	Applications of non-destructive spectroscopic techniques and multivariate statistics for the analysis of Spanish atmospheric aerosol collected on membranes	<i>Not yet published article</i>

According to SCImago Journal Rank (SJR), on 29/10/2021, the Journal Impact Factor quartiles are:

^a Multidisciplinary (Q1)

^b Atmospheric Science (Q1); Environmental Science (miscellaneous) (Q1)

^c Analytical Chemistry (Q2); Atomic and Molecular Physics, and Optics (Q2); Electrical and Electronic Engineering (Q2); Information Systems (Q2); Instrumentation (Q2); Medicine (miscellaneous) (Q2); Biochemistry (Q3)

^d Atmospheric Science (Q1)

^e Chemistry (miscellaneous) (Q1); Pharmaceutical Science (Q1); Analytical Chemistry (Q2); Drug Discovery (Q2); Medicine (miscellaneous) (Q2); Organic Chemistry (Q2); Physical and Theoretical Chemistry (Q2); Molecular Medicine (Q3)

^f Environmental Chemistry (Q1); Environmental Engineering (Q1); Pollution (Q1); Waste Management and Disposal (Q1)

References

- Amann M., Gomez-Sanabria A., Klimont Z., Maas R., Winiwarter W. (2017). Measures to address air pollution from agricultural sources. https://ec.europa.eu/environment/air/pdf/clean_air_outlook_agriculture_report.pdf
- Andreae, M. O. (2007). Atmosphere. Aerosols before pollution. *Science*, 315(5808), 50–51.
- Andreae, M. O., & Gelencsér, A. (2006). Black carbon or brown carbon? The nature of light-absorbing carbonaceous aerosols. *Atmos. Chem. Phys.*, 6(10), 3131–3148. <https://doi.org/10.5194/acp-6-3131-2006>
- Bauer, S. E., Menon, S., Koch, D., Bond, T. C., & Tsigaridis, K. (2010). A global modeling study on carbonaceous aerosol microphysical characteristics and radiative effects. *Atmospheric Chemistry and Physics*, 10(15), 7439–7456
- Bellouin, N., Quaas, J., Gryspeerdt, E., Kinne, S., Stier, P., Watson-Parris, D., Boucher, O., Carslaw, K. S., Christensen, M., Daniau, A.-L., Dufresne, J.-L., Feingold, G., Fiedler, S., Forster, P., Gettelman, A., Haywood, J. M., Lohmann, U., Malavelle, F., Mauritsen, T., ... Stevens, B. (2020). Bounding Global Aerosol Radiative Forcing of Climate Change. *Reviews of Geophysics*, 58(1), e2019RG000660. <https://doi.org/https://doi.org/10.1029/2019RG000660>
- Bimenyimana, S. (2018). Continuous Real-Time Measurement of the Chemical Composition of Submicron Aerosol Particles in Kigali City Using Aerosol Chemical Speciation Monitor (ACSM) (Doctoral dissertation, University of Rwanda).
- Briggs, N. L., & Long, C. M. (2016). Critical review of black carbon and elemental carbon source apportionment in Europe and the United States. *Atmospheric Environment*, 144, 409–427. <https://doi.org/https://doi.org/10.1016/j.atmosenv.2016.09.002>
- Capello, F., & Gaddi, A. V. (2018). *Clinical handbook of air pollution-related diseases*. Springer.
- Chin, M., & Kahn, R. (2009). *Atmospheric aerosol properties and climate impacts (Vol. 2)*. US Climate Change Science Program.
- China S. and Mazzoleni C. (2018). "Preface: Morphology and Internal Mixing of Atmospheric Particles" *Atmosphere* 9, no. 7: 249. <https://doi.org/10.3390/atmos9070249>
- Choi, J. K., Ban, S. J., Kim, Y. P., Kim, Y. H., Yi, S. M., & Zoh, K. D. (2015). Molecular marker characterization and source appointment of particulate matter and its organic aerosols. *Chemosphere*, 134, 482–491.
- Coude-Gaussen, G., Rognon, P., Bergametti, G., Gomes, L., Strauss, B., Gros, J. M., & le Coustumer, M. N. (1987). Saharan dust on Fuerteventura Island (Canaries): Chemical and mineralogical characteristics, air mass trajectories, and probable sources. *Journal of Geophysical Research: Atmospheres*, 92(D8), 9753–9771. <https://doi.org/https://doi.org/10.1029/JD092iD08p09753>
- Cubasch U., (2013). AR5 Climate Change 2013: The Physical Science Basis, Technical Summary. <https://www.ipcc.ch/report/ar5/wg1/technical-summary>
- EEA Report No 9/2020. The Air quality in Europe report provides an annual assessment of the status and impacts of air quality and recent air quality trends. The report supports policy development and implementation in the field of air quality at both European and national levels. <https://www.eea.europa.eu/publications/air-quality-in-europe-2020-report>
- EEA IND-366-en, CSI 040 , AIR 005 Published 04 Sep 2019. Emissions of the main air pollutants in Europe. <https://www.eea.europa.eu/data-and-maps/indicators/main-anthropogenic-air-pollutant-emissions/assessment-6>

- Formenti, P., Caquineau, S., Chevaillier, S., Klaver, A., Desboeufs, K., Rajot, J. L., Belin, S., & Briois, V. (2014). Dominance of goethite over hematite in iron oxides of mineral dust from Western Africa: Quantitative partitioning by X-ray absorption spectroscopy. *Journal of Geophysical Research: Atmospheres*, 119(22), 12, 712–740, 754. <https://doi.org/https://doi.org/10.1002/2014JD021668>
- Fröhlich-Nowoisky, J., Kampf, C. J., Weber, B., Huffman, J. A., Pöhlker, C., Andreae, M. O., Lang-Yona, N., Burrows, S. M., Gunthe, S. S., Elbert, W., Su, H., Hoor, P., Thines, E., Hoffmann, T., Després, V. R., & Pöschl, U. (2016). Bioaerosols in the Earth system: Climate, health, and ecosystem interactions. *Atmospheric Research*, 182, 346–376. <https://doi.org/https://doi.org/10.1016/j.atmosres.2016.07.018>
- Fuzzi, S., Baltensperger, U., Carslaw, K., Decesari, S., Denier van der Gon, H., Facchini, M. C., Fowler, D., Koren, I., Langford, B., Lohmann, U., Nemitz, E., Pandis, S., Riipinen, I., Rudich, Y., Schaap, M., Slowik, J. G., Spracklen, D. v, Vignati, E., Wild, M., ... Gilardoni, S. (2015). Particulate matter, air quality and climate: lessons learned and future needs. *Atmos. Chem. Phys.*, 15(14), 8217–8299. <https://doi.org/10.5194/acp-15-8217-2015>
- Italian Decree Law N.101 31st july 2020. <https://www.gazzettaufficiale.it/eli/id/2020/08/12/20G00121/sg>
- Ginoux, P., Prospero, J. M., Gill, T. E., Hsu, N. C., & Zhao, M. (2012). Global-scale attribution of anthropogenic and natural dust sources and their emission rates based on MODIS Deep Blue aerosol products. *Reviews of Geophysics*, 50(3).
- Harapan, H., Itoh, N., Yufika, A., Winardi, W., Keam, S., Te, H., Megawati, D., Hayati, Z., Wagner, A. L., & Mudatsir, M. (2020). Coronavirus disease 2019 (COVID-19): A literature review. *Journal of Infection and Public Health*, 13(5), 667–673. <https://doi.org/https://doi.org/10.1016/j.jiph.2020.03.019>
- Harrison, R. M., & Kitto, A.-M. N. (1992). Estimation of the rate constant for the reaction of acid sulphate aerosol with NH₃ gas from atmospheric measurements. *Journal of Atmospheric Chemistry*, 15(2), 133–143.
- Haynes, W. M. (Ed.). (2014). *CRC handbook of chemistry and physics*. CRC press.
- Hewitt, C. N. (2001). The atmospheric chemistry of sulphur and nitrogen in power station plumes. *Atmospheric Environment*, 35(7), 1155–1170. [https://doi.org/https://doi.org/10.1016/S1352-2310\(00\)00463-5](https://doi.org/https://doi.org/10.1016/S1352-2310(00)00463-5)
- Heyder, J., & Porstendörfer, J. (1974). Comparison of optical and centrifugal aerosol spectrometry: liquid and non-spherical particles. *Journal of Aerosol Science*, 5(4), 387–400. [https://doi.org/https://doi.org/10.1016/0021-8502\(74\)90135-9](https://doi.org/https://doi.org/10.1016/0021-8502(74)90135-9)
- Hoose, C., Lohmann, U., Bennartz, R., Croft, B., and Lesins, G. (2008). Global simulations of aerosol processing in clouds, *Atmos. Chem. Phys.*, 8, 6939–6963, <https://doi.org/10.5194/acp-8-6939-2008>
- Huneus, N., Schulz, M., Balkanski, Y., Griesfeller, J., Prospero, J., Kinne, S., Bauer, S., Boucher, O., Chin, M., Dentener, F., Diehl, T., Easter, R., Fillmore, D., Ghan, S., Ginoux, P., Grini, A., Horowitz, L., Koch, D., Krol, M. C., ... Zender, C. S. (2011). Global dust model intercomparison in AeroCom phase I. *Atmos. Chem. Phys.*, 11(15), 7781–7816. <https://doi.org/10.5194/acp-11-7781-2011>
- IPCC (2021). *AR6 Climate Change 2021: The Physical Science Basis*. <https://www.ipcc.ch/report/ar6/wg1/#SPM>
- John, W. (2011). Size Distribution Characteristics of Aerosols. In *Aerosol Measurement* (eds P. Kulkarni, P.A. Baron and K. Willeke). <https://doi.org/10.1002/9781118001684.ch4>
- Karagulian, F., Belis, C. A., Dora, C. F. C., Prüss-Ustün, A. M., Bonjour, S., Adair-Rohani, H., & Amann, M. (2015). Contributions to cities' ambient particulate matter

- (PM): A systematic review of local source contributions at global level. *Atmospheric Environment*, 120, 475–483. <https://doi.org/https://doi.org/10.1016/j.atmosenv.2015.08.087>
- Kim, K.-H., Kabir, E., & Kabir, S. (2015). A review on the human health impact of airborne particulate matter. *Environment International*, 74, 136–143. <https://doi.org/https://doi.org/10.1016/j.envint.2014.10.005>
 - Kroll, J. H., & Seinfeld, J. H. (2008). Chemistry of secondary organic aerosol: Formation and evolution of low-volatility organics in the atmosphere. *Atmospheric Environment*, 42(16), 3593–3624. <https://doi.org/https://doi.org/10.1016/j.atmosenv.2008.01.003>
 - Kulmala, M., Kontkanen, J., Junninen, H., Lehtipalo, K., Manninen, H. E., Nieminen, T., Petäjä, T., Sipilä, M., Schobesberger, S., & Rantala, P. (2013). Direct observations of atmospheric aerosol nucleation. *Science*, 339(6122), 943–946.
 - Kumar, A., Chen, F., Mozhi, A., Zhang, X., Zhao, Y., Xue, X., Hao, Y., Zhang, X., Wang, P. C., & Liang, X.-J. (2013). Innovative pharmaceutical development based on unique properties of nanoscale delivery formulation. *Nanoscale*, 5(18), 8307–8325.
 - Kumar, P., Morawska, L., Birmili, W., Paasonen, P., Hu, M., Kulmala, M., ... & Britter, R. (2014). Ultrafine particles in cities. *Environment international*, 66, 1-10. <https://doi.org/10.1016/j.envint.2014.01.013>
 - Lazaridis, M. (2008). Organic Aerosols. In *Environmental Chemistry of Aerosols*, I. Colbeck (Ed.). <https://doi.org/10.1002/9781444305388.ch4>
 - Leelőssy, Á., Molnár, F., Izsák, F., Havasi, Á., Lagzi, I., & Mészáros, R. (2014). Dispersion modeling of air pollutants in the atmosphere: a review. *Central European Journal of Geosciences*, 6(3), 257–278. <https://doi.org/10.2478/s13533-012-0188-6>
 - Lewis, E. R., Lewis, R., Lewis, E. R., & Schwartz, S. E. (2004). Sea salt aerosol production: mechanisms, methods, measurements, and models (Vol. 152). American geophysical union.
 - Linke, C., Möhler, O., Veres, A., Mohácsi, Á., Bozóki, Z., Szabó, G., Schnaiter, M., Optical properties and mineralogical composition of different Saharan mineral dust samples: a laboratory study (2006) *Atmos. Chem. Phys.*, 6 (11), pp. 3315-3323
 - Marani, M., Katul, G. G., Pan, W. K., & Parolari, A. J. (2021). Intensity and frequency of extreme novel epidemics. *Proceedings of the National Academy of Sciences*, 118(35).
 - Margitan, J. J. (1984). Mechanism of the atmospheric oxidation of sulfur dioxide. Catalysis by hydroxyl radicals. *The Journal of Physical Chemistry*, 88(15), 3314–3318. <https://doi.org/10.1021/j150659a035>
 - Molinaroli, E., & Masiol, M. (2006). *Particolato atmosferico e ambiente mediterraneo. Il caso delle polveri sahariane.*
 - Pöschl, U. (2020). Air Pollution, Oxidative Stress, and Public Health in the Anthropocene. In W. K. Al-Delaimy, V. Ramanathan, & M. Sánchez Sorondo (Eds.), *Health of People, Health of Planet and Our Responsibility: Climate Change, Air Pollution and Health* (pp. 79–92). Springer International Publishing. https://doi.org/10.1007/978-3-030-31125-4_7
 - Prinn, R. G. (2003). The cleansing capacity of the atmosphere. *Annual Review of Environment and Resources*, 28(1), 29-57.
 - Raaschou-Nielsen, O., Beelen, R., Wang, M., Hoek, G., Andersen, Z. J., Hoffmann, B., Stafoggia, M., Samoli, E., Weinmayr, G., Dimakopoulou, K., Nieuwenhuijsen, M., Xun, W. W., Fischer, P., Eriksen, K. T., Sørensen, M., Tjønneland, A., Ricceri, F., de Hoogh, K., Key, T., ... Vineis, P. (2016). Particulate matter air pollution components and risk for lung cancer. *Environment International*, 87, 66–73. <https://doi.org/https://doi.org/10.1016/j.envint.2015.11.007>

- Raes, F., Dingenen, R. van, Vignati, E., Wilson, J., Putaud, J.-P., Seinfeld, J. H., & Adams, P. (2000). Formation and cycling of aerosols in the global troposphere. *Atmospheric Environment*, 34(25), 4215–4240. [https://doi.org/https://doi.org/10.1016/S1352-2310\(00\)00239-9](https://doi.org/https://doi.org/10.1016/S1352-2310(00)00239-9)
- Rodríguez, S., Calzolari, G., Chiari, M., Nava, S., García, M.I., López-Solano, J., Rapid changes of dust geochemistry in the Saharan Air Layer linked to sources and meteorology (2020) *Atmos. Environ.*, 223, p. 117186
- Salako, G. O., Hopke, P. K., Cohen, D. D., Begum, B. A., Biswas, S. K., Pandit, G. G., Lodoysamba, S., Wimolwattanapun, W., Bunprapob, S., Chung, Y.-S., Rahman, S. A., Hamzah, M. S., Davy, P., Markwitz, A., & Shagjjamba, D. (2012). Exploring the Variation between EC and BC in a Variety of Locations. *Aerosol and Air Quality Research*, 12(1), 1–7. <https://doi.org/10.4209/aaqr.2011.09.0150>
- Schraufnagel, D. E. (2020). The health effects of ultrafine particles. *Experimental & Molecular Medicine*, 52(3), 311–317. <https://doi.org/10.1038/s12276-020-0403-3>
- Schraufnagel, D. E., Balmes, J. R., Cowl, C. T., de Matteis, S., Jung, S.-H., Mortimer, K., Perez-Padilla, R., Rice, M. B., Riojas-Rodriguez, H., Sood, A., Thurston, G. D., To, T., Vanker, A., & Wuebbles, D. J. (2019). Air Pollution and Noncommunicable Diseases: A Review by the Forum of International Respiratory Societies ’ Environmental Committee, Part 1: The Damaging Effects of Air Pollution. *CHEST*, 155(2), 409–416. <https://doi.org/10.1016/j.chest.2018.10.042>
- Steinfeld, J. I., Pandis S.N. (2016). *Atmospheric chemistry and physics: from air pollution to climate change*, 3rd Edition. ISBN: 978-1-118-94740-1.
- Sierra-Vargas, M. P., Vargas-Domínguez, C., Bobadilla-Lozoya, K., & Aztatzi-Aguilar, O. G. (2018). Health impact of volcanic emissions. *Volcanoes-Geological and Geophysical Setting, Theoretical Aspects and Numerical Modeling, Applications to Industry and Their Impact on the Human Health*, 395, 116–124.
- Tositti, L. (2018). Physical and chemical properties of airborne particulate matter & The relationship between health effects and airborne particulate constituents. In *Clinical Handbook of Air Pollution-Related Diseases* (pp. 7-54). Springer, Cham.
- Turpin, B. J., Saxena, P., & Andrews, E. (2000). Measuring and simulating particulate organics in the atmosphere: problems and prospects. *Atmospheric Environment*, 34(18), 2983–3013. [https://doi.org/https://doi.org/10.1016/S1352-2310\(99\)00501-4](https://doi.org/https://doi.org/10.1016/S1352-2310(99)00501-4)
- Von Schneidmesser, E., Monks, P. S., Allan, J. D., Bruhwiler, L., Forster, P., Fowler, D., ... & Sutton, M. A. (2015). Chemistry and the linkages between air quality and climate change. *Chemical Reviews*, 115(10), 3856-3897. <https://doi.org/10.1021/acs.chemrev.5b00089>
- Watson, J. G., & Chow, J. C. (2007). Receptor models for source apportionment of suspended particles. *Introduction to Environmental Forensics*, 2, 279–316.
- Welker, R. W. (2012). Chapter 4 - Size Analysis and Identification of Particles. In R. Kohli & K. L. Mittal (Eds.), *Developments in Surface Contamination and Cleaning* (pp. 179–213). William Andrew Publishing. <https://doi.org/https://doi.org/10.1016/B978-1-4377-7883-0.00004-3>
- Wang, Ju, Anan Yu, Le Yang, and Chunsheng Fang (2019). "Research on Organic Carbon and Elemental Carbon Distribution Characteristics and Their Influence on Fine Particulate Matter (PM2.5) in Changchun City" *Environments* 6, no. 2: 21. <https://doi.org/10.3390/environments6020021>
- WHO (2012). *Health effects of black carbon*. ISBN 978 92 890 0265 3.
- WHO (2021). *WHO global air quality guidelines: particulate matter (PM2.5 and PM10), ozone, nitrogen dioxide, sulfur dioxide and carbon monoxide*. ISBN 9789240034228. <https://www.who.int/publications/i/item/9789240034228>

- Shindell, D., Myhre, G., Boucher, O., Forster, P., Breon, F. M., & Fuglestedt, J. (2013). Radiative Forcing in the AR5. *Climate Change 2013: The Physical Science Basis - Working Group 1 contribution to the IPCC Fifth Assessment Report*.
- Yadav, S., & Phuleria, H. C. (2020). Oxidative Potential of Particulate Matter: A Prospective Measure to Assess PM Toxicity. In *Measurement, Analysis and Remediation of Environmental Pollutants* (pp. 333-356). Springer, Singapore.
- Zhang, L., Michelangeli, D. V., & Taylor, P. A. (2004). Numerical studies of aerosol scavenging by low-level, warm stratiform clouds and precipitation. *Atmospheric Environment*, 38(28), 4653-4665. <https://doi.org/10.1016/j.atmosenv.2004.05.042>
- Zhao, C.-N., Xu, Z., Wu, G.-C., Mao, Y.-M., Liu, L.-N., Dan, Y.-L., Tao, S.-S., Fan, Y.-G., Emerging role of air pollution in autoimmune diseases (2019) *Autoimmun. Rev.*, 18 (6), pp. 607-614.

CHAPTER 2 - Particulate matter emission sources and meteorological parameters combine to shape the airborne bacteria communities in the Ligurian coast, Italy

by Giorgia Palladino^{1,3}, **Pietro Morozzi**², Elena Biagi^{1,3}, Erika Brattich⁴, Silvia Turroni¹, Simone Rampelli¹, Laura Tositti², Marco Candela^{1,3}

¹ Unit of Microbiome Science and Biotechnology, Department of Pharmacy and Biotechnology, University of Bologna, Bologna, Italy

² Department of Chemistry “Giacomo Ciamician”, University of Bologna, Italy

³ Fano Marine Center (FMC), Fano, Italy

⁴ Department of Physics and Astronomy, University of Bologna, Italy

Scientific Reports volume 11, Article number: 175 (2021), <https://doi.org/10.1038/s41598-020-80642-1>



© 2021 by the authors. This article is an open access article distributed under the terms and conditions of the Creative Commons Attribution (CC BY) license (<http://creativecommons.org/licenses/by/4.0/>).

Abstract

Aim of the present study is to explore how the chemical composition of particulate matter (PM) and meteorological conditions combine in shaping the air microbiome in Savona (Italy), a medium-size, heavily inhabited urban settlement, hosting a wide range of industrial activities. In particular, the air microbiome and PM₁₀ were monitored over six months in 2012. During that time, the air microbiome was highly dynamic, fluctuating between different compositional states, likely resulting from the aerosolization of different microbiomes emission sources. According to our findings, this dynamic process depends on the combination of local meteorological parameters and particle emission sources, which may affect the prevalent aerosolized microbiomes, thus representing further fundamental tools for source apportionment in a holistic approach encompassing chemical as well as microbiological pollution. In particular, we showed that, in the investigated area, industrial emissions and winds blowing from the inlands combine with an airborne microbiome which include faecal microbiomes components, suggesting multiple citizens' exposure to both chemicals and microorganisms of faecal origin, as related to landscape exploitation and population density. In conclusion, our findings support the need to include monitoring of the air microbiome compositional structure as a relevant factor for the final assessment of local air quality.

Subjects: Air microbiology, Environmental monitoring, High-throughput screening, Microbial ecology, Microbiome

1 – Introduction

Airborne Particulate Matter (APM) is a complex system of particles in suspension in the atmosphere, usually defined as aerosol. Atmospheric aerosol is contributed by a multiplicity of sources of both natural and anthropogenic origin, including both biogenic and abiotic chemical components, and producing extremely complex and variable matrices that can be processed and solved for their origin using appropriate analytical processing and computational tools (Tositti et al., 2018a, Tositti et al., 2018b). In particular, the aerosol composition consists of a series of macrocomponents, which make up the mass of APM, as well as an even larger series of different trace components, the latter being of primary relevance as including the most toxic species and providing the highest chemical fingerprinting potential (Hopke, 2016). These aerosol bulk components can be emitted directly into the atmosphere (Primary Aerosol) or, otherwise, they can be abundantly produced within the atmosphere, following chemical reactions on gaseous precursors previously emitted (Secondary Aerosol). Primary Biological Aerosol (PBA), in short bioaerosol, represents the APM fraction including atmospheric particles released from the biosphere to the atmosphere (Fröhlich-Nowoisky et al., 2016). PBA comprise living and dead organisms, their dispersal units (e.g. pollen and spores) as well as tissue fragments from decay processes (Womach et al., 2010; Castillo et al., 2012). The overall mass contribution of PBA to conventional APM metrics is to date a very challenging task though some authors have recently estimated that it may account for about 16% of PM₁₀ in different cities examined (Hyde et al., 2020). The PBA fraction including microorganisms is defined as “airborne microbiome” (AM) and represents a highly dynamic and diversified assemblage of active and inactive microorganisms (Mescioglu et al., 2019). Indeed, AM can originate from multiple terrestrial and marine sources - including resident microbiomes in soil, waterbodies, plants and animal faeces (Fröhlich-Nowoisky et al., 2016; Després et al., 2012; Mhuireach et al., 2019) - whose relative importance depends season, location, altitude and meteorological and atmospheric factors. Further, in agricultural and suburban locations, other sources relevant to AM emissions are represented by man-made systems, such as agricultural waste, composting, and wastewater treatment plants. AM emission mechanisms include erosion or abrasive dislodgement from terrestrial sources and, from open waters, bubble-bursting at the air–water interface (Veron, 2015; Wilson et al., 2015). PBA size spans from a few nanometres up to about a tenth of a millimetre (Castillo et al., 2012), with bacteria-containing particles ranging around 2–4 µm in diameter (Dommergue et al., 2019) and accounting for “5–50% of the total number of atmospheric particles > 0.2 µm in diameter” (Delort et al., 2018). Due to the small size, AM can be transported over large distances, across continents and oceans, and reach the upper troposphere, where it actively contributes to ice nucleation and cloud processing (DeLeon-Rodriguez et al., 2013). In the troposphere, the AM concentration ranges from 10² to 10⁵ cells/m³ (Dommergue et al., 2019), being the densest in the planetary boundary layer, whose thickness depends on micrometeorological factors and geographic location, with marked daily and seasonal fluctuations (Sesartic et al., 2012; Toprak et al., 2013). In particular, the near-ground AM is the one most influenced by local sources, including local meteorology and atmospheric composition. AM is then removed from the troposphere by wet and dry deposition processes. The former is the major sink for atmospheric aerosol particles, in the form of precipitation (Renard et al., 2019), while the latter, being less important on the global scale, is particularly relevant with respect to local air quality (Fröhlich-Nowoisky et al., 2016; Mescioglu et al., 2019).

Recently, an increasing perception of the strategic importance of PBA - AM in particular - for the Earth system and, ultimately, for the planet and human health, has arisen (Cao et al., 2014; Huang et al., 2014; Michaud et al., 2018). For instance, besides its relevance to

atmospheric processes, AM has been found to control the spread of microorganisms over the planet surface, affecting the geographical biome, with key implications on agriculture and, ultimately, human health. This awareness raised concern about the potential impact of anthropic activities on PBA and, in particular, on the AM fraction. For example, changes in aerosol composition due to extensive human influence on the planetary scale give rise to air pollution, the inherent modification of atmospheric reactivity and, ultimately, climate change (von Schneidemesser et al., 2015). These factors may likely interfere with AM, shaping its structure and dispersion throughout the troposphere, with direct consequences on the terrestrial biome (Qin et al., 2020). However, as far as we know, the current state of knowledge on the connections between AM, atmospheric processes and atmospheric pollution is still fragmentary, with relatively few pioneer studies that take into account multidimensional datasets to analyse the connection between air chemical composition and its microbiome structure and variations, e.g. comparing different land-use types (Bowers et al., 2013; Liu et al., 2019), different sites within cities (Woo et al., 2013; Gandolfi et al., 2015; Innocente et al., 2017; Li et al., 2019), or worldwide locations (Mescioglou et al., 2019; Graham et al., 2018; Tignat-Perrier et al., 2019).

Our work fits in this scenario by exploring the ability of an interdisciplinary approach combining chemical speciation and metagenomics in shedding light on the complex relationships among abiotic and microbiome components of local ambient aerosol. The study is based on a series of about one hundred PM₁₀ samples from a coastal district in north-western Italy, collected daily over six months, from February to July 2012, to cover the cold-to-warm seasonal transition. The chemical composition of each sample was obtained, and a receptor modelling approach was used to identify and quantitatively apportion the chemical species determined in the samples to their sources. Owing to the cutoff adopted in APM sampling, the samples were deemed suitable for total DNA extraction and microbiome characterization by Next-Generation Sequencing using the 16S rRNA gene as target. In our work, we were able to finely reconstruct the overall aerosol behavior in an area affected by both natural and anthropogenic emission sources, determining the local bacterial microbiome from PBA contained in PM₁₀ and its main features as a function of local meteorological and environmental characteristics.

2 – Results

2.1 – Particulate matter emission sources and atmospheric parameters

The PMF model application on PM₁₀ samples resulted in a solution with an optimum number of seven source factors at the receptor site, i.e. the station where the PM₁₀ samples were collected. Like other multivariate methods, these factors correspond to linear combinations of the original compositional parameters, each potentially identifiable as an emission source profile. The fractional contribution per sample for each of the seven factors is reported in Supplementary Table S1.

In order to associate the factors with specific emission sources, prior knowledge about the receptor site (Savona, Italy) was used together with a critical analysis of the factor fingerprints (Fig. 1a). Moreover, the percentage contribution of the seven identified sources to the total variable was reported (PM₁₀, Fig. 1b).

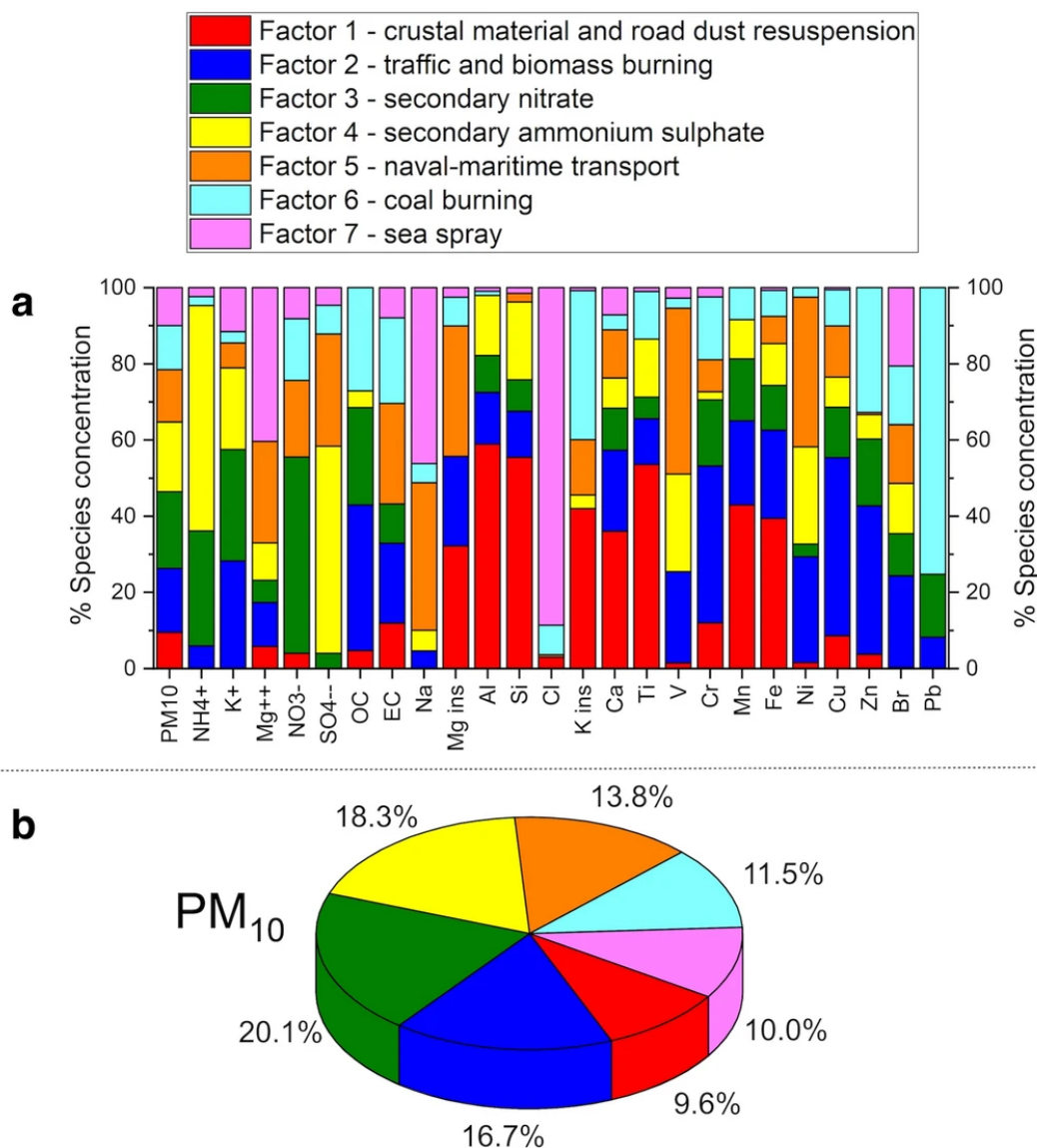


Figure 1. Emission sources identified by PMF analysis. (a) Stacked bar chart of the percentage concentration of each chemical species contributing to each of the seven factors that represent the chemical profile of each source identified in the PMF model. (b) Pie chart representing the contribution of the seven sources to PM₁₀ mass. The seven factors were identified as reported at the top.

As a result, the seven factors extracted by PMF analysis can be described as follows. Factor 1 is characterized by the prevalence of elements attributable to the geochemical composition because of the high percentages of Si, Al, and Ti. Therefore, this factor was identified as “crustal material and road dust resuspension”, deriving from the soil and/or road surface (Tositti et al., 2014; Chow et al., 2015). Factor 2 is linked to organic carbon (OC), Cu, Zn, Cr, and K⁺. OC and K⁺ are strictly related to combustion processes, including biomass burning, as previously described (Pachon et al., 2013). Cu, Zn, and Cr are associated with traffic: Cu and Cr are well-known tracers of the brakes of motor vehicles, while Zn is known as a tracer of tire wear (Alastuey et al., 2007; Thorpe et al., 2008; Gietl et al., 2010). Therefore, this factor was identified as a combination of “traffic and biomass burning” sources. Factor 3 is mainly associated with NO₃⁻ from gas-to-particle conversion of NO_x (g) in the atmosphere to which traffic and other high-temperature combustion processes may

contribute (Schaap et al., 2004; Pathak et al., 2009); as such it can hardly be attributed to a single well-defined source, especially in such a complex emissive scenario. Therefore, this factor was identified collectively as “secondary nitrate”. Factor 4 relates to SO_4^{2-} and NH_4^+ from gas-to-particle reactions, leading to secondary ammonium sulphate (Rodríguez et al., 2004; Vecchi et al., 2004; Hueglin et al., 2005). Similarly to secondary nitrate, this component can be contributed by various sources (both natural and anthropogenic) due to the multiplicity of fossil fuel sources of the precursor gaseous SO_2 and the ubiquity of NH_3 (g) (Behera et al., 2013; Fioletov et al., 2017). Therefore, this factor was collectively identified as “secondary ammonium sulphate”. Factor 5 is associated with Na, Mg ins, V, and Ni. The distinctive association of V and Ni reveals emissions attributable to the combustion of heavy oil (Jang et al., 2007; Becagli et al., 2012; Viana et al., 2014). The association of these species with Na and Mg suggests a “naval-maritime transport” source. Factor 6 is mainly characterized by high scores of Pb, K ins, Zn, OC, and elemental carbon (EC). The fine particles produced by coal combustion are characterized by significant fractions of OC and K together with typical elements such as Zn, while other semi-volatile elements condense on the surface of fine particles of K ins (Yu et al., 2018). Therefore, this factor was identified as “coal burning”. Factor 7 is connected to a large score of Cl⁻, Na, and Mg⁺⁺, and clearly identified as “sea spray” aerosol (Grythe et al., 2014).

In order to confirm the PMF analysis results, the origin of the polluted air masses was investigated by analyzing the PMF factors as a function of wind direction, calculating the respective cumulative distribution functions and generating the corresponding wind polar plots. This method associates the emissive profile obtained by PMF with wind direction and intensity to which the receptor site is downwind. The plots obtained are shown in Supplementary Figure S1. In particular, factors 1, 3, 4, and 6 (respectively crustal material and road dust resuspension, secondary nitrate, secondary ammonium sulphate, and coal burning) are associated with winds blowing from the inland towards the coast covering traffic and industrial sources. Factor 5 (naval-maritime transport) is oriented downwind from the sea, confirming that it is associated with the fuel oil used for sea shipping. Finally, while factor 2 shows a local origin indicating sources in the proximity of the receptor site, factor 7 is meridionally oriented, indicating once more a marine origin. It should be noted, however, that, unlike factor 5 characterized by elements typical of the submicron fraction likely flushed back and forth by sea-land breezes from the harbor, factor 7 is associated with coarse particles requiring different meteorological conditions (possibly more intense winds from the open sea in order to sustain heavier particles).

2.2 – AM overall composition

Next generation sequencing of the V3-V4 hypervariable region of the 16S rRNA gene from the total microbial DNA extracted from PM₁₀ air filters resulted in 98 samples containing more than 1,000 reads per samples which were retained for the rest of the study, for a total of 797,781 high-quality sequences with an average of $8,058 \pm 3,410$ (mean \pm SD) paired-end reads per sample, binned into 4 189 ASVs. According to our data, AM is dominated by the phyla Proteobacteria (mean relative abundance \pm SD = $42.8 \pm 19.4\%$) and Firmicutes ($27.4 \pm 18.9\%$), with Actinobacteria ($14.8 \pm 10.9\%$) and Bacteroidetes ($9.2 \pm 8.6\%$) being subdominant. At the family level, the most represented taxa are *Comamonadaceae* ($6.1 \pm 13.4\%$) and *Sphingomonadaceae* ($4.3 \pm 5.0\%$), both belonging to Proteobacteria. Other represented families are *Ruminococcaceae* ($3.9 \pm 7.6\%$), *Enterobacteriaceae* ($3.7 \pm 5.9\%$), *Clostridiaceae* ($3.6 \pm 6.8\%$), *Bacillaceae* ($3.5 \pm 5.0\%$) and *Flavobacteriaceae* ($3.4 \pm 5.7\%$). Please see Supplementary Figure S2 for a graphical representation of the overall compositional structure of AM throughout the entire sampling period.

In order to explore connections between the AM structure and seasonality, we compared the levels of AM diversity over the different months (Fig. 2). Diversity measurements indicated a general trend of microbial richness to decrease from winter to summer, although the differences did not reach statistical significance (Kruskal–Wallis test, FDR corrected p-value > 0.05) (Fig. 2a). Conversely, the PCoA of unweighted UniFrac distances between the AM compositional profiles showed sample segregation according to the month of sampling (Fig. 2b) (FDR-corrected permutation test with pseudo-F ratio, p-value = 0.012), meaning that seasonality significantly affects the overall compositional AM structure.

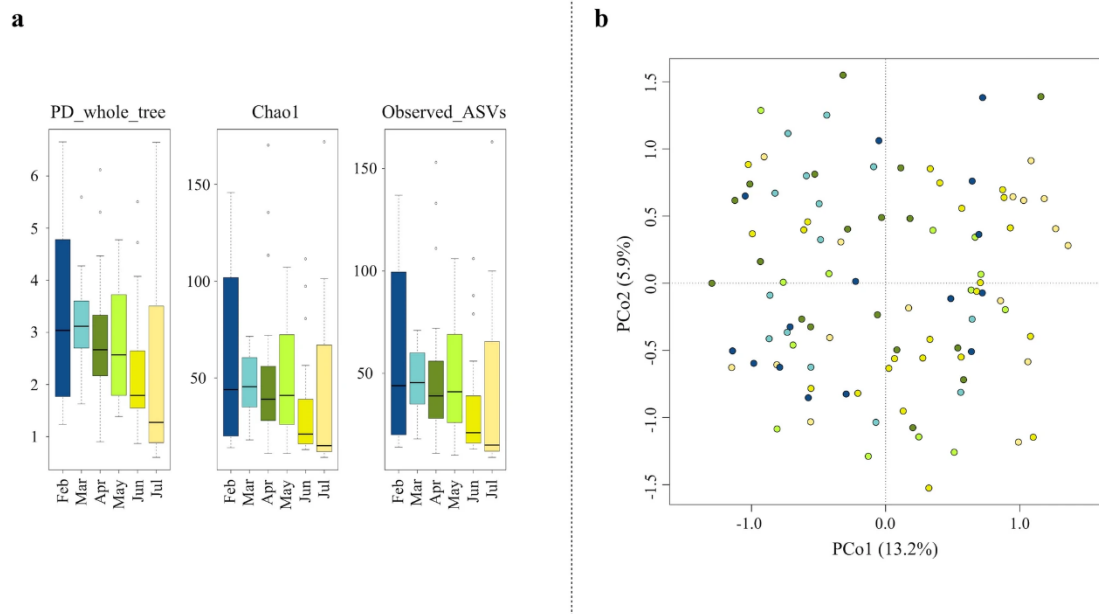


Figure 2. AM alpha and beta diversity throughout the sampling period. (a) Box-and-whiskers distribution of Faith's Phylogenetic Diversity (PD_whole_tree), Chao1 index for microbial richness and number of observed ASVs, for each month of sampling. The data show a trend towards reduced microbial richness from winter to summer, although the differences did not reach statistical significance (Kruskal–Wallis test, FDR-corrected p-value > 0.05). (b) Principal Coordinates Analysis (PCoA) based on unweighted UniFrac distances between AM profiles, showing separation by sampling month (permutation test with pseudo-F ratio, p-value = 0.012) (same colour code as in panel A). The first and second principal components (PCo1 and PCo2) are plotted and the percentage of variance in the dataset explained by each axis is reported.

2.3 - Variation of the AM topological structure and association with PM emission sources and meteorological parameters

To further explore the overall AM variation across the sampling period, a clustering analysis of the AM compositional profiles was carried out. Hierarchical Ward-linkage clustering based on the Spearman correlation coefficients of family-level AM profiles resulted in the significant separation of 4 clusters, named C1, C2, C3 and C4, respectively (FDR-corrected permutation test with pseudo-F ratio, p-value ≤ 0.001) (Fig. 3). Confirming the robustness of the identified clusters, the PCoA of the unweighted UniFrac distances between samples revealed a sharp segregation based on the assigned cluster (Fig. 4). Interestingly, when we searched for correlations between PCoA coordinates and measured meteorological parameters or PMF factors (Supplementary Tables S2 and S1, respectively), we found that factor 5 (naval-maritime transport) and relative humidity (RH) were both positively

correlated with the PCo1 axis (Kendal's test, FDR-corrected p-value ≤ 0.001), while factor 6 (coal burning) was negatively correlated with the PCo1 coordinates (p-value ≤ 0.001) (Fig. 4). This indirect gradient analysis allowed to highlight positive associations between clusters C1 and C3 and factors 6 and 5, respectively. Further, cluster C3 was found to be positively related to RH. As for seasonality, the clusters C3 and C4 are the most prevalent in summer and winter, respectively, while for C1 and C2 we did not observe any prevalence for a particular sampling period. We also compared the microbial diversity values of samples included in the different clusters, using three different diversity metrics. Our data indicated higher biodiversity in clusters C1 and C2 (PD whole tree, chao1, and observed ASVs, mean \pm SD: 3.6 ± 1.3 , 67.2 ± 43.9 , and 65.0 ± 40.5 for C1, 3.2 ± 1.4 , 59.1 ± 38.2 and 57.6 ± 36.0 for C2, respectively) compared to C3 and C4 (1.4 ± 0.7 , 18.7 ± 9.4 , and 18.5 ± 9.3 for C3, 2.4 ± 1.2 , 31.2 ± 18.4 and 31.2 ± 18.3 for C4), with C3 having the lowest biodiversity (Kruskal–Wallis test, FDR corrected p-value ≤ 0.001).

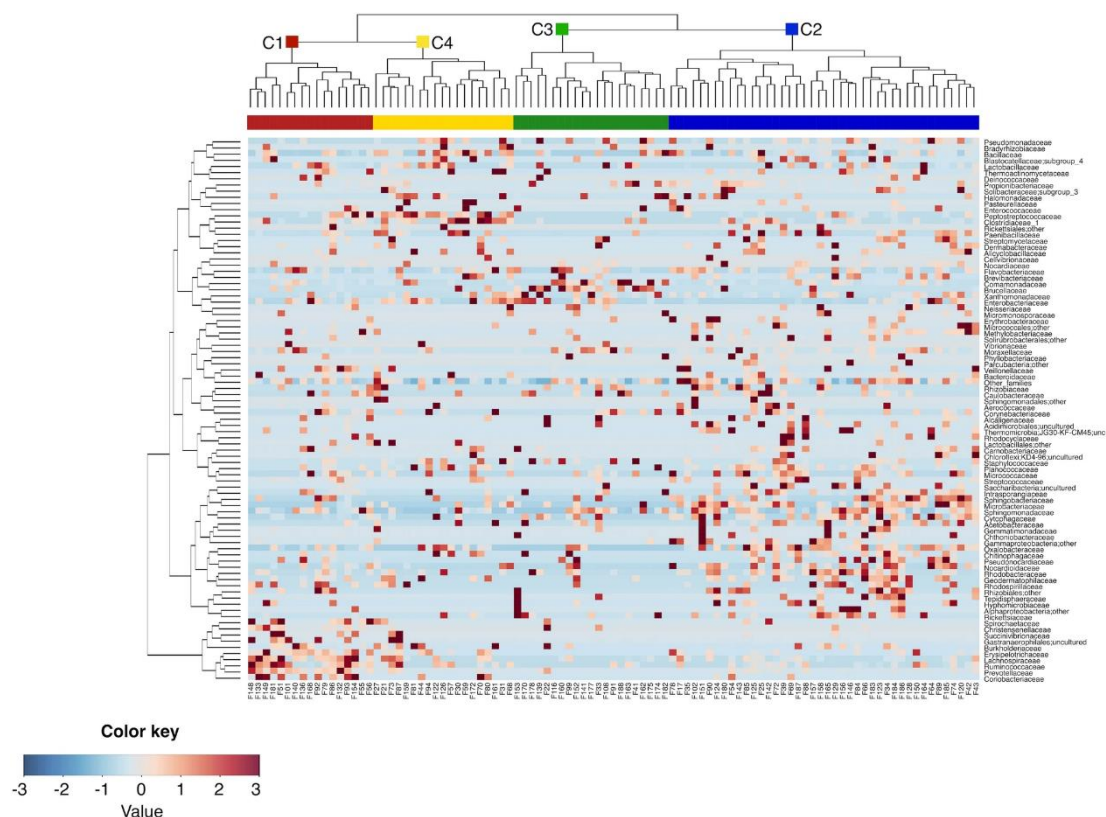


Figure 3. Family-level clusters of the airborne microbiome. Hierarchical Ward-linkage clustering based on the Spearman correlation coefficients of the proportion of families in the AM samples. Only families with relative abundance $> 2\%$ in at least 3 samples were retained. The four identified clusters (FDR-corrected permutation test with pseudo-F ratio, p-value ≤ 0.001) are labelled in the top tree and highlighted by different coloured squares (red, blue, green and yellow for the clusters C1, C2, C3 and C4, respectively).

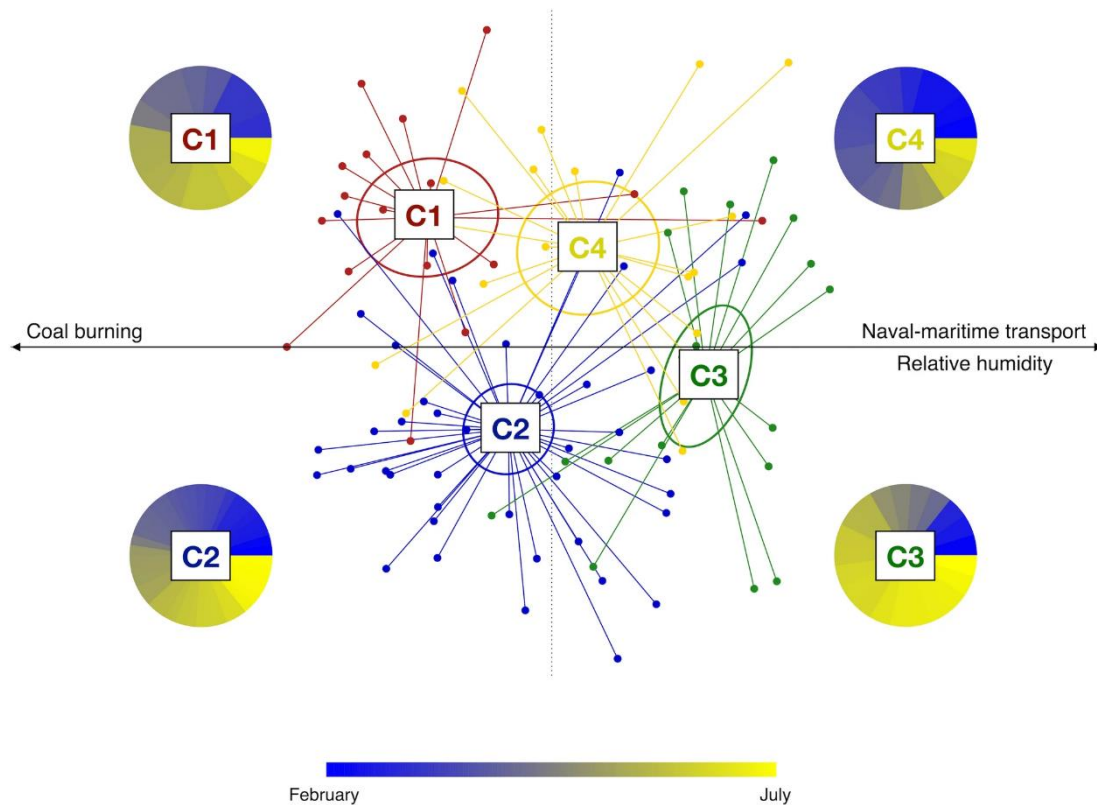


Figure 4. Variation of the AM topological structure and association with PM emission sources and meteorological parameters. Principal coordinates analysis (PCoA) based on the unweighted UniFrac distance shows separation between the microbial clusters (C1 to C4; permutation test with pseudo F-ratio, $p\text{-value} \leq 0.001$; see also Fig. 3). The percentage of variance in the dataset explained by each axis, first and second principal component (PCo1 and PCo2), is 13.2% and 5.9%, respectively. Ellipses include 95% confidence area based on the standard error of the weighted average of sample coordinates. Significant Kendall correlations between PCoA axes and PMF factors and measured meteorological parameters are reported with a black arrow. Specifically, the emission source factor 5 (naval-maritime transport) and relative humidity are both positively correlated with the PCo1 axis (Kendall correlation test, FDR-corrected $p\text{-value} \leq 0.001$), while the emission source factor 6 (coal burning) is negatively correlated with the PCo1 coordinates ($p\text{-value} \leq 0.001$). For each AM cluster, the proportion of samples based on the sampling time (from February (dark blue) to July (yellow)) is shown as a pie chart.

2.4 - Compositional specificity and prevalent microbiological source of the four AM clusters

We subsequently compared the relative abundance of AM families among the four clusters in order to find out the most distinctive families of each of them (Supplementary Figure S3). According to our findings, the discriminating families (i.e. families with significantly different relative abundance, based on Kruskal–Wallis test) for the microbial cluster C1 are *Prevotellaceae*, *Erysipelotrichaceae*, *Coriobacteriaceae*, *Christensenellaceae*, *Lachnospiraceae*, *Ruminococcaceae*, and *Spirochaetaceae*. The microbial cluster C2 is instead characterized by higher abundance in the families *Microbacteriaceae*, *Cytophagaceae*, *Oxalobacteraceae*, *Sphingobacteriaceae*, *Nocardiodaceae*, *Methylobacteriaceae*, *Intrasporangiaceae*, *Rhodobacteraceae* and *Acetobacteraceae*. Only two proteobacterial families, namely *Brucellaceae* and *Comamonadaceae*, have a

significantly higher abundance in cluster C3. Four families show higher abundance in cluster C4, i.e. *Peptostreptococcaceae*, *Clostridiaceae*, *Bacillaceae* and *Enterobacteriaceae*. It is also worth noting that the families *Planococcaceae* and *Paenibacillaceae* are highly represented in both C2 and C4 clusters, whereas *Sphingomonadaceae* members are equally represented in all clusters except for C4.

In an attempt to identify the most likely prevalent microbial origin of the four AM clusters, we first derived the respective compositional peculiarities at the OTU level. To this aim, 16S rRNA gene reads were clustered at 97% homology, resulting in 3 821 OTUs. By linear regression, we subsequently obtained 80 OTUs specifically discriminating the four clusters. In particular, for 52 of these OTUs a significantly different distribution in the four clusters was confirmed by a Kruskal–Wallis test, as shown in Supplementary Figure S4. For each of them, the isolation source of the closest BLAST match within the NCBI 16S rRNA sequence database was recovered (Supplementary Table S3). Interestingly, according to our findings, the cluster C1 is mainly characterized by OTUs of faecal origin. These OTUs include sequences assigned to typical components of the human gut microbiome, such as *Faecalibacterium prausnitzii*, *Ruminococcus faecis*, *Prevotella copri*, *Eubacterium eligens*, *Ruminococcus bromii*, *Roseburia inulinivorans* and *Blautia faecis* (Zhang et al., 2015; Lloyd-Price et al., 2016; Rinninella et al., 2019), the cattle rumen components *Succinivibrio dextrinosolvens* (Wang et al., 2017) and *Oscillibacter ruminantium* (Lee et al., 2012), and the porcine gut microbiome member *Treponema porcinum* (Nordhoff et al., 2005). Differently, the cluster C2 is characterized by OTUs assigned to microorganisms isolated from plant roots and leaves, including *Curtobacterium flaccumfaciens* (Chen et al., 2020), *Glutamicibacter halophytocola* (Feng et al., 2017) and *Frigoribacterium endophyticum* (Wang et al., 2015), as well as by a specific pattern of environmental bacteria, from soil, air, and fresh and marine water ecosystems. Similarly, both clusters C3 and C4 are characterized by a peculiar combination of environmental microorganisms from different sources, including soil, fresh and marine waters, and airborne microbial ecosystems.

3 – Discussion

In order to explore connections between the local air microbiome, atmospheric pollution and meteorological factors, here we provide a longitudinal survey of the near-ground AM, atmospheric particulate and atmospheric parameters in Savona, Italy. According to our findings, the local AM appears dominated by the phyla Proteobacteria, Firmicutes, Actinobacteria and Bacteroidetes, well matching the general layout of an AM community (Fröhlich-Nowoisky et al., 2016; Liu et al., 2019). The application of the PMF receptor modelling on the chemical compositional pattern of the PM₁₀ samples collected during the field campaign allowed the identification of seven emission sources: “crustal material and road dust resuspension”, “traffic and biomass burning”, “secondary nitrate”, “secondary ammonium sulphate”, “naval-maritime transport”, “coal burning” and “sea spray”. Each source factor was subsequently subjected to anemological analysis based on polar plots, allowing each emission source to be associated with the corresponding wind direction to which the receptor site is downwind, similarly to the approach used by Innocente et al., 2017. Specifically, emission sources as “crustal material and road dust resuspension”, “secondary nitrate”, “secondary ammonium sulphate” and “coal burning” were associated with winds blowing from the inland toward the sampling site, intercepting substantially traffic and industrial particulate sources. Conversely, emission sources such as “naval-maritime transport” and “sea spray” were associated with a sea breeze, supporting a marine origin for both. Finally, the “traffic and biomass burning” emission source mostly showed a local origin.

It is known that bacterial communities structure and composition can be influenced by environmental conditions, such as seasons, air masses origin and landscape characteristics (Innocente et al., 2017; Tignat-Perrier et al., 2019; Bowers et al., 2011), as well as PM₁₀ chemical compositional pattern (Gandolfi et al., 2015). When we explored the AM structure variation during the observation period, we were able to identify four distinct clusters of samples, named C1 to C4. Interestingly, the four clusters were associated with a peculiar combination of seasonality, meteorological variables and emission sources, as integrated into factors by PMF analysis.

In particular, the AM cluster C1 was associated with the “coal burning” emission source, suggesting not actually the industrial facility as a microbiome source, but rather the influence of an air mass whose transport over a given district harvests chemical and microbiological components along the same tropospheric path. Instead, the cluster C3, most represented in the warm period, probably has a marine origin due to its association with the “naval-marine transport” emission source and high relative humidity. Finally, the clusters C2 and C4 did not show any specific association with the aerosol sources assessed by PMF, even if they showed a different seasonal behaviour, with C4 being more represented in the cold period. The results obtained by the application of such double-step multivariate analysis - associating multidimensional microbiome and chemical datasets - represent the true novelty of our study. Indeed, we were able to associate the AM composition to well discriminated emission sources, each with a characteristic chemical composition and origin.

The four AM clusters revealed a distinct, well-defined compositional structure, each being enriched with a specific set of microbial families and OTUs. The specificity of each bacterial profile *de facto* serves as a microbiological fingerprint, allowing to single out the probable microbiome sources characterizing each cluster that, similar to what occurs to abiotic particles, allow to trace back the origin of the air mass. In particular, the clusters C3 and C4 substantially reflect interconnected environmental microbiomes, encompassing a specific combination of microorganisms from soil resuspension, as well as from marine and fresh waters (possibly from rivers and streams flowing into the Ligurian Sea) and from the air. C2 cluster reveals the plant microbiome as an additional source, showing a further combination of plant-associated and environmental microorganisms, due to the contact of air masses over a vegetation landscape. Interestingly, the feasibility of air mass tracing also using bacterial species clearly emerges when we observe in detail the compositional structure of C1. This is in fact the only AM cluster carrying a recognizable pool of bacterial moieties of faecal origin, which are consistently part of the animal gut microbiome, suggesting not only a well-defined origin but also the potential use of this information in the assessment of microbiological impacts. Faecal material as a potential source of bacteria was already reported by Bowers et al., 2013. It should be noted that in the area upwind C1 no sewage treatment plant as a possible source of faecal microbiome was present at the time of sampling. However, the area is very densely populated and forested areas populated by local fauna are closely found within a few kilometres.

Taken together, our data on the temporal dynamics of the near-ground AM in Savona, highlight the relevant degree of plasticity of AM over time. As such, we demonstrated how meteorological factors (e.g. wind direction and humidity) and atmospheric pollution (particles emission sources) can combine in shaping the AM configuration. In particular, coal burning and winds blowing from the inlands mix to establish a characteristic AM with a prevalence of aerosolized faecal microorganisms, regardless of seasonality. Conversely, in the summer season, humidity, sea breeze and naval-marine transport pollutants result in an AM mainly originating from environmental microbiomes, including microorganisms that are typically found in seawater and soil. Even if we were not able to establish connections

between the other identified emission sources and specific AM clusters, we would stress the importance of seasonality in shaping the AM structure. Indeed, the variation between the clusters C2 and C4, for which no connection with any emission source was observed, was shown to be dependent on the sampling period, with the cluster C2 most prevalent during the warm season and including plant microbiomes as possible characteristic sources, as previously observed by Franzetti et al., 2011 and Bertolini et al., 2013.

In conclusion, our results suggest that, in an urban settlement, the influence of air masses harvesting chemical components from industrial sources may increase the proportion of aerosolized faecal microorganisms in the atmosphere, ultimately increasing citizens' exposure to faecal microbes. Similar results have recently been obtained by exploring AM in Beijing over 6 months (Qin et al., 2020). Our findings strengthen the importance of including the monitoring of the AM compositional structure as a determinant factor in the currently used air quality indexes. Indeed, in urban areas, the possible increased exposure to faecal-associated microbiomes as a result of increasing pollution can pose a possible threat to human health, particularly in regions with high-intensity animal farming, due to the inherent propensity of opportunistic pathogens to aerosolize.

4 – Materials and methods

4.1 – Site description

The PM₁₀ samples treated in this work were collected in Savona, one of the main towns in the Ligurian region (Fig. 5). The whole region overlooks the Tyrrhenian sea but is entirely occupied by the Apennine range down to the coast, where only a narrow strip of plain is present. Therefore, the coastal area is densely inhabited and crossed by an extremely busy traffic road mainly connecting Italy to France. Besides being occupied by a medium-size heavily inhabited urban settlement, the Savona district also hosts a wide industrial area, including a coal-fired power plant active at the time of our experimental field activity and a large and very busy harbour. The climate of this site is classified as warm-temperate (Csa, according to Köppen and Geiger classification (Köppen, 1900; Geiger, 1954) with an average annual temperature of 14.6 °C and average precipitation of 910 mm (<https://en.climate-data.org>, accessed 28/07/2020). Intense northern winds characterize the circulation in winter (Burlando et al., 2013), while sea-land breeze regimes prevail in the warm season, usually starting from March (Bentamy et al., 2007; Tositti et al., 2018a). The air sampling site was located at an altitude of 12 m on the sea level in a rural area as classified according to the EU Directive 2008/50/EC on Air quality, with a distance of 2 km from the sea.



Figure 5. Location of the sampling site. Map providing the location of Savona in Italy (indicated with a yellow balloon with a star; other Italian cities are indicated with a green balloon) (top panel), and snapshot of the PM₁₀ sampling site with a 3D view of the surroundings (bottom panel) (source: Google Earth; map data: SIO, NOAA, U.S. Navy, NGA, GEBCO, TerraMetrics). Adapted from the original file of P. Christener (<https://commons.wikimedia.org/wiki/File:Vado-Ligure.jpg>), CC BY-SA 3.0 (), via Wikimedia Commons.

4.2 – Sample collection and atmospheric parameters

A total of 184 daily PM₁₀ samples were collected from February 1, 2012, until July 20, 2012 with low-volume samplers (SWAM Dual Channel, 55.6 m³/day, FAI, Italy) to allow simultaneous collection of both quartz (Whatman @QM-A quartz) and PTFE membranes (Whatman PM_{2.5} PTFE). Samples were stored frozen in the dark at -10 °C until processing. In this work, PTFE membranes were used for gravimetry, ion chromatography and elemental analysis with particle induced X-ray emission and inductively coupled plasma mass spectrometry, while quartz membranes were used for the analysis of carbonaceous macrocomponents and microbiology. A subset of 98 samples, uniformly distributed across the sampling period, was used for the analyses reported in the present paper. During the sampling campaign, meteorological parameters were measured simultaneously on site using a Davis Vantage Pro2 Weather Station (Davis Instruments, Hayward, CA), placed in proximity of the PM₁₀ sampler, for the measurement of temperature, pressure, relative humidity, rainfall, and wind direction and speed with a time resolution of 30 min. Subsequently, the data obtained were averaged on a daily scale (Supplementary Table S2), i.e. at the same time resolution as the PM₁₀ samples, using the “openair” package (Carslaw et al., 2012) of the R software (version 3.6.1) (R, 2019).

4.3 – Chemical characterisation of the samples

Chemical characterization of PM₁₀ filters was carried out using several analytical techniques. First, PM₁₀ mass load ($\mu\text{g}/\text{m}^3$) was determined by gravimetric analysis. Elemental and organic carbon were determined on quartz membranes by thermal-optical transmittance analysis (TOT), as previously described (Piazzalunga et al., 2011). For inorganic speciation, several analytical techniques were performed on PTFE filter portions: Ion Chromatography (IC) for the determination of the main water-soluble ion composition (NH_4^+ , K^+ , Mg^{2+} , NO_3^- , SO_4^{2-} , Na^+ , Cl^- , Ca^{2+} , and a few low-level organic compounds, i.e. oxalates and methanesulfonate), and Particle Induced X-ray Emission (PIXE) and Inductively Coupled Plasma Mass Spectrometry (ICP-MS) for the simultaneous analysis of a series of metals and metalloids (Na, Al, Si, Cl, Ca, Ti, V, Cr, Mn, Fe, Ni, Cu, Zn, Br, Pb, Li, Co, Rb, Sr, Cd, La, Ce, Sb, Cs, Ba, Ti, Bi, As, Se, Sn). Elemental analysis by PIXE was carried out at the Tandatron 3 meV of LABEC-INFN, Florence (Italy), according to the method previously reported (Lucarelli et al., 2011). Elemental analysis by ICP-MS was carried out according to the UNI EN 14,902, 2005 for PM₁₀ as an extension of the DL 155, 2010 in agreement with the EU Directive 2008/50/EC on ambient air quality and cleaner air for Europe. In order to prevent data redundancy, insoluble magnesium (Mg ins) and insoluble potassium (K ins) were calculated as the difference between PIXE and IC concentrations and replaced the corresponding elementary concentration data.

4.4 – Positive Matrix Factorization analysis

Positive Matrix Factorization (PMF) is an advanced multivariate factor analysis technique widely used in receptor modelling for the chemometric evaluation and modelling of environmental datasets (Hopke, 2016; Tositti et al., 2014; Paatero et al., 1994; Hopke et al., 2000; Comero et al., 2009; Belis et al., 2019; Belis et al., 2019; Masiol et al., 2020). PMF allows the identification and quantification of the emissive profile of a receptor site, i.e. the monitoring site where an air quality station is operated. We applied EPA PMF 5.0 software (Norris et al., 2014). The dataset was checked and re-arranged prior to PMF modelling according to the model criteria previously described (Norris et al., 2014) and, after data pre-processing, a concentration matrix of 98 samples \times 25 variables was obtained. After careful evaluation of the input data and uncertainty matrices, an optimum number of factors was found by analysing the values of Q, a parameter estimating the goodness of the fit performed (Brown et al., 2015), and the distribution of residuals. In order to assess the reliability of the model reconstruction, measured (input data) and reconstructed (modeled) values together with the distribution of residuals were compared. Our results indicated a good general performance of the model in reconstructing PM₁₀ (coefficient of determination equal to 0.79) for most variables. In order to confirm the results of receptor modelling, the origin of the air masses associated with the factors obtained was investigated through the creation of wind polar plots using the source contribution of the factors produced by PMF. In particular, polar plots were produced for each single PMF factor using the “openair” package of R (Carslaw et al., 2012), utilizing the conditional probability function (CPF) (Ashbaugh et al., 1985) with an arbitrary threshold set to the 75th percentile.

4.5 – Microbial DNA extraction, 16S rRNA gene amplification and sequencing

Microbial DNA extraction was performed on quartz membrane filter using the DNeasy PowerSoil Kit (Qiagen, Hilden, Germany) with the following modifications: the homogenization was performed with a FastPrep instrument (MP Biomedicals, Irvine, CA)

at 5.5 movements per sec for 1 min, and the elution step was preceded by a 5-min incubation at 4 °C (Jiang et al., 2015; Shin et al., 2015). Extracted DNA samples were quantified with NanoDrop ND-1000 (NanoDrop Technologies, Wilmington, DE) and stored at -20 °C until further processing. The V3-V4 hypervariable region of the 16S rRNA gene was PCR amplified in a 50- μ L final volume containing 25 ng of microbial DNA, 2X KAPA HiFi HotStart ReadyMix (Roche, Basel, Switzerland), and 200 nmol/L of 341F and 785R primers carrying Illumina overhang adapter sequences. The thermal cycle was performed as already described (Turroni et al., 2016) using 30 amplification cycles. PCR products were purified using Agencourt AMPure XP magnetic beads (Beckman Coulter, Brea, CA). Indexed libraries were prepared by limited-cycle PCR with Nextera technology and cleaned-up as described above. Libraries were normalized to 1 nM and pooled. The sample pool was denatured with 0.2 N NaOH and diluted to 6 pM with a 20% PhiX control. Sequencing was performed on an Illumina MiSeq platform using a 2 \times 250 bp paired-end protocol, according to the manufacturer's instructions (Illumina, San Diego, CA).

4.6 – Bioinformatics and statistics

A pipeline combining PANDAsseq (Masella et al., 2012) and QIIME 2 (Bolyen et al., 2019) was used to process raw sequences. DADA2 (Callahan et al., 2016) was used to bin high-quality reads (min/max length = 350/550 bp) into amplicon sequence variants (ASVs). After taxonomy assignment using the VSEARCH algorithm (Rognes et al., 2016) and the SILVA database (December 2017 release) (Quast et al., 2013), the sequences assigned to eukaryotes (i.e. chloroplasts and mitochondria) or unassigned were discarded. Three different metrics were used to evaluate alpha diversity - Faith's Phylogenetic Diversity (PD whole tree) (Faith et al., 1992), Chao1 index for microbial richness, and number of observed ASVs - and unweighted UniFrac distance was used for Principal Coordinates Analysis (PCoA). Permutation test with pseudo-F ratio (function "adonis" in the "vegan" package of R), Kruskal–Wallis test or Wilcoxon rank-sum test were used to assess data separation. Kendall correlation test was used to determine associations between the PCoA coordinates of each sample and the factors identified by the PMF analysis. p-values were corrected for multiple testing with the Benjamini–Hochberg method, with a false discovery rate (FDR) \leq 0.05 considered statistically significant. All statistical analyses and respective figures were produced with the R software (R, 2019) using "Made4" (Culhane et al., 2005) and "vegan" (<https://cran.r-project.org/web/packages/vegan/index.html>) packages. Clustering analysis of family-level AM profiles, filtered for family subject prevalence of at least 20%, based on the SILVA taxonomy assignment, was carried out using hierarchical Ward-linkage clustering based on the Spearman correlation coefficients. We verified that each cluster showed significant correlations between samples within the group (multiple testing using the Benjamini–Hochberg method) and that the clusters were statistically significantly different from each other (permutational MANOVA using the Spearman distance matrix as input, function adonis of the vegan package in R).

Additionally, PANDAsseq assembled paired-end reads were also processed with the QIIME1 (Caporaso et al., 2010) pipeline for Operational Taxonomic Units (OTUs) clustering based on 97% similarity threshold. Taxonomy was then assigned using the SILVA database. OTUs were processed through the R package "MaAsLin2" (Mallick et al., 2020) to determine their association with microbial clusters. Kruskal–Wallis test was used to find OTUs whose relative abundance was significantly different among microbial clusters. The resulting OTUs were taxonomically assigned against the NCBI 16S rRNA database using the BLAST algorithm (<https://blast.ncbi.nlm.nih.gov/>).

5 – Data availability

Sequence reads were deposited in the National Center for Biotechnology Information Sequence Read Archive (NCBI SRA; BioProject ID PRJNA664273; reviewer link <https://dataview.ncbi.nlm.nih.gov/object/PRJNA664273?reviewer=k646phv540av66bt8v1jduj699>).

Supplementary Information (only available online)

[Supplementary Information 1.](#)

[Supplementary Information 2.](#)

Acknowledgements

The authors wish to acknowledge Google Earth and the data providers SIO, NOAA, U.S. Navy, NGA, GEBCO and TerraMetrics for providing maps and 3D views of the sampling site. This study represents partial fulfilment of the requirements for the PhD thesis of G. Palladino at the PhD course of Innovative Technologies and Sustainable Use of Mediterranean Sea Fishery and Biological Resources (FishMed – University of Bologna, Italy).

Author contributions

Conceptualization: L.T., M.C.; Data curation: G.P., P.M.; Formal analysis: G.P., P.M., E.Br., S.R.; Investigation: G.P., P.M.; Methodology: E.Br., S.R., L.T., M.C.; Resources: L.T., M.C.; Writing - original draft: G.P., P.M., L.T., M.C.; Writing - review & editing: E.Bi, S.T.

Competing Interests

The authors declare no competing interests.

References

1. Alastuey, A., Contribution of harbour activities to levels of particulate matter in a harbour area: Hada Project-Tarragona Spain (2007) *Atmos. Environ.*, 41, pp. 6366-6378;
2. Ashbaugh, L.L., Malm, W.C., Sadeh, W.Z., A residence time probability analysis of sulfur concentrations at Grand Canyon National Park (1985) *Atmos. Environ.*, 19, pp. 1263-1270;
3. Becagli, S., Evidence for heavy fuel oil combustion aerosols from chemical analyses at the island of Lampedusa: a possible large role of ships emissions in the Mediterranean (2012) *Atmos. Chem. Phys.*, 12, pp. 3479-3492;
4. Behera, S.N., Sharma, M., Aneja, V.P., Balasubramanian, R., Ammonia in the atmosphere: a review on emission sources, atmospheric chemistry and deposition on terrestrial bodies (2013) *Environ. Sci. Pollut. Res. Int.*, 20, pp. 8092-8131;

5. Belis, C., (2019) European Guide on Air Pollution Source Apportionment with Receptor Models, <https://ec.europa.eu/jrc/en/publication/european-guide-air-pollution-source-apportionment-receptor-models>, Revised version 2019;
6. Bentamy, A., Ayina, H.L., Queffeuilou, P., Croize-Fillon, D., Kerbaol, V., Improved near real time surface wind resolution over the Mediterranean Sea (2007) *Ocean Sci.*, 3, pp. 259-271;
7. Bertolini, V., Temporal variability and effect of environmental variables on airborne bacterial communities in an urban area of Northern Italy (2013) *Appl. Microbiol. Biotechnol.*, 97, pp. 6561-6570;
8. Bolyen, E., Reproducible, interactive, scalable and extensible microbiome data science using QIIME 2 (2019) *Nat. Biotechnol.*, 37, pp. 852-857;
9. Bowers, R.M., McLetchie, S., Knight, R., Fierer, N., Spatial variability in airborne bacterial communities across land-use types and their relationship to the bacterial communities of potential source environments (2011) *ISME J.*, 5, pp. 601-612;
10. Bowers, R.M., Seasonal variability in bacterial and fungal diversity of the near-surface atmosphere (2013) *Environ. Sci. Technol.*, 47, pp. 12097-12106;
11. Brown, S.G., Eberly, S., Paatero, P., Norris, G.A., Methods for estimating uncertainty in PMF solutions: examples with ambient air and water quality data and guidance on reporting PMF results (2015) *Sci. Total Environ.*, 518-519, pp. 626-635;
12. Burlando, M., Wind climate analysis in complex terrains (2013) *J. Wind Eng. Ind. Aerod.*, 123, pp. 349-362;
13. Callahan, B.J., DADA2: High-resolution sample inference from Illumina amplicon data (2016) *Nat. Methods*, 13, pp. 581-583;
14. Cao, C., Inhalable microorganisms in Beijing's PM_{2.5} and PM₁₀ pollutants during a severe smog event (2014) *Environ. Sci. Technol.*, 48, pp. 1499-1507;
15. Caporaso, J.G., QIIME allows analysis of high-throughput community sequencing data (2010) *Nat. Methods*, 7, pp. 335-336;
16. Carslaw, D., Ropkins, K., Openair - an R package for air quality data analysis (2012) *Environ. Modell. Softw.*, 27-28, pp. 52-61;
17. Castillo, J.A., Staton, S.J., Taylor, T.J., Herckes, P., Hayes, M.A., Exploring the feasibility of bioaerosol analysis as a novel fingerprinting technique (2012) *Anal. Bioanal. Chem.*, 403, pp. 15-26;
18. Chen, G., Complete genome sequencing provides novel insight into the virulence repertoires and phylogenetic position of dry beans pathogen *Curtobacterium flaccumfaciens* pv. *flaccumfaciens* (2020) *Phytopathology*;
19. Chow, J.C., Lowenthal, D.H., Chen, L.W.A., Wang, X., Watson, J.G., Mass reconstruction methods for PM 2.5: a review (2015) *Air Qual. Atmos. Health*, 8, pp. 243-263;
20. Comero, S., Capitani, L., Gawlik, B.M., Positive Matrix Factorisation (PMF)—an introduction to the chemometric evaluation of environmental monitoring data using PMF (2009) JRC Scientific and Technical Reports, <https://op.europa.eu/it/publication-detail/-/publication/11e6a70c-6048-4442-9421-33a332893b8e/language-en/format-PDF/source-120358304>;
21. Culhane, A.C., Thioulouse, J., Perrière, G., Higgins, D.G., MADE4: an R package for multivariate analysis of gene expression data (2005) *Bioinformatics*, 21, pp. 2789-2790;
22. DeLeon-Rodriguez, N., Microbiome of the upper troposphere: species composition and prevalence, effects of tropical storms, and atmospheric implications (2013) *Proc. Natl. Acad. Sci. USA*, 110, pp. 2575-2580;
23. Delort, A.M., Amato, P., (2018) *Microbiology of aerosols* (John Wiley & Sons, Inc, 2018);

24. Després, V., Primary biological aerosol particles in the atmosphere: a review (2012) *Tellus B*, 64, p. 15598;
25. Dommergue, A., Methods to investigate the global atmospheric microbiome (2019) *Front. Microbiol.*, 10, p. 243;
26. Faith, D.P., Conservation evaluation and phylogenetic diversity (1992) *Biol. Conserv.*, 61, pp. 1-10;
27. Feng, W.W., *Glutamicibacter halophytocola* sp. nov., an endophytic actinomycete isolated from the roots of a coastal halophyte, *Limonium sinense* (2017) *Int. J. Syst. Evol. Microbiol.*, 67, pp. 1120-1125;
28. Fioletov, V., Multi-source SO₂ emission retrievals and consistency of satellite and surface measurements with reported emissions (2017) *Atmos. Chem. Phys.*, 17, pp. 12597-12616;
29. Franzetti, A., Gandolfi, I., Gaspari, E., Ambrosini, R., Bestetti, G., Seasonal variability of bacteria in fine and coarse urban air particulate matter (2011) *Appl. Microbiol. Biotechnol.*, 90, pp. 745-753;
30. Fröhlich-Nowoisky, J., Bioaerosols in the Earth system: climate, health, and ecosystem interactions (2016) *Atmos. Res.*, 182, pp. 346-376;
31. Gandolfi, I., Spatio-temporal variability of airborne bacterial communities and their correlation with particulate matter chemical composition across two urban areas (2015) *Appl. Microbiol. Biotechnol.*, 99, pp. 4867-4877;
32. Geiger, R., (1954) *Landolt-Börnstein – Zahlenwerte und Funktionen aus Physik, Chemie, Astronomie, Geophysik und Technik, alte Serie Vol. 3, Ch. Klassifikation der Klimate nach W. Köppen*, pp. 603-607. , Springer, Berlin;
33. Gietl, J.K., Lawrence, R., Thorpe, A.J., Harrison, R.M., Identification of brake wear particles and derivation of a quantitative tracer for brake dust at a major road (2010) *Atmos. Environ.*, 44, pp. 141-146;
34. Graham, K.E., Prussin, A.J., 2nd, Marr, L.C., Sassoubre, L.M., Boehm, A.B., Microbial community structure of sea spray aerosols at three California beaches (2018) *FEMS Microbiol. Ecol.*, 94, p. fiy005;
35. Grythe, H., Ström, J., Krejčí, R., Quinn, P.K., Stohl, A., A review of sea-spray aerosol source functions using a large global set of sea salt aerosol concentration measurements (2014) *Atmos. Chem. Phys.*, 14, pp. 1277-1297;
36. Hopke, P.K., A guide to positive matrix factorization (2000) EPA Workshop Proceedings Materials from the Workshop on UNMIX and PMF as Applied to PM_{2.5}, Volume II, Appendix 1B, <https://www3.epa.gov/ttn/amtic/unmixmtg.html>;
37. Hopke, P.K., Review of receptor modeling methods for source apportionment (2016) *J. Air Waste Manage.*, 66, pp. 237-259;
38. Huang, R.J., High secondary aerosol contribution to particulate pollution during haze events in China (2014) *Nature*, 514, pp. 218-222;
39. Hueglin, C., Chemical characterisation of PM_{2.5}, PM₁₀ and coarse particles at urban, near-city and rural sites in Switzerland (2005) *Atmos. Environ.*, 39, pp. 637-651;
40. Hyde, P., Mahalov, A., Contribution of bioaerosols to airborne particulate matter (2020) *J. Air Waste Manage.*, 70, pp. 71-77;
41. Innocente, E., Influence of seasonality, air mass origin and particulate matter chemical composition on airborne bacterial community structure in the Po Valley, Italy (2017) *Sci. Total Environ.*, 593-594, pp. 677-687;
42. Jang, H.N., Formation of fine particles enriched by V and Ni from heavy oil combustion: anthropogenic sources and drop-tube furnace experiments (2007) *Atmos. Environ.*, 41, pp. 1053-1063;
43. Jiang, W., Optimized DNA extraction and metagenomic sequencing of airborne microbial communities (2015) *Nat. Protoc.*, 10, pp. 768-779;

44. Köppen, W., Versuch einer Klassifikation der Klimate, vorzugsweise nach ihren Beziehungen zur Pflanzenwelt (1900) *Geographische Zeitschrift*, 6, pp. 593-611;
45. Lee, G.H., Genome sequence of *Oscillibacter ruminantium* strain GH1, isolated from rumen of Korean native cattle (2012) *J. Bacteriol.*, 194, p. 6362;
46. Li, H., Spatial and seasonal variation of the airborne microbiome in a rapidly developing city of China (2019) *Sci. Total Environ.*, 665, pp. 61-68;
47. Liu, H., The distribution variance of airborne microorganisms in urban and rural environments (2019) *Environ. Pollut.*, 247, pp. 898-906;
48. Lloyd-Price, J., Abu-Ali, G., Huttenhower, C., The healthy human microbiome (2016) *Genome Med.*, 8, p. 51;
49. Lucarelli, F., Is PIXE still a useful technique for the analysis of atmospheric aerosols? The LABEC experience (2011) *X-Ray Spectrom.*, 40, pp. 162-167;
50. Mallick, H., Rahnavard, A., McIver, L., (2020) *Maaslin2: Maaslin2. R Package Version 1.2.0*, , <http://huttenhower.sph.harvard.edu/maaslin2>
51. Masella, A.P., Bartram, A.K., Truszkowski, J.M., Brown, D.G., Neufeld, J.D., PANDAseq: paired-end assembler for illumina sequences (2012) *BMC Bioinform.*, 13, p. 31;
52. Masiol, M., Hybrid multiple-site mass closure and source apportionment of PM_{2.5} and aerosol acidity at major cities in the Po Valley (2020) *Sci. Total Environ.*, 704, p. 135287;
53. Mescioglou, E., Aerosol microbiome over the Mediterranean Sea diversity and abundance (2019) *Atmosphere*, 10, p. 440;
54. Mhuireach, G.Á., Betancourt-Román, C.M., Green, J.L., Johnson, B.R., Spatiotemporal controls on the urban aerobiome (2019) *Front. Ecol. Evol.*, 7, p. 43;
55. Michaud, J.M., Taxon-specific aerosolization of bacteria and viruses in an experimental ocean-atmosphere mesocosm (2018) *Nat. Commun.*, 9, p. 2017;
56. Nordhoff, M., *Treponema berlinense* sp. nov. and *Treponema porcinum* sp. nov., novel spirochaetes isolated from porcine faeces (2005) *Int. J. Syst. Evol. Microbiol.*, 55, pp. 1675-1680;
57. Norris, G., Duvall, R., Brown, S., Bai, S., (2014) *Epa Positive Matrix Factorization (PMF) 5.0 Fundamentals and User Guide Prepared for the Us Environmental Protection Agency Office of Research and Development*, , https://www.epa.gov/sites/production/files/2015-02/documents/pmf_5.0_user_guide.pdf, United States Environmental Protection Agency report;
58. Paatero, P., Tapper, U., Positive matrix factorization: a non-negative factor model with optimal utilization of error estimates of data values (1994) *Environmetrics*, 5, pp. 111-126;
59. Pachon, J.E., Weber, R.J., Zhang, X., Mulholland, J.A., Russell, A.G., Revising the use of potassium (K) in the source apportionment of PM_{2.5} (2013) *Atmos. Pollut. Res.*, 4, pp. 14-21;
60. Pathak, R.K., Wu, W.S., Wang, T., Summertime PM_{2.5} ionic species in four major cities of China: nitrate formation in an ammonia-deficient atmosphere (2009) *Atmos. Chem. Phys.*, 9, pp. 1711-1722;
61. Piazzalunga, A., Bernardoni, V., Fermo, P., Valli, G., Vecchi, R., On the effect of water-soluble compounds removal on EC quantification by TOT analysis in aerosol samples (2011) *Atmos. Chem. Phys. Discuss.*, 11, pp. 19851-19880;
62. Qin, N., Longitudinal survey of microbiome associated with particulate matter in a megacity (2020) *Genome Biol.*, 21, p. 55;
63. Quast, C., The SILVA ribosomal RNA gene database project: improved data processing and web-based tools (2013) *Nucl. Acids Res.*, 41, pp. D590-D596;

64. R: A Language and Environment for Statistical Computing (2019), <https://www.R-project.org>, R Foundation for Statistical Computing. Vienna, Austria;
65. Renard, P., Cloud microorganisms, an interesting source of biosurfactants (2019) *Surfactants and Detergents*, <https://www.intechopen.com/books/surfactants-and-detergents/cloud-microorganisms-an-interesting-source-of-biosurfactants>, (ed. Dutta, A. K.), IntechOpen, UK;
66. Rinninella, E., What is the healthy gut microbiota composition? A changing ecosystem across age, environment, diet, and diseases (2019) *Microorganisms*, 7, p. 14;
67. Rodríguez, S., Comparative PM₁₀-PM_{2.5} source contribution study at rural, urban and industrial sites during PM episodes in Eastern Spain (2004) *Sci. Total Environ.*, 328, pp. 95-113;
68. Rognes, T., Flouri, T., Nichols, B., Quince, C., Mahé, F., VSEARCH: a versatile open source tool for metagenomics (2016) *PeerJ*, 4;
69. Schaap, M., Van Loon, M., Ten Brink, H.M., Dentener, F.J., Builtjes, P.J.H., Secondary inorganic aerosol simulations for Europe with special attention to nitrate (2004) *Atmos. Chem. Phys.*, 4, pp. 857-874;
70. Sesartic, A., Lohmann, U., Storelvmo, T., Bacteria in the ECHAM5-HAM global climate model (2012) *Atmos. Chem. Phys.*, 12, pp. 8645-8661;
71. Shin, S.K., Metagenomic insights into the bioaerosols in the indoor and outdoor environments of childcare facilities (2015) *PLoS ONE*, 10;
72. Thorpe, A., Harrison, R.M., Sources and properties of non-exhaust particulate matter from road traffic: a review (2008) *Sci. Total Environ.*, 400, pp. 270-282;
73. Tignat-Perrier, R., Global airborne microbial communities controlled by surrounding landscapes and wind conditions (2019) *Sci. Rep.*, 9, p. 14441;
74. Toprak, E., Schnaiter, M., Fluorescent biological aerosol particles measured with the Waveband Integrated Bioaerosol Sensor WIBS-4: laboratory tests combined with a one year field study (2013) *Atmos. Chem. Phys.*, 13, pp. 225-243;
75. Tositti, L., Airborne particulate matter biotoxicity estimated by chemometric analysis on bacterial luminescence data (2018a) *Sci. Total Environ.*, 640, pp. 1512-1520;
76. Tositti, L., Physical and chemical properties of airborne particulate matter (2018b) *Clinical Handbook of Air Pollution-Related Diseases*, pp. 7-32., Capello F, Gaddi A, (eds), Springer, Cham;
77. Tositti, L., Source apportionment of particulate matter in a large city of southeastern Po Valley (Bologna, Italy) (2014) *Environ. Sci. Pollut. R.*, 21, pp. 872-890;
78. Tositti, L., The relationship between health effects and airborne particulate constituents (2018) *Clinical Handbook of Air Pollution-Related Diseases*, pp. 33-54. , Capello F, Gaddi A, (eds), Springer, Cham;
79. Turrioni, S., Fecal metabolome of the Hadza hunter-gatherers: a host-microbiome integrative view (2016) *Sci. Rep.*, 6, p. 32826;
80. Vecchi, R., Marazzan, G., Valli, G., Ceriani, M., Antoniazzi, C., The role of atmospheric dispersion in the seasonal variation of PM₁ and PM_{2.5} concentration and composition in the urban area of Milan (Italy) (2004) *Atmos. Environ.*, 38, pp. 4437-4446;
81. Veron, F., Ocean spray (2015) *Annu. Rev. Fluid Mech.*, 47, pp. 507-538;
82. Viana, M., Impact of maritime transport emissions on coastal air quality in Europe (2014) *Atmos. Environ.*, 90, pp. 96-105;
83. von Schneidmesser, E., Chemistry and the linkages between air quality and climate change (2015) *Chem. Rev.*, 115, pp. 3856-3897;
84. Wang, H.F., *Frigoribacterium endophyticum* sp. nov., an endophytic actinobacterium isolated from the root of *Anabasis elatior* (C. A. Mey.) Schischk (2015) *Int. J. Syst. Evol. Microbiol.*, 65, pp. 1207-1212;

85. Wang, Y., Bacterial community diversity associated with different levels of dietary nutrition in the rumen of sheep (2017) *Appl. Microbiol. Biotechnol.*, 101, pp. 3717-3728;
86. Wilson, T.W., A marine biogenic source of atmospheric ice-nucleating particles (2015) *Nature*, 525, p. 234;
87. Womack, A.M., Bohannon, B.J., Green, J.L., Biodiversity and biogeography of the atmosphere (2010) *Philos. Trans. R. Soc. B.*, 365, pp. 3645-3653;
88. Woo, A.C., Temporal variation in airborne microbial populations and microbially-derived allergens in a tropical urban landscape (2013) *Atmos. Environ.*, 74, pp. 291-300;
89. Yu, J., Potassium: a tracer for biomass burning in Beijing (2018) *Aerosol Air Qual. Res.*, 18, pp. 2447-2459;
90. Zhang, J., A phylo-functional core of gut microbiota in healthy young Chinese cohorts across lifestyles, geography and ethnicities (2015) *ISME J.*, 9, pp. 1979-1990;

CHAPTER 3 - Ultraviolet–Visible Diffuse Reflectance Spectroscopy (UV–Vis DRS), a rapid and non-destructive analytical tool for the identification of Saharan dust events in particulate matter filters

By **Pietro Morozzi**^a, Barbara Ballarin^b, Sara Arcozzi^c, Erika Brattich^d, Franco Lucarelli^e, Silvia Nava^e, Pedro José Gómez-Cascales^f, J.A.G. Orza^f, Laura Tositti^a

^a Department of Chemistry “G. Ciamician”, University of Bologna, Via Selmi, 2, 40126, Bologna, Italy

^b Department of Industrial Chemistry Toso Montanari, University of Bologna, Viale del Risorgimento, 4, 40136, Bologna, Italy

^c Department of Industrial Chemistry Toso Montanari, University of Bologna, Via Granarolo, 62, 48018, Faenza, Italy

^d Department of Physics and Astronomy, University of Bologna, Via Irnerio, 46, 40126, Bologna, Italy

^e Department of Physics and Astronomy, University of Florence and National Institute of Nuclear Physics (INFN), Florence Section, Via Sansone, 1, 50019, Sesto Fiorentino, Italy

^f SCOLAb, Department of Applied Physics, University Miguel Hernandez de Elche, 03202, Elche, Spain



ELSEVIER

This article was published in Atmospheric Environment, Volume 252, 2021, 118297, ISSN 1352-2310, Copyright Elsevier, <https://doi.org/10.1016/j.atmosenv.2021.118297>

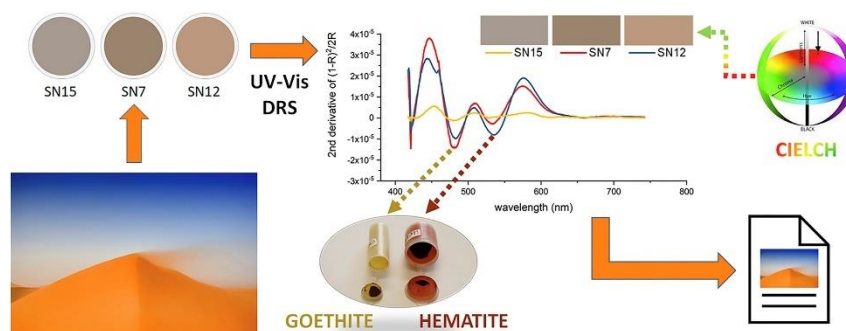
Highlights

- Rapid and non-destructive technique for particulate matter filter analysis.
- Quick identification of filter colour.
- Semi-quantitative analysis of iron oxide minerals.
- Fast detection of Saharan dust events.
- Determination of particular events and/or emission sources of particulate matter.

Abstract

Mineral dust represents one of the main components of particulate matter (PM) in the Mediterranean area. The rapid identification of Saharan dust events in PM samples is desirable and required for several reasons, including their role in direct effect on climate by

radiative forcing as well as their adverse effects on human health. For this purpose, the feasibility of UV–Vis Diffuse Reflectance Spectroscopy (UV–Vis DRS) is described as a rapid, inexpensive and non-destructive method of analysis of PM filters. The method developed allows to parameterize the PM filter colors and to obtain semiquantitative data related to iron oxide minerals, mainly hematite and goethite, two of the most representative minerals of Saharan dust in the Mediterranean area. The obtained results were validated based on the correlation between the spectrophotometric data of iron oxides from the membranes with the quantitative assessment of the concentration of iron by Particle Induced X-ray Emission (PIXE). Moreover, colorimetric parameterization allows setting up a classification approach for filters with potential for *a posteriori* use of this data in the study of the optical behavior of aerosol particles in the air. In this work, it is demonstrated how, as the concentration of iron mineral oxides and especially of hematite increases, the extent of redness color in PM filters grows up. Therefore, this technique can be extremely useful for a rapid, cheap and unambiguous identification of Saharan dust events in PM filters. The diagnosis of Saharan dust events was performed on PM₁₀ filters with a strong mineral dust component and demonstrated with the residence time analysis of back-trajectory ensembles, proving the reliability of this non-destructive methodology. This method has the potential to be adopted by the Environmental Protection Agencies, although further evaluations are necessary and currently underway to assess their applicability not only for PM filters sampled in remote stations but also in urban stations affected by both anthropogenic pollution and Saharan dust events.



Keywords: Saharan dust, Diffuse reflectance spectroscopy, Iron oxide minerals, Colorimetry, Chemometrics, Residence time analysis

1 – Introduction

Mineral dust uplifted into the troposphere by turbulence and wind in the North African desert is often transported across thousands of kilometers including the Mediterranean basin, the European continent sometimes up to the northernmost countries and/or the American continent, according to the season (e.g., Middleton and Goudie, 2002). Overall the Mediterranean basin owing to proximity and average circulation patterns, is directly and frequently affected by the so called Saharan dust incursions throughout the year with events whose intensity and frequency are object of extensive research (Brattich et al., 2015a, 2015b; Cabello et al., 2016; Cuevas et al., 2017; Cusack et al., 2012; Israelevich et al., 2012; Riccio et al., 2009; Tositti et al., 2014). This occurrence is being reported as increasing in likely connection with global warming (Middleton and Goudie, 2002; Soleimani et al., 2020). These events have often been linked with PM₁₀ exceedances in respect to EU air quality standards drawing attention on potential health hazards as well as on their correct

management (Diapouli et al., 2017; Krasnov et al., 2014; Matassoni et al., 2011; Nava et al., 2012; Querol et al., 2019). The current EU Air Quality standards for PM₁₀ are far less stringent than the WHO standards with a threshold of 20 µg/m³ (WHO annual mean) vs. a 40 µg/m³ for the former (WHO, 2006). It is to note that the EU regulation allows to eliminate from the annual inventory of exceedances the natural events such as Saharan dust incursions thus improving the overall environmental performance for this parameter (EEA, 2012).

Saharan dust does not only affect air quality standards, but plays a significant role in climate change by direct and indirect effect, the former by modifying the optical properties of the troposphere (e.g., Chin et al., 2009; Ginoux, 2017; IDSO, 1981; Littmann and Steinrücke, 1989; Sokolik and Toon, 1999), while the latter is associated with cloud processing and nucleation (see for example Reicher et al., 2019). Furthermore, mineral dust strongly influences the atmospheric reactivity through complex surface chemical reactions (Usher et al., 2003). Saharan dust transport is also connected with adverse health effects and increase in the mortality rate among the Mediterranean population (Karanasiou et al., 2012; Querol et al., 2019; Stafoggia et al., 2016).

Mineral particles may also affect the oxidant capacity of the troposphere by catalyzing ozone destruction, an important pollutant and reactive greenhouse gas (Bonasoni et al., 2003; Dickerson et al., 1997; Prospero et al., 1995). Moreover, iron contained in Saharan dust plumes can settle on oceanic surfaces and behave as a nutrient for marine phytoplankton, with beneficial outcome for oligotrophic aquatic systems, but potentially damaging the eutrophic ones (e.g., Bristow et al., 2010; Molinaroli and Masiol, 2006). However, Saharan dust has been often associated with a coral decline in the Caribbean region, suggesting that either mineral or microbiological components of Saharan dust may reveal detrimental to fragile ecosystems (Garrison et al., 2003; Shinn et al., 2000).

The complex role and behavior of mineral dust from Saharan regions, as briefly outlined, clearly shows the importance of identifying its occurrence in a given airshed in a simple, fast and unambiguous way. Common procedures to identify dust outbreaks may use a combination of back-trajectory analysis, satellite retrievals, and the output of dust prediction models. Collectively they provide a reasonable degree of evidence though each of these tools has limitations: a back-trajectory travelling over North Africa is not always associated to dust advection; satellite retrievals are limited by cloud coverage and transit time; uncertainties in dust model estimates remain, due to incomplete representation of several processes. Moreover, though meteorological forecasts are presently very well evolved enabling a timely Saharan dust alerting, most efforts are mainly retrospective and used for confirmation of more focused experimental activities from Lidar experiments and remote sensing to aerosol chemical speciation, preventing an efficient Saharan dust diagnosis (Pérez et al., 2011; Spyrou et al., 2010). All of this information is frequently combined with PM₁₀ levels or columnar aerosol properties at the study site. These levels are compared with local threshold values or background levels obtained by their own time series (Barnaba et al., 2017) or with PM₁₀ concentrations at a close regional background site (EC Commission, 2011; Escudero et al., 2007).

Saharan mineral dust consists mainly of silicates, aluminum oxides, carbonates, gypsum, and iron oxides, with a specific composition that depends on the geological material from its lifting place (e.g., Linke et al., 2006). Chemical speciation analysis is largely used to characterize aerosol composition as a function of its sources. Mineral dust is successfully identified with all the basic techniques devoted to elemental inorganic analysis; X-ray emission techniques such as Particle Induced X-ray Emission (PIXE) and X-ray fluorescence (XRF) are the most efficient and non-destructive ones since they allow a prompt detection

of the abundant lithogenic components, without any demanding and costly chemical processing in advance. Crustal elements like silicon (Si), aluminum (Al), titanium (Ti), calcium (Ca), and iron (Fe) are successfully used to identify Saharan dust events, as reported by, e.g., Alastuey et al. (2016); Formenti et al. (2010); Marconi et al. (2014); Nava et al. (2012); Rodríguez et al. (2020). In most cases, elemental analysis is complemented by ion chromatography wherein the most informative species associated with mineral dust is calcium ion (Ca^{2+}) (Escudero et al., 2005; Flentje et al., 2015; Putaud et al., 2004). This approach can be integrated by the detection of mineral species such as quartz, feldspars, illite, smectite, kaolinite, chlorite, vermiculite, mica, calcite, gypsum, hematite and goethite (Caquineau et al., 2002; Journet et al., 2014) requiring X-Ray Diffraction (XRD) (Menéndez et al., 2007; Shao et al., 2007), and Scanning Electron Microscopy (SEM) (Menéndez et al., 2007; Remoundaki et al., 2011). However, many of these analytical techniques are expensive, time consuming, and require sophisticated instrumental facilities and highly skilled personnel. Furthermore, X-ray emission and diffraction techniques are not routinely adopted by the Environmental Protection Agencies, at least in Europe, where, as required by Air Quality regulation, chemical speciation of PM_{10} is typically based on ion chemistry and on a very limited selection of pollutants including, beside benzo-a-pyrene normalized PAHs, only a few trace elements in most cases requiring wet chemical pre-treatment followed by Atomic Absorption or Inductively Coupled Plasma Spectroscopies (EU, 2008).

In this work, a procedure based exclusively on Ultraviolet–Visible Diffuse Reflectance Spectroscopy (UV–Vis DRS) (Torrent and Barrón, 2008) is proposed as a simple, cheap, efficient, rapid, and non-destructive analysis of particulate samples collected on a membrane for Saharan Dust transport diagnosis. This method is based on the integrated use of aerosol mass load data and the detection of iron oxides, which account for approximately 2–7% in weight of the total amount of mineral dust (Alfaro et al., 2004; Formenti et al., 2008; Goudie and Middleton, 2006) in atmospheric aerosol. Differently from most crustal materials and in spite of comparable concentration range, iron oxides in Saharan Dust mainly consist of goethite (predominant, 52–78% of the total iron oxides) and hematite (22–48% of the total iron oxides) (Formenti et al., 2014; Shi et al., 2012; Lafon et al., 2006). Since these minerals are important markers of mineral dust (Formenti et al., 2014; Lafon et al., 2006; Shi et al., 2012), they can be used as proxies for Saharan dust events in locations characterized by a low background of iron oxides from other more common sources, i.e. the Earth's crust especially by soil resuspension or technogenic ones such as metal works. Hematite and goethite are typically characterized by intense color shades, which can impart a yellowish to red tone to atmospheric dust particles (Arimoto et al., 2002). The proposed methodology is characterized by: (a) color metrological parametrization and (b) iron mineral oxides semi-quantification of the analyzed PM filters, followed by (c) chemometric tools. It can be integrated into routine sampling when no further speciation analysis is needed. This procedure therefore can be deemed as a cheap but robust screening test enabling to associate high PM_{10} values with a measurable and reliable Saharan dust tracer.

2 – Materials and methods

The Materials and Methods section is organized as follows

- a) Subsection 2.1 describes the PM_{10} samples used for the application and characterization of the UV–Vis DRS methodology reported in this work;
- b) Subsection 2.2 describes in detail the method used, paying particular attention to the instrumental configuration and analysis method of PM filters (subsection 2.2.1), how it is possible to parameterize the colour of the analyzed filters (subsection 2.2.2) and

obtain semi-quantitative data of iron oxide minerals from sample reflectance spectra (subsection 2.2.3);

- c) Subsection 2.3 presents the validation of the proposed methodology. After checking the main results of the proposed methodology (subsection 2.3.1), chemometric methods are used to identify the PM filters that have been subjected to a Saharan dust transport event (subsection 2.3.2.1), and the diagnosis obtained are assessed and confirmed by a residence time analysis of back-trajectory ensembles (subsection 2.3.2.2).

2.1 - Particulate matter samples

PM₁₀ samples analyzed in this work were collected at Sierra Nevada, a high altitude site (37.096 N, -3.387 W, 2550 m a.s.l.) in Southern Spain, within the framework of the Spanish national project FRESA (Impact of dust-laden African air masses and of stratospheric air masses in the Iberian Peninsula. Role of the Atlas Mountains, Ref: CGL2015-70741-R). The sampling station is located in an area scarcely influenced by traffic and other anthropogenic sources, but strongly impacted by Saharan dust incursion events due to its proximity to North Africa (Fig. 1).

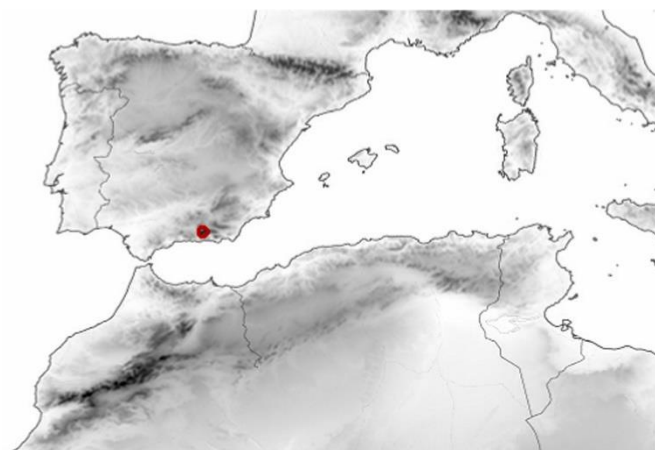


Fig. 1. Map and location of Sierra Nevada sampling station.

PM sampling was carried out using a high volume PM₁₀ sampler (CAV-A/mb, MCV S.A.) on a weekly basis (168 h at 30 m³/h) using quartz filters (Ø 15 cm, Whatman QM-A quartz filters) from 8 June to 11 October 2016. Nineteen weekly PM₁₀ samples (labeled as SN1-SN19) were overall obtained and processed along with three field blanks (labeled as B1-B3).

2.2 - The UV-Vis DRS methodology

2.2.1 - Sample preparation and UV-Vis DRS analysis

UV-Vis Diffuse Reflectance Spectroscopy is a widely used, basic spectrophotometric technique for the analysis of powders and surfaces, requiring a negligible sample preparation (Torrent and Barrón, 2008). It is based on the surface dispersion of a fraction of the UV-Vis incident radiation on it. A UV-Vis collimated light beam is directed with a certain angle onto the sample and, as a result, an ensemble of optical processes leads to radiation reflection by the sample surface on the whole overlying hemisphere. As a rule, the radiation reflected

by a sample can be considered as the sum of two components: regular (or specular) and diffuse (or nondirectional) reflectance (e.g., Torrent and Barrón, 2008). Regular reflectance occurs when incident radiation hits an ideally smooth and planar surface (i.e. without roughness) of the sample, and it is then reflected at an angle equal to the angle of incidence (Fresnel law). Instead, diffuse reflectance is a combination of several optical phenomena, such as multiple reflections, scattering and refraction, which disperse the radiation at all of the angles of the hemisphere of origin of the incident radiation (Blitz, 1998). Diffuse reflectance, which depends on the physico-chemical properties and color of the surface, is therefore the most informative component (Sellitto et al., 2008).

Diffuse reflectance spectroscopy of PM filters has been conducted with an ordinary UV–Vis spectrophotometer (Perkin Elmer Lambda 35, UV–Vis range) equipped with an integrating sphere; In this configuration all the reflected radiation emitted by the sample can be diffused and thereafter efficiently analyzed by the inner walls of the integrating sphere. The analysis does not include any sample chemical preparation: to the scope a square punch of 1.8 cm × 1.8 cm of a quartz PM filter is placed inside a flat sample holder, designed to position the sample for beam irradiation at a 0° incidence angle, and lodged over the reflectance sample port of the integrating sphere, a 50 mm diameter Labsphere RSA-PE-20 (Labsphere, United States). With the 0° sample holder in place, any specular component of reflection from the sample is excluded from measurement, since this component is directed out of the sphere through the transmittance sample entrance port. This integrating sphere configuration is named 0°/diffuse (0°/d) and Fig. 2 shows its operating scheme. Sample aliquots were carefully cut by means of a square die-cutting tool with a side of 1.8 cm. The UV–Vis DRS analysis of the latter is non-destructive since the side containing the particulate material is analyzed as it is, without any treatment and contact with the instrument. Firstly, a Spectralon white standard (USRS-99-010-EPV, Labsphere, United States) was analyzed as a reference and the instrumental autozero was performed. Then, one aliquot from each field blanks (B1–B3) was prepared and B1 portion was used for the background correction. Subsequently, the analysis of the remaining blank portions (B2 and B3) and the PM sampled filters was carried out. In particular, beside blanks, three distinct replicates of each PM sampled filter were prepared and analyzed for statistical purposes as well as to account for filter anisotropy. In this way, a total of 59 analyses were completed for this work. Therefore, the percentage reflectance (% R), i.e. the ratio between the intensity of the radiation reflected by the sample and the intensity of the total radiation reflected by a white diffuse reflectance standard, was determined for each of the analyzed portions. In particular, this parameter was measured as a function of the wavelength λ of the UV–Vis incident radiation (i.e., reflectance spectra were obtained), based on the following instrumental parameters: λ range = 780 - 380 nm; resolution = 0.3 nm; scan speed = 480 nm/min, smoothing = 2 nm, and slit = 2 nm.

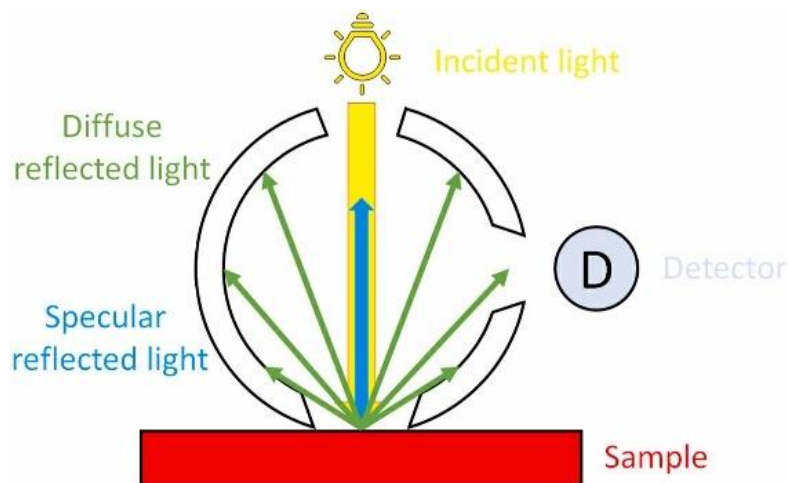


Fig. 2. Scheme of the integrating sphere, 0°/d geometry. The UV–Vis incident light hits the sample perpendicularly. Any specular component of reflection from the sample is excluded from measurement since this component is directed out of the sphere through the transmittance sample entrance port and, therefore, the detector only measures the diffuse reflectance component.

2.2.2 - Color parametrization

Aerosol sample color is measured by means of its UV–Vis reflectance spectrum. Indeed, sample color strongly depends on its diffuse reflection: an object irradiated by a light source disperses part of the incident radiation by diffuse reflection, which is subsequently collected by the eyes of an observer which in turn act as transducers, converting the light signal into appropriate electrical impulses for the brain. Ultimately, these impulses are integrated and processed by the latter, which generates the color perception for the observer (Kremers et al., 2016). Therefore, color is an extremely complex and subjective entity, as it is not a specific feature of the object itself, but depends on many variables such as light source, optical behavior of the object, observer's eyes and brain, etc. Since 1931, the International Commission on Illumination (CIE) has released guidelines to standardize color perception, based on the definition of three elements: light source, observer, and colorimetric spaces. The latter are mathematical models capable to define the color of an object in a rigorous manner (Ibraheem et al., 2012). One of the most used colorimetric space is the CIE $L^*a^*b^*$ (CIELAB) (ISO-CIE 11664-4-2019), which uses three cartesian components to uniquely define color sample: L^* , which indicates the CIELAB lightness in the range 0 (pure black) to 100 (pure white); a^* , measuring the CIELAB redness-greenness coordinate; and b^* , associated with the CIELAB yellowness-blueness coordinate. This colorimetric space can also be defined in polar coordinates, thus obtaining the CIE $L^*C_{ab}^*h_{ab}^\circ$ space (CIELCH) (ISO-CIE 11664-4-2019), wherein: L^* indicates the CIELAB lightness; C_{ab}^* represents the CIELAB chroma, a measure of the color intensity, defining to what extent a given color shade is “contaminated” by gray; and h_{ab}° indicates the CIELAB hue angle, whose value is expressed in degrees and describes the color tone. In particular, the 0° angle represents the red color. Because of their easy interpretability, in this work the mathematical definition of the colors of the analyzed portion samples was carried out employing the CIELAB and CIELCH spaces, starting from the reflectance spectra obtained and using the Color 2.01 software (Perkin Elmer Ltd, United Kingdom). Standard Illuminant D65 was set up as a representation of solar light source, according to CIE (ISO-CIE 11664-2-2020), and an observer angle of 10° was set up with the aim of simulating the average spectral response in human observers (ISO-CIE 11664-1-2019). Average values and the standard deviations of

the colorimetric parameters (L^* , a^* , b^* , C_{ab}^* , and h_{ab}°) were calculated for the blank filter (B) and the 19 samples (SN1,...SN19). The CIELAB average data were used for color visualization through the online tool Nix Color Sensor (<https://www.nixsensor.com/free-color-converter/>).

2.2.3 - Semi-quantification of iron oxide minerals

Diffuse reflectance measurements are extremely useful for the characterization and quantification of solid materials. Indeed, they exhibit attenuation in reflectance spectra due to their light-absorption in specific UV–Vis wavelength ranges. Iron oxide minerals, which are the proper focus of this work, present absorption in association with their electronic transitions within the $3d^5$ shell of Fe^{3+} ion triggered by UV–Vis radiation (Scheinost et al., 1998); as a consequence, reflectance spectra prove as an efficient alternative for their assessment. While past work on PM membranes was mainly based on the first derivative of the UV–Vis reflectance (e.g., Arimoto et al., 2002; Shen et al., 2006), here we compute the second derivative of the Kubelka-Munk (K-M) function spectra. This method has been widely used for the assessment of iron oxides in soil samples (Barrón and Torrent, 1986; Fernandez and Schulze, 1992; Sellitto et al., 2009; Szalai et al., 2013) but less frequently for PM filters analysis (Lafon et al., 2006), while the approach was used in several spectrophotometric applications for the most absorbing aerosol component, i.e. soot (see for example Pandey et al., 2019; Petzold and Schönlinner, 2004). The calculation of the second derivative was performed using the Savitzky-Golay filter (Schafer, 2011), an averaging algorithm that fits a polynomial to the spectral data allowing the calculation of a derivative of this function. In this work a polynomial order of 4 and a number of smoothing points equal to 251 was chosen. Processed spectra thus obtained revealed neat and significant peaks due to the absorption of iron oxide minerals. The heights of these peaks were utilized for semi-quantitative analysis, following peak definition and baseline subtraction. In our work, iron oxide minerals are determined semi-quantitatively for the absence of a series of standards containing known amounts of iron mineral oxides spread on membranes similar to samples. Indeed several efforts were spent to scope, but owing to the lack of homogeneity of artificial hematite-laden filters, standardization was not reached.

The conversion of the reflectance spectra into K-M spectra was carried out using the UV WinLab 2.85 Software (Perkin Elmer Ltd, United Kingdom), while the calculation of the Savitzky-Golay second derivative was performed by the software The Unscrambler V10.4 (Camo, Oslo, Norway), and the quantification of peak heights was carried out using the Peak Analyzer tool of the OriginPro 2018 software (Northampton, USA).

2.3 - Validation of the methodology

2.3.1 - Validation of UV–Vis DRS results

Sample color (subsection 2.2.2) was numerically defined by means of colorimetric parameters described by CIE, and semi-quantitative information about iron oxide minerals (subsection 2.2.3) were achieved by a suitable mathematical treatment of reflectance spectra. In order to validate our spectrophotometric approach, experimental data obtained were compared with elemental iron concentration data ($\mu g\ cm^{-2}$) obtained by Proton Induced X-ray Emission (PIXE) carried out on the same PM_{10} filters using a Tandetron 3 MeV accelerator at LABEC (Laboratorio di tecniche nucleari per l'Ambiente e i Beni Culturali, <https://www.ionbeamcenters.eu/RADIATE-project-partners/infn/>) at the INFN Section of

Florence (Italy) (Lucarelli et al., 2014, 2018). Since the membranes used in this work are made of quartz instead of the typical PTFE suitable for inorganic elemental analysis, PIXE spectra were adequately processed for the intense interference of silicates in the filter medium (Chiari et al., 2018; and Lucarelli et al., 2011; Calzolari et al., 2006). In brief, PM₁₀ samples were irradiated in ambient conditions with a 3.0 MeV proton beam with a 5 nA current for 60 s.

Spearman correlation analysis (Akoglu, 2018) was then performed between the UV–Vis DRS outcomes (color parameters and semi-quantitative data of iron oxide minerals) with elemental iron concentration calculated by PIXE and PM₁₀ mass load obtained by gravimetry, both expressed in $\mu\text{g cm}^{-2}$ for dimensional consistency.

2.3.2 - Diagnosis and validation of Saharan mineral dust events

2.3.2.1 - Diagnosis based on PM filters

The ultimate goal of this work is to sort out quickly, but safely the PM filters exposed to Saharan Dust transport events from the others.

Therefore, Ward's cluster analysis (Ward, 1963) using squared Euclidean distance was employed for the detection of two sample clusters, respectively a cluster indicating the samples subjected to Saharan dust transport events and another cluster for all the other sample cases. After standardization by autoscaling (van den Berg et al., 2006), the colorimetric parameters of CIELCH model (subsection 2.2.2) and the semi-quantitative data of iron oxide minerals (subsection 2.2.3) were used as starting variables. The statistical analysis was carried out by means of the software Statistica V.10 (StatSoft Inc., Tulsa, USA).

The two clusters obtained were subsequently compared with PM₁₀ data ($\mu\text{g/m}^3$) in order to associate or exclude, in a binary way, the occurrence of a Saharan dust incursion.

2.3.2.2 - Back-trajectory ensembles and residence time analysis

A residence time analysis of back-trajectory ensembles (Lin, 2012; Lupu and Maenhaut, 2002; Stohl, 1998) was carried out to assess and confirm the diagnosis made by UV–Vis DRS.

Ensembles of back-trajectories were calculated using the NOAA Hybrid Single Particle Lagrangian Integrated Trajectory (HYSPLIT_4) model (Rolph et al., 2017; Stein et al., 2015). Meteorological data from the ERA-Interim reanalysis (Dee et al., 2011) was used as input for the trajectory calculations with data interpolated into a 0.5-degree grid, in agreement with the 0.5-degree terrain model available in the Hysplit model, and 27 pressure levels from 1000 to 100 hPa. The ensemble is generated by offsetting the meteorological database by one grid point in the horizontal and 0.01 sigma units in the vertical, resulting in 27 back-trajectories (Draxler, 2003). 96-hour kinematic back-trajectory ensembles were calculated starting 200 m above the sampling site at 00, 06, 12, and 18 UTC in the period 8 June – 11 October 2016.

The trajectory ensembles were subsequently grouped together on the basis of sampling PM resolution (weekly). The analysis of residence time was based on the number of trajectory endpoints falling within each sampling period over five broad regions (Africa, America, Europe, Mediterranean Sea, and Atlantic Ocean). Furthermore, two additional specific areas such as Mauritania and the Atlantic Ocean at low altitude (below 800 m) were investigated.

Subsequently, the frequency of residence time across each area per single PM filter (Ashbaugh et al., 1985; Orza et al., 2013; Xu et al., 2006) as the ratio between the total counts and the total number of endpoints. All the calculations were performed with scripts purposely elaborated with the R programming language (R Core Team, 2019). To further support the diagnosis of African dust events, aerosol optical depth (AOD) Collection C6 (Merged Dark Target/Deep Blue) from the Moderate Resolution Imaging Spectroradiometer (MODIS) onboard the Aqua and Terra satellites were retrieved (NASA EOSDIS, worldview tool at <https://worldview.earthdata.nasa.gov>).

3 – Results and Discussion

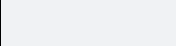
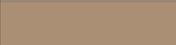
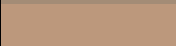
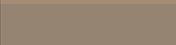
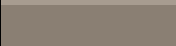
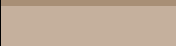
Results and discussion section is organized as follows:

- a) Subsection 3.1 reports the colorimetric parameters and the related digitized colors for the analyzed PM filters, highlighting and discussing their differences.
- b) Subsection 3.2 details the semi-quantitative results of iron oxide minerals, and their processing from raw reflectance spectra.
- c) Subsection 3.3 presents the correlation between the semi-quantitative data of the iron oxide minerals, the elemental iron obtained by Proton Induced X-ray Emission (PIXE) analysis, and the colorimetric parameters.
- d) Subsection 3.4 reveals the PM filters that have been subjected to a Saharan Dust transport event by a multivariate approach validated by residence time analysis.

3.1 - Colorimetric data and results

For each portion of the PM filter analyzed, the sample color was obtained by the procedure described in subsection 2.2.2. The colorimetric parameters related to the CIELAB (L^* , a^* , b^*) and CIELCH (L^* , Cab^* , hab°) models together with the subsequent color obtained for the blank filter (B) and for the 19 PM samples (SN1, ...SN19) are reported in Table 1.

Table 1. Average values and standard deviations (numbers in brackets) of the colorimetric parameters for the analyzed samples. The colors obtained from the conversion to RGB color model by the online tool nix Color Sensor (<https://www.nixsensor.com/free-color-converter/>) are displayed in the last column of this table.

Sample	L*	a*	b*	C _{ab} *	h _{ab} [°]	Color
B	95.46 (0.11)	-0.51 (0.05)	-0.92 (0.13)	1.05 (0.14)	241.15 (0.81)	
SN1	67.49 (2.68)	4.14 (1.19)	13.89 (4.42)	14.49 (4.57)	73.26 (0.64)	
SN2	66.85 (3.60)	1.99 (0.43)	10.27 (1.08)	10.46 (1.13)	79.11 (1.53)	
SN3	62.63 (3.07)	7.37 (0.56)	19.23 (1.36)	20.59 (1.47)	69.03 (0.11)	
SN4	58.53 (2.46)	4.86 (1.55)	14.31 (4.99)	15.11 (5.22)	71.10 (0.71)	
SN5	59.27 (2.79)	6.33 (0.09)	17.16 (1.64)	18.30 (1.56)	69.67 (1.66)	
SN6	64.43 (2.91)	6.84 (0.46)	18.35 (3.35)	19.59 (3.28)	69.27 (2.52)	
SN7	56.77 (2.12)	5.36 (0.39)	16.02 (1.22)	16.89 (1.28)	71.48 (0.14)	
SN8	64.35 (1.41)	5.37 (1.63)	16.20 (4.63)	17.06 (4.90)	71.72 (0.38)	
SN9	57.51 (3.59)	3.94 (0.51)	13.94 (1.26)	14.49 (1.35)	74.27 (0.70)	
SN10	61.20 (3.26)	6.41 (1.31)	17.72 (2.97)	18.85 (3.23)	70.22 (0.79)	
SN11	59.83 (3.63)	4.86 (0.81)	15.04 (2.11)	15.80 (2.25)	72.13 (0.89)	
SN12	65.59 (0.76)	9.41 (1.52)	20.24 (2.92)	22.33 (3.28)	65.11 (0.65)	
SN13	60.28 (3.57)	5.43 (0.80)	16.02 (1.76)	16.91 (1.93)	71.31 (0.78)	
SN14	56.44 (1.09)	3.72 (0.95)	12.65 (2.98)	13.18 (3.13)	73.68 (0.49)	
SN15	64.91 (2.89)	1.94 (0.32)	7.47 (1.86)	7.72 (1.88)	75.19 (1.56)	
SN16	53.75 (2.55)	2.25 (0.27)	7.90 (1.52)	8.22 (1.53)	73.93 (1.58)	
SN17	62.68 (2.65)	4.46 (0.53)	14.27 (2.03)	14.95 (2.09)	72.60 (0.90)	
SN18	61.01 (2.99)	5.80 (0.09)	16.91 (1.04)	17.88 (1.00)	71.04 (0.98)	
SN19	73.23 (2.41)	4.20 (0.56)	12.63 (2.16)	13.34 (1.97)	71.24 (4.53)	

The collected PM samples present distinct color shades (from gray to red) as a function of the dominating aerosol source during the respective sampling time interval. In order to examine how these samples differ in color, a graphical representation based on chroma (C_{ab}*) and hue (h_{ab}[°]) is reported in Fig. 3. Fig. 3 (a), shows how the blank filter (B) remarkably differs from all the others (SN1, ...SN19). In fact, the blank filter is characterized by a whitish color due to the absence of particulate material, while a greyish-yellowish-reddish color characterizes all the sampled filters (see the last column to the right of Table 1). Sampled filters in Fig. 3 (b) show a defined trend: the grayest samples (like SN15) present a higher hue value and a lower chroma value than other filters while the most reddish samples (like SN12) show a higher value of chroma and a lower value of hue. Instead, the samples with intermediate values of chroma and hue (like SN7) exhibit a browner coloration than the others. This observation agrees with the CIELCH color definition: a lower hue value corresponds to a color tone more shifted towards red, while a higher chroma value corresponds to a more marked color intensity (compared to the gray color that occurs at chroma values close to zero). This demonstrates how the CIELCH color space adequately

describes the colors of the analyzed PM filters due to their high chromaticity. In fact, the higher efficiency of the CIELCH model as compared with the CIELAB one in assessing the differences between the more chromatic colors is known, since C_{ab}^* and h_{ab}° allow a better identification of the more saturated colors than a and b (Schloss et al., 2018).

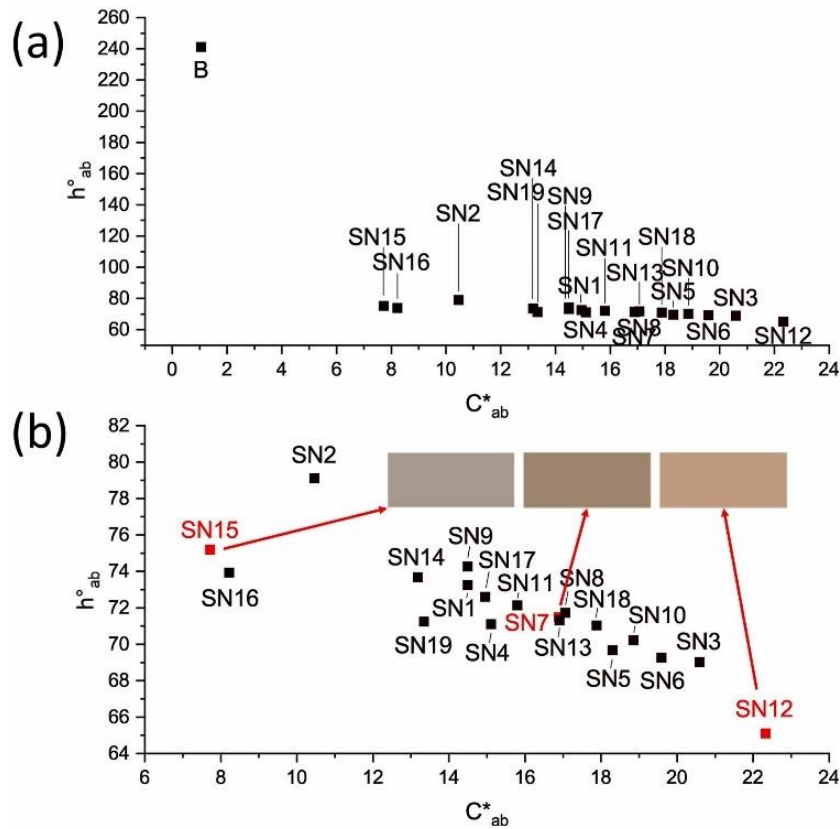


Fig. 3. (a) Graphic representation of blank filter (B) and sampled filters (SN1, ...SN19) based on chroma (C_{ab}^*) and hue (h_{ab}°). (b) Zoomed plot on sampled filters. The colors of three specific samples (SN15, SN7, SN12) are shown.

3.2 - Iron oxide minerals

As previously reported in subsection 2.2.3, the calculation of the second derivative of the Kubelka-Munk function spectra was performed over the UV-Vis DRS spectra. This operation allows to identify attenuated peaks due to light absorption by iron oxide minerals, such as akaganéite, ferroxhyte, ferrihydrite, goethite, hematite, lepidocrocite, maghemite, and schwertmannite (Sherman and Waite, 1985; Torrent and Barrón, 2002), whose characteristics are reported in Fig. 4.

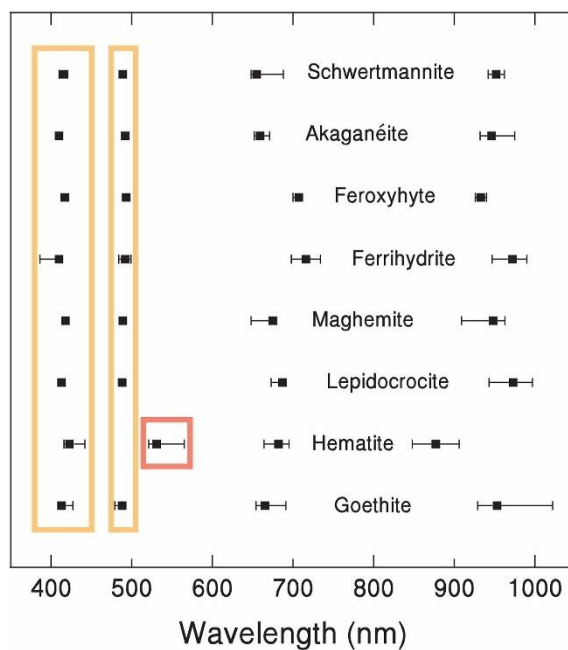


Fig. 4. Median and range of the UV–Vis absorption bands of some iron oxide minerals in the second derivative of K–M function spectra, adapted from Torrent and Barrón, 2008. It can be seen that below 600 nm, there are three absorption bands at around 420, 480, and 535 nm.

According to Scheinost et al., 1998, only the attenuated peak at around 535 nm is specific for a single mineral (hematite), while the other peaks at 420 nm and 480 nm are shared by several other iron oxides. Therefore, the semi-quantitative nature of the spectral data of iron oxide minerals can be deduced for each portion of the PM filter through an appropriate processing of their UV–Vis reflectance spectra. For sake of brevity, from now on graphical plots present the results for only three characteristic filters, namely SN15, SN7, and SN12 (Fig. 5). The selection of the filters is not arbitrary, but is based on their representativeness as described in subsection 3.1.

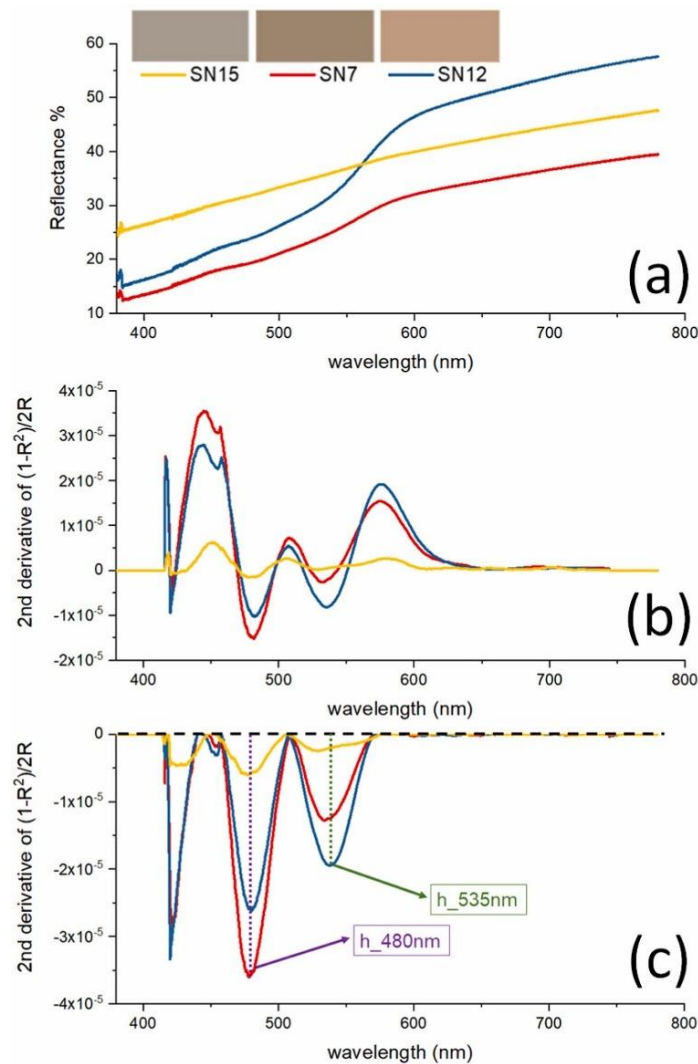


Fig. 5. Reflectance spectra (a), Savitzky-Golay second derivative of Kubelka-Munk (K–M) function spectra (b), and baseline subtraction and quantification of relevant peak heights (c) for SN15 (grayish filter), SN7 (brownish filter), and SN12 (reddish filter).

Fig. 5 (a) depicts the reflectance UV–Vis spectra obtained from our aerosol samples. The raw spectra present a characteristic baseline due to the scattering of the UV–Vis radiation with limited signal decreases. Samples SN7 and SN12 in particular present two bands at around 480 nm and 535 nm characterized by an attenuated reflectance due to the absorption by iron oxides (Gonçalves et al., 2012; Torrent and Barrón, 2002), a spectral feature not observed in the sample SN15. Derivative spectroscopy has been therefore explored in order to: (a) correct for baseline effects in spectra to remove non-chemical effects, (b) enhance spectral detail not appreciable in the raw spectrum, and (c) resolve overlapped bands (Ojeda and Rojas, 2013). The treated spectra finally produced three main peaks at 420, 480 and 535 nm, respectively.

An example is reported in Fig. 5 (c). The 420 nm peak was discarded as significantly affected by an instrumental noise due to the lamp shift from Vis to UV at around 380 nm (see Fig. 5 (a)). Average values and the standard deviations of the peak heights obtained from the signals at h_480 nm and h_530 nm were calculated for the blank filter (B) and for the 19 samples (SN1, ...SN19) starting from the three analyzed portions for each sample, and were reported in Table 2.

Table 2. Average values and standard deviations (numbers in brackets) of the semi-quantitative data of mixed iron oxide minerals (h_480 nm) and hematite (h_535 nm).

Sample	h_480nm (10 ⁻⁵)	h_530nm (10 ⁻⁵)
B	0.025 (0.009)	0.011 (0.005)
SN1	1.32 (0.37)	0.55 (0.08)
SN2	0.83 (0.16)	0.17 (0.04)
SN3	3.27 (0.71)	1.49 (0.20)
SN4	2.53 (1.20)	1.29 (0.17)
SN5	3.03 (0.03)	1.42 (0.06)
SN6	2.99 (0.27)	1.19 (0.19)
SN7	4.01 (0.38)	1.28 (0.11)
SN8	2.38 (0.90)	0.87 (0.08)
SN9	2.50 (0.05)	0.78 (0.16)
SN10	3.17 (0.11)	1.48 (0.09)
SN11	2.74 (0.10)	0.97 (0.18)
SN12	2.57 (0.10)	1.96 (0.22)
SN13	2.92 (0.62)	1.31 (0.33)
SN14	3.02 (0.64)	0.95 (0.15)
SN15	0.72 (0.46)	0.21 (0.13)
SN16	1.29 (0.15)	0.55 (0.26)
SN17	2.20 (0.06)	0.87 (0.19)
SN18	2.69 (0.52)	1.26 (0.31)
SN19	0.78 (0.18)	0.41 (0.09)

3.3 - Validation of UV-Vis DRS results

The similarity between the sample series of iron oxides semi-quantitative data (h_480 nm and h_535 nm) and elemental iron (Fe) concentration by PIXE can be observed in Fig. 6 (a), showing a comparable trend among all the parameters. Scatter plots in Fig. 6 (b) indicate a good correlation between these independent parameters. Table 3 reports the Spearman correlation coefficients between CIELCH parameters, iron oxide minerals semi-quantitative data, elemental iron, and PM₁₀. It is shown that iron (Fe) is highly linearly correlated with PM₁₀ (+0.96), confirming that mineral dust is one of the main components in the analyzed samples. A high positive correlation between peak heights at 480 nm and 535 nm and iron concentration is observed (+0.84 and +0.86 respectively) supporting the association between mineral and elemental components as shown in Fig. 6. In particular the band at h_535 nm is found as the most significantly associated to the filter color (+0.85 with chroma and -0.83 with hue). This result is extremely interesting because, as previously remarked (see section 3.2), this peak is specific to hematite, while the other peak (h_480 nm) is associated with a range of different minerals made of iron oxides, including goethite (which is the most abundant iron oxide in Saharan Dust). An increase in chroma and a decrease in hue leads to

a higher degree in the redness of the PM filters (see subsection 3.1), which is exactly the characteristic color of hematite (Rossman, 1996). As such, the semi-quantitative data on iron oxide minerals (especially hematite) are strongly related to PM filter colors (especially the red color), and both parameters are indicative of Saharan dust transport events.

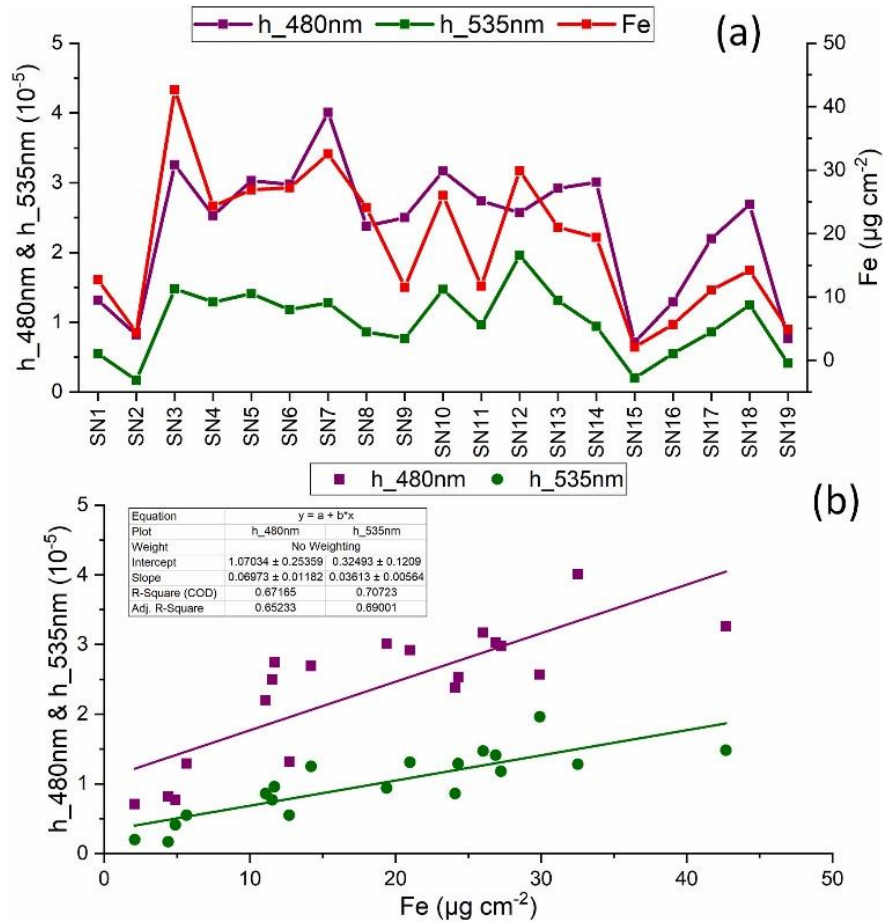


Fig. 6. (a) Sample series of h_480 nm (semi-quantitative data of several iron oxide minerals, mainly goethite), h_535 nm (semi-quantitative data of hematite), and elemental iron concentration (Fe). (b) Scatter plots of h_480 nm vs. Fe and h_535 nm vs. Fe.

Table 3. Spearman correlation coefficients obtained for each pair of variables. L* = CIELAB lightness, C_{ab}* = CIELAB chroma, h_{ab}^o = CIELAB hue, Fe = elemental iron, PM₁₀ = particulate matter, h_480 nm = semi-quantitative data of mixed iron oxide minerals, h_535 nm = semi-quantitative data of hematite.

	L*	C _{ab} *	h _{ab} ^o	Fe	PM ₁₀	h_480nm	h_535nm
L*	1.00						
C _{ab} *	0.08	1.00					
h _{ab} ^o	-0.11	-0.90	1.00				
Fe	-0.20	0.85	-0.80	1.00			
PM ₁₀	-0.11	0.81	-0.74	0.96	1.00		
h_480nm	-0.47	0.69	-0.60	0.84	0.75	1.00	
h_535nm	-0.28	0.85	-0.83	0.86	0.81	0.81	1.00

3.4 - Diagnosis and validation of Saharan mineral dust

Fig. 7 reports the dendrogram obtained from Ward's clustering analysis applied to the UV-Vis DRS results (CIELCH parameters and iron oxide minerals semi-quantitative data), and where two main clusters are identified. In particular, 15 PM samples belong to cluster 1, while the other 4 PM samples belong to cluster 2. These clusters are compared with PM₁₀ data (normalized in air sampled volume, $\mu\text{g}/\text{m}^3$) in Fig. 8 (a). Indeed, the association of mineral dust transport events has already been clearly related to significant increases in PM due to the considerable mass load of this component in particulate material owing to the large fraction of the coarse particles (Krasnov et al., 2014; Matassoni et al., 2011). In order to facilitate the Saharan Dust detection, the UV-Vis DRS results are reported again in Fig. 8(b) and (c). The residence time spent by the air parcels over different areas before reaching the sampling site is also reported in Fig. 9 for each PM sample.

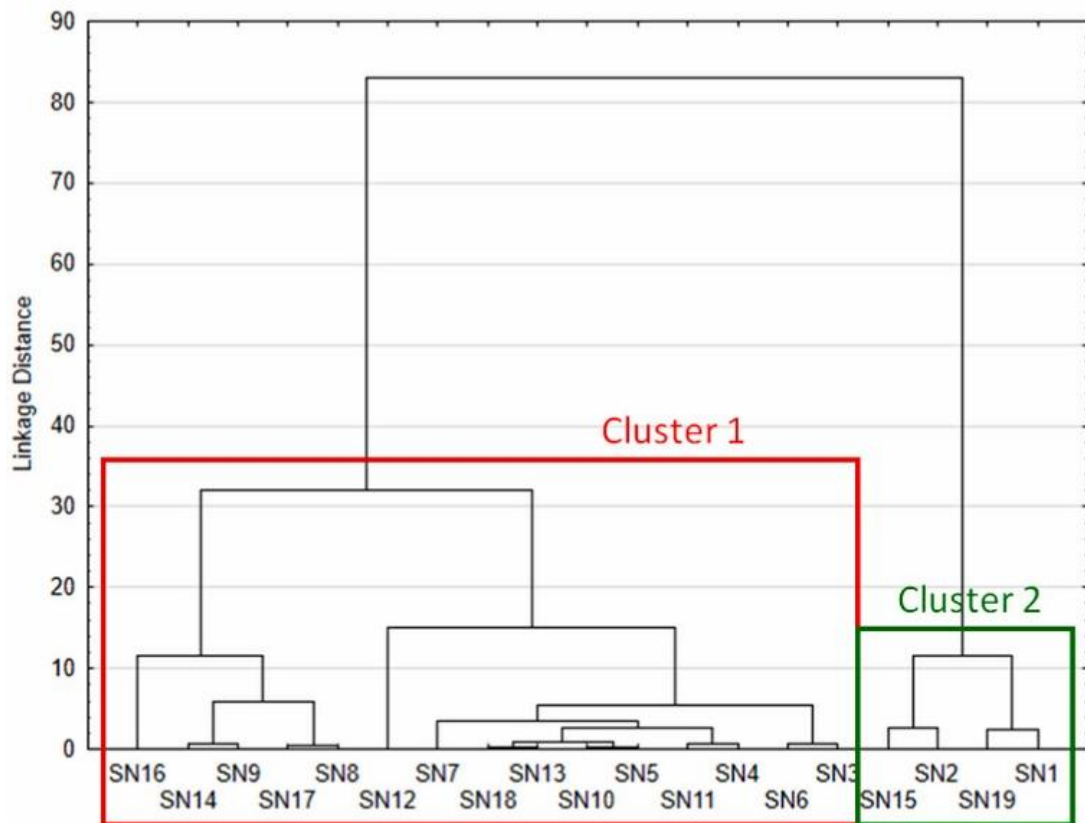


Fig. 7. Dendrogram of Ward's hierarchical clustering method starting from CIELCH parameters and semi-quantitative data of iron oxide minerals. The clustering solution with two clusters is highlighted by squares.

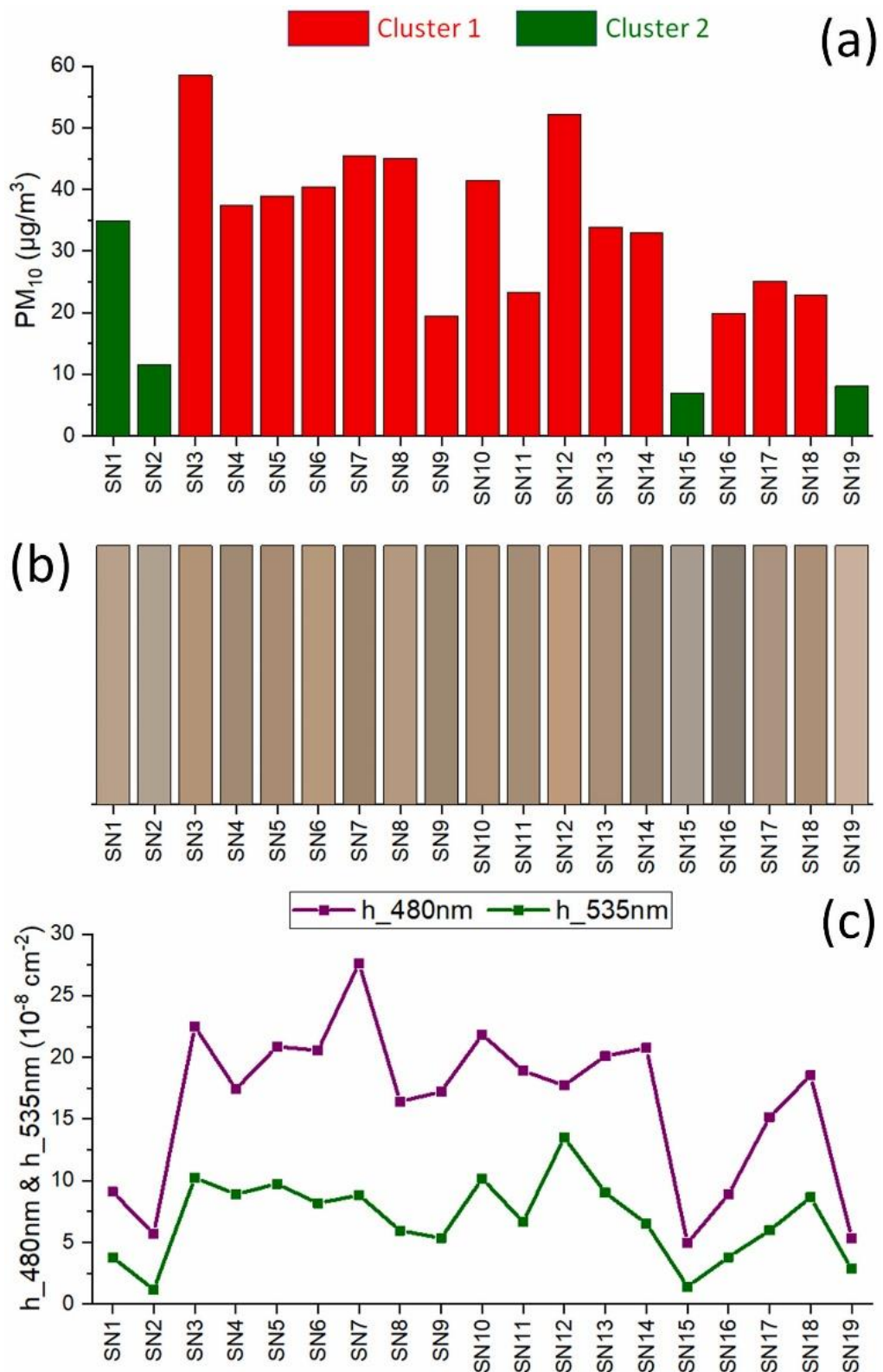


Fig. 8. (a) Sample series of PM₁₀ data (μg/m³) with the association of PM filters to the respective clusters (cluster 1 and cluster 2). (b) Display of PM filters colors, look at subsection 3.1. (c) Sample series of h_{480nm} (semi-quantitative data of several iron oxide minerals) and h_{535nm} (hematite), look at subsection 3.2.

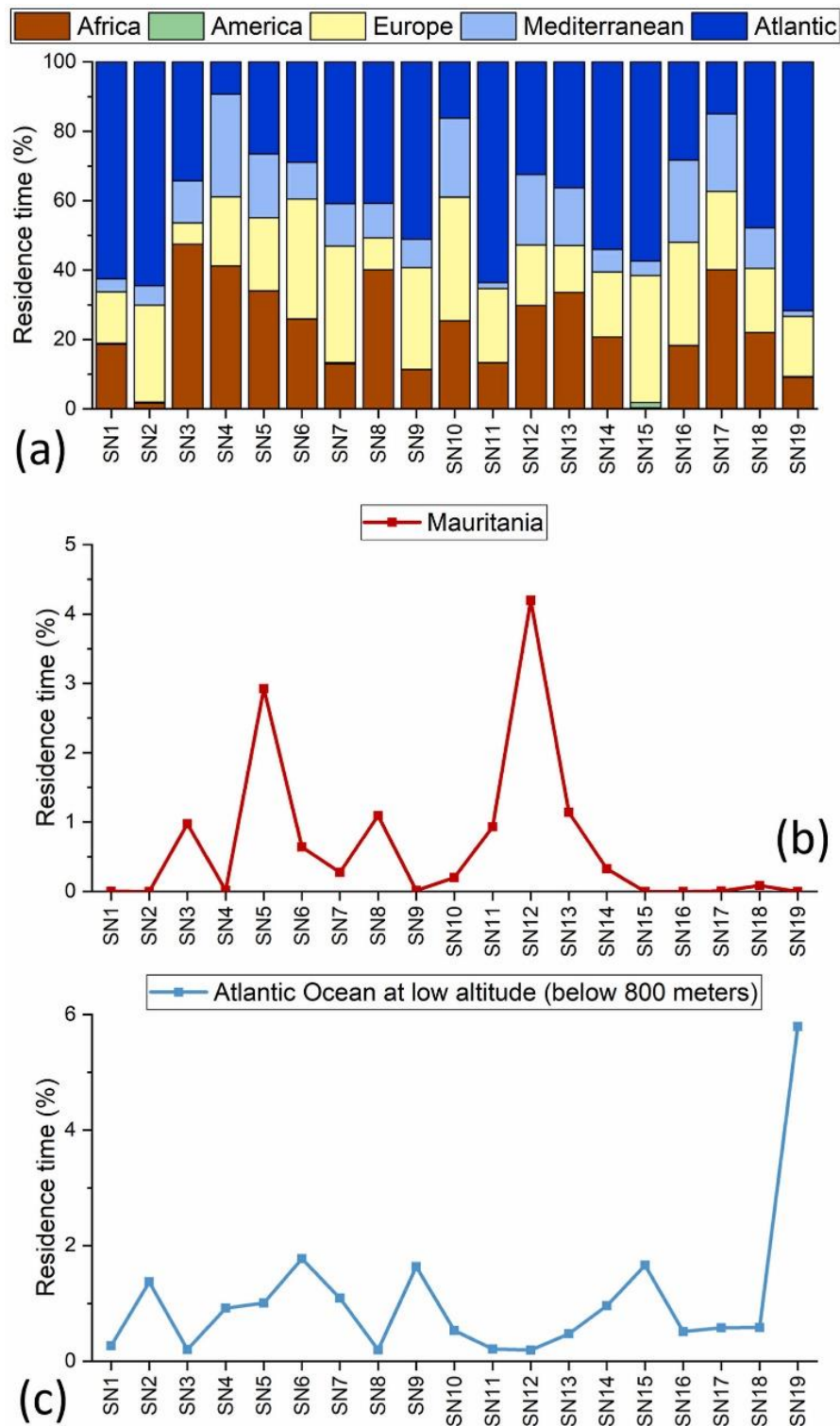


Fig. 9. (a) Stacked bar chart of the percentage residence time over each examined region and PM filter; Sample series of residence time over Mauritania (b) and the Atlantic Ocean, below 800 m (c).

Cluster 1 (highlighted in red) clearly identifies the Saharan dust events while cluster 2 (highlighted in green) identifies air masses from all the other source areas (Fig. 8(a)). Moreover, these results are in agreement with the estimated residence time (Fig. 9 (a)). Indeed, residence time analysis highlights how SN2, SN15, and SN19 samples belonging to

cluster 2 are characterized by shorter residence times (less than 10%) over Africa than other PM filters (higher than 10%), suggesting uplift and rapid transport of mineral dust from the North-African desert without appreciable mixing with other aerosol sources.

Sample SN1 presents an exception being characterized by an elevated PM₁₀ value and a residence time over Africa comparable to the samples belonging to the Saharan dust events cluster (cluster 1). Its assignment to the category of non-Saharan dust events, obtained only by UV–Vis DRS, is linked to its greyish color and to the low concentrations of iron oxide minerals. In order to justify this outcome, an in-depth analysis was carried out by satellite images retrieved from NASA's Earth Observing System Data and Information System (EOSDIS) (Behnke et al., 2019), reported in Fig. 10. Whitish dust from the dried surface of Chott el-Jerid ephemeral lake (Fig. 10(a)), was uplifted by the wind on 05/06/2016 (Fig. 10(b)) and reached the receptor site on 08/06/2016 (from Fig. 10(c)–10(f)), that is the first day of SN1 filter sampling period. Therefore, although the SN1 sample is significantly impacted by this Saharan dust transport event, its chemical-mineralogical composition is unusual compared to other PM samples due to the deficiency of iron oxide minerals, as evidenced by the greyish color of the examined filter.

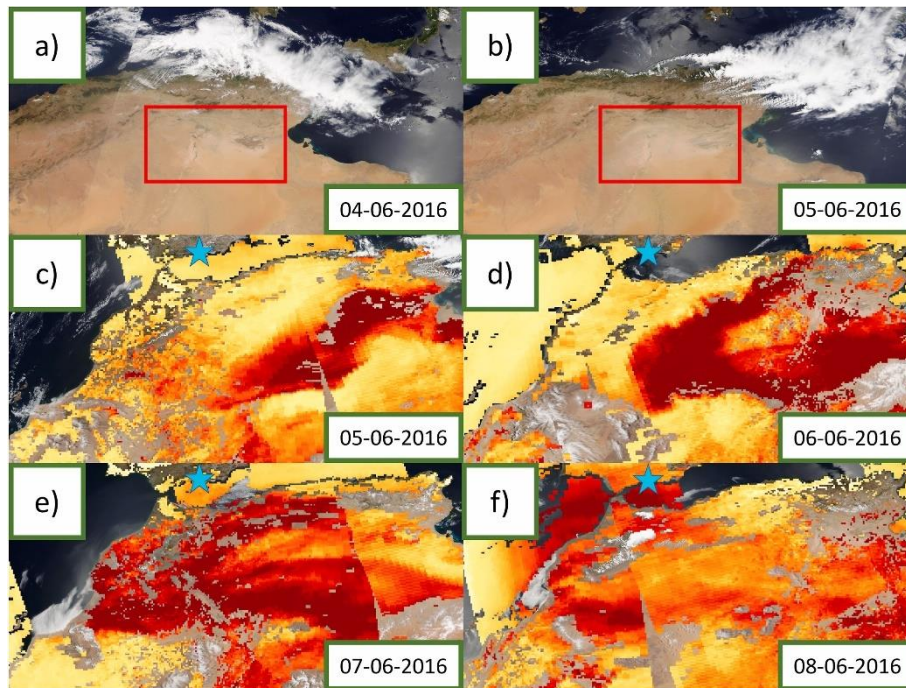


Fig. 10. Corrected reflectance (True Color) Terra/MODIS snapshots for 4 June 2016 (a) and 5 June 2016 (b); Merged DT/DB Aerosol Optical Depth (Land and Ocean) Aqua/MODIS snapshots from 5 June 2016 (c) to 8 June 2016 (f). Higher AOD values are indicated by a more reddish color and allow following the dust plume transport. The red square in a) and b) highlights the Chott el-Jerid Lake (Tunisia) while the light blue star in c), d), e), and f) indicates the PM sampling station in Sierra Nevada (37.096 N, -3.387 W, 2550 m a.s.l.). Images have been retrieved from the NASA EOSDIS, worldview tool at <https://worldview.earthdata.nasa.gov>.

Some particular considerations can be drawn also for two additional specific samples; i.e. SN12 and SN19. SN12 is one of the PM filters more impacted by a Saharan dust events, as results from its high PM₁₀ concentration and the pronounced reddish color (see subsection

3.1). The latter observation may be explained by the higher value of residence time over Mauritania (> 4%), as reported in Fig. 9 (b), whose area is known to be an important source of hematite (Journet et al., 2014; Schlueter, 2006; Waele et al., 2019). As previously assessed, sample SN19 is clearly a PM sample not affected by Saharan dust transport. This filter presents the “whitest” color amongst the samples analyzed, as shown by the highest luminescence value ($L^* = 73.23$, look at Table 1) in the CIELAB/CIELCH colorimetric models. This result can be justified by a significantly long residence time over the Atlantic Ocean at low altitude (>5%), as reported in Fig. 9 (c), which presumably involves a strong influence of colorless sea salt component (mainly defined by sodium chloride and magnesium chloride) in the examined filter.

Conclusions

In this work, the feasibility of UV–Vis Diffuse Reflectance Spectroscopy for a rapid and non-destructive diagnosis of Saharan dust events in particulate matter filters has been explored, assessed, and validated. This method has been applied to a sequence of particulate matter filters sampled at high altitude (2550 m a.s.l.) in an area heavily impacted by Saharan mineral dust incursion events due to its proximity to North Africa (Sierra Nevada, Spain, 37.096 N, -3.387 W).

In particular, this analytical method allowed to identify unequivocally two absorption bands corresponding to a well-defined set of iron mineral oxides contained in Saharan dust: the absorption band at about 480 nm, representative of multiple iron oxide minerals (i.e., goethite, lepidocrocite, maghemite, ferrihydrite, ferroxhyte, akaganéite, and schwertmannite), and another at about 535 nm, specific for hematite and therefore highly selective for diagnostic purposes. Through appropriate processing of the reflectance spectra, a semi-quantitative data for these mineral oxides it was obtained. Furthermore, starting from the reflectance measurements, it was possible to quantitatively parameterize the filter coloring as a function of PM source.

The results obtained from this technique have been validated on the basis of the elemental iron concentration obtained by Proton Induced X-ray Emission (PIXE) analysis. Besides, the relationship between the concentration of hematite increases and the higher reddish color of the filters with an increase in their PM₁₀ content was demonstrated. Therefore, the UV–Vis DRS has been proven to be extremely useful for a fast, cheap, and unambiguous identification of Saharan mineral dust events in PM filters.

The results obtained have been finally proven on the basis of residence time analysis of back-trajectory ensembles, whose outcomes are in excellent agreement with those obtained by UV–Vis DRS, except for one PM sample with a peculiar chemical-mineralogical composition likely associated with the dried Chott el-Jerid Lake (Tunisia). Furthermore, some other samples have been explored by associating the color and the semi-quantitative data of iron oxide minerals with their particular PM sources.

It is important to highlight that in this work the UV–Vis DRS methodology was described, applied, and validated for weekly PM₁₀ samples certainly characterized by a predominance of Saharan Dust but likewise affected by a complex mixture of emission sources. Despite the presence of high number of mixed emission sources, reasonable outcomes were achieved with this technique. The final decision in using this approach is currently under investigation for other daily PM filters presenting significant amounts of anthropogenic particulate matter, e.g. Black and Brown carbon, which can significantly affect the sample membranes' spectral behavior.

CRedit authorship contribution statement

Pietro Morozzi: Conceptualization, Methodology, Formal analysis, Investigation, Writing – original draft, Visualization. Barbara Ballarin: Resources, Writing – review & editing. Sara Arcozzi: Methodology, Resources, Investigation. Erika Brattich: Writing – review & editing. Franco Lucarelli: Validation, Resources, Writing – review & editing. Silvia Nava: Validation, Resources, Writing – review & editing. Pedro José Gómez-Cascales: Investigation. J.A.G. Orza: Software, Formal analysis, Resources, Writing – review & editing, Supervision, Project administration, Funding acquisition. Laura Tositti: Conceptualization, Writing – review & editing, Supervision.

Acknowledgements

This work has been carried out under the Spanish project FRESA (Impact of dust-laden African air masses and of stratospheric air masses in the Iberian Peninsula. Role of the Atlas Mountains, Ref: CGL2015-70741-R). Firstly, Lucas Alados-Arboledas (IISTA-CEAMA) is gratefully acknowledged for making possible the field campaign at the sampling site. We are grateful to prof. María Ángeles Ferro García, and her coworkers Francisco Piñero García and Abel Milena Pérez in the Radiochemistry and Environmental Radiology Laboratory of the Inorganic Chemistry Department of University of Granada (LABRADIQ) for kindly providing the samples used in this work. A Heartfelt thanks to Christian Cingolani, Josep Mestres Sanna, and Adrià Simon Ortiz for the assistance in the experimental activity during their thesis work. Finally, the authors acknowledge the NOAA Air Resources Laboratory (ARL) for the provision of the HYSPLIT transport and dispersion model and/or READY website (<https://www.ready.noaa.gov>) used in this publication and the European Centre for Medium-range Weather Forecast (ECMWF) for making available the ERA-Interim database.

References

- Akoglu, H., User's guide to correlation coefficients (2018) Turkish Journal of Emergency Medicine, 18;
- Alastuey, A., Querol, X., Aas, W., Lucarelli, F., Pérez, N., Moreno, T., Geochemistry of PM10 over Europe during the EMEP intensive measurement periods in summer 2012 and winter 2013 (2016) Atmos. Chem. Phys., 16 (10), pp. 6107-6129;
- Alfaro, S., Lafon, S., Rajot, J., Formenti, P., Gaudichet, A., Maillé, M., Iron oxides and light absorption by pure desert dust: an experimental study (2004) J. Geophys. Res., 109, p. 8208;
- Arimoto, R., Balsam, W., Schloesslin, C., Visible spectroscopy of aerosol particles collected on filters: iron-oxide minerals (2002) Atmos. Environ., 36, pp. 89-96;
- Ashbaugh, L.L., Malm, W.C., Sadeh, W.Z., A residence time probability analysis of sulfur concentrations at grand Canyon National Park (1985) Atmos. Environ., 19 (8), pp. 1263-1270., 1967;
- Barnaba, F., Bolignano, A., di Liberto, L., Morelli, M., Lucarelli, F., Nava, S., Desert Dust Contribution to PM10 Loads in Italy: Methods and Recommendations Addressing the Relevant European Commission Guidelines in Support to the Air Quality Directive 2008/50 (2017) Atmos. Environ., 161;
- Barrón, V., Torrent, J., Use of the Kubelka—Munk theory to study the influence of iron oxides on soil colour (1986) J. Soil Sci., 37 (4), pp. 499-510;

- Behnke, J., Mitchell, A., Ramapriyan, H., NASA's Earth observing data and information system – near-term challenges (2019) *Data Sci. J.*, 18;
- Blitz, J.P., Diffuse reflectance spectroscopy (1998) *Modern Techniques in Applied Molecular Spectroscopy*, 14, p. 185;
- Bonasoni, P., Cristofanelli, P., Sandro, F., Gobbi, G.P., van Dingenen, R., Tositti, L., Balkanski, Y., Ozone and aerosol correlation during Saharan dust transport episodes at Mt. Cimone (2003);
- Brattich, E., Hernández-Ceballos, M.A., Cinelli, G., Tositti, L., Analysis of ²¹⁰Pb peak values at Mt. Cimone (1998–2011) (2015) *Atmos. Environ.*, 112, pp. 136-147;
- Brattich, E., Riccio, A., Tositti, L., Cristofanelli, P., Bonasoni, P., An outstanding Saharan dust event at Mt. Cimone (2165 m asl, Italy) in March 2004 (2015) *Atmos. Environ.*, 113, pp. 223-235;
- Bristow, C.S., Hudson-Edwards, K.A., Chappell, A., Fertilizing the Amazon and equatorial Atlantic with west African dust (2010) *Geophys. Res. Lett.*, 37 (14);
- Cabello, M., Orza, J.G., Dueñas, C., Liger, E., Gordo, E., Cañete, S., Back-trajectory analysis of African dust outbreaks at a coastal city in southern Spain: selection of starting heights and assessment of African and concurrent Mediterranean contributions (2016) *Atmos. Environ.*, 140;
- Calzolari, G., Chiari, M., García Orellana, I., Lucarelli, F., Migliori, A., Nava, S., Taccetti, F., The new external beam facility for environmental studies at the Tandatron accelerator of LABEC (2006) *Nucl. Instrum. Methods Phys. Res. Sect. B Beam Interact. Mater. Atoms*, 249 (1), pp. 928-931;
- Caquineau, S., Gaudichet, A., Gomes, L., Legrand, M., Mineralogy of Saharan dust transported over northwestern tropical Atlantic Ocean in relation to source regions (2002) *J. Geophys. Res.: Atmosphere*, 107 (D15), AAC 4-1-AAC 4-12;
- Chiari, M., Yubero, E., Calzolari, G., Lucarelli, F., Crespo, J., Galindo, N., Comparison of PIXE and XRF analysis of airborne particulate matter samples collected on Teflon and quartz fibre filters (2018) *Nucl. Instrum. Methods Phys. Res. Sect. B Beam Interact. Mater. Atoms*, 417, pp. 128-132;
- Chin, M., Diehl, T., Dubovik, O., Eck, T., Holben, B., Sinyuk, A., Streets, D., Light absorption by pollution, dust, and biomass burning aerosols: a global model study and evaluation with AERONET measurements (2009) *Annales Geophysicae*, 27;
- Cuevas, E., Gómez-Peláez, A.J., Rodríguez, S., Terradellas, E., Basart, S., García, R.D., The pulsating nature of large-scale Saharan dust transport as a result of interplays between mid-latitude Rossby waves and the North African Dipole Intensity (2017) *Atmos. Environ.*, 167, pp. 586-602;
- Cusack, M., Alastuey, A., Pérez, N., Pey, J., Querol, X., Trends of particulate matter (PM_{2.5}) and chemical composition at a regional background site in the Western Mediterranean over the last nine years (2002–2010) (2012) *Atmos. Chem. Phys.*, 12 (18), pp. 8341-8357;
- Dee, D.P.D., Uppala, Simmons, B., Poli, P., The ERA-Interim reanalysis: configuration and performance of the data assimilation system (2011) *Q. J. R. Meteorol. Soc.*, 137, pp. 553-597;
- Diapouli, E., Manousakas, M.I., Vratolis, S., Vasilatou, V., Pateraki, S., Bairachtari, K.A., AIRUSE-LIFE +: estimation of natural source contributions to urban ambient air PM₁₀ and PM_{2.5} concentrations in southern Europe – implications to compliance with limit values (2017) *Atmos. Chem. Phys.*, 17 (5), pp. 3673-3685;
- Dickerson, R., Kondragunta, S., Stenchikov, G., Civerolo, K., Doddridge, B., Holben, B., The impact of aerosol on solar UV radiation and photochemical smog (1997) *Science (New York, N.Y.)*, 278, pp. 827-830;

- Draxler, R.R., Evaluation of an ensemble dispersion calculation (2003) *J. Appl. Meteorol.*, 42 (2), pp. 308-317;
- EC Commission, (2011) Staff Working Paper Establishing Guidelines for Determination of Contributions from the Re-suspension of Particulates Following Winter Sanding or Salting of Roads under the Directive 2008/50/EC on Ambient Air Quality and Cleaner Air for Europe, 2011, p. 207., http://ec.europa.eu/environment/air/quality/legislation/pdf/sec_2011_0207.pdf, European Commission, SEC. 2011;
- Particulate Matter from Natural Sources and Related Reporting under the EU Air Quality Directive in 2008 and 2009 (2012), <https://www.eea.europa.eu/publications/particulate-matter-from-natural-sources>;
- Escudero, M., Castillo, S., Querol, X., Avila, A., Alarcón, M., Viana, M.M., Wet and dry African dust episodes over eastern Spain (2005) *J. Geophys. Res.: Atmosphere*, 110 (D18);
- Escudero, M., Querol, X., Pey, J., Alastuey, A., Pérez, N., Ferreira, F., A methodology for the quantification of the net African dust load in air quality monitoring networks (2007) *Atmos. Environ.*, 41 (26), pp. 5516-5524;
- EU, Directive 2008/50/EC of the European Parliament and of the Council of 21 May 2008 on ambient air quality and cleaner air for Europe (2008) Official Journal of the European Union, , <http://data.europa.eu/eli/dir/2008/50/oj>;
- Fernandez, R.N., Schulze, D.G., Munsell colors of soils simulated by mixtures of goethite and hematite with kaolinite (1992) *Z. für Pflanzenernährung Bodenkunde*, 155 (5), pp. 473-478;
- Flentje, H., Briel, B., Beck, C., Collaud Coen, M., Fricke, M., Cyrys, J., Identification and monitoring of Saharan dust: an inventory representative for south Germany since 1997 (2015) *Atmos. Environ.*, 109, pp. 87-96;
- Formenti, P., Rajot, J., Desboeufs, K., Caquineau, S., Chevallier, S., Nava, S., Regional variability of the composition of mineral dust from western Africa: results from the AMMA SOP0/DABEX and DODO field campaigns (2008) *J. Geophys. Res.*, 113;
- Formenti, P., Nava, S., Prati, P., Chevaillier, S., Klaver, A., Lafon, S., Self-attenuation artifacts and correction factors of light element measurements by X-ray analysis: Implication for mineral dust composition studies (2010) *J. Geophys. Res.*, 115;
- Formenti, P., Caquineau, S., Chevaillier, S., Klaver, A., Desboeufs, K., Rajot, J., Dominance of goethite over hematite in iron oxides of mineral dust from Western Africa: quantitative partitioning by X-ray Absorption Spectroscopy (2014) *J. Geophys. Res.: Atmosphere*, 119;
- Garrison, V.H., Shinn, E.A., Foreman, W.T., Griffin, D.W., Holmes, C.W., Kellogg, C.A., African and Asian dust: from desert soils to coral Reefs (2003) *Bioscience*, 53 (5), pp. 469-480;
- Ginoux, P., Warming or cooling dust? (2017) *Nat. Geosci.*, 10 (4), pp. 246-248;
- Gonçalves, Í.G., Petter, C.O., Machado, J.L., Quantification of hematite and goethite concentrations in kaolin using diffuse reflectance spectroscopy: a new approach to Kubelka-Munk theory (2012) *Clay Clay Miner.*, 60 (5), pp. 473-483;
- Goudie, A., Middleton, N., Desert dust in the global system (2006) *Desert Dust in the Global System*, 1-287;
- Ibraheem, N., Hasan, M., Khan, R.Z., Mishra, P., Understanding color models: a review (2012) *ARPN J. Sci. Technol.*, 2;
- IDSO, S., Climatic change: the role of atmospheric dust (1981) *Spec. Pap. Geol. Soc. Am.*, 186, pp. 207-215;

- IE 11664-1-2019. Colorimetry - CIE Standard Colorimetric Observers. Standard, International Organization for Standardization, Geneva, CH;
- IE 11664-2-2020. Colorimetry - Part 2: CIE Standard Illuminants. Standard, International Organization for Standardization, Geneva, CH;
- IE 11664-4-2019. Colorimetry - Part 4: CIE 1976 L*a*b* Colour Space. Standard, International Organization for Standardization, Geneva, CH;
- Israelevich, P., Ganor, E., Alpert, P., Kishcha, P., Stupp, A., Predominant transport paths of Saharan dust over the Mediterranean Sea to Europe (2012) *J. Geophys. Res.: Atmosphere*, 117 (D2);
- Journet, E., Balkanski, Y., Harrison, S., A new data set of soil mineralogy for dust-cycle modeling (2014) *Atmos. Chem. Phys.*, 14, pp. 3801-3816;
- Karanasiou, A., Moreno, N., Moreno, T., Viana, M., de Leeuw, F., Querol, X., Health effects from Sahara dust episodes in Europe: Literature review and research gaps (2012) *Environ. Int.*, 47, pp. 107-114;
- Krasnov, H., Katra, I., Koutrakis, P., Friger, M., Contribution of dust storms to PM10 levels in an urban arid environment (2014) *J. Air Waste Manag. Assoc.*, 64, pp. 89-94., 1995;
- Kremers, J., Baraas, R., Marshall, N., Human Color Vision (2016);
- Lafon, S., Sokolik, I., Rajot, J., Caquineau, S., Gaudichet, A., Characterization of iron oxides in mineral dust aerosols: implications for light absorption (2006) *J. Geophys. Res.*, 111;
- Lin, J., Lagrangian modeling of the Atmosphere: an introduction (2012) *Geophysical Monograph Series*, 200;
- Linke, C., Möhler, O., Veres, A., Mohácsi, Á., Bozóki, Z., Szabó, G., Schnaiter, M., Optical properties and mineralogical composition of different Saharan mineral dust samples: a laboratory study (2006) *Atmos. Chem. Phys.*, 6 (11), pp. 3315-3323;
- Littmann, T., Steinrücke, J., Atmospheric boundary conditions of recent Saharan dust influx into Central Europe (1989) *Geojournal*, 18, pp. 399-406;
- Lucarelli, F., Nava, S., Calzolari, G., Chiari, M., Udisti, R., Marino, F., Is PIXE still a useful technique for the analysis of atmospheric aerosols? The LABEC experience (2011) *X Ray Spectrom.*, 40, pp. 162-167;
- Lucarelli, F., Calzolari, G., Chiari, M., Giannoni, M., Mochi, D., Nava, S., Carraresi, L., The upgraded external-beam PIXE/PIGE set-up at LABEC for very fast measurements on aerosol samples (2014) *Nucl. Instrum. Methods Phys. Res. Sect. B Beam Interact. Mater. Atoms*, 318, pp. 55-59;
- Lucarelli, F., Calzolari, G., Chiari, M., Nava, S., Carraresi, L., Study of atmospheric aerosols by IBA techniques: the LABEC experience (2018) *Nucl. Instrum. Methods Phys. Res. Sect. B Beam Interact. Mater. Atoms*, 417, pp. 121-127;
- Lupu, A., Maenhaut, W., Application and comparison of two statistical trajectory techniques for identification of source regions of atmospheric aerosol species (2002) *Atmos. Environ.*, 36 (36), pp. 5607-5618;
- Marconi, M., Sferlazzo, D.M., Becagli, S., Bommarito, C., Calzolari, G., Chiari, M., Saharan dust aerosol over the central Mediterranean Sea: PM10 chemical composition and concentration versus optical columnar measurements (2014) *Atmos. Chem. Phys.*, 14 (4), pp. 2039-2054;
- Matassoni, L., Pratesi, G., Centioli, D., Cadoni, F., Lucarelli, F., Nava, S., Malesani, P., Saharan dust contribution to PM 10, PM 2.5 and PM 1 in urban and suburban areas of Rome: a comparison between single-particle SEM-EDS analysis and whole-sample PIXE analysis (2011) *J. Environ. Monit.: JEM*, 13, pp. 732-742;

- Menéndez, I., Díaz-Hernández, J.L., Mangas, J., Alonso, I., Sánchez-Soto, P.J., Airborne dust accumulation and soil development in the north-East sector of gran canaria (canary Islands, Spain) (2007) *J. Arid Environ.*, 71 (1), pp. 57-81;
- Middleton, N., Goudie, A., Saharan dust: sources and trajectories (2002) *Trans. Inst. Br. Geogr.*, 26, pp. 165-181;
- Molinaroli, E., Masiol, M., Particolato atmosferico e ambiente mediterraneo. Il caso delle polveri sahariane (2006);
- Nava, S., Becagli, S., Calzolari, G., Chiari, M., Lucarelli, F., Prati, P., Saharan dust impact in central Italy: an overview on three years elemental data records (2012) *Atmos. Environ.*, 60, pp. 444-452;
- Ojeda, C.B., Rojas, F.S., Recent applications in derivative ultraviolet/visible absorption spectrophotometry: 2009–2011: a review (2013) *Microchem. J.*, 106, pp. 1-16;
- Orza, J.A.G., Cabello, M., Galiano, V., Vermeulen, A.T., Stein, A.F., The association between the north Atlantic Oscillation and the Interannual variability of the tropospheric transport pathways in western Europe (2013) *Lagrangian Modeling of the Atmosphere*, pp. 127-142;
- Pandey, A., Shetty, N.J., Chakrabarty, R.K., Aerosol light absorption from optical measurements of PTFE membrane filter samples: sensitivity analysis of optical depth measures (2019) *Atmos. Meas. Tech.*, 12 (2), pp. 1365-1373;
- Pérez, C., Haustein, K., Janjic, Z., Jorba, O., Huneus, N., Baldasano, J.M., Black, T., Thomson, M., Atmospheric dust modeling from meso to global scales with the online NMMB/BSC-Dust model – Part 1: model description, annual simulations and evaluation (2011) *Atmos. Chem. Phys.*, 11 (24), pp. 13001-13027;
- Petzold, A., Schönlinner, M., Multi-angle absorption photometry—a new method for the measurement of aerosol light absorption and atmospheric black carbon (2004) *J. Aerosol Sci.*, 35 (4), pp. 421-441;
- Prospero, J., Schmitt, R., Cuevas, E., Savoie, D., Graustein, W., Turekian, K., Temporal variability of summer-time ozone and aerosols in the free troposphere over the eastern North Atlantic (1995) *Geophys. Res. Lett.*, 22, pp. 2925-2928;
- Putaud, J.-P., van Dingenen, R., Dell'Acqua, A., Raes, F., Matta, E., Decesari, S., Size-segregated Aerosol Mass Closure and Chemical Composition in Monte Cimone (I) during MINATROC (2004);
- Querol, X., Tobías, A., Pérez, N., Karanasiou, A., Amato, F., Stafoggia, M., Monitoring the impact of desert dust outbreaks for air quality for health studies (2019) *Environ. Int.*, 130, p. 104867;
- R Core Team, R: A Language and Environment for Statistical Computing (2019), <https://www.R-project.org/>, R Foundation for Statistical Computing Vienna, Austria;
- Reicher, N., Budke, C., Eickhoff, L., Raveh-Rubin, S., Kaplan-Ashiri, I., Koop, T., Rudich, Y., Size-dependent ice nucleation by airborne particles during dust events in the eastern Mediterranean (2019) *Atmos. Chem. Phys.*, 19 (17), pp. 11143-11158;
- Remoundaki, E., Bourliva, A., Kokkalis, P., Mamouri, R.E., Papayannis, A., Grigoratos, T., PM10 composition during an intense Saharan dust transport event over Athens (Greece) (2011) *Sci. Total Environ.*, 409 (20), pp. 4361-4372;
- Riccio, A., Chianese, E., Tositti, L., Baldacci, D., Sandrini, S., Modeling the transport of Saharan dust toward the Mediterranean region: an important issue for its ecological implications (2009) *Ecol. Quest.*, 11, pp. 65-72;
- Rodríguez, S., Calzolari, G., Chiari, M., Nava, S., García, M.I., López-Solano, J., Rapid changes of dust geochemistry in the Saharan Air Layer linked to sources and meteorology (2020) *Atmos. Environ.*, 223, p. 117186;

- Rolph, G., Stein, A., Stunder, B., Real-time environmental applications and Display sYstem: READY (2017) *Environ. Model. Software*, 95, pp. 210-228;
- Rossman, G., Why hematite is red: correlation of optical absorption intensities and magnetic moments of Fe³⁺ minerals (1996), 5, pp. 23-27;
- Schafer, R., What is a Savitzky-Golay filter? [Lecture notes] (2011) *IEEE Signal Processing Magazine - IEEE SIGNAL PROCESS MAG*, 28, pp. 111-117;
- Scheinost, A., Chavernas, A., Barrón, V., Torrent, J., Use and limitations of second-derivative diffuse reflectance spectroscopy in the visible to near-infrared range to identify and quantify Fe oxides in soils (1998) *Clay Clay Miner.*, 46, pp. 528-536;
- Schloss, K.B., Lessard, L., Racey, C., Hurlbert, A.C., Modeling color preference using color space metrics (2018) *Vis. Res.*, 151, pp. 99-116;
- Schlueter, T., *Geological Atlas of Africa: with Notes on Stratigraphy, Tectonics, Economic Geology, Geohazards and Geosites of Each Country* (2006);
- Sellitto, V., Barrón, V., Palumbo, G., Salzano, R., Colombo, C., Uso della spettrometria di riflettanza diffusa (DRS) e bi-direzionale (BRF) per lo studio dei suoli vulcanici europei (2008);
- Sellitto, V.M., Fernandes, R.B.A., Barrón, V., Colombo, C., Comparing two different spectroscopic techniques for the characterization of soil iron oxides: diffuse versus bi-directional reflectance (2009) *Geoderma*, 149 (1-2), pp. 2-9;
- Shao, L., Li, W., Yang, S., Shi, Z., Lü, S., Mineralogical characteristics of airborne particles collected in Beijing during a severe Asian dust storm period in spring 2002 (2007) *Sci. China Earth Sci.*, 50 (6), pp. 953-959;
- Shen, Z.X., Cao, J.J., Zhang, X.Y., Arimoto, R., Ji, J.F., Balsam, W.L., Spectroscopic analysis of iron-oxide minerals in aerosol particles from northern China (2006) *Sci. Total Environ.*, 367 (2-3), pp. 899-907;
- Sherman, D.M., Waite, T.D., Electronic spectra of Fe³⁺ oxides and oxide hydroxides in the near IR to near UV (1985) *Am. Mineral.*, 70 (11-12), pp. 1262-1269., <http://pubs.er.usgs.gov/publication/70012311>;
- Shi, Z., Krom, M.D., Jickells, T.D., Bonneville, S., Carslaw, K.S., Mihalopoulos, N., Impacts on iron solubility in the mineral dust by processes in the source region and the atmosphere: a review (2012) *Aeolian Research*, 5, pp. 21-42;
- Shinn, E.A., Smith, G.W., Prospero, J.M., Betzer, P., Hayes, M.L., Garrison, V., Barber, R.T., African dust and the demise of caribbean coral Reefs (2000) *Geophys. Res. Lett.*, 27 (19), pp. 3029-3032;
- Sokolik, I.N., Toon, O.B., Incorporation of mineralogical composition into models of the radiative properties of mineral aerosol from UV to IR wavelengths (1999) *J. Geophys. Res.: Atmosphere*, 104 (D8), pp. 9423-9444;
- Soleimani, Z., Teymouri, P., Darvishi Bolorani, A., Mesdaghinia, A., Middleton, N., Griffin, D.W., An overview of bioaerosol load and health impacts associated with dust storms: a focus on the Middle East (2020) *Atmos. Environ.*, 223, p. 117187;
- Spyrou, C., Mitsakou, C., Kallos, G., Louka, P., Vlastou, G., An improved limited area model for describing the dust cycle in the atmosphere (2010) *J. Geophys. Res.: Atmosphere*, 115 (D17);
- Stafoggia, M., Zauli-Sajani, S., Pey, J., Samoli, E., Alessandrini, E., Basagaña, X., Desert dust outbreaks in Southern Europe: contribution to daily PM₁₀ concentrations and short-term associations with mortality and hospital admissions (2016) *Environ. Health Perspect.*, 124 (4), pp. 413-419;
- Stein, A.F., Draxler, R.R., Rolph, G.D., Stunder, B.J.B., Cohen, M.D., Ngan, F., NOAA's HYSPLIT atmospheric transport and dispersion modeling system (2015) *Bull. Am. Meteorol. Soc.*, 96 (12), pp. 2059-2077;

- Stohl, A., Computation, accuracy and applications of trajectories—a review and bibliography (1998) *Atmos. Environ.*, 32 (6), pp. 947-966;
- Szalai, Z., Kiss, K., Jakab, G., Sipos, P., Belucz, B., Németh, T., The use of UV-VIS-NIR reflectance spectroscopy to identify iron minerals (2013) *Astron. Nachr.*, 334 (9), pp. 940-943;
- Torrent, J., Barrón, V., Diffuse reflectance spectroscopy of iron oxides (2002) *Encyclopedia of Surface and Colloid Science*, 1;
- Torrent, J., Barrón, V., *Methods of Soil Analysis. Part 5. Mineralogical Methods, Chapter 13 Diffuse Reflectance Spectroscopy* (2008), pp. 367-385., SSSA Book Series USA No. 5;
- Tositti, L., Brattich, E., Cinelli, G., Baldacci, D., 12 years of ⁷Be and ²¹⁰Pb in Mt. Cimone, and their correlation with meteorological parameters (2014) *Atmos. Environ.*, 87, pp. 108-122;
- Usher, C.R., Michel, A.E., Grassian, V.H., Reactions on mineral dust (2003) *Chem. Rev.*, 103 (12), pp. 4883-4940;
- van den Berg, R., Hoefsloot, H., Westerhuis, J., Smilde, A., van der Werf, M., Van den Berg, R.A., Hoefsloot, H.C.J., Van der Werf, M.J., Centering, scaling, and transformations: improving the biological information content of metabolomics data. *BMC Genomics* 7: 142-157 (2006) *BMC Genom.*, 7, p. 142;
- Waele, B.D., Aitken, A., Mourik, M.V., Laab Laab, K.O., Elhacen Ould Med Yeslem, M., Mohamedou, T., From a mining Mindset to regional discovery: a case study for hematite iron Ore Exploration in Mauritania (2019) *ASEG Extended Abstracts*, (1), pp. 1-3., 2019;
- Ward, J.H., Hierarchical groupings to optimize an objective function (1963) *J. Am. Stat. Assoc.*, pp. 234-244;
- WHO, WHO Air Quality Guidelines for Particulate Matter, Ozone, Nitrogen Dioxide and Sulfur Dioxide: Global Update 2005: Summary of Risk Assessment (2006), World Health Organization WHO/SDE/PHE/OEH/06.02). p. WHO/SDE/PHE/OEH/06.02;
- Xu, J., DuBois, D., Pitchford, M., Green, M., Etyemezian, V., Attribution of sulfate aerosols in Federal Class I areas of the western United States based on trajectory regression analysis (2006) *Atmos. Environ.*, 40 (19), pp. 3433-3447

CHAPTER 4 - Chemiluminescent fingerprints from airborne particulate matter: A luminol-based assay for the characterization of oxidative potential with kinetical implications

by **Pietro Morozzi**^a, Luca Bolelli^b, Erika Brattich^c, Elida Nora Ferri^b, Stefano Girotti^b, Stefano Sangiorgi^b, J.A.G. Orza^d, Francisco Piñero-García^{e,f}, Laura Tositti^a

^a Department of Chemistry “G. Ciamician”, University of Bologna, Via Selmi, 2, 40126 Bologna, Italy

^b Department of Pharmacy and Biotechnology, University of Bologna, Via S. Donato 15, 40127 Bologna, Italy

^c Department of Physics and Astronomy, University of Bologna, Via Irnerio, 46, 40126 Bologna, Italy

^d SCOLAb, Department of Applied Physics, University Miguel Hernandez de Elche, 03202 Elche, Spain

^e Radiochemistry and Environmental Radiology Laboratory, Inorganic Chemical Department, Faculty of Sciences, University of Granada, 18077 Granada, Spain

^f Department of Radiation Physics, Institute of Clinical Sciences, Sahlgrenska Academy, University of Gothenburg, Gula Stråket 2B, SE-413 45, Gothenburg, Sweden



ELSEVIER

This article was published in Science of The Total Environment, Volume 789, 2021, 148005, ISSN 0048-9697, <https://doi.org/10.1016/j.scitotenv.2021.148005>

Highlights

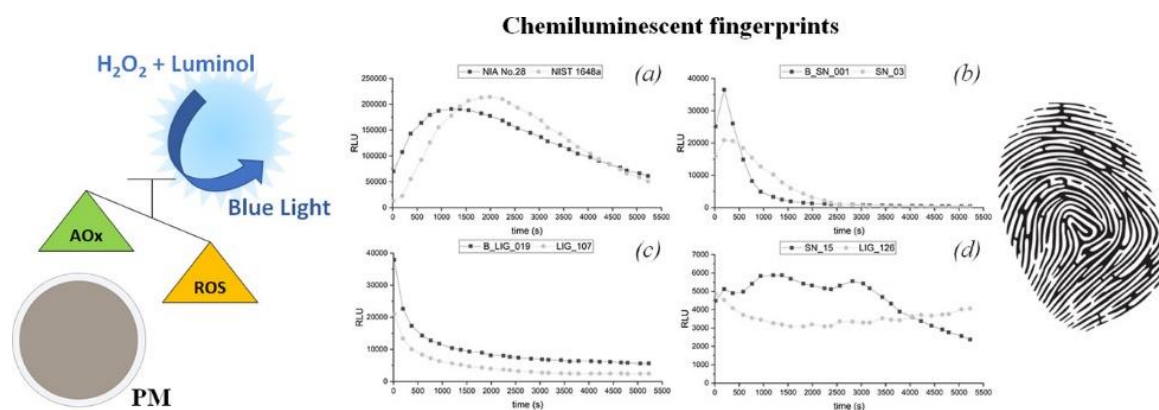
- Screening evaluation of particulate matter oxidative potential
- Luminol light emission over time as chemiluminescent fingerprint
- Relationship between the luminescence data and aerosol emission sources
- Effective discrimination of different particulate matter filters by chemometrics

Abstract

In this study, a new chemiluminescent method based on the dependence of luminol light emission induced by free radicals in airborne particulate matter (PM) is proposed as a screening assay for the rapid characterization of samples from different sources based on their redox properties. This parameter is considered critical for assessing particulate matter toxicity and its impacts on human health. We propose a cell-free, luminescent assay to evaluate the redox potential of particulate matter directly on the filters employed to collect it. A joint chemometric approach based on Principal Component Analysis and Hotelling Analysis was applied to quickly sort out ambient particulate samples with a significantly different light emission profile caused by Luminol reaction. Based on Spearman correlation analysis, the association of the samples light emission intensity with their chemical composition and emission sources was attempted.

The overall methodology was tested with certified reference materials and applied to two series of particulate matter samples previously subjected to thorough chemical speciation and subsequent source apportionment.

The results show the effectiveness of the luminescent method, allowing the quick assessment of particulate matter oxidative potential, but providing further evidence on the complexity of the oxidative potential determination in this kind of samples. The chemometric processing of the whole dataset clearly highlights the distinct behavior among the two series of samples, the certificate standard reference materials, and the blank controls, supporting the suitability of the approach.



Keywords: Airborne particulate matter, Oxidative potential, Chemiluminescence, Chemometrics, Luminol

1 – Introduction

Airborne particulate matter (from now on PM) is one of the most serious and challenging pollutants to which the human population is exposed (Landrigan et al., 2018). The health hazard from PM is historically recognized since ancient times (Claxton, 2014), though it is only in recent decades that the cause-effect relationships are being systematically investigated. To date, the outcomes of PM on human health account for a myriad of different diseases ranging from the lung-related ones to the cardiovascular (Cohen et al., 2005; Pope and Dockery, 2006; Rajagopalan et al., 2018), autoimmune (Zhao et al., 2019), and non-communicable diseases (Schraufnagel et al., 2019), which presently include diabetes, cognitive impairment, Alzheimer, and many others. For these reasons, environmental legislation is continuously evolving with regulations aiming to reduce the PM concentration within thresholds to minimize the risks to both the population and the environment. The

main shreds of evidence are extensively collected from epidemiological inference (Pope and Dockery, 2006; Shiraiwa et al., 2017; Zhao et al., 2019) and are accompanied by concurrent investigations aimed to associate the complex PM chemical composition with toxicity data and related health effects, proposing plausible mechanisms of cell-PM interactions.

Nowadays, the most accredited hypothesis is that health hazard from PM is due to a synergy between its chemical composition and size distribution of the particles, as well as that the potential damages depend both on exposure and dose, while a univocal mechanistic paradigm concerning what is triggering health effects in humans is not available yet, mainly due to the complexity of aerosol chemistry. In fact, PM chemical speciation continues to be challenging, reflecting source composition and complexity as well as the impacts of atmospheric recirculation and processing, which lead to the addition/formation of new pollutants over time.

PM mass load has been long recognized as the fundamental metric to assess aerosol environmental levels and inherent health risk in the range 20–50 $\mu\text{g}/\text{m}^3$ for PM_{10} (i.e., particles with an aerodynamic diameter smaller than or equal to 10 μm). However, some major components accounting for a large fraction of the PM mass load display relatively limited reactivity, such as Secondary Inorganic Aerosol (SIA; ammonium, sulfates, and nitrates), sea salt, some of the mineral components, while organic and elemental carbon are associated with more critical compounds (Mauderly and Chow, 2008). PM hazard is mainly associated with trace elements and organic compounds involved in electron transfer processes though all these species are generally in concentration several orders of magnitude lower than the PM carrier mass load (Tositti, 2017; Kelly and Fussell, 2020; Pardo et al., 2020). For example, EU air quality standards include regulations for PM_{10} and for a few of its chemical components such as Pb, Ni, Cd, As, BaP (i.e. benzo-a-pyrene) and assimilated PAHs (Polycyclic Aromatic Hydrocarbons) with concentration thresholds from the units up to hundreds of ng/m^3 (EU Directive 2008/50/EC, 2008), clearly showing the hazard derived from minor constituents rather than bulk PM concentration.

To date, there is a consensus that airborne particulate toxicity is mainly attributed to oxidative stress, the pathological condition originated from the breakdown of the physiological balance between the generation of Reactive Oxygen Species (ROS, including H_2O_2 , $\text{O}_2^{\cdot-}$, $^1\text{O}_2$, $\cdot\text{OH}$, O_3 , hypohalous acids, organic peroxides, ...) and the antioxidant capacity of human tissues (see for example Janssen et al., 2014; Riediker et al., 2019; Pardo et al., 2020). Non-neutralized free radicals lead to the damage of cells, tissues, and organs, as reported by Averill-Bates et al., 2018.

Therefore, ROS concentration is considered as an efficient predictor of PM harmfulness and the term “oxidative potential” (OP), i.e., the ability to produce oxidative stress, has been consequently introduced as a suitable metric (Ayres et al., 2008; Delfino et al., 2013, and references therein).

Many different cell-free and cell-based methodologies have been proposed in the last decades for the evaluation of OP in PM, but so far no official standard method has been selected and accredited for routine use.

Cell-free assays, recently reviewed by Taylor Bates et al. (2019) and Pietrogrande et al. (2019), stand out for the assessment of PM's oxidative potential owing to their rapidity, limited costs, and the absence of highly specialized personnel compared to the cell-based analysis. They are ideal for analyzing the large number of PM filter samples collected on a routine basis by adopting different experimental approaches: the measurement of the depletion rate of natural antioxidants like ascorbic acid (AA) or glutathione (GSH); the

measurement of the depletion rate of a chemical reductant like dithiothreitol (DTT); the measurement of the formation rate of ROS by Electronic Spin Resonance (ESR), High-Performance Liquid Chromatography or fluorescent probes.

These assays return different and even contrasting results due to the different sensitivity that each method shows with respect to the different redox-active compounds (Visentin et al., 2016; Xiong et al., 2017; Taylor Bates et al., 2019). PM samples contain thousands of different chemicals, including several pro- and anti-oxidant, producing a net signal resulting from contrasting effects of difficult interpretation. Moreover, the different experimental procedures employed in each method such as sampling procedure (Yang et al., 2014), sample storage conditions (Fuller et al., 2014), solvents used for the extraction (Verma et al., 2012; Yang et al., 2014; Calas et al., 2017), extracting procedure (Miljevic et al., 2014), or even reagent concentration (Lin and Zhen Yu, 2019) can lead to biased results.

In the attempt both to shed light on the factors affecting the assessment of PMs' OP and to find a rapid screening assay to characterize the different PMs, in this work we propose a new method for the assessment of OP based on the Total Oxidant Capacity determination by using the highly sensitive luminol (5-Amino-2,3-dihydrophthalazine-1,4-dione) chemiluminescent assay. This molecule is largely employed in various conditions to determine the amount of free radicals produced by a sample, the antioxidant power of different molecules and their amount, as well as the final balance of these two phenomena in the same matrix (Girotti et al., 2000; Ferri et al., 2006; Khan et al., 2014).

Compared to other assays currently used in PM OP determination, which are mainly based on antioxidant molecules consumption, the luminol assay works completely different since it is based on its activation by oxidative reactions and then on the measurement of light emission intensity and kinetics (Agarwal et al., 2004). Indeed, the analytical signal appears after its oxidation produced by free radicals, mainly H₂O₂ derived radicals, a reaction triggered by enzymes like peroxidases (Zhang et al., 2018). PM was tested directly on the filters, cut to obtain various subsamples, without extraction procedures and analyzing many samples in short time on multiwall plates. Pragmatic and easy procedures of PM sample processing were selected while chemometric techniques, including multivariate and untargeted techniques, were extensively applied for the treatment of instrumental signals, data reduction, and classification.

2 – Materials and Methods

2.1 –Particulate matter and certified PM reference materials samples

Two series of particulate matter samples, the SN and the LIG series, were collected on filters in Sierra Nevada (Spain) and in Liguria (NW Italy), respectively.

The Sierra Nevada sampling station, in southern Spain, is located at high altitude (2550 m a.s.l., 37.096 N, -3.387 W). The PM₁₀ samples were collected in the framework of the FRESA Project (Impact of dust-laden African air masses and of stratospheric air masses in the Iberian Peninsula. Role of the Atlas Mountains, Ref: CGL2015–70741-R) on quartz filters (Ø 15 cm) by a high volume sampler, 30 m³/h, (CAV-A/mb, MCV S.A., Spain) for a week (air volume sampled per filter = 5040 m³). A total of 19 weekly filters were collected mainly during the summer period (from June to October 2016) and 3 field blank filters (i.e., filters that are taken to the field through the same procedure as samples, including transport to and from the sampling site, and storage in the field, and analysis, but are not used for

collecting particulate matter, to ensure prevention of contamination of field samples), were processed.

The Liguria sampling station (NW Italy) is located in a narrow valley secluded by a complex mountainous topography with a small town, an industrial area with a large chemical plant and limited vehicular traffic. PM₁₀ samples were collected on quartz filters (Ø 4.7 cm) by a HYDRA Dual Sampler, (Fai Instruments S.r.l., Italy), for 24 h at 2.3 m³/h, (air volume sampled = 55.2 m³). A total of 130 daily filters were collected from November 2014 to April 2015, plus 4 field blank filters.

Two standard reference materials of particulate matter were also analyzed: CRM No.28 Urban Aerosols by NIES (National Institute for Environmental Studies, Ibaraki Prefecture, Japan) and SRM 1648a - Urban Particulate Matter, by NIST (National Institute for Standards and Technology, MD, USA).

A home-made device was designed and assembled according to Fermo et al., 2006 and Cuccia et al., 2011 to collect the standards on filters. The system consists of a vacuum pump, a filter holder, plastic tubes for the connections, and a resuspension chamber. The system was carefully assembled to guarantee air-tightness. A scheme is shown in Fig. 1.

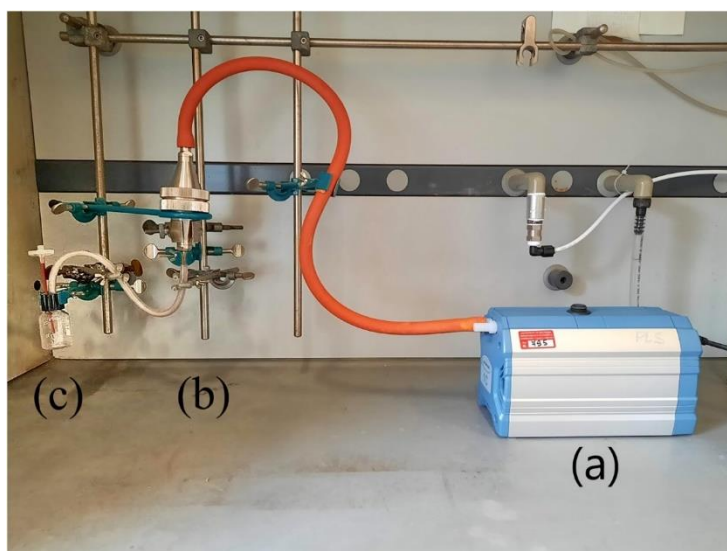


Fig. 1. Assembled experimental set up of the resuspension chamber. From right to left: (a) Vacuubrand 1C pump (flow rate = 0.4/0.5 cfm), (b) 47 mm in-line filter holder, and (c) a resuspension chamber, a 25 ml KITASATO flask. The flask was modified by connecting the side-arm at a certain angle to the flask axis, in order to maximize the turbulence and the resulting resuspension of particles. During air suction, the flask was continuously kept under vibrational stirring to improve particulate homogeneity during the resuspension.

The device allowed to obtain filters simulating typical PM samples based on known amounts of powdered reference materials determined by accurate weighing. The surface densities of the standards obtained were respectively 0.44 mg cm⁻² for the NIES CRM No.28 and 0.34 mg cm⁻² for the NIST SRM 1648a.

2.2 – Chemical speciation and source apportionment of PM₁₀

Sierra Nevada (SN) and Ligurian (LIG) particulate matter samples were stored frozen in the dark at -10 °C and then subjected to an extensive chemical speciation as follows.

Shortly, the SN samples were analyzed by gravimetry to determine the PM₁₀ mass ($\mu\text{g}/\text{m}^3$), by Ion Chromatography (IC) for the determination of the main water-soluble ions composition (EN 16913, 2017), and by Particle Induced X-ray Emission (PIXE) for multielemental non-destructive analysis using the method already described in Lucarelli et al., 2011 and Chiari et al., 2018.

LIG samples have been subjected to the same analyses as those of SN, plus Inductively Coupled Plasma Mass Spectrometry (ICP-MS) determination of trace elements according to EN 14902 (2005), IC determination of anhydrous sugars (Piazzalunga et al., 2010), Thermal-optical analysis (TOA) for elemental carbon (EC) and organic carbon (OC) assessment (Piazzalunga et al., 2011), and Gas Chromatography-Mass Spectrometry (GC-MS) for the determination of Polycyclic Aromatic Hydrocarbons (PAHs) (EPA, 1998; EPA, 2007).

A receptor modeling for Source Apportionment (SA) was applied in order to derive information about their sources and their contribution to PM levels (Belis et al., 2019).

Owing to the limited number of samples available, source apportionment of SN samples (19 sample \times 19 variables) was performed by means of the Chemical Mass Balance (CMB) approach, using the EPA-CMB 8.2 software (EPA, 2004). Suitable source profiles were selected from the European data base for PM source profiles (Pernigotti et al., 2016). After several runs, the final CMB solution was chosen on the basis of its best statistical performance indexes, i.e. R-square (R^2 ; target = 0.8–1.0), Chi-square (χ^2 ; target = 0–4), and calculated-to-measured ratios for the chemical species used (C/M; target = 0.5–2.0).

Source Apportionment of LIG samples (129 sample \times 42 variables) was performed by Positive Matrix Factorization (PMF) (Paatero and Tapper, 1993), a multivariate factor analysis technique which uses experimental uncertainty for scaling matrix elements and constrains factor elements to be non-negative. This analysis employed the EPA PMF5.0 software (Norris et al., 2014).

2.3 – Chemiluminescent assay

Chemiluminescence reagents were all from the WesternSure® PREMIUM kit (LI-COR, Lincoln, NE, USA).

The chemiluminescent assay was carried out on environmental samples, blanks, and standard samples using 96-well plates (8 \times 12 well strips). Quartz filter punches ($\text{Ø} = 8$ mm) were obtained by die-cutting quartz membranes. Each punch was carefully transferred face-up to the bottom of each well directly from the die-cutting tool. 100 μl of the mixture (1:1) of solution A (containing luminol and enhancer) and solution B (fresh H₂O₂ solution) were added to each well of the plate using a multichannel pipette. Immediately after the reagent addition, the light emission intensity was measured using a VICTOR Light microplate luminometer and expressed as Relative Luminescence Units (RLU). The luminometer recorded sequentially the light emitted in one second by each well, taking 124 s to read the whole plate. The chemiluminescence values were recorded for about 1 h (28 values), obtaining a light emission profile (RLU vs. Time, in seconds). The precision of the measurements was quantified as the relative standard deviation of a set of replicates, computed from the analysis of six punches of a single filter, chosen to the scope. The result

was about 11% and included the PM filter anisotropy, i.e. the not homogeneous distribution of the particulate materials on the filter, which cannot be precisely the same in every point of the filter.

2.4 – Chemometrics

The experimental dataset was extensively processed by chemometric tools for a) data classification and reduction, and b) for correlation.

After suitable data standardization by subtracting the column-average from every element in the column (i.e. centering, van den Berg et al., 2006), Principal Components Analysis (PCA) (Bro and Smilde, 2014) and Hotelling analysis were applied to the whole dataset including chemiluminescence data using The Unscrambler V. 10.4 (Camo, Oslo, Norway).

PCA and Hotelling analyses were computed at a confidence level of 95% (Jolliffe, 2005). While PCA allowed to identify sample groupings, Hotelling analysis provides a geometrical representation of PCA scores relatively to an ellipsoid. The samples outside the ellipsoid are considered significantly different from those inside it (at the confidence level of 95%) therefore highlighting distinct sample behavior in terms of OP and composition.

A Spearman correlation analysis between emission source contributions and OP data, defined as the integrals of luminol light emission over the acquisition time, was performed for each a priori class (Wissler, 1905). Spearman analysis is a more appropriate measure of association than Pearson's for describing the monotonic relationship between two variables instead of a linear relationship and, therefore, best suited in this case study (Schober et al., 2018).

Before the correlation analysis, all OP data were normalized by filter surface and volume of sampled air in order to provide dimensional consistency and homogeneity with the source contributions deduced by source apportionments, expressed as μg in the whole filter per m^3 of sampled air. In this way, an OP value was defined as the chemiluminescence (from now on, CL) value of the whole filter on m^3 of sampled air (RLU/m^3).

The Spearman correlation analyses were carried out by the software OriginPro 2018 (OriginLab, Northampton, USA).

3 – Results and discussion

3.1 – The chemiluminescent assay: Analysis of the chemiluminescence profile

CL luminol assays are based on instrumental data representing the light emission intensity over time. The kinetics of the luminol oxidation, which leads to an excited intermediate and then to its decay to a stable final product accompanied by light emission, can be completely different in the various experimental conditions since the reaction mechanism is quite complicated, as shown in Rose and Waite, 2001.

It depends on the reagents' ratio in the sample, on the rate and/or chemical nature of radicals production, on the presence of enhancers or scavenging molecules which can be consumed or produced during the reaction. Their simultaneous presence will result in a signal dependent on their balanced effects. Owing to PM complexity, we firstly examined the spectral output obtained, in order to define the best instrumental conditions to apply and to identify possible, characterizing differences among the samples. The trend of the light emission values vs. time clearly showed different kinetic patterns in luminol oxidation and,

consequently, in ROS production rate or in oxidant/antioxidant capacity balance. The luminescence emission intensity vs. time trends can be basically classified according to diagrams depicted in Fig. 2.

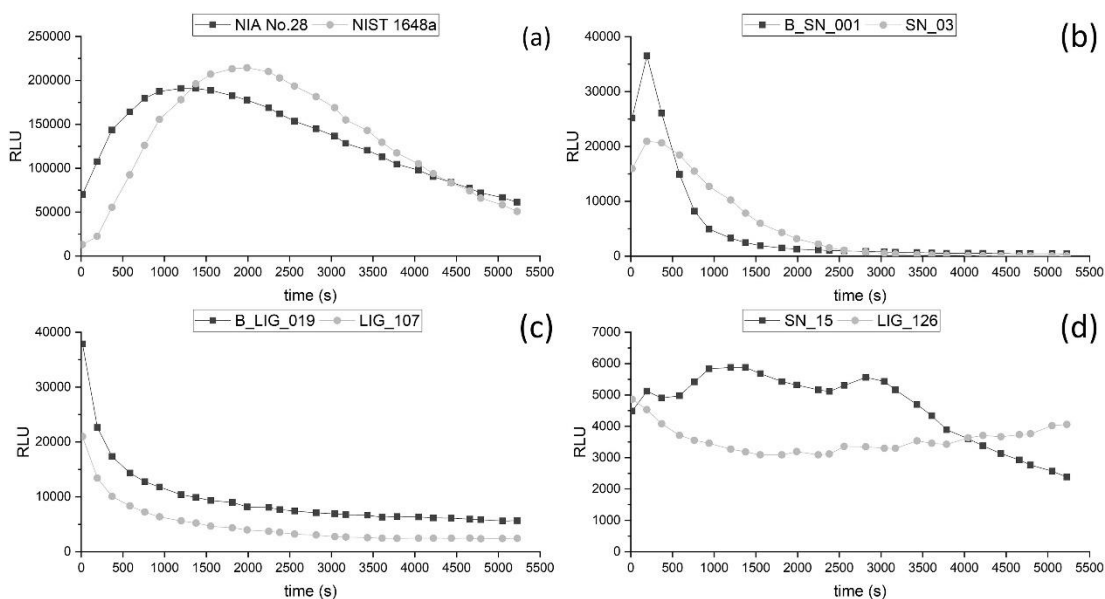


Fig. 2. Light emission kinetics generated by luminol-based chemiluminescence analysis of different particulate matter samples: a) the two certified standards, b) one Sierra Nevada (SN) sample with its blank (B_SN) filter, c) one Ligurian (LIG) sample with its blank (B_LIG) filter, and d) two peculiar samples.

The differences in the luminescence kinetics are plausibly associated with the chemical complexity and unicity of each individual PM sample and with the consequent relative stability and balance of the free radicals production-scavenging phenomena (Squadrito et al., 2001; Dellinger et al., 2007; Feld-Cook et al., 2017; Tong et al., 2018). The emission profile is implicitly informative of the nature and half-life of the ROS active species originated in the collected PM, as well as of the interactions between them and other components, information that can be used as a proxy of the particulate oxidative potential. The attempt to identify this intriguing connection between the chemical composition and the reactive species highlighted by the chemiluminescent reaction was the basic challenge to justify the application of this method. Our observation shows clearly how source profiles affect PM composition and the associated availability of redox active species, each one with its specific properties, including solubilization in the liquid medium (possibly critical for elements like the Fe(II)/Fe(III) couple, to which luminol is extremely sensitive by the way) (Khan et al., 2014). With the exception of samples with a flat CL profile, the major differences are observed at the beginning of the emission profile when maximum intensity is reached with very variable rates, after which these samples reveal an asymptotic relaxation of CL. It is to note how the certified reference materials (CRMs) used to check the procedure performance are particularly slow in CL development (up to tenths of minutes as compared to hundreds of seconds for our samples) possibly indicating not only different PM composition and source profile mixtures, but possibly aging of CRMs and/or an influence of handling procedures and inherent environmental/atmospheric redox conditions.

Our findings show quite clearly that in the conditions observed the choice of a maximum for OP assessment is extremely arbitrary. For this reason, on account of metrologic requisites, we decided to use the integral of RLU over the 0–5000 s time interval as the spectral parameter on which quantifying the differences in the PM redox behavior.

3.2 – Chemometric analyses

3.2.1 – Comprehensive PCA and evaluation of luminol chemiluminescence as a proxy for PM oxidation potential

The calculation of the Principal Components (PCs) of a given dataset allowed identifying groups of variables with similar and coherent behavior as compared to the other groups. In this case the discriminating parameter is the “chemiluminescent fingerprints” linking their oxidative potentials to their composition.

As shown in the scores plot reported in Fig. 3, PC-1 and PC-2 together covered almost the entire explained variance ($\approx 100\%$), which means an exceptionally high capability to describe the initial dataset. High discrimination between NIA No.28, NIST 1648a, as compared to all the other analyzed samples, is observed. Good discrimination between LIG and SN samples is found (except for some LIG samples). Even the respective blanks are well separated from each other. The LIG blanks are entirely resolved from the LIG samples, while the SN blanks are slightly overlapped to the SN samples.

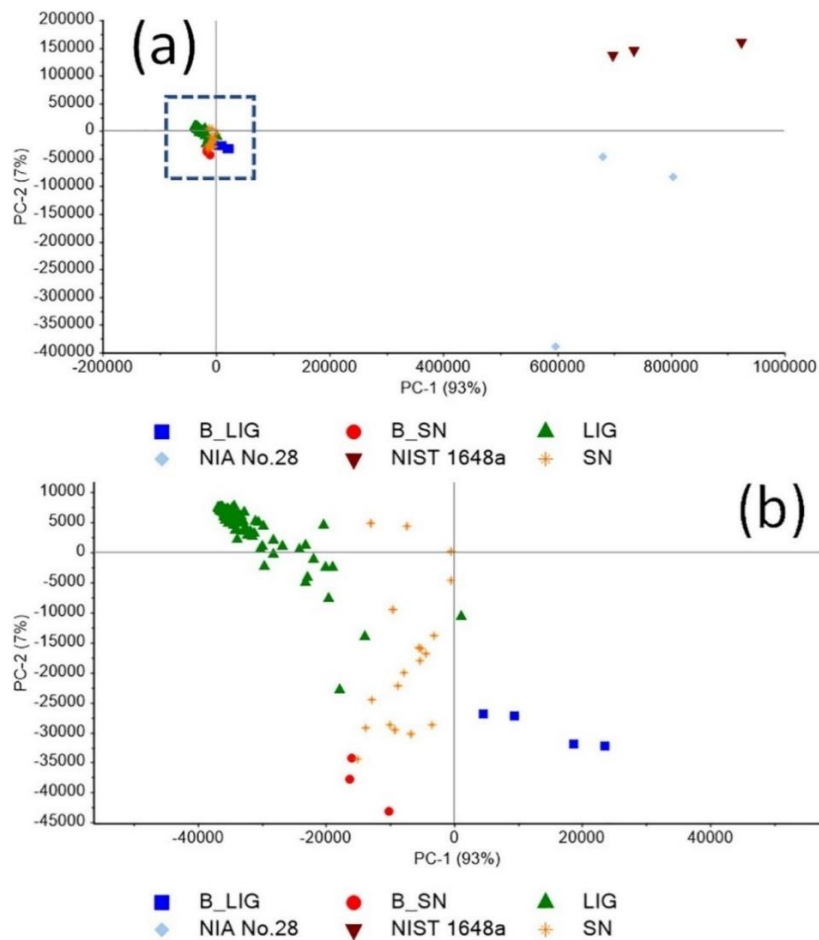


Fig. 3. (a) Principal Component Analysis (PCA) scores plot including all the analyzed samples, PC-1 vs. PC-2. The graph portion inside the smaller dashed square is magnified into (b).

These results reveal that the CL profiles are significant, and can be therefore taken as meaningful measurements of OPs in connection with their respective composition and redox properties and, therefore, of a given receptor site.

3.2.2 – Class-PCA and Hotelling analysis

Two different class-PCA were performed and the relative scores plots are reported in Fig. 4 (a, LIG samples) and (b, SN samples). Hotelling analysis calculates an ellipsoid for the PCA scores plot. The samples outside such ellipsoid are considered significantly different from those inside of it (at the confidence level of 95%) and therefore are highlighted as samples with significantly different OP is with respect to all the others.

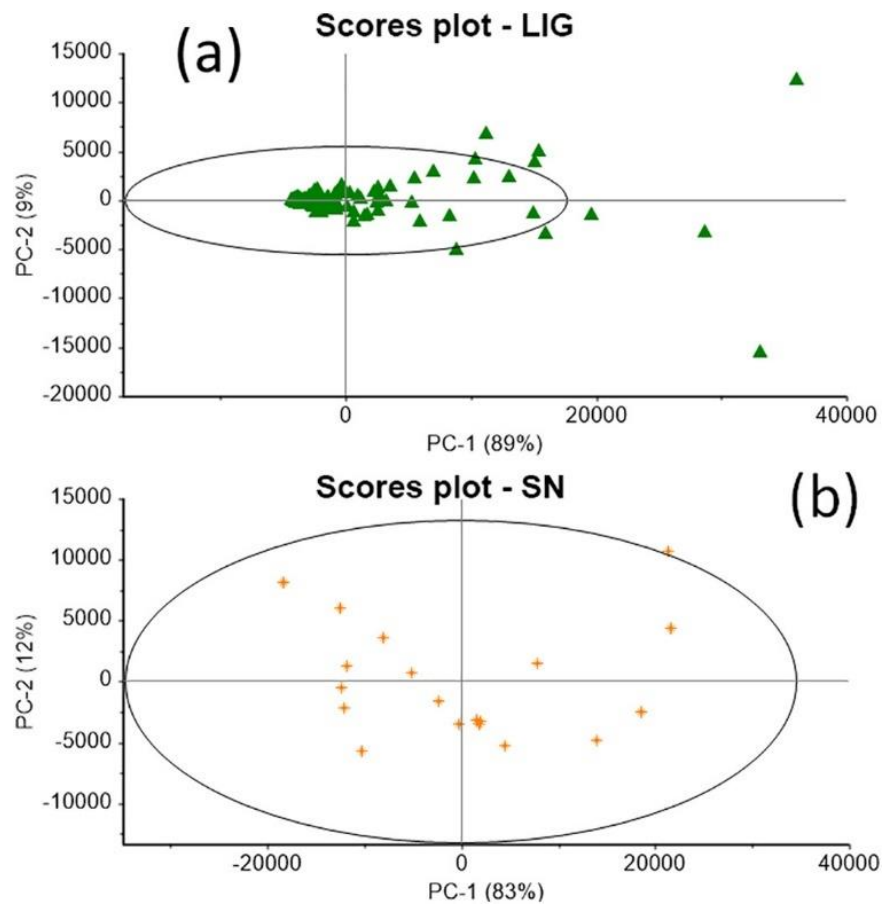


Fig. 4. Scores plots of (a) LIG class-PCA (PC-1 vs. PC-2) and (b) SN class-PCA (PC-1 vs. PC-2).

The Hotelling ellipses at the 95% confidence level were computed and displayed in both scores plots. This method allows to distinguish the samples with significantly different CL profile though within the same group.

In both cases, the explained variance is very high for the first two principal components (PC-1 + PC-2): respectively 98% for LIG class-PCA and 95% for SN class-PCA. This confirms the representativeness of the starting dataset.

In Fig. 4 (a), almost all the samples are enclosed within the Hotelling ellipse: only nine LIG samples appeared to be significantly different, possibly in connection with the seasonal variation in atmospheric circulation leading to a higher degree of data scattering. These samples were collected during the cold season characterized by a different circulation pattern as compared to the warm season and being, therefore, affected by distinct emissive profiles.

On the contrary, the Sierra Nevada samples were highly coherent, being all sampled during a single season.

3.3 – Source apportionment of the PM samples

In order to associate statistically the OPs based on luminol CL with the chemical fingerprints of the emission sources of PM₁₀ in the location studied, in this paragraph we describe the results of receptor modeling obtained at the two locations herein investigated.

3.3.1 – Sources of SN samples

As previously described, the SN dataset includes a small number of weekly samples (19) not suitable for the use of PMF which is a comparatively more frequently used approach in source apportionment (Belis et al., 2019). The best solution of the Chemical Mass Balance (CMB) for the source apportionment of Sierra Nevada (SN) samples was achieved by the selection of four SPECIEUROPE (Pernigotti et al., 2016) source profiles: 17 - Soil Dust Composite Rural (cr), 157 - Aged sea spray (ss), 288 - Nitrate_PMF5 (nt), and 291 – Sulphate (sp). The PM₁₀ fraction of reconstructed mass (%) is 85% and the results are in agreement with the PM mass reconstruction based on empirical equations performed on the basis of chemical speciation data (see for example Chow et al., 2015).

Soil Dust Composite Rural basically captures the Saharan dust incursion events typical of high-altitude locations across the Mediterranean region (Riccio et al., 2009; Cusack et al., 2012; Israelevich et al., 2012; Tositti et al., 2014; Brattich et al., 2015a, Brattich et al., 2015b; Cabello et al., 2016; Cuevas et al., 2017) representing most of the mass of the PM₁₀ (about 75%). Secondary Inorganic Aerosol (SIA; ammonium, sulfates, and nitrates) derives from the gas-to-particle conversion from SO₂ and NO_x in the atmosphere (Schaap et al., 2004; Pathak et al., 2009). These sources contribute respectively to 5% and 3% of the PM₁₀ at SN. The Aged sea spray source contributes 2% to PM₁₀ mass, mainly constituted of sodium chloride (NaCl), which undergoes atmospheric aging processes due to their long-range atmospheric transport. The pie chart representing the contribution of the four sources to PM₁₀ mass is reported in Fig. 5.

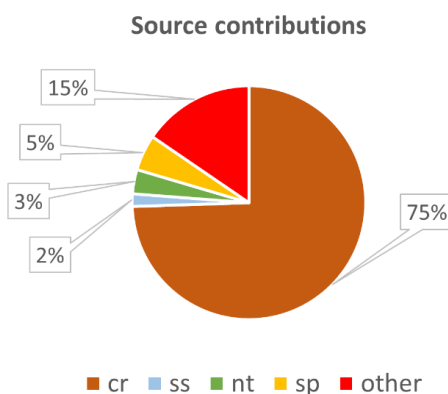


Fig. 5. Source contributions (SN) of 17 - Soil Dust Composite Rural (cr), 157 - Aged sea spray (ss), 288 - Nitrate_PMF5 (nt), and 291 – Sulphate (sp) to PM₁₀ mass. “Other” covers undetermined PM₁₀ components.

3.3.2 – Sources of LIG samples

PMF model requires an accurate and detailed knowledge in terms of number of observed data and of chemical parameters across the studied area in order to capture a reliable quantitative source profile. A six-factor solution was selected as the best result on the basis of the fitting parameters, the convergence of calculated Q to the expected value, a parameter estimating the goodness of the fit and the distribution of residuals (Brown et al., 2015). The six factors obtained are: secondary nitrate, biomass burning, industrial emissions, road dust, fuel oil burning, and sea salt. The comparison between measured (input data) and modeled values together with the distribution of residuals was evaluated, indicating a good model performance in reconstructing PM₁₀, with a coefficient of determination equal to 0.96 and accounting for 80% of the total PM mass. The Factor Fingerprints screen is reported in Fig. 6.

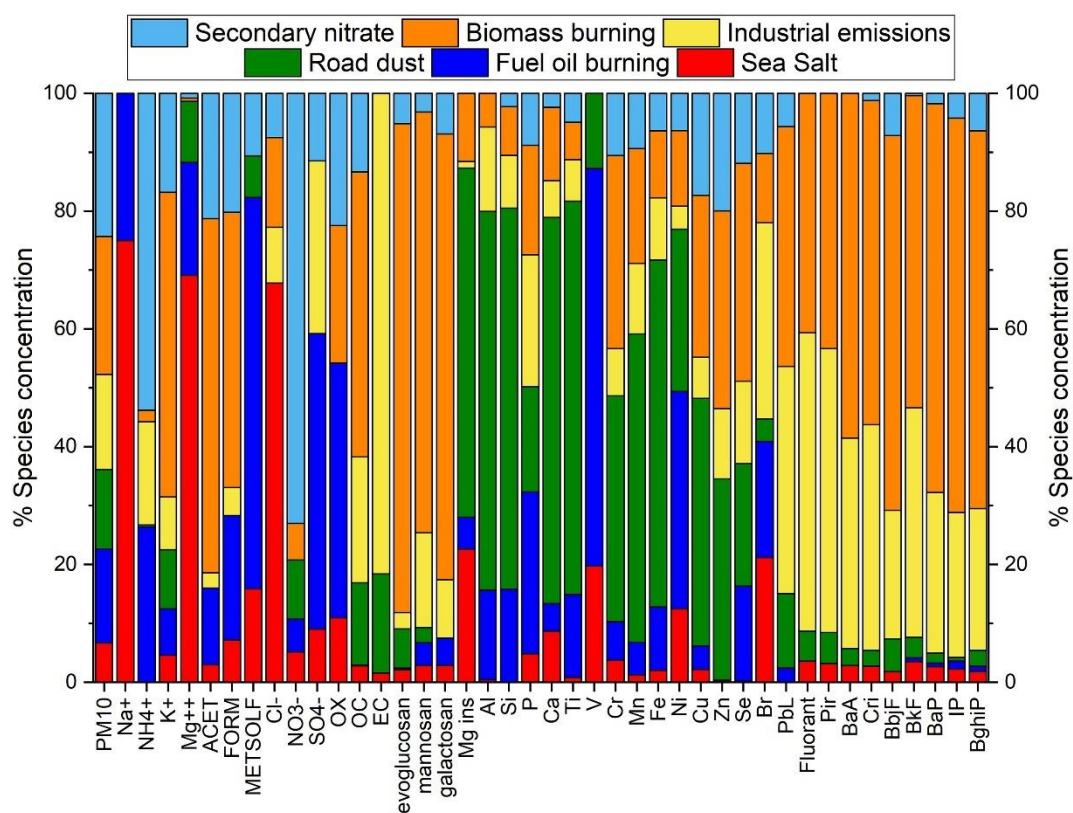


Fig. 6. Source Fingerprints corresponding to the factors resolved by the PMF model (LIG).

The secondary nitrate source (23.7%) includes all the high-temperature active sources, e.g. biomass combustion, the industrial settlement, and traffic. The biomass burning source (24.7%) is mainly due to wood burning during the winter period. The industrial high temperature facility emissive contribution covers about 17.1% of the PM₁₀ at the receptor site contributing however substantially to OC, EC, and sulfates beside nitrates. Road dust (11.7%) comprises mainly coarse mineral particles from friction and wear of the mechanic components such as brakes, tires, and asphalt including trace elements of potential toxicological relevance, e.g. Ni and others. Fuel oil burning (16.7%) identifies the combustion of heavy oils due to trucks, diesel, and marine traffic. The sea salt source (6.1%) has the typical “marine aerosol” imprint.

3.4 – Spearman correlation analysis

For each class (SN and LIG samples), a Spearman correlation analysis between source contributions data from CMB (SN samples) or PMF (Ligurian samples) and the OPs was computed; the obtained correlation coefficients are reported in Table 1.

Table 1. Spearman correlation coefficients (r_s) between the emission sources and the luminol-based oxidative potential (OP) for the Sierra Nevada (SN) and Ligurian (LIG) samples. The emission sources of these samples have already been described in Section 3.3. The most significant correlations ($|r_s| > 0.6$) have been marked with an asterisk.

(SN)		(LIG)	
emission source	r_s OP	emission source	r_s OP
Aged sea spray	+0.73*	Road dust	+0.23
Nitrate	+0.72*	Secondary Nitrate	+0.15
Sulphates	+0.72*	Fuel oil burning	+0.12
Soil dust Composite rural	+0.66*	Sea salt	-0.05
		Industrial emissions	-0.14
		Biomass Burning	-0.71*

Concerning SN samples, all the emission sources were significantly and positively correlated with the light emission intensity. Therefore, all these emission sources contribute significantly to the increase of free radicals in these samples, i.e. to the particulate material's oxidative potential. It is interesting to note how the mineral dust source (cr) does not show the highest correlation, despite its high weight contribution (75% of the total PM_{10}).

The results for the LIG samples were completely different: OP is negatively correlated with biomass burning emission source, which quantitatively is one of the most relevant emission sources (14.7% of the total PM_{10}) while the other emission sources were not significantly correlated with the oxidative potential. The absence of significant correlations with other emission sources may be related to the sampling period of the Ligurian filters (from November 2014 to April 2015), which are mainly in the cold season and, therefore, with a significant contribution of biomass burning sensibly affecting oxidative potential with respect to other sources. Correlation analysis on a semi-seasonal basis indicates how the biomass burning component is more negatively correlated with the oxidative potential in the coldest months of the sampling campaign ($r_s = -0.83$) and then decreases the negative correlation moving towards the hot season ($r_s = -0.51$).

Despite the statistical significance of LIG results, this anticorrelation has drawn our attention since it has been widely demonstrated how combustion PM led to an increase in vivo of oxidative damages (Lighty et al., 2000; Mauderly and Chow, 2008).

One plausible explanation is that Biomass Burning components in PM operate free radical scavenging activity mechanism, neutralizing many of the radical species during the chemiluminescence assay.

As previously reported for LIG class in Fig. 4(a), 9 samples behaved significantly different from the others.

Fig. 7 represents the boxplots of the oxidative potential and biomass burning components for the samples inside the 95%-Hotelling ellipses and for the samples outside the latter, respectively.

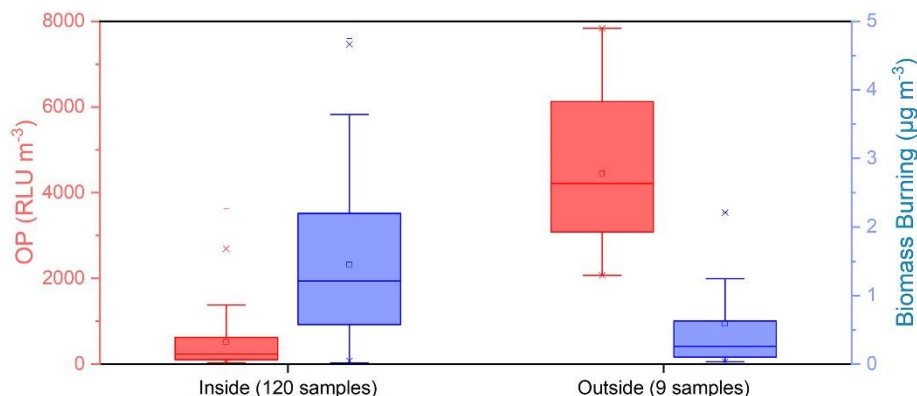


Fig. 7. Comparison of the light intensity (OP) and the amount of Biomass Burning products box chart graph between the Ligurian samples inside the 95%-Hotelling ellipse shown earlier in Fig. 4(a) (on the left) and outside the 95%-Hotelling ellipse (on the right).

As shown in Fig. 7, the 9 LIG samples outside the Hotelling ellipse were characterized by higher light emission and lower Biomass Burning component compared to the other 120 samples. In particular, the higher emission of these specific samples seems due to the lower biomass burning component, as evidenced by the significant negative correlation seen above. This could be in agreement with seasonality, as these filters were sampled in the hot season characterized by less heating through wood combustion. The color of the filters, less dark than the others, also supports this hypothesis suggesting the presence of a smaller amount of biomass burning components.

Therefore, the 9 LIG samples highlighted by the screening method proposed in this paper turn out to be those with the lower biomass burning components, those with higher light intensity from oxidized luminol and with the lighter color of the filters.

4 – Conclusions

In this article, a new chemiluminescence method based on the sensitivity of luminol to radicals is proposed for particulate matter samples rapid characterization.

This method allows to simultaneously analyses up to 96 PM filter portions without any chemical sample pre-treatment (no liquid extraction) and in a short time (approximately 1 h). The cost of this kind of analysis, estimated as the ratio between the price of the used reagents and the number of tests that can be carried out with them, is around 50 cents per sample. All these advantages make this technique a screening one, which can also be performed by non-highly specialized personnel.

The primary purpose of this methodology is the rapid identification of PM samples that significantly differ from all others as regards their composition. Subsequently, it is necessary to understand why these samples behave differently, through a comparison of

chemiluminescence values with the chemical-physical characterization data or, even better, information on their emission sources.

Two different series of samples were used for the technique validation, well characterized on their emission sources through the application of Source Apportionment techniques: Sierra Nevada (S-Spain) samples, which contain mainly mineral dust from North Africa, and Ligurian (NW-Italy) samples, composed mainly by organic compounds deriving from biomass burning and industrial combustions.

The chemiluminescence signals obtained from this method are profiles of light emission over time dependent on free radicals amount resulting from the balance between the radical producing components and the radicals trapping ones, i.e. from the PM chemical composition. This emission kinetics showed different shapes and represented the final result of all chemical phenomena occurring in that specific, and complex, mixture each PM sample is made of. Indirectly, the light intensity indicated the OP of each sample in terms of the amount of active free radicals.

These light emission profiles were interpreted and considered holistically for the application of non-targeted chemometric techniques which allowed the identification of distinct samples. Subsequently, Spearman's correlation analysis allowed to determine the relationship between luminescence and emission source contributions, specifically linking the PM filters selected by the screening method as samples attributed to a well-defined source of emission.

This screening method did not identify any Sierra Nevada sample with chemiluminescence profile significantly different from the other ones of this set, while 9 Ligurian samples significantly different were identified. The latter have a higher light emission, and therefore a higher oxidative potential, associated with a lower presence of the Biomass Burning component on these filters. Although this, clearly demonstrated, correlation could seem contradictory to a first sight, it can be simply explained by the specific mechanism of luminol emission, which reveals both the pro- and antioxidant components at the same time.

Based on what was previously reported, the effectiveness of the proposed screening technique was proven, and this means that this method can join the others analytical techniques used for PM OP assessment already reported in the scientific literature.

Funding

This work was funded by Fundamental Oriented Research (RFO) 2018–2019 and 2019–2020, University of Bologna (Italy).

CRedit authorship contribution statement

Pietro Morozzi: Methodology, Formal analysis, Writing – original draft, Visualization. Luca Bolelli: Methodology, Investigation, Writing – review & editing. Erika Brattich: Writing – review & editing. Elida Nora Ferri: Writing – review & editing. Stefano Girotti: Conceptualization, Resources, Writing – review & editing, Supervision, Funding acquisition. Stefano Sangiorgi: Investigation, Writing – review & editing. J.A.G. Orza: Writing – review & editing. Francisco Piñero-García: Supervision. Laura Tositti: Conceptualization, Writing – review & editing, Supervision.

Acknowledgements

We are grateful to prof. María Ángeles Ferro García and Abel Milena Pérez in the Radiochemistry and Environmental Radiology Laboratory of the Inorganic Chemistry Department of University of Granada (LABRADIQ) for kindly providing the Sierra Nevada (SN) samples used in this work. Heartfelt thanks to Josep Mestres Sanna and Adrià Simon Ortiz for the assistance in the experimental activity.

References

- Agarwal, A., Allamaneni, S.R., M Said, T., Chemiluminescence technique for measuring reactive oxygen species (2004) *Reprod. BioMed. Online*, 9, pp. 466-468;
- Averill-Bates, D., Chow-shi-yée, M., Grondin, M., Ouellet, F., Activation of apoptosis signaling pathways by reactive oxygen species (2018) *Cryobiology*, 80, p. 170;
- Ayres, J.G., Borm, P., Cassee, F.R., Castranova, V., Donaldson, K., Ghio, A., Harrison, R.M., Kooter, I.M., Evaluating the toxicity of airborne particulate matter and nanoparticles by measuring oxidative stress potential—a workshop report and consensus statement (2008) *Inhal. Toxicol.*, 20 (1), pp. 75-99;
- Belis, C., Favez, O., Mircea, M., Diapouli, E., Manousakas, M.-I., Vratolis, S., Gilardoni, S., Decesari, S., (2019), European Guide on Air Pollution Source Apportionment With Receptor Models - Revised Version 2019;
- Brattich, E., Hernández-Ceballos, M.A., Cinelli, G., Tositti, L., (2015), Analysis of ²¹⁰Pb peak values at Mt. Cimone (1998–2011). *Atmos. Environ.*, 112, 136–147, pp. 223-235;
- Brattich, Erika, Riccio, A., Tositti, L., Cristofanelli, P., & Bonasoni, P. (2015b). An outstanding Saharan dust event at Mt. Cimone (2165 m asl, Italy) in March 2004. *Atmos. Environ.*, 113; Bro, R., Smilde, A., Principal component analysis (2014) *Anal. Methods*, 6, p. 2812;
- Brown, S.G., Eberly, S., Paatero, P., Norris, G.A., Methods for estimating uncertainty in PMF solutions: examples with ambient air and water quality data and guidance on reporting PMF results (2015) *Sci. Total Environ.*, 518, pp. 626-635;
- Cabello, M., Orza, G., Dueñas, J., Liger, C., Gordo, E., (2016), E., & Cañete, S. Back-trajectory analysis of African dust outbreaks at a coastal city in southern Spain: selection of starting heights and assessment of African and concurrent Mediterranean contributions. *Atmos. Environ.*, 140;
- Calas, A., Uzu, G., Martins, J., Voisin, D., Spadini, L., Lacroix, T., Jaffrezo, J.-L., The importance of simulated lung fluid (SLF) extractions for a more relevant evaluation of the oxidative potential of particulate matter (2017) *Sci. Rep.*, 7;
- Chiari, M., Yubero, E., Calzolari, G., Lucarelli, F., Crespo, J., Galindo, N., Nicolás, J.F., Nava, S., Comparison of PIXE and XRF analysis of airborne particulate matter samples collected on Teflon and quartz fibre filters (2018) *Nucl. Instrum. Methods Phys. Res., Sect. B*, 417, pp. 128-132;
- Chow, J.C., Lowenthal, D.H., Chen, L.-W.A., Wang, X., Watson, J.G., Mass reconstruction methods for PM_{2.5}: a review (2015) *Air Qual. Atmos. Health*, 8 (3), pp. 243-263;
- Claxton, L.D., The history, genotoxicity, and carcinogenicity of carbon-based fuels and their emissions. Part 2: solid fuels (2014) *Mutat. Res. Rev. Mutat. Res.*, 762, pp. 108-122;

- Cohen, A.J., Ross Anderson, H., Ostro, B., Pandey, K.D., Krzyzanowski, M., Künzli, N., Gutschmidt, K., Samet, J.M., The global burden of disease due to outdoor air pollution (2005) *J. Toxic. Environ. Health A*, 68 (13-14), pp. 1301-1307;
- Cuccia, E., Piazzalunga, A., Bernardoni, V., Brambilla, L., Fermo, P., Massabò, D., Molteni, U., Vecchi, R., Carbonate measurements in PM10 near the marble quarries of Carrara (Italy) by infrared spectroscopy (FT-IR) and source apportionment by positive matrix factorization (PMF) (2011) *Atmos. Environ.*, 45 (35), pp. 6481-6487;
- Cuevas, E., Gómez-Peláez, A.J., Rodríguez, S., Terradellas, E., Basart, S., García, R.D., García, O.E., Alonso-Pérez, S., The pulsating nature of large-scale Saharan dust transport as a result of interplays between mid-latitude Rossby waves and the North African Dipole Intensity (2017) *Atmos. Environ.*, 167, pp. 586-602;
- Cusack, M., Alastuey, A., Pérez, N., Pey, J., Querol, X., (2012), pp. 8341-8357., Trends of particulate matter (PM2.5) and chemical composition at a regional background site in the Western Mediterranean over the last nine years (2002–2010). *Atmos. Chem. Phys.*, 12(18);
- Delfino, R.J., Staimer, N., Tjoa, T., Gillen, D.L., Schauer, J.J., Shafer, M.M., Airway inflammation and oxidative potential of air pollutant particles in a pediatric asthma panel (2013) *J. Expo. Sci. Environ. Epidemiol.*, 23 (5), pp. 466-473;
- Dellinger, B., Lomnicki, S., Khachatryan, L., Maskos, Z., Hall, R.W., Adoukpe, J., McFerrin, C., Truong, H., Formation and stabilization of persistent free radicals (2007) *Proc. Combust. Inst.*, 31 (1), pp. 521-528;
- EN 14902, Ambient air quality - standard method for the measurement of Pb, Cd, As and Ni in the PM10 fraction of suspended particulate matter (2005);
- EN 16913, Ambient air - standard method for measurement of NO₃, SO₄²⁻, Cl⁻, NH₄⁺, Na⁺, K⁺, Mg²⁺, Ca²⁺ in PM_{2,5} as deposited on filters (2017);
- EPA. 1998. "Method 8270D (SW-846): Semivolatile Organic Compounds by Gas Chromatography/ Mass Spectrometry (GC/MS)," Revision 4, www.epa.gov;
- EPA, EPA-CMB8.2 User's manual (2004), www.epa.gov;
- EPA, Method 3550C (SW-846): ultrasonic extraction (2007), www.epa.gov;
- EU Directive 2008/50/EC, Directive 2008/50/EC of the European Parliament and of the Council of 21 May 2008 on ambient air quality and cleaner air for Europe (2008) *Off. J. Eur. Union*;
- Feld-Cook, E.E., Bovenkamp-Langlois, L., Lomnicki, S.M., Effect of particulate matter mineral composition on environmentally persistent free radical (EPFR) formation (2017) *Environ. Sci. Technol.*, 51 (18), pp. 10396-10402;
- Fermo, P., Piazzalunga, A., Vecchi, R., Valli, G., Ceriani, M., A TGA/FT-IR study for measuring OC and EC in aerosol samples (2006) *Atmos. Chem. Phys.*, 6 (1), pp. 255-266;
- Ferri, E., Girotti, S., Cerretani, L., Bendini, A., Various luminescent methods applied to evaluate olive oil total antioxidant capacity (2006) *Luminescence*, 21 (6), pp. 358-359;
- Fuller, S.J., Wragg, F.P.H., Nutter, J., Kalberer, M., Comparison of on-line and off-line methods to quantify reactive oxygen species (ROS) in atmospheric aerosols (2014) *Atmos. Environ.*, 92, pp. 97-103;
- Girotti, S., Fini, F., Ferri, E., Budini, R., Piazzzi, S., Cantagalli, D., Determination of superoxide dismutase in erythrocytes by a chemiluminescent assay (2000) *Talanta*, 51 (4), pp. 685-692;
- Israelevich, P., Ganor, E., Alpert, P., Kishcha, P., Stupp, A., (2012), Predominant transport paths of Saharan dust over the Mediterranean Sea to Europe. *J. Geophys. Res.- Atmos.*, 117(D2);

- Janssen, N.A.H., Yang, A., Strak, M., Steenhof, M., Hellack, B., Gerlofs-Nijland, M.E., Kuhlbusch, T., Brunekreef, B., Oxidative potential of particulate matter collected at sites with different source characteristics (2014) *Sci. Total Environ.*, 472, pp. 572-581;
- Jolliffe, I. (2005). Principal component analysis. 2nd ed. [http://Lst-liep.liep-unesco.org/Cgi-Bin/Wwwi32.Exe/\[In=epidoc1.in\]/?T2000=017716/\(100\)](http://Lst-liep.liep-unesco.org/Cgi-Bin/Wwwi32.Exe/[In=epidoc1.in]/?T2000=017716/(100),), 98. <https://doi.org/10.1002/0470013192.bsa501>;
- Kelly, F.J., Fussell, J.C., Toxicity of airborne particles—established evidence, knowledge gaps and emerging areas of importance (2020) *Philos. Trans. R. Soc. A Math. Phys. Eng. Sci.*, 378 (2183);
- Khan, P., Idrees, D., Moxley, M.A., Corbett, J.A., Ahmad, F., von Figura, G., Sly, W.S., Hassan, M.I., Luminol-based chemiluminescent signals: clinical and non-clinical application and future uses (2014) *Appl. Biochem. Biotechnol.*, 173 (2), pp. 333-355;
- Landrigan, P.J., Fuller, R., Acosta, N.J.R., Adeyi, O., Arnold, R., Baldé, A.B., Bertollini, R., Breyse, P.N., The Lancet commission on pollution and health (2018) *Lancet*, 391 (10119), pp. 462-512;
- Lighty, J., Veranth, J., Sarofim, A., (2000), Combustion aerosols: factors governing their size and composition and implications to human health. *J. Air Waste Manage. Assoc.*, 50, 1565–1618; discussion 1619. doi: 1995;
- Lin, M., Zhen Yu, J., Dithiothreitol (DTT) concentration effect and its implications on the applicability of DTT assay to evaluate the oxidative potential of atmospheric aerosol samples (2019) *Environ. Pollut.*, 251;
- Lucarelli, F., Nava, S., Calzolari, G., Chiari, M., Udisti, R., Marino, F., Is PIXE still a useful technique for the analysis of atmospheric aerosols? The LABEC experience (2011) *X-Ray Spectrom.*, 40, pp. 162-167;
- Mauderly, J.L., Chow, J.C., Health effects of organic aerosols (2008) *Inhal. Toxicol.*, 20 (3), pp. 257-288;
- Miljevic, B., Hedayat, F., Stevanovic, S., Fairfull-Smith K., E., Bottle, S., Ristovski, Z., To sonicate or not to sonicate PM filters: reactive oxygen species generation upon ultrasonic irradiation (2014) *Aerosol Sci. Technol.*, 48;
- Norris, G., Duvall, R., Brown, S., Bai, S., EPA positive matrix factorization (PMF) 5.0 fundamentals and user guide (2014), www.epa.gov;
- Paatero, P., Tapper, U., Analysis of different modes of factor analysis as least squares fit problems (1993) *Chemom. Intell. Lab. Syst.*, 18 (2), pp. 183-194;
- Pardo, M., Qiu, X., Zimmermann, R., Rudich, Y., Particulate matter toxicity is Nrf2 and mitochondria dependent: the roles of metals and polycyclic aromatic hydrocarbons (2020) *Chem. Res. Toxicol.*, 33 (5), pp. 1110-1120;
- Pathak, R.K., Wu, W.S., Wang, T., Summertime PM_{2.5} ionic species in four major cities of China: nitrate formation in an ammonia-deficient atmosphere (2009) *Atmos. Chem. Phys.*, 9 (5), pp. 1711-1722;
- Pernigotti, D., Belis, C.A., Spano, L., SPECIEUROPE: the European data base for PM source profiles (2016) *Atmos. Pollut. Res.*, 7 (2), pp. 307-314;
- Piazzalunga, A., Bernardoni, V., Fermo, P., Valli, G., Vecchi, R., On the effect of water-soluble compounds removal on EC quantification by TOT analysis in aerosol samples (2011) *Atmos. Chem. Phys. Discuss.*, 11 (7);
- Piazzalunga, A., Fermo, P., Bernardoni, V., Vecchi, R., Valli, G., de Gregorio, M.A., A simplified method for levoglucosan quantification in wintertime atmospheric particulate matter by high performance anion-exchange chromatography coupled with pulsed amperometric detection (2010) *Int. J. Environ. Anal. Chem.*, 90 (12), pp. 934-947;
- Pietrogrande, M.C., Russo, M., Zagatti, E., Review of PM oxidative potential measured with acellular assays in urban and rural sites across Italy (2019) *Atmosphere*, 10 (10);

- Pope, C.A., III, Dockery, D.W., Health effects of fine particulate air pollution: lines that connect (2006) *J. Air Waste Manage. Assoc.*, 56 (6), pp. 709-742;
- Rajagopalan, S., Al-Kindi, S.G., Brook, R.D., Air pollution and cardiovascular disease: JACC state-of-the-art review (2018) *J. Am. Coll. Cardiol.*, 72 (17), pp. 2054-2070;
- Riccio, A., Chianese, E., Tositti, L., Baldacci, D., Sandrini, S., Modeling the transport of Saharan dust toward the Mediterranean region: an important issue for its ecological implications (2009) *Ecol. Quest.*, 11, pp. 65-72;
- Riediker, M., Zink, D., Kreyling, W., Oberdörster, G., Elder, A., Graham, U., Lynch, I., Cassee, F., Particle toxicology and health - where are we? (2019) *Part. Fibre Toxicol.*, 16 (1), p. 19;
- Rose, A.L., Waite, T.D., Chemiluminescence of luminol in the presence of iron(II) and oxygen: oxidation mechanism and implications for its analytical use (2001) *Anal. Chem.*, 73 (24), pp. 5909-5920;
- Schaap, M., van Loon, M., ten Brink, H.M., Dentener, F.J., Builtjes, P.J.H., Secondary inorganic aerosol simulations for Europe with special attention to nitrate (2004) *Atmos. Chem. Phys.*, 4 (3), pp. 857-874;
- Schober, P., Boer, C., Schwarte, L.A., Correlation coefficients: appropriate use and interpretation (2018) *Anesth. Analg.*, 126 (5), https://journals.lww.com/anesthesia-analgesia/Fulltext/2018/05000/Correlation_Coefficients__Appropriate_Use_and.50.aspx;
- Schraufnagel, D.E., Balmes, J.R., Cowl, C.T., De Matteis, S., Jung, S.H., Mortimer, K., Perez-Padilla, R., Wuebbles, D.J., Air pollution and noncommunicable diseases: A review by the Forum of International Respiratory Societies' Environmental Committee, Part 2: Air pollution and organ systems (2019) *Chest*, 155 (2), pp. 417-426;
- Shiraiwa, M., Ueda, K., Pozzer, A., Lammel, G., Kampf, C.J., Fushimi, A., Enami, S., Fujitani, Y., Aerosol health effects from molecular to global scales (2017) *Environ. Sci. Technol.*, 51 (23), pp. 13545-13567;
- Squadrito, G.L., Cueto, R., Dellinger, B., Pryor, W.A., Quinoid redox cycling as a mechanism for sustained free radical generation by inhaled airborne particulate matter (2001) *Free Radic. Biol. Med.*, 31 (9), pp. 1132-1138;
- Taylor Bates, J., Fang, T., Verma, V., Zeng, L., Weber, R., Tolbert, E., P. Y., Russell, A., Review of acellular assays of ambient particulate matter oxidative potential: methods and relationships with composition, sources, and health effects (2019) *Environ. Sci. Technol.*, 53;
- Tong, H., Lakey, P.S.J., Arangio, A.M., Socorro, J., Shen, F., Lucas, K., Brune, W.H., Shiraiwa, M., Reactive oxygen species formed by secondary organic aerosols in water and surrogate lung fluid (2018) *Environ. Sci. Technol.*, 52 (20), pp. 11642-11651;
- Tositti, L., Brattich, E., Cinelli, G., Baldacci, D., 12 years of ⁷Be and ²¹⁰Pb in Mt. Cimone, and their correlation with meteorological parameters (2014) *Atmos. Environ.*, 87, pp. 108-122;
- Tositti, L., The relationship between health effects and airborne particulate constituents (2017) *Clinical Handbook of Air Pollution-Related Diseases*;
- van den Berg, R., Hoefsloot, H., Westerhuis, J., Smilde, A., & van der Werf, M. Van den Berg RA, Hoefsloot HCJ, Westerhuis JA, Smilde AK, Van der Werf MJ. Centering, scaling, and transformations: improving the biological information content of metabolomics data. *BMC Genomics* 7: 142–157. *BMC Genomics*, 7, 142. doi:;
- Verma, V., Rico-Martínez, R., Kotra, N., King, L., Liu, J., Snell, T., Weber, R., Contribution of water-soluble and insoluble components and their hydrophobic/hydrophilic subfractions to the reactive oxygen species-generating potential of fine ambient aerosols (2012) *Environ. Sci. Technol.*, 46, pp. 11384-11392;

- Visentin, M., Pagnoni, A., Sarti, E., Pietrogrande, M.C., Urban PM2.5 oxidative potential: importance of chemical species and comparison of two spectrophotometric cell-free assays (2016) *Environ. Pollut.*, 219, pp. 72-79;
- Wssler, C., (1905), The Spearman correlation formula. *Biometrika*, 22, 309–311. doi:;
- Xiong, Q., Yu, H., Wang, R., Wei, J., Verma, V., Rethinking dithiothreitol-based particulate matter oxidative potential: measuring dithiothreitol consumption versus reactive oxygen species generation (2017) *Environ. Sci. Technol.*, 51 (11), pp. 6507-6514;
- Yang, A., Jedyńska, A., Hellack, B., Kooter, I., Hoek, G., Brunekreef, B., Kuhlbusch, T.A.J., Janssen, N., Measurement of the oxidative potential of PM2.5 and its constituents: the effect of extraction solvent and filter type (2014) *Atmos. Environ.*, 83;
- Zhang, Y., Dai, M., Yuan, Z., Methods for the detection of reactive oxygen species (2018) *Anal. Methods*, 10 (38), pp. 4625-4638;
- Zhao, C.-N., Xu, Z., Wu, G.-C., Mao, Y.-M., Liu, L.-N., Dan, Y.-L., Tao, S.-S., Fan, Y.-G., Emerging role of air pollution in autoimmune diseases (2019) *Autoimmun. Rev.*, 18 (6), pp. 607-614.

CHAPTER 5 - How to Get the Best from Low-Cost Particulate Matter Sensors: Guidelines and Practical Recommendations

by Erika Brattich¹, Alessandro Bracci¹, Alessandro Zappi², **Pietro Morozzi**², Silvana Di Sabatino¹, Federico Porcù¹, Francesca Di Nicola¹, and Laura Tositti²

¹ Department of Physics and Astronomy, Alma Mater Studiorum University of Bologna, 40126 Bologna, Italy

² Department of Chemistry “G. Ciamician”, Alma Mater Studiorum University of Bologna, 40126 Bologna, Italy

Sensors 2020, 20(11), 3073; <https://doi.org/10.3390/s20113073>



© 2020 by the authors. Licensee MDPI, Basel, Switzerland. This article is an open access article distributed under the terms and conditions of the Creative Commons Attribution (CC BY) license (<http://creativecommons.org/licenses/by/4.0/>).

Abstract

Low-cost sensors based on the optical particle counter (OPC) are increasingly being used to collect particulate matter (PM) data at high space and time resolution. In spite of their huge explorative potential, practical guidelines and recommendations for their use are still limited. In this work, we outline a few best practices for the optimal use of PM low-cost sensors based on the results of an intensive field campaign performed in Bologna (44°30' N, 11°21' E; Italy) under different weather conditions. Briefly, the performances of a series of sensors were evaluated against a calibrated mainstream OPC with a heated inlet, using a robust approach based on a suite of statistical indexes capable of evaluating both correlations and biases in respect to the reference sensor. Our results show that the sensor performance is sensibly affected by both time resolution and weather with biases maximized at high time resolution and high relative humidity. Optimization of PM data obtained is therefore achievable by lowering time resolution and applying suitable correction factors for hygroscopic growth based on the inherent particle size distribution.

Keywords: low-cost sensors; air quality; particulate matter; optical particle counter; particle mass concentration; PM₁₀; PM_{2.5}; PM₁; particle size distribution

1 – Introduction

The assessment of high-resolution air quality data in highly inhomogeneous areas such as the urban environment is a major requirement for the understanding of the complex physico-chemical processes behind the accumulation of atmospheric pollutants. This is especially true for airborne particulate matter (PM), a pollutant characterized by multiple emission sources simultaneously active at a single place; complex chemical phenomenology affects both composition and particle size, strongly affected not only by local advection pattern but also by local turbulence.

In order to comply with governmental air quality standards, monitoring stations are deployed and managed by regional environmental protection agencies which collect systematic and routine data of particle and gaseous pollutants using highly reliable but costly, large and usually static certified reference instruments, according to the environmental prescription and regulations (Castell et al., 2017). Due to the high costs of the installation and maintenance of reference monitoring stations in terms of economic and human resources, this approach is limited to a few sparse stations over single urban areas. The urban canopy is highly complex in terms of spatial patterns (Ratti et al., 2006), topography, dispersion and deposition conditions (Tan et al., 1998), and emission profiles, which induce localized gradients in ground-level concentrations of air pollutants (Hewitt et al., 2020). Therefore, the available monitoring stations, though satisfying the legislative requirements, are hardly representative of the whole urban surface, preventing an accurate assessment of spatially resolved environmental conditions and the inherent risks for the population. Environmental protection agencies usually complement air quality monitoring from static monitoring stations with mobile monitoring stations sampling additional local sites not covered by the reference network for fixed periods (Castell et al., 2017). Mobile laboratories use the same instrumentation as the permanent monitoring stations, and therefore suffer the same high maintenance and calibration costs. In addition, though data collected from mobile laboratories are precious in terms of accuracy and for specific purposes under intensive field campaigns, they are affected by significant temporal limitations, not representative of the whole annual and interannual variability. For this reason, the deployment of low-cost sensors networks is becoming increasingly popular, allowing not only integration of the environmental information at a high space and time resolution but also raising citizen awareness (Castell et al., 2017; Camprodon et al., 2019) and involvement in the management of environmental issues (Mao et al., 2019). In addition, recent approaches to complement data from low-cost sensors in air quality models have been proposed to increase spatial and temporal resolution and reduce biases and systematic errors (Ahangar et al., 2019; Schneider et al., 2017; Popoola et al., 2018). The success of these initiatives within the broader framework of IoT (Internet of Things) is very promising; however, from a metrological standpoint, one of the main drawbacks of this approach is the lack of a suitable evaluation of the consistency and reliability of the experimental data collected with low cost sensors, a non-negligible aspect for the subsequent data elaborations and deductions.

In the case of PM sensors, many factors should be accounted for, owing to a series of intrinsic and extrinsic factors. On the global scale, PM metrics included in the air quality networks rely on the official method (EN 12341:2014), which consists of the collection of PM₁₀ and PM_{2.5} usually on quartz fiber filters by sequential certified samplers and successive gravimetric analysis, or by continuous detection based on beta-attenuation technique or tapered element oscillating microbalance (TEOM) (Hauck et al., 2004; Patashnick et al., 1991). However, scientists widely agree that a more informative and accurate approach should also include the assessment of the corresponding size distribution closely related to PM atmospheric residence time, transport and health effects (Hidy et al., 2019; Strak et al., 2012; Tositti, 2018). In this framework, the use of optical particle counters (OPCs) is highly valued since they allow for the collection of information on particle size distributions and for the conversion of number densities obtained with the aid of suitable parameterizations and assumptions usually based on empirical data into mass concentration data easily interpretable as a function of air quality standards.

While OPCs are widely used instruments in atmospheric research, they are not routinely employed in air quality networks. Therefore standardization protocols are not widely applied, even if recently the ISO 21501 (and in particular the recent Part 4:2018 Determination of particle size distribution - single particle light interaction methods - light

scattering airborne particle counter for clean spaces) has been made available after the dismissal of ASTM F 328-98(2003). This standard method is usually carried out by the manufacturer. As a result, owing to the need for special experimental facilities, even research-oriented instruments usually rely solely on calibration procedures carried out at the manufacturers with a frequency dictated by a single laboratory's responsibility and awareness.

Therefore, even research-based instrumentation poses some fundamental questions in terms of PM data quality and assimilation to be employed in whatever environmental application.

Low-cost PM sensors are based on the same technology. In order to obtain reliable data, it is necessary to evaluate their uncertainties, performance and accuracy with laboratory tests and field comparisons with reference instruments (Tagle et al., 2020).

Further sources of uncertainty in PM data assessments arise from the meteorological variability, since different weather and dispersion conditions may change the physico-chemical nature of the particles observed at the receptor site over time. In particular, the variability of wind circulation and boundary layer mixing affect the ventilation, dilution and upwind emission sources (Jacob et al., 2009). Temperature and relative humidity conditions affect the stability of aerosol components, such as NH_4NO_3 and several carbonaceous components, and the kinds and rates of chemical reactions, leading to the formation of secondary inorganic and organic aerosols (Seinfeld et al., 2016; Leung et al., 2018; Sun et al., 2013). In addition, atmospheric fluctuations in relative humidity (RH) which in turn depend not only on the air masses transiting over a given place but also on the setting of different thermodynamic and microphysical conditions, are capable of modifying the particle size distribution sensibly as a result of aerosol hygroscopicity (Wang et al., 2018).

Recently, several papers focusing on the evaluation of the affordability of low-cost sensors from laboratory tests and experimental field campaigns have been published (Crilley et al., 2019; Sayahi et al., 2019; Bulot et al., 2019; Chatzidiakou et al., 2019; Kuula et al., 2019; Jiao et al., 2016; Kelly et al., 2017; Mukherjee et al., 2017; Sousan et al., 2016; Zheng et al., 2019). However, previous studies often failed in deriving practical guidelines and recommendations for the best practices with which to use low-cost sensors in terms of time resolution and different weather conditions. In this work, we present the results of an intercomparison exercise performed during a long-term (more than six months of monitoring) experimental field campaign aimed at assessing the performance of a series of low-cost sensors in terms of accuracy and reproducibility under different time resolution and weather conditions.

As such, this work aims to:

- Characterize the performances and reproducibility of different brands of low sensors in comparison to reference instruments;
- Assess instrument variability using batches of the same kind of low-cost sensors from the same producer;
- Perform a comparative analysis of the various OPCs under different meteorological conditions capable of sensibly affecting the PM size distribution, and consequently, the estimated mass concentration data.

This work is organized as follows. Following the Introduction section, Section 2 presents the material and methods used in this work, including the site where the experimental field campaign was performed, the instrumentation adopted, the algorithm used to convert number densities to mass concentration and the statistical parameters used to evaluate the performances of low-cost sensors. Section 3 presents and discusses the results in terms of

particulate matter concentrations and particle number densities, and finally, Section 4 draws the main conclusions of the work.

2 – Materials and Methods

In this work, we evaluated the performances of a set of different low-cost and research-oriented laser particle counters in outdoor ambient conditions during two distinct experimental field campaigns performed during the periods June 6th 2019 - August 4th 2019 and September 23rd 2019 - February 12th 2020 in Bologna (44°30' N, 11°21' E; Northern Italy), a city located in the Po Valley, a region representing one of the major pollution hotspots in Europe (e.g., Tositti et al., 2014; Diémoz et al., 2019). The study periods included a range of different meteorological conditions, well representative of the typical weather conditions affecting the city and the surrounding region in the warm and cold seasons.

Bologna is characterized by a humid temperate climate (Cfa following Köppen climate classification), with quite cold, humid and damp winters and hot and muggy summers. Humidity is generally quite high during both summer and winter periods, while the wind circulation is characterized by frequent stagnation conditions under calm and breeze regimes. Precipitation is moderate and quite well distributed over the seasons, with two peaks in spring and autumn and relative minima in winter and summer.

2.1 Instrumentation

For the purpose of investigating and comparing the performances of the sensors in measuring particle size distributions and particle mass concentrations, they were co-located on the rooftop of the Department of Physics and Astronomy of the University of Bologna. Optical sensors included: one Profiler Model 212 (MetOne Instruments, Inc., Grants Pass, OR 97526, USA), a couple of OPC-N2 low-cost sensors (Alphasense Ltd., Braintree CM77 7AA, UK; price around 300–400 €), a couple of iSCAPE Citizen Kits (SCK, Fab Lab Barcelona 08002, Barcelona, Spain; based on the Smart Citizen Kit 2.0 and PMS 7003 particle sensors, price around 100–200 €) low-cost sensors and one LOAC (light optical aerosol counter; MeteoModem, 77760 Ury, France).

All the sensors utilized in this work are optical particle monitors that use laser beams to detect and count particles, thereby evaluating the scattering signal from suspended particulate to provide a semi-continuous real-time measurement of airborne particulate as a function of size. In particular, the MetOne Profiler 212 is a robust mainstream optical particle counter widely employed in air monitoring (see for example Mamali et al., 2018; Pal et al., 2014), regularly re-calibrated on an annual basis and employed in this work as a reference instrument; i.e., following a heating step causing particle dehydration and classification of particles based on their dry diameters.

The OPC-N2 and the SCK sensors are low-cost sensors characterized by a low price, extreme portability and small weight (e.g., Sayahi et al., 2019; Sousan et al., 2016; Zheng et al., 2019). According to Karagulian et al., 2019, the low-cost sensors herein evaluated can be classified respectively as OEM (original equipment manufacturers) and SSys (sensor systems); i.e., equipment based on low-cost sensors mounted by the customers or already available in a “ready-to-use” format. The Alphasense OPC-N2 sensors were mounted at our lab in a waterproof case together with other meteorological and gaseous pollutant sensors not treated in this work; the whole system (ABBA; Arduino Board Based Air quality monitoring system) was designed and built within the team authoring this paper.

Finally, the LOAC is a versatile optical particle counter characterized by low weight and extreme compactness, which enables it to perform measurements not only at the surface but dynamic applications such as balloon platforms in the troposphere and the stratosphere (Renard et al., 2016; Brattich et al., 2019).

The optical counters used in this work are characterized by different size ranges, flow rates, time resolution, scattering angles and laser wavelengths; all the devices use a mirror to ensure the photodetector collects efficiently all scattered light. In the case of LOAC, the size distribution is estimated from two scattering angles: one around 12° almost insensitive to the refractive index of the particles and one around 60° strongly sensitive to the refractive index of the particles (Renard et al., 2016). This enables the sensor to determine not only the size distribution but also the typology of the dominant aerosol (droplets, carbonaceous, salts and mineral particles). An important characteristic of an optical particle counter is the counting efficiency; i.e., the maximum number of particles or maximum concentration of particles that can be detected by the sensor (ISO 21501-4:2018). The counting efficiency of the sensors used in this work is quite variable and also depends on the diameter and meteorological conditions for the LOAC. Table 1 summarizes the main technical specifications of the sensors used in this work.

Table 1. Technical specifications of the MetOne Profiler-212, OPC-N2 from Alphasense, Smart Citizen Kit (SCK), and LOAC (Light Optical Aerosol Counter) optical particle counters.

Instrument	MetOne Profiler-212	OPC-N2	SCK	LOAC
Size (cm)	114.3×190.5 + 30.5 for inlet tube	$7.5 \times 6 \times 6.46 \times 6 \times 220 \times 10 \times 5$		
Weight (g)	1200	<105	65	300
Size range (μm)	0.3–10	0.38–16	0.3–10	0.2–50
Size bins	8 (selectable)	16	3	19
Flow rate (L min^{-1})	1	1.2	≈ 0.1	≈ 2
Measurement frequency (s)	1–60	1–5	30	1–60
Laser wavelength (nm)	808	658	680	650
Scattering angle ($^\circ$)	90	30	90	12 and 60

The measurement time resolution of the MetOne Profiler 212 (hereafter MetOne), OPC-N2 and LOAC sensors was set to 60 s. Instead, the SCKs made measurements integrated over 30 s, which were averaged to the same time resolution of the other sensors for the sake of homogeneity.

Observations of meteorological variables (atmospheric pressure, air temperature, air relative humidity, wind speed and wind direction) were collected by a Davis Vantage Pro2 (Davis Instruments, Hayward, CA 94545, USA) on a 10-min time basis.

2.2 Number Concentration to Mass Conversion

Optical particle counters are typically based on light scattering by aerosol particles in a flow cell (e.g., Jaenicke et al., 1972; Liu et al., 1974; Welker et al., 2012). As a result, this broad family of instruments is designed to assess particle number densities as a function of particle size bins based on suitable scattering parameterization. Particle number density is, therefore, a fundamental metric to integrate efficiently aerosol gravimetry-based metrics. The MetOne herein used as a reference provides, therefore, the number densities in the particle size intervals previously detailed. In order to make all the data comparable, signals from the MetOne were converted into mass concentration ($\mu\text{g m}^{-3}$).

Conversely, as previously described, the OPC-N2 and the SCK sensors estimate PM_{10} , $\text{PM}_{2.5}$ and PM_{10} mass concentrations from count measurements using embedded proprietary algorithms not yet disclosed to the public. Similarly, the LOAC sensor estimates $\text{PM}_{2.5}$ and PM_{10} mass concentrations from count measurements. In general, the algorithms used by the optical sensors assume a default particle density (1650 kg m^{-3} in the case of OPC-N2; unknown for the SCKs); a volume-weighting factor (default set to 1) to account for errors in sizing due to differences in the refractive index of particles used for calibration and those being measured (Renard et al., 2010); and for SCK, an atmospheric correction factor used in field evaluation whose details are not available from the manufacturer.

Number density data obtained by the MetOne was therefore subjected to a suitable inversion procedure for the planned comparison with the other devices. The following computation was used based on the assumptions of spherical particles with uniform density, a standard approximation, though actually not complying with real ambient aerosol particles (Crilley et al., 2018).

For each size bin of the instrument, a weighted volume diameter was computed according to (Crilley et al., 2018):

$$D = \text{LB} \left[\frac{1}{4} \left(1 + \left(\frac{\text{UB}}{\text{LB}} \right)^2 \right) \left(1 + \frac{\text{UB}}{\text{LB}} \right) \right]^{1/3} \quad (1)$$

(1) where LB and UB are respectively the lower and upper boundaries of each size bin. The particle volume (V_p) and mass are then calculated as follows:

$$V_p = \frac{\pi D^3 n}{6} \quad (2)$$

$$m = \rho V_p \quad (3)$$

where n is the particle count and ρ is the particle density in g cm^{-3} . According to Tittarelli et al., 2008 and Di Antonio et al., 2018, the value of particle density was assumed equal to 1.65 g cm^{-3} , a widely accepted approximation well representative of urban average particle mixture (Crilley et al., 2018; Di Antonio et al., 2018). The particle mass is eventually divided by the sampled air volume to provide aerosol mass concentration per unit air volume. Note that in the case of the LOAC instrument, m is not the particle mass, but it is already the volume mass concentration.

Particle mass concentrations for the MetOne (PM_{10} , $\text{PM}_{2.5}$, and PM_{10}) and the LOAC (PM_{10}) were finally estimated by summing the concentration masses in the various size bins fitting to the respective aerosol cutoff.

2.3 Sensor Performance Metrics

For the purpose of investigating the performances of the OPC-N2, SCK and LOAC particle sensors, their measurements were compared to those obtained from the co-located MetOne instrument. In particular, the choice to use the measurements retrieved from the MetOne as the reference values derived from the fact that this instrument is widely used internationally and therefore fairly well characterized, at least compared to the others (e.g., Mamali et al., 2018; Invernizzi et al., 2011; Zhu et al., 2011; Gaston et al., 2016; Huang et al., 2019; Che et al., 2019). This instrument is endowed with a humidity sensor and an inlet heater to prevent moisture from being sampled as particulate mass.

In order to detect and remove outliers from the 1-min time series recorded by all the sensors, we used the Hampel filter based on the calculation of the median and the standard deviation expressed as median absolute deviation (MAD) over a sliding window (Hampel, 1974; Liu et al., 2004). The filter identifies as outliers values differing from the window median by more than x standard deviations and substitutes them with the median. The filter has two configurable parameters; namely, the size of the sliding window and the number of standard deviations which identify the outlier (x). In this case, we selected a sliding window of 7 observations (given observation and the 2×7 surrounding elements) and a value of $2 \times \text{MAD}$ to detect outliers.

In particular, besides visual comparisons of the time series, scatterplots and histograms produced with the “psych” package (Revelle, 2020) for the R language, version 3.6.1, and density scatter plots built using “ksdensity” Matlab function, a set of statistical indexes was calculated. Indexes include widely used metrics (e.g., Pal, 2017), such as the mean bias error (MBE), the mean absolute error (MAE), the root mean square error (RMSE), the correlation coefficient (r), the coefficient of determination (R^2) and the t-score (t). In addition, normalized values were also calculated for MBE, MAE and RMSE, using the observation range (NMBE, NMAE and NRMSE) or the observation average (CVMBE, CVMAE and CVRMSE) as a factor for normalizations. Calculations were performed using the “tdr” package (Perpinan Lamigueiro, 2020) for the R language. Formulas are provided in Appendix A. Our approach, using a combination of qualitative and quantitative analyses including statistical parameters such as the bias, the RMSE and the MAE, besides the correlation coefficient, is very robust and complete for characterizing the performances of the sensors completely (Karagulian et al., 2019).

3 – Results and Discussion

In this study, we evaluated the performances of a suite of particle sensors in terms of mass concentrations and particle number densities, as evaluated from the comparison with a co-located reference instrument under different sampling conditions. This section presents and discusses the main results of this intercomparison exercise, focusing firstly on mass concentrations and secondly on particle number densities to better understand the reasons for the different behaviors.

3.1 Particle Mass Concentrations

3.1.1 Effect of Seasonal Variability

Figure 1 and Figure 2 present the time series of hourly particle mass concentrations (PM_{10} , $PM_{2.5}$ and PM_{10}) observed by the two SCKs (4E59 and BC60), the two OPC-N2s (ABBA1 and ABBA2), the LOAC (during autumn) and the MetOne during the summer, autumn and winter experimental campaigns. Notwithstanding the application of the Hampel filter, as detailed in Section 2, Figure 1 and Figure 2 highlight clearly that data collected from low-cost sensors in both seasons and from the LOAC during autumn are characterized by evident spikes in mass concentrations, usually not observed or at least less evident in the observations from the MetOne instrument. In addition, biases between the two types of low-cost sensors and the reference instrument are larger during the summer season (Figure 1) than during autumn (Figure 2). During both seasons, the most significant biases affect PM_1 , while biases seem to be reduced for PM_{10} . Finally, Figure 1 and Figure 2 highlight that the two couples of SCKs and OPC-N2s are characterized by high correlations and very similar temporal patterns.

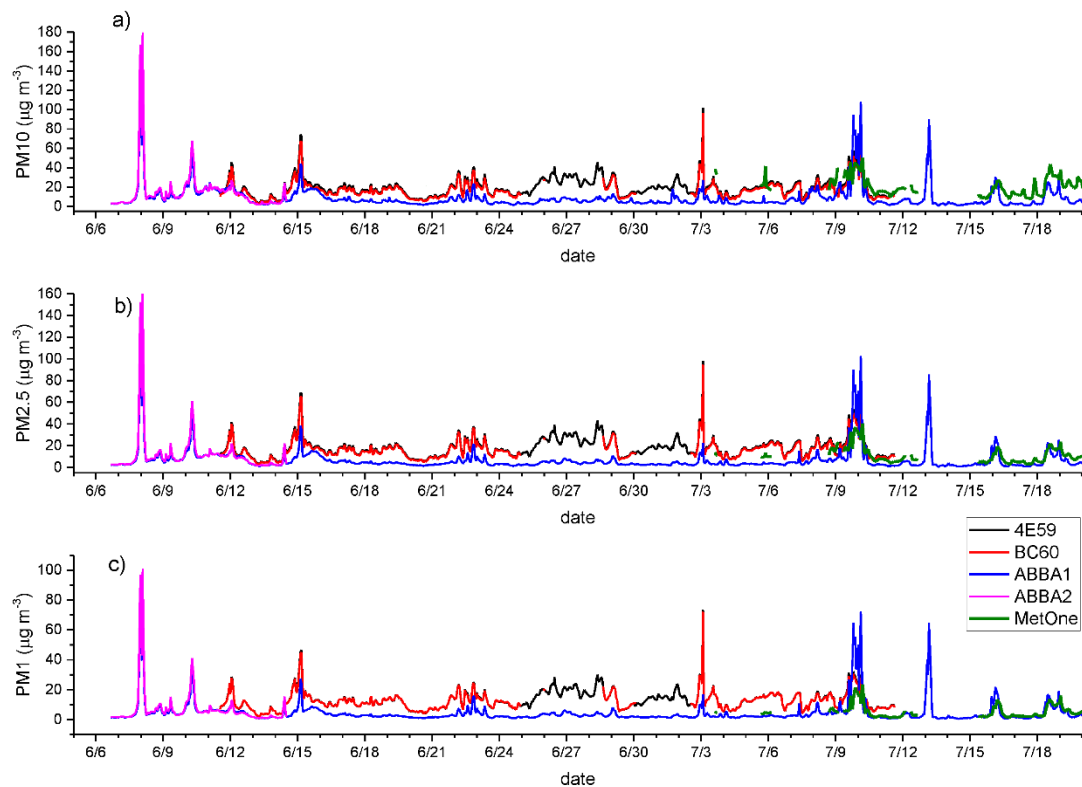


Figure 1. Comparison of hourly PM_{10} (a), $PM_{2.5}$ (b) and PM_1 (c) ($\mu\text{g m}^{-3}$) mass concentrations from the co-located particle sensors during the summer measurement period. 4E59 (black line) and BC60 (red line) are the two SCK (Smart Citizen Kit) sensors; ABBA1 (blue line) and ABBA2 (pink line) are the two OPC-N2 sensors from Alphasense. MetOne (thick green line) is the reference instrument.

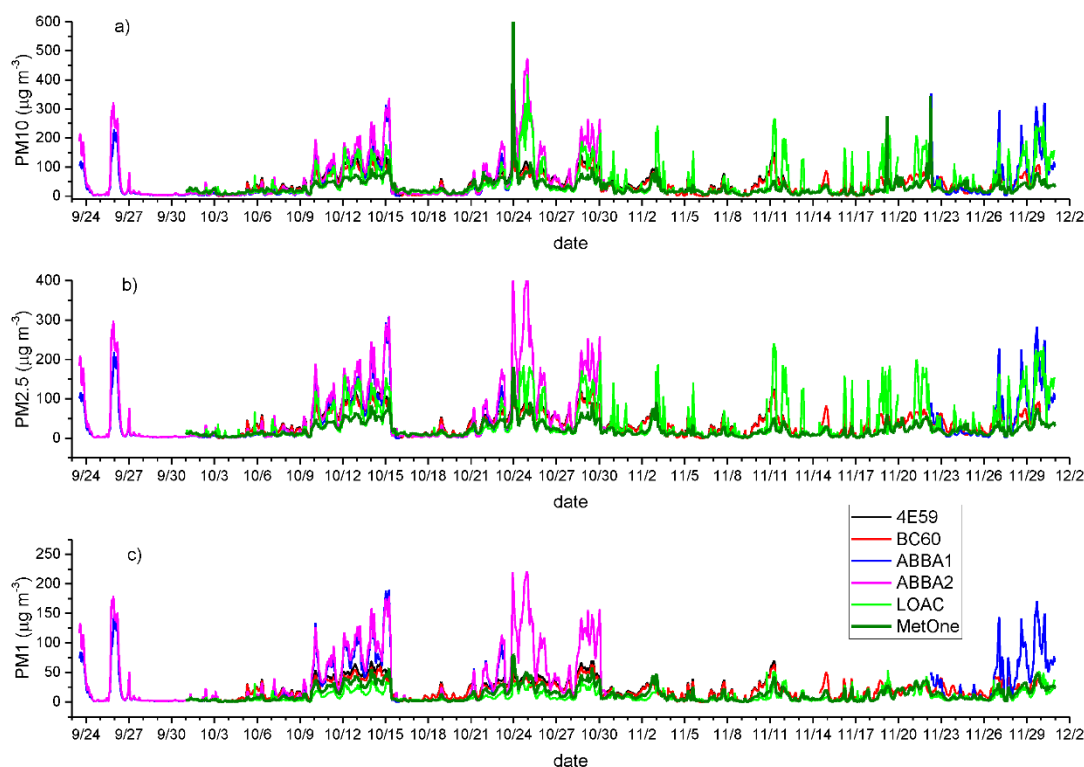


Figure 2. Comparison of hourly PM_{10} (a), $PM_{2.5}$ (b) and PM_1 (c) ($\mu\text{g m}^{-3}$) mass concentrations from the co-located particle sensors during the autumn measurement period. 4E59 (black line) and BC60 (red line) are the two SCK sensors; ABBA1 (blue line) and ABBA2 (pink line) are the two OPC-N2s sensors. LOAC (Light Optical Aerosols Counter) is the light green line. MetOne (thick olive green line) is the reference instrument.

Comparisons of hourly observations of $PM_{2.5}/PM_{10}$ and $PM_1/PM_{2.5}$ concentration ratios are reported in Appendix B. The hourly resolution of these time series has been chosen with respect to the 10-min resolution to improve the graphic representation of the long-term time series. This comparison highlights that, in general, the two SCKs are characterized by very high concentration ratios with respect to the MetOne, while observations from the OPC-N2s show a better agreement with those from MetOne, particularly as far as the $PM_{2.5}/PM_{10}$ ratio is concerned. The very high ratios observed by the two SCKs might derive from the reduced particle-size selectivity of the Plantower PMS5003 particle sensor of the SCKs, as evidenced by Kuula et al., 2019.

A better understanding of how data collected from different particle sensors are related derives from the visual inspection of density plots, scatterplots and histograms of 1-min observations during the two measurement campaigns (Figure 3 and Figure 4 and Appendix C).

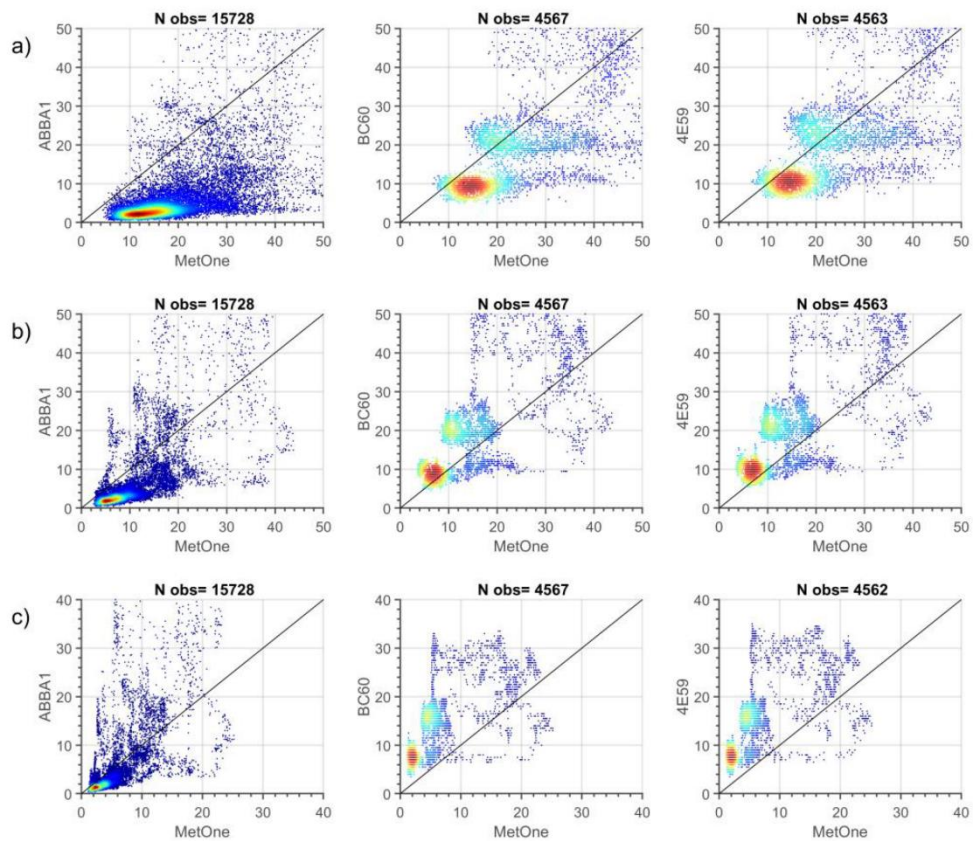


Figure 3. Density scatter plot for of 1-min PM₁₀ (a), PM_{2.5} (b) and PM₁ (c) ($\mu\text{g m}^{-3}$) mass concentrations from the co-located particle sensors during the summer measurement period. Points are colored based on data density ranging from dark red (high density) to dark blue (low density). N obs is the number of measurements for each pair of sensors.

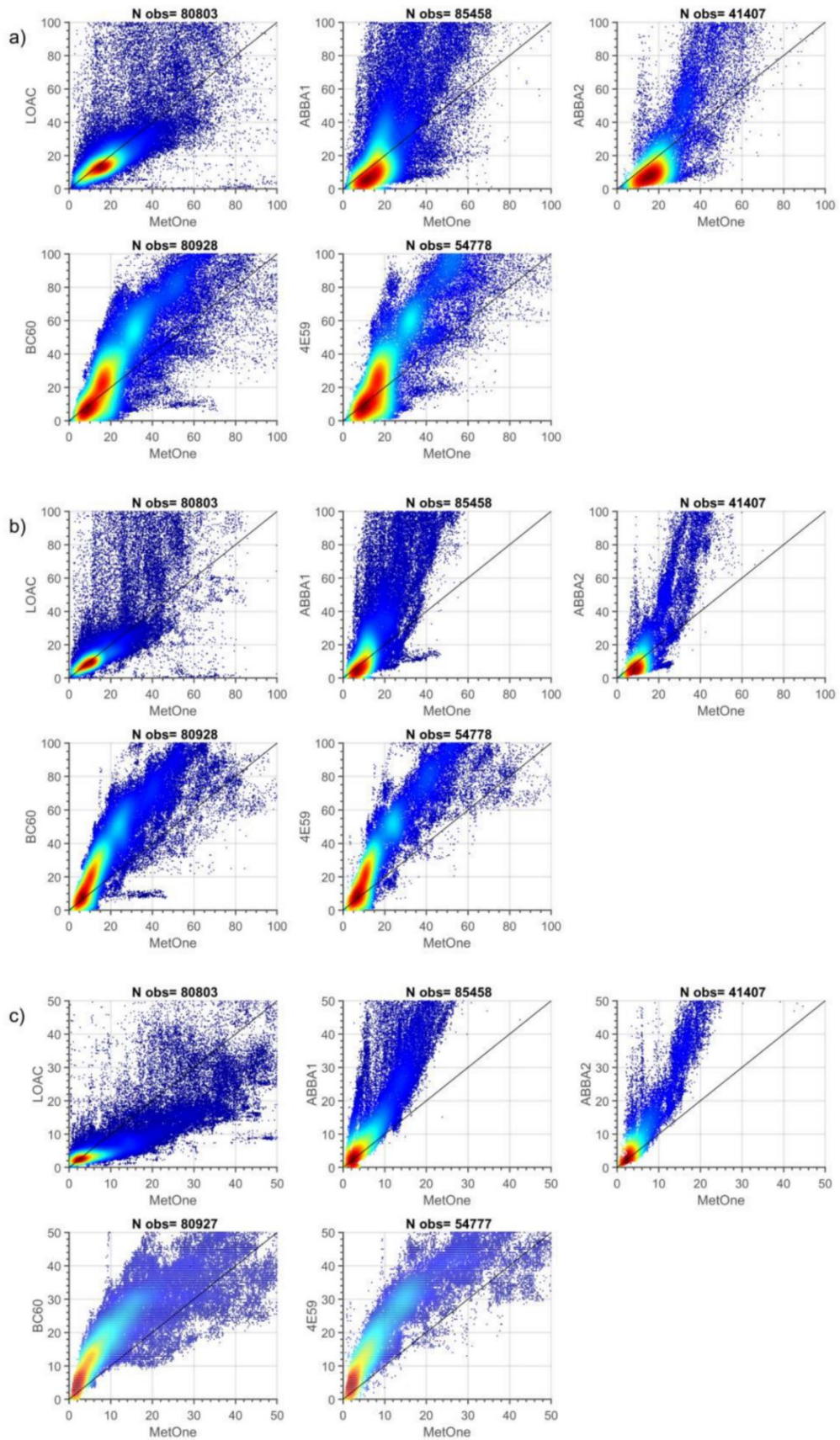


Figure 4. Density scatter plot for of 1-min PM₁₀ (a), PM_{2.5} (b) and PM₁ (c) ($\mu\text{g m}^{-3}$) mass concentrations from the co-located particle sensors during the autumn measurement period. Points are colored based on data density ranging from dark red (high density) to dark blue (low density). N obs is the number of measurements for each pair of sensors.

The comparison of summer data (Figure 3 and Appendix C) highlights even more some patterns previously observed: observations of the two SCKs are very well correlated ($R = 0.98, 0.99$ and 0.99 respectively for PM_{10} , $PM_{2.5}$ and PM_1) and similarly distributed, while observations from the two OPC-N2s, even though similarly well correlated between each other ($R = 0.91, 0.99$ and 0.99 respectively for PM_{10} , $PM_{2.5}$ and PM_1) seem to slightly deviate from a linear regression line, indicating some biases between the two sensors though of the same type.

When comparing observations from SCKs and OPC-N2s with those from the MetOne during summer (Figure 3), the density scatterplots show a better agreement for the $PM_{2.5}$ cut-off. At the same time, lower correlations are observed for PM_1 and even worse for PM_{10} . Indeed, low-cost sensors present evident tails in their populations, a feature particularly marked for the two SCKs (4E59 and BC60), in spite of their better correlation with respect to OPC-N2s (ABBA1 and ABBA2) for PM_{10} and $PM_{2.5}$. These tails are likely caused by the occurrence of instrumental spikes not removed by the Hampel filter, as observed by data clusters departing from the main data clouds in the scatter plots.

The comparison of autumn data (Figure 4 and Appendix C) shows again that data from the two couples of low-cost sensors are reciprocally well correlated, particularly in the case of the two SCKs ($R = 0.91, 0.95$ and 0.98 respectively for PM_{10} , $PM_{2.5}$ and PM_1), but also in the case of OPC-N2s for $PM_{2.5}$. The comparison with observations from the MetOne highlights higher correlations with respect to the summer season for PM_1 and $PM_{2.5}$ for both kinds of low-cost sensors and especially for the OPC-N2s, while for PM_{10} autumn correlations are higher than the summer ones only for OPC-N2s. Biases and tails are evidenced in the histograms and scatterplots for both types of low-cost sensors, even though clear clusters emerge in the case of the two SCKs. Moreover, all the data are mostly positioned above the bisector, suggesting that owing to the generally higher relative humidity of the autumn season at this latitude and the heating inlet of the MetOne, particle size measured by the sensors is different; the MetOne does not show the effect of the hygroscopic growth, as seen in detail later on. The observations from LOAC, instead, show a different behavior, showing a general tendency to underestimate aerosol mass concentration with respect to the MetOne.

3.1.2 Effect of Time Resolution

Figure 5 presents the evaluation of the performances of the sensors through the RMSE and the r correlation coefficient at different time resolutions (from 1 min to 1 day) during the two measurement periods, while the complete series of the statistical indicators is presented in Appendix D. During both measurement periods, the values highlight a tendency for the performance of the low-cost sensors to improve with lower time resolutions, as evidenced by the increasingly higher correlation coefficients and the lower biases. The comparison of the summer and autumn values shows that as previously observed, the agreement of the sensors is higher during autumn, though also accompanied by higher biases in this season. The performances of the two couples of low-cost sensors within the brand type are very similar. In general, during both measurement periods, the SCKs are more consistent with MetOne than the OPC-N2s in the case of PM_{10} concentrations, while OPC-N2s reveal lower biases for $PM_{2.5}$ and PM_1 . In addition, the MBE values confirm the SCKs' tendency to overestimate compared to MetOne; conversely, the OPC-N2s tend to underestimate $PM_{2.5}$ and PM_{10} observations during summer. As previously described, the LOAC shows reduced correlations for all size fractions at high time resolution, while correlations greatly improve

at lower time resolutions. Finally, the bias for the LOAC is particularly low for PM_{10} , which might indicate its better counting efficiency for the smaller particles.

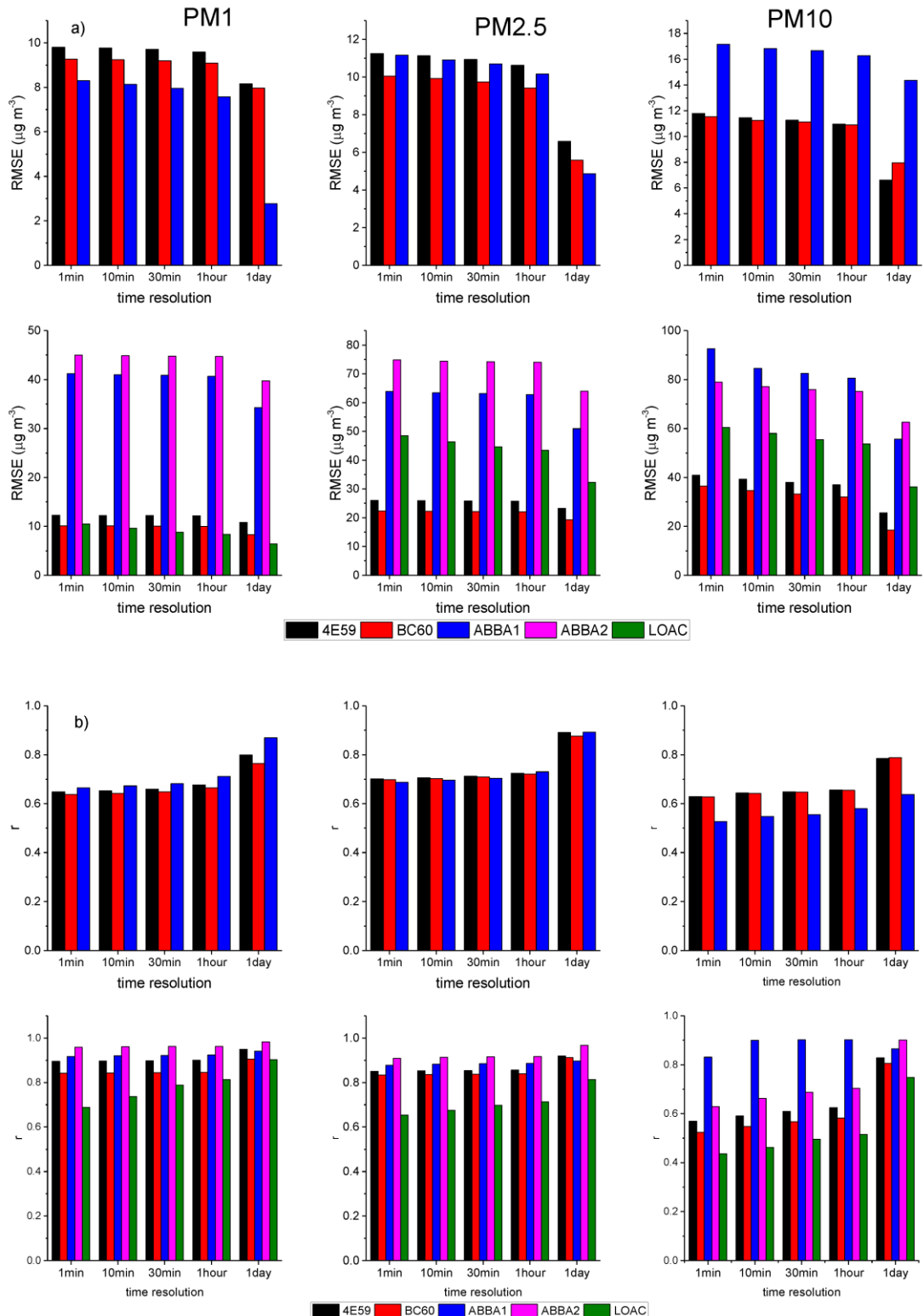


Figure 5. RMSE (root mean square error) (a) and r Pearson's correlation coefficient (b) of the optical sensors in measuring PM_1 , $PM_{2.5}$ and PM_{10} mass concentrations under varying time resolution (1 min, 10 min, 30 min, 1 h and 1 day) using the MetOne as the reference sensor and during the two-measurement periods (summer in the upper panel, autumn in the lower panel).

3.1.3 Effects of Meteorological Conditions

As reported in Section 2, the measurement period included different meteorological conditions typical of the warm and cold seasons in the measurement site. Specifically, with the aim of understanding the effects of different weather conditions on the performances of the optical sensors, we investigated the effects of the prevailing weather conditions based on the meteorological variables observed in situ from the co-located meteorological station and a WMO (World Meteorological Organization) synoptic meteorological station located at the Bologna airport; synoptic weather charts; atmospheric vertical soundings at a nearby meteorological station; drop size distribution observations obtained from a co-located OTT-Parsivel disdrometer, OTT Hydromet GmbH, 87437 Kempten, Germany; and maps of dust transport over the Mediterranean region, as simulated by the BSC-DREAM 8b model from the Barcelona Supercomputing Center (<https://ess.bsc.es/bsc-dust-daily-forecast>). Briefly, the weather conditions observed were the following:

- Thunderstorm on 9th July 2019;
- Saharan dust transport on 10th July 2019;
- Rain on 7th October 2019;
- Mist on 14th October 2019;
- Fair weather on 20th October 2019;
- Cloudy conditions on 23rd October 2019;
- Fog on 25th October 2019;
- Drizzle on 1st November 2019.

Figure 6 presents the performances of the optical sensors during these different weather conditions as evaluated from the calculations of MAE, MBE and RMSE indexes, and correlation coefficients using the MetOne sensor as a reference instrument.

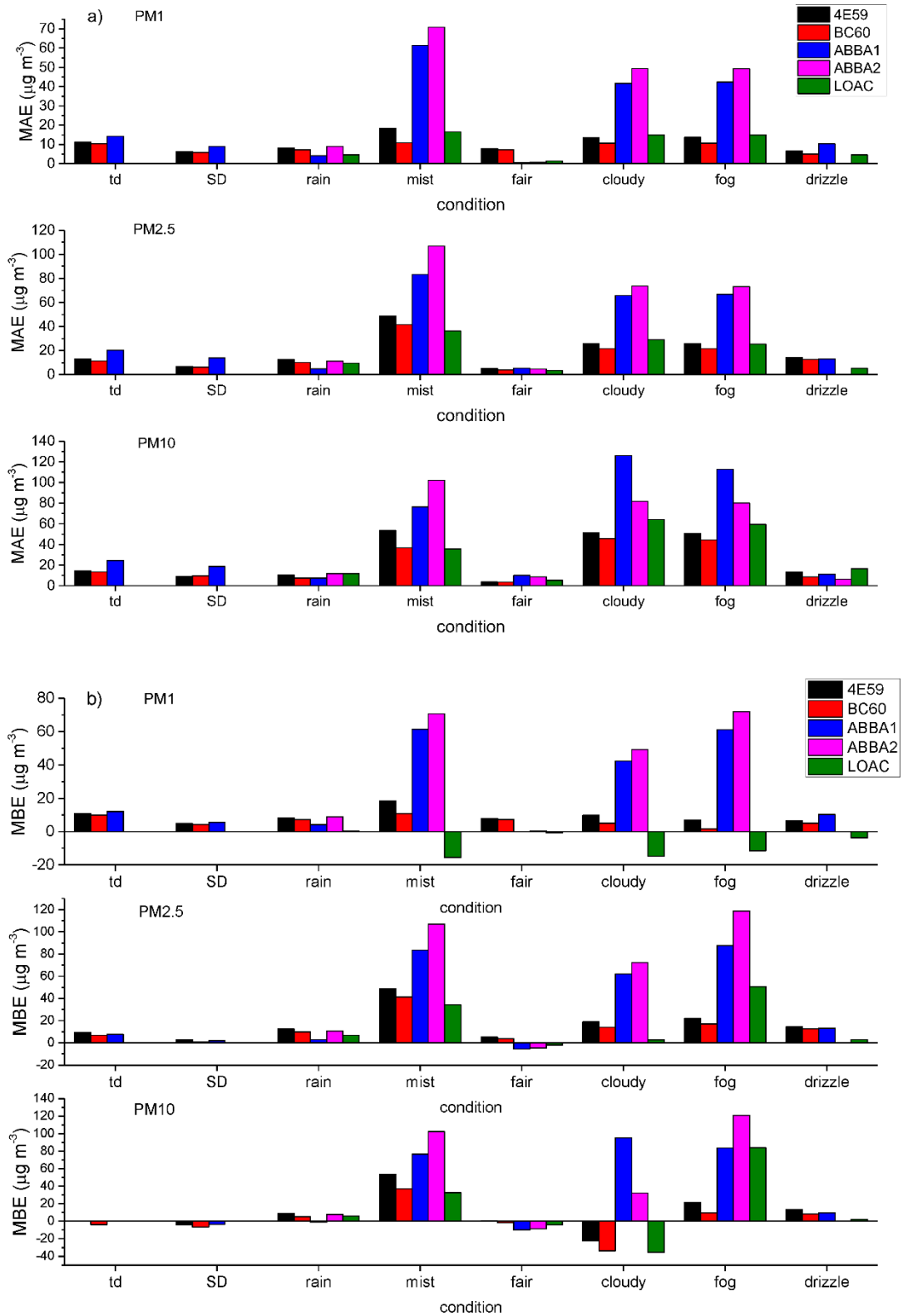


Figure 6. Evaluation of the performances of the different optical sensors in measuring PM_{10} , $\text{PM}_{2.5}$ and PM_1 mass concentrations under varying weather conditions (thunderstorm = td, Saharan dust transport = SD, rain, mist, fair weather, cloudy, fog, drizzle) using the MetOne as the reference sensor by calculating the following indexes: (a) MAE (mean absolute error); (b) MBE (mean bias error); (c) RMSE (root mean square error); (d) r (Pearson's correlation coefficient).

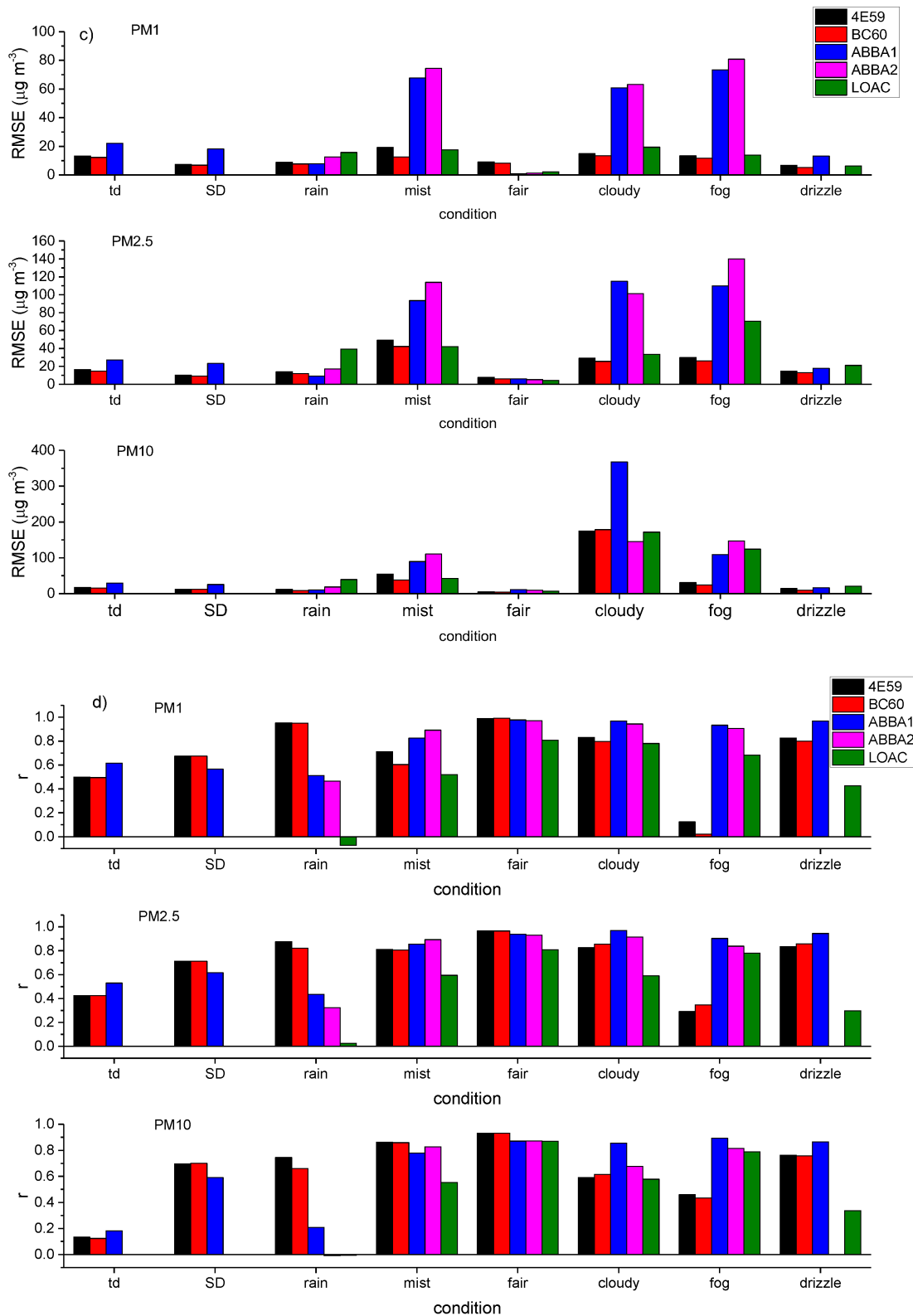


Figure 6 - continued

As seen in Figure 6, the performances of all the sensors are the highest during fair weather conditions, when the lowest values of the MAE, MBE and RMSE are reported, associated with high correlation coefficients (>0.80) for all size fractions. Conversely, the performances of the sensors sensibly worsen under mist, cloudy and fog conditions, as expected given the

hygroscopic behavior of aerosols. The comparison among the different sensors shows the higher performance of the OPC-N2s and the LOAC in capturing PM_{10} concentrations under fair weather, while the SCKs perform better for $PM_{2.5}$ and particularly for PM_{10} concentrations. Figure 6 shows how the SCKs present a satisfactory, even though never exceptional performance under all weather conditions, while the OPC-N2s and the LOAC reveal very variable behaviors ranging from the excellent performance with fair weather down to fairly biased and poorly correlated under mist, cloudy and fog conditions. The OPC-N2s present high average correlations (>0.6) for most weather conditions except for the Saharan dust transport and rain events. The differentiated behavior of the other sensors may stem from several factors differently affecting particle counts in the various size bins and how they are used in PM assessment. One of the primary factors is basically the different particle size bins and the overall size intervals of each model, leading to an approximation in the instrumental comparison. Secondly, as previously reported, optical sensors are characterized by distinct particle size-selectivity (Kuula et al., 2019). Thirdly, the use of a constant density factor across the various size ranges to convert number densities to mass concentrations is likely an oversimplification, owing to the intrinsic complexity of PM composition highly inhomogeneous across the size distribution and to the direct and indirect influence of meteorology on particle size and composition (Johnson et al., 2018). In fact, the enhanced bias among the various sensors observed during the Saharan dust transport should be ascribed to the use of a density factor unsuitable for capturing the prevailing mineral component of the particles associated with this kind of transport. All the other biases instead are attributable mainly to the influence of relative humidity on particle size as a result of variable hygroscopic growth leading to an overestimation of particle mass by the optical sensors with respect to the MetOne sensor endowed with the inlet heater.

The effect of relative humidity can be better assessed by observing the scatter plots of the aerosol masses obtained for the various devices. Figure 7, Figure 8 and Figure 9 report the comparison of 10-min averaged PM_{10} , $PM_{2.5}$ and PM_{10} concentrations of the MetOne vs. those obtained from all the others with different color tones as a function of relative humidity and temperature, during the autumn measurement period (results for the summer measurement period are reported in Appendix E).

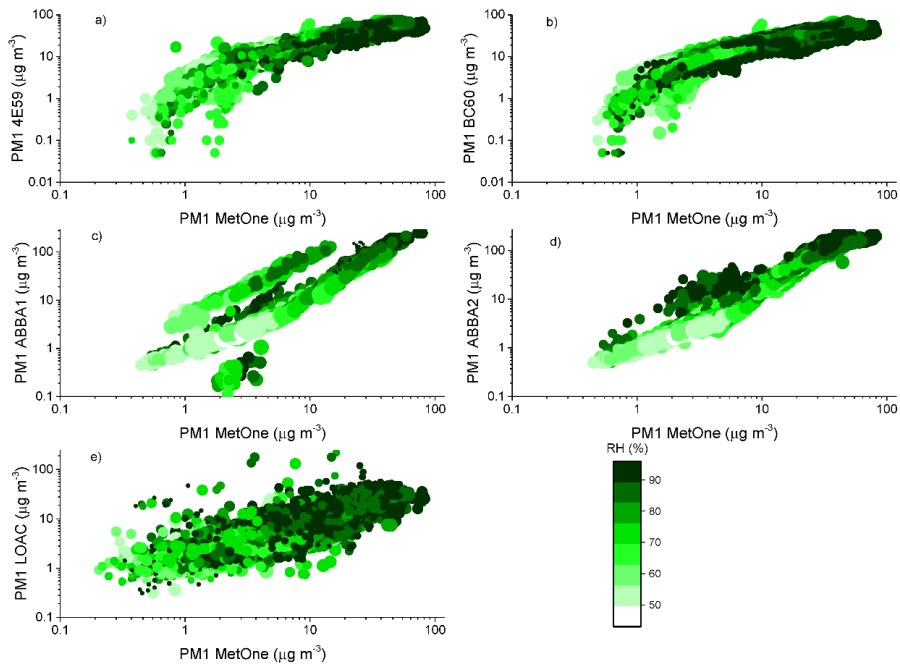


Figure 7. Comparison of 10-min PM_1 mass concentrations observed by the MetOne and the other optical sensors: (a,b) the two SCKs (4E59 and BC60); (c,d) are the two OPC-N2s (ABBA1 and ABBA2); (e) is the LOAC during the autumn measurement period. The color scale indicates the relative humidity (%) value at the time of the measurements, while the size of the marker is proportional to the value of temperature at the time of the measurements.

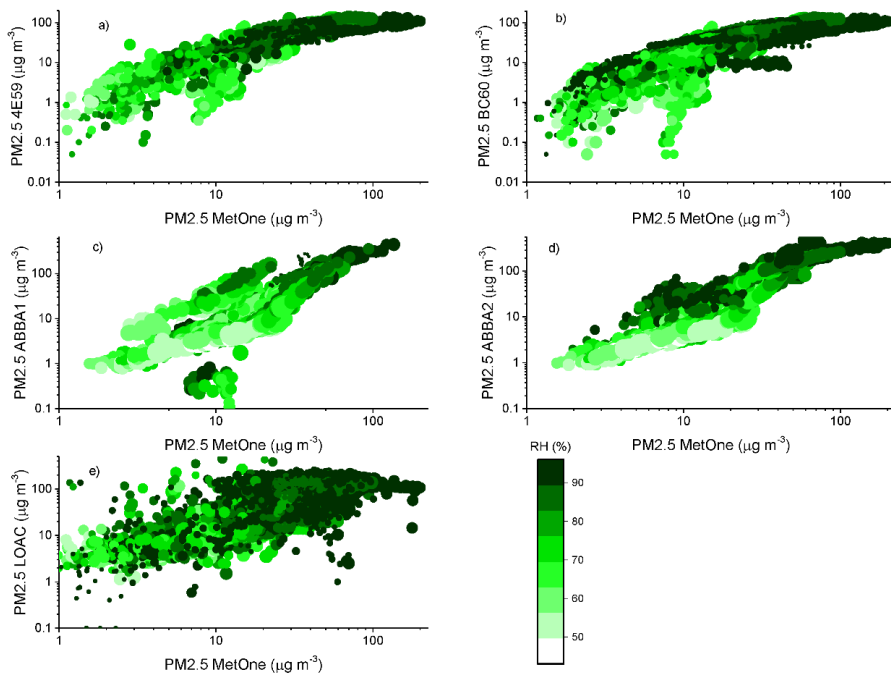


Figure 8. Comparison of 10-min $PM_{2.5}$ mass concentrations observed by the MetOne and the other optical sensors: (a,b) are the two SCKs (4E59 and BC60), (c,d) are the two OPC-N2s (ABBA1 and ABBA2) and (e) is the LOAC during the autumn measurement period. The color scale indicates the relative humidity (%) value at the time of the measurements, while the size of the marker is proportional to the value of temperature at the time of the measurements.

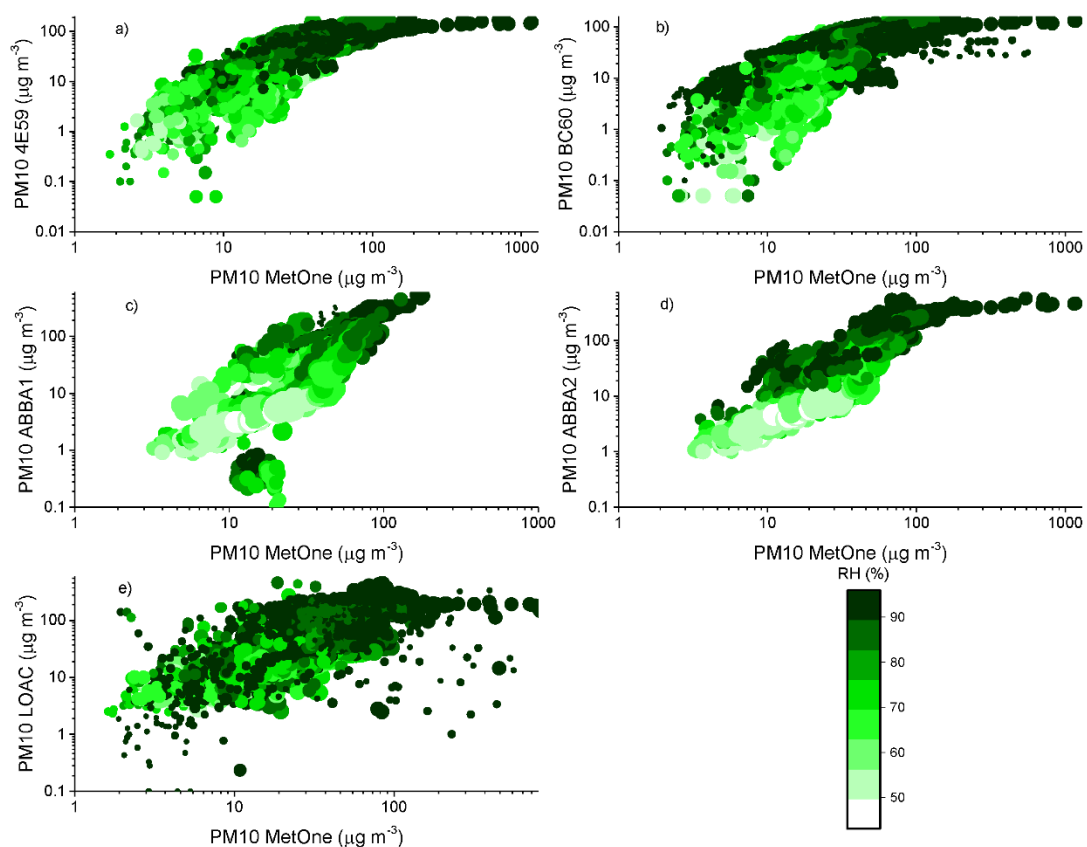


Figure 9. Comparison of 10-min PM_{10} mass concentrations observed by the MetOne and the other optical sensors: (a,b) are the two SCKs (4E59 and BC60), (c,d) are the two OPC-N2s (ABBA1 and ABBA2) and (e) is the LOAC during the autumn measurement period. The color scale indicates the relative humidity (%) value at the time of the measurements, while the size of the marker is proportional to the value of temperature at the time of the measurements.

During the autumn measurement period, the temperature in Bologna varied between 5 and 28 °C, while relative humidity varied in the range 43-96%. Overall, Figure 5, Figure 6 and Figure 7 highlight the effects of relative humidity conditions on PM concentrations observed by all the optical particle counters. In particular, OPC-N2 sensors tend to overestimate particulate matter concentrations under high relative humidity conditions, while they seem to underestimate PM concentrations under low relative humidity, especially for $PM_{2.5}$ and PM_{10} . The behavior of the two SCKs seems more coherent and less affected by humidity conditions than that of the OPC-N2s, while the PM_{10} readings from this sensor type present also the effect of temperature conditions, possibly associated with the protective case used to house the two sensors. The more significant effect of relative humidity conditions on $PM_{2.5}$ and PM_{10} concentrations, related with the condensation of water vapor and hygroscopic growth of particles (Malings et al., 2020), is in agreement with the previous results on the dependence of hygroscopicity on particle size, previously observed by Wu et al., 2016. The hygroscopic growth of particles inevitably affects the response of all the particle counters, resulting in a possible overestimation of the mass because of the reduced molecular mass of water (Bagtasa et al., 2007). The differences against the MetOne reference instrument can be ascribed to the thermal dehydration of particles within the instrument body, leading to a decrease in particle size, and therefore, to a shift in the size distribution in this instrument. Since size distribution affects the retrieved mass data through the application

of the conversion previously described in the experimental section, the bias between instruments might be larger at higher relative humidity values owing to enhanced hygroscopic growth.

Figure 10 presents a focus of the PM₁₀ concentrations and of relative humidity values observed on the week of 7-14 October 2019, enlightening the occurrence of a bias among the sensors. In particular, an overestimation of mass concentrations was observed in the data from low-cost sensors and by the LOAC, when relative humidity was higher than 70-80%, and under fog conditions, in agreement with previous observations (Johnson et al., 2018; Han et al., 2017; Jayaratne et al., 2018), likely due to the use of an inadequate density factor in these conditions.

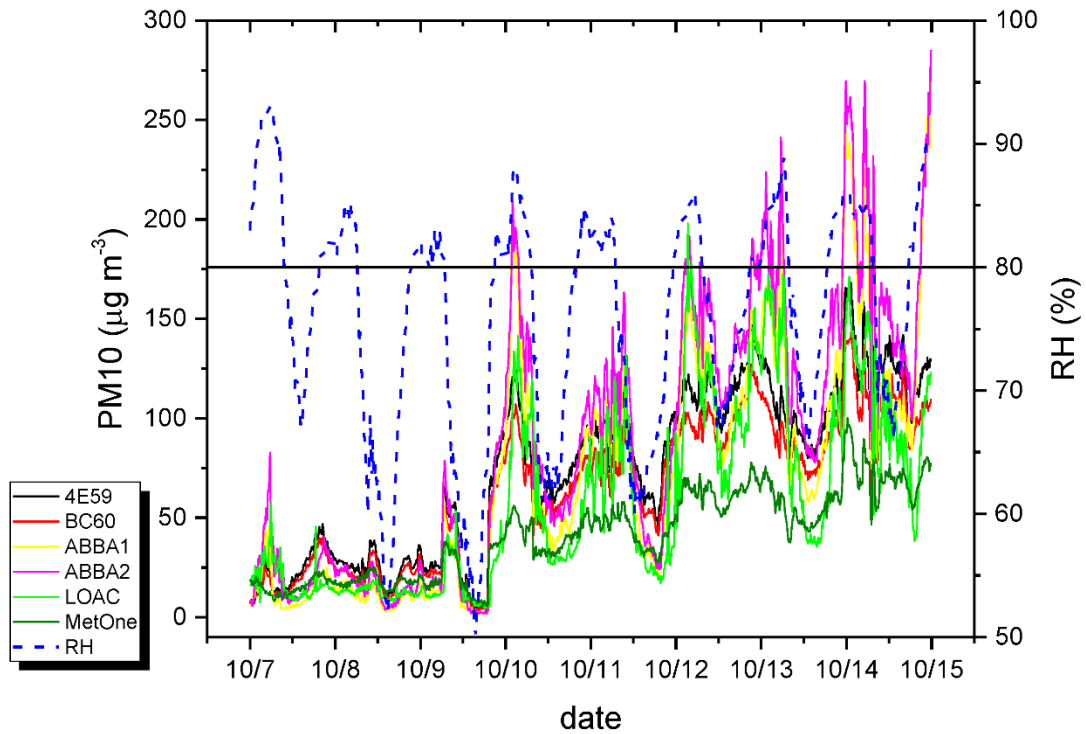


Figure 10. Time series of 10-min PM₁₀ mass concentrations observed by the various optical sensors and relative humidity values during the week of 7-14 October 2019.

Under these circumstances of high relative-humidity conditions, we tested the use of the hygroscopic growth factor developed by Di Antonio et al., 2018 based on the κ -Köhler theory. Specifically, the particle diameters of the OPC-N2 and of the LOAC sensors (as reported previously, the SCKs do not provide particle counts explicitly in the various size bins and therefore cannot be subjected to this correction) were corrected by a hygroscopic growth factor (Gaston et al., 2016) to take into account the changes in particle size due to water uptake:

$$g(\text{RH}) = \left(1 + \kappa \frac{\text{RH}}{100 - \text{RH}} \right)^{1/3} \quad (4)$$

$$D_{\text{wet}} = D \cdot g(\text{RH}) \quad (5)$$

where RH is the relative humidity obtained by the weather station, and κ is a parameter that describes the particle hygroscopicity and is assumed to be 0.62, an optimized value for a

mixture of organic and inorganic particles in polluted environments fitting Bologna airshed characteristics. “Corrected” particle mass concentrations were then estimated by summing the concentration masses in the various size bins fitting to the respective aerosol cutoff. Figure 11 reports the scatterplots for the PM₁₀ mass concentrations observed by one of the two OPC-N2s (the ABBA2) and the LOAC vs. those observed by the MetOne during October 2019, both with and without the use of the correction with the hygroscopic growth factor.

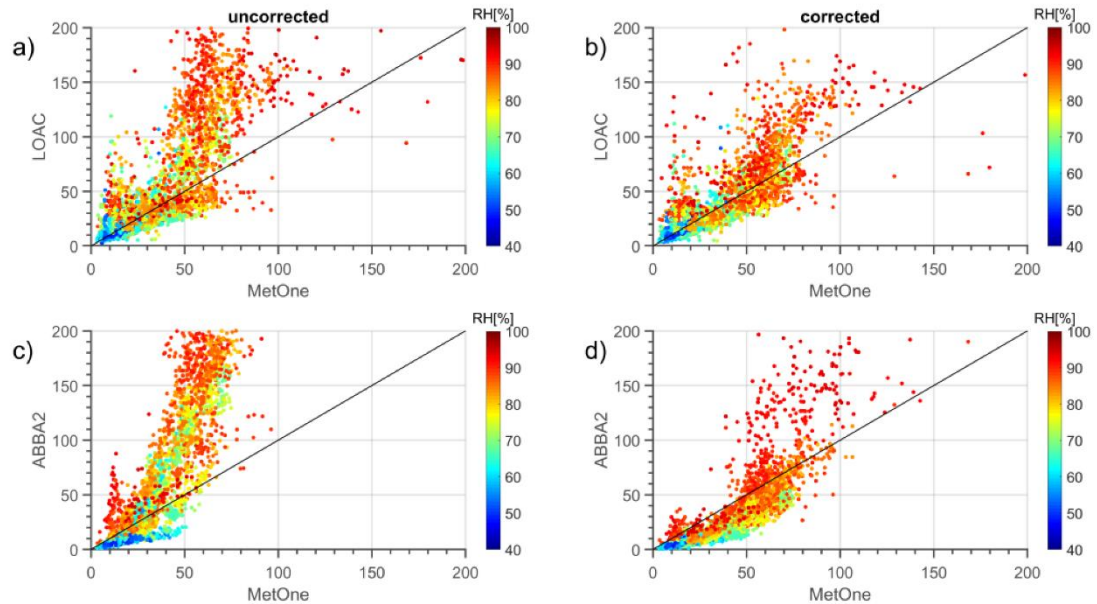


Figure 11. Comparison of 10-min PM₁₀ mass concentrations observed by the MetOne, by one of the two OPC-N2 (ABBA2) and by the LOAC during October 2019, both without (left panels, a,c) and with (right panels, b,d) the correction with the hygroscopic growth factor. The color scale indicates the relative humidity (%) value at the time of the measurements.

The comparison of the regression for corrected and uncorrected mass concentrations indicates that the correction performs well and improves the agreement with the MetOne reference instrument, even though in the case of the OPC-N2 sensor seems to lower also the values observed under moderate or low relative humidity conditions. Therefore, it seems useful to adopt a threshold value of RH (Relative Humidity) beyond which the correction can be applied.

3.2 Particle Number Densities and Particle Size Distributions

The correlations of particle number densities observed by the instruments were evaluated over three weeks, considering in particular, two periods of weak synoptic forcing respectively in summer (19-24 July 2019) and in winter (5-11 February 2020), characterized by constant high atmospheric pressure, low wind speeds and absence of precipitation, and one in autumn (19-26 October 2019) was characterized by the presence of frequent fog and cloudy conditions. These analyses were carried out by comparing the particle number densities retrieved by the two OPC-N2s and by the LOAC with those collected by the MetOne. In this framework, the SCKs, which might be classified as SSys ready-to-use out of the box systems according to Karagulian et al., 2019, do not provide particle number

densities explicitly, and therefore, could not be evaluated against the other ones. Moreover, during the summer week, only one of the OPC-N2 (ABBA1) and the MetOne were operating.

The correlations were evaluated by estimating seven fractions, obtained by summing the proper bins of each instrument: “fr0.5” (considered as the fraction 0.3–0.5 μm), “fr0.7” (0.5–0.7 μm), “fr1” (0.7–1.0 μm), “fr1_2” (1.0–2.0 μm , not present for LOAC), “fr1_3” (1.0–3.0 μm), “fr5” (3.0–5.0 μm) and “fr10” (5.0–10.0 μm). All data were mediated over 10 min, and the Hampel filter presented in the experimental section was applied to remove outliers.

Table 2 summarizes the results in terms of the coefficient of determination (R^2) and Pearson and Spearman correlation coefficients.

Table 2. Comparison of the particle sensors evaluated by determination coefficients (R^2), Pearson and Spearman correlation indexes, with respect to the MetOne reference instrument, during the three considered weeks.

JULY 19–24, 2019									
				ABBA1					
	R^2	Pearson	Spearman						
fr0.5	0.481	0.694	0.785						
fr0.7	0.480	0.693	0.850						
fr1	0.381	0.617	0.688						
fr1_2	0.344	0.587	0.617						
fr1_3	0.348	0.590	0.632						
fr5	0.107	0.328	0.415						
fr10	0.0007	0.027	0.041						

OCTOBER 19–26, 2019											
			ABBA1			ABBA2			LOAC		
	R^2	Pearson	Spearman	R^2	Pearson	Spearman	R^2	Pearson	Spearman		
fr0.5	0.860	0.927	0.971	0.877	0.936	0.966	0.491	0.701	0.866		
fr0.7	0.867	0.931	0.990	0.812	0.901	0.985	0.723	0.850	0.947		
fr1	0.769	0.877	0.963	0.651	0.807	0.944	0.557	0.747	0.939		
fr1_2	0.844	0.919	0.935	0.580	0.762	0.861	--	--	--		
fr1_3	0.758	0.870	0.893	0.487	0.698	0.803	0.254	0.504	0.803		
fr5	0.818	0.905	0.833	0.126	0.351	0.776	0.016	0.128	0.724		
fr10	0.976	0.988	0.651	0.076	0.276	0.571	0.011	0.103	0.713		

FEBRUARY 5–11, 2020											
			ABBA1			ABBA2			LOAC		
	R^2	Pearson	Spearman	R^2	Pearson	Spearman	R^2	Pearson	Spearman		
fr0.5	0.819	0.905	0.986	0.752	0.867	0.985	0.460	0.678	0.887		
fr0.7	0.778	0.882	0.987	0.771	0.878	0.978	0.610	0.781	0.934		
fr1	0.500	0.707	0.920	0.462	0.680	0.908	0.593	0.770	0.958		
fr1_2	0.066	0.507	0.966	0.209	0.457	0.953	--	--	--		
fr1_3	0.252	0.502	0.944	0.203	0.451	0.920	0.130	0.360	0.941		
fr5	0.803	0.896	0.585	0.841	0.917	0.581	0.328	0.572	0.780		
fr10	0.931	0.965	0.203	0.843	0.918	0.278	0.533	0.730	0.651		

The lower fractions (fr0.5, fr0.7 and fr1) show, in general, higher correlations than the higher ones, as shown by the low R^2 and correlation coefficients. This is ascribed to the higher mass contribution of the coarse fraction to PM_{10} in the warm and substantially drier season, but also to the influence of gravity and therefore to the remarkable stochasticity of suspended

coarse particles (Seinfeld et al., 2016; Raes et al., 2000). Similar results were reported in other papers focusing on OPC comparison (see for example, Han et al., 2017).

In the summer week, poor R^2 and Pearson correlations were observed between MetOne and ABBA1, while the Spearman correlations were higher, in agreement with the non-normal distribution. During the autumn and winter weeks, instead, high (>0.6 and even >0.9 in most cases) Spearman correlation coefficients were observed between all instruments against the MetOne for almost all fractions. The LOAC sensor presents the lowest correlations with the MetOne in terms of R^2 and Pearson indexes. This is attributed to the frequent spikes present in LOAC data (even if partially removed by the application of the Hampel filter) in all the size classes simultaneously possibly due to electronic noise during the experiment. The Spearman coefficient, indeed, being a non-parametric alternative for evaluating the correlation, shows a better skill in evaluating it in the presence of spikes. ABBA1 and ABBA2 are both strongly correlated to MetOne, particularly considering the Spearman indexes. Moreover, the correlation coefficients between these two OPCs are always higher than 0.9 for all fractions (data not shown), suggesting, as reported before, that instruments of the same manufacturer tend to behave similarly.

Figure 12 shows the time series of particle counts in the different size fractions observed by the two OPC-N2s, the LOAC and the MetOne, together with the corresponding values of relative humidity, during the week of October characterized by frequent fog and cloudy conditions (22–26 October 2019). Particle counts observed by the two OPC-N2s were corrected with the previously cited hygroscopic growth factor. The plots evidence interesting features of the instruments: first of all, the MetOne and the LOAC sensors observe regularly more particles in the smallest size fraction, in agreement with the lower instrumental limit of these two instruments with respect to the OPC-N2 low-cost sensors; secondly, during fog (24th of October) and rain events (24–25 October) and with values of relative humidity close to saturation (95%), the MetOne observes more particles in the second bin than the other sensors; in the coarsest fractions, the LOAC greatly overestimates the number of particles during rain events, but not during fog events, while on the contrary MetOne and ABBA1 seem to perform better under fog than under rainy conditions.

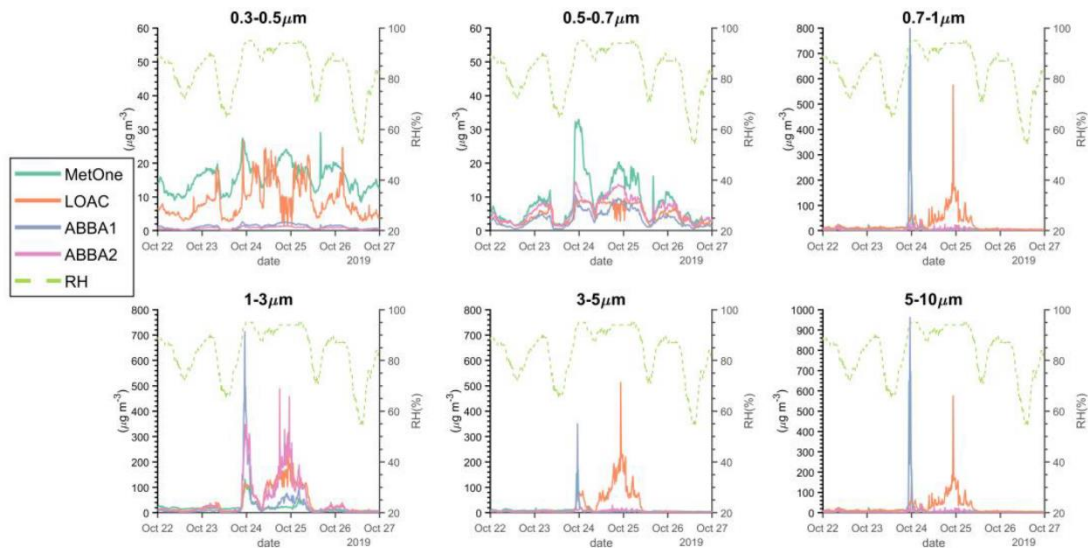


Figure 12. Time series of 1-min particle number densities in the various size fractions (0.3–0.5; 0.5–0.7; 0.7–1; 1–3; 3–5; 5–10 μm) observed by the various optical sensors and relative humidity value during the week of 19–26 October 2019.

The comparison of particle size distributions observed by the MetOne and one of the two OPC-N2s during the same week of October (Figure 13) shows very clearly that under high relative humidity conditions the disagreement between the two instruments is due to the higher counts of the OPC-N2 in the 1–3 μm size fraction.

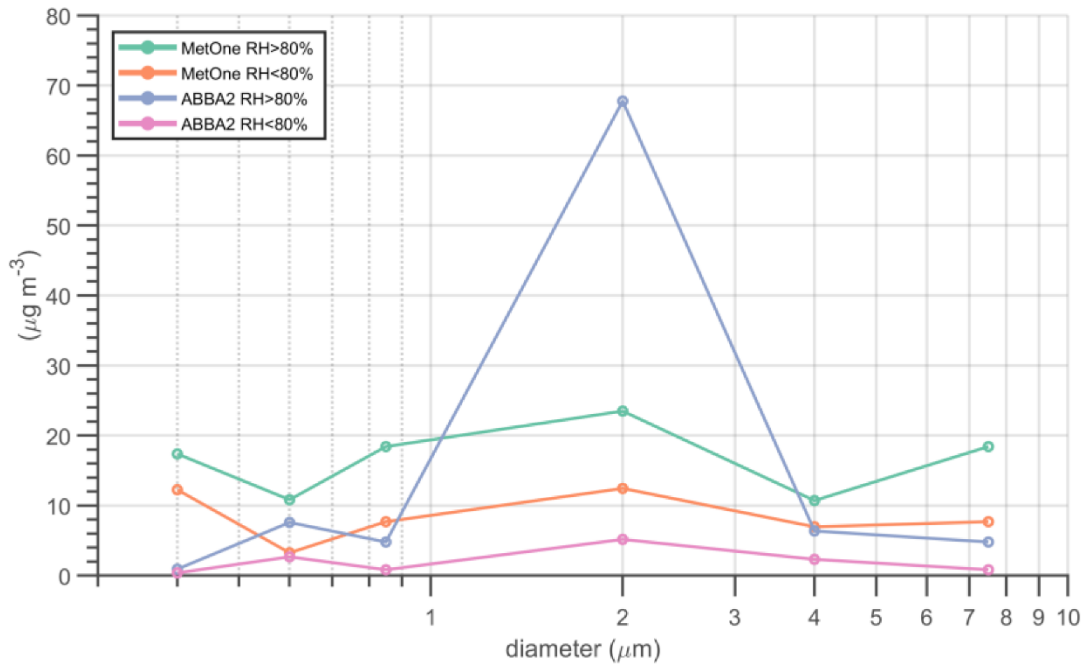


Figure 13. Particle size distributions observed by the MetOne and by one of the two OPC-N2s (ABBA2) for relative humidity values lower and higher than 80% during the week of 19–26 October 2019.

4 – Conclusions

This work describes and discusses the results of an intercomparison exercise that aimed at evaluating the performances of a series of OPCs representative of both research and low-cost devices, the latter becoming extremely popular and extensively used at all scientific levels.

To that end, an intensive long-term experimental field campaign was carried out. The performances of the sensors were evaluated through a robust comprehensive approach considering a mainstream OPC with a heated inlet as the reference instrument, and calculating a series of statistical parameters to capture not only the correlation but also the biases from the reference OPC.

The results of this study indicate that low-cost sensors, and all OPCs, are affected by relevant biases and low correlations when working at elevated time resolution, while the performance improves when lowering the time resolution to hourly or daily averages.

Other biases that emerged from our work are tightly connected with aerosol complexity, and as such, cannot be ignored, since the PM data might be seriously misleading if not considered and suitably corrected. In particular the main deviations were observed using flat density correction factors when converting particle number densities into mass, suggesting a post field campaign reassessment and post-processing of data. This is especially important in countries/areas affected by mineral dust outbreaks whose properties and size distribution spectrum are significantly different from the urban background.

In addition, the performance of a sensor is highly impacted by the prevailing weather conditions, suggesting particular caution in their use for estimating PM concentrations at high relative humidity conditions, such as rain and fog events. Conversely, their performances under conditions of weak synoptic forcing and prevailing anticyclonic conditions were in general characterized by low biases and elevated correlation coefficients. The detailed analysis of the effect of relative humidity suggests/shows that the application of a hygroscopic growth factor to account for the condensation of water vapor on aerosol particles can improve the agreement; however, this approach requires some caution as it may lead to artefacts and shifts in the size distribution which may ultimately result in errors in the estimated PM concentrations.

To conclude, our results show that whatever the application of OPCs is, and the adoption of either research, or in particular, of low-cost PM sensors, the intelligent use of the data is advised based on the following recommendations:

- Data from these devices are precious and extremely informative;
- They can be used reasonably confidently in fair weather conditions and with low time resolution;
- Careful data treatment and evaluation are required in two main cases: airsheds affected by mineral dust, and more generally, during relatively high humidity conditions, rain and fog are observed.

Our results may be extended using longer time series comprehensive of different seasons and analyzing more specifically the effect of PM size and chemical composition on the estimate of PM concentrations from OPCs, taking advantage of the use of ancillary data collected with the suite of co-located instruments. Future research studies focusing on how to automatically adjust data from low-cost sensors under conditions such as high relative humidity or transportation of mineral dust, affecting the observations from optical particle counters may greatly benefit from our results.

Funding

The iSCAPE Smart Citizen Kits were developed under the iSCAPE (“Improving the Smart Control of Air Pollution”) H2020 Project, grant number 689954.

Acknowledgements

The authors wish to acknowledge the Institut for Advanced Architecture of Catalonia (IAAC) and the Fab Lab Barcelona, particularly Guillem Camprodom, Victor Barberan and Oscar Gonzalez, for providing the Smart Citizen Kits and for support for their use during the field campaigns. Massimo Bacchetti and Simone Cangiamila from the Department of Physics and Astronomy of the University of Bologna are acknowledged for their support in the installation of the instrumentation and in data collection.

Conflicts of Interest

The authors declare no conflict of interest. The funders had no role in the design of the study; in the collection, analyses, or interpretation of data; in the writing of the manuscript, or in the decision to publish the results.

Appendices

Appendix A, B, C, D, and E are available online: <https://doi.org/10.3390/s20113073>

References

1. Ahangar, F.E.; Freedman, F.R.; Venkatram, A. Using Low-Cost Air Quality Sensor Networks to Improve the Spatial and Temporal Resolution of Concentration Maps. *Int. J. Environ. Res. Public Health* **2019**, *16*, 1252. [[Google Scholar](#)] [[CrossRef](#)]
2. Bagtasa, G.; Takeuchi, N.; Fukagawa, S.; Kuze, H.; Naito, S. Correction in aerosol mass concentration measurements with humidity difference between ambient and instrumental conditions. *Atmos. Environ.* **2007**, *41*, 1616–1626. [[Google Scholar](#)] [[CrossRef](#)]
3. Brattich, E.; Serrano Castillo, E.; Guilietti, F.; Renard, J.-B.; Tripathi, S.N.; Ghosh, K.; Berthet, G.; Vignelles, D.; Tositti, L. Measurements of aerosols and charged particles on the BEXUS18 stratospheric balloon. *Ann. Geophys.* **2019**, *37*, 389–403. [[Google Scholar](#)] [[CrossRef](#)]
4. Bulot, F.; Johnston, S.; Basford, P.; Easton, N.; Apetroaie-Cristea, M.; Foster, G.; Morris, A.; Cox, S.; Loxham, M. Long-term field comparison of multiple low-cost particulate matter sensors in an outdoor urban environment. *Sci. Rep.* **2019**, *9*, 1–13. [[Google Scholar](#)] [[CrossRef](#)] [[PubMed](#)]
5. Camprodon, G.; González, Ó.; Barberán, V.; Pérez, M.; Smári, V.; de Heras, M.Á.; Bizzotto, A. Smart Citizen Kit and Station: An open environmental monitoring system for citizen participation and scientific experimentation. *HardwareX* **2019**, *6*, e00070. [[Google Scholar](#)] [[CrossRef](#)]
6. Castell, N.; Dauge, F.R.; Schneider, P.; Vogt, M.; Lerner, U.; Fishbain, B.; Broday, D.; Bartonova, A. Can commercial low-cost sensor platforms contribute to air quality monitoring and exposure estimates? *Environ. Int.* **2017**, *99*, 293–302. [[Google Scholar](#)] [[CrossRef](#)] [[PubMed](#)]
7. Chatzidiakou, L.; Krause, A.; Popoola, O.; Di Antonio, A.; Kellaway, M.; Han, Y.; Squires, F.; Wang, T.; Zhang, H.; Wang, Q.; et al. Characterising low-cost sensors in highly portable platforms to quantify personal exposure in diverse environments. *Atmos. Meas. Tech.* **2019**, *12*, 4643–4657. [[Google Scholar](#)] [[CrossRef](#)] [[PubMed](#)]
8. Che, W.W.; Tso, C.Y.; Sun, L.; Danny, Y.K.; Lee, H.; Chao, C.Y.H.; Lau, A.K.H. Energy consumption, indoor thermal comfort and air quality in a commercial office with retrofitted heat, ventilation and air conditioning (HVAC) system. *Energy Build.* **2019**, *201*, 202–215. [[Google Scholar](#)] [[CrossRef](#)]
9. Crilley, L.R.; Shaw, M.; Pound, R.; Kramer, L.J.; Price, R.; Young, S.; Lewis, A.C.; Pope, F.D.; Alphasense Ltd.; Liu, D.; et al. Long-term field evaluation of the Plantower PMS low-cost particulate matter sensors. *Atmos. Meas. Tech. Discuss.* **2019**, *245*, 932–940. [[Google Scholar](#)]
10. Crilley, L.R.; Shaw, M.; Pound, R.; Kramer, L.J.; Price, R.; Young, S.; Lewis, A.C.; Pope, F.D. Evaluation of a low-cost optical particle counter (Alphasense OPC-N2) for ambient air monitoring. *Atmos. Meas. Tech.* **2018**, *11*, 709–720. [[Google Scholar](#)] [[CrossRef](#)]
11. Di Antonio, A.; Popoola, O.A.M.; Ouyang, B.; Saffell, J.; Jones, R.L. Developing a relative humidity correction for low-cost sensors measuring ambient particulate matter. *Sensors* **2018**, *18*, 2790. [[Google Scholar](#)] [[CrossRef](#)] [[PubMed](#)]
12. Diémoz, H.; Gobbi, G.P.; Magri, T.; Pession, G.; Pittavino, S.; Tombolato, I.K.F.; Campanelli, M.; Barnaba, F. Transport of Po Valley aerosol pollution to the northwestern

- Alps-Part 2: Long-term impact on air quality. *Atmos. Chem. Phys.* **2019**, *19*, 10129–10160. [[Google Scholar](#)]
13. Gaston, C.J.; Lopez-Hilfiker, F.D.; Whybrew, L.E.; Hadley, O.; McNair, F.; Gao, H.; Jaffe, D.A.; Thornton, J.A. Online molecular characterization of fine particulate matter in Port Angeles, WA: Evidence for a major impact from residential wood smoke. *Atmos. Environ.* **2016**, *138*, 99–107. [[Google Scholar](#)] [[CrossRef](#)]
 14. Hampel, F.R. The influence curve and its role in robust estimation. *J. Am. Stat. Assoc.* **1974**, *69*, 382–393. [[Google Scholar](#)] [[CrossRef](#)]
 15. Han, I.; Symanski, E.; Stock, T.H. Feasibility of using low-cost portable particle monitors for measurement of fine and coarse particulate matter in urban ambient air. *J. Air Waste Manag. Assoc.* **2017**, *67*, 330–340. [[Google Scholar](#)] [[CrossRef](#)] [[PubMed](#)]
 16. Hauck, H.; Berner, A.; Gomisack, B.; Stopper, S.; Puxbaum, H.; Kundi, M.; Preining, O. On the equivalence of gravimetric PM data with TEOM and beta-attenuation measurements. *J. Aerosol Sci.* **2004**, *35*, 1135–1149. [[Google Scholar](#)] [[CrossRef](#)]
 17. Hewitt, C.N.; Ashworth, K.; MacKenzie, A.R. Using green infrastructure to improve urban air quality (GI4AQ). *Ambio* **2020**, *49*, 62–73. [[Google Scholar](#)] [[CrossRef](#)] [[PubMed](#)]
 18. Hidy, G.M. Atmospheric Aerosols: Some Highlights and Highlighters, 1950 to 2018. *Aerosol Sci. Eng.* **2019**, *3*, 1–20. [[Google Scholar](#)] [[CrossRef](#)]
 19. Huang, Y.; Kok, J.F.; Martin, R.L.; Swet, N.; Katra, I.; Gill, T.E.; Reynolds, R.L.; Freire, L.S. Fine dust emissions from active sands at coastal Oceano Dunes, California. *Atmos. Chem. Phys.* **2019**, *19*, 2947–2964. [[Google Scholar](#)] [[CrossRef](#)]
 20. Invernizzi, G.; Sascio, A.; Ruprecht, A.A. A portable device capable to deliver to the airways filtered air with a submicrometric particle removal efficiency of about 90%. *Epidemiology* **2011**, *22*, S189–S190. [[Google Scholar](#)] [[CrossRef](#)]
 21. Jacob, D.J.; Winner, D.A. Effect of climate change on air quality. *Atmos. Environ.* **2009**, *43*, 51–63. [[Google Scholar](#)] [[CrossRef](#)]
 22. Jaenicke, R. The optical particle counter: Cross-sensitivity and coincidence. *J. Aerosol Sci.* **1972**, *3*, 95–111. [[Google Scholar](#)] [[CrossRef](#)]
 23. Jayaratne, R.; Liu, X.; Thai, P.; Dunbabin, M.; Morawska, L. The influence of humidity on the performance of a low-cost air particle mass sensor and the effect of atmospheric fog. *Atmos. Meas. Tech.* **2018**, *11*, 4883–4890. [[Google Scholar](#)] [[CrossRef](#)]
 24. Jiao, W.; Hagler, G.; Williams, R.; Sharpe, R.; Brown, R.; Garver, D.; Judge, R.; Caudill, M.; Rickard, J.; Davis, M.; et al. Community Air Sensor Network (CAIRSENSE) project: Evaluation of low-cost sensor performance in a suburban environment in the southeastern United States. *Atmos. Meas. Tech.* **2016**, *9*, 5281–5292. [[Google Scholar](#)] [[CrossRef](#)]
 25. Johnson, K.K.; Bergin, M.H.; Russell, A.G.; Hagler, G.S.W. Field test of several low-cost particulate matter sensors in high and low concentration urban environments. *Aerosol Air Qual. Res.* **2018**, *18*, 565–578. [[Google Scholar](#)] [[CrossRef](#)]
 26. Karagulian, F.; Barbieri, M.; Kotsev, A.; Spinelle, L.; Gerboles, M.; Lagler, F.; Redon, N.; Crunaire, S.; Borowiak, A. Review of the performance of low-cost sensors for air quality monitoring. *Atmosphere* **2019**, *10*, 506. [[Google Scholar](#)] [[CrossRef](#)]
 27. Kelly, K.E.; Whitaker, J.; Petty, A.; Widmer, C.; Dybwad, A.; Sleeth, D.; Martin, R.; Butterfield, A. Ambient and laboratory evaluation of a low-cost particulate matter sensor. *Environ. Pollut.* **2017**, *221*, 491–500. [[Google Scholar](#)] [[CrossRef](#)]
 28. Kuula, J.; Mäkelä, T.; Aurela, M.; Teinilä, K.; Varjonen, S.; Gonzales, O.; Timonen, H. Laboratory evaluation of particle size-selectivity of optical low-cost particulate matter sensors. *Atmos. Meas. Tech. Discuss.* **2019**, *13*, 1–21. [[Google Scholar](#)] [[CrossRef](#)]
 29. Leung, D.M.; Tai, A.P.K.; Mickley, L.J.; Moch, J.M.; Van Donkelaar, A.; Shen, L.; Martin, R.V. Synoptic meteorological modes of variability for fine particulate matter

- (PM_{2.5}) air quality in major metropolitan regions of China. *Atmos. Chem. Phys.* **2018**, *18*, 6733–6748. [[Google Scholar](#)] [[CrossRef](#)]
30. Liu, B.Y.H.; Berglund, R.N.; Agarwal, J.K. Experimental studies of optical particle counters. *Atmos. Environ.* **1974**, *8*, 717–732. [[Google Scholar](#)] [[CrossRef](#)]
 31. Liu, H.; Sirish, S.; Wei, J. On-line outlier detection and data cleaning. *Comput. Chem. Eng.* **2004**, *28*, 1635–1647. [[Google Scholar](#)] [[CrossRef](#)]
 32. Malings, C.; Tanzer, R.; Hauryliuk, A.; Saha, P.K.; Robinson, A.L.; Presto, A.A.; Subramanian, R. Fine particle mass monitoring with low-cost sensors: Corrections and long-term performance evaluation. *Aerosol Sci. Technol.* **2020**, *54*, 160–174. [[Google Scholar](#)] [[CrossRef](#)]
 33. Mamali, D.; Marinou, E.; Sciare, J.; Pikridas, M.; Kokkalis, P.; Kottas, M.; Biniotoglu, I.; Tsekeri, A.; Keleshis, C.; Engelmann, R.; et al. Vertical profiles of aerosol mass concentration derived by unmanned airborne in situ and remote sensing instruments during dust events. *Atmos. Meas. Tech.* **2018**, *11*, 2897–2910. [[Google Scholar](#)] [[CrossRef](#)]
 34. Mao, F.; Khamis, K.; Krause, S.; Clark, J.; Hannah, D.M. Low-Cost Environmental Sensor Networks: Recent Advances and Future Directions. *Front. Earth Sci.* **2019**, *7*, 221. [[Google Scholar](#)] [[CrossRef](#)]
 35. Mukherjee, A.; Stanton, L.G.; Graham, A.R.; Roberts, P.T. Assessing the utility of low-cost particulate matter sensors over a 12-week period in the Cuyama valley of California. *Sensors* **2017**, *17*, 1805. [[Google Scholar](#)] [[CrossRef](#)]
 36. Pal, R. Chapter 4-Validation methodologies. In *Predictive Modeling of Drug Sensitivity*; Academic Press: Cambridge, MA, USA, 2017; pp. 83–107. ISBN 978-0-12-805274-7. [[Google Scholar](#)]
 37. Pal, S.; Lee, T.R.; Phelps, S.; De Wekker, S.F.J. Impact of atmospheric boundary layer depth variability and wind reversal on the diurnal variability of aerosol concentration at a valley site. *Sci. Total Environ.* **2014**, *496*, 424–434. [[Google Scholar](#)] [[CrossRef](#)] [[PubMed](#)]
 38. Patashnick, H.; Rupprecht, E.G. Continuous PM-10 measurements using the tapered element oscillating microbalance. *J. Air Waste Manage. Assoc.* **1991**, *41*, 1079–1083. [[Google Scholar](#)] [[CrossRef](#)]
 39. Perpignan Lamigueiro, O. Tdr: Target Diagram. R Package Version 0.13. Available online: <https://cran.r-project.org/package=tdr> (accessed on 1 May 2020).
 40. Popoola, O.A.M.; Carruthers, D.; Lad, C.; Bright, V.B.; Mead, M.I.; Stettler, M.E.J.; Saffell, J.R.; Jones, R.L. Use of networks of low cost air quality sensors to quantify air quality in urban settings. *Atmos. Environ.* **2018**, *194*, 58–70. [[Google Scholar](#)] [[CrossRef](#)]
 41. R Development Core Team 3.0.1. A Language and Environment for Statistical Computing. Available online: <http://www.r-project.org> (accessed on 1 May 2020).
 42. Raes, F.; Van Dingenen, R.; Vignati, E.; Wilson, J.; Putaud, J.-P.; Seinfeld, J.H.; Adams, P. Formation and cycling of aerosols in the global troposphere. *Atmos. Environ.* **2000**, *34*, 4215–4240. [[Google Scholar](#)] [[CrossRef](#)]
 43. Ratti, C.; Di Sabatino, S.; Bitter, R. Urban texture analysis with image processing techniques: Wind and dispersion. *Theor. Appl. Climatol.* **2006**, *84*, 77–99. [[Google Scholar](#)] [[CrossRef](#)]
 44. Renard, J.-B.; Dulac, F.; Berthet, G.; Lurton, T.; Vignelles, D.; Jégou, F.; Tonnelier, T.; Jeannot, M.; Couté, B.; Akiki, R.; et al. LOAC: A small aerosol optical particle counter/sizer for ground-based and balloon measurements of the size distribution and nature of atmospheric particles-Part 1: Principle of measurements and instrument evaluation. *Atmos. Meas. Tech.* **2016**, *9*, 1721–1742. [[Google Scholar](#)] [[CrossRef](#)]

45. Renard, J.-B.; Thauray, C.; Mineau, J.-L.; Gaubicher, B. Small-angle light scattering by airborne particulates: Environment S.A. continuous particulate monitor. *Meas. Sci. Technol.* **2010**, *21*, 085901. [[Google Scholar](#)] [[CrossRef](#)]
46. Revelle, W. Psych: Procedures for Psychological, Psychometric, and Personality Research. Available online: <https://cran.r-project.org/web/packages/psych/index.html> (accessed on 1 May 2020).
47. Sayahi, T.; Butterfield, A.; Kelly, K.E. Long-term field evaluation of the Plantower PMS low-cost particulate matter sensors. *Environ. Pollut.* **2019**, *245*, 932–940. [[Google Scholar](#)] [[CrossRef](#)]
48. Schneider, P.; Castell, N.; Vogt, M.; Dauge, F.R.; Lahoz, W.A.; Bartonova, A. Mapping urban air quality in near real-time using observations from low-cost sensors and model information. *Environ. Int.* **2017**, *106*, 234–247. [[Google Scholar](#)] [[CrossRef](#)]
49. Seinfeld, J.H.; Pandis, S.N. *Atmospheric Chemistry and Physics: From Air Pollution to Climate Change*, 3rd ed.; John Wiley & Sons: Hoboken, NJ, USA, 2016; ISBN 978-1-118-94740-1. [[Google Scholar](#)]
50. Sousan, S.; Koehler, K.; Hallett, L.; Peters, T.M. Evaluation of the Alphasense optical particle counter (OPC-N2) and the Grimm portable aerosol spectrometer (PAS-1.108). *Aerosol Sci. Technol.* **2016**, *50*, 1352–1365. [[Google Scholar](#)] [[CrossRef](#)]
51. Strak, M.; Janssen, N.A.; Godri, K.J.; Gosens, I.; Mudway, I.S.; Cassee, F.R.; Lebret, E.; Kelly, F.J.; Harrison, R.M.; Brunekreef, B.; et al. Respiratory Health Effects of Airborne Particulate Matter: The Role of Particle Size, Composition, and Oxidative Potential—The RAPTES Project. *Environ. Health Perspect.* **2012**, *120*, 1183–1189. [[Google Scholar](#)] [[CrossRef](#)] [[PubMed](#)]
52. Sun, Y.L.; Jiang, Q.; Wang, Z.F.; Fu, P.Q.; Li, J.; Yang, T.; Yin, Y. Investigation of the sources and evolution processes of severe haze pollution in Beijing in January 2013. *J. Geophys. Res.* **2014**, *119*, 4380–4398. [[Google Scholar](#)] [[CrossRef](#)]
53. Tagle, M.; Rojas, F.; Reyes, F.; Vásquez, Y.; Hallgren, F.; Lindén, J.; Kolev, D.; Watne, Å.; Oyola, P. Field performance of a low-cost sensor in the monitoring of particulate matter in Santiago, Chile. *Environ. Monit. Assess.* **2020**, *192*, 171. [[Google Scholar](#)] [[CrossRef](#)]
54. Tan, D.G.H.; Haynes, P.H.; MacKenzie, A.R.; Pyle, J.A. Effects of fluid dynamical stirring and mixing on the deactivation of stratospheric chlorine. *J. Geophys. Res.* **1998**, *103*, 1585–1605. [[Google Scholar](#)] [[CrossRef](#)]
55. *The British Standard Institution ISO 21501-4:2018 Determination of Particle Size Distribution—Single Particle Light Interaction Methods—Part 4: Light Scattering Airborne Particle Counter for Clean Spaces*; ISO/TC 24/SC 4 Particle characterization: Geneva, Switzerland, 2018; Volume 2018, ISBN 978 0 580 86373 8.
56. Tittarelli, A.; Borgini, A.; Bertoldi, M.; De Saeger, E.; Ruprecht, A.; Stefanoni, R.; Tagliabue, G.; Contiero, P.; Crosignani, P. Estimation of particle mass concentration in ambient air using a particle counter. *Atmos. Environ.* **2008**, *42*, 8543–8548. [[Google Scholar](#)] [[CrossRef](#)]
57. Tositti, L. Physical and chemical properties of airborne particulate matter. In *Clinical Handbook of Air Pollution-Related Diseases*; Capello, F., Gaddi, A., Eds.; Springer: Cham, Switzerland; Berlin, Germany, 2018; pp. 7–32. [[Google Scholar](#)]
58. Tositti, L.; Brattich, E.; Masiol, M.; Baldacci, D.; Ceccato, D.; Parmeggiani, S.; Stracquandano, M. Source apportionment of particulate matter in a large city of southeastern Po Valley (Bologna, Italy). *Environ. Sci. Pollut. Res. Int.* **2014**, *21*, 872–890. [[Google Scholar](#)] [[CrossRef](#)]
59. Wang, X.; Shen, X.J.; Sun, J.Y.; Zhang, X.Y.; Wang, Y.Q.; Zhang, Y.M.; Wang, P.; Xia, C.; Qi, X.; Zhong, J. Size-resolved hygroscopic behavior of atmospheric aerosols during

- heavy aerosol pollution episodes in Beijing in December 2016. *Atmos. Environ.* **2018**, *194*, 188–197. [[Google Scholar](#)] [[CrossRef](#)]
60. Welker, R.W. Size Analysis and Identification of Particles. In *Developments in Surface Contamination and Cleaning: Detection, Characterization, and Analysis of Contaminants*; Kohli, R., Mittal, K.L., Eds.; William Andrew Inc.: Waltman, WA, USA; Elsevier: London, UK, 2012; pp. 179–213. [[Google Scholar](#)]
61. Wu, Z.J.; Zheng, J.; Shang, D.J.; Du, Z.F.; Wu, Y.S.; Zeng, L.M.; Wiedensohler, A.; Hu, M. Particle hygroscopicity and its link to chemical composition in the urban atmosphere of Beijing, China, during summertime. *Atmos. Chem. Phys.* **2016**, *16*, 1123–1138. [[Google Scholar](#)] [[CrossRef](#)]
62. Zheng, T.; Bergin, M.H.; Johnson, K.K.; Tripathi, S.N.; Shirodkar, S.; Landis, M.S.; Sutaria, R.; Carlson, D.E. Field evaluation of low-cost particulate matter sensors in high- and low-concentration environments. *Atmos. Meas. Tech.* **2019**, *11*, 4823–4846. [[Google Scholar](#)] [[CrossRef](#)]
63. Zhu, D.; Kuhns, H.D.; Gillies, J.A.; Etyemezian, V.; Gertler, A.W.; Brown, S. Inferring deposition velocities from changes in aerosol size distributions downwind of a roadway. *Atmos. Environ.* **2011**, *43*, 957–966. [[Google Scholar](#)] [[CrossRef](#)]

CHAPTER 6 - Development and evolution of an anomalous Asian dust event across Europe in March 2020

By Laura Tositti¹, Erika Brattich², Claudio Cassardo³, **Pietro Morozzi**¹, Alessandro Bracci², Angela Marinoni⁴, Silvana Di Sabatino², Federico Porcù², and Alessandro Zappi¹

¹ Department of Chemistry “G. Ciamician”, Alma Mater Studiorum University of Bologna, Via F. Selmi, 2, 40126 Bologna (Italy)

² Department of Physics and Astronomy “Augusto Righi”, Alma Mater Studiorum University of Bologna Viale Berti Pichat 6/2, 40127 Bologna (Italy)

³ Department of Physics, via P. Giuria 1, 10125 Torino (Italy)

⁴ National Research Council of Italy, Institute of Atmospheric Sciences and Climate (CNR-ISAC), Via P. Gobetti, 101, 40129 Bologna (Italy)

Atmos. Chem. Phys. Discuss. [preprint], <https://doi.org/10.5194/acp-2021-429>, in review, 2021.



© 2021 by the authors. This article is an open access article distributed under the terms and conditions of the Creative Commons Attribution 4.0 (CC BY) license ().

Abstract

This paper concerns an in-depth analysis of an exceptional incursion of mineral dust over Southern Europe in late March 2020. This event was associated with an anomalous circulation pattern leading to several days of PM₁₀ exceedances in connection with a dust source located in Central Asia a rare source of dust for Europe, more frequently affected by dust outbreaks from the Sahara desert. The synoptic meteorological configuration was analyzed in detail, while aerosol evolution during the transit of the dust cloud over Northern Italy was assessed at high time resolution by means of optical particle counting at three stations in northern Italy, namely Bologna, Trieste, and Mt. Cimone allowing to reveal transport timing among the three locations. Back-trajectory analyses supported by AOD (Aerosol Optical Depth) maps allowed to locate the mineral dust source area in the Aralkum region. The event was therefore analyzed through the observation of particle number size distribution with the support of chemical composition analysis. It is shown that PM₁₀ exceedance recorded is associated with a large fraction of coarse particles in agreement with mineral dust properties. Both in-situ number size distribution and vertical distribution of the dust plume were cross-checked by Lidar Ceilometer and AOD data from two nearby stations, showing that the dust plume, differently from those originated in the Sahara desert, traveled close to the ground up to a height of about 2 km. The limited mixing layer height caused by high concentrations of absorbing and scattering aerosols caused the mixing of mineral dust with other locally-produced ambient aerosols, thereby potentially increasing its morbidity effects.

1 – Introduction

Mineral dust originating in desert regions is one of the main components of the ambient aerosol affecting air quality and human health, cloud formation, ocean ecosystems, and climate (Knippertz and Stuut, 2014; Schepanski, 2018). Despite its significance, mineral dust still represents one of the largest uncertainties in climate modeling (Adebiyi and Kok, 2020; IPCC Working Group I, 2013). Mineral dust is often transported at large a scale influencing vast continental and ocean areas (Barkan and Alpert, 2010). The most immediate effect of mineral dust in a specific area is the increase, sometimes dramatic, of particulate matter (PM) mass loading (Brattich et al., 2015a), mainly in the coarse fraction. Several studies also demonstrated that mineral dust can affect cloud processing (Bangert et al., 2012) and biogeochemical cycles of ecosystems (Okin et al., 2004). Numerous studies documented the health effects of mineral dust transport in various parts of the world (Domínguez-Rodríguez et al., 2021; Fubini and Fenoglio, 2007; Keil et al., 2016; Sajani et al., 2011; Stafoggia et al., 2016), owing to the conjunct impact of mineralogy, allergens, and pathogens (García-Pando et al., 2014). For these reasons, it is essential to study mineral dust composition in connection with its atmospheric path, source region, physicochemical properties, and modifications associated with environmental, climatic, and health issues.

The most important dust sources regions at the global scale are the North African Sahara region, the Arabian desert, the central Asia desert, the Dasht-e Margo (the desert region between Pakistan, Iran, and Afghanistan), the Great Basin (USA), the Kalahari desert (Southern Africa), and the central Australia deserts (Calidonna et al., 2020; Prospero et al., 2002; Washington et al., 2003). Recently another prominent source of mineral dust is drawing research interest, i.e., the semi-arid region between the Persian Gulf and the Caspian Sea. Several studies (Gholamzade Ledari et al., 2020; Kaskaoutis et al., 2018; Rashki et al., 2018) reported the transport of mineral dust originating in this region usually towards central and eastern Asia. With the purpose to evaluate the wind regime and dust activity in this region, a particular index, the Caspian Sea - Hindu Kush Index (CasHKI), has been introduced and studied in a long-term time series in previous studies (Kaskaoutis et al., 2018).

The primary source of desert dust reaching Southern Europe, including Italy, is the Saharan desert (Brattich et al., 2015a; Calidonna et al., 2020). In general, dust storms are more frequent in the spring-summer periods, while these are rare in the cold seasons (Brattich et al., 2015a; Duchi et al., 2016) to late winter (Fubini and Fenoglio, 2007; IPCC Working Group I, 2013). Saharan dust outbreaks are connected with several factors, among which the high temperatures, relatively intense winds, associated with cloud-free conditions, strong and perhaps increasing meridian gradients of pressure (African highs), while thermal convection, promotes dust lifting and subsequent transport (Varga et al., 2013). Saharan dust outbreaks in Italy are mainly driven by pressure lows south of the peninsula, causing counterclockwise northward pulling of African desert air masses. While typically keeping its meridional character, this synoptic condition has been found to shift seasonally from the eastern in the spring to the western northern African coastal boundaries in the summer (Brattich et al., 2015a).

Different from the vast literature on Saharan dust, the present work examines an outstanding mineral dust event whose characteristics are unprecedented to the best of our knowledge. The event described, indeed, concerns a singular and massive incursion of mineral dust reaching Europe from central Asia in late March 2020, a period marked by a series of peculiarities, not necessarily connected, such as an extensive, persistent, and intense eastern circulation, fairly infrequent at these latitudes, owing to basic dynamic constraints, the SARS

COV-2 lockdown, and the concurrent, though seemingly out of context, large ozone hole in the Arctic (Manney et al., 2020).

The mineral dust incursion originating from the Caspian region widely bounced across the Italian media, as it led to PM₁₀ concentration levels well above the EU air quality threshold, wedging over an area historically characterized by frequent and significant exceedances of this pollutant such as the Po valley (Tositti et al., 2014), mainly due to the accumulation of anthropogenic emissions. As a result, this contingency brought to harsh, though controversial connections between air quality across the regional airshed and the virus spread (Belosi et al., 2021; Prather et al., 2020).

Differently from the extensive literature on Saharan dust, as previously reminded, mineral dust from the Caspian region is far less investigated, though it is recently drawing ever-increasing attention by researchers owing to a multitude of climatic and environmental implications. This arid region is indeed an area of increasing desertification owing to climate change as well as to decades of disastrous environmental management, including the desiccation of the Aral Sea, with a loss of 90% of its original water volume in the last decades (Behzod et al., 2012; Breckle and Wucherer, 2012; Loodin, 2020; Sharma et al., 2018; Shen et al., 2016; Shi et al., 2014; Zhang et al., 2020).

The event of mineral dust incursion from Central Asia herein described occurred at the end of March 2020 and, to the best of our knowledge, has not been so far the object of an in-depth analysis though it was mentioned in a few papers devoted to other topics (Masic et al., 2020; Šikoparija, 2020) or described qualitatively in remote sensing or meteorological web pages (Mahovic et al., 2020; SNPA, 2020).

In this work, we present an in-depth analysis of this outstanding event based on the collection of high-resolution Optical Particle Counter number size distribution observed at three sites of NE Italy, i.e., at the two urban observatories in Bologna and Trieste, and the high altitude WMO-GAW Global observatory of Mt. Cimone (<https://cimone.isac.cnr.it/>). Data analysis includes an accurate meteorological assessment in order to identify the peculiar synoptic conditions leading to the event. Back-trajectories analysis was used to identify the source region. Aerosol behavior during transport over Italy was analyzed by Optical particle spectrometry, while multiple data based on remote sensing (satellites, LIDAR, and AERONET sun photometers) were employed to gain a dynamical 3D characterization of the mineral dust transport.

After the Introduction section and a description of the measurement techniques, the discussion of the results is organized as follows: 1) In-depth synoptic analysis and directional analysis of the event; 2) Analysis of aerosol size distribution in Bologna, Trieste, and Mt. Cimone before, during and after the event; 3) Influence on aerosol mass load 4) Trend of AOD, aerosol vertical behavior and chemical composition of the dust event from satellite platforms. Finally, the main conclusions are summarized.

2 – Materials and methods

2.1 – Sampling sites

The Caspian dust event was highlighted during a long-term air-quality campaign by three Optical Particle Counters (see paragraph 2.3 for details) located in three different sampling sites.

Sampling in Bologna (BO) was carried out with one LOAC (Light Optical Aerosol Counter; MeteoModem, 77760 Ury, France) (Brattich et al., 2020b; Renard et al., 2016b, 2016c). The instrument was installed on the rooftop of the Department of Physics and Astronomy of the University of Bologna (44°29'58"N, 11°21'14"E, 62 m a.s.l.). Meteorological conditions (temperature, pressure, relative humidity, rain rate, wind speed and direction) in Bologna were also collected by a Davis Vantage Pro2 (Davis Instruments, Hayward, CA 94545, USA) on a 10-min time basis, close to LOAC.

In Trieste (TS), an OPC Multichannel Monitor (FAI Instruments S.r.l., Roma, Italy) (Dinoi et al., 2017) was placed in the air quality station of via Pitacco (45°37'29"N, 13°46'46"E, 30m a.s.l.), managed by the Regional Environmental Protection Agency (ARPA FVG - Agenzia Regionale per la Protezione dell'Ambiente del Friuli Venezia Giulia). Meteorological data for Trieste are available as open data on the ARPA FVG website (<https://www.osmer.fvg.it/>) on a 1-h time basis.

At the summit of Mt. Cimone (CMN, 44°11'37"N, 10°42'02"E, 2165 m a.s.l.), is located the only WMO-GAW global station in Italy and within the Mediterranean basin. The atmospheric measurements carried out at CMN can be considered representative for the baseline conditions of the Mediterranean basin free troposphere. An OPC (GRIMM 1.108) is continuously running since August 2002 to observe accumulation and coarse aerosol number size distribution. The OPC is placed on a TSP heated air inlet designed in the framework of EUSAAR project and following the ACTRIS recommendation for aerosol inlets.

For all sites, data analysis for the present work covers the period between 20 March and 5 April 2020, i.e. from a week before the beginning of the dust event (27 March) and until one week after the end of the event (31 March).

2.2 - Synoptic-scale conditions

The synoptic-scale main patterns related to the dust transport have been reconstructed and investigated based on the meteorological fields provided by the Global Forecast System (GFS) coupled model, produced by the National Centers for the Environmental Prediction (NCEP). In particular, we have analyzed the pressure field at the sea level (SLP) and the geopotential height at 500 (Z500) and 850 (Z850) hPa at 00:00 UTC for each day during the period of the event.

Besides, to locate and follow such long-range transport, we have coupled to the GFS weather model the regional air quality products of the Copernicus Atmosphere Monitoring Service (CAMS) (Marécal et al., 2015) in terms of particulate matter concentration (specifically PM₁₀ fraction) at the height of 50 m above the surface. In detail, we have used the analysis output provided by the CAMS that merges model and observation data and ensures a high spatial resolution (~0.1 degrees) (CAMS, 2015).

Back-trajectories were also evaluated to confirm the origin of the studied mineral dust event from Central Asia. Back-trajectories are computed simulating the transport of air masses for

a determined time frame until these reach a given “receptor” point at a specific time instant (Fleming et al., 2012; Rolph et al., 2017). In the specific case, 96-h back-trajectories were computed by Hybrid Single Particle Lagrangian Integrated Trajectory (HYSPLIT_4) model (Rolph et al., 2017; Stein et al., 2015) considering as receptor sites the three locations of the OPCs (see paragraph 2.3) over the whole period of the event. The computation was performed every six hours starting from 27 March 00:00 UTC until 31 March 18:00 UTC using GFS meteorological data at a 0.25-degree (27.8 km) resolution (National Centers for Environmental Prediction/National Weather Service/NOAA/US Department of Commerce, 2015). For each receptor site, trajectories were computed at three different heights to determine the impact of the arrival height on the trajectory analysis: 100, 1000, and 2000 m a.g.l. for Bologna (BO) and Trieste (TS), and 1700, 2200, 2700, and 3200 m a.g.l. for Mt. Cimone (CMN).

2.3 - Optical Aerosol Counters (OPCs)

Optical particle counters (OPCs) are widely used for aerosol characterization (Brattich et al., 2015a, 2019, 2020b; Bulot et al., 2019; Kim et al., 2019). The advantages of this class of aerosol instrumentation over the traditional filter-based instruments are their portability, the relatively low cost, the availability of aerosol size distribution, and the possibility of acquiring PM data continuously and at high time resolution (down to 1 measurement s⁻¹) (Brattich et al., 2020b).

The three instruments employed in the sample sites (LOAC in BO, FAI in TS, and GRIMM at CMN, see paragraph 2.1), usually operated simultaneously for long-term data collection, are typically based on the principle of light scattering from aerosol particles, generally using a monochromatic high energy source such as a laser beam to detect and count particles. According to Mie scattering theory (Mie, 1908; Renard et al., 2016a), the intensity of scattered light is related to the particles’ size, while the number of pulses of scattered light reaching the detector is related to the number of particles. This kind of instrument can retrieve a semi-continuous real-time analysis of the suspended particulate matter as a function of its diameter. In particular, the LOAC evaluates the scattering at two angles, 12° and 60°, the first being almost insensitive to the particles’ refractive index, whereas the second is strongly sensitive to the refractive index (Renard et al., 2016b). GRIMM spectrometer detects aerosol particles from the scattered signal at 90°. All the OPC sensors operate at a 1 L min⁻¹ air volume flow rate and with a scan frequency of 1 min. For the sake of homogeneity, all the data were averaged at 1-hour time resolution. All OPC data are reported as number concentration, in counts dm⁻³ (# L⁻¹).

Particle size distribution is obtained over 19 size bins for LOAC, 8 size bins for the FAI instrument, and 15 size bins for the GRIMM instrument, as reported in Table 1. A mean bin diameter was calculated for each size interval as previously indicated by Eq. 1 (Crilley et al., 2018):

$$D = LB \left[\frac{1}{4} \left(1 + \left(\frac{UB}{LB} \right)^2 \right) \left(1 + \frac{UB}{LB} \right) \right]^{1/3}$$

where LB and UB are respectively the lower and the upper bin boundaries. While LOAC and GRIMM have well-defined minimum and maximum particle diameters for each bin, FAI OPC works in an integral mode: the count value of each bin was obtained by subtracting the value of the following one and for the computation of D, LB of the latter bin was set as UB.

Table 1. Size bins of the three OPCs. All reported values are in μm

Bin n ^o	LOAC OPC		FAI OPC		GRIMM OPC	
	Boundaries	Mean diameter	Boundaries	Mean diameter	Boundaries	Mean diameter
1	0.2 ÷ 0.3	0.253	> 0.28	0.343	0.3 ÷ 0.4	0.352
2	0.3 ÷ 0.4	0.352	> 0.4	0.452	0.4 ÷ 0.5	0.452
3	0.4 ÷ 0.5	0.452	> 0.5	0.606	0.5 ÷ 0.65	0.578
4	0.5 ÷ 0.6	0.551	> 0.7	0.915	0.65 ÷ 0.8	0.728
5	0.6 ÷ 0.7	0.651	> 1.1	1.59	0.8 ÷ 1.0	0.904
6	0.7 ÷ 0.9	0.804	> 2.0	2.53	1.0 ÷ 1.6	1.32
7	0.9 ÷ 1.1	1.00	> 3.0	4.08	1.6 ÷ 2.0	1.81
8	1.1 ÷ 3.0	2.19	> 5.0 ÷ 10.0	7.77	2.0 ÷ 3.0	2.53
9	3.0 ÷ 5.0	4.08			3.0 ÷ 4.0	3.52
10	5.0 ÷ 7.5	6.33			4.0 ÷ 5.0	4.52
11	7.5 ÷ 10.0	8.81			5.0 ÷ 7.5	6.33
12	10.0 ÷ 12.5	11.3			7.5 ÷ 10.0	8.81
13	12.5 ÷ 15.0	13.8			10.0 ÷ 15.0	12.7
14	15.0 ÷ 17.5	16.3			15.0 ÷ 20.0	17.6
15	17.5 ÷ 20.0	18.8			> 20.0	
16	20.0 ÷ 22.0	21.0				
17	22.0 ÷ 30.0	26.2				
18	30.0 ÷ 40.0	35.2				
19	40.0 ÷ 50.0	45.2				

The LOAC aerosol range is between 0.20 and 50 μm , while the FAI working range is between 0.30 and 10 μm and the GRIMM working range lies between 0.3 and 20 μm .

Owing to the different ranges and number of bins of the used OPCs (Table 1), experimental data were homogenized as follows. Seven aerosol fractions were considered for comparison of the three OPC outputs, while two additional fractions were evaluated for LOAC only: “fr0.3”, “fr0.4”, “fr0.5”, “fr0.7”, “fr1.1”, “fr3”, and “fr5” for all OPCs; “fr0.2” and “fr10” for LOAC only. Table 2 describes the processed fractions and the bin combination used for the comparison. Table 1 shows that also the GRIMM instrument could be used to evaluate “fr10”. However, previous studies (Duchi et al., 2016; Marinoni et al., 2008; Sajani et al., 2012) highlighted that the presence of coarse particles is unusual on the top of CMN, except in cases of Saharan dust (Marinoni et al., 2008). Moreover, as described further on, the event herein analyzed, had limited vertical development and did not affect significantly the top of Mt. Cimone as shown by the low counts of the coarser bins at this station. Therefore, we decided to not consider “fr10” for CMN.

Table 2. Fractions analyzed with LOAC, FAI OPC, and GRIMM, with the corresponding bin combinations (sums or differences)

Fraction	Size interval (μm)	LOAC	FAI	GRIMM
fr0.2	0.2 ÷ 0.3	bin1	--	--
fr0.3	0.3 ÷ 0.4	bin2	bin1 – bin2	bin1
fr0.4	0.4 ÷ 0.5	bin3	bin2 – bin3	bin2
fr0.5	0.5 ÷ 0.7	bin4 + bin5	bin3 – bin4	bin3
fr0.7	0.7 ÷ 1.1	bin6 + bin7	bin4 – bin5	bin4 + bin5
fr1.1	1.1 ÷ 3.0	bin8	bin5 – bin7	bin6 + bin7 + bin8
fr3	3.0 ÷ 5.0	bin9	bin7 – bin8	bin9 + bin10
fr5	5.0 ÷ 10.0	bin10 + bin11	bin8	bin11 + bin 12
fr10	> 10.0	Sum from bin11 to bin 19	--	--

Computations and graphs of time-series, particle size distributions, and number concentration to mass conversions were performed with R software (R Core Team, Vienna, Austria). Polar plots of the OPC fractions were calculated considering all data from 20 March to 6 April with the R package “openair” (Carslaw and Beevers, 2013; Carslaw and Ropkins, 2012).

2.4 - Particulate matter concentrations and chemical speciation data

In addition to measurements from the OPCs, daily mean PM₁₀ concentrations at two air quality stations of the ARPAE (Agenzia Prevenzione Ambiente Energia Emilia Romagna) Regional Environmental Protection Agency in Bologna (Porta San Felice and Giardini Margherita, respectively urban traffic and urban background station) were used. Data were obtained through the “saqgetr” R package (Grange, 2019).

Furthermore, chemical speciation data (ions, carbonaceous fraction, and elements) sampled in Bologna and available as open data from ARPAE (<https://www.arpae.it/it>) were also analyzed to complement the other analyses.

2.5 - AERONET (AERosol RObotic NETwork)

Aerosol optical depth (AOD) data retrieved from Aerosol Robotic Network (AERONET) ground-based remote sensing aerosol network at the site of Venice (Acqua Alta Oceanographic Tower - AAOT; 45°19'N, 12°30'E) were used as an independent method to confirm the dust aerosol transport event at the end of March 2020.

AERONET collaboration provides globally distributed observations of spectral aerosol optical depth (AOD), inversion products, and precipitable water in diverse aerosol regimes. For this work, version 3 AOD data and inversions computed for Level 2.0, i.e., quality assured (with pre- and post-field calibration applied, automatically cloud cleared, and manually inspected), were utilized. Total mode, fine mode, and coarse mode AOD at 500 nm were computed using a best-fit second-order polynomial. Finally, the AERONET inversion code provides aerosol optical properties in the total atmospheric column derived

from the direct and diffuse radiation measured by AERONET Cimel sun/sky-radiometers (NASA, 2006). The output includes both retrieved aerosol parameters, which comprehends the volume size distribution, and parameters calculated based on the retrieved aerosol properties. The inversion algorithms are based on the following assumptions, i.e.: the atmosphere is considered as plane-parallel; the vertical distribution of aerosol is assumed homogeneous in the almucantar inversion and bi-layered for the principal plane inversion; aerosol particles are assumed to be partitioned in spherical and non-spherical components.

2.6 - LIDAR Ceilometer

Aerosol vertical profiles collected in Milan (Diémoz et al., 2019; Ferrero et al., 2020) (45°31'N 9°12'E, 130 m asl, ~200 km northwest of Bologna) have been used to identify the signature of dust transport as well as to investigate its vertical extension and altitude. Such profiles were gathered by a Nimbus CHM15K system (Lufft, Germany) running within the Italian Automated Lidar Ceilometer network – Alice-net (www.alice-net.eu), coordinated by ISAC-CNR in partnership with other Italian research institutions and environmental agencies. It is a high-performance system providing vertical profiles of aerosols and clouds in the first 15 km of the atmosphere with a temporal resolution of 30 s and a vertical resolution of 15 m (Dionisi et al., 2018). Alice-net measurements have been and are usefully employed to detect altitude and temporal evolution of cloud layers (Ferrero et al., 2020) and to track transport of polluted (Diémoz et al., 2019) or mineral dust aerosol plumes (Gobbi et al., 2019) at different sites along the Italian peninsula.

3 – Results and discussions

3.1 – Synoptic analysis

As documented later on, the likely source of the investigated episode of severe dust transport is the Central Asian southern desert region, arid but ecologically active, located between the eastern coast of the Caspian Sea and the steppes near the central Asia mountain ranges. Most of Turkmenistan and eastern Uzbekistan, as well as the Central Asian desert ecoregion to the North, can be considered a cold desert, in agreement with the inherent climatic class (BWk, according to the Köppen classification), with hot summers and cold winters, and annual precipitation of 125–170 mm year⁻¹, with winter and spring as the driest seasons. For these reasons, we have decided to analyze the pressure field at the sea level (SLP) and the geopotential height at 500 (Z500) and 850 (Z850) hPa in the period from 20 March to 30 March 2020. Figure 1 shows the geopotential maps (Z500) and the corresponding PM₁₀ (50 m height) concentration maps derived from satellite observations for the most relevant days of the event, 25 - 28 March 2020.

On 20 March, at 500 hPa the geopotential height was high on the western Mediterranean basin and western Europe, due to a ridge expanded from Libya to Italy and Poland, while the pressure field at the sea level and the geopotential height at 850 hPa were uniform. On the Caspian deserts, the circulation was weak, even if, in the northern area, southern winds were flowing towards Uzbekistan and Kazakhstan. In the following three days, regarding Z500 the European anticyclone elongates versus northeast reaching Scandinavia on 23 March, and at the same time a trough developed from Russia extending to Bosnia and Albania; regarding SLP and Z850, an anticyclone developed on southern Sweden, activating a weak eastern flow directed from the southern Urals to Croatia. A southern flow established over the Caspian deserts, so designating the onset of the dust transport towards Europe and

therefore Italy. On 24 March, at Z500 a narrow ridge was extending from the Azores to Baltic Republics, while a minimum formed between Caspian deserts and Italy; regarding SLP and Z850, a strong anticyclone was present over Lithuania and Belarus and a minimum north of the Caspian Sea were collaborating in originating both an intense eastern flow from the Caspian desert to the eastern Black Sea and another flow from the western Black Sea towards Italy. At that time, the Italian Adriatic regions were already affected by a strong NE flow, but still without dust, since the cloud on the evening of this day was just approaching the eastern Black Sea. On 25 March, at Z500 a cutoff was gradually filling over Italy, surrounded by a ridge from the UK to Belarus and another one west of Urals, in Asia. Regarding SLP, isobars in Fig 1a outline an almost linear corridor of flow between the Caspian deserts and Bosnia and Croatia, which veers North across the Bora door entering NE Italy, with a double curvature in correspondence of the Balkans; regarding Z850, the only remarkable flow is present between Romania and Croatia. At this stage, the dust cloud was crossing the Black Sea (Fig. 1b), still traveling near the surface. Important for the next evolution was also the minimum present in the SLP and at Z850 over Tunisia. On 26 March (Fig. 1c), the anticyclone extended towards the Black sea, joining with the one over Egypt, while the cutoff retreated to Italy and the western Mediterranean sea, promoting the shift of the SLP and Z850 anticyclone to the north of the Black sea; the minimum over Tunisia shifted to Ionian sea, thus strengthening the flow along a corridor extended from the Caspian desert across the Black sea up to Romania and Bulgaria (Fig. 1d), and then from there to the Adriatic sea. Under these conditions, the most intense flow was observed. In the evening, the dust cloud reached Croatia. On 27 March (Fig. 1e), the trough at Z500 was located on the western Mediterranean basin, surrounded by anticyclones and ridges; SLP and Z850 cyclone moved over the Tyrrhenian sea, while the anticyclone expanded also over Romania; as a consequence, the main flow from the Caspian deserts, moving across the Black sea, headed towards Greece (Fig. 1f), veering toward NW thereafter affecting the Adriatic Sea and eastern Italy. The dust cloud touched down on the coast of the Adriatic regions (Friuli Venezia Giulia, Emilia Romagna, and Marche) in the evening. On 28 March (Fig. 1g), due to the weakening of the geopotential field at Z500 and Z850, as well as the SLP field, the flow from Romania to Italy weakened considerably. The circulation over NE Italy changed due to the influence of the anticyclonic curvature induced by a large high of SLP located between Iceland and Ireland, pivoting a strong surface southern flow from Scandinavia: a first impulse of cool easterly air mass shifted along the surface across the Po valley in the early morning, forming a shallow front (with few clouds) able to transport the dust cloud up to the border of Piedmont during the afternoon (Fig. 1h). In eastern Italy, instead, the local breeze circulation was prevailing. During the evening, a second easterly impulse crossed the Po Valley, this time accompanied by more clouds but without precipitations, and during the morning of 29 March reached also the northwestern Italian regions (Piedmont, Valle d'Aosta, and Liguria). At this time, approximately half of Italy was affected by the central Asian dust cloud, though over the NE sector the concentration had already decreased owing to a northerly air mass from the Alps. On this date, SLP and geopotential at Z850 and Z500 decreased abruptly in a corridor from Baltic republics to Greece, thus completely interrupting the easterly flow of dusty air. During the afternoon of the 29 March, the inflow of the arctic air mass moving across the Alps displaced southwards the mineral dust rich air mass over the Po Valley. Finally, on the 30 March, the cold front pushed by the Arctic airflow fully embraced the Po valley, thus definitely cleaning most of northern Italy.

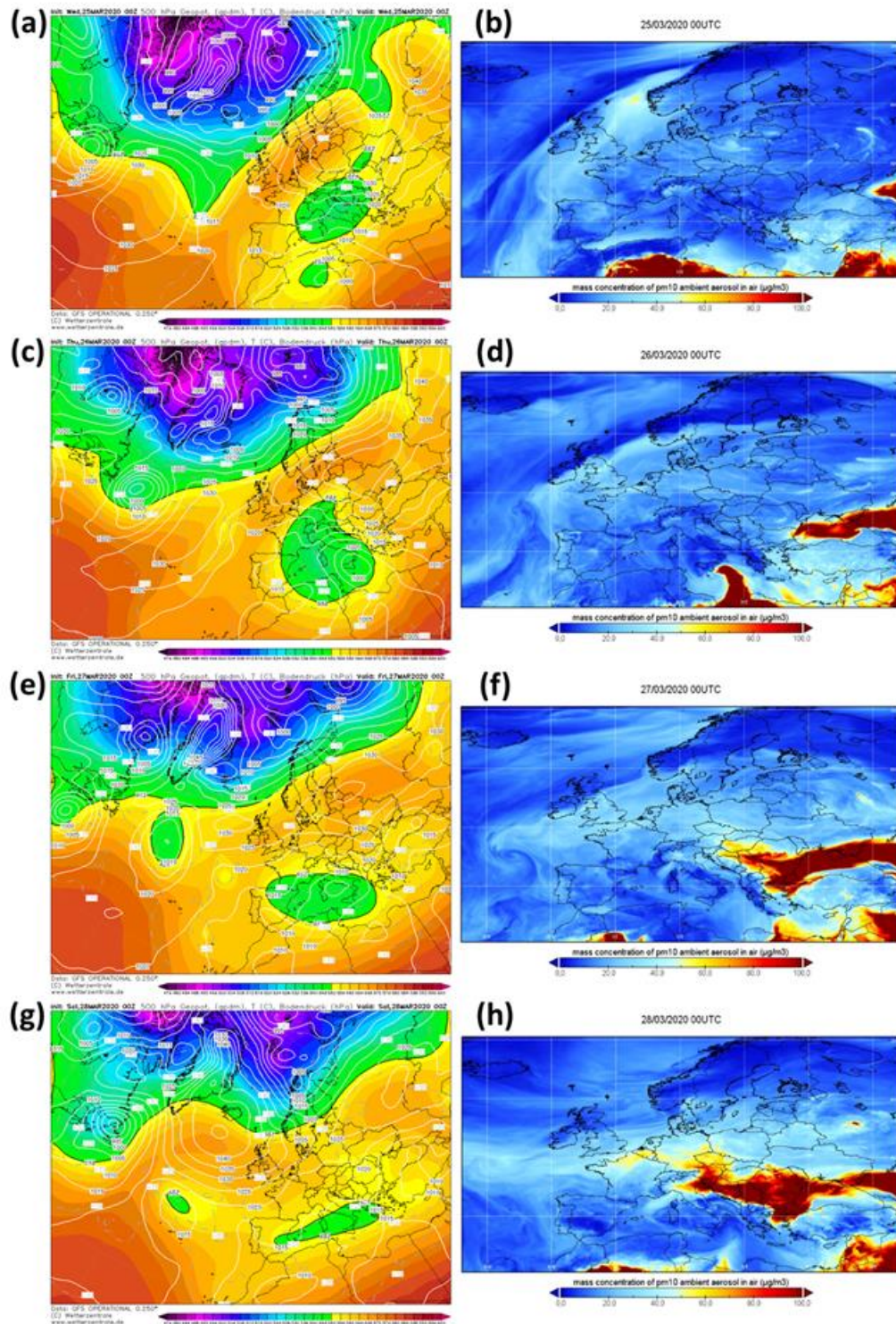


Figure 1. Left part: analysis maps showing: 500 hPa geopotential height (colors, in dam) and temperature (dotted dashed grey lines, in °C) and surface pressure (white lines, in hPa) relative to the days a) 25 March; c) 26 March; e) 27 March; g) 28 March, chosen as the most significant synoptic maps for the episode studied. Source: Wetterzentrale.de (<https://www.wetterzentrale.de/>). Right part: PM₁₀ concentration maps generated by Copernicus Atmosphere Monitoring Service (2020) at the height of 50 m above the surface, relative to the days b) 25 March; d) 26 March; f) 27 March; h) 28 March.

The easterly origin of the air mass originating the dust event over northern Italy was also confirmed by back-trajectory analyses. 96-h back-trajectories were computed using the three measurement sites (BO, TS, and CMN) as receptor points. The most relevant back-trajectories are reported in Figure 2 (for BO) and in the supplementary materials Figure S1 (for TS) and Figure S2 (for CMN).

Fig. 2a shows, in particular, the back-trajectory ending on 27 March 18:00 UTC in BO. Such date corresponds to the first peak due to the Caspian dust observed in TS by FAI-OPC, considered as the beginning of the event in Italy. Fig. 2a already indicates an airflow originating in the area between Caspian and Aral seas, with some intrusions from the Black and Mediterranean seas. The Caspian origin of air masses becomes even more evident in the following days (Fig. 2b and 2c). Then (Fig. 2d), on 30 March, a northern stream started to flow over northern Italy cleaning the air from the dust. The observation drawn from these back-trajectories confirms what was suggested by the synoptic analysis. The calculated trajectories, in the limits of the computational error, suggest that the Caspian dust, before arriving in Bologna, reached Trieste passing through the “Bora door” (a section of the Alps through which the Bora wind reaches Italy from the Balkan region).

This evidence is also confirmed by the computed back-trajectories for the TS measurement site shown in Figure S1. The ending times in Fig. S1 are the same as Fig. 2, and the conclusions that can be drawn are similar: an airflow originating in the Caspian region reached Trieste on 27 March (Fig S1a) and it continued in the following days (Fig. S1b and S1c) until a northern stream cleaned the air starting from 30 March (Fig. S1d).

Figure S2 shows, instead, some of the calculated back-trajectories for Mt. Cimone. In this case, an air mass with a possible north-African origin, with a strong component from the Aegean Sea, reached the site on 27 March (Fig. S2a), however, it did not give origin to visible peaks in the OPC time-series (Fig. 3c). Then, again (Fig. S2b and S2c), the peaks observed on 28 – 29 March can be associated with an airflow deriving from the Caspian region.

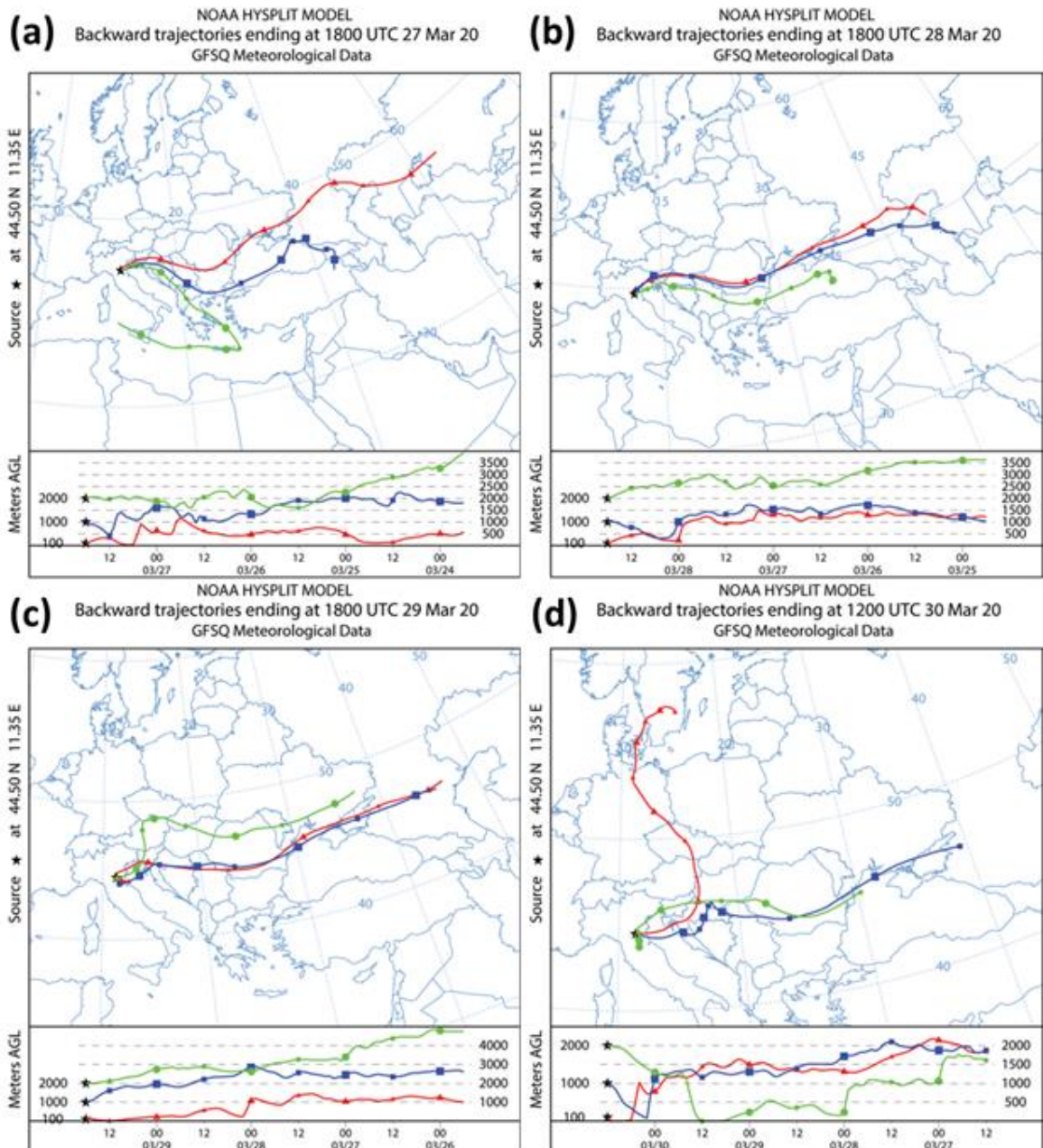


Figure 2. Back-trajectories (96-h backwards) ending at Bologna on a) 27 March 18:00 UTC; b) 28 March 18:00 UTC; c) 29 March 18:00 UTC; d) 30 March 12:00 UTC

3.2 – Optical Aerosol Counters (OPCs)

3.2.1 – Temporal trends and particle size distributions

The mineral dust outbreak produced a remarkable increase in particle number densities at all the three sites investigated, i.e., Bologna, Trieste, and at the top of Mt. Cimone. This increase was remarkably high for the coarse fractions, a typical feature of mineral dust, in particular at both the urban stations.

Figure 3 reports the temporal trend of the coarse fractions limited, for sake of simplicity, to fr5 (diameter 5-10 μm) for BO and TS, and the fraction fr3 (3-5 μm) for CMN. For the latter, fr3 was considered, instead of fr5, due to a large number of data below the detection limit for size bins > 7.5 microns, as previously reported in the Materials and methods section. This

is consistent with a possible loss of larger particles due to gravitational settling during the transport at higher altitude. The complete OPC series are available as supplementary material (Fig. S3).

As reported in Figure 3, coarse particle number densities were very low both before and after the event, reflecting the typical size distribution at urban locations in the cold season, while the fairly low level in the fine fraction (Fig. S3) is likely due (besides the seasonal evolution pattern naturally leading to a decrease going towards the warmer season at this latitude) at least in part to the lockdown imposed to stem the spread of the SARS-COV2 pandemic in Italy, from early March 2020 (Chauhan and Singh, 2020). The Asian dust plume impacted TS first, on 27 March during the afternoon, reaching BO (about 200 km east) the day after (please note the time lag of the order of one day at the two stations in Fig. 3a and 3b). Overall the event duration was of about three days, ceasing on 30 March in Trieste and on 31 March in Bologna. During this period, a general increase in suspended particle concentration, especially in the coarse fraction, was observed at all the stations in agreement with mineral dust properties and its resulting influence on PM mass load recorded at the time throughout several European stations (Mahovic et al., 2020). The dust plume reached CMN (Figure 3c) on 28 March, but the maximum concentrations were slightly lagged peaking between the afternoon of 29 March until 30 March. Another peak in CMN series is visible on 21 March, likely due to a genuine “high-pass” Saharan dust, which is not herein discussed being beyond the scope of the present work.

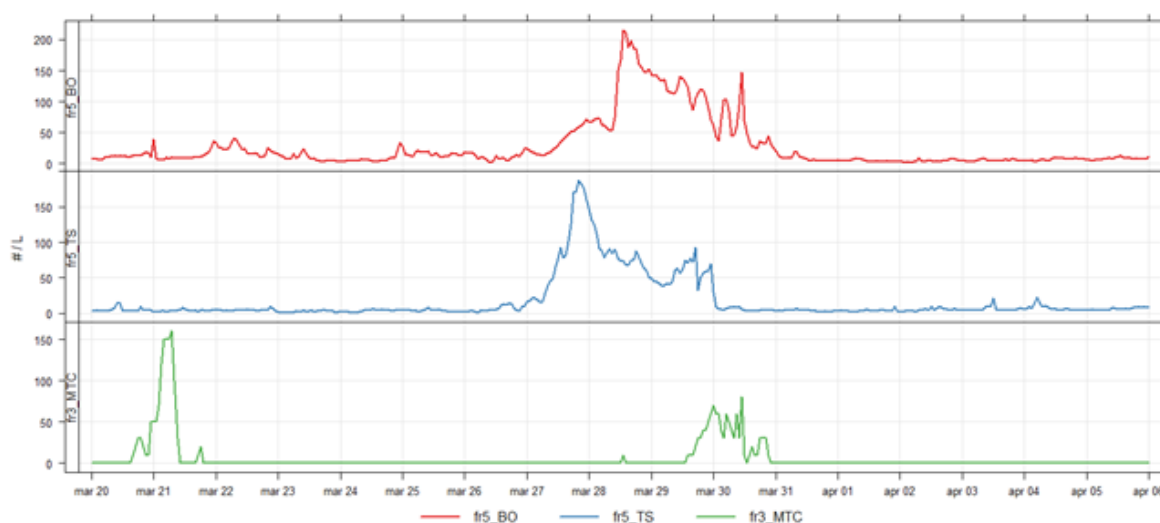


Figure 3. Temporal trends of fr5 (5.0 to 10.0 μm) at Bologna, red line, and Trieste, blue line, and of fr3 (3.0 to 5.0 μm) at Mt. Cimone, green line. Values are in Counts dm^{-3} ($\#/L$)

OPC data were associated with the meteorological parameters collected at the three sites, in particular, the connection with local wind speed and direction was evaluated using polar plots (Carslaw and Beevers, 2013). For the present study, we computed polar plots for fr5 of both cities and for fr3 of CMN as reported in Fig. 4. A conditional probability function (CPF) at the 90th percentile was used for computation in order to minimize pollution source effects and focus the computation only on the event of dust transport (Kurniawati et al., 2019). Polar plots of both cities (Fig. 4a and 4c) show a maximum CPF probability corresponding to the wind blowing from the east direction, in agreement with the advection of dust from the Caspian region to the study area. The wind speed corresponding to the two wind intensity maxima was about 3 m s^{-1} for Bologna and 7 m s^{-1} for Trieste. Fig. 4b and 4d

report the wind intensity and direction pattern observed in the two cities during the study period. In particular, the plot highlights how the dust event was preceded and followed by weak winds, lower than 2 m s^{-1} and typical of the Po Valley basin, while during the event wind speed of about 15 up to 20 m s^{-1} was recorded in TS. The Easterly direction remains the most remarkable feature since this source area for air masses is fairly infrequent in Italy though acknowledged especially in the spring (Battison et al., 1988; Brattich et al., 2015b, 2020a; Dimitriou and Kassomenos, 2014).

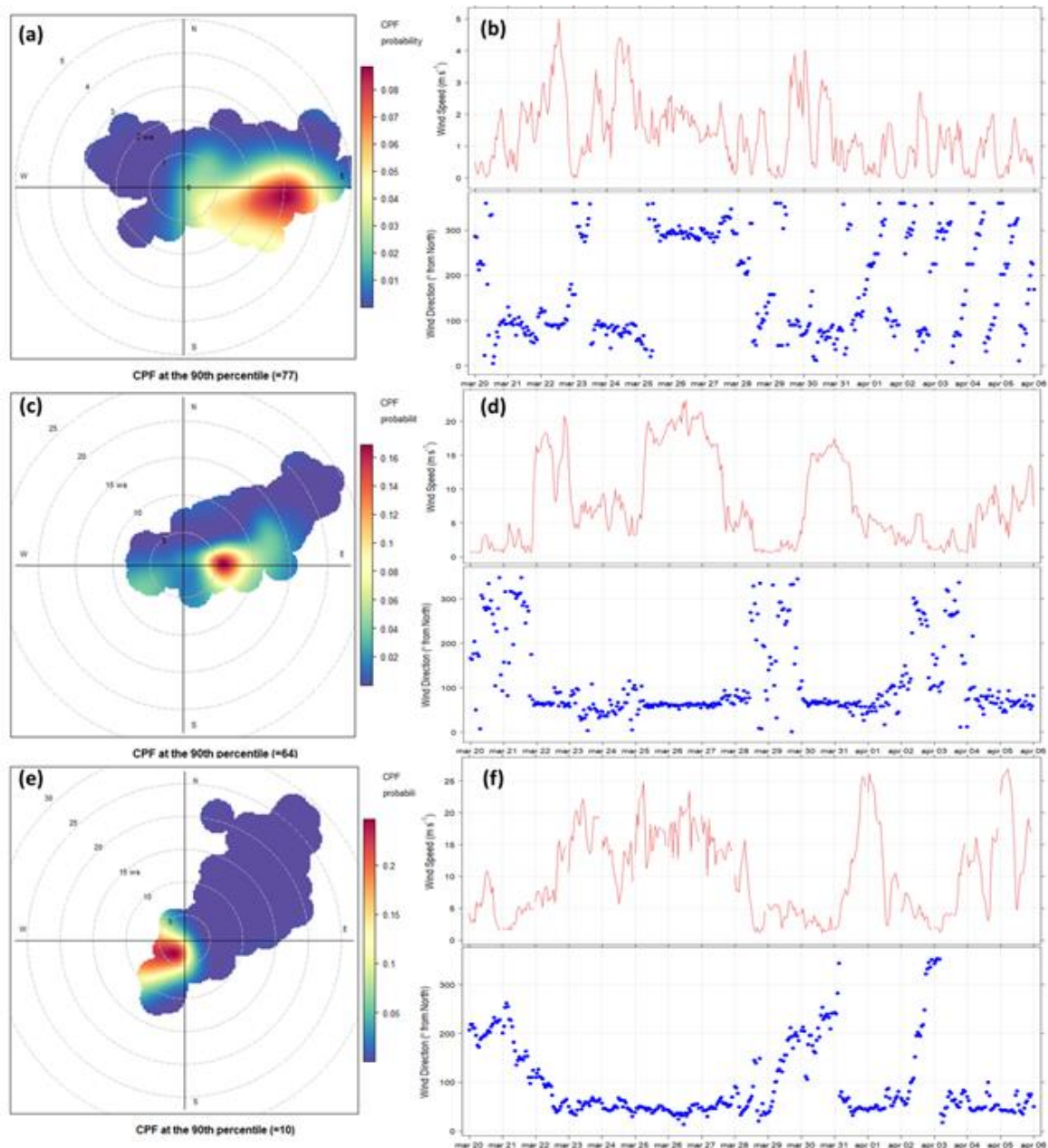


Figure 4. Right part: polar plots of a) fr5 for Bologna; c) fr5 for Trieste; e) fr3 for Mt. Cimone. Gray dashed circumferences indicate wind speed in m s^{-1} . Left part: wind speed (red line) and wind direction (blue points) from 20 March to 6 April 2020 for b) Bologna; d) Trieste; f) Mt. Cimone

The temporal behavior of particle number densities as a function of size is not the same (Fig. S3). At the three stations, mineral dust transport showed a stronger increase for the coarse fraction, while the increase in fine particles, although present, is generally slighter. Mt. Cimone, instead, showed an apparent strong increase in the fine fractions, but not in the coarse ones suggesting a depletion due to the influence of gravitational selection on particles with height.

This information can be summarized by comparing particle size distributions at the three stations before, during, and after the event, as reported in Fig. 5. An overall increase in number densities is observed at all sites during the dust event. However, as reported in Fig. 5, the most significant deviations of the within-the-event period from both before- and after-event periods were observed starting from 0.7 μm in BO and TS, while at CMN also the finest particles undergo an increase during the event. This confirms the primary influence of the dust on coarse particles, rather than on finer ones, at least in the two cities. This finding is different from Saharan dust outbreaks since, in this latter case, also the finest fractions increase, at least among the size range determined by OPC and/or from LIDAR observations (Brattich et al., 2015a; Denjean et al., 2016).

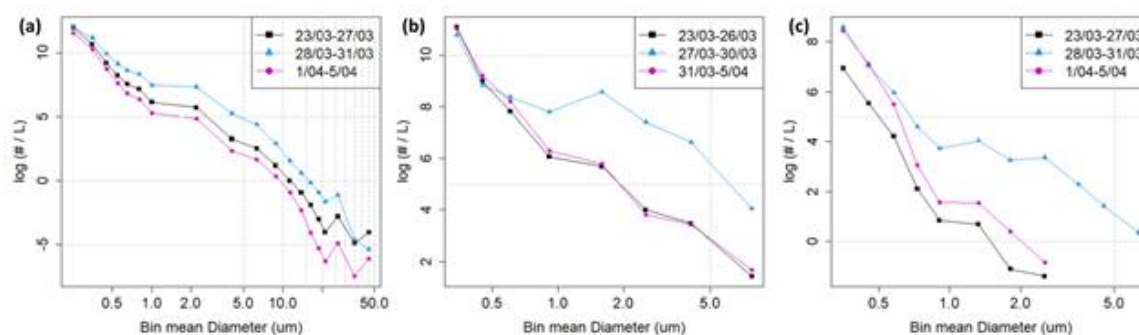


Figure 5. Particle size distributions for the OPCs: a) LOAC (Bologna); b) FAI (Trieste); c) GRIMM (Mt. Cimone). Abscissa values are in μm , ordinate values in $\log(\# \text{ L}^{-1})$. Abscissa axis is on logarithmic scale

3.2.2 – Particle Mass Concentrations

Number densities were eventually converted into daily PM_{10} mass loads using an algorithm based on an average PM density of 1.65 g cm^{-3} , usually applied to urban aerosol composition, which may not accurately fit mineral dust aerosols with a different chemical composition (Brattich et al., 2020b; Gholamzade Ledari et al., 2020). Calculated daily PM_{10} mean in BO reached values of 79 and $74 \mu\text{g m}^{-3}$ respectively on 28 and 29 March (with an absolute maximum of $168 \mu\text{g m}^{-3}$ on 28 March 13:00 UTC), with a negative bias of about 12% with respect to the experimental values recorded by the Regional Environmental Protection Agency in Bologna revealing an expected underestimate (Figure 6a). Calculated PM_{10} values are even higher at TS, where values of 107 and $124 \mu\text{g m}^{-3}$ were reached on 27 and 28 March (with maxima of 275 at 19:00 UTC and $246 \mu\text{g m}^{-3}$ at 23:00 UTC on 27 March). Recorded PM_{10} values in Bologna and Trieste are remarkably higher than the EU PM_{10} threshold (European Parliament, 2008) and 3-5 times the WHO recommendation (WHO for European, 2006) and the estimation of the desert dust load following the method suggested by Barnaba et al. (2017) indicates values in the range of $66\text{-}108 \mu\text{g m}^{-3}$ at these two cities (Figure 6b).

In BO, PM_{10} was slightly above the EU threshold also on 30 March, ($54 \mu\text{g m}^{-3}$), while two relative maxima were detected on 27 March ($36.4 \mu\text{g m}^{-3}$) and 22 March ($35.0 \mu\text{g m}^{-3}$). The PM_{10} mean of the days before the event (excluding 22 March), which can be considered as

representative of the typical background of the region likely due to the limited influence of vehicular emissions during the lockdown and the low influence of industrial activities in Bologna, were $15.0 \mu\text{g m}^{-3}$ $10.3 \mu\text{g m}^{-3}$ respectively prior and after the mineral dust outbreak event. A tail of the event was observed also in TS on 29 March with $79.4 \mu\text{g m}^{-3}$. The PM_{10} daily mean value of the days before the event in TS was $11.4 \mu\text{g m}^{-3}$, while that of the days immediately following the event was $13.9 \mu\text{g m}^{-3}$.

An increase of calculated PM_{10} was observed also at Mt. Cimone with a maximum of $11 \mu\text{g m}^{-3}$ on 30 March 11:00 UTC. Although this value is very low compared to the ones of Bologna and Trieste, the increase is outstanding if compared with the mean PM_{10} values observed before and after the event: 0.11 and $0.35 \mu\text{g m}^{-3}$, respectively in agreement with winter relative minima previously reported, due to the height (2173 m a.s.l.) and the cold-season decoupling of the mountain top from the PBL (Tositti et al., 2013).

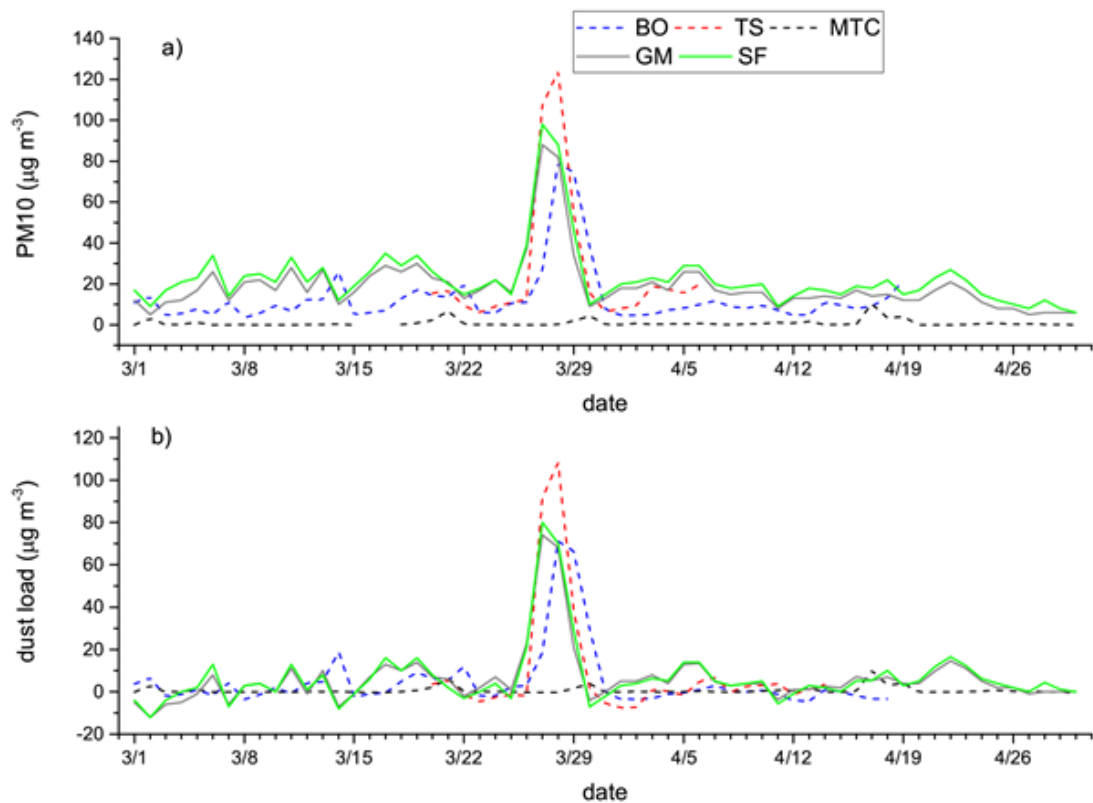


Figure 6. a) Daily mean PM_{10} values (a) and dust load (b) calculated over the March-April 2020 period. Dashed lines represent values calculated from the counts of the three optical particle counters in Bologna (BO), Trieste (TS), and Mt. Cimone (CMN), while solid lines represent concentration values recorded in Bologna at three air quality stations from the ARPAE network (Giardini Margherita GM, Porta San Felice SF).

3.3 – Ancillary analyses

3.3.1 – AERONET (AERosol RObotic NETwork)

Figure 7 shows the Aerosol Optical Depth (AOD) data retrieved from AERONET ground-based remote sensing aerosol network at the site of Venice (Acqua Alta Oceanographic Tower - AAOT; $45^{\circ}19'N$, $12^{\circ}30'E$) around the period of the mineral dust outbreak event herein analyzed. Figure 7 shows very clearly the peculiar, steadily high aerosol optical depth value in the period 28 – 30 March and the simultaneously low value of the fine mode fraction,

confirming the abrupt change in dust optical properties in agreement with the OPC data previously described.

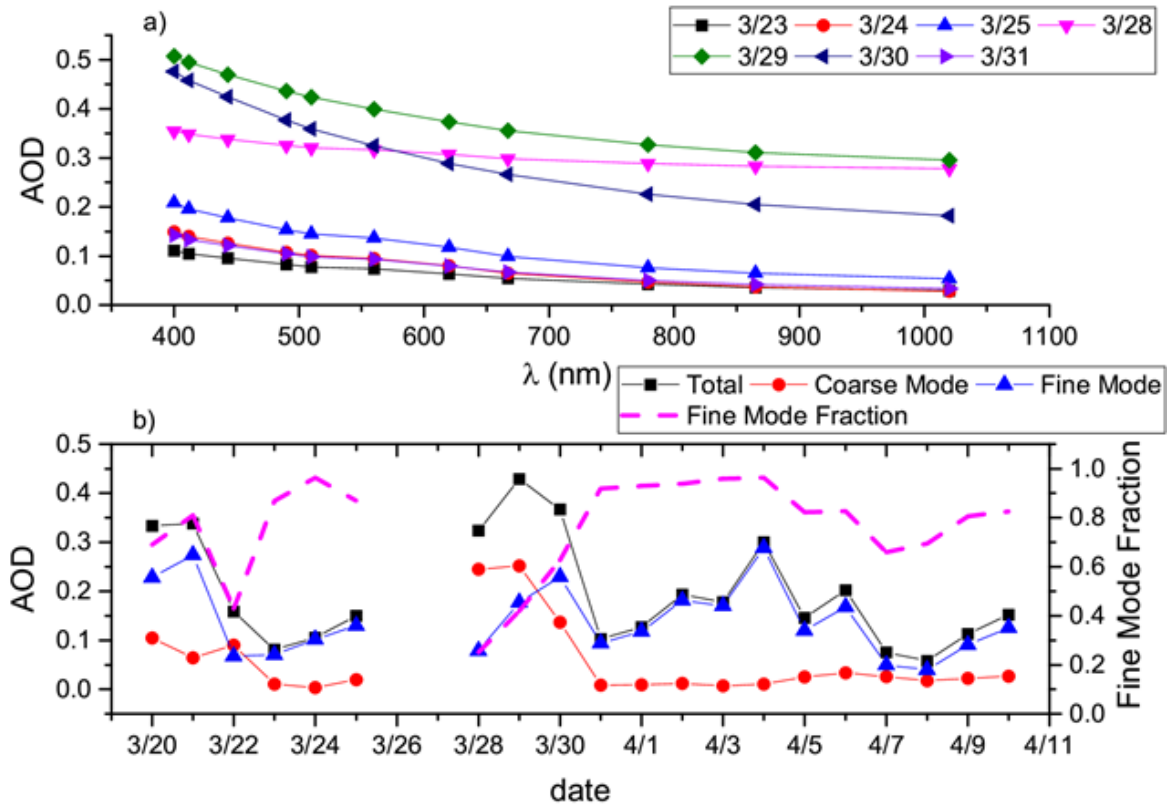


Figure 7. a) Aerosol Optical Depth (AOD) at different wavelengths and for different days of March 2020 detected at the AERONET site of Venice; b) time series of the total, coarse, and fine mode AOD, and fine mode fraction observed in March-April 2020 at the AERONET site of Venice.

Even the volumetric size distributions retrieved by AERONET indicate the prominence of the mode, i.e. of particles with an aerodynamic diameter $> 1 \mu\text{m}$, on 28 and 29 March in agreement with this observation and with the particle size distributions from OPC readings in BO and TS (Fig. S4).

3.3.2 – LIDAR Ceilometer

Images from a LIDAR ceilometer from Alice-net (Dionisi et al., 2018) located in Milan were employed to derive information on aerosol vertical distribution and of the dynamics of the atmospheric lowest layers. Figure 8 shows the vertical profiles observed during the event, showing an approximate thickness of about 2 km above ground level. This observation indicates another peculiarity of this mineral dust event, which, differently from Saharan dust plumes typically reaching and shifting aloft between 1500 and 4000 m a.s.l. (Jorba et al., 2004; Soupiona et al., 2020), traveled at relatively low atmospheric altitude, reasonably due to the low temperatures at the source and to the reduced convective activity resulting from the higher latitude and season as compared to the Saharan desert. The relatively low travel height of the dust plume caused the gravitational settling of the heaviest particles in the proximity of the ground, in agreement with the size distribution data observed at Mt. Cimone as shown in Figure S3c.

Figure 8 shows also that the yellow layer was somewhat deeper during the first three hours of 28 March than during the rest of the day; this observation likely indicates that early in the morning the dust plume was capped by a cloud top, reasonably caused by the irruption of the easterly cold front towards the Po Valley. The layer was shallower from 4:00 UTC on. Signals of convective activity appeared between 10:00 - 15:00 UTC, as indicated by the more intense orange vertical swipes linked to the rising thermals. In the evening, the layer was even shallower, due to the nocturnal cooling suppressing vertical motions. In general, the thinning of the mixing layer during dust transports, confirmed also by the analysis of the radiosoundings of the period, is linked to the high concentrations of aerosols in the troposphere which reduce the amount of solar radiation reaching the ground, in turn reducing sensible heat fluxes that drive the diurnal evolution of temperature and the PBL (Li et al., 2017; Pandolfi et al., 2014; Salvador et al., 2019). From 20:00 UTC on, 2 km high clouds appeared, probably linked to the arrival of the cold front from N-NE, while the yellow layer rose again because of wind-induced turbulence. The following day, thermals appeared again between 8:00 and 15:00 UTC, while the signal of Arctic air masses can be observed from 20:00 UTC on.

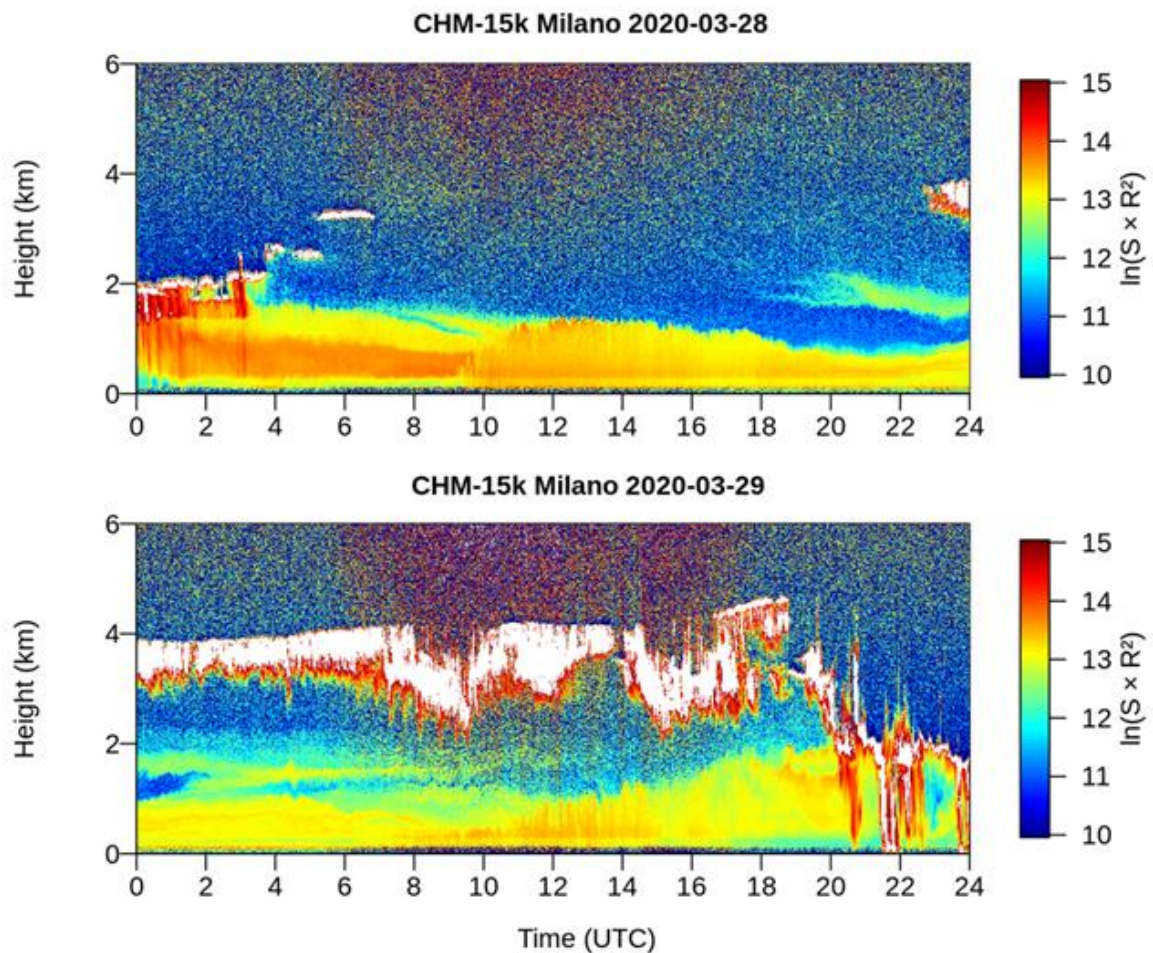


Figure 8. Vertical profiling from the automated LIDAR ceilometer located in Milan on 28 and 29 March 2020.

3.3.3 – Chemical composition

The change in dust optical properties is in agreement with the concurrent change in aerosol composition at the Bologna Gobetti ARPAE station (Figure 9). Indeed, the arrival of the dust plume from the Aralkum desert was connected with an increase in some major particulate components (i.e., nitrate, sulfate, K, Pb) and elemental carbon likely in association with the entrainment of air pollution when the air mass passed over the Balkans (Evangelidou et al., 2021) as well as of some trace elements (Na, Ca, Mg, Fe), some of which typically crustal (Ca and Mg, Fe) due to the mineral dust matrix or marine (Na), most likely from the Adriatic Sea. The entrainment of anthropogenic pollution and marine aerosols together with the crustal material originated from the Aralkum might have been favored by the low boundary layer previously observed, an aspect which has been put in connection with the exacerbation of the toxicological properties of dust aerosols (Pandolfi et al., 2014).

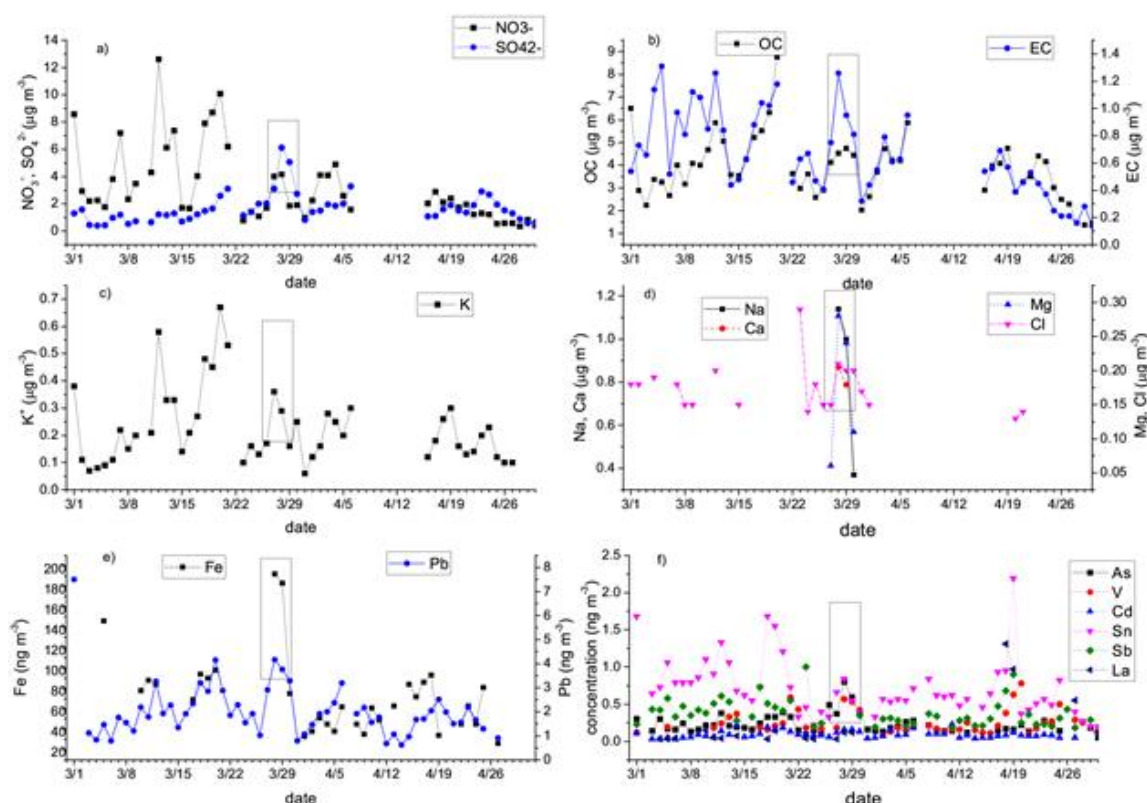


Figure 9. Concentration of major components and trace elements analyzed in PM_{2.5} particulate samples at the Bologna Gobetti ARPAE air quality station during March-April 2020 period: a) nitrate NO₃⁻ and sulfate SO₄²⁻; b) carbonaceous components organic and elemental carbon (OC and EC); c) potassium ion (K⁺); d) Na, Ca, Mg and Cl; e) Fe and Pb; f) As, V, Cd, Sn, Sb, and La. The boxes enclose the dates of the dust incursion over Northern Italy.

4 – Conclusions

This work presents a detailed investigation of a mineral dust event that reached northern Italy at the end of March 2020. The peculiarity of this event is mainly associated with its origin, which can be traced back to the desert region surrounding the Caspian Sea, in central Asia. Its origin was confirmed by the concurrent analysis of the synoptic configuration together with satellite data of AOD and the calculation of back-trajectories for the study

period. In particular, while it is well known how Southern Europe is often subjected to mineral dust incursions from the Sahara desert, transport of mineral dust originated in the Caspian area impacts frequently eastern Asia rather than Europe.

Data collected from three optical particle counters (OPCs), located at two different cities, Bologna and Trieste, and at one high-altitude i.e. the WMO-GAW Mt. Cimone station, all in northern Italy, was used to study the event at high time resolution. The use of OPCs allowed characterizing accurately the size distribution of this anomalous mineral dust event, to understand its features over time.

The results demonstrated that the transport of mineral dust affected mostly the concentration of coarse fraction at all three sites, in particular those with a mean diameter higher than 0.7 μm . The fine fraction appeared negligibly affected by the central Asian mineral dust outburst, its concentration being similar to that observed before and after the event. Anyhow, the coarse fraction was affected by the event to the point that PM_{10} concentration in Bologna exceeded up to twice - three times the WHO limit, in a period in which anthropogenic emissions were strongly reduced by the lockdown imposed in Italy to contrast the spread of the SARS-COV2 virus.

Overall, these results demonstrate how the concurrent analysis of multiple meteorological information and atmospheric composition data is needed to deepen our understanding of the variety of physicochemical processes connected with aerosols and their interactions. These results can be extremely important for their potential climatological implications owing to the projected increases in the frequency of dust storms resulting from the combined effects of increasing temperatures, increasing drought, and soil erosion.

Data availability

OPC observations and HYSPLIT back-trajectories used for this investigation are available upon request to the corresponding author (laura.tositti@unibo.it).

Synoptic maps are available on the wetterzentrale web archive: <https://www.wetterzentrale.de/>.

NASA AERONET observations are available at: <https://aeronet.gsfc.nasa.gov/>.

The lidar ceilometer images from the Alice-net automated images from Milan are available by contacting the PI Luca Di Liberto (l.diliberto@isac.cnr.it).

Aerosol chemical speciation data are available on the ARPAE open data portal at: <https://dati.arpae.it/>.

Author contributions

LT, EB, and FP designed the study. CC led the synoptic analysis. PM led calculation and analysis of HYSPLIT back-trajectories. AZ, EB, and AB developed the analysis methodology and led the analysis of observational data with contributions from all coauthors. AM provided and analyzed data for the Mt. Cimone station. LT, EB, and AZ wrote the manuscript with contributions from all coauthors.

Competing interests

The authors declare that they have no conflict of interest.

Acknowledgments

We gratefully acknowledge Dr. Marco Bellini and Dr. Fulvio Stel from ARPA FVG Regional Environmental Protection Agency for providing data at the Trieste via Pitacco and via del Ponticello stations. Open data of PM chemical speciation at the Bologna via Gobetti sampling site were provided ARPAE Regional Environmental Protection Agency. The HYSPLIT transport and dispersion model and/or READY website (<https://www.ready.noaa.gov>) used in this publication were provided by the NOAA Air Resources Laboratory (ARL). We wish to thank the NASA-GSFC AERONET team, and the PI Giuseppe Zibordi and his staff for establishing and maintaining the AAOT Venice site used in this investigation. We also thank the Alice-net automated LIDAR ceilometer network and the PI Luca Di Liberto from ISAC-CNR Rome for providing access to the LIDAR ceilometer images from Milan.

Financial support

This paper is published with the contribution of the Department of Excellence program financed by the Ministry of Education, University and Research (MIUR, L. 232 del 01/12/2016). Monte Cimone station has received funding from the European Union's Horizon 2020 research and innovation programme under grant agreement No 654109.

Appendix

Appendix is available online: <https://doi.org/10.5194/acp-2021-429>

References

- Adebisi, A. A. and Kok, J. F.: Climate models miss most of the coarse dust in the atmosphere, *Sci. Adv.*, 6(15), doi:10.1126/sciadv.aaz9507, 2020.
- Bangert, M., Nenes, A., Vogel, B., Vogel, H., Barahona, D., Karydis, V. A., Kumar, P., Kottmeier, C. and Blahak, U.: Saharan dust event impacts on cloud formation and radiation over Western Europe, *Atmos. Chem. Phys.*, 12(9), 4045–4063, doi:10.5194/acp-12-4045-2012, 2012.
- Barkan, J. and Alpert, P.: Synoptic analysis of a rare event of Saharan dust reaching the Arctic region, *Weather*, 65(8), 208–211, doi:10.1002/wea.503, 2010.
- Barnaba, F., Bolignano, A., Di Liberto, L., Morelli, M., Lucarelli, F., Nava, S., Perrino, C., Canepari, S., Basart, S., Costabile, F., Dionisi, D., Ciampichetti, S., Sozzi, R. and Gobbi, G. P.: Desert dust contribution to PM10 loads in Italy: Methods and recommendations addressing the relevant European Commission Guidelines in support to the Air Quality Directive 2008/50, *Atmos. Environ.*, 161, 288–305, doi:10.1016/j.atmosenv.2017.04.038, 2017.
- Battison, G. A., Degetto, S., Gerbasi, R., Sbrignadello, G. and Tositti, L.: Fallout distribution in Padua and Northeast Italy after the chernobyl nuclear reactor accident, *J. Environ. Radioact.*, 8(2), 183–191, doi:10.1016/0265-931X(88)90025-2, 1988.

- Behzod, G., Su-Chin, C. and Dilmurod, G.: Changes in water volume of the Aral Sea after 1960, *Appl. Water Sci.*, 2, 285–291, doi:<https://doi.org/10.1007/s13201-012-0048-z>, 2012.
- Belosi, F., Conte, M., Gianelle, V., Santachiara, G. and Contini, D.: On the concentration of SARS-CoV-2 in outdoor air and the interaction with pre-existing atmospheric particles, *Environ. Res.*, 193, doi:10.1016/j.envres.2020.110603, 2021.
- Brattich, E., Riccio, A., Tositti, L., Cristofanelli, P. and Bonasoni, P.: An outstanding Saharan dust event at Mt. Cimone (2165 m a.s.l., Italy) in March 2004, *Atmos. Environ.*, 113, 223–235, doi:10.1016/j.atmosenv.2015.05.017, 2015a.
- Brattich, E., Hernández-Ceballos, M. A., Cinelli, G. and Tositti, L.: Analysis of 210Pb peak values at Mt. Cimone (1998-2011), *Atmos. Environ.*, 112, 136–147, doi:10.1016/j.atmosenv.2015.04.020, 2015b.
- Brattich, E., Serrano Castillo, E., Guilietti, F., Renard, J.-B., Tripathi, S. N., Ghosh, K., Berthet, G., Vignelles, D. and Tositti, L.: Measurements of aerosols and charged particles on the BEXUS18 stratospheric balloon, *Ann. Geophys.*, 37, 389–403, doi:10.5194/angeo-37-389-2019, 2019.
- Brattich, E., Orza, J. A. G., Cristofanelli, P., Bonasoni, P., Marinoni, A. and Tositti, L.: Advection pathways at the Mt. Cimone WMO-GAW station: Seasonality, trends, and influence on atmospheric composition, *Atmos. Environ.*, 234, doi:10.1016/j.atmosenv.2020.117513, 2020a.
- Brattich, E., Bracci, A., Zappi, A., Morozzi, P., Sabatino, S. Di, Porcù, F., Nicola, F. Di and Tositti, L.: How to get the best from low-cost particulate matter sensors: Guidelines and practical recommendations, *Sensors (Switzerland)*, 20(11), 1–33, doi:10.3390/s20113073, 2020b.
- Breckle, S.-W. and Wucherer, W.: *The Aralkum, a Man-Made Desert on the Desiccated Floor of the Aral Sea (Central Asia)*, edited by L. A. Dimeyeva and N. P. Ogar, Springer., 2012.
- Bulot, F. M. J., Johnston, S. J., Basford, P. J., Easton, N. H. C., Apetroaie-Cristea, M., Foster, G. L., Morris, A. K. R., Cox, S. J. and Loxham, M.: Long-term field comparison of multiple low-cost particulate matter sensors in an outdoor urban environment, *Sci. Rep.*, 9(1), doi:10.1038/s41598-019-43716-3, 2019.
- Calidonna, C. R., Avolio, E., Gullì, D., Ammoscato, I., De Pino, M., Donateo, A. and Feudo, T. Lo: Five years of dust episodes at the Southern Italy GAW regional coastal mediterranean observatory: Multisensors and modeling analysis, *Atmosphere (Basel)*, 11(5), doi:10.3390/ATMOS11050456, 2020.
- CAMS: CAMS documentation Webpage, [online] Available from: <https://confluence.ecmwf.int/display/CKB/CAMS+Regional%3A+European+air+quality+analysis+and+forecast+data+documentation> (Accessed 10 May 2021), 2015.
- Carslaw, D. C. and Beevers, S. D.: Characterising and understanding emission sources using bivariate polar plots and k-means clustering, *Environ. Model. Softw.*, 40, 325–329, doi:10.1016/j.envsoft.2012.09.005, 2013.
- Carslaw, D. C. and Ropkins, K.: Openair - An r package for air quality data analysis, *Environ. Model. Softw.*, 27–28, 52–61, doi:10.1016/j.envsoft.2011.09.008, 2012.
- Chauhan, A. and Singh, R. P.: Decline in PM_{2.5} concentrations over major cities around the world associated with COVID-19, *Environ. Res.*, 187, doi:10.1016/j.envres.2020.109634, 2020.
- Crilley, L. R. ., Shaw, M. ., Pound, R. ., Kramer, L. J. ., Price, R. ., Young, S. ., Lewis, A. C. . and Pope, F. D.: Evaluation of a low-cost optical particle counter (Alphasense OPC-N2) for ambient air monitoring, *Atmos. Meas. Tech.*, 11, 709–720, doi:10.5194/amt-11-709-2018, 2018.

- Denjean, C., Cassola, F., Mazzino, A., Triquet, S., Chevaillier, S., Grand, N., Bourriane, T., Momboisse, G., Sellegri, K., Schwarzenbock, A., Freney, E., Mallet, M. and Formenti, P.: Size distribution and optical properties of mineral dust aerosols transported in the western Mediterranean, *Atmos. Chem. Phys.*, 16(2), 1081–1104, doi:10.5194/acp-16-1081-2016, 2016.
- Diémoz, H., Barnaba, F., Magri, T., Pession, G., Dionisi, D., Pittavino, S., Tombolato, I. K. F., Campanelli, M., Ceca, L. S. Della, Hervo, M., Di Liberto, L., Ferrero, L. and Gobbi, G. P.: Transport of Po Valley aerosol pollution to the northwestern Alps-Part 1: Phenomenology, *Atmos. Chem. Phys.*, 19(5), 3065–3095, doi:10.5194/acp-19-3065-2019, 2019.
- Dimitriou, K. and Kassomenos, P.: Indicators reflecting local and transboundary sources of PM_{2.5} and PMCOARSE in Rome - impacts in air quality, *Atmos. Environ.*, 96, 154–162, doi:10.1016/j.atmosenv.2014.07.029, 2014.
- Dinoi, A., Donateo, A., Conte, M., Conte, M. and Belosi, F.: Comparison of atmospheric particle concentration measurements using different optical detectors: Potentiality and limits for air quality applications, *Meas. J. Int. Meas. Confed.*, 106, 274–282, doi:10.1016/j.measurement.2016.02.019, 2017.
- Dionisi, D., Barnaba, F., Diémoz, H., Di Liberto, L. and Gobbi, G. P.: A multiwavelength numerical model in support of quantitative retrievals of aerosol properties from automated lidar ceilometers and test applications for AOT and PM₁₀ estimation, *Atmos. Meas. Tech.*, 11(11), 6013–6042, doi:10.5194/amt-11-6013-2018, 2018.
- Domínguez-Rodríguez, A., Báez-Ferrer, N., Abreu-González, P., Rodríguez, S., Díaz, R., Avanzas, P. and Hernández-Vaquero, D.: Impact of Desert Dust Events on the Cardiovascular Disease: A Systematic Review and Meta-Analysis, *J. Clin. Med.*, 10(4), 727, doi:10.3390/jcm10040727, 2021.
- Duchi, R., Cristofanelli, P., Landi, T. C., Arduini, J., Bonafe, U., Bourcier, L., Busetto, M., Calzolari, F., Marinoni, A., Putero, D. and Bonasoni, P.: Long-term (2002-2012) investigation of Saharan dust transport events at Mt. Cimone GAW global station, Italy (2165 m a.s.l.), *Elementa*, 2016, doi:10.12952/journal.elementa.000085, 2016.
- European Parliament: Directive 2008/50/EC of the European Parliament and of the Council of 21 May 2008 on Ambient Air Quality and Cleaner Air for Europe, European Commission, Brussels, Belgium. [online] Available from: <http://eur-lex.europa.eu/legal-content/EN/TXT/PDF/?uri=CELEX:32008L0050&from=EN>, 2008.
- Evangeliou, N., Platt, S. M., Eckhardt, S., Lund Myhre, C., Laj, P., Alados-Arboledas, L., Backman, J., Brem, B. T., Fiebig, M., Flentje, H., Marinoni, A., Pandolfi, M., Yus-Díez, J., Prats, N., Putaud, J. P., Sellegri, K., Sorribas, M., Eleftheriadis, K., Vratolis, S., Wiedensohler, A. and Stohl, A.: Changes in black carbon emissions over Europe due to COVID-19 lockdowns, *Atmos. Chem. Phys.*, 21(4), 2675–2692, doi:10.5194/acp-21-2675-2021, 2021.
- Ferrero, L., Gregorič, A., Močnik, G., Rigler, M., Cogliati, S., Barnaba, F., Di Liberto, L., Gobbi, G. P., Losi, N. and Bolzacchini, E.: The impact of cloudiness and cloud type on the atmospheric heating rate of black and brown carbon, *Atmos. Chem. Phys.*, 1–33, doi:10.5194/acp-2020-264, 2020.
- Fleming, Z. L., Monks, P. S. and Manning, A. J.: Review: Untangling the influence of air-mass history in interpreting observed atmospheric composition, *Atmos. Res.*, 104–105, 1–39, doi:10.1016/j.atmosres.2011.09.009, 2012.
- Fubini, B. and Fenoglio, I.: Toxic potential of mineral dusts, *Elements*, 3(6), 407–414, doi:10.2113/GSELEMENTS.3.6.407, 2007.
- García-Pando, C. P., Stanton, M. C., Diggle, P. J., Trzaska, S., Miller, R. L., Perlwitz, J. P., Baldasano, J. M., Cuevas, E., Ceccato, P., Yaka, P. and Thomson, M. C.: Soil dust

- aerosols and wind as predictors of seasonal meningitis incidence in niger, *Environ. Health Perspect.*, 122(7), 679–686, doi:10.1289/ehp.1306640, 2014.
- Gholamzade Ledari, D., Hamidi, M. and Shao, Y.: Evaluation of the 13 April 2011 frontal dust storm in west Asia, *Aeolian Res.*, 44, doi:10.1016/j.aeolia.2020.100592, 2020.
 - Gobbi, G. P., Barnaba, F., Di Liberto, L., Bolignano, A., Lucarelli, F., Nava, S., Perrino, C., Pietrodangelo, A., Basart, S., Costabile, F., Dionisi, D., Rizza, U., Canepari, S., Sozzi, R., Morelli, M., Manigrasso, M., Drewnick, F., Struckmeier, C., Poenitz, K. and Wille, H.: An inclusive view of Saharan dust advections to Italy and the Central Mediterranean, *Atmos. Environ.*, 201, 242–256, doi:10.1016/j.atmosenv.2019.01.002, 2019.
 - Grange, S. K.: Technical note: saqgetr R package (Version 0.1). [online] Available from: <https://drive.google.com/file/d/1IgDODHqBHewCTKLdAAxRyR7ml8ht6Ods/view>, 2019.
 - IPCC Working Group I: WORKING GROUP I CONTRIBUTION TO THE IPCC FIFTH ASSESSMENT REPORT CLIMATE CHANGE 2013: THE PHYSICAL SCIENCE BASIS, Final Draft Underlying Scientific-Technical Assessment, Ippc, (January 2014), 103, doi:10.1017/CBO9781107415324, 2013.
 - Jorba, O., Pérez, C., Rocadenbosch, F. and Baldasano, J. M.: Cluster analysis of 4-day back trajectories arriving in the Barcelona area, Spain, from 1997 to 2002, *J. Appl. Meteorol.*, 43(6), 887–901, doi:10.1175/1520-0450(2004)043<0887:CAOBDT>2.0.CO;2, 2004.
 - Kaskaoutis, D. G., Houssos, E. E., Minvielle, F., Rashki, A., Chiapello, I., Dumka, U. C. and Legrand, M.: Long-term variability and trends in the Caspian Sea – Hindu Kush Index: Influence on atmospheric circulation patterns, temperature and rainfall over the Middle East and Southwest Asia, *Glob. Planet. Change*, 169, 16–33, doi:10.1016/j.gloplacha.2018.07.004, 2018.
 - Keil, D. E., Buck, B., Goossens, D., Teng, Y., Pollard, J., McLaurin, B., Gerads, R. and DeWitt, J.: Health effects from exposure to atmospheric mineral dust near Las Vegas, NV, USA, *Toxicol. Reports*, 3, 785–795, doi:10.1016/j.toxrep.2016.09.009, 2016.
 - Kim, S., Park, S. and Lee, J.: Evaluation of performance of inexpensive laser based PM2.5 sensor monitors for typical indoor and outdoor hotspots of South Korea, *Appl. Sci.*, 9(9), doi:10.3390/app9091947, 2019.
 - Knippertz, P. and Stuut, J. B. W.: Mineral dust: A key player in the earth system., 2014.
 - Kurniawati, S., Santoso, M., Lestiani, D. D., Atmodjo, D. P. D., Sari, D. K. and Kusmartini, I.: Identification of Potential Source Location of Sulfur at Urban Area Bandung using Conditional Probability Function (CPF), *IOP Conf. Ser. Earth Environ. Sci.*, 303(1), doi:10.1088/1755-1315/303/1/012042, 2019.
 - Li, Z., Guo, J., Ding, A., Liao, H., Liu, J., Sun, Y., Wang, T., Xue, H., Zhang, H. and Zhu, B.: Aerosol and boundary-layer interactions and impact on air quality, *Natl. Sci. Rev.*, 4(6), 810–833, doi:10.1093/nsr/nwx117, 2017.
 - Loodin, N.: Aral Sea: an environmental disaster in twentieth century in Central Asia, *Model. Earth Syst. Environ.*, 6(4), 2495–2503, doi:10.1007/s40808-020-00837-3, 2020.
 - Mahovic, N. S., Prieto, J., Jericevic, A., Gasparac, G. and Smiljanic, I.: EUMETSAT Webpage, [online] Available from: <https://www.eumetsat.int/aralkum-desert-dust-pollutes-air-south-east-europe> (Accessed 26 April 2021), 2020.
 - Manney, G. L., Livesey, N. J., Santee, M. L., Froidevaux, L., Lambert, A., Lawrence, Z. D., Millán, L. F., Neu, J. L., Read, W. G., Schwartz, M. J. and Fuller, R. A.: Record-Low Arctic Stratospheric Ozone in 2020: MLS Observations of Chemical Processes and

- Comparisons With Previous Extreme Winters, *Geophys. Res. Lett.*, 47(16), doi:10.1029/2020GL089063, 2020.
- Marécal, V., Peuch, V. H., Andersson, C., Andersson, S., Arteta, J., Beekmann, M., Benedictow, A., Bergström, R., Bessagnet, B., Cansado, A., Chéroux, F., Colette, A., Coman, A., Curier, R. L., Van Der Gon, H. A. C. D., Drouin, A., Elbern, H., Emili, E., Engelen, R. J., Eskes, H. J., Foret, G., Friese, E., Gauss, M., Giannaros, C., Guth, J., Joly, M., Jaumouillé, E., Josse, B., Kadygrov, N., Kaiser, J. W., Krajsek, K., Kuenen, J., Kumar, U., Liora, N., Lopez, E., Malherbe, L., Martinez, I., Melas, D., Meleux, F., Menut, L., Moinat, P., Morales, T., Parmentier, J., Piacentini, A., Plu, M., Poupkou, A., Queguiner, S., Robertson, L., Rouil, L., Schaap, M., Segers, A., Sofiev, M., Tarasson, L., Thomas, M., Timmermans, R., Valdebenito, Van Velthoven, P., Van Versendaal, R., Vira, J. and Ung, A.: A regional air quality forecasting system over Europe: The MACC-II daily ensemble production, *Geosci. Model Dev.*, 8(9), 2777–2813, doi:10.5194/gmd-8-2777-2015, 2015.
 - Marinoni, A., Cristofanelli, P., Calzolari, F., Roccatò, F., Bonafè, U. and Bonasoni, P.: Continuous measurements of aerosol physical parameters at the Mt. Cimone GAW Station (2165 m asl, Italy), *Sci. Total Environ.*, 391(2–3), 241–251, doi:10.1016/j.scitotenv.2007.10.004, 2008.
 - Masic, A., Bibic, D., Pikula, B., Blazevic, A., Huremovic, J. and Zero, S.: Evaluation of optical particulate matter sensors under realistic conditions of strong and mild urban pollution, *Atmos. Meas. Tech.*, 13(12), 6427–6443, doi:10.5194/amt-13-6427-2020, 2020.
 - Mie, G.: Beiträge zur Optik trüber Medien, speziell kolloidaler Metallösungen, *Ann. Phys.*, 330(3), 377–445, doi:10.1002/andp.19083300302, 1908.
 - NASA: AERONET Inversion Products, Weather, 1–6, 2006.
 - National Centers for Environmental Prediction/National Weather Service/NOAA/US Department of Commerce: NCEP GFS 0.25 Degree Global Forecast Grids Historical Archive, , doi:https://doi.org/10.5065/D65D8PWK, 2015.
 - Okin, G. S., Mahowald, N., Chadwick, O. A. and Artaxo, P.: Impact of desert dust on the biogeochemistry of phosphorus in terrestrial ecosystems, *Global Biogeochem. Cycles*, 18(2), doi:10.1029/2003GB002145, 2004.
 - Pandolfi, M., Tobias, A., Alastuey, A., Sunyer, J., Schwartz, J., Lorente, J., Pey, J. and Querol, X.: Effect of atmospheric mixing layer depth variations on urban air quality and daily mortality during Saharan dust outbreaks, *Sci. Total Environ.*, 494–495, 283–289, doi:10.1016/j.scitotenv.2014.07.004, 2014.
 - Prather, K. A., Wang, C. C. and Schooley, R. T.: Reducing transmission of SARS-CoV-2: Masks and testing are necessary to combat asymptomatic spread in aerosols and droplets, *Science (80-.)*, 368(6498), 1422–1424, doi:10.1126/science.abc6197, 2020.
 - Prospero, J. M., Ginoux, P., Torres, O., Nicholson, S. E. and Gill, T. E.: Environmental characterization of global sources of atmospheric soil dust identified with the Nimbus 7 Total Ozone Mapping Spectrometer (TOMS) absorbing aerosol product, *Rev. Geophys.*, 40(1), 2-1-2–31, doi:10.1029/2000RG000095, 2002.
 - Rashki, A., Kaskaoutis, D. G. and Sepehr, A.: Statistical evaluation of the dust events at selected stations in Southwest Asia: From the Caspian Sea to the Arabian Sea, *Catena*, 165, 590–603, doi:10.1016/j.catena.2018.03.011, 2018.
 - Renard, J.-B., Dulac, F., Berthet, G., Lurton, T., Vignelles, D., Jégou, F., Tonnelier, T., Jeannot, M., Couté, B., Akiki, R., Verdier, N., Mallet, M., Gensdarmes, F., Charpentier, P., Mesmin, S., Duverger, V., Dupont, J.-C., Elias, T., Crenn, V. and Sciare, D.: LOAC: a small aerosol optical particle counter/sizer for ground-based and balloon measurements of the size distribution and nature of atmospheric particles-Part 1: Principle of

- measurements and instrument evaluation, *Atmos. Meas. Tech.*, 9, 1721–1742, doi:10.5194/amt-9-1721-2016, 2016a.
- Renard, J. B., Dulac, F., Berthet, G., Lurton, T., Vignelles, D., Jégou, F., Tonnelier, T., Jeannot, M., Couté, B., Akiki, R., Verdier, N., Mallet, M., Gensdarmes, F., Charpentier, P., Mesmin, S., Duverger, V., Dupont, J. C., Elias, T., Crenn, V., Sciare, J., Zieger, P., Salter, M., Roberts, T., Gobbi, M., Hamonou, E., Olafsson, H., Dagsson-Waldhauserova, P., Camy-Peyret, C., Mazel, C., Décamps, T., Piringer, M., Surcin, J. and Daugeron, D.: LOAC: A small aerosol optical counter/sizer for ground-based and balloon measurements of the size distribution and nature of atmospheric particles-Part 1: Principle of measurements and instrument evaluation, *Atmos. Meas. Tech.*, 9(4), 1721–1742, doi:10.5194/amt-9-1721-2016, 2016b.
 - Renard, J. B., Dulac, F., Berthet, G., Lurton, T., Vignelles, D., Jégou, F., Tonnelier, T., Jeannot, M., Couté, B., Akiki, R., Verdier, N., Mallet, M., Gensdarmes, F., Charpentier, P., Mesmin, S., Duverger, V., Dupont, J. C., Elias, T., Crenn, V., Sciare, J., Zieger, P., Salter, M., Roberts, T., Giacomoni, J., Gobbi, M., Hamonou, E., Olafsson, H., Dagsson-Waldhauserova, P., Camy-Peyret, C., Mazel, C., Décamps, T., Piringer, M., Surcin, J. and Daugeron, D.: LOAC: A small aerosol optical counter/sizer for ground-based and balloon measurements of the size distribution and nature of atmospheric particles-Part 2: First results from balloon and unmanned aerial vehicle flights, *Atmos. Meas. Tech.*, 9(8), 3673–3686, doi:10.5194/amt-9-3673-2016, 2016c.
 - Rolph, G., Stein, A. and Stunder, B.: Real-time Environmental Applications and Display sYstem: READY, *Environ. Model. Softw.*, 95, 210–228, doi:10.1016/j.envsoft.2017.06.025, 2017.
 - Sajani, S. Z., Miglio, R., Bonasoni, P., Cristofanelli, P., Marinoni, A., Sartini, C., Goldoni, C. A., De Girolamo, G. and Lauriola, P.: Saharan dust and daily mortality in Emilia-Romagna (Italy), *Occup. Environ. Med.*, 68(6), 446–451, doi:10.1136/oem.2010.058156, 2011.
 - Sajani, S. Z., Bonasoni, P., Cristofanelli, P., Marinoni, A. and Lauriola, P.: Only coarse particles from the sahara?, *Epidemiology*, 23(4), 642–643, doi:10.1097/EDE.0b013e318258c23f, 2012.
 - Salvador, P., Molero, F., Fernandez, A. J., Tobías, A., Pandolfi, M., Gómez-Moreno, F. J., Barreiro, M., Pérez, N., Marco, I. M., Revuelta, M. A., Querol, X. and Artúñano, B.: Synergistic effect of the occurrence of African dust outbreaks on atmospheric pollutant levels in the Madrid metropolitan area, *Atmos. Res.*, 226, 208–218, doi:10.1016/j.atmosres.2019.04.025, 2019.
 - Schepanski, K.: Transport of mineral dust and its impact on climate, *Geosci.*, 8(5), doi:10.3390/geosciences8050151, 2018.
 - Sharma, A., Huang, H. P., Zavialov, P. and Khan, V.: Impact of Desiccation of Aral Sea on the Regional Climate of Central Asia Using WRF Model, *Pure Appl. Geophys.*, 175(1), 465–478, doi:10.1007/s00024-017-1675-y, 2018.
 - Shen, H., Abuduwaili, J., Samat, A. and Ma, L.: A review on the research of modern aeolian dust in Central Asia, *Arab. J. Geosci.*, 9(13), doi:10.1007/s12517-016-2646-9, 2016.
 - Shi, W., Wang, M. and Guo, W.: Long-term hydrological changes of the Aral Sea observed by satellites, *J. Geophys. Res. Ocean.*, 119(6), 3313–3326, doi:10.1002/2014JC009988, 2014.
 - Šikoparija, B.: Desert dust has a notable impact on aerobiological measurements in Europe, *Aeolian Res.*, 47, doi:10.1016/j.aeolia.2020.100636, 2020.

- SNPA: Sistema Nazionale Protezione Ambiente (SNPA) Webpage, [online] Available from: <https://www.snpambiente.it/2020/03/31/polveri-dal-mar-caspio-allitalia/> (Accessed 26 April 2021), 2020.
- Soupiona, O., Papayannis, A., Kokkalis, P., Foskinis, R., Sánchez Hernández, G., Ortiz-Amezcu, P., Mylonaki, M., Papanikolaou, C. A., Papagiannopoulos, N., Samaras, S., Groß, S., Mamouri, R. E., Alados-Arboledas, L., Amodeo, A. and Psiloglou, B.: EARLINET observations of Saharan dust intrusions over the northern Mediterranean region (2014-2017): Properties and impact on radiative forcing, *Atmos. Chem. Phys.*, 20(23), 15147–15166, doi:10.5194/acp-20-15147-2020, 2020.
- Stafoggia, M., Zauli-Sajani, S., Pey, J., Samoli, E., Alessandrini, E., Basagaña, X., Cernigliaro, A., Chiusolo, M., Demaria, M., Díaz, J., Faustini, A., Katsouyanni, K., Kelessis, A., Linares, C., Marchesi, S., Medina, S., Pandolfi, P., Pérez, N., Querol, X., Randi, G., Ranzi, A., Tobias, A., Forastiere, F., Angelini, P., Berti, G., Bisanti, L., Cadum, E., Catrambone, M., Davoli, M., de Donato, F., Gandini, M., Grosa, M., Ferrari, S., Pelosini, R., Perrino, C., Pietrodangelo, A., Pizzi, L., Poluzzi, V., Priod, G., Rowinski, M., Scarinzi, C., Stivanello, E., Dimakopoulou, K., Elefteriadis, K., Maggos, T., Michalopoulos, N., Pateraki, S., Petrakakis, M., Rodopoulou, S., Sypsa, V., Agis, D., Artiñano, B., Barrera-Gómez, J., de la Rosa, J., Diaz, J., Fernandez, R., Jacquemin, B., Karanasiou, A., Ostro, B., Salvador, P., Sanchez, A. M., Sunyer, J., Bidondo, M., Declercq, C., Le Tertre, A., Lozano, P., Pascal, L. and Pascal, M.: Desert dust outbreaks in Southern Europe: Contribution to daily PM10 concentrations and short-term associations with mortality and hospital admissions, *Environ. Health Perspect.*, 124(4), 413–419, doi:10.1289/ehp.1409164, 2016.
- Stein, A. F., Draxler, R. R., Rolph, G. D., Stunder, B. J. B., Cohen, M. D. and Ngan, F.: NOAA's Hysplit atmospheric transport and dispersion modeling system, *Bull. Am. Meteorol. Soc.*, 96(12), 2059–2077, doi:10.1175/BAMS-D-14-00110.1, 2015.
- Tositti, L., Riccio, A., Sandrini, S., Brattich, E., Baldacci, D., Parmeggiani, S., Cristofanelli, P. and Bonasoni, P.: Short-term climatology of PM10 at a high altitude background station in southern Europe, *Atmos. Environ.*, 65, 142–152, doi:10.1016/j.atmosenv.2012.10.051, 2013.
- Tositti, L., Brattich, E., Masiol, M., Baldacci, D., Ceccato, D., Parmeggiani, S., Stracquadanio, M. and Zappoli, S.: Source apportionment of particulate matter in a large city of southeastern Po Valley (Bologna, Italy), *Environ. Sci. Pollut. Res.*, 21(2), 872–890, 2014.
- Varga, G., Kovács, J. and Újvári, G.: Analysis of Saharan dust intrusions into the Carpathian Basin (Central Europe) over the period of 1979-2011, *Glob. Planet. Change*, 100, 333–342, doi:10.1016/j.gloplacha.2012.11.007, 2013.
- Washington, R., Todd, M., Middleton, N. J. and Goudie, A. S.: Dust-storm source areas determined by the total ozone monitoring spectrometer and surface observations, *Ann. Assoc. Am. Geogr.*, 93(2), 297–313, doi:10.1111/1467-8306.9302003, 2003.
- WHO for Europe: Air Quality Guidelines, *Air Qual. Guidel.*, 2006.
- Zhang, X. X., Claiborn, C., Lei, J. Q., Vaughan, J., Wu, S. X., Li, S. Y., Liu, L. Y., Wang, Z. F., Wang, Y. D., Huang, S. Y. and Zhou, J.: Aeolian dust in Central Asia: Spatial distribution and temporal variability, *Atmos. Environ.*, 238, doi:10.1016/j.atmosenv.2020.117734, 2020.

CHAPTER 7 - ATR-FTIR Spectroscopy, a New Non-Destructive Approach for the Quantitative Determination of Biogenic Silica in Marine Sediments

by Dora Melucci¹, Alessandro Zappi¹, Francesca Poggioli¹, Pietro Morozzi¹, Federico Giglio², and Laura Tositti¹

¹ Department of Chemistry “G. Ciamician”, University of Bologna, 40126 Bologna, Italy

² Polar Science Institute-National Research Council ISP-CNR, Via P. Gobetti 101, 40129 Bologna, Italy

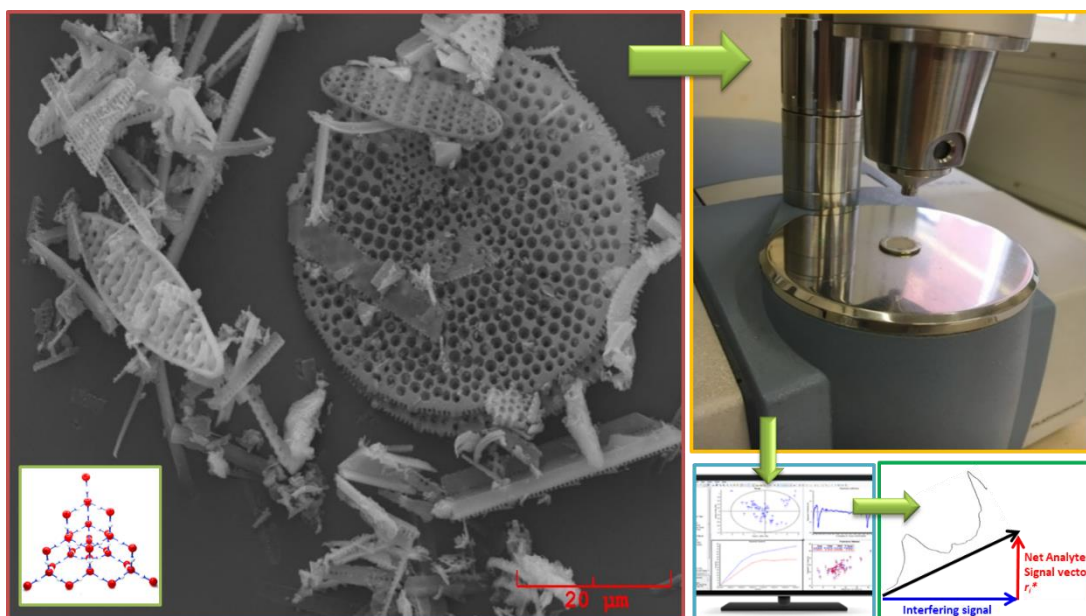
Molecules 2019, 24(21), 3927; <https://doi.org/10.3390/molecules24213927>



© 2019 by the authors. Licensee MDPI, Basel, Switzerland. This article is an open access article distributed under the terms and conditions of the Creative Commons Attribution (CC BY) license (<http://creativecommons.org/licenses/by/4.0/>).

Abstract

Biogenic silica is the major component of the external skeleton of marine micro-organisms, such as diatoms, which, after the organisms death, settle down onto the seabed. These micro-organisms are involved in the CO₂ cycle because they remove it from the atmosphere through photosynthesis. The biogenic silica content in marine sediments, therefore, is an indicator of primary productivity in present and past epochs, which is useful to study the CO₂ trends. Quantification of biosilica in sediments is traditionally carried out by wet chemistry followed by spectrophotometry, a time-consuming analytical method that, besides being destructive, is affected by a strong risk of analytical biases owing to the dissolution of other silicatic components in the mineral matrix. In the present work, the biosilica content was directly evaluated in sediment samples, without chemically altering them, by attenuated total reflection Fourier transform infrared (ATR-FTIR) spectroscopy. Quantification was performed by combining the multivariate standard addition method (MSAM) with the net analyte signal (NAS) procedure to solve the strong matrix effect of sediment samples. Twenty-one sediment samples from a sediment core and one reference standard sample were analyzed, and the results (extrapolated concentrations) were found to be comparable to those obtained by the traditional wet method, thus demonstrating the feasibility of the ATR-FTIR-MSAM-NAS approach as an alternative method for the quantification of biosilica. Future developments will cover in depth investigation on biosilica from other biogenic sources, the extension of the method to sediments of other provenance, and the use higher resolution IR spectrometers.



Keywords: diatoms; biogenic silica; ATR-FTIR; chemometrics; NAS

1 – Introduction

In the present work, we introduce an innovative and non-destructive method for the quantification of biogenic silica in marine sediments through the use of infrared spectroscopy combined with chemometrics. The proposed method was applied to sediment samples coming from Terra Nova Bay, Antarctica.

Antarctica is a unique natural laboratory because it is the coldest, driest, highest, windiest, and most isolated continent. Therefore, it is almost unaffected by anthropogenic influence (Casalino et al., 2013). The Southern Ocean allows the diffusion of atmospheric carbon dioxide into the deep sea, which is partially used by sea plants for growth and for the production of organic matter (Toggweiler et al., 2006). Therefore, this region is one of the most important for the study of climate changes and conditions of the ocean (Sprenk et al., 2013).

In particular, an important tool to control the chemical composition of seawater and to reconstruct paleo-ocean conditions is represented by marine sediments, which are a reservoir and a sink of chemical species involved and cycled in the marine food chain (Casalino et al., 2013). Among nutrients, silicon is an essential element in the ocean ecosystems, because it is responsible for the growth of Radiolaria, Sponges, Phaeodaria, and particularly Diatoms, which represent a major portion of planktonic primary producers (Kamatani et al., 2000). Diatoms are planktonic unicellular microalgae, known to form an external skeleton called frustule, constituted by amorphous silica and organic components (usually including long-chain polyamines and silaffins) (Kröger et al., 2008; Sumper et al., 2002). After their death, the diatom siliceous skeleton settles down through the water column. The extent of diatom deposition in the sediments will be a function of the sea bottom depth and of the degree of solubilization of opal silica in the water column (DeMaster et al., 1981). Siliceous microfossils, therefore, can represent a large part of the mass of biogenic sediments accumulating on the deep-sea floor (Broecker et al., 1983).

In the whole Southern Ocean, the Ross Sea is the region of the most widely extensive algal blooms, usually initiating in the Ross Sea polynya (Sullivan et al., 1993), an ice-free area of

enhanced bio-productivity that can be considered as a biological “hot spot” compared with the surrounding waters. This area extends to the open sea surface as soon as the austral summer develops and the sea ice melts (Smith et al., 1997; Arrigo et al., 2000). It plays a key climatic role on a global scale. Indeed, the Ross Sea is one of the main sink areas for the tropospheric CO₂, widely contributing to counterbalancing its budget and the associated role in climate change (Sandrini et al., 2007; Manno et al., 2007). In the western Ross Sea, the polynya of Terra Nova Bay (TNB) is an area of high accumulation of biogenic silica in the sediments (Ledford-Hoffman et al., 1986; Frignani et al., 2003).

Biogenic silica (BSi) content in marine sediment can be considered as a good proxy to characterize the bio-productivity of the Southern Ocean (Petrovskii et al., 2016; Maldonado et al., 2019). However, the quantification of BSi is complicated by the presence of lithogenic silica, which is chemically equivalent to BSi (SiO₂), with the only difference being crystalline, while BSi is amorphous. Several methods have been proposed to estimate BSi in marine sediments: (1) X-ray diffraction after the conversion of opal to cristobalite at a high temperature (Calvert et al., 1966); (2) direct X-ray diffraction of amorphous silica (Eisma et al., 1971); (3) direct infrared spectroscopy of amorphous opal (Chester et al., 1968); (4) elemental partitioning of sediment chemistry (Nancy Ann, 2008; Leinen, 1977); (5) microfossil counts (Leinen et al., 1985; Pokras et al., 1986); and (6) several wet-alkaline extraction methods (DeMaster et al., 1981; Donald et al., 2003; Mortlock et al., 1989)

Among the above-mentioned techniques, the wet alkaline methods are the most popular because they are the most sensitive techniques for BSi assessment. According to these methods, BSi is extracted and distinguished from lithogenic silica based on hot alkaline solutions (DeMaster et al., 1981). Wet methods exploit a different rate of dissolution of lithogenic and biogenic silica in alkaline solution, with BSi dissolving more quickly than the mineral component. Solubilized BSi can, therefore, be collected in the supernatant of the solution, and subsequently determined by spectrophotometry. Such separations are extremely demanding and time-consuming, and above all, they do not ensure the quantitative recovery of BSi, owing to inherent systematic problems; that is, dependence on matrix effects, incomplete opal recovery, and contamination by non-biogenic silica (Maldonado et al., 2019; Leinen et al., 1985).

The increasing success of chemometric tools applied to basic spectrophotometric techniques such as Fourier transform infrared (FTIR), together with the compelling need for understanding key biogeochemical processes of global importance, have recently inspired the introduction of an alternative approach to solve the problem of BSi assessment. In particular, FTIR spectroscopy has been applied to lacustrine sediments for the analysis of silica and other minerals by Rosén et al., 2000 and Rosén et al., 2005. Vogel et al. 2008 and Rosén et al. 2011 showed that FTIR spectroscopy in the mid-infrared region is highly sensitive to chemical components present in minerogenic and organic material, such as sediments; this fact provides an efficient tool for qualitative and quantitative characterization of these fundamental, but complex environmental matrices.

Moreover, a method based on attenuated total reflectance (ATR)-FTIR measurements has also been proposed in the literature to quantify inorganic components in marine sediments (Mecozzi et al., 2001; Khoshmanesh et al., 2012). ATR-FTIR spectroscopy is particularly appealing for the analysis of sediments because no chemical sample pre-treatment is required: it may in principle by-pass all the drawbacks of the wet-chemical method; moreover, it works with small amounts of sample material (0.05–0.1 g, dry weight) and it is rapid, inexpensive, and efficient. Besides, ATR-FTIR is a non-destructive method, allowing to recover the sample for further analyses, and it can be carried out even off the lab.

In the present work, we developed and present an analytical method based on ATR-FTIR for the quantitative determination of biosilica content in marine sediments. The feasibility of the method was evaluated by quantifying BSi in a series of sediment samples collected in the Ross Sea. Optimization of the experimental procedures such as the drying process, homogenization, and deposition of the sample on the ATR crystal are discussed in detail, in order to provide a reliable background useful to solve reproducibility problems, which may constitute a drawback of such a simple instrumental approach. Furthermore, the strong matrix effect intrinsic to environmental samples is faced and solved by applying a multivariate standard addition method (MSAM) (Melucci et al., 2012), improved by net analyte signal (NAS) computation (Lorber et al., 1997; Bro et al., 2003).

2 – Results and Discussion

2.1 ATR Spectra

For each of the 22 analyzed sediment samples (21 coming from Mooring D and one 53%_{w/w} reference standard), four standard-added (add.x) samples were prepared: the zero-added sample (add.0) is the pure sample, add.1 has an added concentration of diatomite at 5%_{w/w}, add.2 at 10%_{w/w}, and add.3 at 15%_{w/w}. All added samples (and a pure diatomite sample) were analyzed by ATR-FTIR.

In the ATR spectra of marine sediments, the contribution of silica, both biogenic and lithogenic, is dominant. Such spectra exhibit four characteristic vibrational bands. The two main bands at 1100 and 471 cm^{-1} are attributed to triply degenerated stretching and bending vibration modes, respectively, of the $[\text{SiO}_4]$ tetrahedron (Malandrino et al., 2010). The band at 800 cm^{-1} corresponds to an inter-tetrahedral Si–O–Si bending vibration mode, and the band near 945 cm^{-1} to an Si–OH vibration mode (Dunbar et al., 1985). Previous studies have shown that the absorbance centered around 1640 cm^{-1} and between 3000 and 3750 cm^{-1} can be attributed to hydroxyl vibrations because hydroxyl ions are major constituents of clay minerals, opal, and organic compounds present in marine sediments (Liu et al., 1999). However, these bands are not specific for silica, their intensity is generally low (about one-tenth of the main band); moreover, they are overlapped with the residual absorption bands of H_2O . Therefore, to reduce the noise in the spectral data acquired, we decided to discard the IR region between 4000 and 1300 cm^{-1} and to apply the chemometric procedure only in the region between 1300 and 400 cm^{-1} .

Figure 1 shows the raw spectra of sample D10 (as an example of the spectra obtained for all sediment samples) and the replicates of a pure-diatomite sample. In Figure 1a, spectra obtained by instrumental analysis are shown, while Figure 1b highlights the effect of the spectral pre-treatments: uninformative-band removal and MSC.

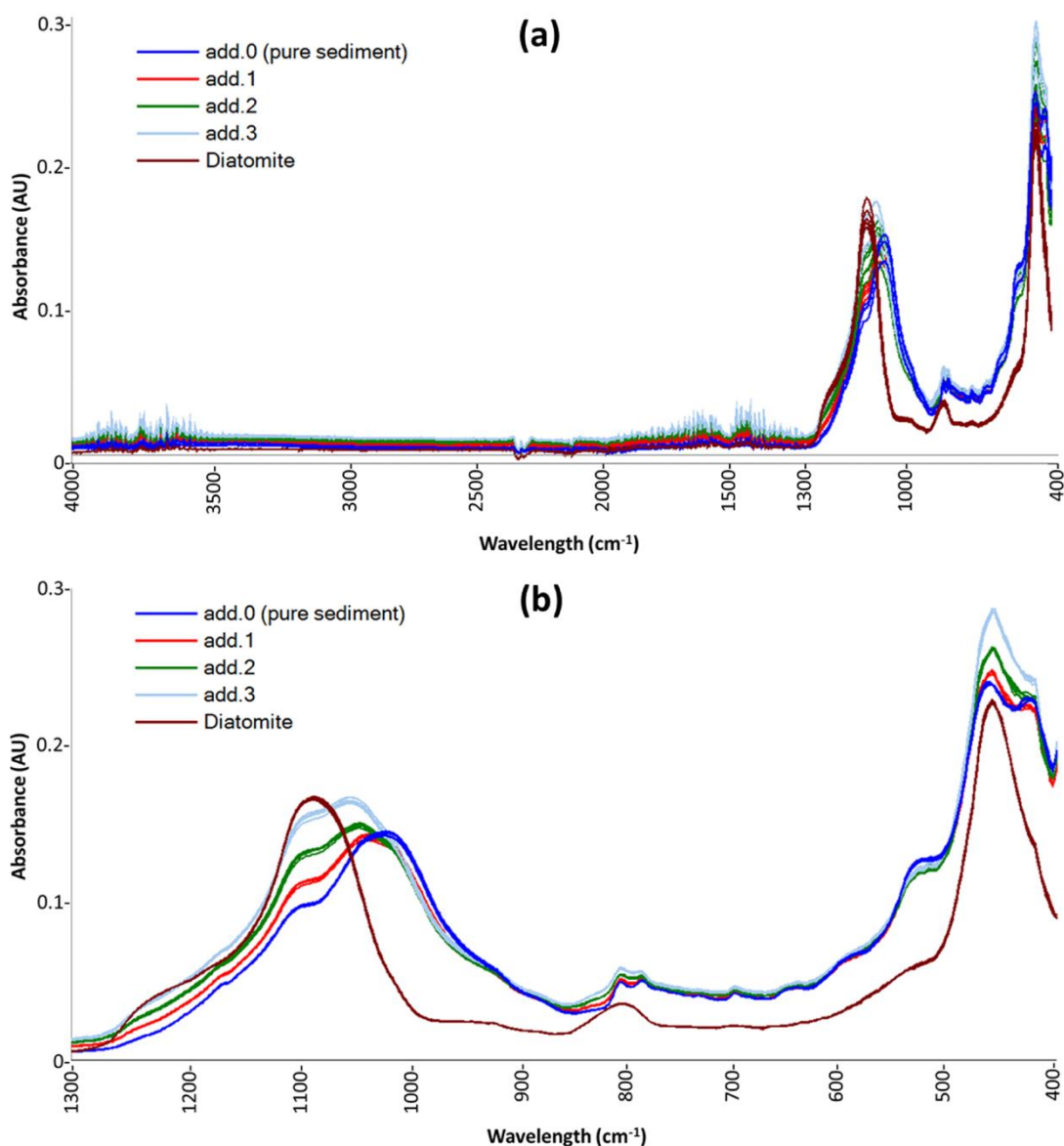


Figure 1. (a) ATR raw spectra of sample D10, as obtained from the spectrophotometer; (b) the same spectra after band removal (discarding the IR range 4000–1300 cm⁻¹) and after multiplicative scatter correction (MSC) pre-treatment. “add.” in the legends indicates standard added samples.

On the spectra reported in Figure 1b, the two chemometric procedures described in Section 3.4 were carried out for all sediment samples, and the results are reported in Table 1. The expected values reported in Table 1 are the BSi concentrations obtained by wet analyses that were carried out only on five sediment samples (and on 53% w/w-standard): D4, D6, D9, D18, and D21.

Table 1. Net analyte signal (NAS) results for the two pre-processing methods. All the numbers are formatted with three significant digits to allow for a detailed comparison. LoD, limit of detection.

Sample code	Expected Value \pm Standard Deviation (% _{ow/w})	Procedure 1				Procedure 2			
		NAS Extr. C (% _{ow/w})	Standard Deviation	R ²	LoD	NAS Extr. C (% _{ow/w})	Standard Deviation	R ²	LoD
Std 53%	53 \pm 3	53.6	6.02	0.992	1.01	50.2	2.74	0.988	7.76
D0	-	3.23	0.903	0.996	0.0265	8.64	3.01	0.956	2.39
D1	-	3.24	1.92	0.993	0.190	-	-	-	-
D2	-	9.88	1.70	0.994	0.416	9.28	1.23	0.990	6.24
D3	-	7.55	0.315	0.993	0.743	8.40	0.436	0.999	4.08
D4	13 \pm 2	12.0	1.16	0.988	0.469	12.8	2.01	0.988	3.58
D5	-	5.41	1.10	0.993	0.0214	5.38	1.75	0.995	2.88
D6	14 \pm 2	14.2	1.54	0.989	0.00946	14.2	2.71	0.997	1.41
D7	-	5.87	1.27	0.999	0.646	-	-	-	-
D8	-	9.45	0.671	0.993	0.380	-	-	-	-
D9	8 \pm 1	8.26	3.16	0.986	0.654	8.91	0.514	0.982	4.68
D10	-	12.0	1.18	0.997	0.515	12.1	2.12	0.995	0.267
D11	-	2.94	0.646	0.994	0.0666	3.84	0.803	0.993	1.76
D12	-	-	-	-	-	10.6	2.32	0.995	2.32
D13	-	-	-	-	-	3.72	1.81	0.987	3.82
D14	-	9.00	0.146	0.998	0.133	10.9	0.433	0.998	7.62
D15	-	3.25	0.184	0.993	0.0784	5.19	0.122	0.996	2.22
D16	-	-	-	-	-	5.63	1.38	0.989	3.60
D17	-	2.71	0.535	0.994	0.0647	13.7	1.41	0.984	1.93
D18	4.2 \pm 0.6	4.80	1.67	0.996	0.0900	5.16	1.70	0.992	4.34
D19	-	4.04	0.332	0.998	0.0459	3.22	0.345	0.997	1.23
D20	-	2.36	0.535	0.999	0.610	4.26	1.19	0.991	8.46
D21	3.4 \pm 0.5	3.12	1.86	0.998	0.653	4.12	0.296	0.993	3.93

2.2 Results: Procedure 1

To assess the reliability of the new methodology proposed here, the BSi results obtained here can be compared to those achieved through the traditional wet method, taken as a reference. Table 1 shows that the results obtained with Procedure 1 (band removal and MSC) are in good agreement with the expected values obtained when samples were analyzed with the wet method. Indeed, the confidence intervals obtained for these five sediment samples by NAS are not significantly different from the ones obtained by the wet method (at 0.05 significance). Also, the result obtained for the standard sample (Std 53%_{w/w}) is in agreement with the expected concentration. The coefficients R² of the NAS standard addition lines are all higher than 0.98, indicating a good correlation between added concentrations (dependent variable) and the pseudo-univariate NAS values calculated by the chemometric procedure. The LoD values are also very good, being, in general, in the order of magnitude of one-tenth (or even lower) with respect to the corresponding extrapolated BSi concentration.

Moreover, Frignani et al., 2003 reported that BSi concentration in surface sediments in this area is usually relatively low, $<10\%_{w/w}$; the results obtained by NAS are in agreement with this consideration, as D0, D1, D2, and D3 extrapolated concentrations are lower than the indicated value.

All these considerations confirm that NAS applied to ATR spectra of the standard added samples can be a valuable and reliable alternative to the time-consuming wet method for the quantification of BSi in marine sediments.

The main drawbacks concern the three samples for which no results were obtained: D12, D13, and D16. In these cases, the NAS standard addition lines had, for all PLS-factors, either a negative slope or intercept, giving negative extrapolated values, or not acceptable R^2 (lower than 0.7), that make any possible result unreliable. The reason for such behavior is still under study, but we can hypothesize that there is still some source of noise in ATR analysis that was not taken into account, although several precautions were taken during instrumental analyses, as described in Section 3.3. We, therefore, decided to proceed with further chemometric assessments, also to test the hypothesis of a possible defect in the NAS procedure.

2.3 Results: Procedure 2

As described in Section 3.4, a variable selection was carried out on baseline-corrected spectra. Correlation loadings on PLS-factor 1 were used to select the most important variables to describe the regression model. Although a different variable selection was carried out for each sediment sample, not always giving the same variables, a general description of the selected IR bands can be drawn and is resumed in Figure 2. High correlation loading values in the PLS-factor 1 are computed in the regions of $1260\text{--}1060\text{ cm}^{-1}$, $830\text{--}800\text{ cm}^{-1}$, and $467\text{--}436\text{ cm}^{-1}$. These regions of the IR spectra correspond to the characteristic SiO_2 absorbance maxima as reported by Vogel et al., 2008. On these selected variables, NAS computation was carried out and the results are reported in the last vertical section of Table 1.

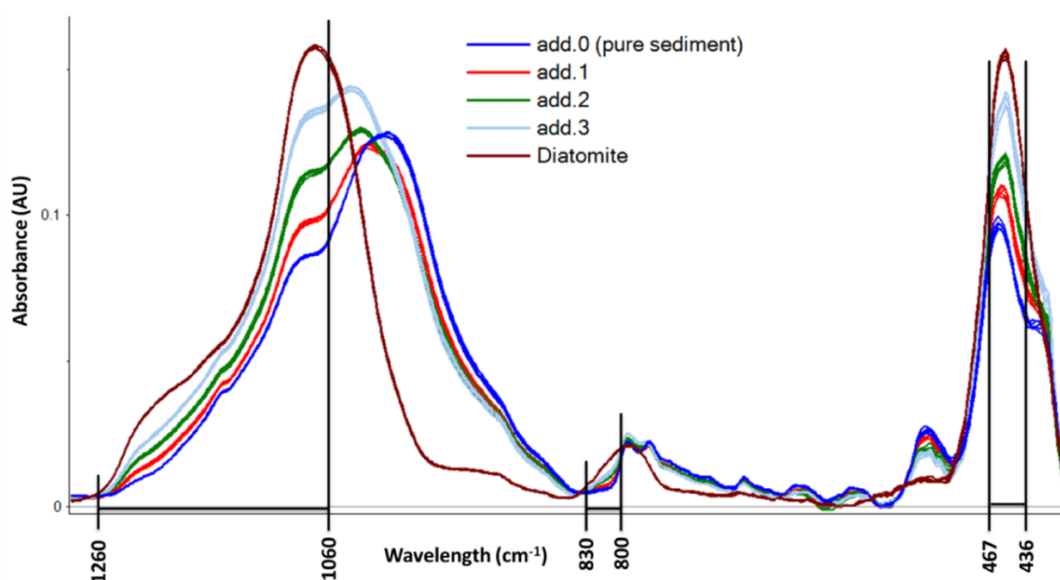


Figure 2. Baseline-corrected ATR spectra of sample D10. Black lines indicate the variables considered most important by partial least square (PLS) correlation loadings.

Again, concentrations extrapolated by NAS are not significantly different from the “wet method-based” values, with high R^2 (>0.95). After the application of this second procedure (baseline correction and variable selection before NAS), significant differences were detected only for D0 and D17, which, in this case, also have a lower R^2 compared with the other samples. In this case, some problems arise from LoDs, which, in most cases, are comparable to the extrapolated value (and also higher than that for D20). Such a drawback might, therefore, be because of the spectral pre-treatment; in order to calculate LoD, a blank spectrum is necessary. However, such a blank spectrum has to be pre-treated as all the other spectra, and in this case, it has to be baseline corrected. In this way, the pre-treatment can likely produce some spikes in the blank spectrum (that is, a noisy signal oscillating around the zero), thus affecting the computation of LoD.

The three samples that did not give results with the computation by Procedure 1 (D12, D13, and D16) in this case have an acceptable extrapolated concentration. However, there are again three samples (D1, D7, and D8) with no result. This strengthens the hypothesis of the presence of a noise source that was not taken into account. Indeed, variable selection may reduce the noise present in the whole spectrum, but, at the same time, if noise is present in the selected variables, its effect may be enhanced. Therefore, the two chemometric methods presented in this work may be considered to be complementary for this study.

3 – Materials and Methods

3.1 Study Area

Sediment samples for the present study were collected in “mooring D” (or “site D”), which is located in Antarctica, in the western sector of the Ross Sea continental shelf within the polynya of Terra Nova Bay at $75^{\circ}06' S$ and $164^{\circ}28'5'' E$ (Figure 3). The box-core, from which the sediments were collected, was sampled at a depth of 972 m during the 2003–2004 Italian PNRA (Programma Nazionale di Ricerca in Antartide) Campaign (Ramer et al., 2013), whose basis was situated in the “Mario Zucchelli” station.

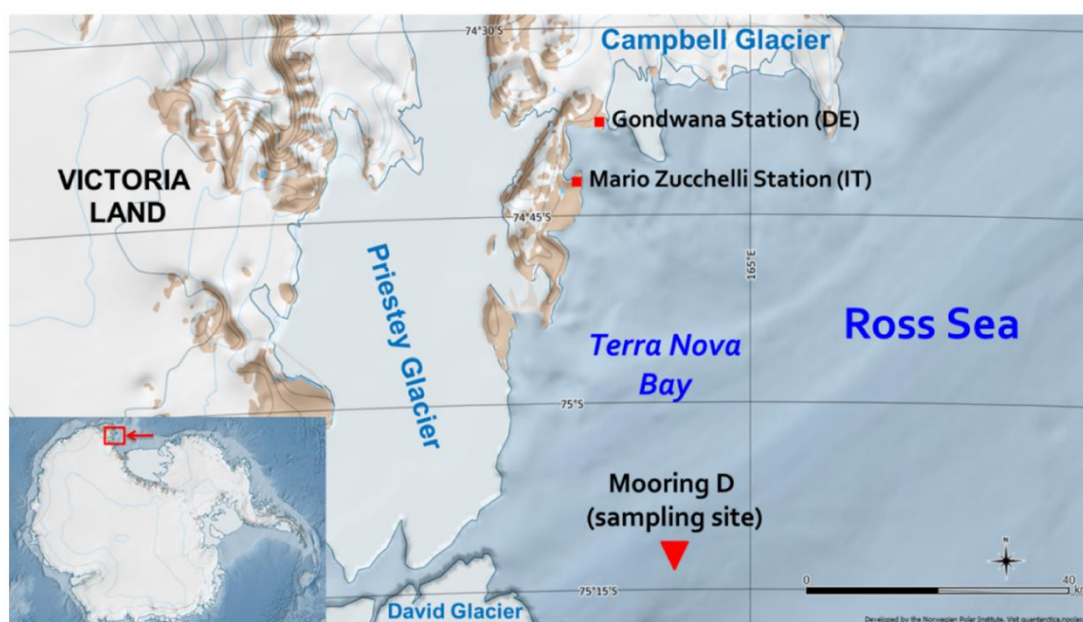


Figure 3. Sampling site (Mooring D) in Terra Nova Bay, Antarctica.

In the Ross Sea, surface sediments are generally composed of unsorted ice-rafted debris, terrigenous silts and clays, and siliceous and calcareous biogenic debris (Rinnan et al., 2009). In site D, in particular, coarse terrigenous deposits are predominant, owing to the proximity of Priestley, David, and Campbell glaciers (Frignani et al., 2003).

3.2 Samples

The sediment collected in site D was sampled using a 1T Oceanic box corer. A sub core 22 cm long was collected by means of a polyvinyl chloride (PVC) liner. The short core was subsampled with a resolution of 1 cm (Ramer et al., 2013). Twenty-two sediment sections were thus obtained and named with a two-digit code: a letter, “D”, indicating the sampling place; and a number, from 0 to 21, indicating the core height, with D0 being the top, corresponding to the sediment surface. Sediments were then stored at $-21\text{ }^{\circ}\text{C}$ in a polycarbonate Petri capsule and oven-dried at $50\text{ }^{\circ}\text{C}$ just prior to the analyses. The BSi content of five of these samples was also quantified by a wet method analysis, according to the DeMaster method (DeMaster et al., 1981; Frignani et al., 2003), thus providing some comparison values for the ATR analyses. In the absence of a commercial certified reference material for BSi, the “internal reference standard” used in the Polar Science Institute-National Research Council (CNR-ISP) laboratory was adopted for the purpose of this paper. This sample consists of an Antarctic marine sediment analyzed repeatedly both in CNR and other biogeochemical laboratories, resulting in a BSi content of $(53 \pm 3)\%_{\text{w/w}}$ and a remaining $47\%_{\text{w/w}}$ of alkaline halide.

For the sake of readability, a flowchart concerning the sample preparation is reported in Figure 4. Before sample preparation, all samples were manually ground in an agate mortar for approximately 15 min and heated in a ventilated oven at $105\text{ }^{\circ}\text{C}$ for 1 h to remove atmospheric moisture. Afterward, each sample was split into four aliquots, three of which were added with known amounts ($5\%_{\text{w/w}}$, $10\%_{\text{w/w}}$, $15\%_{\text{w/w}}$) of Diatomite (Celite® 545 AW, Sigma-Aldrich, Darmstadt, Germany), in order to apply the multivariate standard addition method. The total weight of each standard-added sample was 200 mg. Diatomite was chosen as a proxy of standard biogenic silica, because it is composed of frustulae of biogenic silica, similar to what we wanted to quantify in marine sediments. Such a similarity was visually evaluated by analyzing some samples with a scanning electron microscope (SEM) Philips 515B (Philips, Amsterdam, Netherlands), equipped with an EDAX DX4 microanalytical device (EDAX Inc., Mahwah, NJ, USA). Figure 5 shows the pictures obtained by SEM. From Figure 5c,d, it can be seen that samples D1 and D4 contain the same radiolaria present in the Diatomite (Figure 5a) used as a proxy of BSi.

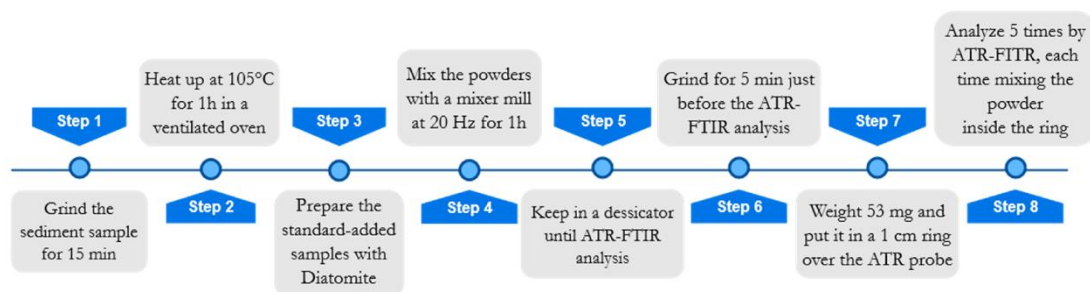


Figure 4. Sample preparation flowchart. ATR-FTIR, attenuated total reflection Fourier transform infrared.

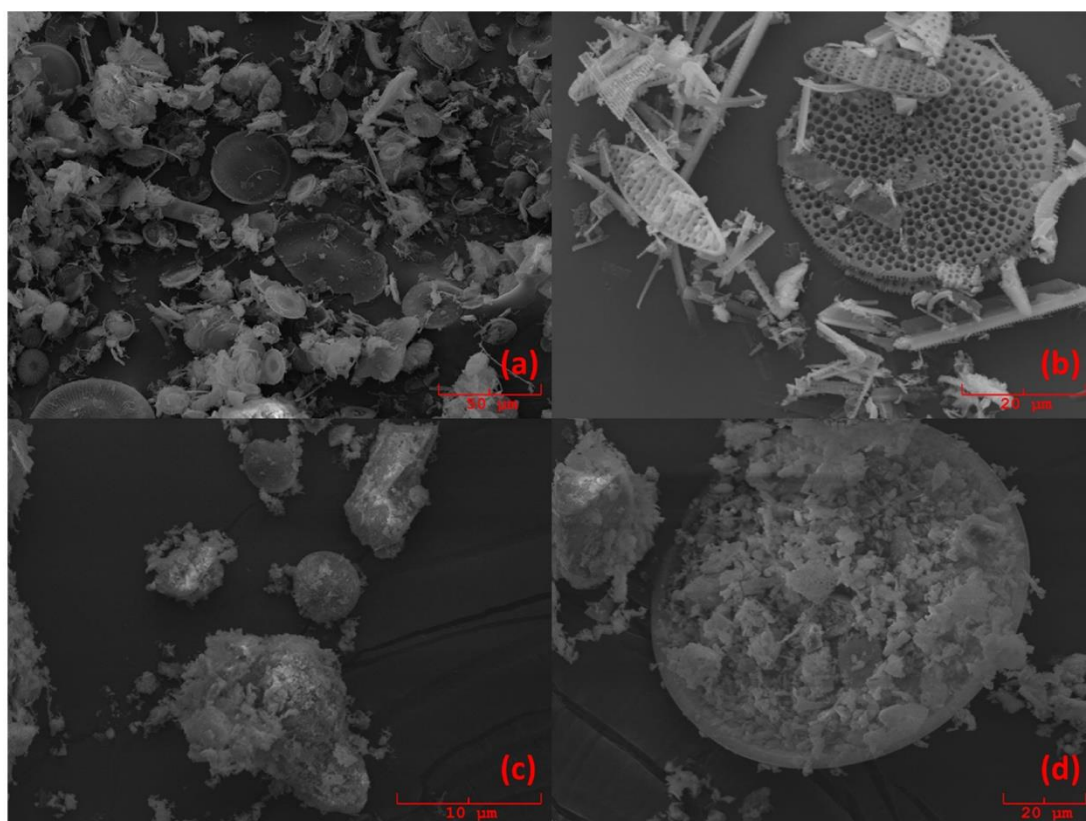


Figure 5. Scanning electron microscope (SEM) images of samples (a) pure diatomite; (b) 53% standard; (c) D1 sample, which is characterized by the presence of both radiolaria and bulks of sedimentary material; and (d) D4 sample.

To ensure better homogenization of the powders, a Mixer Mill “MM20” (Retsch Inc., Düsseldorf, Germany) was used. Each added sample was placed in stainless steel cylinders of 1.5 mL volume and left in the ball mill for 60 min at 20 Hz. Before the instrumental analysis, samples were kept in a desiccator filled with silica gel to prevent the absorption of atmospheric moisture. Standard added samples were then analyzed by ATR-FTIR spectroscopy.

3.3 ATR-FTIR Analysis

Attenuated total reflection spectra were collected using a Bruker ALPHA FT-IR spectrometer (Bruker Optics GmbH, Billerica, MA, USA) equipped with a single-reflection diamond ATR accessory (Bruker Platinum ATR, Billerica, MA, USA) with an approximately 0.6 mm × 0.6 mm active area and a mercury–cadmium–telluride detector. Spectra were collected in the mid-IR range, 400–4000 cm⁻¹, with an optical resolution of 4 cm⁻¹; the registered spectrum is the mean of 64 scans, executed in 3 min. For each sample aliquot, five replicate spectra were recorded to assess precision and ensure the reproducibility of each sample. All measurements were performed at ambient conditions. Before spectra acquisition, a background spectrum (air) was collected with the same operational parameters. Such a background was automatically subtracted to each sample spectrum.

To optimize the analytical reproducibility, some precautions were taken for ATR analysis. Indeed, it is widely reported in the literature how an imprecise sample preparation (especially drying process), sample deposition, and instrumental calibration may cause poor instrumental repeatability and accuracy, fundamental characteristics for quantification purposes (Mecozzi et al., 2001; Lorber et al., 1986). For these reasons, a suitable experimental protocol was developed and evaluated (Figure 4).

Before the instrumental analysis, samples were manually ground again for 5 min in an agate mortar, in order to homogenize powder granulometry. Moreover, for each added sample, an aliquot (53 mg) was carefully weighted and lodged in a steel ring of 1 cm in diameter, which was then placed over the spectrophotometer probe. The same amount of material was taken for all the analyzed samples, to maximize reproducibility and reduce scattering and other problems resulting from not optimal (or not constant) contact between the sample and crystal. These problems become relevant in ATR analysis when used for quantification purposes owing to the geometry of ATR irradiation and reflectance, which need an accurate evaluation and the adoption of a suitable experimental protocol (Wold et al., 2001).

3.4 Chemometrics

Prior to chemometric analysis, the five replicated spectra of each added sample were pre-treated by multiplicative scatter correction (MSC) (Stute et al., 1996). MSC allows the reduction of the effects of scattering noise on IR spectra, increasing the reproducibility of sample replicates.

Subsequently, in order to calculate the BSi content in each sediment sample by MSAM, the NAS procedure was applied (Bro et al., 2003; Hemmateenejad et al., 2009). NAS is a mathematical procedure that allows extracting, from a multivariate signal (in this case, an ATR spectrum), that part of the signal that is only due to the analyte, removing the other signals due to the other interfering species present in the matrix (Bro et al., 2003). In this way, the multivariate problem can be reduced to a pseudo-univariate problem, whose results can be obtained by a univariate treatment. NAS computations were performed as follows.

The NAS procedure starts from a partial least square (PLS) regression (Lorho et al., 2006), using the ATR spectra as independent variables (X) and the added concentrations vector as dependent one (y). The best PLS-factor (A) has to be selected and the corresponding PLS-regression coefficient vector (bA) is used to compute a projection matrix (H) as follows:

$$H = b_A(b_A b_A^t)^{-1} b_A^t \quad (1)$$

(1) where t indicates transpose and superscript “-1” indicates matrix inversion. H matrix is then used to compute NAS vectors (x_i^*):

$$x_i^* = H x_i \quad (2)$$

(2) where x_i are the rows of matrix X, which means samples of ATR spectra. Each calculated x_i^* corresponds to the net signal (devoid of interfering signals) of each replicate of the added samples. The Euclidean norms of such net signals can be then used as pseudo-univariate signals to compute a univariate standard addition linear regression line, from which BSi concentration can be obtained by extrapolation.

The selection of the optimal PLS-factor (A) is a crucial point of the procedure, because, in most of the cases, the final extrapolated concentration varies (also dramatically) while varying A. Therefore, A was chosen (sample by sample) as the PLS-factor that optimizes both the PLS root mean squared error (RMSE), by minimizing it, and the determination

coefficient (R^2) of the final pseudo-univariate line, by maximizing it. When these two conditions were not simultaneously achievable for one PLS-factor, A was chosen as the factor giving the best compromise between these two parameters, based on the highest R^2 .

The standard deviations of the extrapolated concentration values were computed by the jackknife method (Gendron-Badou et al., 2003). Once the optimal PLS-factor is selected, the jackknife procedure replicates the NAS computation as many times as the number of objects (x_i), each time keeping out one object. In this way, i different extrapolated values are obtained for each NAS computation and the overall standard deviation is estimated as the standard deviation of the jackknife-extrapolated values.

Limits of detection (LoDs) were computed collecting five replicates (the same number of the other samples) of a blank spectrum (empty sample holder) and projecting them onto the NAS space by Equation (2) as if they were real samples (Meyer-Jacob et al., 2014). The so obtained NAS-blank signals were mediated to obtain the vector ε , and the LoD was computed as follows (Meyer-Jacob et al., 2014):

$$LoD = 3 \frac{\|\varepsilon\|}{\|b_A\|} \quad (3)$$

(3) where $\|\cdot\|$ indicates the Euclidean norm.

The so far described procedure (Procedure 1) was applied to raw spectra, as they were obtained from the spectrophotometer. This procedure gave reasonable results for the majority of the samples, while it failed for three of them; in those cases, for all PLS-factors, the final NAS standard addition line had either a negative slope or intercept, producing a negative extrapolated concentration. The reason behind such behavior is still under evaluation. In order to obtain a result for each sediment sample, another chemometric procedure (Procedure 2) has thus been developed. Instead of using raw spectra, a baseline correction was applied directly by the software controlling the instrument, OPUS v.7.2 (Bruker). MSC was applied to baseline-corrected spectra and, before NAS computation, a variable selection was applied. For variable selection, another PLS regression was computed (previously to the one used for NAS). Only factor 1, always retaining more than 95% of the explained variance, was considered, and the variables giving correlation loadings (Colthup et al., 1990) higher than 0.7 (in absolute value) were retained as important. NAS computation was then applied only with these selected variables. The standard deviations on the extrapolated values and LoDs were calculated as before.

MSC and variable selection pre-processing were performed by the software The Unscrambler v.10.3 (CAMO, Oslo, Norway), while NAS and jackknife procedures were computed by a homemade code in R environment (R Core Team, Vienna, Austria).

4 – Conclusions

In this study, we demonstrated the feasibility of a new approach for the quantification of biogenic silica based on IR spectroscopy coupled with chemometrics. Biogenic silica content in marine sediments from Terra Nova Bay in West Antarctica was evaluated with Fourier-transform infrared spectroscopy in attenuated total reflection mode (ATR-FTIR). For quantification, the multivariate standard addition method (MSAM) was applied, and the net analyte signal (NAS) procedure was used to solve the problems deriving from the strong matrix effect affecting such analyses.

Twenty-one subsequent core samples and one reference standard were analyzed. Reliable results were obtained, as observed from the comparison with homologous data from the traditional wet method.

Some drawbacks remain. The chemometric procedure did not give acceptable results for some samples, even if a variable selection was carried out. Moreover, the limits of detection, and perhaps also standard deviations, are in some cases still too high.

However, it has to be taken into account that the quantification of biosilica, in this work, has been carried out with an analytical technique (ATR) that has several intrinsic drawbacks when performing quantitative analysis. In particular, owing to the optical behavior of photons at such low angles as in ATR, extremely careful handling of samples and highly reproducible sample geometry are required when analyzing powdered samples. Moreover, the analyzed samples are powders, which, despite all the precautions taken before and during the analysis, can still have some problems concerning homogeneity and granulometry. The BSi content was also evaluated in natural samples without any chemical pre-treatment, thus its analytical signal may be strongly affected by the presence of lithogenic silica, besides all the other species composing the sediments.

Considering all these aspects, the analytical and chemometric procedure presented in this work, although requiring some more refinements, can be considered a promising alternative to the traditional time-consuming wet method for the quantification of biosilica in marine sediments. In paleolimnological research, the ATR-FTIR technique is seldom used. The results presented here, as well as the fact that this method is fast and cost-effective, requiring only small quantities of sediment sample, should encourage more researchers to use it. Moreover, marine sediments are precious samples, which are difficult to collect; thus, a non-destructive method would be preferable to analyze them, although ATR-FTIR cannot yet entirely replace conventional analytical tools in paleolimnology.

Author Contributions

Conceptualization, D.M., F.G., and L.T.; Methodology, D.M., A.Z., F.G., and F.P.; Software, A.Z. and F.P.; Validation, A.Z. and P.M.; Formal Analysis, F.P., A.Z., and P.M.; Investigation, F.P.; Resources, F.G. and L.T.; Data Curation, D.M., A.Z., and F.P.; Writing—Original Draft Preparation, A.Z. and F.P.; Writing—Review & Editing, D.M., A.Z., P.M., and L.T.; Visualization, F.P. and F.G.; Supervision, D.M.; Project Administration, L.T.

Funding

This study has been conducted with the financial support of the Italian National Research Program for Antarctica (PNRA).

Acknowledgements

We are indebted to the Italian participants to the XIX Expedition to Antarctica, in the year 2003/04, for carrying out the samplings. We are deeply grateful to Prof. Giorgio Gasparotto, of the Department of Biological, Geological, and Environmental Sciences, University of Bologna for kindly providing the access to his SEM facility and the precious support in producing the diatom images employed herein.

Conflicts of Interest

The authors declare no conflict of interest.

References

1. Arrigo, K.R.; DiTullio, G.R.; Dunbar, R.B.; Robinson, D.H.; VanWoert, M.; Worthen, D.L.; Lizotte, M.P. Phytoplankton taxonomic variability in nutrient utilization and primary production in the Ross Sea. *J. Geophys. Res. Ocean.* **2000**, *105*, 8827–8846. [[Google Scholar](#)] [[CrossRef](#)]
2. Bro, R.; Andersen, C.M. Theory of net analyte signal vectors in inverse regression. *J. Chemom.* **2003**, *17*, 646–652. [[Google Scholar](#)] [[CrossRef](#)]
3. Broecker, W.S. Tracers in the sea. *Geochim. Cosmochim. Acta* **1983**, *47*, 1336. [[Google Scholar](#)]
4. Calvert, S.E. Accumulation of diatomaceous silica in the sediment of the Gulf of California. *Geol. Soc. Am. Bull.* **1966**, *77*, 569–572. [[Google Scholar](#)] [[CrossRef](#)]
5. Casalino, C.E.; Malandrino, M.; Giacomino, A.; Abollino, O. Total and fractionation metal contents obtained with sequential extraction procedures in a sediment core from Terra Nova Bay, West Antarctica. *Antarct. Sci.* **2013**, *25*, 83–98. [[Google Scholar](#)] [[CrossRef](#)]
6. Chester, R.; Elderfield, H. The infrared determination of opal in siliceous deep-sea sediments. *Geochim. Cosmochim. Acta* **1968**, *32*, 1128–1140. [[Google Scholar](#)] [[CrossRef](#)]
7. Colthup, N.B.; Daly, L.H.; Wiberley, S.E. *Introduction to Infrared and Raman Spectroscopy*, 3rd ed.; Academic Press: San Diego, CA, USA, 1990; ISBN 978-0-12-182554-6. [[Google Scholar](#)]
8. DeMaster, D.J. The supply and accumulation of silica in the marine environment. *Geochim. Cosmochim. Acta* **1981**, *45*, 1715–1732. [[Google Scholar](#)] [[CrossRef](#)]
9. Donald, W.; Eggimann, F.T.M. Dissolution and Analysis of Amorphous Silica in Marine Sediments. *SEPM J. Sediment. Res.* **2003**, *50*, 215–225. [[Google Scholar](#)]
10. Dunbar, R.B.; Anderson, J.B.; Domack, E.W.; Jacobs, S.S. Oceanographic influences on sedimentation along the Antarctic continental shelf. In *Antarctic Research Series*; American Geophysical Union: Washington, DC, USA, 1985; pp. 291–312. [[Google Scholar](#)]
11. Eisma, D.; Van Der Gaast, S.J. Determination of opal in marine sediments by X-ray diffraction. *Netherlands J. Sea Res.* **1971**, *5*, 382–389. [[Google Scholar](#)] [[CrossRef](#)]
12. Frignani, M.; Giglio, F.; Accornero, A.; Langone, L.; Ravaioli, M. Sediment characteristics at selected sites of the Ross Sea continental shelf: Does the sedimentary record reflect water column fluxes? *Antarct. Sci.* **2003**, *15*, 133–139. [[Google Scholar](#)] [[CrossRef](#)]
13. Gendron-Badou, A.; Coradin, T.; Maquet, J.; Fröhlich, F.; Livage, J. Spectroscopic characterization of biogenic silica. *J. Non Cryst Solids* **2003**, *316*, 331–337. [[Google Scholar](#)] [[CrossRef](#)]
14. Hemmateenejad, B.; Yousefinejad, S. Multivariate standard addition method solved by net analyte signal calculation and rank annihilation factor analysis. *Anal. Bioanal. Chem.* **2009**, *394*, 1965–1975. [[Google Scholar](#)] [[CrossRef](#)] [[PubMed](#)]
15. Kamatani, A.; Oku, O. Measuring biogenic silica in marine sediments. *Mar. Chem.* **2000**, *68*, 219–229. [[Google Scholar](#)] [[CrossRef](#)]
16. Khoshmanesh, A.; Cook, P.L.M.; Wood, B.R. Quantitative determination of polyphosphate in sediments using attenuated total reflectance-fourier transform infrared

- (ATR-FTIR) spectroscopy and partial least squares regression. *Analyst* **2012**, *137*, 3704–3709. [[Google Scholar](#)] [[CrossRef](#)] [[PubMed](#)]
17. Kröger, N.; Poulsen, N. Diatoms—From Cell Wall Biogenesis to Nanotechnology. *Annu. Rev. Genet.* **2008**, *42*, 83–107. [[Google Scholar](#)] [[CrossRef](#)]
 18. Ledford-Hoffman, P.A.; Demaster, D.J.; Nittrouer, C.A. Biogenic-silica accumulation in the Ross Sea and the importance of Antarctic continental-shelf deposits in the marine silica budget. *Geochim. Cosmochim. Acta* **1986**, *50*, 2099–2110. [[Google Scholar](#)] [[CrossRef](#)]
 19. Leinen, M. A normative calculation technique for determining opal in deep-sea sediments. *Geochim. Cosmochim. Acta* **1977**, *41*, 671–676. [[Google Scholar](#)] [[CrossRef](#)]
 20. Leinen, M. Techniques for determining opal in deep-sea sediments: A comparison of radiolarian counts and x-ray diffraction data. *Mar. Micropaleontol.* **1985**, *9*, 375–383. [[Google Scholar](#)] [[CrossRef](#)]
 21. Liu, W.; Sun, Z.; Ranheimer, M.; Forsling, W.; Tang, H. A flexible method of carbonate determination using an automatic gas analyzer equipped with an FTIR photoacoustic measurement chamber. *Analyst* **1999**, *124*, 361–365. [[Google Scholar](#)] [[CrossRef](#)]
 22. Lorber, A. Error Propagation and Figures of Merit for Quantification by Solving Matrix Equations. *Anal. Chem.* **1986**, *58*, 1167–1172. [[Google Scholar](#)] [[CrossRef](#)]
 23. Lorber, A.; Faber, K.; Kowalski, B.R. Net Analyte Signal Calculation in Multivariate Calibration. *Anal. Chem.* **1997**, *69*, 1620–1626. [[Google Scholar](#)] [[CrossRef](#)]
 24. Lorho, G.; Westad, F.; Bro, R. Generalized correlation loadings. Extending correlation loadings to congruence and to multi-way models. *Chemom. Intell. Lab. Syst.* **2006**, *84*, 119–125. [[Google Scholar](#)] [[CrossRef](#)]
 25. Malandrino, M.; Mentasti, E.; Giacomino, A.; Abollino, O.; Dinelli, E.; Sandrini, S.; Tositti, L. Temporal variability and environmental availability of inorganic constituents in an antarctic marine sediment core from a polynya area in the Ross Sea. *Toxicol. Environ. Chem.* **2010**, *92*, 453–475. [[Google Scholar](#)] [[CrossRef](#)]
 26. Maldonado, M.; López-Acosta, M.; Sitjà, C.; García-Puig, M.; Galobart, C.; Ercilla, G.; Leynaert, A. Sponge skeletons as an important sink of silicon in the global oceans. *Nat. Geosci.* **2019**, *12*, 815–822. [[Google Scholar](#)] [[CrossRef](#)]
 27. Manno, C.; Sandrini, S.; Tositti, L.; Accornero, A. First stages of degradation of *Limacina helicina* shells observed above the aragonite chemical lysocline in Terra Nova Bay (Antarctica). *J. Mar. Syst.* **2007**, *68*, 91–102. [[Google Scholar](#)] [[CrossRef](#)]
 28. Mecozzi, M.; Pietrantonio, E.; Amici, M.; Romanelli, G. Determination of carbonate in marine solid samples by FTIR-ATR spectroscopy. *Analyst* **2001**, *126*, 144–146. [[Google Scholar](#)] [[CrossRef](#)] [[PubMed](#)]
 29. Melucci, D.; Locatelli, C. Multivariate calibration in differential pulse stripping voltammetry using a home-made carbon-nanotubes paste electrode. *J. Electroanal. Chem.* **2012**, *675*, 25–31. [[Google Scholar](#)] [[CrossRef](#)]
 30. Meyer-Jacob, C.; Vogel, H.; Boxberg, F.; Rosén, P.; Weber, M.E.; Bindler, R. Independent measurement of biogenic silica in sediments by FTIR spectroscopy and PLS regression. *J. Paleolimnol.* **2014**, *52*, 245–255. [[Google Scholar](#)] [[CrossRef](#)]
 31. Mortlock, R.A.; Froelich, P.N. A simple method for the rapid determination of biogenic opal in pelagic marine sediments. *Deep Sea Res. Part A Oceanogr. Res. Pap.* **1989**, *36*, 1415–1426. [[Google Scholar](#)] [[CrossRef](#)]
 32. Nancy Ann, B. Chapter 18 The Determination of Biogenic Opal in High Latitude Deep Sea Sediments. *Dev. Sedimentol.* **2008**, *36*, 317–331. [[Google Scholar](#)]
 33. Petrovskii, S.K.; Stepanova, O.G.; Vorobyeva, S.S.; Pogodaeva, T.V.; Fedotov, A.P. The use of FTIR methods for rapid determination of contents of mineral and biogenic

- components in lake bottom sediments, based on studying of East Siberian lakes. *Environ. Earth Sci.* **2016**, *75*, 226. [[Google Scholar](#)] [[CrossRef](#)]
34. Pokras, E.M. Preservation of fossil diatoms in Atlantic sediment cores: Control by supply rate. *Deep Sea Res. Part A Oceanogr. Res. Pap.* **1986**, *33*, 893–902. [[Google Scholar](#)] [[CrossRef](#)]
 35. Ramer, G.; Lendl, B. Attenuated Total Reflection Fourier Transform Infrared Spectroscopy. In *Encyclopedia of Analytical Chemistry*; John Wiley & Sons: Hoboken, NJ, USA, 2013; pp. 1–27. [[Google Scholar](#)]
 36. Rinnan, Å.; van den Berg, F.; Engelsen, S.B. Review of the most common pre-processing techniques for near-infrared spectra. *TrAC Trends Anal. Chem.* **2009**, *28*, 1201–1222. [[Google Scholar](#)] [[CrossRef](#)]
 37. Rosén, P. Total organic carbon (TOC) of lake water during the Holocene inferred from lake sediments and near-infrared spectroscopy (NIRS) in eight lakes from northern Sweden. *Biogeochemistry* **2005**, *76*, 503–516. [[Google Scholar](#)] [[CrossRef](#)]
 38. Rosén, P.; Dåbakk, E.; Renberg, I.; Nilsson, M.; Hall, R. Near-infrared spectrometry (NIRS): A new tool for inferring past climatic changes from lake sediments. *Holocene* **2000**, *10*, 161–166. [[Google Scholar](#)] [[CrossRef](#)]
 39. Rosén, P.; Vogel, H.; Cunningham, L.; Hahn, A.; Hausmann, S.; Pienitz, R.; Zolitschka, B.; Wagner, B.; Persson, P. Universally applicable model for the quantitative determination of lake sediment composition using fourier transform infrared spectroscopy. *Environ. Sci. Technol.* **2011**, *45*, 8858–8865. [[Google Scholar](#)] [[CrossRef](#)]
 40. Sandrini, S.; Ait-Ameur, N.; Rivarolo, P.; Massolo, S.; Touratier, F.; Tositti, L.; Goyet, C. Anthropogenic carbon distribution in the Ross Sea, Antarctica. *Antarct. Sci.* **2007**, *19*, 395–407. [[Google Scholar](#)] [[CrossRef](#)]
 41. Smith, W.O.; Gordon, L.I. Hyperproductivity of the Ross Sea (Antarctica) polynya during austral spring. *Geophys. Res. Lett.* **1997**, *24*, 233–236. [[Google Scholar](#)] [[CrossRef](#)]
 42. Sprenk, D.; Weber, M.E.; Kuhn, G.; Rosén, P.; Frank, M.; Molina-Kescher, M.; Liebetrau, V.; Röhling, H.-G. Southern Ocean bioproductivity during the last glacial cycle—New detection method and decadal-scale insight from the Scotia Sea. *Geol. Soc. Lond. Spec. Publ.* **2013**, *381*, 245–261. [[Google Scholar](#)] [[CrossRef](#)]
 43. Stute, W. The jackknife estimate of variance of a Kaplan-Meier integral. *Ann. Stat.* **1996**, *24*, 2679–2704. [[Google Scholar](#)] [[CrossRef](#)]
 44. Sullivan, C.W.; Arrigo, K.R.; McClain, C.R.; Comiso, J.C.; Firestone, J. Distributions of phytoplankton blooms in the Southern Ocean. *Science* **1993**, *262*, 1832–1837. [[Google Scholar](#)] [[CrossRef](#)] [[PubMed](#)]
 45. Sumper, M. A phase separation model for the nanopatterning of diatom biosilica. *Science* **2002**, *295*, 2430–2433. [[Google Scholar](#)] [[CrossRef](#)]
 46. Toggweiler, J.R.; Russell, J.L.; Carson, S.R. Midlatitude westerlies, atmospheric CO₂, and climate change during the ice ages. *Paleoceanography* **2006**, *21*. [[Google Scholar](#)] [[CrossRef](#)]
 47. Vogel, H.; Rosén, P.; Wagner, B.; Melles, M.; Persson, P. Fourier transform infrared spectroscopy, a new cost-effective tool for quantitative analysis of biogeochemical properties in long sediment records. *J. Paleolimnol.* **2008**, *40*, 689–702. [[Google Scholar](#)] [[CrossRef](#)]
 48. Wold, S.; Sjöström, M.; Eriksson, L. PLS-regression: A basic tool of chemometrics. *Chemom. Intell. Lab. Syst.* **2001**, *58*, 109–130. [[Google Scholar](#)] [[CrossRef](#)]

CHAPTER 8 - Deposition processes over complex topographies: Experimental data meets atmospheric modeling

by Laura Tositti^a, Beatrice Moroni^b, Enrico Dinelli^{cd}, Pietro Morozzi^a, Erika Brattich^e, Bartolomeo Sebastiani^b, Chiara Petroselli^f, Stefano Crocchianti^b, Roberta Selvaggi^b, Goretti Enzo^b, David Cappelletti^b

^a Department of Chemistry “G. Ciamician”, University of Bologna, Bologna (BO) 40126, Italy

^b Department of Chemistry, Biology and Biotechnologies, University of Perugia, Perugia (PG) 06123, Italy

^c Department of Biological, Geological and Environmental Sciences (BiGeA), University of Bologna, Bologna (BO) 40126, Italy

^d Department of Biological, Geological and Environmental Sciences (BiGeA), U.O.S. Ravenna, Ravenna (RA) 48123, Italy

^e Department of Physics and Astronomy, University of Bologna, Bologna (BO), 40126 Bologna (BO), Italy

^f Faculty of Engineering and Physical Sciences, University of Southampton, 12 University Road, SO17 1BJ Southampton, UK



ELSEVIER

This article was published in *Science of The Total Environment*, Volume 744, 2020, 140974, ISSN 0048-9697, Copyright Elsevier, <https://doi.org/10.1016/j.scitotenv.2020.140974>

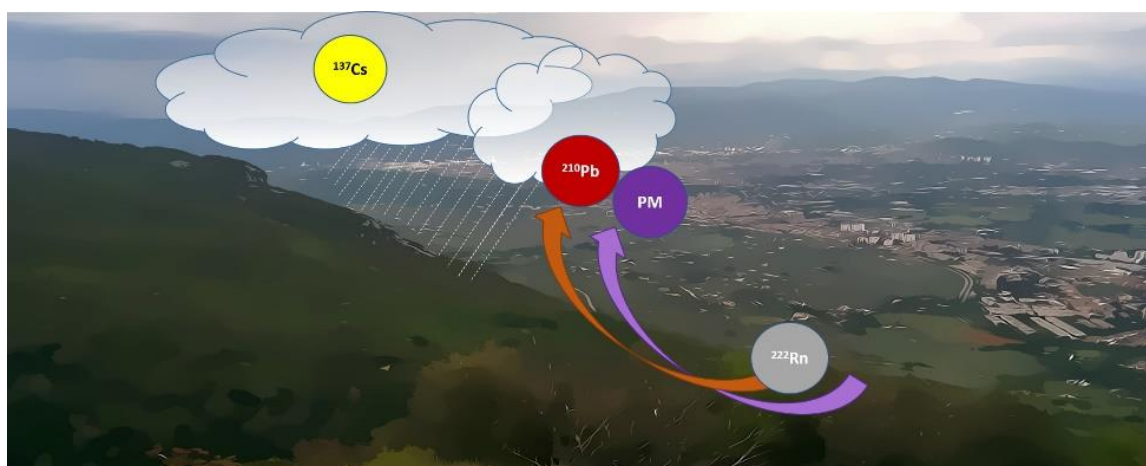
Highlights

- Atmospheric deposition along a soil transect as a function on the altitude
- Concentration vs. depth profile of atmospheric radionuclides
- Increase of deposition with height and asymmetrical deposition on the two branches
- Seeder-feeder process confirmed by Calpuff modeling

Abstract

The present paper describes the assessment of the atmospheric deposition processes in a basin valley through a multidisciplinary approach based on the data collected within an extensive physico-chemical characterization of the soils, combined with the local meteorology. Surface soil cores were collected on a NNW-SSE transect across the Terni basin (Central Italy), between the Monti Martani and the Monti Sabini chains (956 m a.s.l.), featuring the heavily polluted urban and industrial enclave of Terni on its bottom. Airborne radiotracers, namely ^{210}Pb and ^{137}Cs , have been used to highlight atmospheric deposition.

We observed an increased deposition flux of ^{210}Pb and ^{137}Cs at sites located at the highest altitudes, and the associated concentration profiles in soil allowed to evaluate the role of atmospheric deposition. We also obtained a comprehensive dataset of stable anthropogenic pollutants of atmospheric origin that showed heterogeneity along the transect. The behavior has been explained by the local characteristic of the soil, by seeder-feeder processes promoted by the atmospheric circulation, and was reconciled with the concentration profile of radiotracers by factor analysis. Finally, the substantial impact of the local industrial activities on soil profiles and the role of the planetary boundary layer has been discussed and supported by simulations employing a Lagrangian dispersion model.



Keywords: Atmospheric deposition, Airborne radiotracers, ^{210}Pb , ^{137}Cs , Soil, CALPUFF model

1 – Introduction

Soil plays a fundamental role in environmental biogeochemical cycling through a wide range of different processes, both naturally and anthropogenically driven. It is characterized by endogenous processes such as soil development, use, and management, as well as by exogenous processes e.g., climatic factors, atmospheric deposition, and runoff, which may add complexity in terms of chemical components transfer, mixing and reworking on not easily predictable space and time scales. As a result, soil behaves as a receptor for atmospheric deposition, reflecting the influence of atmospheric aerosols with the mediation of wet and, to a lesser extent, dry scavenging according to local climatology and pluviometric regime. Atmospheric deposition flux includes numerous chemical species from gas-to-particle reactions derived nutrients such as nitrate, ammonium, and sulfate, to metals, metalloids, and carbonaceous species (Vet et al., 2014a, Vet et al., 2014b; Zhang and Vet, 2006). Once deposited, substances may permeate and migrate to depth throughout the soil

pores as a function of the relative interaction strength with soil components. Therefore, each atmospherically originated chemical species will produce a vertical concentration profile reflecting the interplay among its own physicochemical properties and soil properties. In particular, the mobility and adsorption processes of a pollutant in soil will depend on the soil mineralogical composition, porosity, water, and organic matter content, pH, and redox conditions. As time goes by, soil itself will evolve leading to temporal accretion and burial of older layers wherein both endogenous and exogenous substances can be stored and redistributed (Vet et al., 2014a; Fowler et al., 2004; Kaste et al., 2003; Lamborg et al., 2000).

Owing to both the morphology and intrinsic complexity of the soil chemical matrix, the assessment of atmospherically-derived components in a soil profile is usually a challenging task because they represent a minor fraction as compared to bulk soil components. In this context, however, environmental radionuclides represent an exception, since both natural and artificial radioisotopes have been historically investigated to trace the fate of atmospheric pollution in depositional environments including soil matrices, posing the basis for modern biogeochemistry, geophysical radiotracer research, and geochronology (Baskaran, 2011).

The efficacy of natural and artificial radiotracers in environmental investigations is based on two substantial properties. Firstly, radiotracers can be measured very accurately, even at their lowest molar concentration on a routine basis. Secondly, they are emitted by unambiguous sources, which make them easily recognizable and widely used as surrogates of stable pollutants or as geochronometers and radiotracers (Landis et al., 2016; Fowler et al., 1995; Graustein and Turekian, 1986).

Soil contains two main groups of radionuclides: geogenic radionuclides, intrinsically associated to the soil parent material, and atmospherically derived radionuclides, transferred to the soil environment through wet and dry deposition. Geogenic radionuclides are mainly represented by uranium and thorium families together with the primordial ^{40}K . The atmospherically derived fraction includes among others ^{210}Pb ($t_{1/2} = 22.3$ years) and ^{137}Cs ($t_{1/2} = 30.2$ years) both widely employed in the study of depositional processes (Baskaran, 2011); ^7Be ($t_{1/2} = 55$ d) is another frequently used atmospheric radiotracer, but owing to the relatively short half-life its use is conditioned by the time elapsed between sampling and measurement.

While ^{137}Cs is an artificial radionuclide deriving from both the global fallout (peak emissions from nuclear weapon testing in 1963) and, in the northern hemisphere, from the Chernobyl accident in 1986 (IAEA, 2006), ^{210}Pb is a natural radionuclide from the ^{238}U radioactive family including ^{222}Rn and ^{210}Pb formed at intermediate stages of the radioactive chain. In particular, ^{210}Pb belongs to ^{222}Rn progeny, but differently from the parent nuclide which is a noble gas, all its progeny including ^{210}Pb , is particle reactive and similarly to ^{137}Cs , gets efficiently associated to submicron aerosol particles, tracing airborne particulate and eventually the aerosol sinks (Graustein and Turekian, 1989; Preiss et al., 1996; Persson and Holm, 2011; Mabit et al., 2014; Landis et al., 2014). All these radionuclides are highly particle-reactive. Therefore, after being produced/emitted to the air, they quickly get associated with ambient aerosol, usually in the accumulation mode (i.e., submicrometric in size), with an atmospheric residence time of the order of days up to a few weeks. As a result, they are excellent tracers of both atmospheric aerosol (Tositti et al., 2014a; Brattich et al., 2015a, Brattich et al., 2015b, Brattich et al., 2016), and of atmospheric deposition (Battiston et al., 1987; Bettoli et al., 1995; Tositti et al., 2006).

Airborne radionuclides establish negative concentration gradients in soil with depth. These profiles reflect both their origin and the processes they undergo within the soil, linked to its

properties and management. Atmospherically deposited radionuclides are in most cases confined in the upper 15–20 cm of soil which outlines the need for high-resolution sectioning when dealing with soil and the possibility of efficiently detect the influence of atmospheric contribution independently on the nature of the pollutant investigated, as reported in the literature (Suchara et al., 2016; Landis et al., 2014; Graustein and Turekian, 1989).

Radionuclides profiles in soil depend on the extent of atmospheric deposition, which in turn depends on a number of meteorological processes and orographical features. In fact, many studies have observed how the deposition rate of wet-removed chemical species increases with increasing altitude. In areas characterized by complex topographies, this differential behavior has been attributed to the influence of orographic clouds which produce an enrichment in aerosol particles being removed by nucleation through the so-called “seeder-feeder mechanism” (see for example Le Roux et al., 2008; Likuku, 2006 and references therein). Airborne radiotracers, whose environmental sources and sinks are known in remarkable detail, have been successfully applied to constrain the fate of stable substances and pollutants with similar environmental behavior contributing to enlighten their atmospheric source (Vet et al., 2014a; Fowler et al., 2004; Kaste et al., 2003; Lamborg et al., 2000).

The present paper concerns the assessment of the depositional pollution features in the Terni basin, an area heavily impacted by human activities in Umbria, Central Italy. The present investigation of biogeochemical cycling of pollutants in the Terni area, accounting for its topographical complexity, is part of a comprehensive environmental study where earlier research shed light on the role of the planetary boundary layer in atmospheric dispersion of pollution in the area (Moroni et al., 2012, Moroni et al., 2013; Ferrero et al., 2012, Ferrero et al., 2014). The present work describes the assessment of the atmospheric deposition processes in the Terni basin through a multidisciplinary approach based on the data collected within an extensive chemical-physical characterization of Terni soils, combined with the local meteorology. Specifically, this paper is based on a transect of surface soil cores collected at ten stations along with a mountainous profile across the Terni basin. At each station, radionuclide, inorganic, and organic components concentrations were determined as a function of station height and soil depth. Finally, their connections with atmospheric deposition have been analyzed.

The paper is organized as follows:

- assessment of radionuclidic and chemical vertical profiles at the ten sampling stations;
- identification of atmospheric inputs of radionuclides and station classification by multivariate techniques;
- assessment of differential depositional behavior with elevation;
- qualitative comparison between experimental results and the numerical outputs of a Lagrangian Gaussian puff dispersion model.

2 –Materials and methods

2.1 Site description and sample collection

The Terni district is a densely populated and industrialized area located at the margins of the Central Apennines range in Umbria, Central Italy (Fig. 1). The town of Terni (170 m a.s.l.) lies in a vast plain area (about 2% of the territory) surrounded by medium-range geographical elevations (average elevation 800–1200 m a.s.l.).

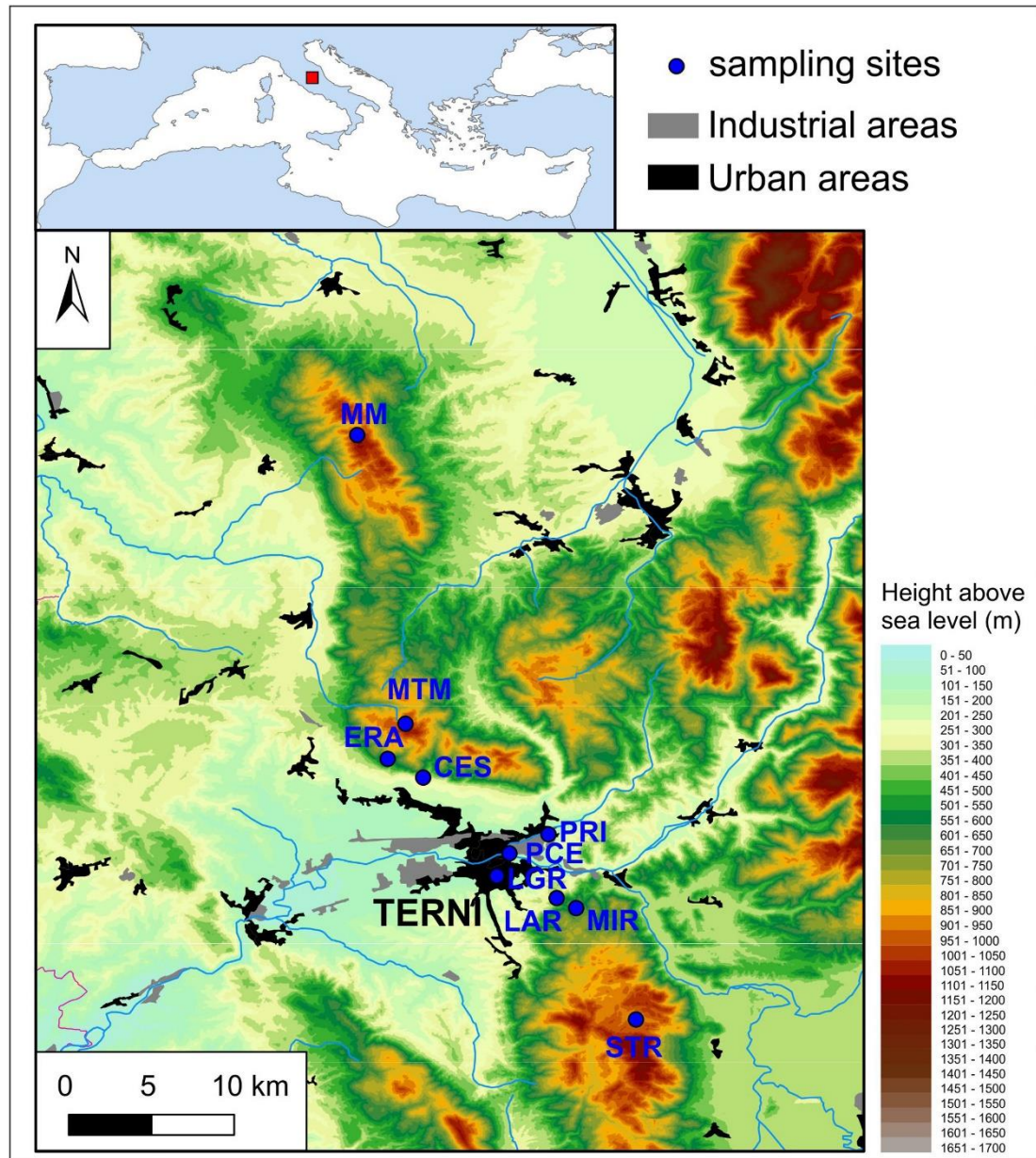


Fig. 1. Map of the Terni district depicting topography and name/location of the sampling stations occupied in this work. The color scale depicts the altitude (meters above sea level).

The local climate is classified as Csa (Köppen classification), i.e., as mid-latitude temperate, with warm, humid summers and cold rainy winters. The mean annual temperature is 14.5 °C, while yearly mean rainfall is 854 mm/y (ARPA-Umbria, 2013). Weak winds, due to the local topography, are typically oriented along the course of the Nera river, predominantly along with the N-NE, NE, and S-SW directions (Meloni and Carpine, 2004). Terni began its

industrial development as far back as 1884, with the building of the Italian largest forge, for the production of armor and guns for the Navy. Since then the Acciai Speciali Terni (AST) became the strongest industrial asset of the area, focusing on stainless steel production for more than one hundred years, until the most recent owner, Thyssen-Krupp. Besides the steel industry, three waste incinerators are located in the Terni area for industrial and municipal waste management. Previous assessments on the local source profile identified traffic and agricultural activities as significant contributions of both fine and coarse particulate (Moroni et al., 2012). Considerable efforts have been made to mitigate the impact of industrial emissions, wood-burning, and road traffic, but only a modest improvement of air quality standards has been achieved so far. In particular, long-lasting high pollution level events are frequently observed in the cold season, in association with intense thermal inversion episodes (Ferrero et al., 2012, Ferrero et al., 2014; Moroni et al., 2013).

Soil was sampled in summer 2014 at 10 stations located along a roughly NNW-SSE transect crossing the whole Terni basin roughly along a parabolic section with the bottom coinciding with the Terni urban area in the valley (Fig. 1 and Table 1).

Table 1. Location and lithology of the bedrock of the sampling sites.

SITE	LABEL	HEIGHT (M A.S.L.)	LATITUDE	LONGITUDE	BEDROCK
MT. Martano	MM	1094	42.789168	12.597780	Limestones and marly limestones in pelagic facies (Palaeogene-Upper Cretaceous)
Mt. Torre Maggiore	MTM	967	42.632315	12.600922	Micritic limestones and pelagic micritic shales (Cretaceous-Upper Jurassic)
S. Erasmo	ERA	724	42.613036	12.591092	Limestones and sometimes dolomites in neritic and carbonate platform facies (Jurassic)
Cesi	CES	338	42.603063	12.610602	Lacustrine and fluviolacustrine deposits (Pleistocene and Pliocene)
Prisciano	PRI	156	42.572104	12.678502	Micritic limestones and pelagic micritic shales (Cretaceous-Upper Jurassic)
Pineta Centurini	PCE	133	42.561713	12.657302	Lacustrine and fluviolacustrine deposits (Pleistocene and Pliocene)
Le Grazie	LGR	149	42.549633	12.650519	Lacustrine and fluviolacustrine deposits (Pleistocene and Pliocene)
Larviano	LAR	385	42.537563	12.683046	Limestones, marly limestones and marls, marls (cherty) of pelagic facies (Jurassic)
Miranda	MIR	618	42.532231	12.693726	Limestones, marly limestones and marls, marls (cherty) of pelagic facies (Jurassic)
Piani di Stroncone	STR	956	42.471502	12.726271	Limestones, marly limestones and marls, marls (cherty) of pelagic facies (Jurassic)

The stations are classified into three main groups:

- Stations located close to the main pollution sources within the urban territory (Prisciano-PRI, Pineta Centurini-PCE, and Le Grazie-LGR);
- Stations located north and south from the main emission area, but at a higher elevation and distance from the direct influence of the pollution sources (Mt. Torre Maggiore-MTM, S. Erasmo-ERA, Cesi-CES to the north, Miranda-MIR, Larviano-LAR and Piani di Stroncone-STR south from Terni);

- Mt. Martano-MM (1094 m a.s.l.), at about 45 km north of Terni is a background mid-altitude station chosen as reference site distant from pollution sources and influenced by the boundary layer only during summertime (Moroni et al., 2015).
- Mt. Torre Maggiore (IT5220013) and Piani di Stroncone (IT5220021) are Natura 2000 protected areas (<https://natura2000.eea.europa.eu/>, accessed 21/04/2020).

At each station, 3 shallow cores 20 cm long were drilled using a PTFE liner (diameter = 7 cm) and sectioned every 5 cm. Soil samples were air-dried in a low humidity environment for about 2 weeks in a hood, then crushed and sieved (2 mm certified mesh).

Each core was splitted and one portion of the sample was weighed and oven-dried at 105 °C for 16 h and then weighted again to determine the residual moisture.

According to the documentation on soil management available through the local administration, all the Terni area is characterized by a high degree of human exploitation. The basic information about the sampling stations as well as information about the bedrock lithology, were recovered and classified using the layer “geology of Italy” downloaded from the “Portale Cartografico Nazionale” (<http://www.pcn.minambiente.it/mattm/servizio-discaricamento-wfs/>, accessed 21/04/2020), is reported in Table 1.

2.2 Analytical methods

2.2.1 Elemental analysis by WD-XRF analysis

Soil samples were further homogenized and milled in an agate mortar to obtain the fraction <10 µm. Powder pellets were prepared for the XRF analysis to determine major and trace element concentrations with a Panalytical Axios4000 spectrometer equipped with a Rh tube. Matrix corrections were applied during data processing (Franzini et al., 1972, Franzini et al., 1975). Precision and accuracy for trace element determination were better than 5% except for elements at 10 ppm or lower (10–15%), as estimated from the analysis of international reference materials (Lancianese and Dinelli, 2016). The investigated chemical components include SiO₂, TiO₂, Al₂O₃, Fe₂O₃, MnO, MgO, CaO, Na₂O, K₂O, P₂O₅, As, Ba, Ce, Co, Cr, Cu, Ga, La, Mo, Nb, Ni, Pb, Rb, S, Sc, Sn, Sr, Th, V, Y, Zn, Zr. The minimum and maximum values at each sampling station are reported in Table S1 of the Supplementary Material (hereafter SM).

2.2.2 High-resolution γ-ray spectrometry

Natural and artificial radionuclides including among others ²¹⁰Pb (E_γ = 46.5 keV), ²²⁶Ra (E_γ = 186 keV) and ¹³⁷Cs (E_γ = 661.7 keV) were determined in soil samples by a HPGe (High Purity Germanium) extended-range detector (PROFILE Hyper Pure Germanium detector by Ortec-Ametek Inc.). The detector (relative efficiency of 20% and resolution (Full Width at Half Maximum, FWHM) of 1.9 keV at 1332.5 keV) was calibrated for energy and efficiency using a multiple radionuclide liquid source (DKD, Eckert & Ziegler Nuclitec GmbH) in a jar geometry (diameter = 54 mm and thickness = 1 cm). Soil samples were measured in the same jar geometry, weighed and then counted for 24 h each to optimize peak counting statistics. Spectra were subsequently analyzed with Gamma Vision-32 software (version 6.07, Ortec-Ametek) allowing also for self-attenuation at low energy on the basis of the apparent density. ²²⁶Ra activity was determined at 186 keV correcting the peak area for ²³⁵U emission according to the procedure reported by Gilmore (2008). Atmospheric ²¹⁰Pb defined as ²¹⁰Pb_{ex}, i.e. “in excess” of the fraction supported by in situ production by ²²⁶Ra, was

calculated by subtracting the activity fraction of ^{210}Pb in equilibrium with ^{226}Ra from the mineral soil component from the total ^{210}Pb detected in each sample (Swarzenski, 2014), after correcting for self-absorption. Further details on γ -spectrometry determinations are available elsewhere (Cinelli et al., 2014; Tositti et al., 2016). Uncertainty (here defined as one standard deviation) on the γ photopeaks was calculated propagating the error resulting from the efficiency calibration fit previously determined over the counting error. Minimum detectable activity (MDA) was determined using the Traditional ORTEC method (ORTEC, 2003) with a peak-cut-off limit of 40%. Analytical quality control has been assessed using certified reference materials DH-1a and UTS-3, both by CANMET. The minimum and maximum radionuclides concentration data are reported in Table S2 of the SM.

2.2.3 PAHs and n-alkanes

The determination of PAHs and n-alkanes were performed by GC–MS on a Varian-Chrompack 3800 gas-chromatograph coupled with a tandem mass spectrometry ion trap detector (ITD-MS) (Varian Saturn 2000) and equipped with a split–splitless inlet and a low bleed Factor Four VF-5 ms analytical capillary column (Chrompack). The analytical procedure was described in detail in Cartechini et al. (2015). PAHs and n-alkanes concentration data analyzed in Terni soils are reported in Table S3 of the SM.

2.2.4 Loss-On-Ignition LOI, TOC and N

Total loss on ignition (LOI) was gravimetrically estimated after overnight heating on 1 g of sample at 950 °C in a muffle furnace.

A LECO Truspec CN analyzer was employed for the determination of total organic carbon (TOC) and total nitrogen (N). About 20 mg of soil sieved at 0.5 mm were weighed in a tin capsule. TOC was obtained by difference to between total carbon and inorganic carbon made on the same samples kept in the muffle for 5 h at 550 °C. The accuracy at which the instrument operates is 0.3 ppm or 0.5% RSD for carbon and 40 ppm 0.5% RSD for nitrogen. The minimum and maximum values at each sampling station of LOI, TOC, and N data are reported in Table S1 of the SM.

2.3 Statistical methods and elaboration tools

2.3.1 Principal Component Analysis (PCA) and Gabriel Biplot

Factor Analysis based on Principal Component Analysis (PCA) was applied to the complete transect dataset derived from the application of the analytical techniques detailed above, with the aim of classifying soil samples and assessing similarities/differences among the sampling stations.

Missing data or data below detection limits (LOD) were substituted in the data matrices by LOD/2 in order to optimize the modeling outcome. The dataset was normalized before performing PCA by means of autoscaling, i.e. subtracting the mean value to each observation and dividing by the standard deviation. This process produces new variables with zero mean and unit standard deviation, so that each of them has the same importance regardless their original variances and units of measure as explained by van den Berg et al. (2006) and Jolliffe and Cadima (2016).

Gabriel biplot (Gabriel, 1971) was also used in order to represent both variables and cases together in two dimensions.

2.3.2 CALPUFF

Calpuff (CALPUFF, 2001) is a Lagrangian Gaussian Puff model and has been one of the preferred models adopted for regulatory purposes to assess pollutants transport in the range from tens to hundreds of kilometers (USEPA, 2005). Similar to other Lagrangian models, it is still recommended as a screening model (USEPA, 2017). Its advantage over gaussian-based models is based on its capability to simulate the transport of pollutants in calm and stagnant condition (Daly and Zannetti, 2007), i.e. eventually those typically affecting the Terni valley.

The Calpuff dispersion model (version 7.2.1) was used in the present work in combination with CALMET (version 6.327), a diagnostic meteorological model that develops wind and temperature fields on a three-dimensional gridded domain. Associated two-dimensional fields such as mixing height, surface characteristics, and dispersion properties are also included in its output file.

The domain of the simulation was a square grid 20 km wide centered on the Terni city. The meteorological data was produced by ARPA Emilia Romagna for the year 2014 on the basis of the LAMA (Limited Area Meteorological Analysis) dataset (Jongen and Bonafe, 2006) that covers the Italian territory and the surrounding regions with a horizontal resolution of 0.0625° (~7 km) and a temporal resolution of 1 h. Boundary conditions were provided by the global scale analysis model ECMWF. The diagnostic model requires both geophysical and meteorological data. Among the former ones, terrain elevations were derived from Umbria high-resolution regional thematic cartography, the 25 m resolution Digital Terrain Models of regional coverage. Domain points falling outside Umbria were obtained from the 3 arc-seconds Shuttle Radar Topography Mission dataset. The land-use categories were computed starting from the Corine Land Cover 2000 (22 Oct 2009 update).

Calpuff model allows to specify the source size and type, as well as to assume the source emission as constant or variable in a known mode according to cycle, time of the day, year, etc. (see the discussion in the following).

The code resolution enables to account for spatial inhomogeneities deriving from orography localized land use as well as wind circulation and pollutants dispersion in the domain, leading to adequately reproduce calm and breeze regimes. Moreover, the use of a Lagrangian dispersion model allows to evaluate the effects both in proximity and at distance from the simulated sources, including the area of maximum fallout of total suspended particles (TSP). Results of the Calpuff model are expressed as soil concentrations isopleths. In this work, we chose to evaluate mean annual concentrations and maximum daily concentrations. This last value produces the maximum annual value reached by the pollutant in each cell (side 200×200 m).

Most of the Calpuff technical options were left to the default settings. However, for the purpose of this work, we chose to simulate the vertical wind shear, without considering the chemical transformation from source to receptor, and to calculate the dispersion coefficients from the values of micrometeorological variables. As far as the PM_{10} size parameters for dry deposition are concerned, a geometric mass mean diameter of $0.48 \mu\text{m}$ with a geometric standard deviation of $2.0 \mu\text{m}$ was selected.

In the Calpuff simulation, we included as a source only the major industrial plant of the region, i.e. the AST steel plant. The plant stacks were modeled as constant 47 points sources. The emission rates adopted were proposed by the plant operator in the Application for Site Certification submitted in 2010 or the certified self-monitored concentrations of the emission gases for the year 2010. This source configuration is deemed emitting 96% of NO_x and PM₁₀ mass on an annual basis. Since each source was assumed to emit at the highest constant rate for the whole period, the simulation could be considered as a worst-case scenario. However, fugitive emissions such as those associated with the volatilization and vapor emission from open vessels and the releases from materials handling, especially the north-east on-site disposal, were not included.

3 –Results and discussion

3.1 Atmospheric radionuclides and depositional patterns

In this work, the radionuclides ¹³⁷Cs and ²¹⁰Pb_{ex} have been determined in a series of ten surface soil profiles to trace the occurrence and the extent of stable pollution fallout across the study area. These radiotracers have been detected at all the stations investigated, suggesting that the influence of atmospheric deposition is active across the whole Terni district.

In order to outline different depositional patterns among the stations, concentration vertical profiles and inventories of both radiotracers were examined. ¹³⁷Cs and ²¹⁰Pb_{ex} activity concentration depth profiles are reported in Fig. 2.

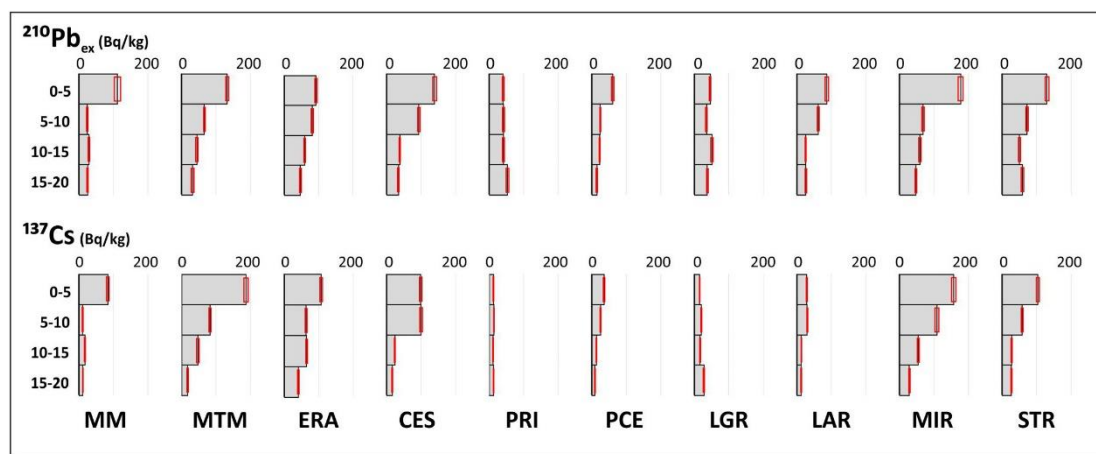


Fig. 2. Vertical profiles of ²¹⁰Pb_{ex} and ¹³⁷Cs along the soil sampling transect. The experimental errors associated with each radionuclide data are defined as error bars. Layer depth ranges in cm.

At best, an undisturbed profile of atmospheric ²¹⁰Pb shows a monotonic decrease with depth, a situation controlled mainly by the organic fraction to which this radionuclide (as well as the corresponding element) is firmly bound, leading even the possibility of dating when high-resolution sectioning is carried out (Landis et al., 2016). Differently from ²¹⁰Pb, ¹³⁷Cs shows ideally two distinct activity peaks corresponding to the 1963 and 1986 horizons, well preserved in the case of undisturbed depositional environments; this is not granted in soil wherein the complex behavior of this radionuclide is hardly predictable, especially when long time from deposition has elapsed. ¹³⁷Cs can be initially bound to surface organics from vegetable litter and subsequently released through rain permeation leading to a lagged

association to the clay and organic components fractions at depth as described in detail in Suchara et al. (2016). However, vertical profiles of radionuclides along a soil profile at every single location reflect their behavior in terms of physicochemical interaction between the mobile phase(s) containing the radionuclides and the solid matrix; also the perturbation (disturbance) caused by local soil management, if any, can play a role.

In most cases, soil concentration for both airborne radionuclides showed maxima in the top layer confirming the influence of active deposition from the atmospheric compartment. In most of the profiles, concentrations monotonically decreased as a function of the depth. In some cases, the decrease was noteworthy for ^{137}Cs , even down to the fourth layer. ^{137}Cs , a monovalent soft cation, has a greater vertical mobility and showed consistently a broader distribution with respect to $^{210}\text{Pb}_{\text{ex}}$. Thanks to its strong association with the soil organic fraction, $^{210}\text{Pb}_{\text{ex}}$ is on average less mobile than ^{137}Cs , remaining usually confined in the uppermost first and second layers (Mabit et al., 2014; Suchara et al., 2016).

Altogether, the profiles of the two radiotracers also reflect different post-depositional behavior contributing to a more complete understanding of the atmosphere/soil relationships. The most disturbed (i.e. not decreasing) radiotracer profiles are those collected at the bottom stations (i.e. PRI, LGR, and PCE) all in proximity of residential and/or industrial sides. Specifically, the high degree of perturbation at LGR and PRI largely results from the strong anthropogenic influence from urban and industrial activities. In particular, PRI is in the core of the industrial Terni district while LGR is located in the Terni residential area, connecting the randomized distribution of radionuclides to the local remarkable degree of soil disturbance from human activities (e.g. reworking). On the other side, PCE maintains a slight degree of atmospheric deposition identifiable by the decreasing concentration trend with depth. Atmospheric deposition at PCE is sensibly affected by the airshed of Terni conurbation in terms of chemical composition and is possibly supported by the pine stand, a park area dating back about fifty years ago. Atmospheric deposition is therefore detectable in the area owing both to the absence of soil reworking in the last five decades whereas throughfall and foliar interception may have played a role in soil enrichment of the fallout species (Fowler et al., 2004; Likuku et al., 2006).

These differences in concentration vs. depth profiles arise mainly from the distinct soil characteristics. For this reason, depth profiles of atmospheric radionuclides have been evaluated individually for each sampling station. In order to assess the extent of deposition rate, comparing the different stations, we calculated the radionuclide inventory, a parameter conceptually close to a depositional flux. The inventory, expressed in Bq/m^2 , is the integral of the radionuclide activity concentration over depth accounting for soil geometry (unit surface and layer thickness) and soil mass density, and was calculated according to the method proposed by Graustein and Turekian, 1986, Graustein and Turekian, 1989.

The results are reported in Fig. 3 where ^{137}Cs and $^{210}\text{Pb}_{\text{ex}}$ inventories are represented along a profile cross section. Minimum inventories are observed at the three valley bottom stations while maxima are observed at the three most elevated stations, namely at MTM, and, with slightly lower values, at MM to the north and STR on the opposite branch of the transect (see Fig. 1). These results are in agreement with previous studies observing an increased deposition flux with height (Fowler et al., 1988; Le Roux et al., 2008; Stankwitz et al., 2012; Blackwell and Driscoll, 2015).

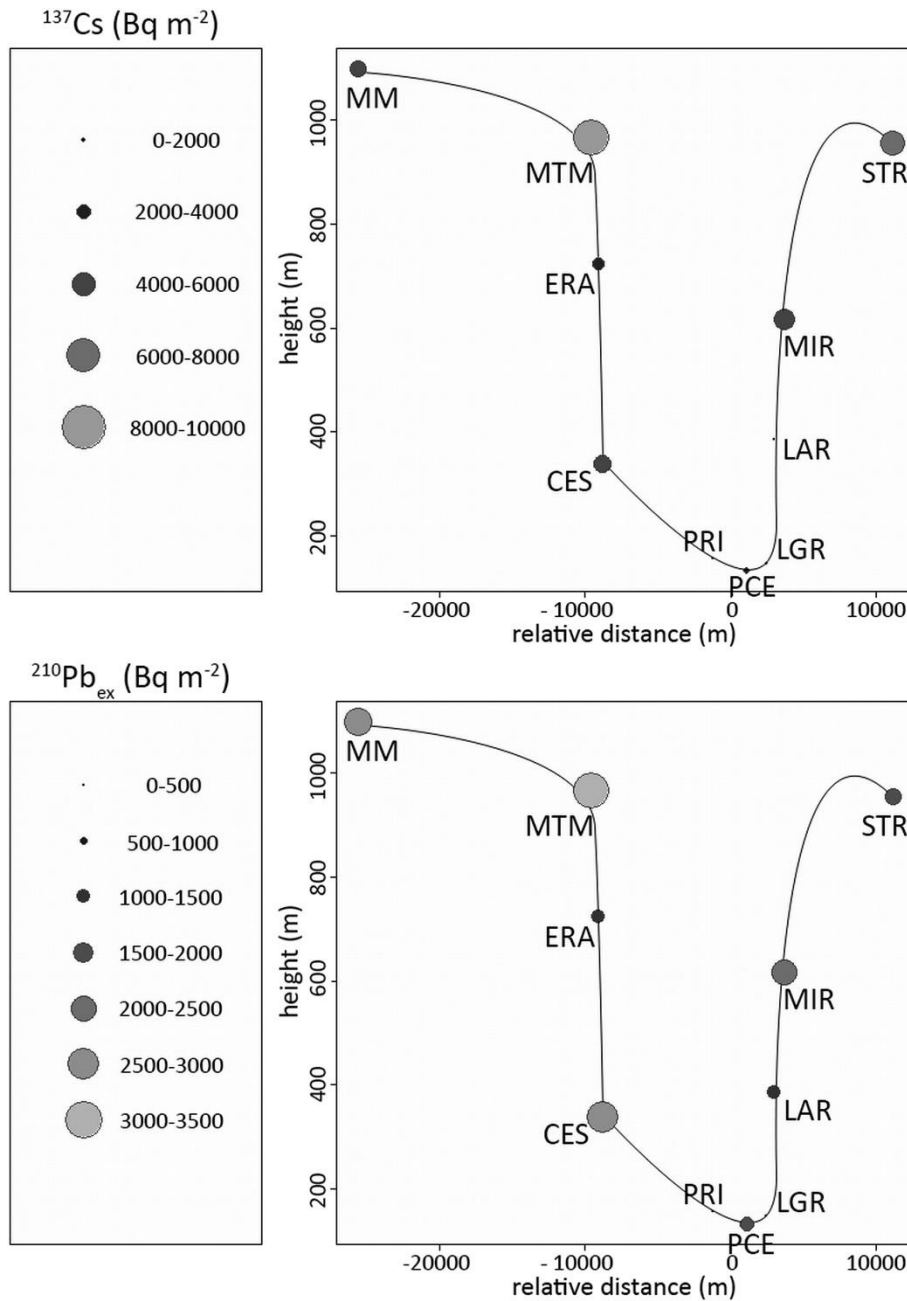


Fig. 3. ^{137}Cs and $^{210}\text{Pb}_{\text{ex}}$ inventories (expressed in Bq m⁻²) in the investigated sites as a function of relative distance and altitude from Terni (both expressed in m). The size of the circles is proportional to the flux, with scales reported to the left of the figure.

Atmospheric deposition appears to be higher on the NNW side of the transect with respect to the SSE side, with the exception of ERA station where both ^{137}Cs and $^{210}\text{Pb}_{\text{ex}}$ inventories are lower possibly due to local disturbances.

This difference in the inventories has been evaluated by the Unpaired Two-Samples Wilcoxon Test at a significance level of 95%. This non-parametric test allows comparing the means in two independent groups of samples without any prior assumption regarding data distribution. The results of the test indicate a statistically significant difference between the NNW (defined by MM, MTM, and ERA stations) and the SSE (defined by PRI, PCE, and LGR stations) sides of the Terni transect (p-value less than 0.05 for both ^{137}Cs and

$^{210}\text{Pb}_{\text{ex}}$) and the exceedance in deposition in the NNW side might be due to the combination of the meteorological conditions of the district, of the dominant circulation pattern along the transect under the influence of both mesoscale and mountain/valley breeze regime (see further on in this paper), as well as of the distinct origin of the two radionuclides. In fact, while ^{137}Cs has been emitted in a pulsed way by point sources and its transport through the troposphere over the investigated region has occurred well above the atmospheric boundary layer, $^{210}\text{Pb}_{\text{ex}}$ is generated in the lowest layers of the troposphere through radon exhalation and decay, which means a continuous and extended source area. As a result, it cannot be excluded that $^{210}\text{Pb}_{\text{ex}}$ deposition flux is contributed by both local and distant sources. As such, the former component may be affected by the seeder-feeder phenomenology through the uplift of radon enriched air masses from the plain, while the latter can be supported also by mesoscale/synoptic processes.

As a whole, we can conclude that the radionuclidic signature traces the atmospheric deposition along the soil transect in a fairly satisfactory way, though with differences that deserve a thorough inspection and evaluation.

3.2 Sampling stations and their association with atmospheric radiotracers

We will focus herein on the strategy adopted for detecting associations between atmospheric radiotracers and sampling stations. Owing to the extensive dataset collected, a multivariate approach was selected in order to detect data patterns and significant associations as widely applied in atmospheric science (e.g., Tositti et al., 2014b, Tositti et al., 2018; Núñez-Alonso et al., 2019, Petroselli et al., 2019) and in general in environmental science (e.g., Perez-Bendito and Rubio, 1999).

Factor analysis based on Principal Component Analysis (PCA) was applied to compositional data including the atmospherically derived radionuclides from all stations and in all the sections for station classification and solved for station affinity; Gabriel biplot showing the two atmospheric radionuclides ($^{210}\text{Pb}_{\text{ex}}$ and ^{137}Cs) is reported in Fig. 4, while factor scores (that are the observations coordinates on the PCA dimensions) are reported in Table 2. While each soil station has its own peculiarities, and will be object of a dedicated paper, the station score distribution shows that all the stations are clustered in groups reflecting substantially their mean height. Similarities are found between MM and MTM, i.e. the high-altitude stations on the NNW branch of the transect, and between STR and MIR on the opposite edge, in connection with minimal human disturbances as compared to bottom stations. A second larger group includes CES, LGR, LAR, PRI, i.e. the stations at low-altitude within the transect, while PCE and ERA appear as isolated with respect to all the others.

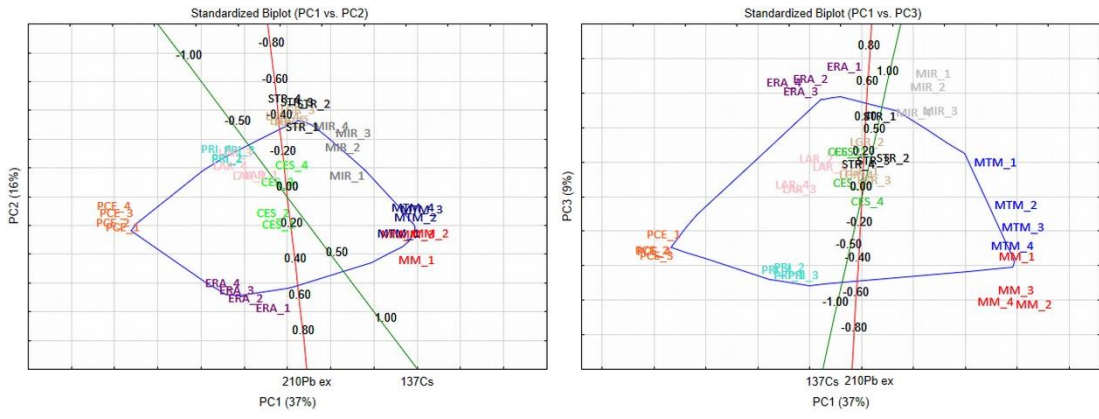


Fig. 4. Gabriel biplot of Principal Component Analysis (PCA) with $^{210}\text{Pb}_{\text{ex}}$ and ^{137}Cs , PC1 vs. PC2 and PC1 vs. PC3.

Table 2. Scores of the first six Principal Component Analysis factors (PC1, ...PC6).

Sample	PC1	PC2	PC3	PC4	PC5	PC6
MM_1	6.81	-3.84	-2.35	0.15	-0.32	0.19
MM_2	7.55	-2.46	-3.95	0.24	0.84	-0.43
MM_3	6.78	-2.52	-3.50	-0.08	1.11	0.18
MM_4	5.87	-2.52	-3.86	-0.47	1.11	0.39
MTM_1	5.87	-2.47	0.77	-1.32	-0.41	0.11
MTM_2	6.75	-1.64	-0.64	-0.23	0.16	-0.54
MTM_3	7.08	-1.21	-1.38	-0.18	0.18	-0.42
MTM_4	6.60	-1.14	-2.01	-0.19	0.61	-0.91
ERA_1	-0.75	-6.34	3.98	1.84	-1.82	-0.12
ERA_2	-2.21	-5.81	3.57	1.60	-1.41	-0.19
ERA_3	-2.66	-5.43	3.15	1.36	-1.16	-0.10
ERA_4	-3.41	-5.07	3.44	1.24	-1.55	-0.86
CES_1	-0.48	-1.99	1.13	0.53	1.21	1.47
CES_2	-0.75	-1.41	1.15	0.92	1.52	1.19
CES_3	-0.52	0.20	0.10	1.57	1.95	1.52
CES_4	0.25	1.08	-0.51	1.49	2.20	0.62
PRI_1	-3.17	1.39	-2.98	0.30	-5.19	0.11
PRI_2	-3.18	1.43	-2.71	0.17	-4.76	0.18
PRI_3	-2.55	1.87	-2.98	0.35	-4.13	-0.66
PRI_4	-3.74	1.90	-2.80	0.54	-4.97	0.51
PCE_1	-8.64	-2.17	-1.62	-1.92	1.04	-1.25
PCE_2	-9.15	-1.90	-2.16	-2.12	2.09	-1.67
PCE_3	-8.97	-1.43	-2.33	-1.57	3.19	-2.06
PCE_4	-9.10	-1.05	-2.19	-1.15	2.80	-2.74
LGR_1	-0.01	3.36	0.48	4.93	0.89	-0.81
LGR_2	0.23	3.32	1.45	5.27	0.42	-1.63
LGR_3	0.56	3.94	0.19	4.76	1.25	-1.14
LGR_4	-0.25	3.62	0.36	4.72	1.04	-0.54
LAR_1	-1.39	0.55	0.62	-1.00	0.55	4.20
LAR_2	-1.98	0.50	0.90	-0.59	0.82	4.22
LAR_3	-2.72	1.72	-0.10	-1.62	0.14	4.37
LAR_4	-3.03	1.05	0.03	-0.78	0.92	4.15
MIR_1	3.12	0.52	3.73	-3.44	-0.65	-1.75
MIR_2	2.91	1.98	3.30	-3.28	-0.94	-1.35
MIR_3	3.46	2.75	2.50	-3.25	-0.52	-1.88
MIR_4	2.30	3.12	2.43	-2.94	-0.70	-1.25
STR_1	0.78	3.06	2.32	-1.52	0.44	0.15
STR_2	1.39	4.23	0.94	-1.25	0.76	-0.73
STR_3	0.53	4.32	0.84	-1.31	0.59	-0.36
STR_4	-0.14	4.51	0.71	-1.78	0.68	-0.19

Fig. 4 shows as PC1 is poorly described by atmospheric radiotracers ($^{210}\text{Pb}_{\text{ex}}$ and ^{137}Cs), unlike PC2 and PC3. The use of $^{210}\text{Pb}_{\text{ex}}$ and ^{137}Cs suggests a clear separation among the ERA, MIR, and PRI stations, which conversely does not appear among the PCE, MM, and

MTM. The distinction of the ERA station is in agreement with what previously observed. Also, the PRI station can be justified by an anomaly in the concentration profiles of both ^{210}Pb and ^{137}Cs , which is correlated with disturbances related to local soil use (see Fig. 2 and Section 3.1).

It is therefore, concluded that the radiotracer approach is efficient in solving atmospheric deposition in soil, even if the extension of the approach to the whole compositional dataset in order to detect unambiguously atmospherically derived components would require an increase of resolution in soil sampling and associated vertical profile, as performed, for instance, by Landis et al. (2016).

3.3 Organic compounds

Differently from elements and radionuclidic components discussed above, PAHs and paraffins, chosen for their likely atmospheric origin similarly to the airborne radiotracers on which this paper is based, were analyzed in the bulk cores, mixing the whole upper soil 20 cm without sectioning. In this case, no vertical profiles of organics were available, therefore data and correlations were studied considering exclusively inventories of organic pollutants in analogy and association with $^{210}\text{Pb}_{\text{ex}}$ and ^{137}Cs inventories. Total PAH has a high linear coefficient of determination with soil TOC ($R^2 \approx 0.85$), owing to the high affinity with this macro soil component.

The comparison of PAH's inventories across the soil transect (Fig. 5A) reveals that the bottom stations (LGR, PRI and PCE), all located within the Terni conurbation, present the maximum deposition of these pollutants.

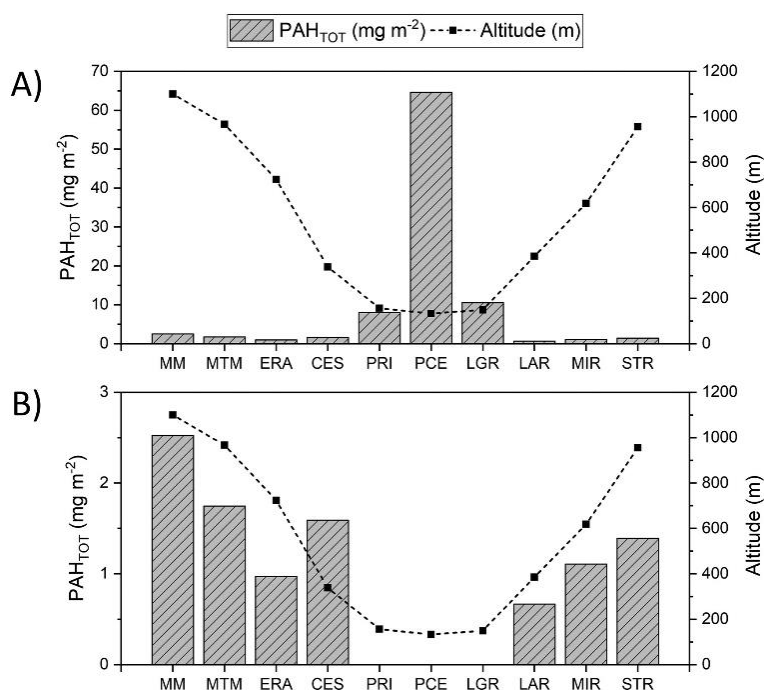


Fig. 5. Total PAH inventory (expressed in mg m^{-2}) as a function of altitude from Terni (expressed in m) for all the investigated sites (A) and excluding the three bottom stations in Terni area (B).

In particular, all the three urban stations present PAH concentration values 7–45 times higher than the average of all the remaining stations, indicating an extremely high degree of local pollution; in addition PCE presents by far the highest total PAH concentration level together with the highest HMW (high molecular weight) PAH's concentrations, possibly in association again with enhanced aerosol interception by the tree canopy. The highest LMW (Low Molecular Weight) PAH's fraction was detected at LGR, a site more exposed to vehicular traffic. Outside the urban environment, the concentration profile of PAHs along the two sides of the transect, showed a certain degree of increase with height and deposition pattern similar to the radionuclidic inventories with higher depositions on the left branch suggesting the potential for similar depositional behavior with height (see Fig. 5B). However, the complex environmental behavior of PAH's ranging from different volatilities as a function of molecular mass to photodegradation and/or nitrification in the troposphere, prevent from conclusive deductions on this class of organic pollutants.

Paraffins do not show any clear depositional pattern with height, nor specific trends were found for the carbon preference index - CPI (Lichtfouse and Eglinton, 1995) or low vs. high molecular weight paraffins. This observation is in agreement with the findings of Luo et al. (2012), who attributed a large part of the variance of paraffins in soil samples vs. elevation to vegetation and bacterial processing rather than to atmospheric transport.

3.4 Pollutant dispersion in the Terni basin valley: CALPUFF modeling

The atmospheric deposition detected along the soil transect is supported by the output of the CALPUFF dispersion model. The model was run for the full 2014 meteorological year and showed higher cumulate precipitations at the higher elevation sites (Fig. 6) which are in reasonably satisfactory agreement with measured total precipitations recorded by the Regional Hydrographic Network (<https://servizioidrografico.regione.umbria.it>, accessed 21/04/2020) reported in Table 3. Measured precipitations show a slight prevalence of the NW stations. We note that the highest depositions of radionuclides and chemical species have been observed on the NW branch of the transect, although relative maxima have also been observed in the SE branch. Since the major mechanism of removal of the accumulation mode (300–700 nm) is wet scavenging, this observation is expected to be in agreement with the pattern of the measured precipitation.

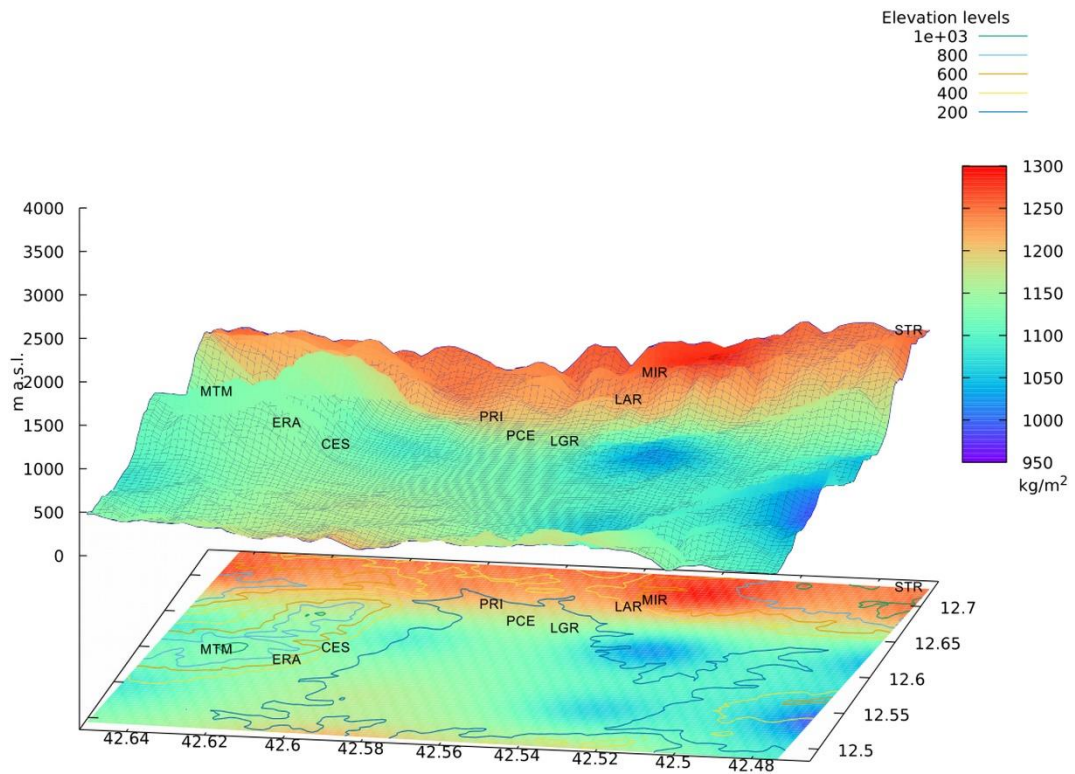


Fig. 6. Cumulative precipitation.

Table 3. Location and total precipitation data.

<i>Site</i>	<i>Height (m a.s.l.)</i>	<i>Latitude</i>	<i>Longitude</i>	<i>Precipitation (kg/m²)</i>	<i>Position in the transect</i>
Montemartano	618	42.7881	12.5947	1343	NNW
Castagnacupa	778	42.6700	12.6539	1415	NNW
Terni	130	42.5597	12.6503	955	CENTRAL
Arrone	285	42.5823	12.7612	1031	SSW
Piediluco	370	42.5342	12.7672	1261	SSW

The wind roses obtained with the same model runs (Fig. 7) show a consistent northerly-northwesterly pattern compatible with an excess accumulation of atmospheric deposition on the north-western branch of the sampling transect, mainly if a seeder-feeder driven phenomenology with mediation by orographic clouds is invoked.

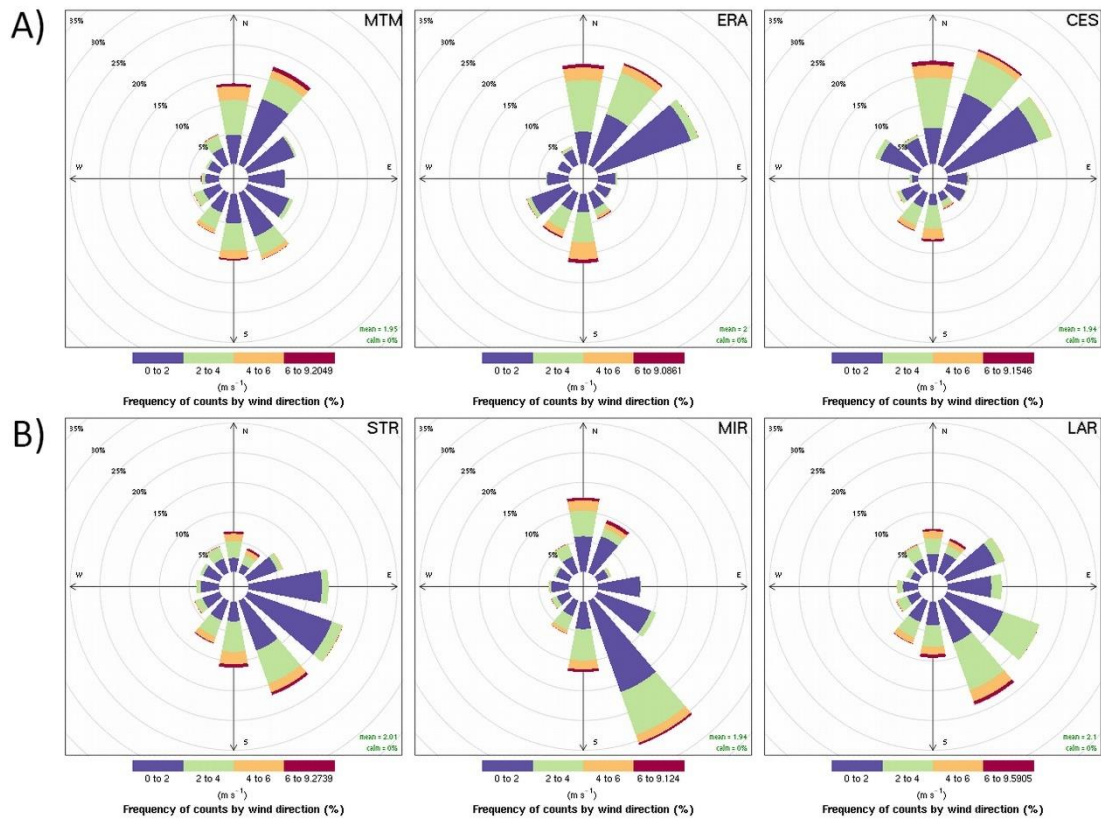


Fig. 7. Wind roses for the north-western branch (A) and for the Eastern branch (B).

The total wet and dry deposition pattern obtained as an outcome of the model is shown in Fig. 8. Maxima are located in the valley bottom, near the PCE, LGR, and PRI sites, but the TSP extends, consistent with the precipitation pattern, towards the higher elevation areas of the computational grid with a slight prevalence of the northern sectors.

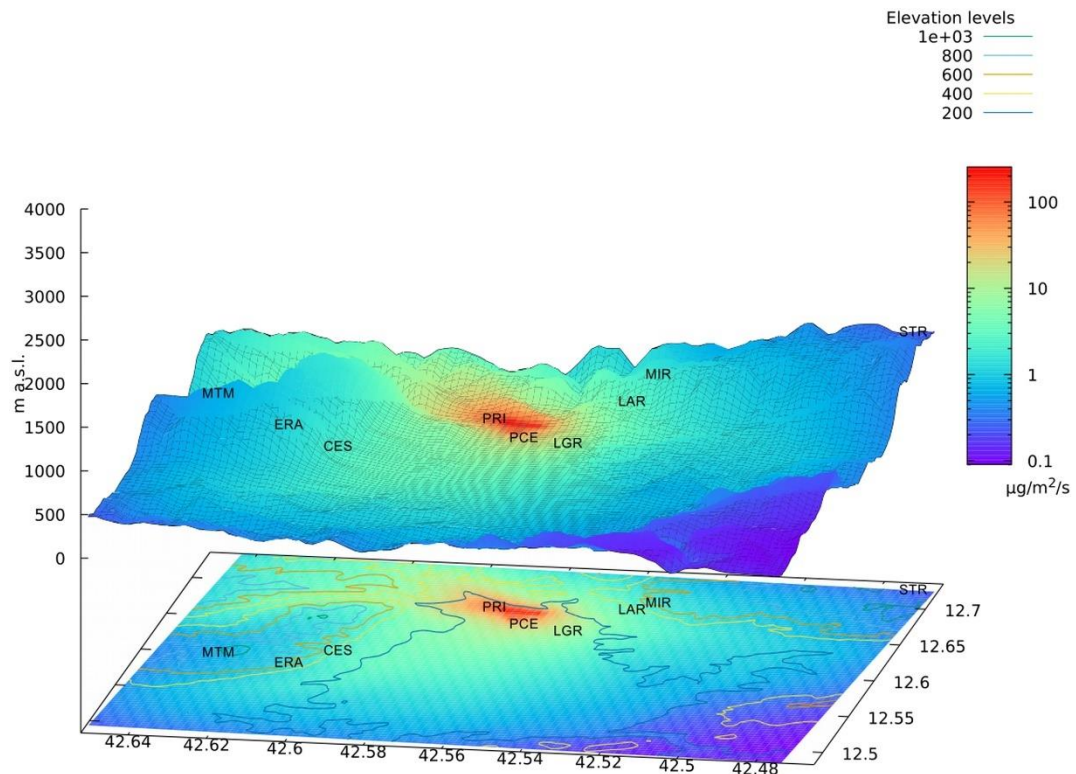


Fig. 8. Wet and dry deposition as obtained by the CALPUF model (see text).

Based on the results from numerical simulations together with the previous pattern of radionuclides and soil composition, we speculate that the plume developing in the Terni bottom airshed enriched in secondary inorganic aerosol, heavy metals, organic pollutants, and radon from which $^{210}\text{Pb}_{\text{ex}}$ is generated, might be uplifted and wet-removed through a seeder-feeder process promoted by the atmospheric circulation. Considering that the CALPUFF modeling is based de facto on a single source, the qualitative agreement of the model simulations with the observations along the transect can be considered as a reasonable support of the reasonings herein presented.

4 –Conclusions

In this paper, we have presented a systematic approach capable of evaluating and describing the deposition process over the Terni district by intercepting the occurrence of the atmospheric components into the soil and atmospheric modeling. The experimental method is based on the use of airborne radionuclides as tracers of atmospheric deposition in a complex mixture of chemical species ranging from inorganic elements to organic molecular species, directly determined in soil profiles. The similarity between soil sampling stations and their association with atmospheric radionuclides is also achieved by means of multivariate statistical analysis.

A significant anthropic impact at low altitude across the Terni basin stations has been detected, because of their proximity of residential and industrial sides, with respect to higher altitude stations. This piece of information is evidenced both by the presence of higher concentrations of PAHs, linked to more anthropogenic pollution, and in a more considerable disturbance of the depth profiles of atmospheric radionuclides. The significant role of the planetary boundary layer in trapping pollutants within a shallow mixing height has been

already pointed out in other studies conducted in the Terni valley (Ferrero et al., 2012, Ferrero et al., 2014; Massimi et al., 2019). Herein, we confirm that this is the prevalent atmospheric process that regulates the dispersion of locally generated pollutants in basin valleys. A higher deposition of atmospheric radionuclides has also been assessed in stations at higher altitudes, in particular on the NNW side of the transect. This process is more related to long-range transport of pollutants and enlightens the important role of medium- or high-altitude monitoring sites to study transboundary pollution (Petroselli et al., 2018, Petroselli et al., 2019; Federici et al., 2018; Moroni et al., 2019).

The comparison of atmospheric deposition data with the output of a Calpuff application to the Terni district shows a satisfactory agreement, even though part of the phenomenology that we assume as being related to orographic precipitation, is not sufficiently captured due to the limited model resolution.

This work represents a multidisciplinary approach for assessing the atmospheric deposition process into soils, and further studies will be carried out in order to deepen also the soil contamination across the Terni district.

CRedit authorship contribution statement

Laura Tositti: Conceptualization, Writing - original draft, Writing - review & editing, Visualization, Resources. Beatrice Moroni: Investigation, Writing - review & editing. Enrico Dinelli: Investigation, Resources, Visualization, Writing - review & editing. Pietro Morozzi: Formal analysis. Erika Brattich: Formal analysis, Writing - review & editing, Investigation. Bartolomeo Sebastiani: Investigation. Chiara Petroselli: Investigation, Writing - review & editing. Stefano Crocchianti: Formal analysis. Roberta Selvaggi: Investigation, Writing - review & editing. Goretti Enzo: Investigation, Writing - review & editing. David Cappelletti: Resources, Investigation, Writing - review & editing, Funding acquisition.

Declaration of competing interest

The authors declare that they have no known competing financial interests or personal relationships that could have appeared to influence the work reported in this paper.

Acknowledgements

The authors thank MIUR and Perugia University for financially supporting the research through the AMIS project (“Dipartimenti di Eccellenza-2018-2022”) and Arpa Umbria for collaboration in the CALPUFF dispersion model.

Appendix A. Supplementary data

Download: [Download Word document \(46KB\)](#)

References

- Arpa (Agenzia Regionale per la protezione ambientale) Umbria, Qualità dell'aria nella provincia di Terni tra il 2002 e il 2011 (2013), <https://www.arpa.umbria.it/pagine/la-qualita-dellaria-nella-provincia-di-terni-tra-i>, Available at (Accessed 21 April 2020);
- Baskaran, M., (2011) Handbook of Isotope Geochemistry, 1, p. 951., Springer-Verlag Berlin Heidelberg;
- Battiston, G.A., Degetto, S., Gerbasi, R., Sbrignadello, G., Tositti, L., Croatto, U., The deposition of chernobyl fallout in North-east Italy (1987) *Inorg. Chim. Acta*, 140 (100), pp. 327-329;
- Bettoli, M.G., Cantelli, L., Degetto, S., Tositti, L., Tubertini, O., Valcher, S., Preliminary investigations on ⁷Be as a tracer in the study of environmental processes (1995) *J. Radioanal. Nucl. Chem. Artic.*, 190 (1), pp. 137-147;
- Blackwell, B.D., Driscoll, C.T., Deposition of mercury in forests along a montane elevation gradient (2015) *Environ. Sci. Technol.*, 49, pp. 5363-5370;
- Brattich, E., Hernandez-Ceballos, M.A., Cinelli, G., Tositti, L., Analysis of ²¹⁰Pb peak values at Mt. Cimone (1998-2011) (2015) *Atmos. Environ.*, 112, pp. 136-147;
- Brattich, E., Riccio, A., Tositti, L., Cristofanelli, P., Bonasoni, P., An outstanding Saharan dust event at Mt. Cimone (2165 m a.s.l., Italy) in March 2004 (2015) *Atmos. Environ.*, 113, pp. 223-235;
- Brattich, E., Hernández-Ceballos, M.A., Orza, J.A.G., Bolívar, J.P., Tositti, L., The western Mediterranean basin as an aged aerosols reservoir. Insights from an old-fashioned but efficient radiotracer (2016) *Atmos. Environ.*, 141, pp. 481-493;
- CALPUFF, Modeling system version 6 user instructions (2001), <http://www.src.com/calpuff/>; Cartechini, L., Castellini, S., Moroni, B., Palmieri, M., Scardazza, F., Sebastiani, B., Selvaggi, R., Cappelletti, D., Acute episodes of black carbon and aerosol contamination in a museum environment: results of integrated real-time and off-line measurements (2015) *Atmos. Environ.*, 116, pp. 130-137;
- Cinelli, G., Tositti, L., Capaccioni, B., Brattich, E., Mostacci, D., Soil gas radon assessment and development of a radon risk map in Bolsena, Central Italy (2014) *Environ. Geochem. Health*, 37 (2), pp. 305-319;
- Daly, A., Zannetti, P., Air pollution modeling - an overview (2007) *Ambient air pollution*, pp. 15-28;
- Federici, E., Petroselli, C., Montalbani, E., Casagrande, C., Ceci, E., Moroni, B., La Porta, G., Cappelletti, D., Airborne bacteria and persistent organic pollutants associated with an intense Saharan dust event in the Central Mediterranean (2018) *Sci. Tot. Environ.*, 645, pp. 401-410;
- Ferrero, L., Cappelletti, D., Moroni, B., Sangiorgi, G., Perrone, M.G., Crocchianti, S., Bolzacchini, E., Wintertime aerosol dynamics and chemical composition across the mixing layer over basin valleys (2012) *Atmos. Environ.*, 56, pp. 143-153;
- Ferrero, L., Castelli, M., Ferrini, B.S., Moscatelli, M., Perrone, M.G., Sangiorgi, G., Rovelli, G., Cappelletti, D., Impact of Black Carbon Aerosol over Italian basin valleys:

- high resolution measurements along vertical profiles, radiative forcing and heating rate (2014) *Atmos. Chem. Phys.*, 14, pp. 9641-9664;
- Fowler, D., Cape, J.N., Leith, I.D., Choularton, T.W., Gay, M.J., Jones, A., The influence of altitude on rainfall composition at Great Dun Fell (1988) *Atmos. Environ.*, 22 (7), pp. 1355-1362;
 - Fowler, D., Mourne, R., Branford, D., The application of 210Pb inventories in soil to measure long-term average wet deposition of pollutants in complex terrain (1995) *Water Air Soil Pollut.*, 85, pp. 2113-2118;
 - Fowler, D., Skiba, U., Nemitz, E., Choubedar, F., Branford, D., Donovan, R., Rowland, P., Measuring aerosol and heavy metal deposition on urban woodland and grass using inventories of 210Pb and metal concentrations in soil (2004) *Water, Air and Soil Pollution Focus*, 4, pp. 483-499;
 - Franzini, M., Leoni, L., Saitta, M., A simple method to evaluate the matrix effects in X-ray fluorescence analysis (1972) *X-Ray Spectrom.*, 1, pp. 151-154;
 - Franzini, M., Leoni, L., Saitta, M., Revisione di una metodologia analitica per fluorescenza-X basata sulla correzione completa degli effetti di matrice (1975) *Rendiconti della Società Italiana di Mineralogia e Petrologia*, 31, pp. 365-378;
 - Gabriel, K.R., The biplot graphic display of matrices with application to principal component analysis (1971) *Biometrika*, 58 (3), pp. 453-467;
 - Gilmore, G.R., *Practical Gamma-Ray Spectrometry* (2008), 2nd edition John Wiley & Sons, Ltd;
 - Graustein, W.C., Turekian, K.K., 210Pb and 137Cs in air and soils measure the rate and vertical profile of aerosol scavenging (1986) *J. Geophys. Res.*, 91D, pp. 14355-14366;
 - Graustein, W.C., Turekian, K.K., The effects of forests and topography on the deposition of sub-micrometer aerosols measured by lead-210 and cesium-137 in soils (1989) *Agric. For. Meteorol.*, 47 (2-4), pp. 199-220;
 - IAEA, *Environmental Consequences of the Chernobyl Accident and their Remediation: Twenty Years of Experience/Report of the Chernobyl Forum Expert Group 'Environment'* (2006), International Atomic Energy Agency Vienna;
 - Jolliffe, I.T., Cadima, J., *Principal component analysis: a review and recent developments* (2016) *Philos. Trans. R. Soc. A Math. Phys. Eng. Sci.*, 374 (2065);
 - Jongen, S., Bonafe, G., LAMI verification for air quality forecast and assessment purposes. Internal report ARPAE-SIM (2006), https://www.arpae.it/smr/archivio/downloads/ambiente/report_lm_verif_fv.pdf;
 - Kaste, J.M., Friedland, A.J., Stürup, S., Using stable and radioactive isotopes to trace atmospherically deposited Pb in montane forest soils (2003) *Environ Sci Technol*, 37, pp. 3560-3567;
 - Lamborg, C.H., Fitzgerald, W.F., Graustein, W.C., Turekian, K.K., An examination of the atmospheric chemistry of mercury using 210Pb and 7Be (2000) *J. Atmos. Chem.*, 35, pp. 325-338;

- Lancianese, V., Dinelli, E., Geochemical mapping based on geological units: a case study from the Marnoso-arenacea formation (Northern Apennines, Italy) (2016) *Chemie der Erde – Geochemistry*, 76 (1), pp. 49-62;
- Landis, J.D., Renshaw, C.E., Kaste, J.M., Quantitative retention of atmospherically deposited elements by native vegetation is traced by the fallout radionuclides ⁷Be and ²¹⁰Pb (2014) *Environ. Sci. Technol.*, 48 (20), pp. 12022-12030;
- Landis, J.D., Renshaw, C.E., Kaste, J.M., Beryllium-7 and Lead-210 chronometry of modern soil processes: the Linked Radionuclide ACcumulation model (LCA) (2016) *Geochim. Cosmochim. Acta*, 180, pp. 109-125;
- Le Roux, G., Pourcelot, L., Masson, O., Duffa, C., Vray, F., Renaud, P., Aerosol deposition and origin in French mountains estimated with soil inventories of ²¹⁰Pb and artificial radionuclides (2008) *Atmos. Environ.*, 42 (7), pp. 1517-1524;
- Lichtfouse, E., Eglinton, T.I., ¹³C and ¹⁴C evidence of pollution of a soil by fossil fuel and reconstruction of the composition of the pollutant (1995) *Org. Geochem.*, 23 (10), pp. 969-973;
- Likuku, A.S., Wet deposition of ²¹⁰Pb aerosols over two areas of contrasting topography (2006) *Environ. Res. Lett.*, 1 (1);
- Likuku, A.S., Branford, D., Fowler, D., Weston, K.J., Inventories of fallout ²¹⁰Pb and ¹³⁷Cs radionuclides in moorland and woodland soils around Edinburgh urban area (UK) (2006) *J. Environ. Radioact.*, 90 (1), pp. 37-47;
- Luo, P., Peng, P.A., Lü, H.Y., Zheng, Z., Wang, X., Latitudinal variations of CPI values of long-chain n-alkanes in surface soils: evidence for CPI as a proxy of aridity (2012) *Sci China Earth Sci*, 55, pp. 1134-1146;
- Mabit, L., Benmansour, M., Abril, J.M., Walling, D.E., Meusburger, K., Iurian, A.R., Bernard, C., Alewell, C., Fallout ²¹⁰Pb as a soil and sediment tracer in catchment sediment budget investigations: a review (2014) *Earth Sci. Rev.*, 138, pp. 335-351;
- Massimi, L., Conti, M.E., Mele, G., Ristorini, M., Astolfi, M.L., Canepari, S., Lichen transplants as indicators of atmospheric element concentrations: a high spatial resolution comparison with PM10 samples in a polluted area (Central Italy) (2019) *Ecol. Indic.*, 101, pp. 759-769;
- Meloni, D., Carpine, F., (2004) Cinquanta anni (1953–2002) di osservazioni meteo a Terni, p. 79., Provincia di Terni;
- Moroni, B., Cappelletti, D., Marmottini, F., Scardazza, F., Ferrero, L., Bolzacchini, E., Integrated single particle-bulk chemical approach for the characterization of local and long range sources of particulate pollutants (2012) *Atmos. Environ.*, 50, pp. 267-277;
- Moroni, B., Ferrero, L., Crocchianti, S., Perrone, M.G., Sangiorgi, G., Bolzacchini, E., Cappelletti, D., Aerosol dynamics upon Terni basin (Central Italy): results of integrated vertical profile measurements and electron microscopy analyses (2013) *Rendiconti Lincei*, 24, pp. 319-328;
- Moroni, B., Castellini, S., Crocchianti, S., Piazzalunga, A., Fermo, P., Scardazza, F., Cappelletti, D., Ground-based measurements of long-range transported aerosol at the

- rural regional background site of Monte Martano (central Italy) (2015) *Atmos. Res.*, 155, pp. 26-36;
- Moroni, B., Crocchianti, S., Petroselli, C., Selvaggi, R., Becagli, S., Traversi, R., Cappelletti, D., Potential source contribution function analysis of long-range transported aerosols in the Central Mediterranean: a comparative study of two background sites in Italy (2019) *Rend. Fis. Acc. Lincei*, 30, pp. 337-349;
 - Núñez-Alonso, D., Pérez-Arribas, L.V., Manzoor, S., Cáceres, J.O., Statistical tools for air pollution assessment: multivariate and spatial analysis studies in the Madrid region (2019) *Journal of analytical methods in chemistry*, 2019;
 - ORTEC, Gamma-Vision 32 A66-B32 User's Manual. ORTEC USA, Part. No. 783620 Manual Revision D (2003);
 - Perez-Bendito, D., Rubio, S., Chapter 14 Chemometrics in environmental analysis (1999) *Environmental Analytical Chemistry*, pp. 747-833;
 - Persson, B.R.R., Holm, E., Polonium-210 and lead-210 in the terrestrial environment: a historical review (2011) *J. Environ. Radioact.*, 102 (5), pp. 420-429;
 - Petroselli, C., Crocchianti, S., Moroni, B., Castellini, S., Selvaggi, R., Nava, S., Calzolari, G., Cappelletti, D., Disentangling the major source areas for an intense aerosol advection in the Central Mediterranean on the basis of Potential Source Contribution Function modeling of chemical and size distribution measurements (2018) *Atmos. Res.*, 204, pp. 67-77;
 - Petroselli, C., Moroni, B., Crocchianti, S., Selvaggi, R., Vivani, R., Soggia, F., Grotti, M., Cappelletti, D., Iron speciation of natural and anthropogenic dust by spectroscopic and chemical methods (2019) *Atmosphere*, 10 (1), p. 8;
 - Preiss, N., Mélières, M.-A., Pourchet, M., A compilation of data on lead 210 concentration in surface air and fluxes at the air-surface and water-sediment interfaces (1996) *Journal of Geophysical Research: Atmospheres*, 101 (D22), pp. 28847-28862;
 - Stankwitz, C., Kaste, J.M., Friedland, A.J., Threshold increases in soil lead and mercury from tropospheric deposition across an elevational gradient (2012) *Environ Sci Technol*, 46, pp. 8061-8068;
 - Suchara, I., Sucharova, J., Hola, M., Pilatova, H., Rulik, P., Long-term retention of ¹³⁷Cs in three forest soils with different soil properties (2016) *J. Environ. Radioact.*, 158-159, pp. 102-113;
 - Swarzenski, P.W., ²¹⁰Pb Dating in *Encyclopedia of Scientific Dating Methods* (2014), Springer Science+Business Media Dordrecht;
 - Tositti, L., Mingozi, M., Sandrini, S., Buoso, S., De Poli, M., Ceccato, D., Zafiropoulos, D., A multitracer study on peat profiles from Tunguska, Siberia (2006) *Glob. Planet. Chang.*, 53, pp. 278-289;
 - Tositti, L., Brattich, E., Cinelli, G., Baldacci, D., 12 years of ⁷Be and ²¹⁰Pb in Mt. Cimone, and their correlation with meteorological parameters (2014) *Atmos. Environ.*, 87, pp. 108-122;
 - Tositti, L., Brattich, E., Masiol, M., Baldacci, D., Ceccato, D., Parmeggiani, S., Stracquadanio, M., Zappoli, S., Source apportionment of particulate matter in a large city

of southeastern Po Valley (Bologna, Italy) (2014) *Environ. Sci. Pollut. Res. Int.*, 21, pp. 872-890;

- Tositti, L., Cinelli, G., Brattich, E., Galgaro, A., Mostacci, D., Mazzoli, C., Massironi, M., Sassi, R., Assessment of lithogenic radioactivity in the Euganean Hills magmatic district (NE Italy) (2016) *J. Environ. Radioact.*, 166 (2), pp. 259-269;
- Tositti, L., Brattich, E., Parmeggiani, S., Bolelli, L., Ferri, E., Girotti, S., Airborne particulate matter biotoxicity estimated by chemometric analysis on bacterial luminescence data (2018) *Sci. Total Environ.*, 640-641, pp. 1512-1520;
- USEPA, Revision to the Guideline on Air Quality Models: Adoption of a Preferred Long Range Transport Model and Other Revisions; Final Rule, 40 CFR Part 51, Federal Register/Vol. 70, No. 216/Wednesday, November 9, 2005/Rules and Regulations, 68218 (2005);
- USEPA, Revision to the Guideline on Air Quality Models: Adoption of a Preferred Long Range Transport Model and Other Revisions; Final Rule, 40 CFR Part 51, Federal Register/Vol. 82, No. 10/January 17, 2017/Rules and Regulations, 5182 (2017);
- van den Berg, R.A., Hoefsloot, H.C., Westerhuis, J.A., Smilde, A.K., van der Werf, M.J., Centering, scaling, and transformations: improving the biological information content of metabolomics data (2006) *BMC Genomics*, 7 (1), p. 142;
- Vet, R., Artz, R.S., Carou, S., Shaw, M., Ro, C.-H., Aas, W., Baker, A., Reid, N.W., A global assessment of precipitation chemistry and deposition of sulfur, nitrogen, sea salt, base cations, organic acids, acidity and pH, and phosphorus (2014) *Atmos. Environ.*, 93, pp. 3-100;
- Vet, R., Artz, R.S., Carou, S., Shaw, M., Ro, C.-H., Aas, W., Baker, A., Reid, N.W., Addendum to: "A global assessment of precipitation chemistry and deposition of sulfur, nitrogen, sea salt, base cations, organic acids, acidity and pH, and phosphorus" (2014) *Atmos. Environ.*, 93, pp. 101-116., 2014;
- Zhang, L., Vet, R., A review of current knowledge concerning size-dependent aerosol removal (2006) *China Particuology*, 4 (6), pp. 272-282

CHAPTER 9 - Chemical characterization of drip and river waters in the Pertosa Auletta cave (SA, Italy)

1 – Introduction

This study presents the preliminary results of a research concerning the characterization of drip- and river water samples in the Pertosa-Auletta cave (Italy, SA), in collaboration with Integrated Environmental Museum (MIIdA) Foundation and the University of Salerno (UNISA). This activity represents only a part of a broader project named AEROCAVE-MIIdA, whose aim is improving our knowledge on the complex meteorological and climatic phenomenologies, investigates the atmospheric aerosols dynamics, and outline the best strategies for the correct management of the cave, presently exploited as a touristic attraction and, therefore, vulnerable from both the chemical and biological point of view.

An intensive chemical characterization of drip and river waters can be extremely informative about the underground karst ecosystem.

Karstification is a hydrogeological phenomenon that denotes the physico-chemical action carried out by water on soil and rocks, that is dissolution and, subsequently, the precipitation of the a few chemical components they contain and basically concerning the complexities of the carbonatic system. The principle of karst is the following: water passes from a dissolution regime (phase of erosion of surface rocks, known as physical and chemical weathering), to a precipitation regime (phase in which the solutes are chemically precipitated owing to saturation conditions) with formation of concretions. The topsoil above karst regions receives atmospheric deposition (rain, snow) typically acidic (pH = 5.7) owing to the equilibrium between the hydrometeor and atmospheric CO₂; Moreover, biochemical degradative processes within soil pores lead to an increase of acidity enhancing, in turn, the solvent capacities of percolating water and leading to the dissolution of mineral carbonates in the soil phase. As soon as water reaches the subsoil, the acidity is typically neutralized so that the conditions favourable to carbonate re-precipitation are reached. The chemical processes underlying the karst phenomenon are illustrated in Figure 1.

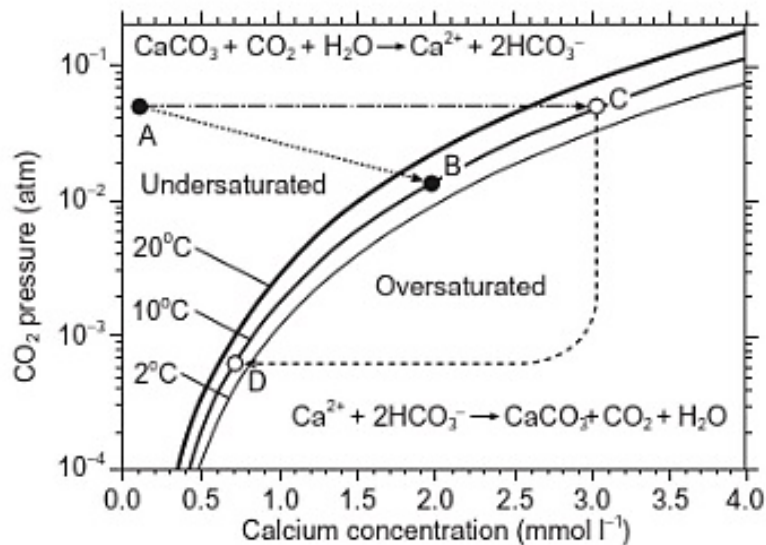


Figure 1. Karst process (Fairchild & Baker, 2012).

As can be seen, high partial pressures of CO₂, connected to respiration and decomposition of organic material on the surface, erode the soil (point A) because of induced acidification in aqueous phase (carbonic acid equilibria). When the acidified percolating water reaches the carbonate minerals, it dissolves them, increasing the calcium concentrations in the solution. If CO₂ is not renewed/replenished, water follows the pattern of a closed system up to the saturation point (B). Instead, if additional CO₂ is fed to the system, the saturation will be reached at point C. As water is further leached to depth into the karst system, it can encounter environments where the partial pressure of CO₂ is lower than the original soil. Water then reaches the supersaturation field and tends to precipitate CaCO₃ (line from C to D).

The amount of calcite (CaCO₃) and dolomite (CaMg(CO₃)₂) that can be dissolved by water depends on its acidity, usually expressed as a partial pressure of carbon dioxide (pCO₂) in aqueous solution. Although strong acids (e.g. sulfuric acid from the oxidation of minerals such as pyrite, FeS₂) can influence the phenomenon of chemical weathering operated by water at the local level, usually the dissolution process is mainly related to pCO₂, which can also reach up to 0.01-0.1 atm (Fairchild & Baker, 2012).

The acidic water then descends through the deeper rocky layers, making its way through porosities, fractures, or layers of stratification. This process generates caves and tunnels (when they develop in a sub-horizontal direction) and/or wells and abysses (when the development is vertical). Ultimately, the flowing water encounters a gas phase with a lower pCO₂ than the previous one. This causes the release of CO₂ from the solution and the precipitation of CaCO₃. Figure 1 shows that the difference in pCO₂ between the surface and the hypogean is a key parameter, which affects the amount of calcium ion removed from water and, therefore, the precipitation rate of calcium carbonate with the formation of concretions (Figure 2).



Figure 2. Calcareous concretions in the Pertosa-Auletta cave (photo by L. Tositti)

Rainwater that falls on the surface of a karst landscape follows gravity, percolating through the soil and underlying epicarsal, or descending more rapidly through relatively large openings. When the descent of the waters occurs simply by means of a permeation of the most superficial layers of the karst system up to reach the underground environments, we witness the origin of drip water (Figure 3).



Figure 3. Active dripping site in the Pertosa-Auletta Cave (photo by L. Tositti)

The underground karst environments continuously evolve over time as a function of the hydrological cycle, and it has been shown that they reflect the chemical composition of the precipitation and of the aerosol from which they developed within cloud processing and below-cloud impaction. The composition of dripping water, in turn, can be extremely variable, owing to the influence of:

- depositional and tectonic processes;
- properties and processes at the surface, which are then combined with the characteristic parameters of the hypogeum.

Owing to the typical environmental inhomogeneities, differences in top soil may produce distinct properties and characteristics in dripping water within the same cave.

The surface and hypogeal factors indicated above as causes of the particular chemistry of dripping waters can be:

- chemical mobility in the soil vertical profile and in the underlying epikarst of local chemical species and the hydrological processes of water infiltration (Fairchild & Treble, 2009);
- the contact time of waters in the soil and epikarst compartments, which, when slow, enhances the interactions with the mineral background of the system;
- temperature, promoting dissolution rates upon increasing, but disrupting the karstic cycling in case of aridity (in a period of global warming the increase in temperature might prove extremely critical since a part the risk for aridity, the intermediate phase of temperature increase might lead to excess solubilization with risk of collapse of the hypogean structures);
- water pH since, as previously described, the more acidic the waters, the higher the solvent power towards the soil phases.

Furthermore, water composition accessing the depths of the karst system, as for all natural waters, is strongly influenced at the origin by the atmospheric chemistry, since cloud water and hydrometeors (rain, snow, hail) are formed through complex nucleation processes mediated by atmospheric aerosols, consequently reflecting their composition (Tositti et al., 2018).

Figure 4 schematically summarizes the wide range of sources of chemical compounds for drip waters.

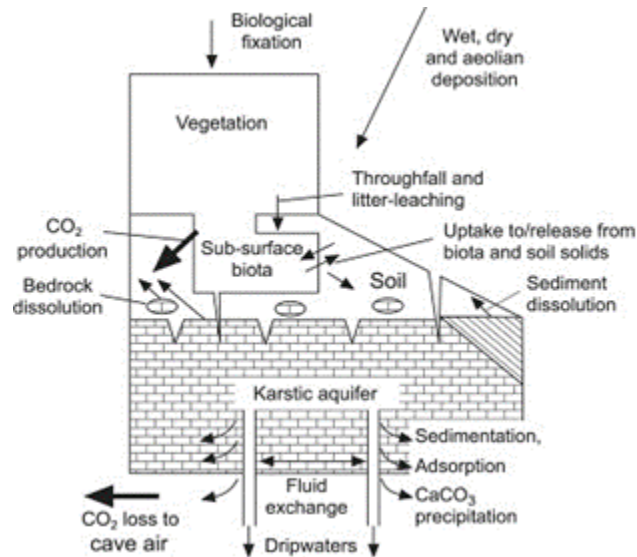


Figure 4. Sources, transport, and deposition processes of chemical compounds in the cave environment (Fairchild & Treble, 2009)

As can be seen, important contributions to the material cycling within the karst system are various types of materials such as aerosol and gaseous components conveyed by atmospheric circulation, dry and humid atmospheric deposition, weathering of rocky substrate, superficial sediment deposits, inorganic soil constituents, and substances recycled through biological activity. In the framework of the complexity of processes active in cave ecosystems, it is to emphasize the role of the so-called speleothems, more commonly known as stalactites and stalagmites whose formation tightly connected to the precipitation phase of carbonates in a cave environment is presently of remarkable interest in the field of global change studies. In fact, these carbonatic formations not only grow in subsequent layers as a function of time, but present a composition in each layer revealing tight connections with the atmospheric composition at the time of formation of the precipitation, thus acting as powerful environmental archives, providing the basis for studying the paleo-atmosphere in terms of air quality and climate change issues.

2 – Materials and methods

2.1 – *Pertosa-Auletta* cave

Pertosa-Auletta cave (Figure 5) is a karst show cave system situated at 263 m asl at the foot of the Alburni massif, one of the most important karst areas in southern Italy characterized by about 300 caves and cavities, some of which are still unexplored. More specifically, the cave is located on the left bank of the Tanagro river positioned in two small municipalities, *Pertosa* and *Auletta* (Salerno, Campania).

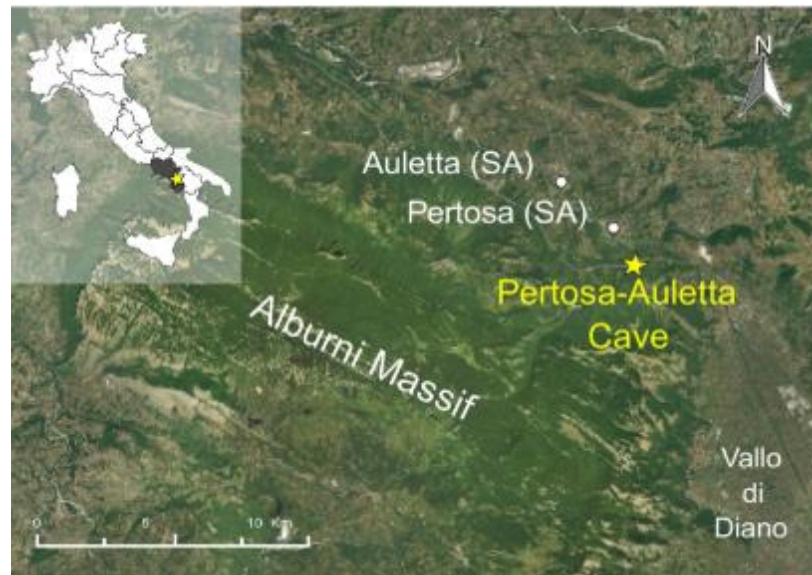


Figure 5. Geographical framework of the Pertosa-Auletta cave (Addesso et al., 2019).

It consists almost exclusively of limestone dating back to the Middle-Upper Jurassic era (from about 175 to 152 M years). These limestone beds have a thickness ranging from a few decimetres to several meters and are separated by thin layers (thickness from cm to dm) of marl (sedimentary rocks, characterized by a lower content of CaCO_3 than limestone) and clays. Locally, some of these layers show signs of emergence, together with red-orange layers of bauxite (sedimentary rock consisting mainly of aluminum hydroxides) (Addesso et al., 2019).

The Alburni massif has several water sources. The Pertosa-Auletta cave is part of the local Pertosa aquifer, that has an average water temperature around $12\text{ }^\circ\text{C}$, is characterized by a flow rate between 350 and 600 L s^{-1} (depending on the season) and has its outflow into the Tanagro river which flows 40 m lower than the cave. In 1924, the Southern Electricity Society (SME) started the hydroelectric exploitation of this source, building a dam at its entrance and generating a navigable lake inside the cave (Pastore, 2016).

The Pertosa-Auletta cave, also known as “Grotta dell'Angelo”, is an underground karst system about 3 km long. It constitutes a fundamental speleological and archeological site. Indeed, the cave is estimated to have formed about 780 000 years ago and terracotta manufacts, stones, bones and metals have been brought to light, which testify to a human presence associated with a period ranging from late Prehistory to Hellenistic-Roman period (Larocca, 2010). Furthermore, it is possible to identify structures of ancient pile dwellings present along the entire extension of the entrance to the Caves.

The underground system of the Pertosa-Auletta Cave (Figure 6), open to the public for tourist visits since the 1930s, is about 3 km long and consists of three parallel branches with two entrances, one artificial and one natural (the natural one is still closed due to collapses).

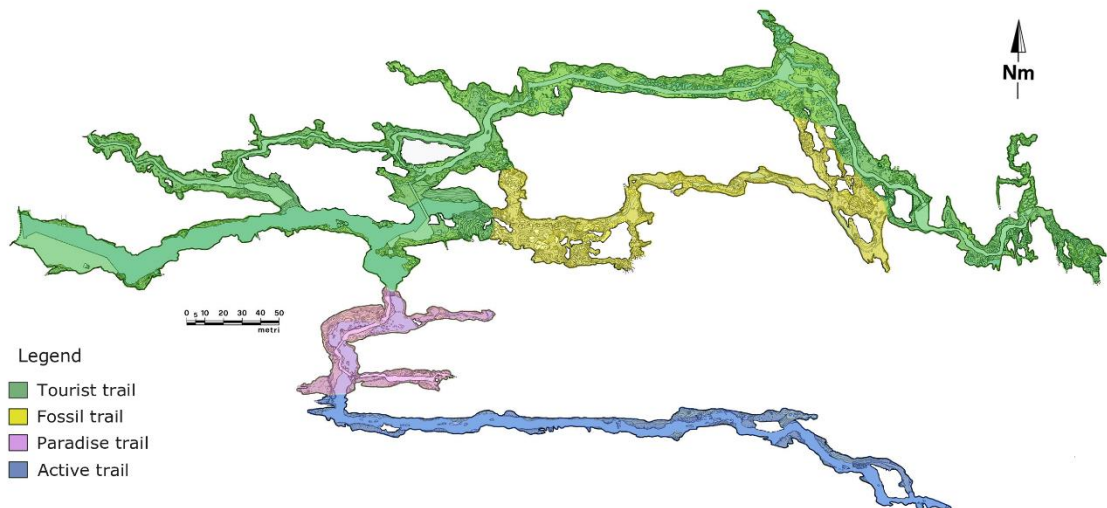


Figure 6. Map of the Pertosa-Auletta Cave (image kindly offered by Dr. Rosangela Adesso)

The northernmost branch is 800 meters long and includes the “Tourist trail” (in green in Figure 6), full of extraordinary speleothems. It is illuminated with artificial light for several hours a day and is intensely visited by tourists. The other two branches, the central one and the southernmost one, are not artificially illuminated and are less affected by human presence. Therefore, the latter represent less-impacted sections of the underground environment. The intermediate branch, called “Fossil trail” (in yellow in Figure 6) is 350 m long and is connected to the Tourist trail by a series of fractures and lateral passages. This tract is completely devoid of speleothems, but rich in muddy deposits and cracks in the rock. It also hosts bat colonies, both in winter and summer, responsible for the presence of fresh guano deposits. The southernmost branch, on the other hand, is known as the “Active trail” (in blue in Figure 6). It is about 500 meters long, almost completely crossed by a perennial underground stream, named as Negro River. The presence of this aquifer represents a peculiarity, enhancing the ecological interest of the Pertosa karst system. Near the junction with the other two branches, the stream forms a 3 m high waterfall, and then continues west for another 200 m, exiting the cave from the natural entrance. The “Paradise trail” is a short path (about 100 m long, in pink in Figure 6) of the Active Tract, illuminated, and open for regular tourist visits.

Another peculiarity of this underground environment is the development of Lampenflora, photobiotic communities that proliferate thanks to the humidity and the abundance of artificial light, but able to compete and probably compromise the fragile ecosystem of the caves (Adesso et al., 2019).

2.2 – Sampling and chemical characterization

Water sampling in the Pertosa-Auletta cave was performed over four seasons, from May 2020 to January 2021. The collection of drip water was carried out using polyethylene (PE) bottles positioned at the ground and always under concretions (stalactites or cannulas), according to the times and methods illustrated in Table 1.

Table 1. Drip water sampling in the Pertosa-Auletta cave

Season	Sampling month	Sampling period
Spring 2020	May 2020	1 week
Summer 2020	September 2020	1 week
Autumn 2020	November 2020	1 week
Winter 2020	January 2021	1 week

Drip waters were always sampled at the same pre-selected dripping points, based on intensity and stability over time of the dripping activity. Similarly, the waters of the Negro River were sampled using PE bottles. In these cases, the river water samples were collected at the time of withdrawal of the weekly drip-water bottles.

Immediately after sampling, the drip and river water samples were stored frozen at -10°C before chemical analysis. All the samples were subjected to an extensive range of chemical characterizations by Ion Chromatography (IC), Inductively coupled plasma - optical emission spectrometry (ICP-OES), and Total Organic Carbon and Total Nitrogen (TOC-TN) analyser (Shimadzu). Furthermore, pH, redox potential, and conductivity were determined *in situ* by a multiparameter water probe (HI-98196 Hanna Instrument) and a Pioneer 65 Radiometer Analytical.

IC allows the quantification of the main water-soluble cations and anions, and analyses were carried out at the by two different Thermo-Dionex ion chromatographs: ICS-2000 for the anions run, and ICS-90 for the cations run. Before analysis, the samples were filtered by PTFE syringe filters with pore size of $0.22\ \mu\text{m}$, to remove any solid residue suspended in the water; details of the chromatographic conditions are given in Table 2.

Table 2. Instrumental parameters of the ion chromatographs setup used

Instruments	ICS90 (Dionex)	ICS2000 (Dionex)
Analyzed ions	Na^+ , NH_4^+ , K^+ , Mg^{2+} , Ca^{2+}	F^- , Cl^- , NO_2^- , Br^- , NO_3^- , SO_4^{2-} , PO_4^{3-} , Acetate, Formate, Methanesulfonate, Succinate, Malonate, Oxalate
Condition	Isocratic	Gradient
Acquisition time	18 min	45 min
Sample volume	10 μL	25 μL
Flow	1.0 mL/min	0.38 mL/min
Eluent	Methanesulfonic acid (20 mM)	KOH (0.8 mM to 30 mM)
Column	Dionex IonPack™ CS12A 4x250 mm (ThermoFisher)	Dionex IonPack™ AS11-HC 2x250 mm (ThermoFisher)
Suppressor	CMMS_III 4mm	AERS_500 2mm
Detector	DS5 Detection stabilizer model (Dionex)	DS6 Heated conductivity cell (Dionex)

Calibration was carried out using suitable mixtures of standard ion solutions in the range $0.01 \div 10\ \text{ppm}$ for organic anions (Acetate, Formate, Methanesulfonate, Succinate,

Malonate, Oxalate) and 0.01 ÷ 50 ppm for cations (Na⁺, NH₄⁺, K⁺, Mg²⁺, Ca²⁺) and inorganic anions (F⁻, Cl⁻, NO₂⁻, Br⁻, NO₃⁻, SO₄²⁻, PO₄³⁻). Method detection limit (LOD) was estimated for each ion from the calibration lines, using the formula:

$$x_{LOD} = 3 \frac{s_{y/x}}{b}$$

where: b is the slope and $s_{y/x}$ is the covariance of the calibration line.

Chemical variables with most of the data below the LoDs thus calculated (> 50% data less than LoD) were discarded from subsequent statistical processing. Quality control was carried out using certified ERM-CA408 simulated rainwater to provide continuous validation for the analysis step and the determined concentrations were always within 7% of the stated values.

Inductively coupled plasma - optical emission spectrometry (ICP-OES) was performed to speciate several elements, which are Al, B, Ba, Ca, Cd, Co, Cr, Cu, Fe, K, Li, Mg, Mn, Mo, Na, Ni, P, Pb, S, Si, Sr, Ti, V, and Zn. Water analyses were performed by a PerkinElmer Optima 7000 DV ICP-OES without any chemical preparations. Instrumental accuracy was continuously assessed during the analysis by a Standard Reference Material (SRM 1575a Pine Needles; NIST, 2004).

Total Organic Carbon and Total Nitrogen (TOC-TN) analyser (Shimadzu) allow determining organic carbon (C org), inorganic carbon (C inorg), and Nitrogen (N) contained in the water samples.

2.3 – Classification and factor analysis

The analyzed samples were distinguished and grouped on the basis of two different classification modes: sampling season, and sampling site. "Negro" sampling site distinguishes river waters from drip waters. A total of 91 samples were analyzed and grouped as follows in Table 3:

Table 3. Sampled waters and their classification

Season	Location	N
Summer (N = 20)	Tourist	10
	Fossil	6
	Paradise	1
	Negro	3
Spring (N = 26)	Tourist	11
	Fossil	10
	Paradise	2
	Negro	3
Autumn (N = 21)	Tourist	9
	Fossil	6
	Paradise	3
	Negro	3
Winter (N = 20)	Tourist	9
	Fossil	5
	Paradise	3
	Negro	3

All the statistical analyses carried out are aimed at highlighting any differences or similarities between the samples grouped based on these two classes. In particular, Non-Negative Matrix Factorization (NMF, Gaujoux & Seoighe, 2010) was applied to reduce the number of the original variables of the system (chemical variables, all expressed in parts per million / ppm), and identify the new variables thus obtained from a chemical-hydrogeological point of view. This advanced multivariate factor analysis technique was performed by an R package named NMF (Gaujoux, 2020) on a concentration matrix of 91 samples x 36 variables. After careful evaluation of the best NMF algorithm, an optimum number of six factors was found by evaluating the key fit parameters, that are cophenetic coefficient, and residual sum of squares (RSS). In order to assess the reliability of the model reconstruction, measured (input data) and reconstructed (modeled) values together with the distribution of residuals were compared. Our results indicated a good general performance of the model in reconstructing most of the variables.

Finally, significant differences in the contributions of the six factors thus obtained as a function of the two classes were examined by Multivariate Analysis of Variance (MANOVA) and boxplots. In our case, each boxplot refers to a Factor or a chemical-physical parameter and the abscissa represents the kind of sample studied.

3 – Results and discussions

3.1 – Non-Negative Matrix Factorization (NMF)

Non-Negative Matrix Factorization (NMF) was performed by Brunet algorithm (standard NMF, Brunet et al., 2004) and six new variables (factors) were calculated as a linear combination of the 36 original variables (chemical variables) of the analyzed waters. Figure 7 show the stacked bar chart of the percentage concentration of each chemical species contributing to each of the six factors. Each factor represents the chemical profile of each source identified in the factorial analysis.

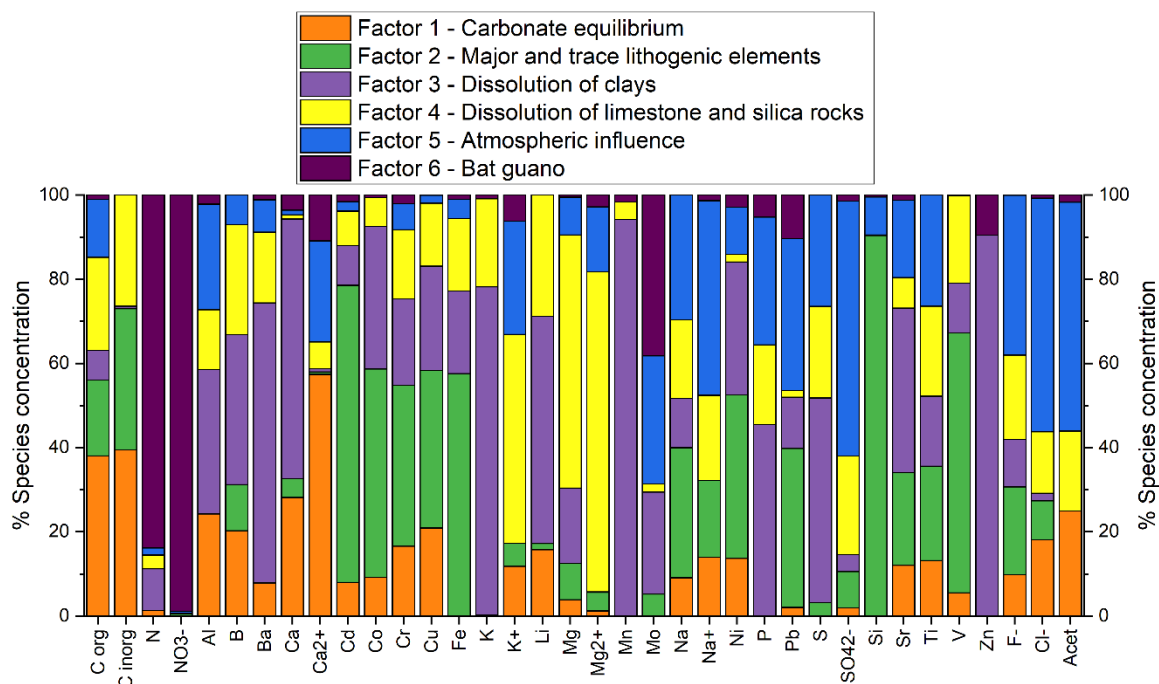


Figure 7. Factor Fingerprints screen.

Factor 1 is mainly characterized by organic carbon (C org), inorganic carbon (C inorg), and Ca^{2+} . Therefore, this factor defines the carbonate system in water samples, central point of the karst process previously described in the Introduction.

Factor 2 is mainly defined by Si, Cd, Fe, V, Co, Cr, and Cu. This factor includes major and trace chemicals of lithogenic origin (Tadros et al., 2019).

Factor 3 is mainly defined by K, Zn, and Mn, elements expected to have some association with the dissolution of clays (Tadros, 2018; Tremaine et al., 2016).

Factor 4 is mainly defined by Mg^{2+} , Mg, K^{+} and can be associated with dissolution of potassium silicates, that constitute the typical continental sediments, and Cretaceous limestone, very rich in dolomite-enriched cretaceous limestone (Pastore et al., 2017).

Factor 5 is mainly defined by SO_4^{2-} , Na^{+} , Cl^{-} revealing an atmospheric influence (Tremaine et al., 2016). Indeed, as widely described in the Introduction, drip waters derive from meteoric waters whose composition is closely linked to the hygroscopic atmospheric aerosol components acting as cloud condensation nuclei (CCN) and triggering precipitation formation. In particular, Na^{+} and Cl^{-} are mainly associated with the sea-salt component of atmospheric aerosols (Raes et al., 2000), while SO_4^{2-} is linked with secondary inorganic aerosol (SIA) component (Tremaine et al., 2016; Raes et al., 2000).

Factor 6 is mainly defined by N e NO_3^{-} , chemical species typically associated with bat guano (Misra et al., 2019; Sakoui et al., 2020). A low P loading is observed in this Factor, as it is presumably more linked to chemical fertilizers used for olive tree groves above the cave (Katz, 2019).

3.2 – Boxplots and Analysis of variance (ANOVA)

Multivariate analysis of variance (MANOVA) was performed on the contributions of the six chemical factors and chemical-physical parameters (Conductivity, Oxidation-Reduction Potential (ORP), and pH) in order to evaluate significant differences between classes (Season and Location).

MANOVA test showed significant differences, at a significance level of 5%, for both the sampling season (p-value $\approx 2.2 \cdot 10^{-16}$) and location (p-value $\approx 4.9 \cdot 10^{-10}$). Also, ANOVA tests were carried out for each variable and in the Figures below are shown the boxplots divided by classes and related to the most significant differences at a significant level of 5% (p-value < 0.05).

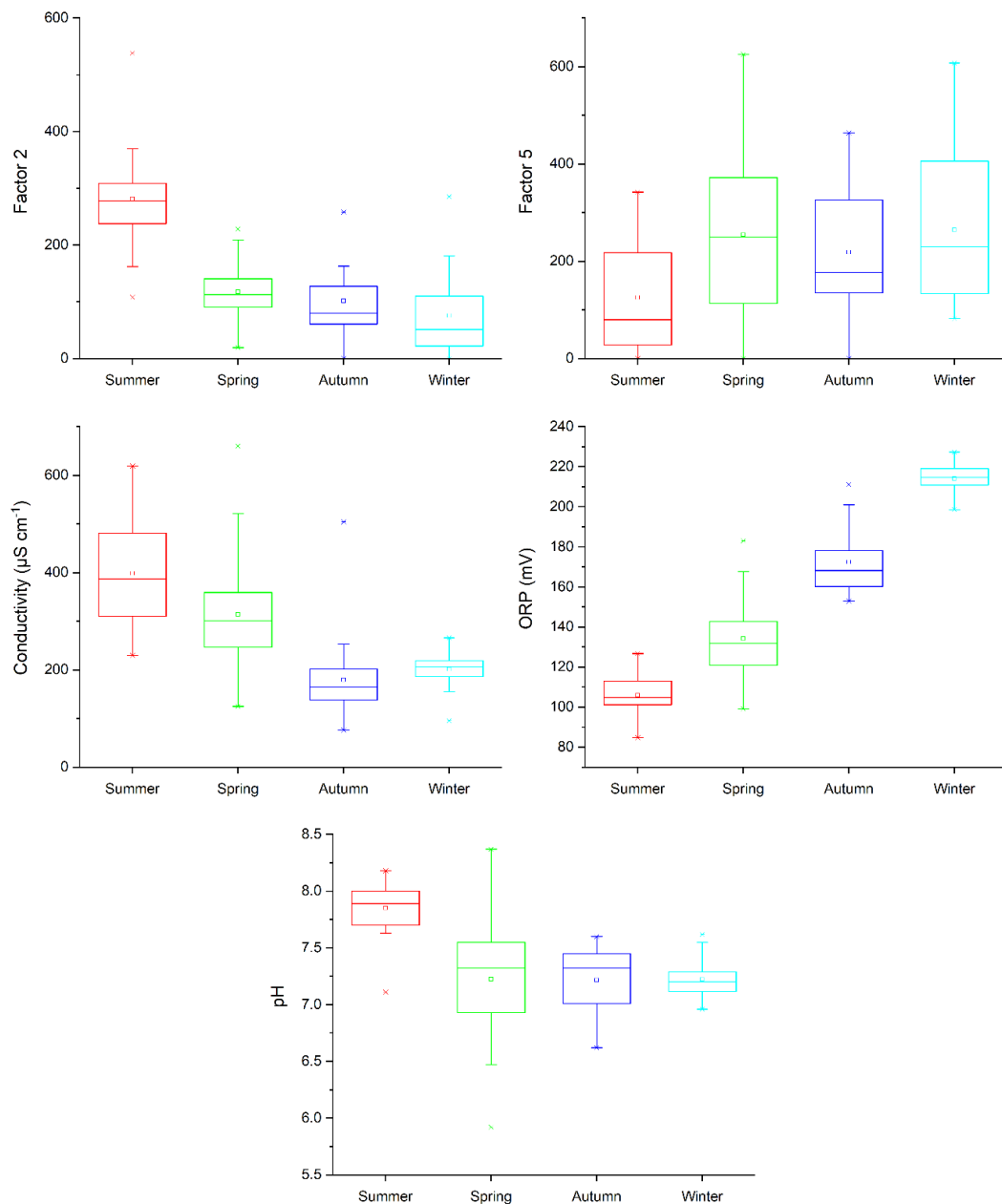


Figure 8. Boxplot of the NMF factors and chemical-physical parameters showing significant seasonal differences.

Higher pH and conductivity values are observed in summer which progressively decrease towards winter. The opposite trend occurs instead for ORP, as it strongly depends on hydrogen ion concentration. The seasonal behavior of pH is likely related to the scarcity of precipitations in the summer season, which reduces the dilution effect while increasing the duration of water-rock interaction with and subsequent leaching of the mineral background of the system.

As for the chemical factors, the most significant seasonal difference is associated with summer, which shows higher values for Factor 2 (major and trace lithogenic elements) and lower values for factor 5 (atmospheric factor). Such behavior may still be due to the dry, less rainy, summer period and, consequently, the deficiency of dripping water arising by rainwater mediated by nucleating aerosol components (Factor 2). Instead, as previously stated, major and minor elements (Factor 2) can be enriched in the drip water because of a greater water-rock interaction explained previously that increase the concentration of dissolved salts.

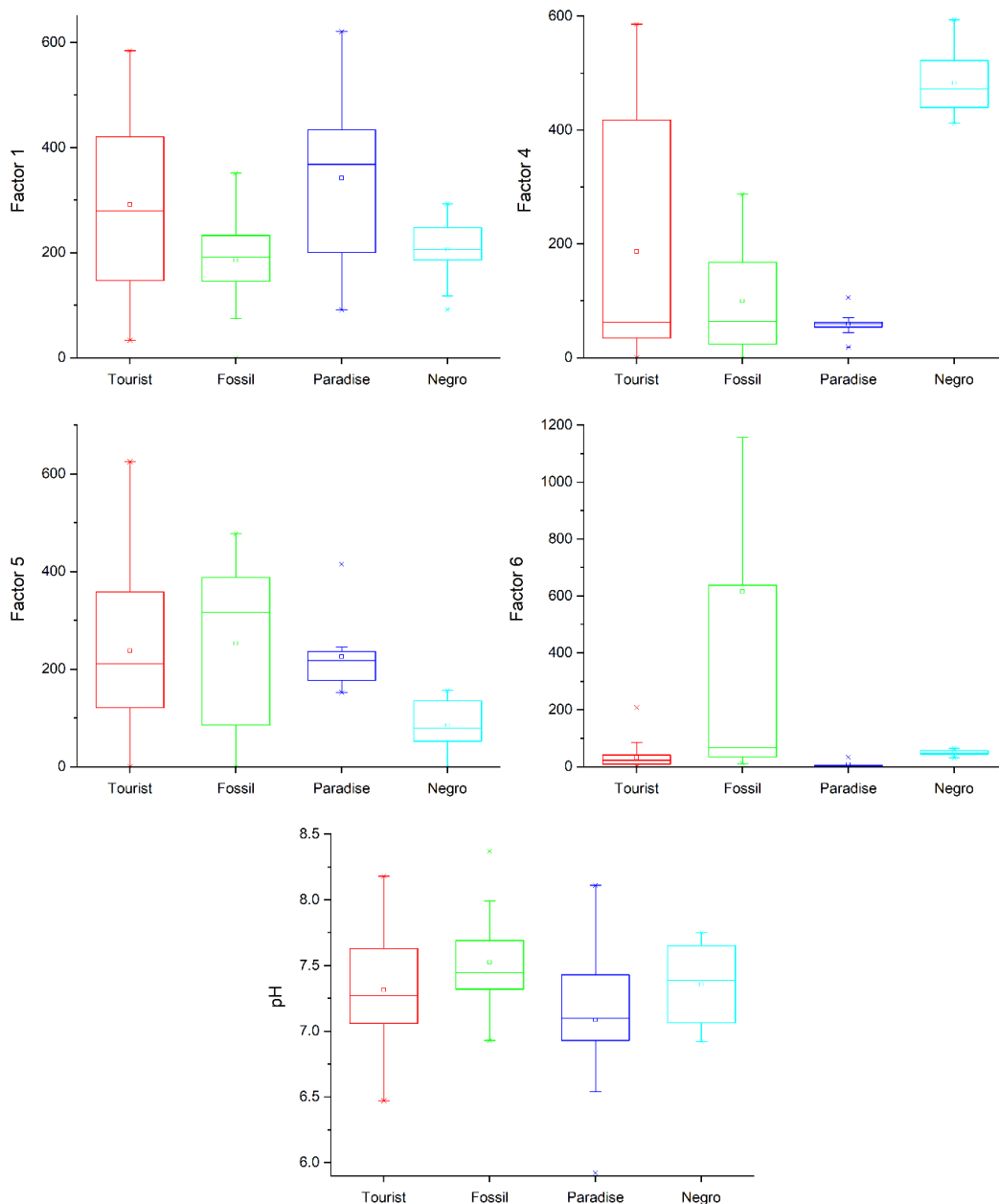


Figure 9. Boxplot of NMF factors and chemical-physical parameters showing significant locational differences.

The most significant differences are observed between the waters of the Negro River and the dripping waters. Indeed, river water samples are characterized by higher values of the factor 4 (dissolution of limestone and silica rocks) and lower values of the factor 5 (atmospheric factor). This evidence is plausibly due to the path of the Negro River to reach the Pertosa-Auletta cave which runs processes of dissolution of silicate and limestone rocks.

Furthermore, the Fossil trail is characterized by very high values of the Factor 6 (bat guano), due to the high aqueous concentrations of N and NO_3^- . This result agrees with the intense presence of bats that inhabit this part of the cave both in summer and in winter (look at section 2.1).

Factor 1 (carbonate equilibrium factor) instead presents lower values for the drip water samples from the Fossil section in respect to the others, highlighting how this area is located

relatively far from the two entrances. Indeed, it is hypothesized that, natural ventilation, promotes carbon dioxide (CO₂) degassing from water, with consequent decrease of water acidity (increase of pH) as compared to Paradise area and precipitation of CaCO₃.

4 – Conclusions

This Chapter shows the preliminary results from the characterization of drip and river water samples in the Pertosa-Auletta cave (SA, Italy). The sampling was carried out over four seasons (annual sampling) and on different parts of the cave. Significant differences are found, both on a seasonal and spatial basis. Additional investigations on new samples from further sampling campaigns are required for a comprehensive long-scale evaluation. Next investigations will include also the study of the cave ventilation with and without visitors in order to understand the connections with outdoor and the factors affecting aerosol population in the cave.

References

- Adesso, R., Bellino, A., D'Angeli, I. M., de Waele, J., Miller, A. Z., Carbone, C., & Baldantoni, D. (2019). Vermiculations from karst caves: The case of Pertosa-Auletta system (Italy). *CATENA*, 182, 104178. <https://doi.org/https://doi.org/10.1016/j.catena.2019.104178>
- Brunet, J.-P., Tamayo, P., Golub, T. R., & Mesirov, J. P. (2004). Metagenes and molecular pattern discovery using matrix factorization. *Proceedings of the National Academy of Sciences*, 101(12), 4164–4169.
- Camuffo, D., & Pagan, E. (2003). Analisi di serie storiche di temperatura e precipitazione in località prossime agli speleotemi. *Studi Trent Sci Nat Acta Geol*, 80, 37–47.
- Fairchild, I., & Baker, A. (2012). Speleothem Science: From Process to Past Environments. In *Quaternary geosciences series*. <https://doi.org/10.1002/9781444361094.app1>
- Fairchild, I. J., & Treble, P. C. (2009). Trace elements in speleothems as recorders of environmental change. *Quaternary Science Reviews*, 28(5), 449–468. <https://doi.org/https://doi.org/10.1016/j.quascirev.2008.11.007>
- Gaujoux, R., & Seoighe, C. (2010). A flexible R package for nonnegative matrix factorization. *BMC Bioinformatics*, 11(1), 367. <https://doi.org/10.1186/1471-2105-11-367>
- Gaujoux, R. (2020). An introduction to NMF package. Version 0.23.0. <https://cran.r-project.org/web/packages/NMF/vignettes/NMF-vignette.pdf>
- Katz, B. G. (2019). Nitrate contamination in karst groundwater. In: D.C. Culver, W.B. White, T. Pipan (Eds.), *Encyclopedia of Caves* (pp. 756–760). Elsevier. doi: 10.1016/B978-0-12-814124-3.00091-1
- Larocca, F. (2010). *Le Grotte dell'Angelo a Pertosa: Il sistema sotterraneo e il giacimento archeologico*. Pertosa: Fondazione Musei Integrati Dell'Ambiente.
- Misra, P. K., Gautam, N. K., & ELANGO VAN, V. (2019). Bat guano: a rich source of macro and microelements essential for plant growth. *Annals of Plant and Soil Research*, 21(1), 82–86.
- Pastore, C. (2016). Hydrogeological analysis of the Alburni's karstic area (Campania, Italy). *Analisi idrogeologica dell'area carsica dei Monti Alburni (Salerno, Campania)*.

- Pastore, C., de Waele, J., Vigna, B., & Fiorucci, A. (2017). Nuovi contributi idrogeologici sull'area carsica dei Monti Alburni. Atti del III Convegno Regionale di Speleologia - Campania Speleologica 2017. 2 - 4 giugno 2017, Napoli.
- Raes, F., Van Dingenen, R., Vignati, E., Wilson, J., Putaud, J. P., Seinfeld, J. H., & Adams, P. (2000). Formation and cycling of aerosols in the global troposphere. *Atmospheric environment*, 34(25), 4215-4240. [https://doi.org/10.1016/S1352-2310\(00\)00239-9](https://doi.org/10.1016/S1352-2310(00)00239-9)
- Sakoui, S., Derdak, R., Addoum, B., Serrano-Delgado, A., Soukri, A., & el Khalfi, B. (2020). The Life Hidden Inside Caves: Ecological and Economic Importance of Bat Guano. *International Journal of Ecology*, 2020, 9872532. <https://doi.org/10.1155/2020/9872532>
- Tadros, C. V. (2018). Inorganic elements: from sources to cave drip water, Yarrangobilly, south-eastern Australia.
- Tadros, C. V., Treble, P. C., Baker, A., Hankin, S., & Roach, R. (2019). Cave drip water solutes in south-eastern Australia: Constraining sources, sinks and processes. *Science of The Total Environment*, 651, 2175-2186.
- Tositti, L., Pieri, L., Brattich, E., Parmeggiani, S., & Ventura, F. (2018). Chemical characteristics of atmospheric bulk deposition in a semi-rural area of the Po Valley (Italy). *Journal of Atmospheric Chemistry*, 75, 97–121. <https://doi.org/10.1007/s10874-017-9365-9>
- Tremaine, D. M., Sinclair, D. J., Stoll, H. M., Lagerström, M., Carvajal, C. P., & Sherrell, R. M. (2016). A two-year automated dripwater chemistry study in a remote cave in the tropical south Pacific: Using [Cl⁻] as a conservative tracer for seasalt contribution of major cations. *Geochimica et Cosmochimica Acta*, 184, 289–310. <https://doi.org/https://doi.org/10.1016/j.gca.2016.03.029>

CHAPTER 10 - Radioactivity measurements of innovative and sustainable building materials: Geopolymers

1 – Introduction

This work presents up-to-date and attractive research now in progress concerning the characterization and quantification of naturally occurring radionuclides (NORM) in innovative building materials defined as “Geopolymers”, i.e. inorganic polymers obtained by the alkali activation of an aluminosilicate precursor. This application might provide many advantages and opportunities such as reducing the amount of waste materials to manage, and limit the environmental hazards they often pose owing to the frequently high content of toxic pollutants by efficiently immobilizing them in a consolidated and basically resistant new material. Moreover, differently from cement production, CO₂ emission from this new productive approach for building materials, is much lower, suggesting its suitability in terms of climatic issues and inherent sustainability constraints.

Despite the environmental and economic benefits so far outlined, it is mandatory to estimate the health risk associated with the radioactivity of building materials as required by the recent Euratom Directive on Radiation Protection (Italian Decree Law N.101 31st July 2020, as from the EU Directive 59/2013/EURATOM).

The preparation of the geopolymer samples was carried out at the Laboratory of Prof. Maria Bignozzi in the Department of Civil, Chemical, Environmental and Materials Engineering at the University of Bologna (DICAM - UNIBO). My role in this work consists of the analysis of geopolymers and their precursors by High-Resolution Gamma-Ray Spectroscopy, (available at the Laboratory of Environmental chemistry and radioactivity under the supervision of my tutor), data interpretation, and calculation of dosimetric indices for health risk assessment as required by the DL 101/2020 (Italian Decree Law N.101 31st July 2020).

Preliminary results on the range of materials analysed show how these new building materials in most cases, but not all, fulfil the current regulation requirements on radioactivity; more samples are being analysed both for extending the survey and to check some results.

2 – Materials and methods

2.1 – *Geopolymers and their precursors*

Geopolymers are inorganic polymers, obtained by activating an aluminosilicate precursor through an alkaline solution. The main sources of aluminosilicates can be natural minerals such as: clays, kaolinite, etc. but also industrial waste materials, e.g. red mud (waste from industrial production of aluminum), fly ash (by-product of coal combustion), slag produced by the separation of a metal from its ore, etc. The most widely used alkaline activator is sodium hydroxide (NaOH).

Geopolymers are considered eco-sustainable materials thanks to the potential reuse of waste materials for their synthesis and to the economic advantage in their production chain (Coletti et al., 2020). Furthermore, their production does not require large amounts of energy and some of these materials can be prepared at room temperature. In particular, the production of a Geopolymer with the same mechanical properties of a Portland cement may even

represents a saving of 45% of CO₂ emission (169 Kg CO₂ m⁻³ vs. 306 Kg CO₂ m⁻³, according to Habert et al., 2011).

In the scientific literature there are different representations of geopolymeric structures but, typically, a Geopolymer has a three-dimensional (3D) form composed of silico-aluminate bonds (sialate) of SiO₄ and AlO₄, with tetrahedral units connected by oxygen atoms (Figure 1).

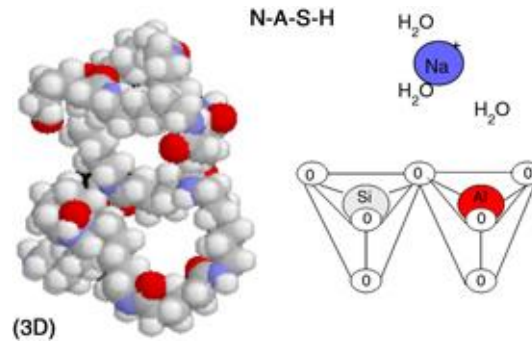


Figure 1. Three-dimensional structure of a N-A-S-H gel (a fly ash-based geopolymer) (Palomo et al., 2015).

The geopolymerization process leads to the formation of a polymer with a wide cross-linking where the bond between the tetrahedral units is balanced by ions generally deriving from the alkaline agent used, e.g. K⁺, Na⁺, and Li⁺ (Nergis et al., 2018). The properties of these materials depend on: the material used as a source of Al & Si, the activator, amount of water added, the relative quantities of the precursors, the hardening time, the size of the particles, and any thermal treatments. Generally, they are comparable to the properties of Portland cement and, for this reason, they can be used as sustainable building materials, low-cost ceramic materials, protective coatings, 3D printer materials, biomedical materials, etc. (Wu et al., 2019).

In this Chapter, I present the preliminary radioactivity results from three different kind of Geopolymer and their relative precursors. The examined waste precursors were coal Fly Ash (FA), Metakaolin (MK), and Brick Waste powder (BP).

Fly ash (FA), are glassy spherical particles obtained upon solidification of volatilized/liquified substances released during coal burning mainly for energy production at more than 1500 °C. These in consolidated materials are classified according to their origin: class F powders are obtained by combustion of bituminous coal or anthracite, while class C powders are produced by combustion of sub-bituminous coal or lignite (Nergis et al., 2018). In this work, Class F fly ash (ASTM C618) sourced by BauMineral (EFA-Füller®, Germany) has been investigated (Provis et al., 2019).

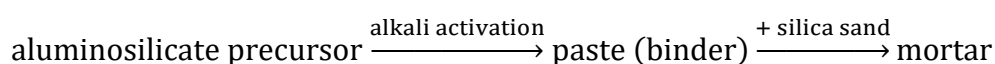
Metakaolin (MK) (Al₂O₃·2SiO₂) is an aluminosilicate obtained by thermal treatment of the mineral Kaolinite. Kaolinite is an aluminum hydroxy silicate consisting of alternating layers of silicon and aluminum with tetrahedral and octahedral coordination, respectively. The calcination process causes a loss of 14% of the mass (Rashad et al., 2013) due to dehydroxylation, with consequent loss of the crystalline layer structure. The product of this treatment is metakaolin, an amorphous material suitable for applications in building materials (Rashad et al., 2013). In this work, metakaolin sourced by Argical™ M1000 (France) has been investigated (San Nicolas et al., 2013).

Brick Waste Powder (BP) is a waste material resulting from brick production. Bricks are produced by thermal treatment of clayey materials. During this process, a certain amount of amorphous aluminosilicate waste phase is produced (Brînduș-Simuț et al., 2018) which can be used as a precursor in the synthesis of geopolymers. In this work, Brick Waste Powder supplied by Wienerberger S.p.A. (industrial plant of Villabruna di Feltre, Belluno, Italy) has been investigated (Sassoni et al., 2016).

From the alkaline activation (AA) of these three aluminosilicates, both the relative pastes (P_AAFA, P_AAMK, P_AABP) and the mortars (M_AAFA, M_AAMK, M_AABP) have been prepared and analysed. Also pastes and mortars are Geopolymers. Mortars are formally obtained from the relative pastes through the further addition of silica sand.

Alkaline activators (sodium and aluminum silicates) and sand were also analyzed.

A summary scheme of the Geopolymer production chain is shown below:



2.2 – High-Resolution Gamma-Ray Spectroscopy

The samples described in the previous paragraph were analysed by a HPGe (High Purity Germanium) extended-range detector (PROFILE Hyper Pure Germanium detector by Ortec-Ametek Inc.). High-Resolution Gamma-Ray Spectroscopy is a powerful and consolidated non-destructive technique widely used for the quali-quantitative analysis of radioactivity. The analysis is based on the recognition of radionuclides by characteristic energy values at which these nuclei emit γ photons. The latter are intercepted with a known probability by a semiconductor high purity detector which transforms the signal from each single incident photon into a measurable electrical signal. Further details on γ -spectrometry determinations are available elsewhere (Cinelli et al., 2015; Tositti et al., 2017).

All the samples were measured in the same jar geometry (diameter = 54 mm and thickness = 1 cm), weighed, and then counted for 24 h each to optimize peak counting statistics (Figure 3).

γ -spectra were subsequently analyzed with Gamma Vision-32 software (version 6.07, Ortec-Ametek) allowing also for self-attenuation at low energy on the basis of the apparent density. ^{226}Ra activity was determined at 186 keV correcting the peak area for ^{235}U emission.

Uncertainty (here defined as one standard deviation) on the γ photopeaks was calculated propagating the error resulting from the efficiency calibration fit previously determined over the counting error. Minimum detectable activity (MDA) was determined using the Traditional ORTEC method (ORTEC, 2003) with a peak-cut-off limit of 40%.

Gamma spectroscopy allowed the quantification of the activity concentrations expressed in Bq Kg^{-1} of the following radionuclides: ^{214}Pb , ^{214}Bi , ^{226}Ra , ^{234}Th , ^{228}Ac , ^{212}Pb , ^{212}Bi , ^{40}K . The latter represent the most representative radionuclides, after excluding the species characterized by most values below the MDA.



Figure 3. Analysis of a geopolymer sample placed on the PROFILE detector.

2.3 – Data processing

Firstly, principal component analysis (PCA) on the activity concentrations data was performed. PCA is an exploratory data analysis technique allowing to reduce the number of variables that describe a set of data, limiting the loss of information as much as possible (Jolliffe & Cadima, 2016). Thus, new orthogonal variables are obtained, called principal components (PCs), which are extremely informative. The graphical representation of the PCs allows to observe any similarities and differences between the samples studied (scores plot), to distinguish the most representative original variables from the less representative ones, and to determine any variables that possess similar information (loadings plot).

In order to visualize the characteristic properties of the samples, boxplots were used.

Eventually, the relative dosimetric indices for the analyzed samples were calculated. In particular, the dosimetric index specified by the the current radioprotection regulation (Italian Decree Law N.101 31st July 2020) was computed from activity concentrations for each sample, as reported below:

$$I = \frac{(228_{Ac} + 212_{Pb})/2}{200} + \frac{226_{Ra}}{300} + \frac{40K}{3000}$$

where all the data required for I calculation are the activity concentrations of a series of natural radionuclides determined in each sample by high resolution gamma-ray spectrometry determined.

3 – Results and discussions

3.1 – Principal Component Analysis (PCA)

Figure 4 reports the main graphs of the Principal Components Analysis (PCA) on activity concentrations data of geopolymers and their precursors.

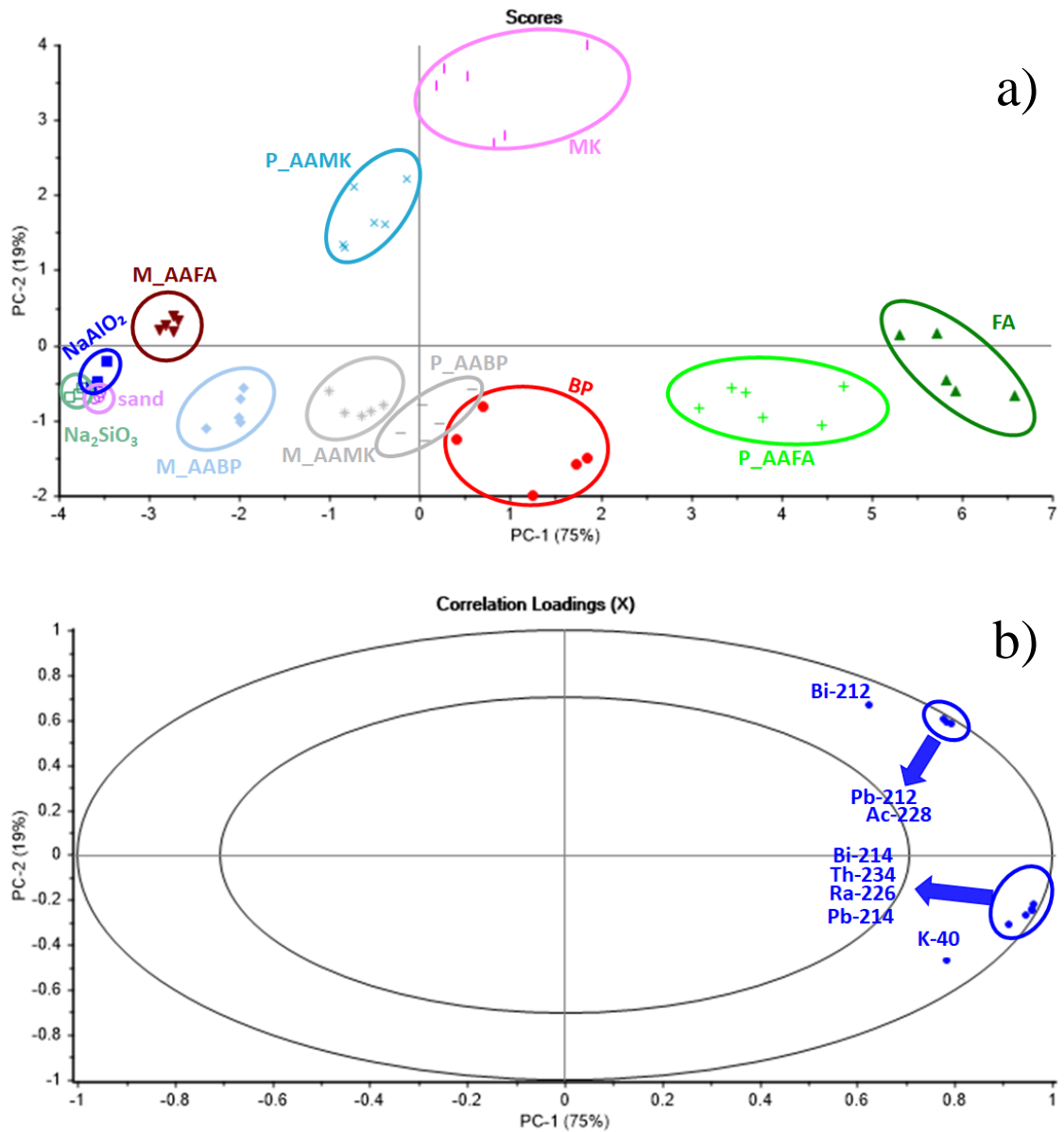


Figure 4. Scores plot (a) and loadings plot (b) of Principal Component Analysis (PCA), PC-1 vs. PC-2.

The scores plot (Figure 4a) basically displays the analysed samples in the first two principal component space (PC-1 & PC-2), that together explained 94% of the X-explained variance. Geopolymer samples (pastes /P/ and mortars /M/ of FA, MK, and BP) are well grouped and separated from each other. Furthermore, the aluminosilicate precursors are distinct from each other and from the corresponding alkaline-activated materials. Instead, alkaline activators and sand are not well separated and mixed.

The loadings plot (Figure 4b) shows the relevance of the original variables (radionuclides). Positive larger values of PC-1 describe more radioactive samples.

The comparison between the scores plot and the loadings plot allows to qualitatively highlight the correspondences between the samples and the original variables, that is the associations between the analyzed materials and the activity concentrations of the radionuclides. In this case, the samples of FA, P_AAFA, and BP are defined by higher positive values along the PC-1 and, therefore, are characterized by higher concentrations of ^{40}K , ^{226}Ra , ^{214}Pb , ^{234}Th and ^{214}Bi (variables that significantly contribute to the definition of positive PC-1). Instead, MK and P_AAMK are described by higher positive PC-2 values, and characterized by higher concentrations of ^{228}Ac , ^{212}Pb , and ^{212}Bi (variables that significantly contribute to the definition of positive PC-2). The alkaline activators (NaAlO_2 and NaSiO_3) and sand are characterized by the lowest values of PC-1 and, therefore, are the least radioactive samples.

3.2 – Radionuclide Boxplots

The boxplots showing the activity concentrations of the different radionuclides as a function of the kind of sample (grouped by the production chain of the three different geopolymers /GP/, and the alkaline activators & sand) have been reported from Figure 5 to Figure 12.

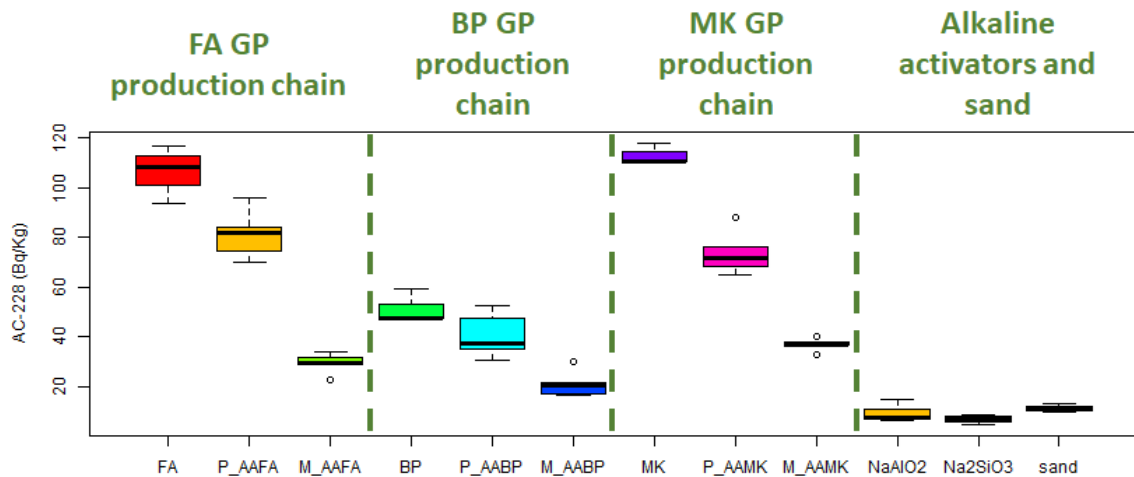


Figure 5. ^{228}Ac boxplots

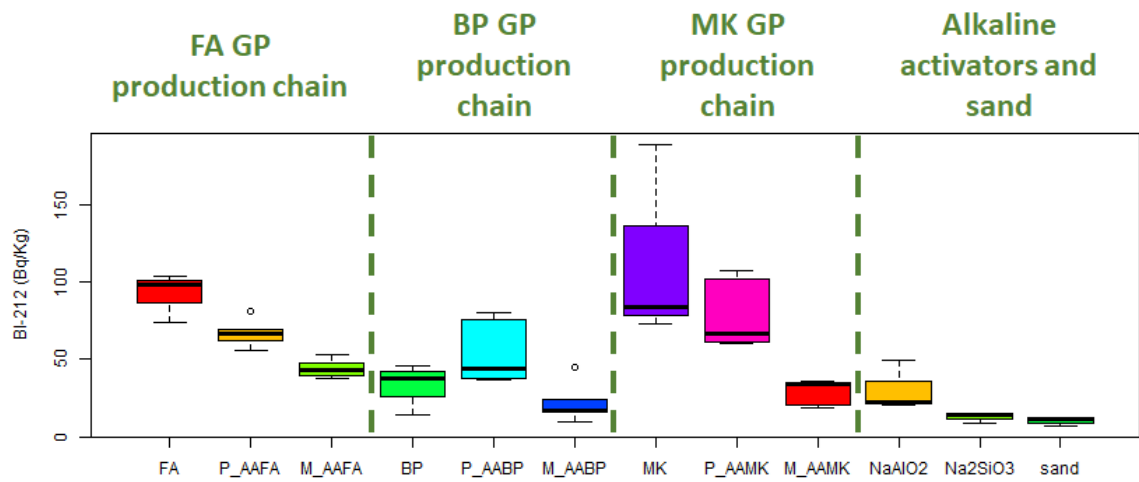


Figure 6. ^{212}Bi boxplots

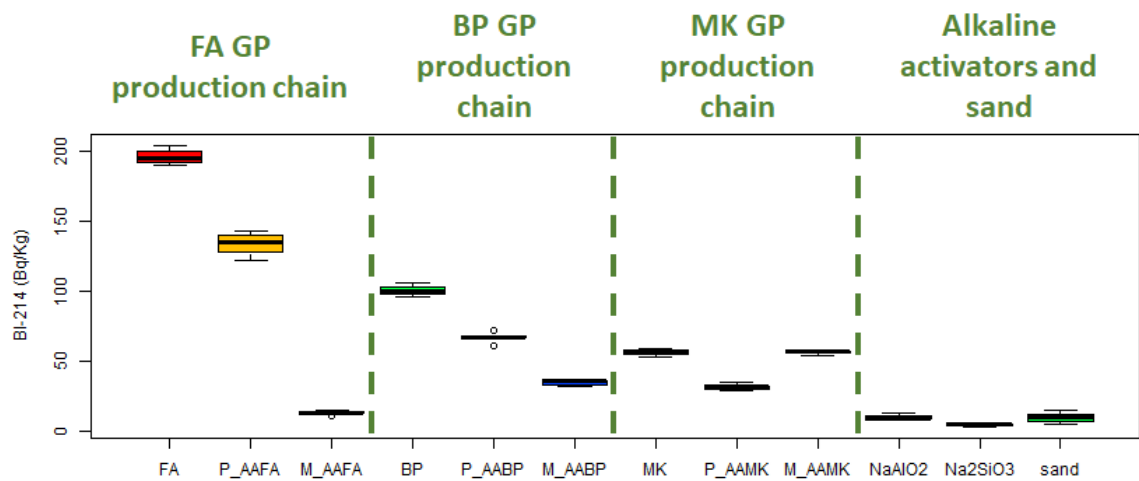


Figure 7. ^{214}Bi boxplots

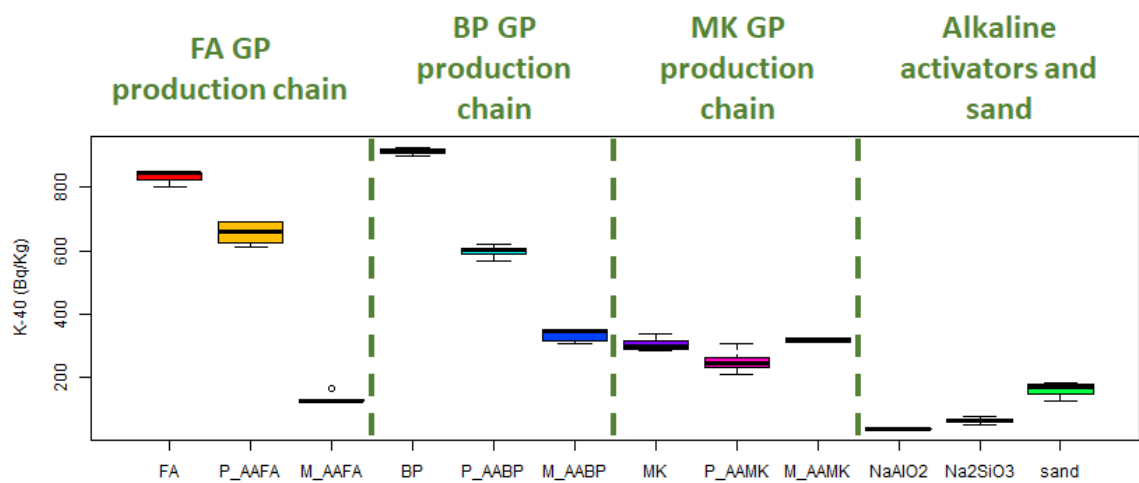


Figure 8. ^{40}K boxplots

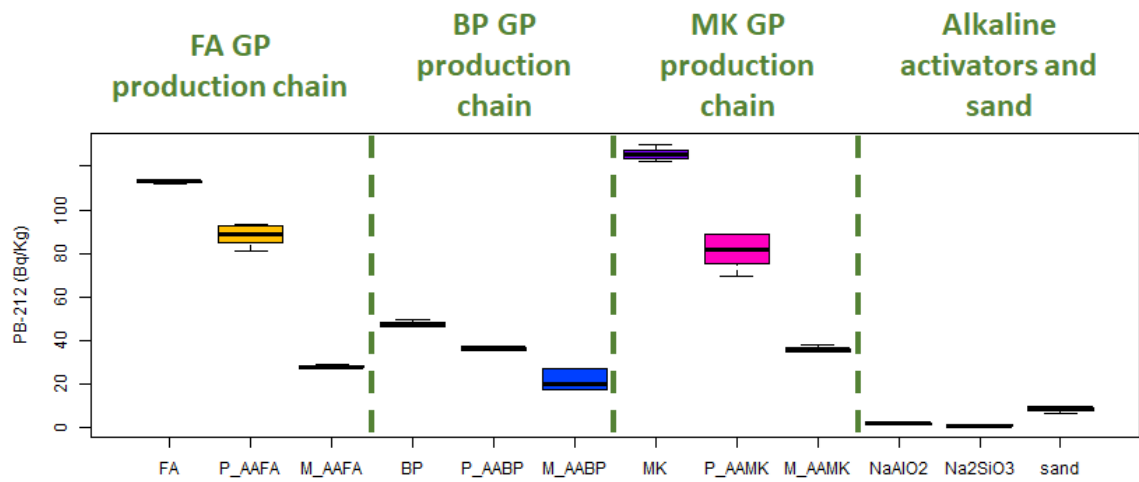


Figure 9. ^{212}Pb boxplots

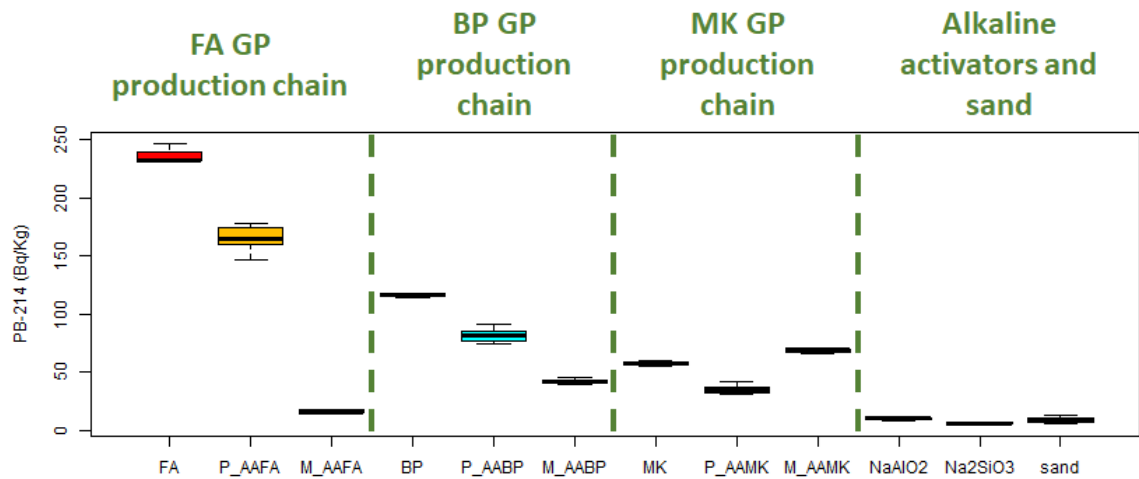


Figure 10. ^{214}Pb boxplots

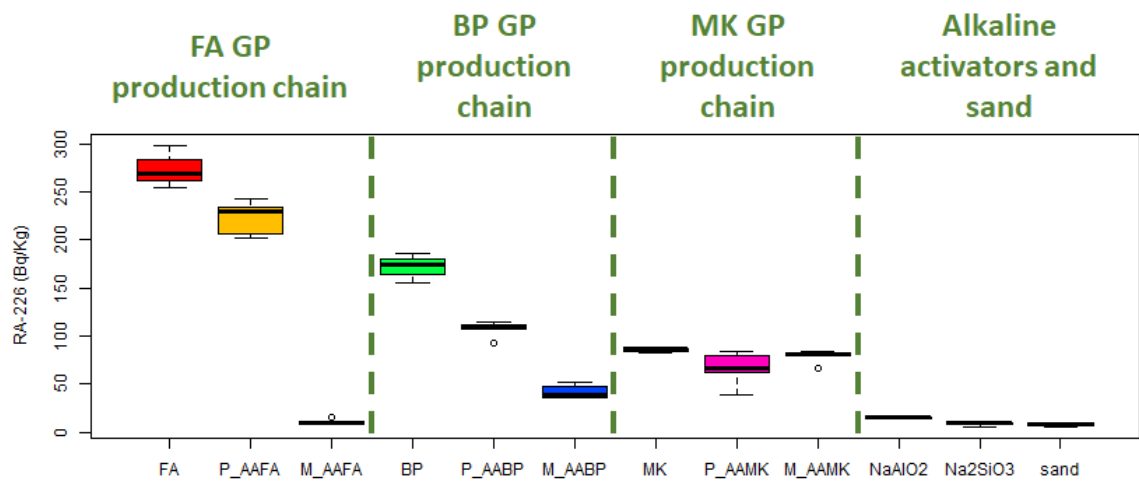


Figure 11. ^{226}Ra boxplots

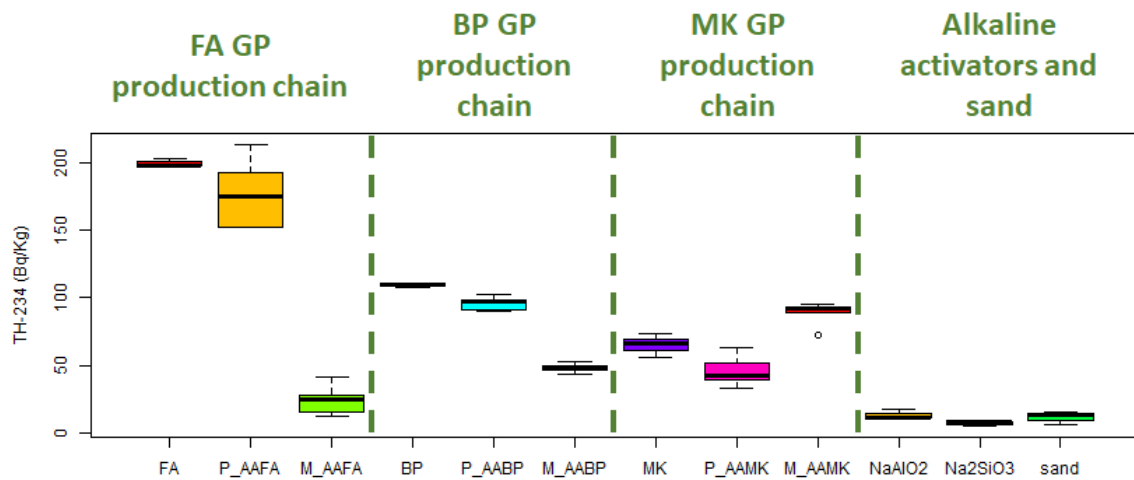


Figure 12. ^{234}Th boxplots

As previously described in section 2.1, the production chain of geopolymers involves the addition of alkaline activators (in the case of pastes) and sand (in the case of mortars) to the aluminosilicate precursor. Since the alkaline activators and sand have low radioactivity as compared to the aluminosilicates (see paragraph 3.1), the outcome in the geopolymers production is generally a progressive dilution of the activity concentrations of radionuclides from the precursor to the paste and, ultimately, to the mortar.

3.3 – Dosimetric indices

Figure 13 shows the boxplots of the dosimetric index (I), as previously described in the paragraph 2.3. This Figure shows a horizontal line at $I = 1$, which represents the safety threshold of I as required by the same legislation. Present regulation allows the use of building materials only when I is less than 1.

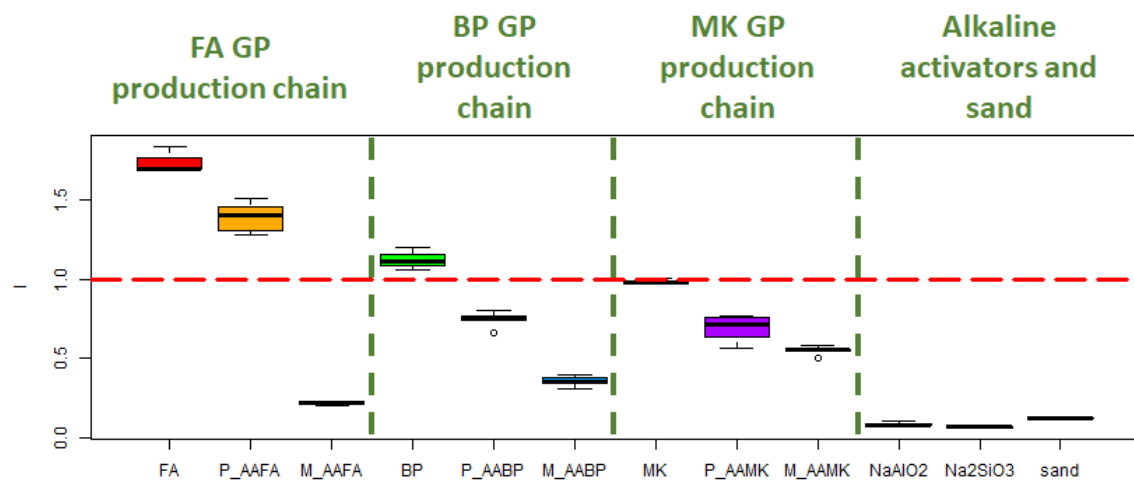


Figure 13. Dosimetric index (I) boxplots

Fly ash (FA) and Brick powder (BP) presents I values above the legal limit ($I > 1$), because of a significant presence of K-40 in these samples. All the geopolymer samples (pastes and

mortars) are below the legal limit of 1, except for the alkaline activated fly ash paste (P_AAFA) and, consequently, this material cannot be used as a building material.

4 – Conclusions

This Chapter shows the preliminary results of radioactivity measurements on innovative and sustainable building materials named as Geopolymers. All the samples involved in the production chain of three different kind of materials were analyzed by High-Resolution Gamma-Ray Spectroscopy for assessing the activity concentrations of several radionuclides. Furthermore, dosimetric indices for health-risk assessment were computed as required by the DL 101/2020. Generally, a progressive decrease of activity concentrations and dosimetric indexes was found in the final products (geopolymers) in respect to their precursors, revealing the method efficacy in reducing the level of NORM in aluminosilicate supplies to then be used as building materials. Further investigations to extend the material range based on new aluminosilicate precursors (e.g blast furnace slag) are in progress for a complete radiochemical characterization on these materials thus increasing their sustainability and safety properties.

References

- Brînduș-Simuț, J., Vyšvařil, M., Bayer, P., Keppert, M., & Rovnaníková, P. (2018). Effect of particle size of waste brick powder on the properties of alkaline activated materials. *IOP Conference Series: Materials Science and Engineering*, 379(1), 012019.
- Cinelli, G., Tositti, L., Capaccioni, B., Brattich, E., & Mostacci, D. (2015). Soil gas radon assessment and development of a radon risk map in Bolsena, Central Italy. *Environmental Geochemistry and Health*, 37(2), 305–319.
- Coletti, C., Brattich, E., Cinelli, G., Cultrone, G., Maritan, L., Mazzoli, C., Mostacci, D., Tositti, L., & Sassi, R. (2020). Radionuclide concentration and radon exhalation in new mix design of bricks produced reusing NORM by-products: The influence of mineralogy and texture. *Construction and Building Materials*, 260, 119820. <https://doi.org/https://doi.org/10.1016/j.conbuildmat.2020.119820>
- Italian Decree Law N.101 31st july 2020. <https://www.gazzettaufficiale.it/eli/id/2020/08/12/20G00121/sg>
- Habert, G., d’Espinoze de Lacaillerie, J. B., & Roussel, N. (2011). An environmental evaluation of geopolymer based concrete production: reviewing current research trends. *Journal of Cleaner Production*, 19(11), 1229–1238. <https://doi.org/https://doi.org/10.1016/j.jclepro.2011.03.012>
- Jolliffe, I. T., & Cadima, J. (2016). Principal component analysis: a review and recent developments. *Philosophical Transactions of the Royal Society A: Mathematical, Physical and Engineering Sciences*, 374(2065), 20150202.
- Nergis, D. D. B., Abdullah, M., Vizureanu, P., & Tahir, M. F. M. (2018). Geopolymers and their uses. *IOP Conference Series: Materials Science and Engineering*, 374(1), 012019.
- ORTEC, Gamma-Vision 32 A66-B32 User's Manual. ORTEC USA, Part. No. 783620 Manual Revision D (2003)
- Palomo, Á., Kavalerova, E., Fernández-Jiménez, A., Krivenko, P., García-Lodeiro, I., & Maltseva, O. (2015). A review on alkaline activation: new analytical perspectives.
- Provis, J. L., Arbi, K., Bernal, S. A., Bondar, D., Buchwald, A., Castel, A., Chithiraputhiran, S., Cyr, M., Dehghan, A., Dombrowski-Daube, K., Dubey, A.,

- Ducman, V., Gluth, G. J. G., Nanukuttan, S., Peterson, K., Puertas, F., van Riessen, A., Torres-Carrasco, M., Ye, G., & Zuo, Y. (2019). RILEM TC 247-DTA round robin test: mix design and reproducibility of compressive strength of alkali-activated concretes. *Materials and Structures*, 52(5), 99. <https://doi.org/10.1617/s11527-019-1396-z>
- Rashad, A. M. (2013). Metakaolin as cementitious material: History, scours, production and composition – A comprehensive overview. *Construction and Building Materials*, 41, 303–318. <https://doi.org/https://doi.org/10.1016/j.conbuildmat.2012.12.001>
 - San Nicolas, R., Cyr, M., & Escadeillas, G. (2013). Characteristics and applications of flash metakaolins. *Applied Clay Science*, 83–84, 253–262. <https://doi.org/https://doi.org/10.1016/j.clay.2013.08.036>
 - Sassoni, E., Pahlavan, P., Franzoni, E., & Bignozzi, M. C. (2016). Valorization of brick waste by alkali-activation: A study on the possible use for masonry repointing. *Ceramics International*, 42(13), 14685–14694. <https://doi.org/https://doi.org/10.1016/j.ceramint.2016.06.093>
 - Tositti, L., Cinelli, G., Brattich, E., Galgaro, A., Mostacci, D., Mazzoli, C., Massironi, M., & Sassi, R. (2017). Assessment of lithogenic radioactivity in the Euganean Hills magmatic district (NE Italy). *Journal of Environmental Radioactivity*, 166, 259–269.
 - Wu, Y., Lu, B., Bai, T., Wang, H., Du, F., Zhang, Y., Cai, L., Jiang, C., & Wang, W. (2019). Geopolymer, green alkali activated cementitious material: Synthesis, applications and challenges. *Construction and Building Materials*, 224, 930–949. <https://doi.org/https://doi.org/10.1016/j.conbuildmat.2019.07.112>

CHAPTER 11 - Applications of non-destructive spectroscopic techniques and multivariate statistics for the analysis of Spanish atmospheric aerosol collected on membranes

1 – Introduction

Last but certainly not least, this study presents an innovative application of non-destructive spectroscopic techniques and multivariate statistics for the analysis of Spanish atmospheric aerosol collected on membranes simultaneously at Sierra Nevada and Granada stations in 2018, as part of the FRESA⁴ Project. This chapter describes only a limited part of this huge project which involves, in addition to the chemical speciation of PM filters through both traditional and innovative techniques, also meteorological characterization, paying particular attention to the dynamics of air masses on a synoptic scale (affecting the mobilization, transport, and deposition of airborne particles) based on the application of circulation models and back-trajectories.

For sake of completeness, the experimental activity carried out within this project, based on over 700 PM₁₀ samples collected in Granada and Sierra Nevada in southern Spain, includes:

- Ion chromatography (IC, double run for cations and anions – completed)
- Elemental analysis (elements with atomic number Z from 11 upward) with Particle Induced X-ray Emission (PIXE) at the accelerator facility of the National Institute of Nuclear Physics at Legnaro-Padova (around 80% samples analysed)
- Ultraviolet–Visible Diffuse Reflectance Spectroscopy (UV–Vis DRS) analysis (completed)
- Fourier transform InfraRed (FT-IR) analysis (completed)
- Chemometric analysis: spectral processing and multivariate analysis, including source apportionment (performed on 50% of the samples)
- Meteorodynamic analysis for environmental and climatologic diagnostics: in progress

It is to note that, apart from the parallel samplings at the two stations already described in some of the published papers included in thesis concerning FRESA project, the huge number of samples treated is necessarily required mainly by the high variance of atmospheric composition, PM included, as dictated by the strong influence of meteorology on the redistribution and photochemistry of airborne chemical species as well as of sources behavior. The understanding of aerosol properties and effects on climate and health relies basically on its chemical speciation (very complex as shown in the introduction) and its variability as a function of time and space. This makes aerosol science an extremely demanding and time-consuming research field, in spite of the need of knowledge owing to the climatic and health- related issues in which PM is involved.

This is the main reason why this latter part of my thesis not only concerns the use of a traditional experimental approach, but includes the development of new “light” methodologies enabling to collect as much chemical information as possible at the least reasonable cost under all points of views.

⁴ Impact of dust-laden African air masses and of stratospheric air masses in the Iberian Peninsula. Role of the Atlas Mountains, Ref: CGL2015-70741-R

This chapter therefore is mainly focused on some relevant achievements I reached based on the innovative application of two traditional (cheap) instrumental techniques and the smart use of chemometrics proving extremely efficient in aerosol sample characterization: Ultraviolet-Visible diffuse reflectance spectroscopy (UV-VIS DRS) and Fourier transform - Infrared spectroscopy (FT-IR) in transmission mode. Both techniques allow to analyze directly PM filters without any chemical preparation and in a short time. These non-destructive spectroscopic methods allow to obtain fast, but complex spectra owing to the complexity in composition and morphology of aerosol matrices, which can be resolved only by means of advanced chemometric techniques, mainly based on multivariate statistics. The combination of simple and cheap instrumental techniques and advance computational methods therefore provide access to quali-quantitative chemical information that can be used for chemical speciation and source apportionment purposes, provided that the new methods can be cross-checked and validated with the support of traditional speciation data.

In this framework, I have used the traditional approach to validate the outcome of the new methods with results that so far appear extremely encouraging. This Chapter therefore demonstrates how these quick and non-destructive metrologies can support and integrate the gold standard analytical approaches in atmospheric aerosol science.

2 – Materials and methods

2.1 – Sampling sites

This section describes the results obtained on the 2018 campaign samples, including only 364 PM₁₀ samples over the 700 collected. For the others, the chemometric analysis is currently in progress. PM₁₀ samples were collected on 47mm-diameter Teflon (PTFE) membranes, within the framework of the Spanish national FRESA project. PM sampling was carried out using a 2.3 m³ h⁻¹ air sampler (55.2 m³ of sampled air per day). PM₁₀ sampled filters derive from two sampling stations located in Andalusia (Southern Spain): Sierra Nevada and Granada (Figure 1).



Figure 1. Satellite image of the two sampling sites. (Adapted from Google Maps)

Figure 1 shows the proximity of the two stations that are relatively close to each other, with a distance of about 20 kilometers. However, Sierra Nevada station have an altitude of almost 2000 meters higher than Granada. The two stations therefore differ in other atmospheric parameters, such as rainfall, wind, pressure, temperatures, and type of ventilation, i.e. meteorological dynamic conditions, as a consequence of the different altitudes of the two sites. This affects the deposition of particulate matter and, therefore, its relative composition.

The sampling site of Granada is located on the roof of the Chemistry Department of the University of Granada - UGR in an urban background area. Instead, the Sierra Nevada PM₁₀ sampler is located on the top of a mountain range, near the Pico Veleta and the Sierra Nevada University Hotel. Therefore, the latter does not show the typical anthropogenic pollution features resulting from smog, vehicle emissions and industrial emissions, but is mainly and strongly influenced by the Saharan dust outbreaks, due to its proximity to the African continent (Mladenov et al., 2008; Morales-Baquero et al., 2013).

2.2 – Traditional chemical speciation and source apportionment of PM₁₀

The samples herein discussed include 172 filters from Granada (GRA) and 192 filters from Sierra Nevada (SN). PM samples were stored in the dark at -10°C until analysis and then analyzed by two golden analytical techniques for chemical characterization: Ion Chromatography (IC) for the quantification of the main water-soluble cations and anions (EN16913, 2017), which represent a large mass fraction of ambient PM, and Particle Induced X-ray Emission (PIXE), an IBA (Ion Beam Analysis) technique allowing to identify and quantify simultaneously and, in a non-destructive way, a significant number of chemical elements present in the analyzed sample (Chiari et al., 2018; Lucarelli et al., 2011). More details on the analyses are included in the previous references.

Receptor modeling for Source Apportionment (SA) was then applied to chemical data in order to derive information about their sources and their mass contribution to PM levels (Belis et al., 2019).

Two different SA methods were performed by Positive Matrix Factorization (PMF) (Paatero & Tapper, 1993) and PMF5.0 software (Norris et al., 2014), respectively for SN samples (192 sample x 24 var) and GRA samples (172 sample x 27 var). These computations were carried out carefully following the European guidelines recently issued for this advanced chemometric tool allowing to rule out the qualitative role of each aerosol emission source active in a given district (Belis et al., 2019); these multivariate techniques, besides providing quantitative resolution of PM source apportionment, prove to be extremely accurate and safe (as compared to other similar techniques), due to the careful processing of data below the limit of detections (LoDs) it provides, together with the inclusion of experimental uncertainties for scaling matrix elements within factor analysis, allowing the variable selection and choice of the best factorial solution.

2.3 – Fourier transform InfraRed (FT-IR) analysis

Fourier Transform InfraRed (IR) analysis of the PM₁₀ filters were carried out by an ALPHA Bruker FT-IR spectrometer (Bruker Optics GmbH, Billerica, MA, USA) in transmission mode (Figure 2a).

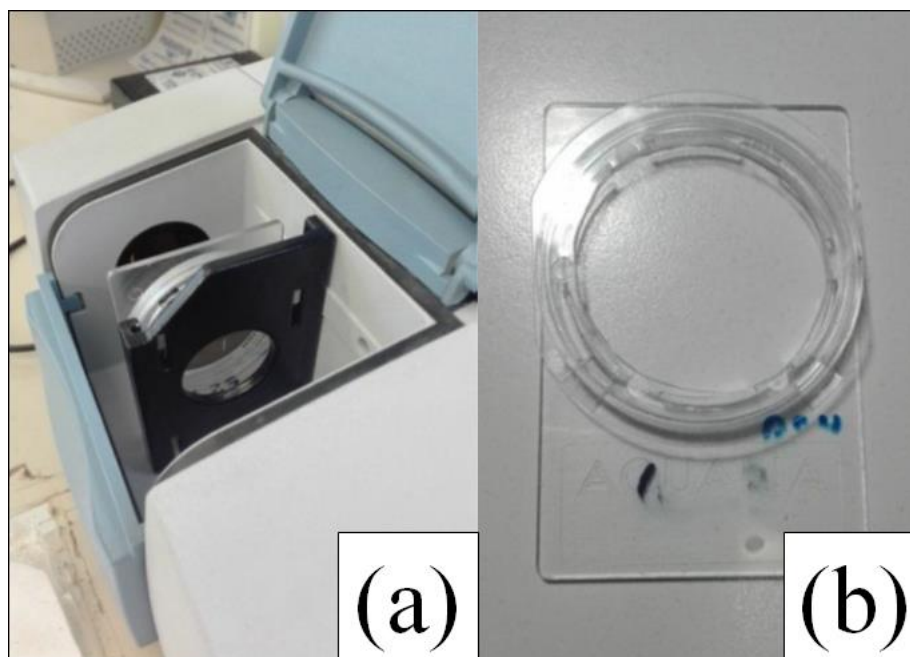


Figure 2. (a) PM₁₀ filter placed inside the measuring chamber of the ALPHA Bruker FT-IR spectrometer and (b) IR sample holder.

This kind of analysis represents an unusual analytical technique for PM membranes owing to the chemical complexity of this type of environmental samples and allows to obtain, in a non-destructive way, fingerprints of the IR-active functional groups, i.e. groups of atoms (mainly from the carbonaceous fraction but also from the mineral component) that can rotate and/or vibrate when irradiated by an IR radiation.

For the repeatability of the IR analysis, it is critical to present the samples in a reproducible geometric configuration and, for this purpose, I designed and built a specific support using a polystyrene (PS) filter holder (Figure 2b). The incident IR radiation impacts orthogonally the PM filter placed inside the support with a reproducible geometry so that the transmitted radiation can reach correctly the Mercury Cadmium Telluride (HgCdTe) detector of the instrument. PM filters were analyzed as follows:

- measurement of the instrumental background, i.e. the cell without any membrane in the filter holder and the air contained inside it. This background was automatically subtracted to each sample spectrum;
- measurement of the "reference pseudo-standard" chosen for the evaluation of instrumental repeatability;
- measurement of a sequence of ten real samples from Granada and Sierra Nevada;
- extension of the cycle from the first bullet point, starting from the measurement of the background.

The IR spectra were acquired using the OPUS 7.2 software on a PC interfaced with the ALPHA Bruker instrument. Spectra were collected in the mid-IR range, 400–4000 cm⁻¹, with an optical resolution of 4 cm⁻¹; the registered spectrum is the mean of 64 scans, (acquisition duration= 3 min). Owing to the unavailability of a gas flushing system, all the measurements were performed at ambient conditions but applying the *atmospheric*

compensation tool allowing to eliminate the IR signal of CO₂ (g) and H₂O (g) included in the measuring chamber (Takahama et al., 2013).

The raw IR spectra obtained from the atmospheric aerosol samples are not very informative on a first approximation, due to the extreme complexity of the PM matrix. As previously explained in the introduction, atmospheric aerosols are chemically very complex and wide-ranging. Therefore, the acquisition of IR signals of these variable mixtures returns spectra with overlapping bands which are difficult to resolve and interpret. In order to extrapolate qualitative-quantitative information, a procedure for processing spectra is therefore required. Moreover, the raw spectra present the scattering produced by the Teflon membranes (support on which the aerosol is deposited). PTFE absorbs in the IR range, and the resulting bands due to the vibrations of the CF₂ functional group significantly interfere in the region of the spectrum useful for the study. An example of an IR spectrum is shown in Figure 3:

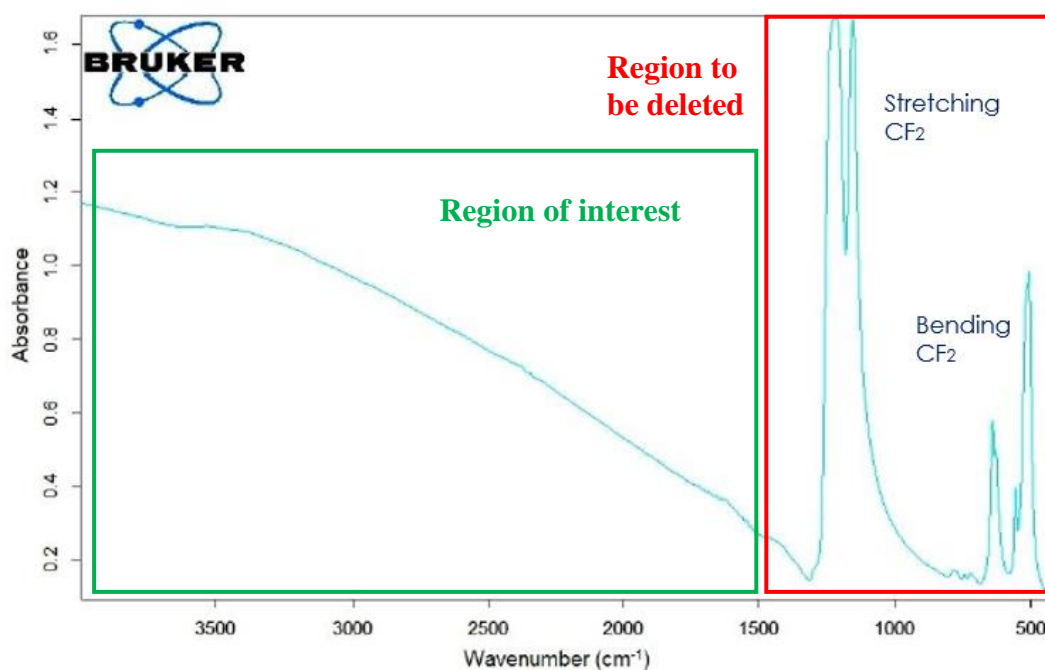


Figure 3. Example of raw IR spectrum of a PM₁₀ sample collected on PTFE membrane.

As from Figure 3, the spectrum can be split into two sections: the first, which ranges from 4000 to 1500 cm⁻¹, where the sample + membrane chemical information is located, and the second one (1500 - 420 cm⁻¹) which presents absorption peaks due to the stretching and bending of the CF₂ bonds of the membrane. The IR peaks attributable to PTFE in this region add to the peaks attributed to the atmospheric aerosol, further complicating the interpretation of the data. The region of interest is presented as an almost linear band with a decreasing trend, in which it is impossible to distinguish IR absorption signals without a proper processing of the spectra. The latter operation can be performed by the AIRspec platform (Reggente et al., 2019a), recently developed by the École polytechnique fédérale de Lausanne (EPFL)'s Laboratory of Atmospheric Processes and their Impacts (LAPI), coordinated by Prof. Satoshi Takahama.

Firstly, this open-source platform available in R language allows for the baseline correction and the removal of the signal due to the PTFE support (Kuzmiakova et al., 2016; Reggente et al., 2019b). Briefly, this procedure is based on a smoothing spline as a function of the

effective degrees of freedom (EDF). A proper evaluation of EDFs allows obtaining high-quality baseline-corrected IR spectra, as depicted in Figure 4.

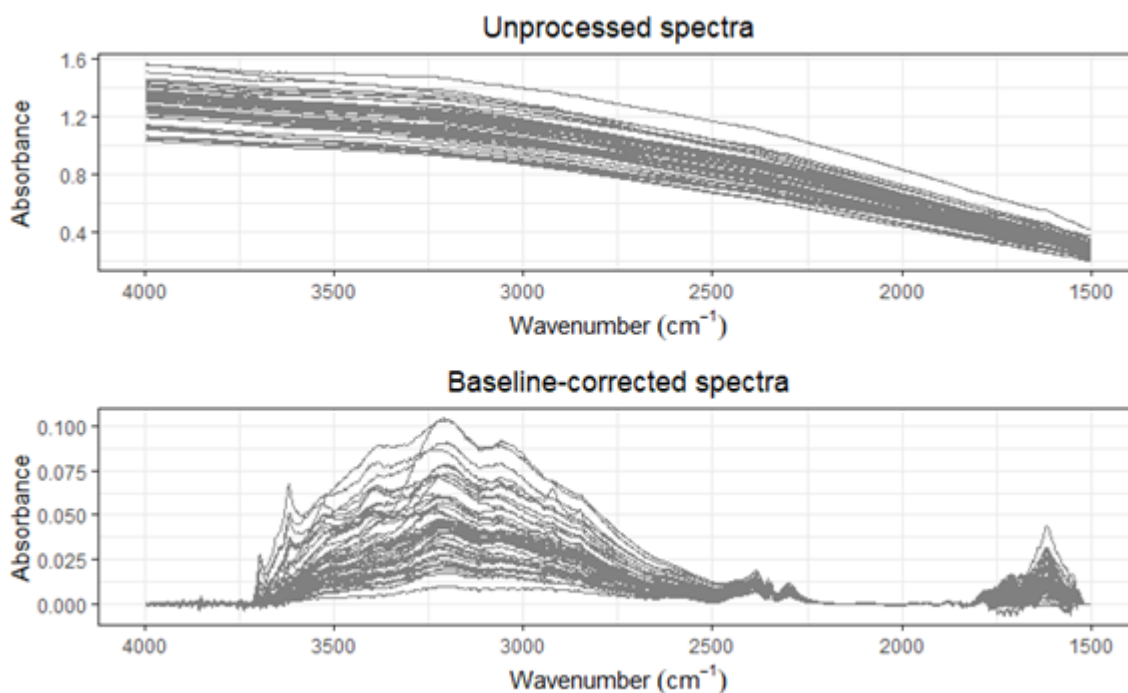


Figure 4. Baseline correction of 50 random FRESA PM₁₀ filters.

Then, the application of Source Apportionment by Positive Matrix Factorization (PMF) on treated spectra may provide reliable qualitative and quantitative information on ambient aerosol sources (Belis et al., 2019). PMF was performed by the EPA PMF 5.0 software (Norris et al., 2014) on IR fingerprints normalized on the volume of sampled air, and uncertainty values computed as the standard deviation of multiple field blank filters plus 6% of additional model uncertainty to incorporate the error associated with the sampling volume of the PM₁₀ filters (EN 12341, 2014).

2.4 - Ultraviolet–Visible Diffuse Reflectance Spectroscopy (UV–Vis DRS) analysis

UV-VIS DRS is a non-destructive analytical method that allows to parameterize the color of the analyzed filter, by a mathematical model known as colorimetric space, and obtain semi-quantitative information on the iron oxide minerals present; these concepts have already been described and discussed extensively in the material and methods section of Chapter 4 (Morozzi et al., 2021) and for sake of brevity are not going to be repeated in this section.

Ultraviolet-Visible (UV-Vis) analysis of the PM₁₀ filters in reflectance mode were carried out, also in this work, by Perkin Elmer Lambda 35 (UV–Vis range) equipped with an integrating sphere. The analysis of PM₁₀ filters were performed in the same modalities and operating conditions reported in Chapter 4 (Morozzi et al., 2021), except for *ad hoc* design, 3D-print, and use of a sample holder in polylactic acid (PLA) I personally introduced in order to improve the reproducibility in terms of geometry and instrumental set-up (Figure 5).

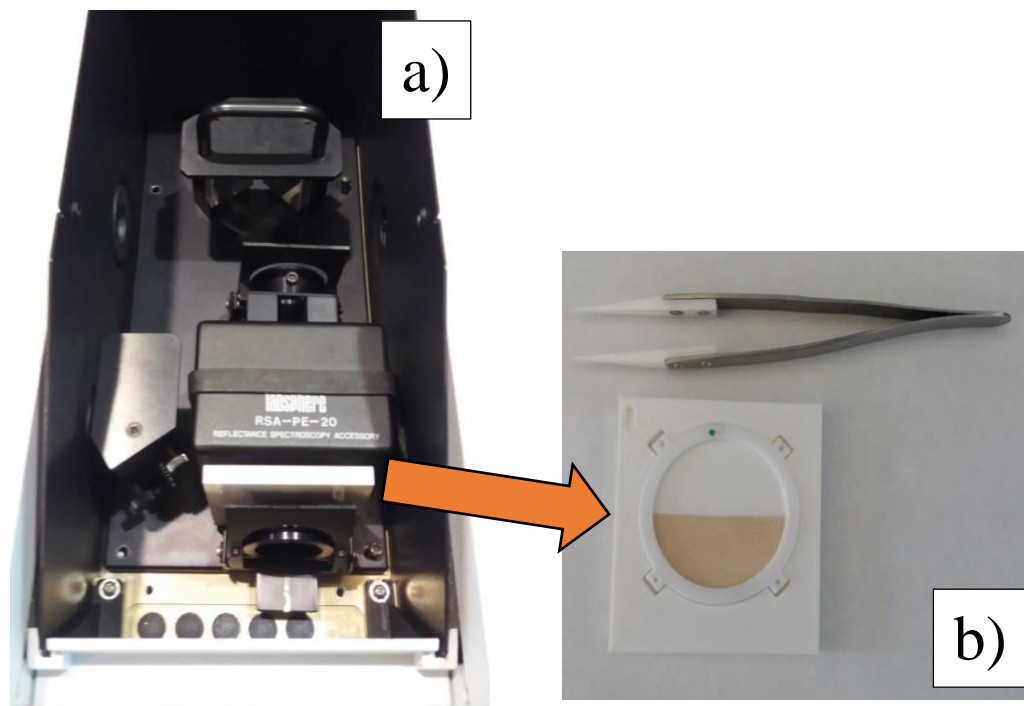


Figure 5. (a) Perkin Elmer Lambda 35 measuring chamber and (b) sample holder

The final outcomes are UV-Vis reflectance spectra that can be used for extracting colorimetric data for color parametrization and digitalization (see for example Table 1 of Chapter 4). This conversion was carried out using the Color 2.01 software (Perkin Elmer Ltd, United Kingdom), taking into account the illuminant and the viewing inclination commonly used for color parameterization: D65/10° (ISO-CIE 11664-2-2020; ISO-CIE 11664-1-2019).

A cluster analysis was applied to all the reflectance spectra of the analyzed samples, regardless of their place of origin (Granada and Sierra Nevada). In particular, in this work, the agglomerative hierarchical method was used, which starts from n clusters, equal to the number of objects that compose the starting dataset, and proceeds to gradually merge into increasingly larger (and obviously decreasing in number) clusters, on the basis of the similarity between the different objects (Murtagh & Contreras, 2012). Specifically, it was performed an agglomerative hierarchical cluster analysis with squared Euclidean distance and the Ward's method (Ward, 1963).

3 – Results and discussions

3.1 – PMF on traditional chemical data

This paragraph describes the results of receptor modeling obtained at the two locations herein investigated. The data used are from Ion Chromatography (IC) and Particle Induced X-ray Emission (PIXE), which have been completed differently from other FRESA campaigns.

For Sierra Nevada (SN) station, a four-factor solution was selected as the best results (Brown et al., 2015), that are respectively: aged sea salt (Factor 1), Secondary Inorganic Aerosol (SIA, Factor 2), Saharan Dust (Factor 3), and a non-well-resolved photochemical smog factor (Factor 4). The factor fingerprint screen is reported in Figure 6.

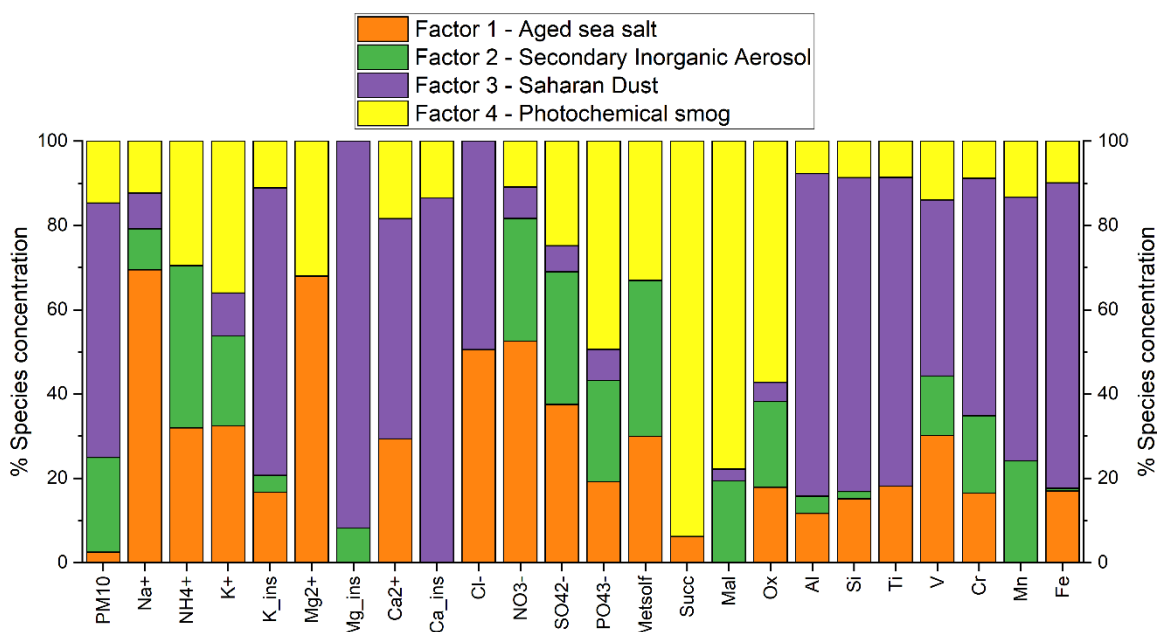


Figure 6. Source Fingerprints corresponding to the factor resolved by the PMF model (SN).

The predominant source is the Saharan Dust one (60.4%_{w/w}), followed by SIA (22.4%_{w/w}), photochemical smog (14.7 %_{w/w}), and aged sea salt (2.5%_{w/w}). Saharan Dust source captures the desert dust incursion events across the western Mediterranean region (already described previously) and is defined by a significant amount of specific markers such as Al, Si, Ti, Ca, K, and Fe. SIA source includes SO_4^{2-} , NO_3^- , NH_4^+ . Photochemical smog factor mainly comprises anions of dicarboxylic acids (Succinate, Malonate, and Oxalate), from photochemical reactions of both natural and man-derived VOCs. Eventually, aged sea salt comprises Na^+ , Cl^- , Mg^{2+} , and NO_3^- wherein nitrates partially substitutes chlorides by double exchange reaction (Pio & Lopes, 1998).

This factor analysis outcome presents a good reconstruction of the total variable (PM_{10}) with a modelled vs. experimental PM_{10} mass reconstruction coefficient of determination equal to 0.88. However, the obtained factors seem not well resolved, plausibly due to the low number of variables processed in PMF.

Also for Granada (GRA) station a four-factor solution was selected as the best results (Brown et al., 2015), that are respectively: Saharan Dust (Factor 1), two anthropic factors (Factor 2 and Factor 3), and sea salt (Factor 4). The factor fingerprint screen is reported in Figure 7.

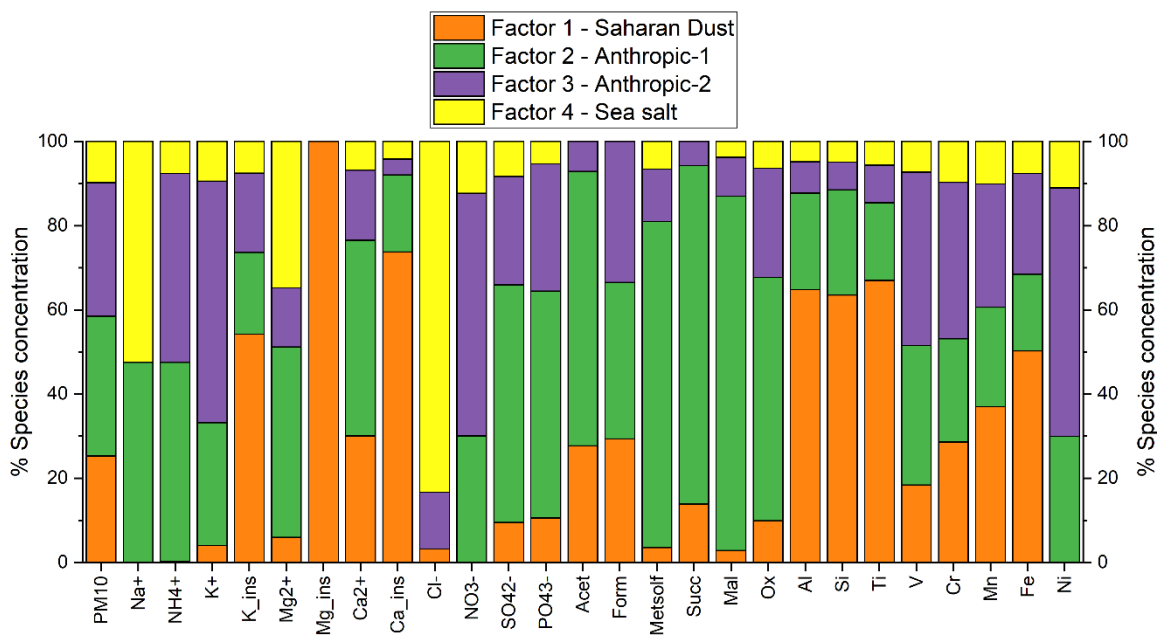


Figure 7. Source Fingerprints corresponding to the factor resolved by the PMF model (GRA).

The predominant sources are the two Anthropic factors (respectively, 33.2%_{w/w} and 31.7%_{w/w}), followed by Saharan Dust (25.3%_{w/w}), and aged sea salt (2.5%_{w/w}). Anthropic-1 factor (Factor 2) includes anions of dicarboxylic acids (Succinate, Malonate, and Oxalate) and monocarboxylic acid (Malonate), from photochemical reaction of natural and anthropic VOCs. Anthropic-2 factor (Factor 3) suggests the combustion of biomass and traffic as non-resolved high temperature sources, described by chemical markers such as K⁺, Ni, NO₃⁻, and NH₄⁺. As SN factor solution, Saharan Dust source (Factor 1) is captured by typical mineral markers such as Al, Si, Ti, Ca, K, and Fe. Eventually, sea salt factor (Factor 4) is described by Na⁺, Mg²⁺, and Cl⁻.

This factor analysis outcome presents a good reconstruction of the total PM₁₀ mass with a modelled vs. original coefficient of determination equal to 0.89. Similarly to SN factors, the obtained factors seem not well resolved.

These PMF results are preliminary and adequate for the current state of the FRESA project. Both SN and GRA factors are going to be recalculated to all chemical composition data relating to the 3-years campaign (not only 2018), when available (elemental analysis by PIXE is still in progress). The computation of the factors are going to be studied in depth together with the validation of the results by minimization of the absolute scaled residuals, evaluation of edges, assessment of profile uncertainties calculated by bootstrap and displacement methods (or combined), application of constraints, etc. (Belis et al., 2019).

3.2 – IR results

The Positive Matrix Factorization (PMF) analysis on baseline-corrected IR spectra by the AIRspec platform allow obtaining IR factors, qualitative information on ambient aerosol sources from IR-fingerprints. Therefore, this outcome provides data on PM₁₀ emission sources from a different perspective respect to the PMF on traditional chemical data, not only as far as the spectral technique is concerned, but mostly because it provides

access also to the carbonaceous fraction that is known to be a relevant mass fraction of ambient aerosol, though constituted by hundreds to thousands of different compounds as previously outlined in the introduction. Clearly the characterization of the organic fraction is still an extremely challenging issue whatever is approach and the resources available in a given lab (NB, the FT-IR based approach was originally introduced about 15 years ago and subsequently developed to the recent levels in highly experienced, extremely well-equipped and renowned USA labs therefore reflecting the ongoing needs of knowledge in this research field).

A 3-factor PMF solution was selected based on the Q parameter (Norris et al., 2014) and on the quality of the mass reconstruction of PM₁₀, that represents the total variable of this study. In particular: $Q_{\text{calculated}} \approx Q_{\text{theoretical}}$ ($Q \approx 123690$) and a respectable original to calculated R² index on PM₁₀ ($R^2 \approx 0.69$). Figure 8 shows the three IR emission source profiles.

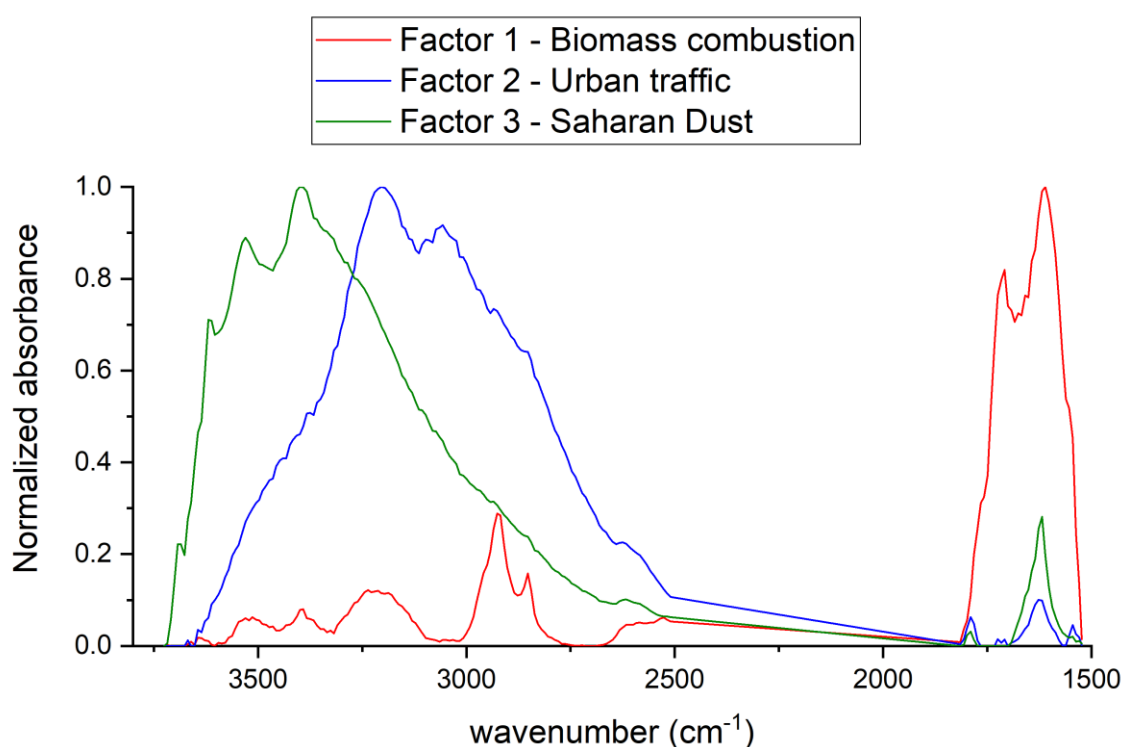


Figure 8. Normalized IR profiles of the 3 factors obtained from the PMF analysis.

The percent contributions of each factor on the average PM₁₀ value are 13%, 40%, and 47% respectively for Factor 1, Factor 2, and Factor 3. Various considerations can be drawn from the obtained IR profiles and the contributions to the total variable.

Factor 3 profile shows the typical trends of mineral dust, recognizable by the IR peaks between 3700 and 3500 cm⁻¹ and at around 1600 cm⁻¹. Indeed, these bands have recently been attributed to the stretching (3700 - 3500 cm⁻¹) and bending (1600 cm⁻¹) of the OH bond due to the water adsorbed on the mineral particles, or to the OH between the layers of the peculiar minerals contained in abundant concentrations in the desert sands, e.g. kaolinite, sepiolite, nacrite etc. (Boose et al., 2019; Reggente et al., 2019b; Senthil Kumar & Rajkumar, 2014).

Factors 1 and 2, on the other hand, can be considered as factors that contain almost anthropogenic contributions, according to the comparison of the peaks obtained with the

results of Corrigan et al., 2013. Factor 2 presents IR peaks due to alcohols ($3700 - 3000 \text{ cm}^{-1}$) which, however, can be attributed to both mineral and organic components; in this factor there are also peaks due to ammonium ($3400 - 2800 \text{ cm}^{-1}$, and consequently to the SIA component) and carboxylic acids, from 3250 to 2900 cm^{-1} to a large extent due to the photooxydation of precursor VOC's. This factor contributes significantly to PM_{10} mass, in agreement with the literature (Liu et al., 2009; Raes et al., 2000; Russell et al., 2009; Takahama et al., 2013) and, therefore, it can be assumed that it is mainly linked to the secondary inorganic aerosol. On the other hand, Factor 1 contributes much less to the reconstruction of the total variable, suggesting the lower contribution of the mineral component, probably due to seasonality, i.e. cold season. This factor is indeed associated with the organic component, mainly with the combustion of biomass, as can be supposed from the peaks around 2900 cm^{-1} which refer to the presence of alkanes. Factor 1 is also dominated by amines and carbonyls, as peaks of 1700 to 1500 cm^{-1} suggest (Takahama et al., 2013).

Therefore, in this work, this method can solve three emission sources: Factors 1 and 2 that are linked with anthropogenic emissions from biomass combustion and urban traffic, respectively (not completely resolved); and Factor 3 that is associated with mineral dust transport.

3.3 – UV-Vis DRS results

Figure 9 presents the color of the analyzed FRESA filters in the tridimensional (3D) scatter plot defined by the colorimetric space CIELAB (ISO-CIE 11664-4-2019).

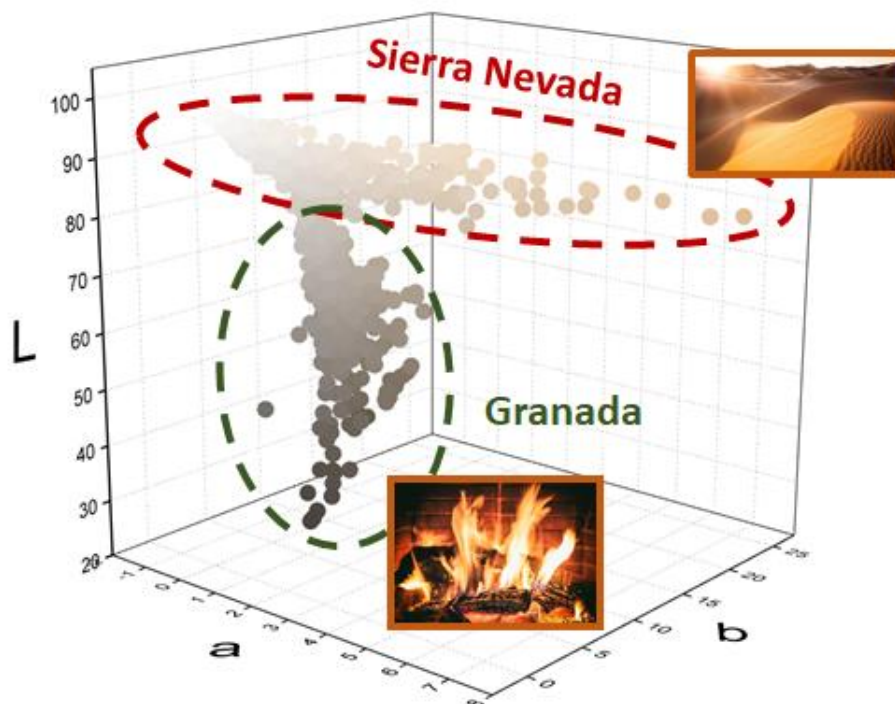


Figure 6. Parameterization and digitization of the PM filter colours obtained from UV-Vis diffuse reflectance spectra and colorimetric spaces.

It can be noted how the color of the samples strongly depends on the sampling station. The color of the Sierra Nevada filters gradually changes from white to red, associated with increasing mineral dust component. Instead, the color of the Granada filters gradually changes from gray to black, associated with increasing organic matter component, partly due to the biomass burning in the winter period.

Figure 10 shows the dendrogram yielded by cluster analysis on the reflectance spectra allowing to define classes of PM₁₀ samples with similar colors in connection with specific peculiar emission sources.

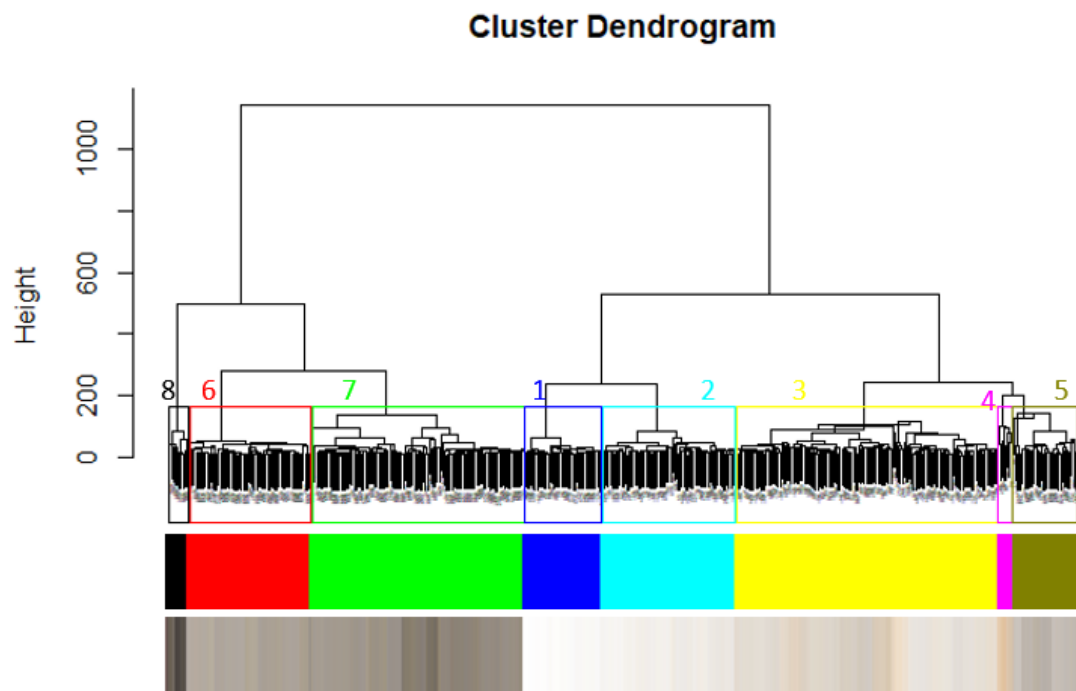


Figure 10. Dendrogram obtained from the UV-Vis spectra of FRESA PM₁₀ samples in which eight clusters and their respective digitized colors are highlighted.

These color-based clusters offer potential information on the chemical composition and related emission sources of PM from a different perspective. Table 1 lists the percentage of PM samples for each of the obtained clusters.

Table 1. The percentage of the samples that frame the eight clusters respect to the total of the samples, and the relative percentages to the SN and GRA class

Cluster	%TOT	%SN	%GRA
1	8	100	-
2	15	100	-
3	29	99	1
4	2	100	-
5	7	3	97
6	14	-	100
7	23	1	99
8	2	-	100

Comparing the clusters depicted in Figure 10 with the percentages reported in Table 1, we have a complete picture of how the PM samples are distributed: the first 4 clusters mainly represent the Sierra Nevada filters here distinguished according to the color of the filters, i.e. from the cluster containing the whitest filters (cluster 1), to the cluster containing the reddest filters (cluster 4); the remaining 4 clusters represent the Granada filters and have been numbered according to the same logic, i.e from the lightest cluster (cluster 5) to the darkest cluster (cluster 8).

3.4 – Validation of non-destructive spectroscopic techniques results

The validation of the outcomes obtained by InfraRed (FT-IR) analysis in transmission mode and Ultraviolet–Visible Diffuse Reflectance Spectroscopy (UV–Vis DRS) analysis with the results obtained by the traditional chemical speciation is extremely auspicious.

Figure 11 confirms as the color of the particulate matter filters agrees with the relative emission sources. In this Figure are reported only the two most significant factors about the coloring of the filters: Biomass Burning source as regards the GRA filters, and Desert Dust source as regards the SN filters.

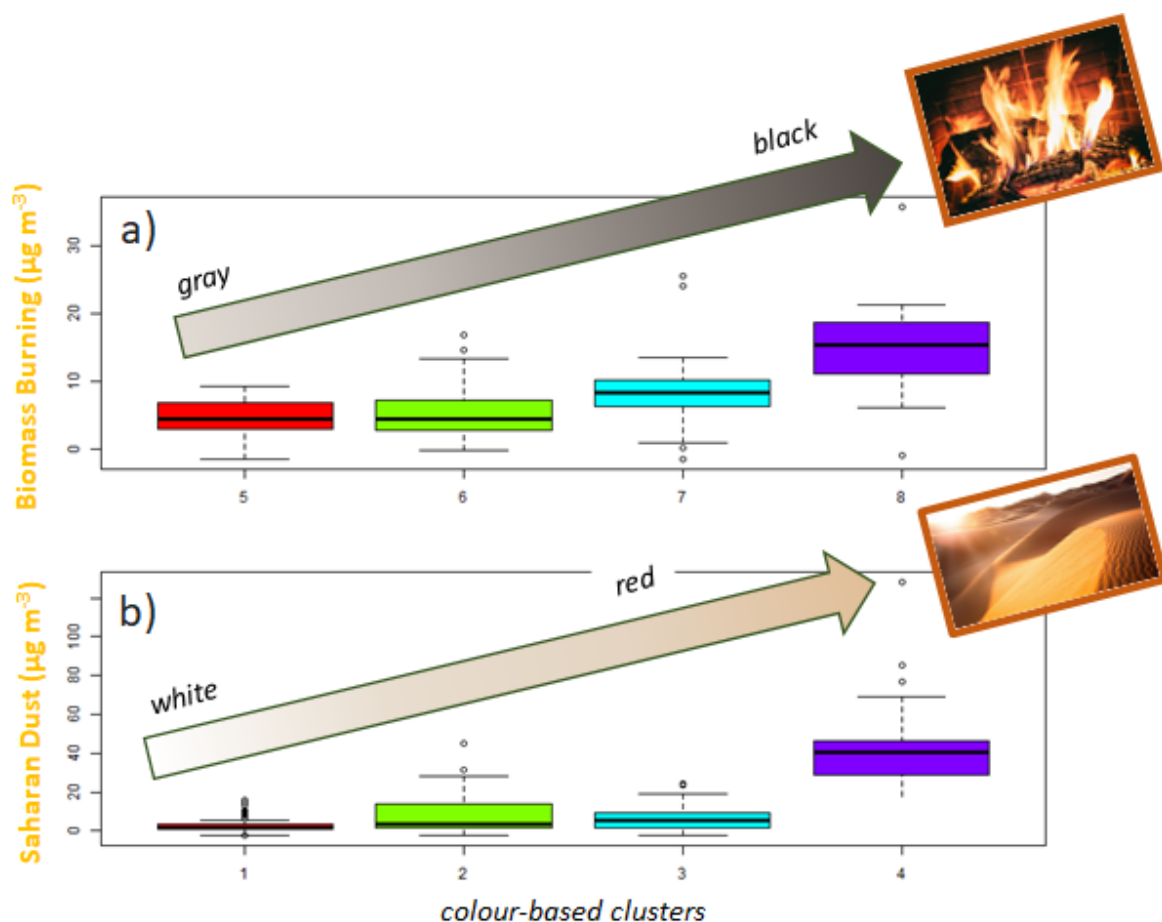


Figure 11. Boxplots of the (a) Biomass Burning GRA source and (b) Saharan Dust SN source contributions ($\mu\text{g m}^{-3}$) obtained by PMF analysis on traditional chemical data (see paragraph 3.1) according to the colour-based clusters shown in the previous section (see paragraph 3.3).

This picture shows how color-based clusters obtained by UV–Vis DRS are in excellent agreement with the PMF factors obtained from traditional chemical analysis.

Figure 12 reveals the time plot of the Saharan Dust contributions obtained from the PMF of IR spectra (in orange) and of chemical data (in blue) for both SN (a) and GRA (b), respectively. Figure 13 also shows the associated scatter plots with related linear regressions.

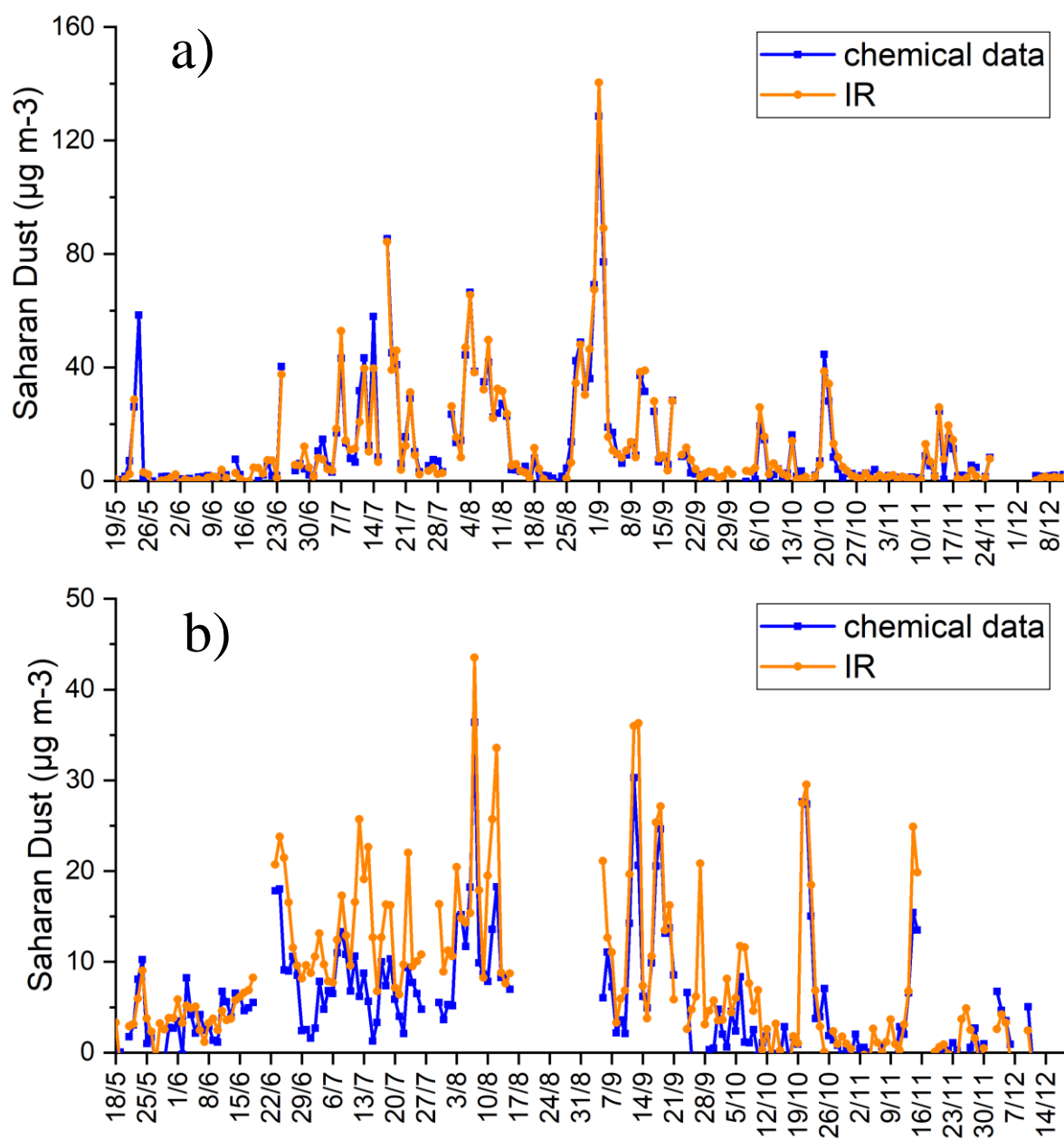


Figure 12. Time plot of the Mineral Dust contributions of SN (a) and GRA (b) obtained from the PMF analysis of IR spectra (in orange, paragraph 3.2) and of chemical data (in blue, paragraph 3.1), respectively.

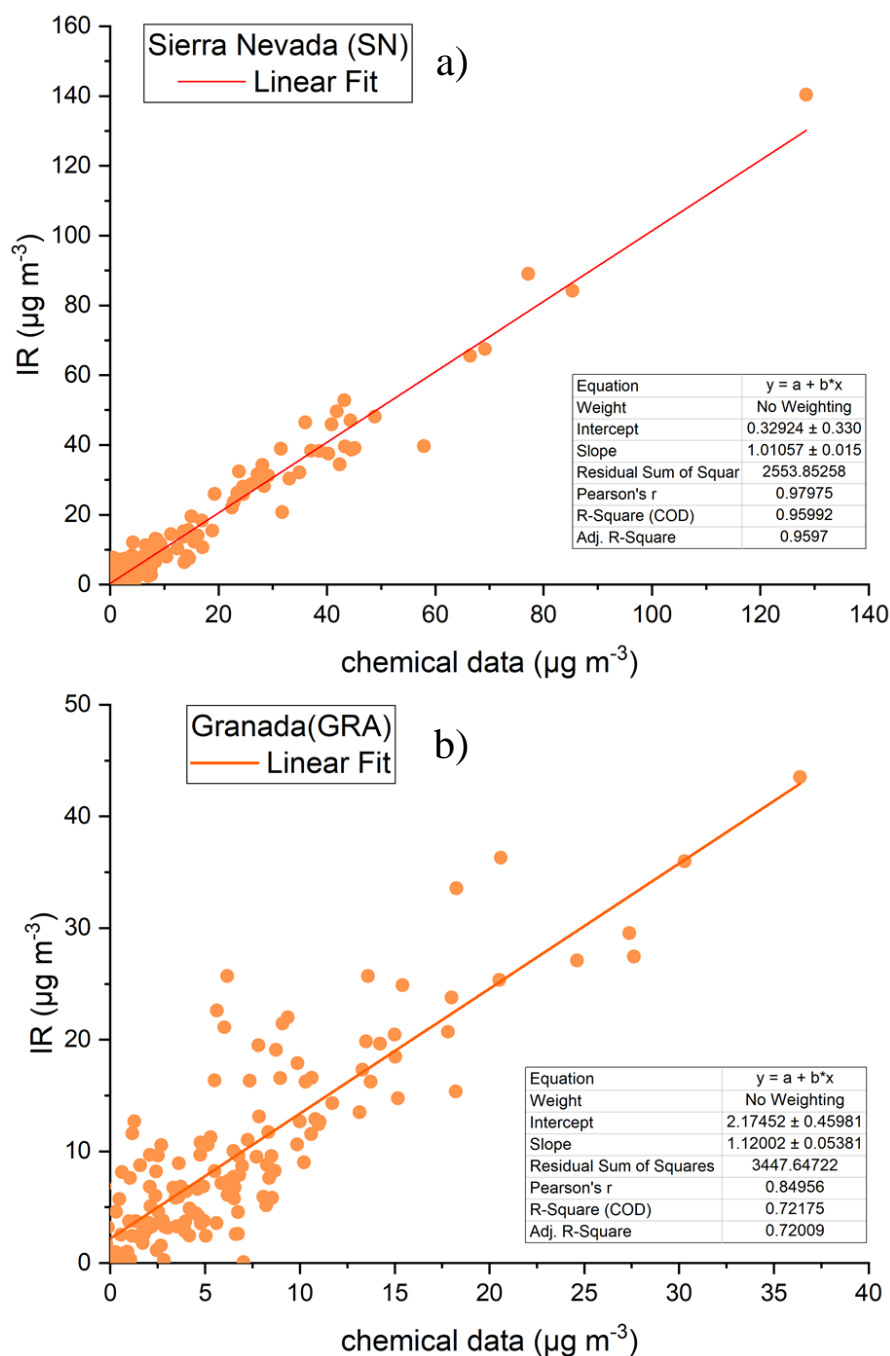


Figure 13. Scatter plot of the Mineral Dust contributions of SN (a) and GRA (b) obtained from the PMF analysis of IR spectra and of chemical data, respectively.

The overlap between the amount of the “traditional” Saharan dust component assessed by chemical speciation and the “innovative” one by FT-IR is quantitatively almost identical for SN filters (whose mineral component is predominant, see paragraph 3.1), with a coefficient of determination (R^2) equal to 0.96. Yet, the overlapping of contributions is acceptable but not (yet) optimal for GRA filters (mineral component less present than the anthropogenic one, see paragraph 3.1), with a R^2 equal to 0.72.

It demonstrates the good ability of IR spectroscopy to correctly quantify the mineral dust source of atmospheric aerosol, even in PM filters in the presence of significant amounts of confounding components.

4 – Conclusions

This Chapter shows how quick and non-destructive metrologies can support and integrate the gold standard analytical approaches in atmospheric aerosol science in spite of the complex spectral signals they produce. This work is still in progress as these results concern exclusively to the 2018 campaign of FRESA project (three-year campaign, from 2017 to 2019), which represent only half of the PM₁₀ filters available. Moreover, as specified in the Introduction, this chapter lacks of all the meteorological and synoptic analyses envisaged by the project and in progress of elaboration, playing a non-negligible role in data elaboration and above all interpretation which cannot be achieved without a suitable dynamic framing.

As regards the Ultraviolet-Visible diffuse reflectance spectroscopy (UV-VIS DRS), a good correlation was observed between the colors of the filters and the Saharan Dust and Biomass Burning source contributions obtained by traditional Positive Matrix Factorization (PMF) analysis. Further studies will need to be done to evaluate possible significant correlations with other colors and emission sources.

Instead, as regards Fourier transform - Infrared spectroscopy (FT-IR), only Saharan dust component of PM has been studied in detail. In fact, actually we have demonstrated how this analytical technique can optimally separate the mineral component from the organic one. However, as regards the latter, further investigations are needed.

References

- Belis, C., Favez, O., Mircea, M., Diapouli, E., Manousakas, M.-I., Vratolis, S., Gilardoni, S., Paglione, M., Močnik, G., Mooibroek, D., Takahama, S., Vecchi, R., Paatero, P., Salvador, P., & Decesari, S. (2019). European guide on air pollution source apportionment with receptor models - Revised version 2019. <https://doi.org/10.2760/439106>
- Boose, Y., Baloh, P., Plötze, M., Ofner, J., Grothe, H., Sierau, B., Lohmann, U., & Kanji, Z. A. (2019). Heterogeneous ice nucleation on dust particles sourced from nine deserts worldwide – Part 2: Deposition nucleation and condensation freezing. *Atmos. Chem. Phys.*, 19(2), 1059–1076. <https://doi.org/10.5194/acp-19-1059-2019>
- Brown, S. G., Eberly, S., Paatero, P., & Norris, G. A. (2015). Methods for estimating uncertainty in PMF solutions: Examples with ambient air and water quality data and guidance on reporting PMF results. *Science of the Total Environment*, 518, 626–635.
- Chiari, M., Yubero, E., Calzolari, G., Lucarelli, F., Crespo, J., Galindo, N., Nicolás, J. F., Giannoni, M., & Nava, S. (2018). Comparison of PIXE and XRF analysis of airborne particulate matter samples collected on Teflon and quartz fibre filters. *Nuclear Instruments and Methods in Physics Research Section B: Beam Interactions with Materials and Atoms*, 417, 128–132. <https://doi.org/https://doi.org/10.1016/j.nimb.2017.07.031>
- Corrigan, A. L., Russell, L. M., Takahama, S., Äijälä, M., Ehn, M., Junninen, H., Rinne, J., Petäjä, T., Kulmala, M., Vogel, A. L., Hoffmann, T., Ebben, C. J., Geiger, F. M., Chhabra, P., Seinfeld, J. H., Worsnop, D. R., Song, W., Auld, J., & Williams, J. (2013). Biogenic and biomass burning organic aerosol in a boreal forest at Hyytiälä, Finland, during HUMPPA-COPEC 2010. *Atmos. Chem. Phys.*, 13(24), 12233–12256. <https://doi.org/10.5194/acp-13-12233-2013>
- EN 12341, Ambient air - Standard gravimetric measurement method for the determination of the PM₁₀ or PM_{2,5} mass concentration of suspended particulate matter (2014);

- EN 16913, Ambient air - standard method for measurement of NO₃, SO₄²⁻, Cl⁻, NH₄⁺, Na⁺, K⁺, Mg²⁺, Ca²⁺ in PM_{2.5} as deposited on filters (2017).
- IE 11664-1-2019. Colorimetry - CIE Standard Colorimetric Observers. Standard, International Organization for Standardization, Geneva, CH;
- IE 11664-2-2020. Colorimetry - Part 2: CIE Standard Illuminants. Standard, International Organization for Standardization, Geneva, CH;
- IE 11664-4-2019. Colorimetry - Part 4: CIE 1976 L*a*b* Colour Space. Standard, International Organization for Standardization, Geneva, CH;
- Kuzmiakova, A., Dillner, A. M., & Takahama, S. (2016). An automated baseline correction protocol for infrared spectra of atmospheric aerosols collected on polytetrafluoroethylene (Teflon) filters. *Atmos. Meas. Tech.*, 9(6), 2615–2631. <https://doi.org/10.5194/amt-9-2615-2016>
- Liu, S., Takahama, S., Russell, L. M., Gilardoni, S., & Baumgardner, D. (2009). Oxygenated organic functional groups and their sources in single and submicron organic particles in MILAGRO 2006 campaign. *Atmospheric Chemistry and Physics*, 9(18), 6849–6863.
- Lucarelli, F., Nava, S., Calzolari, G., Chiari, M., Udusti, R., & Marino, F. (2011). Is PIXE still a useful technique for the analysis of atmospheric aerosols? The LABEC experience. *X-Ray Spectrometry*, 40, 162–167. <https://doi.org/10.1002/xrs.1312>
- Mladenov, N., Pulido-Villena, E., Morales-Baquero, R., Ortega-Retuerta, E., Sommaruga, R., & Reche, I. (2008). Spatiotemporal drivers of dissolved organic matter in high alpine lakes: Role of Saharan dust inputs and bacterial activity. *Journal of Geophysical Research: Biogeosciences*, 113(G2). <https://doi.org/https://doi.org/10.1029/2008JG000699>
- Morales-Baquero, R., Pulido-Villena, E., & Reche, I. (2013). Chemical signature of Saharan dust on dry and wet atmospheric deposition in the south-western Mediterranean region. *Tellus B: Chemical and Physical Meteorology*, 65(1), 18720. <https://doi.org/10.3402/tellusb.v65i0.18720>
- Morozzi, P., Ballarin, B., Arcozzi, S., Brattich, E., Lucarelli, F., Nava, S., Gómez-Cascales, P. J., Orza, J. A. G., & Tositti, L. (2021). Ultraviolet–Visible Diffuse Reflectance Spectroscopy (UV–Vis DRS), a rapid and non-destructive analytical tool for the identification of Saharan dust events in particulate matter filters. *Atmospheric Environment*, 252, 118297. <https://doi.org/https://doi.org/10.1016/j.atmosenv.2021.118297>
- Murtagh, F., & Contreras, P. (2012). Algorithms for hierarchical clustering: an overview. *WIREs Data Mining and Knowledge Discovery*, 2(1), 86–97. <https://doi.org/https://doi.org/10.1002/widm.53>
- Norris, G., Duvall, R., Brown, S., & Bai, S. (2014). EPA Positive Matrix Factorization (PM F) 5.0 Fundamentals and User Guide. www.epa.gov
- Paatero, P., & Tapper, U. (1993). Analysis of different modes of factor analysis as least squares fit problems. *Chemometrics and Intelligent Laboratory Systems*, 18(2), 183–194. [https://doi.org/https://doi.org/10.1016/0169-7439\(93\)80055-M](https://doi.org/https://doi.org/10.1016/0169-7439(93)80055-M)
- Pio, C. A., & Lopes, D. A. (1998). Chlorine loss from marine aerosol in a coastal atmosphere. *Journal of Geophysical Research: Atmospheres*, 103(D19), 25263–25272.
- Raes, F., Dingenen, R. van, Vignati, E., Wilson, J., Putaud, J.-P., Seinfeld, J. H., & Adams, P. (2000). Formation and cycling of aerosols in the global troposphere. *Atmospheric Environment*, 34(25), 4215–4240. [https://doi.org/https://doi.org/10.1016/S1352-2310\(00\)00239-9](https://doi.org/https://doi.org/10.1016/S1352-2310(00)00239-9)
- Reggente, M., Dillner, A. M., & Takahama, S. (2019a). Analysis of functional groups in atmospheric aerosols by infrared spectroscopy: systematic intercomparison of

- calibration methods for US measurement network samples. *Atmos. Meas. Tech.*, 12(4), 2287–2312. <https://doi.org/10.5194/amt-12-2287-2019>
- Reggente, M., Höhn, R., & Takahama, S. (2019b). An open platform for Aerosol InfraRed Spectroscopy analysis – AIRSpec. *Atmos. Meas. Tech.*, 12(4), 2313–2329. <https://doi.org/10.5194/amt-12-2313-2019>
 - Russell, L. M., Takahama, S., Liu, S., Hawkins, L. N., Covert, D. S., Quinn, P. K., & Bates, T. S. (2009). Oxygenated fraction and mass of organic aerosol from direct emission and atmospheric processing measured on the R/V Ronald Brown during TEXAQS/GoMACCS 2006. *Journal of Geophysical Research: Atmospheres*, 114(D7).
 - Senthil Kumar, R., & Rajkumar, P. (2014). Characterization of minerals in air dust particles in the state of Tamilnadu, India through FTIR, XRD and SEM analyses. *Infrared Physics & Technology*, 67, 30–41. <https://doi.org/https://doi.org/10.1016/j.infrared.2014.06.002>
 - Takahama, S., Johnson, A., & Russell, L. M. (2013). Quantification of Carboxylic and Carbonyl Functional Groups in Organic Aerosol Infrared Absorbance Spectra. *Aerosol Science and Technology*, 47(3), 310–325. <https://doi.org/10.1080/02786826.2012.752065>
 - Ward, J.H., Hierarchical groupings to optimize an objective function (1963) *J. Am. Stat. Assoc.*, pp. 234-244;

General Conclusions

This Thesis presents the main published and unpublished scientific results achieved during my 3-years PhD activity. The leitmotif of this Thesis comprises the application of multivariate statistical methods to environmental chemistry and, in particular, to the study of atmospheric aerosols.

Several and multidisciplinary topics have been faced, involving **primarily** the design and optimization of innovative methodologies for the Particulate Matter (PM) analysis and data interpretation, as related to human health and climate change. In this framework, methods of analysis of particulate matter collected on membranes have been developed and applied, such as Microbial DNA extraction from PM₁₀ samples (Chapter 2), Ultraviolet–Visible Diffuse Reflectance Spectroscopy of aerosol mineral and/or anthropogenic components (UV–Vis DRS, Chapter 3 and 11), airborne particulate toxicity testing based on Luminol assay (Chapter 4), and Fourier Transform InfraRed (FT-IR) spectroscopy for qualitative analysis of aerosol components based on functional groups (Chapter 11). It has been demonstrated in this Thesis how these methodologies can successfully increase our knowledge on atmospheric aerosols if connected with golden and traditional analytical techniques and *ad hoc* multivariate statistical techniques. Specifically, these techniques allow to obtain an overall improvement on bioaerosol speciation, emission sources identification, and evaluation of the oxidative potential. The work in progress within the FRESA project (Chapter 11) deserves particular mention as it reveals how non-destructive techniques associated with multivariate statistics can corroborate traditional analysis results on atmospheric aerosol chemistry and source apportionment.

Secondly, the mindful use of particulate matter (PM) low-cost sensors such as optical particle counters (OPCs) may be extremely useful for air quality monitoring and in-depth studies of atmospheric dynamics. For a proper collection and interpretation of OPC data it is essential to follow certain guidelines and recommendations (Chapter 5). Only if this condition is met, it is possible to use authenticated and validated data that can be used for studying peculiar events, e.g an exceptional incursion of Asian mineral dust over Southern Europe in late March 2020 (Chapter 6). Clearly, the data obtained by these low-cost sensors should be accompanied by other methods for a comprehensive investigation, e.g Back-trajectories analysis, weather maps, and remote sensing.

Thirdly, this Thesis presents analysis of other environmental matrices (different from airborne particulate matter) and data interpretation. Example of samples are marine sediments (Chapter 7), soils (Chapter 8), cave drip and river water samples (Chapter 9), and geopolymers (Chapter 10). A wide range of different analytical techniques have been used, such as attenuated total reflection Fourier transform infrared (ATR-FTIR) spectroscopy, Wavelength Dispersive X-Ray Fluorescence (WD-XRF), Gas Chromatography - Mass Spectrometry (GC-MS), Inductively coupled plasma - optical emission spectrometry (ICP-OES), Elemental Analyzer, Ion Chromatography (IC), and High-resolution γ -ray spectrometry. The applications are the most varied, including the quantification of biogenic silica in marine sediments, evaluation of the atmospheric deposition process over the Terni district, characterization of the drip and river waters in the touristic Pertosa-Auletta cave (Italy, SA), and evaluation of radiochemistry and dosimetric indices for health risk assessment of Geopolymers.

Overall, this Thesis demonstrates how the sensible application of basic as well as advanced statistical methods enable to extract tangible and exhaustive environmental and atmospheric evidence.